THE STRUCTURE OF THE EARTH'S MANTLE

FROM BODY WAVE OBSERVATIONS

by

MRINAL KANTI SEN GUPTA

S.M. Massachusetts Institute of Technology,
Cambridge, Mass. U.S.A. (1972)

M.Sc. Indian Institute of Technology,
Kharagpur, India (1969)

SUBMITTED IN

PARTIAL FULFILLMENT

OF THE REQUIREMENTS FOR THE

DEGREE OF DOCTOR OF SCIENCE

at the

MASSACHUSETTS INSTITUTE OF TECHNOLOGY

May, 1975

Signature of Author.....
Department of Earth and Planetary Sciences

Certified by.....
Thesis Supervisor

Accepted by.....
Chairman, Departmental Committee on Graduate Students

MASS. INST. TECH.
SEP 24 1975
LIBRARIES

ABSTRACT

The Structure of the Earth's Mantle From Body Wave Observations

by

Mrinal Kanti Sen Gupta

Submitted to the Department of Earth and Planetary Sciences on May 28, 1975 in partial fulfillment of the requirements for the degree of Doctor of Science

Radial and lateral variation in compressional and shear wave velocities in the earth's mantle are investigated using body wave travel time and amplitude data from deep focus earthquakes. Any significant evidence for radial and lateral inhomogeneities in the earth's deep mantle has been obscured so long by geographical variations of velocity in the earth's crust and upper mantle. In this study, data

from deep focus earthquakes were chosen to remove the effect of near source heterogeneity in the upper mantle. Near-receiver heterogeneity in the upper mantle has been eliminated on the other hand through estimation of station anomaly terms. The impulsive nature of signals, enrichment of short period energy and virtual absence of surface waves in the seismograms of deep focus earthquakes have added to the precision in reading the data. As a result of these merits in deep focus earthquake data, standard deviations of average travel times and station anomalies of this study are about two-fold smaller than those determined from shallow focus earthquakes.

Radial variation in P and S wave velocity were obtained from the average travel times through the technique of first order perturbation (Julian and Anderson, 1968) using the Bl model of Jordan and Anderson (1974) as the starting model. In the scheme of Backus and Gilbert (1970) these one dimensional velocity models were characterized below 1000 km depth by a standard error in velocity of 0.02 km/sec and a half "spread" of 70 km as compared to the layer thickness of 75 km. These models did not show any pronounced velocity reversal at the base of the mantle as suggested by some authors (Cleary, 1974), though a small velocity decrease could not be ruled out either from travel time or amplitude data. Some anomalous rapid changes in

P wave velocity gradient were, however, found centered around 1600 km, 2400 km and 2600 km depth. These anomalies in the velocity gradient were also supported by evidence of $dT/d\Delta$ data. The good fit of the observed amplitudes with the computed geometric spreading factors from these one dimensional velocity models, required further that 'Q' should be increasing with depth in the lower mantle. A possibility of decrease in Q in the lowest 200 km of the mantle is not refuted however.

Based on the evidence of lateral variation in the earth's mantle from the observations of P and S wave travel times, three dimensional models of P and S wave velocities were also constructed for the earth's whole mantle. A method of successive approximation was used for computing relative perturbations to P and S wave velocities of one dimensional models as constants over blocks of size 10° in latitude and longitude and 500 km in depth. Lateral heterogeneity in the earth's mantle seemed to be the most pronounced in the surface layer (0-500 km of depth) and near the core-mantle boundary (2500-3000 km of depth) compared to the middle mantle which was found to be relatively homogeneous. Inverted lateral variation of velocities in the surface layer agreed well with the known knowledge of surface tectonics but lateral variations

in the deep mantle revealed no such relationship with surface tectonics. An extensive region near the core-mantle boundary beneath the central and part of the eastern Pacific was found to have a laterally homogeneous anomaly in the sense that this zone showed small lateral variation in P wave velocity and gravitational potential for up to sixth degree in spherical harmonics and also was characterized by small non-dipole intensity in the earth's magnetic field.

Thesis supervisors:

Prof. M.N. Toksöz
Professor of Geophysics
Department of Earth and Planetary Sciences, M.I.T.

and

Dr. Bruce R. Julian
Staff Scientist, Lincoln Laboratory, M.I.T.
(now at National Earthquake Information Center, U.S.G.S., Golden, Colorado)

Acknowledgement

The inspiration for this work stemmed from the large response of a small publication by Julian and Sengupta (1973). The guidance and encouragement of both Prof. Nafi Toksöz and Dr. Bruce Julian never let this fountain of inspiration dry up amidst adversities but helped to develop it into a stream of thoughts and analyses. So, I owe my sincerest gratitude and the most profound thanks to them as my advisors, as my friends and above all as two of the fair-minded, rare people who make this world beautiful. I must also add that Nafi's comments have substantially improved this manuscript.

For parts of this thesis I benefitted very much from my discussions with Prof. Keiti Aki and Prof. Sean Solomon. Their expertise and suggestions have both clarified some of my thinking and helped to strengthen the scientific arguments. Also, constructive was discussions with Drs. Raul Madariaga and Clint Frasier. Apart from intellectual guidance, there are many an ingredient for completion of a thesis - one of them being 'peace of mind'. In this connection I am indebted to my fellow student, Mr. Raymon Brown and his wife without whose timely help this thesis would not have seen light at all.

I should also acknowledge my gratefulness to the Group 22 personnel of Lincoln Laboratory for allowing me to use their computational and administrative facilities, with a special mention of the programming assistance given by Mr. Peter Neilson and Ms. Leslie Turek.

The last but not the least, my heartfelt thanks are due to Ms. Dorothy Frank who has typed this voluminous manuscript - silently and gladly, diligently and efficiently. More creditable is her patience and intelligence by which she could recover the text in its entirety from my scribblings in the manuscript. Ms. Susan Swim of Group 22 also did me a favor by typing several of the tables at the earlier stage of this manuscript.

The work conducted at Lincoln Laboratory was supported by the U.S. Advanced Research Projects Agency. The research performed at the Department of Earth and Planetary Sciences was supported by the Advanced Research Projects Agency, monitored by the Air Force Office of Scientific Research under contract F44620-71-C-0049.

THEME

"The woods are thick, dark and deep;
And I have miles to go and miles to go before I sleep."

(A modification of Robert Frost's verse)

TABLE OF CONTENTS

ABSTRACT		i
ACKNOWLEDGEMENT		v
THEME		vii
1.	INTRODUCTION AND REVIEW	1
	1.1 WHY?	1
	1.2 STATE OF AFFAIRS IN THE STRUCTURE OF THE EARTH'S MANTLE	2
	1.3 HOW?	11
2.	DATA AND METHOD OF ANALYSIS	16
	Introduction	16
	2.1 THE USEFULNESS OF DEEP FOCUS EARTHQUAKE DATA	17
	2.2 DATA OF THIS STUDY	22
	2.2.1 Reading error in the data	24
	2.3 DETERMINATION OF AVERAGE TRAVEL TIME-DISTANCE CURVE	28
	2.3.1 Absolute travel times vs. differential travel times	28
	2.3.2 Correction due to ellipticity of the earth	31
	2.3.3 Correction for mislocation using an inaccurate travel time curve	32
	2.3.4 Correction for station anomalies	34
	2.4 DETERMINATION OF AVERAGE AMPLITUDE-DISTANCE CURVE	36
	2.4.1 Correction for station anomalies	40

2.5 LIMITATIONS IN THE METHOD 42

2.5.1 Insufficiency of the data 47

Tables 48

Figures 55

3. RADIAL VARIATION OF COMPRESSIONAL AND SHEAR VELOCITIES IN THE MONOPOLE (AVERAGE) EARTH 63

Introduction 63

3.1 "AVERAGE EARTH" MODEL AND AVERAGING THEOREM FOR TRAVEL TIME DATA 64

3.2 "GROSS EARTH" TRAVEL TIME DATA FROM DEEP EARTHQUAKES 65

3.2.1 Characteristic features of deep focus travel time data in relation to those from shallow earthquakes 67

3.2.2 Some anomalous features for deep focus travel time data 70

3.2.3 Baseline difference in deep focus travel time data with respect to other earth models 71

3.3 INVERSION OF DEEP FOCUS TRAVEL TIME DATA TO OBTAIN THE VELOCITY MODELS 76

3.3.1 Choice of radius of the earth's outer core 78

3.3.2 Choice of velocity variation in the upper mantle 80

3.3.3 Determination of P and S velocity variation in the lower mantle and their fit to the observed data 82

3.4 NON-UNIQUENESS IN THE DERIVED VELOCITY MODELS 86

3.4.1 Application of Backus and Gilbert method of resolving kernels to our velocity models 89

3.4.2 Some properties of the averaging kernels and their usefulness related to this study 92

3.4.3 Some properties of the trade-off curves and their usefulness related to this study 95

3.4.4 Summary of resolvability of our P and S velocity models for the lower mantle 97

3.5 COMPARISON OF OUR EARTH MODELS (FOR P AND S VELOCITY VARIATION IN THE LOWER MANTLE) WITH OTHER EARTH MODELS IN LITERATURE 98

3.5.1 Comparison of the shapes of velocity models 99

3.5.2 Comparison of the predicted travel times against the observed travel times 103

3.5.3 Comparison of the predicted $dT/d\Delta$ data against the observed data 106

3.6 SUMMARY AND DISCUSSIONS ON THE SIGNIFICANT FEATURES OF OUR P AND S WAVE VELOCITY MODELS FOR THE LOWER MANTLE 108

3.6.1 Small velocity reversal near the core-mantle boundary 109

3.6.2 Wiggly variation in the velocity gradient 112

Tables 115

Figures 138

4. INVESTIGATION OF ELASTIC AND ANELASTIC PROPERTIES OF THE EARTH'S MANTLE BY USE OF DEEP FOCUS EARTHQUAKE AMPLITUDE DATA 172

Introduction 172

4.1 BODY WAVE AMPLITUDE-DISTANCE DATA FOR DEEP FOCUS EARTHQUAKES 173

4.1.1 Characteristic features of deep focus P wave amplitudes 173

4.1.2 Comparison of deep focus P wave amplitude data with other studies 175

4.1.3 Characteristic features of deep focus S wave amplitudes 178

4.1.4 Comparison of deep focus S wave amplitude data with other works 180

4.2 ON THE COMPUTATION OF THEORETICAL AMPLITUDE-DISTANCE CURVES FOR BODY WAVES 181

4.3 USE OF AMPLITUDE DATA FOR THE VERIFICATION OF SEISMIC VELOCITY PROFILES 185

4.4 WORKING Q(r) MODELS FOR P AND S WAVES 191

4.5 ON THE DETERMINATION OF BODY WAVE MAGNITUDE 196

Tables 201

Figures 219

5. LATERAL VARIATION IN THE STRUCTURE OF THE EARTH'S MANTLE 239

Introduction 239

5.1 EVIDENCE OF LATERAL VARIATION IN THE EARTH'S UPPER MANTLE 240

5.1.1 Station anomalies for deep focus travel time data 241

5.1.1A Interpretation of station anomalies for travel times 244

5.1.2 Station anomalies for amplitudes of P, SV and SH waves 248

5.2 EVIDENCE OF LATERAL VARIATION IN THE DEEP MANTLE 251

5.2.1 Evidence from P wave travel time data 252

5.2.2 Evidence from S wave travel time data 256

5.3 METHOD OF ESTIMATING LATERAL VARIATION OF VELOCITY IN THE EARTH'S MANTLE 259

5.3.1 Inversion procedures and results for laterally heterogeneous earth models 264

5.4 ON THE ASPECT OF MAGNITUDE AND CAUSES OF LATERAL HETEROGENEITY IN THE EARTH'S MANTLE 268

5.5 DESCRIPTION OF THE THREE DIMENSIONAL VELOCITY MODELS 272

5.5.1 Comparison of existing studies of lateral variation in the earth's upper mantle 275

5.5.2 Comparison of other studies of lateral variation in the deep mantle 279

Tables 288

Figures 303

6. CONCLUSIONS 347

REFERENCES 358

APPENDICES 388

APPENDIX A: Relocation of Hypocenters 388

APPENDIX B: Instrument Response Correction for Observed Amplitudes 401

APPENDIX C:	Correction of Amplitudes for the Effect of Reflection and Transmission at the Major Discontinuities of the Earth	405
APPENDIX D:	Determination of SH and SV Amplitudes and Calculation of S polarization angles	414
APPENDIX E:	Determination of the Focal-mechanisms of the Deep Earthquakes Used in the Study and Calculation of the Radiation Correction	418
APPENDIX F:	The Method of Inversion of Travel Time Data in a Spherically Symmetric Earth	440
APPENDIX G:	Backus-Gilbert Method of Calculating the Averaging Kernels and the Trade-off Curves for the Inversion of Travel Time Data in a Spherically Symmetric Earth	446
APPENDIX H:	Reading Errors for the First Arrival Times of P and S Phases	456
APPENDIX I:	Identification of the Seismic Phases	465
APPENDIX J:	The Averaging Theorem for Travel Times	481
APPENDIX K:	The Baseline Correction in the P Wave Travel Times of the Jeffreys-Bullen Tables (1940)	484
APPENDIX L:	Station Anomalies for P and S Wave Travel Times	498
APPENDIX M:	Station Anomalies for P and S wave Amplitudes	512
APPENDIX N:	Three Dimensional Models for P and S Wave Velocities	521
APPENDIX O:	List of Deep Focus Travel Time and Amplitude Data	538
BIOGRAPHICAL NOTES		577

CHAPTER 1

INTRODUCTION AND REVIEW

1.1 WHY?

This study is related to the determination of radial and lateral structure of the mantle with special emphasis on the division of lower mantle or "mesosphere", if we want to be up-to-date. Through the concerted efforts for studies on crust and upper mantle during the Upper Mantle Project (UMP) (Knopoff, 1971), we have learned that the upper mantle is heterogeneous radially and laterally and the present day surface tectonics are controlled to a great extent by processes in the mantle. Especially, it is known today that lateral inhomogeneity holds the key to an understanding of many of the large scale processes in the crust and upper mantle. But at the present time, the problem of the state of the lower mantle and its interaction with the upper mantle has remained largely untouched. Recently in a study of deep focus P wave travel times, Julian and Sengupta (1973) have shown a reliable evidence that large scale lateral heterogeneity may also exist in the lower mantle. This piece of work is an extension to that study using both P and S wave travel time and amplitude data. A complete picture of radial and lateral inhomogeneity in the earth's

whole mantle is important both for its chemical and thermal implications as well as for studying the driving mechanisms for plate motions which are not yet understood.

1.2 STATE OF AFFAIRS IN THE STRUCTURE OF THE EARTH'S MANTLE

Until recently most models of the earth's interior have been based on a concept of spherical symmetry on a global scale or lateral homogeneity on a regional or local scale. Though world-wide features in these one dimensional models may give clues to the state of the earth's interior, such models are undoubtedly over-simplifications. Plate tectonics have confirmed that pronounced lateral heterogeneity exists in the crust and upper mantle up to the depths at which the deepest earthquakes are found (see for example Isacks *et al.*, 1968). At this stage, prospects for constructing a successful three dimensional earth model are brighter than ever (see for example Aki *et al.*, 1974) because a definite pattern in space has been established in the large scale behavior of lateral heterogeneity of the earth's crust and upper mantle. For example, even the crustal structure which varies from one locality to the adjacent locality, reveals a distinct pattern to the scale of oceans and continents. To a more

refined scale, there also emerges a pattern for lateral variation in the crust as shown by Brune (1969) in dividing the earth's crust into nine types like Shield, Basin and Range, Alpine, Deep Ocean Basin and so on in terms of surface wave dispersion, thickness, Pn wave velocity, heat flow, Bouguer anomaly, etc.

In contrast to the crust, inhomogeneities in the earth's upper mantle, radial and lateral, display more distinct patterns which have led to successful exploration on the problem of lateral heterogeneity in the deep mantle. Throughout this study, the upper mantle will be defined to be the region below the well known Mohorovicic discontinuity at 30-40 km depth to a depth of 700 km where ends the so-called "transition zone" (Bullen, 1963, p. 222). This region is earmarked by two world-wide rapid increases in seismic velocity at a depth of around 350-400 km and 650-700 km plus a low velocity-low Q - partially melt zone (which may not be world-wide) between a depth of about 70-250 km (Toksöz et al., 1967; Johnson 1967; Solomon, 1972; Press and Siever, 1974). It is known today that these two discontinuities in velocity gradient correspond to phase changes respectively of olivine to a spinel-type lattice structure and then to post-spinel phases which are

mixtures of (Fe, Mg)O and SiO_2 (stishovite). This latter phase boundary has an additional significance in that downgoing slabs beneath the subduction zone are unable to penetrate this transition region, as a result of which no deep earthquakes are known to occur below a depth of 700 km (see for example, Toksöz et al., 1973). Simpson et al. (1971) indicated the presence of another discontinuity at depth of 280-300 km from measurements of P wave travel time gradients. Strong underside reflections from this discontinuity are also known to cause precursors to the PKPPKP (P'P') phase (Whitcomb and Anderson, 1970). Whitcomb and Anderson accounted further for this discontinuity by the pyroxene-garnet transformation which precedes the olivine-spinel transformation (see for example Ringwood, 1972). Because of lack of observations, this discontinuity at 280-300 km depth may not be a world wide phenomenon.

Lateral heterogeneity in the upper mantle was established even before the plate tectonics came into prominence. Surface wave dispersion data (Aki and Press, 1961; Toksöz et al., 1967; Dziewonski, 1971) and body wave travel times (Bath and Arroyo, 1963; Hales et al., 1970) have long indicated that oceanic upper mantle is slower than continental upper mantle. Low

velocity channels beneath the oceans appear to be better developed in terms of thickness and velocity contrast than those under the shield area of the continents. In the low velocity channel, shield structure may have as much as 10% higher velocity than the corresponding regions in ocean, and lateral variation between these two structures may continue well up to 300 km of depth or more. A correlation has been found between the thickness of these low velocity channels and the absolute motions of the plates (Masse, 1973c) which can explain higher drag on and slower motion of continental plates as compared to their rivals in the ocean (Minster et al., 1974; Solomon and Sleep, 1974; Kaula, 1975). The plate tectonic era in fact accentuated all kinds of studies relating lateral heterogeneity in the upper mantle to the plate-motions and as a result it is now known that pronounced lateral variations also occur near the mid-oceanic ridges where new lithosphere is being created and in the subduction zone where old lithosphere is being consumed. Body wave studies on attenuation of short period Sn phase (Molnar and Oliver, 1969) and long period S wave (Solomon, 1973) as well as fault plane solutions from P wave first motions (Solomon and Julian, 1974) indicate that ridge structure is soft

with 'Q' as low as 10 requiring extensive partial melting in the depth range of about 10-50 km. Surface wave studies have confirmed that lid to low velocity channel is thinner near ridge crest, velocity is smaller at the ridge than the surrounding ocean basin by about 10% or more at depth of about 20 km but levels off gradually with depth extending up to 100 km or more (Weidner, 1974; Leeds et al., 1974). In contrast to ridges, subduction zones are cold with about 5-10% higher seismic velocity (Toksöz et al., 1971; Mitronovas and Isacks, 1971) and about ten times higher Q (Oliver and Isacks, 1967; Isacks and Barazangi, 1973) than average mantle. The high velocity-high Q subduction zone is found to be accompanied also by a thick low velocity-low Q (partially melted) zone on the continental side below the island arcs (Kanamori, 1970; Hatherton, 1970). Between the source and sink, there are also lateral variations in upper mantle beneath a plate. It has been observed (Hart and Press, 1973; Forsyth, 1974) that as ocean floor grows older in a direction from ridge to trench, it has lower and lower temperature, thicker and thicker lithosphere and higher and higher seismic velocity (at least up to a depth of 70-100 km). It is also known from studies of body wave travel times and amplitudes (see for example, Masse et al., 1972,

Masse, 1973a; Yasar and Nuttli, 1974; Helmberger and Engen, 1974), surface wave dispersions (Masse, 1973b; Biswas and Knopoff, 1974) and attenuation measurement (Solomon, 1971) that within the upper mantle beneath the continental North American plate, pronounced lateral variations of the order of 3-4% in P wave velocity and 5-6% in S wave velocity and a variation in Q by a factor of three exist down to about 400 km depth between the region of western North America and the region of Canadian Shield and central and eastern USA. Similar lateral variation in seismic velocity within a continental region also has been found in Australia (Cleary, 1967b) and Africa (Gumper and Pomeroy, 1970). These large scale patterns in lateral variations in the upper mantle <u>within</u> oceanic or continental plate along with small scale anomalous features like extensive volcanism in the Hawaiian Islands or the active seismic zone near New Madrid, Missouri (Turcotte and Oxburgh, 1973; Sykes and Sbar, 1973) may unravel the driving mechanism of plates when we gather knowledge about the state of the lower mantle.

In contrast to the vast wealth of our knowledge about the earth's crust and upper mantle, little is known today, quantitative or qualitative, on the problem

of homogeneity of the lower mantle, especially on the postulates of its radial symmetry. Though in the past, evidence also was given in favor of lateral heterogeneity in deep mantle (see for example, Alexander and Phinney, 1966; Toksöz et al., 1967), it is only recently that data and interpretations are accumulating in growing numbers (see for example, Davies and Sheppard, 1972; Julian and Sengupta, 1973; Niazi, 1973; Jordan and Lynn, 1974; Wright and Lyons, 1975) relating to significant lateral variations of seismic velocity in lower mantle. It has been possible now to take into account the geographical variations in the velocities near the surface which used to obscure the evidence for inhomogeneity in deep mantle. New interpretations of precursors to PKIKP waves (see for example Doornbos and Vlaar, 1973; King et al., 1973; Haddon and Cleary, 1973) in terms of scattering from the deep mantle, have strengthened the evidence for lateral heterogeneity near the core-mantle boundary. A global quantitative picture of these lateral variations in lower mantle has now become necessary more than ever before.

The question of radial variation of seismic velocity in deep mantle also appears to be far from resolved. For example, there is a major conflict in interpretation

of seismic velocity in the lowest 200 km of the mantle. In P wave velocity, for example, one class of models (Ergin, 1967; Buchbinder, 1971; Adam, 1972; Bolt, 1972) suggests pronounced velocity reversals whereas another class of models (Herrin et al., 1968; Richards, 1973, Jordan and Anderson, 1974; Gilbert and Dziewonski, 1974; Dziewonski et al., 1975) shows velocity gradients close to or little higher than critical as given in Jeffreys' model (Jeffreys, 1970, p. 149). Studies on shear wave velocity also present conflicting evidence in this respect. Models of Cleary (1969), Bolt et al. (1970), Randall (1971) and Robinson and Kovach (1972) show a sharp decrease in shear velocity near the core-mantle boundary whereas Mitchell and Helmberger (1973) favor a 20-100 km thick layer of high S wave velocity in this region. There are also suggestion (Press, 1970; Hales and Roberts, 1970; Jordan and Anderson, 1974; Gilbert and Dziewonski, 1974; Dziewonski et al., 1975) that shear velocity varies smoothly down to the core-mantle boundary. Similar disagreements also exist for the Q-model in deep mantle as to whether Q is high (see for example, Archambeau et al., 1969) or low (Teng, 1968; Mikumo and Kurita, 1968).

Evidence of other radial inhomogeneities in the lower mantle have come only through the measurements of

$dT/d\Delta$ because of their sensitivity to velocity gradient. Johnson (1969) pioneered such evidence indicating increased velocity gradient near the depths of 830, 1000, 1230, 1540, 1910 and 2370 km. Several possible phase changes also have been suggested (see for example Ringwood, 1972) corresponding to those discontinuities in velocity gradients. It appears, however, that there are also disagreements as to the nature and depth of these radial inhomogeneities in the lower mantle. For example, measuring $dT/d\Delta$ at the Large Aperture Seismic Array (LASA), Chinnery and Toksöz (1967) found that velocity changes slowly at depths of about 800, 1300 and 2000 km. Subsequently with accumulation of more data, Chinnery (1969) revised the estimates of depth of the first two anomalous regions to 700 and 1150 km but still did not find agreement with the model of Johnson (1969). A comparison of evidence from array $dT/d\Delta$ studies has been given by Wright and Cleary (1972) and Wiggins et al. (1973) for existence of P wave velocity anomalies in the lower mantle. Those comparisons clearly show the regional dependence in the anomalies found from $dT/d\Delta$ data, which may partly be due to the fact that different array measurements of $dT/d\Delta$ have different sensitivity to local crustal-upper mantle structure

whose effect has not been adequately removed (see also Hales and Herrin, 1972). In light of this discussion, we cannot also attach much world-wide significance to the increasing velocity gradient of S wave velocity at the depth of 1550-2100 km as found by Fairborn (1969) from measurement of $dT/d\Delta$ at LASA.

The apparent diverging views concerning the world average structure for lower mantle also call for further investigation. This can be achieved by using a set of data which will remove, as far as possible, the regional dependence as well as reduce the measurement error and other systematic biases to increase the accuracy in the velocity model.

1.3 HOW?

At the present stage of art, it appears that body wave data are the most effective tools to explore the lateral variation in deep mantle. These lateral variations are generally small in percentage; so a three dimensional earth model can be constructed as perturbation to one dimensional model, i.e. the "average earth" in which material property like seismic velocity is assumed to vary only radially. Being better "gross earth data" (Backus and Gilbert, 1968), free oscillation eigenperiods have an

edge here over body wave data for the construction of the one dimensional model. In fact, our present knowledge of shear vleocity in the earth's lower mantle rests heavily on the models derived from free oscillation data for lack of precision in measuring shear wave travel time or $dT/d\Delta$ data. But for reasons, not unequivocal at the present time, there is a pronounced difference in the shear wave velocity models derived from free oscillation data and those from travel time data (see for example Hales, 1974; Jordan and Anderson, 1974; Gilbert and Dziewonski, 1974), which cannot be explained solely in terms of measurement error. In this context, we have preferred to select also the body wave standards for the average earth model to be consistent with our use of body wave data for exploring the lower mantle. Establishment of the precise nature of lateral variation in the upper mantle (see previous section) has made us aware of the different biases one needs to take into account in construction of a body wave 'average earth' velocity model. Unfortunately all major studies relating to the experimental determination of travel time curves for the average earth model have not so far properly taken into account the bias due to near source heterogeneity in the upper mantle (see Hales and Herrin,

1972). Such source bias is particularly severe for shallow earthquakes at island arcs (see for example Cleary, 1967c, Davies and McKenzie, 1969; Toksöz et al., 1971).

In this present study, the average earth model of P and S wave velocity and their relative perturbations over a block size of 10° in latitude and longitude and 500 km in depth have been determined from an analysis of travel time and amplitude data from deep focus earthquakes for which source bias may be less severe than shallow events (see also Chap. 2). Use of the first arrival travel time data are, however, not suitable to detect the small but rapid increase in velocity gradient at the lower mantle but $dT/d\Delta$ data also cannot achieve this goal at the present stage of resolution as mentioned earlier.

With this introduction to our study, we show in detail in the next chapter how we separated the effect of the path through the lower mantle from the observed travel time and amplitude anomaly for the whole ray path and what kind of assumptions we needed for such separation. We point out in particular the advantages and disadvantages one has to face in using deep focus earthquake data in this respect.

The third chapter has been devoted to discussing our one dimensional velocity models - how we obtained them from the observed travel times, what the features are and what quantitative measure we can attach to their reliability. We point out in particular the measure of success one gains by using data from deep focus earthquakes instead of shallow focus earthquakes for experimental determination of travel time curves.

In the fourth chapter, we describe the analysis of amplitude data to test the features of our one dimensional velocity model and to estimate 'Q' for the lower mantle. We also present our version of amplitude-distance curves and station anomalies for both short period (1-2 second) and long period (10-12 second) P wave amplitudes and mention their effect on body wave magnitude determination.

The fifth chapter marks the 'goal' of this study. There we present first the estimates and reliability of corrections to the travel time and amplitude anomaly for the lateral variations in the upper mantle. Then we extract the evidence based on P and S wave travel time anomalies in support of lateral inhomogeneity in the deep mantle. In the second part, we describe a method of inversion for a three dimensional velocity model and the result of inversion when applied to our P and S

wave travel time data. From these inversions, we draw 'quantitative' conclusions on the nature of lateral variation of velocity in the earth's mantle.

In the sixth and final chapter we summarize our major conclusions and mention some possible direction of future work.

A tip to the faithful reader

Before you pore over this thesis and get electrified by some unwanted/unsatisfactory results here and there, just remember the following famous quotation from the prime Hindu philosophy book, called Bhagavat-Gita (i.e. The Gospel):

> "Your right is to work only, not to the fruit thereof."

and you will be saved.

CHAPTER 2

DATA AND METHOD OF ANALYSIS

Introduction

Our aim is to determine the path effect through the earth's lower mantle (depth ≃ 700-3000 km) using the body wave observations of travel times and amplitudes. Success in such efforts lies in effectively removing the source and receiver effects from the observed data. The problem is more complicated because of the unknown positions of the hypocenters. Source, path, and receiver effects often jointly mislocate these hypocenters. To avoid the problem of mislocation of hypocenters, it may be tempting to use the data from explosions whose origin times and locations are known precisely. Heterogeneity in the upper mantle (see Chap. 1, section 1.2) and a severe limitation in the geographic distribution of the large explosions, however, reduce the merit of explosion data for determining the path effect through the earth's lower mantle. We will show in this chapter that the data from deep earthquakes, on the other hand, may be very useful in this respect.

The body wave path effect through the earth's lower mantle is best described by radial and lateral variation in velocity. In our method, observed travel times and amplitude data were fitted first to radial variation of velocity and the remaining residuals to lateral variation. In other words, we have implicitly assumed that the

possibility of radial inhomogeneity, if any, is more likely than lateral heterogeneity in the earth's interior which is already marked with a pronounced variation in the radial structure by the presence of the light crust and heavy core. The idea of lateral inhomogeneity in the lower mantle has been invoked only at the last stage when radial heterogeneity alone could not satisfy the observed data.

In this chapter, we will mainly concentrate on the determination of radial variation of velocity in the lower mantle. Determination of lateral variation in velocity will be discussed in more detail in Chap. 5.

2.1 THE USEFULNESS OF DEEP FOCUS EARTHQUAKE DATA

For our study on the structure of the lower mantle, we found that deep earthquakes are more useful than shallow earthquakes for the following reasons:

1) The quality of the signals from deep events for any body wave phase is better than that of shallow events. This is illustrated in Fig. 2-1 where the body wave signals from two shallow events (depths = 33 and 65 km) at the Tonga Arc are compared with those from a 627 km deep earthquake occurring in the same region and having the same body wave magnitude of 5.9. The longer periods and relatively poor onsets seem to be the characteristics of the signals for the shallow events as compared to those from the deep event. The difference in quality has been remarkably pronounced for the

signals of short period S waves which were not observed at all for the shallowest event and were recorded with highly attenuated amplitude for the 65 km deep event. On the other hand the deep event recorded distinctly both the short period S and SKS signals. The shallowest event did not record also the SKS phase even on the long period records.

The radiation pattern at the source does not appear to explain the high attenuation of both P and S wave signals from the shallow earthquakes (cf. Fig. E-3 in Appendix E). Significantly, fault plane solutions given by Isacks et al. (1969) also show that the projection of station ALQ on the focal sphere of the 65 km deep earthquake appears to lie further from the P wave nodal plane than that for the deep earthquake. The poor quality, in general, of the observed P and S wave signals from shallow earthquakes seems to be primarily due to high attenuation along the ray path through the upper mantle in tectonic regions. Some shallow earthquakes like those occurring in the middle of plates, however, show enrichment in short period energy of body wave phases (Sykes and Sbar, 1973).

Sharp onsets, virtual absence of surface waves, and higher signal to noise (S/N) ratios for deep events are very helpful to read the arrival times of different body wave phases. For example, shear wave arrival times from shallow earthquakes could not be read better than a precision of 2-3 seconds from the long period seismograms. On the other hand, precision

in reading the arrival time data of shear waves from deep events is about one second (see Appendix H). Moreover, the short period records of shear waves from deep events (see Fig. 2-2) helped to enrich our collection of good quality arrival time data. In fact, our travel time analysis for S waves was made with 207 short period S data along with 327 long period data.

2) Not only the arrival time data, but also amplitudes, could be measured more accurately from the records of deep focus earthquakes than from those of shallow events. Moreover, the recorded amplitudes of the first motions of deep events can be related proportionally to the integrated displacement of the ground motion since the peak frequency of signals is generally high compared to the peak frequency of seismographs (long period). This correspondence relationship between the recorded first motion amplitudes and the ground motion amplitudes does not in general hold good for shallow focus earthquakes. Signals of shallow focus earthquakes often do not act as an impulse to the instrument and thus the recorded wave form of the signal may be quite different from that of ground motion.

3) The fact that the signals from deep focus earthquakes have been relatively less biased by the near source heterogeneity in the upper mantle as compared to the signals

from shallow focus earthquakes has other significant effects apart from reducing reading error. The effect of near source heterogeneity is possibly the most crucial factor for biasing the travel time, amplitude data and mislocating the hypocenters. This source bias is particularly severe for shallow focus earthquakes on island arcs. For example, it is known that P wave travel times from shallow focus earthquakes on the Tonga or Aleutian arcs are shorter than normal mantle travel times by about 2-4 seconds (Davies and McKenzie, 1969; Toksöz, Minear and and Julian, 1971). Amplitudes also were found to be affected by focusing, defocusing and the multipathing effect by the strong heterogeneity under island arcs (Davies and Julian, 1972; Sleep, 1973).

The heterogeneity at the island arcs is primarily caused by the downgoing lithospheric slabs which are colder and thereby have higher velocity compared to the surrounding mantle (see for example, Sleep, 1973). Figure 2-3 shows the theoretical temperature distribution and corresponding P wave velocity in a typical downgoing slab at island arcs as reproduced from Fig. 2 of Sleep's paper. It is at once seen from these figures that for the downgoing slab that has penetrated down to a depth of about 700 km, the velocity anomaly inside the slab disappears

below about 600 km. At a depth around 500 km, the velocity inside the slab is higher by about 5% compared to the surrounding mantle and this velocity contrast reaches a maximum of about 15% at a depth of about 300 km. Such a velocity anomaly, no doubt, can cause a severe source bias to the data from shallow events.

It has been hypothesized by many workers (see for example Toksöz, Sleep and Smith, 1974) that intermediate and deep events at island arcs originate within the coldest part of the slab mainly because of the gravity stress induced by the temperature anomaly. From the above discussion it transpires that if earthquakes are so chosen that they are among the deepest ones from a specific island arc, it may be safe to assume that the travel time data and amplitude data will be largely uncontaminated by the slab (see also section 2.5 in this chapter). Moreover, the choice of deep focus earthquakes also eliminates the possibility of biasing by the variation in thickness and velocity contrast in the low velocity channel beneath the island arcs (Kanamori, 1970).

4) Variation in the crust and upper mantle structure from one station to another can be corrected more reliably for deep focus earthquake data than for the data of shallow focus earthquakes. Deep focus earthquakes have only a one

way ray path through the upper mantle, unlike the shallow focus earthquakes for which rays have to go twice through the upper mantle, once beneath the source and once beneath the receiver. Due to this geometry of the rays, separation of receiver effect from the observed travel times and amplitudes is likely to be more effective for deep earthquake data than shallow earthquake data.

In the next three chapters, we will show quantitatively how these four qualities of deep focus earthquake data have resulted in an improvement over the shallow focus earthquake data for experimental determination of travel times and amplitudes of body waves. We like to stress that such improvements are particularly necessary for shear waves whose travel times and amplitudes are not known today to a satisfactory accuracy not because of "instrumentation" but because of lack of good quality data and the presence of strong near source heterogeneities. These two errors have plagued S wave studies more than P wave studies.

2.2 DATA OF THIS STUDY

In our work we have chosen the deepest possible earthquakes in different Benioff zones throughout the world, particularly the ones which extend beyond 450 km depth. We purposely deleted the data from shallower Benioff zones

to avoid the problem of "unification" of data for different depths of focii (see section 2.5) and also to avoid as much as possible the effect of upper mantle heterogeneity. On the other hand we faced the problem of limited distribution of very deep Benioff zones. In order to increase the distribution of sources and receivers on the surface of the earth, we made two exceptions by choosing two intermediate focus earthquakes - one at Hindukush and the other at Greece. We should point out here that we could not always choose the deepest earthquakes in a Benioff zone because of magnitude limitations. We have chosen a body wave magitude threshold of 5.0, and with this threshold of magnitude, the selected earthquakes are possibly the deepest in the respective Benioff zones. The locations of these 14 selected deep earthquakes have been listed in Table 2-1 and are shown on the world map in Fig. 2-4. The corresponding station distribution on the earth's surface is shown in Fig. 2-5.

For each selected earthquake, we collected 70 mm film chips of records from all stations of the World Wide Standard Seismograph Network (WWSSN) and read the seismograms in the epicentral distance range of 30°-100°. To avoid the effect of upper mantle heterogeneity, we chose 30° to be the lower margin of the epicentral distance range of our study whereas the upper limit of 100° was necessitated

by the shadow zone of the velocity discontinuity at the core-mantle boundary. In this range of epicentral distances, we tried to pick all clear arrivals of body wave phases from all three (vertical, north-south, and east-west) components of short period and long period seismograms at each station. The major effort to pick arrival times and amplitudes was concentrated on for phases like P, S, PcP and ScS including depth phases pP and sP. All measurements were taken on the projection screen of an ITEK machine. Optical distortion was avoided largely by taking the measurement on the same spot of the screen.

2.2.1 Reading error in the data

Estimates of the reading error are very important in our analysis as the significance of the determination of path effect and receiver effect has to be tested against these estimates of the reading error. The reading error in the data arises from two sources - first from the uncertainty of time and amplitude picks and the second from the problems of identifying the phases. These two parts of the reading error have been discussed separately in the following paragraphs. We must mention here that though the objectivity of the process of measuring times and amplitudes and identifying phases has been enhanced in recent times through improved instrumentation and

revised travel time charts, the entire process is still a subjective procedure.

In Appendix H, we made an estimation of reading error for first arrival times of P and S waves. From those estimates, we would conclude that first arrival times of P waves could be measured more reliably than those of S waves (or other phases) as expected. A generous estimate of error in measuring P wave first arrival times from short period records is of the order of ±0.3 seconds and could not be more than ±0.5 seconds for long period readings. For S and ScS phases, the reading error is larger and is of the order of ±0.5 seconds for short period readings and about ±1 second for long period recordings. The reading errors of arrival times for other pahses like PcP, pP and sP fall between ±0.3 and ±1.0 second. Also note that our calculation of signal front delay (Papoulis, 1962, p. 134) for WWSSN short period and long period seismographs (Appendix H) shows that there should be no systematic difference between the short period readings and the long period readings. We found this conclusion to be true from our observations.

Amplitude measurements are generally less reliable than arrival time measurements. In section 2.1, we already mentioned that the first motion amplitudes from

deep events should be proportional to the ground motion amplitudes. For this reason, we have consistently measured the first peak to peak amplitude of the signal; in rare cases the second peak to peak amplitude was measured only because amplitude of the first peak was about 5 times (or more) smaller than that of the second peak. In order to reduce the reading error, we have preferred to measure peak to peak amplitude rather than the amplitude (zero to peak) of the signal itself. Our measurement was halved to obtain the actual amplitude. We would generously estimate that long period peak to peak amplitudes have been measured, possibly within a factor of $\sqrt{2}$ and the short period ones within a factor of 2 (two).

Of all the measurements, the measurements of periods are probably the most crude. We measured the time difference between the zero crossing of the first peak to peak trace and the onset of the signal. This measurement was doubled to get the full period. Unlike the amplitude measurement, period measurements from short period records are better compared to those from long period records.

The second part of the reading error concerns us with misidentification of phases associated with a particular signal. To avoid misidentification, redundant information is generally sought whenever necessary. A qualitative

study of the amplitudes on all six components of the seismograms along with the travel time charts prepared by Gutenberg and Richter (1936) have sufficed (see Appendix I) to identify the corresponding phases of almost all the prominent signals. Allowance of ±5-10 seconds was given for the travel times predicted from the reference charts. We must stress here that in our analysis, we have used only the data from those signals for which we could identify the phases confidently and mark the onset times clearly.

Our own readings of the seismograms have provided finally 414 short period (SP) and 213 long period (LP) P wave data of arrival times and amplitudes, 207 SP and 327 LP data for S wave, 44 SP and 43 LP data for ScS phase and 13 SP and 11 LP data for PcP phase. In addition, we had at least five first arrival data of depth phases (pP and/or sP) for each event. In order to enhance the path distribution (see next section) we have added to this dataset about 1200 more data of P wave first arrival times of the selected 14 earthquakes as recorded by all available stations throughout the world (Fig. 2-5). These data were chosen from the times reported in the bulletins of ISC and USCGS/NOAA (see Appendix K for selection procedure).

2.3 DETERMINATION OF AVERAGE TRAVEL TIME-DISTANCE CURVE

To determine radial variation in velocity for a spherically symmetric earth, one must first determine the average travel time-distance curve for a particular focal depth (see Chap. 3, section 3.1). These average travel time-distance curves could be biased by the errors introduced through mislocation of events, incorrect identification of arrival times, effect of lateral heterogeneity, inadequacies of ray theory, etc. Most of the systematic errors in the average travel time distance curve however, can be corrected in two ways - either using absolute travel times of a single phase (e.g. Tucker et al., 1968) or using differential travel times of two suitable phases (e.g. Jordan, 1973).

2.3.1 Absolute travel times vs. differential travel times

In order to use absolute travel times for determining the average travel time-distance curve, the various systematic errors must be estimated individually to correct the absolute times. These systematic errors include the effect of lateral variation of velocity beneath the sources and receivers, use of inaccurate travel time tables for location of hypocenters and error due to ellipticity of the earth. It is, in fact, a laborious linearization-iteration process (see for example Tucker et al., 1968)

where these errors are estimated from a given set of computed hypocenters and then those hypocenters are recomputed after taking into account the estimated biases through linearization. Convergence for this method can always be checked during the process of iteration. Because of the non-linear relationship between the correction of travel times and the changes in hypocenters, the solution in general is non-unique. If, however, different sets of data are seen to produce similar estimates of the systematic errors, we could rely upon those estimates for correction of absolute times.

The second way of removing systematic errors in the average travel times is to use differential travel times instead of absolute travel times. A differential travel time is the difference between the absolute times of two different phases. These phases ought to be so chosen that the systematic errors in the absolute times of two phases are almost the same, so their difference is an unbiased quantity. Two commonly used types of differential times are PcP-P and ScS-S times. It is true (Jordan, 1973) that error in location or lateral heterogeneity in the upper mantle will affect those differential travel times considerably less than the absolute times of corresponding individual phases. These facts tend to support the idea

that the average travel time-distance curve (or radial variation in velocity) could be better determined from differential times rather than from absolute times. Our ultimate goal however, is also to find the travel time anomalies associated with different ray paths, so that we can make our conclusions about the lateral heterogeneity in the deep mantle. But reducing the differential travel time anomalies to path anomalies is difficult and ambiguous as there are two different ray paths to consider. Jordan and Lynn (1974), for example, tried to reduce the differential travel time anomalies of ScS-S to path anomalies associated separately with S and ScS rays. In doing so, they found the correlation between ScS-S travel time anomalies against the absolute travel time anomalies of S and ScS. A better correlation of ScS-S anomalies was observed with S anomalies and they interpreted that all differential travel time anomalies of ScS-S originated along the ray paths of the S wave. This ingenious method of interpretation, however, is liable to face two objections. First, in the presence of the systematic errors in the absolute travel time anomalies of S, it is not clear how reliable is the correlation of ScS-S residuals with S residuals. Second, it is unreasonable to assume that ray paths associated with ScS will be always free from any anomaly. If there are in fact anomalies along ray paths

of both S and ScS, the above method of interpretation will fail. For these two reasons, it might be preferable to use absolute travel times instead of differential travel times to study the lateral heterogeneity in the deep mantle. Also, we should note that our samples of ScS and PcP travel time data are few and far between compared to S and P wave data. So we had almost no option for using the differential travel time data, even for determining the radial variation of velocity.

Instead of using absolute travel times, we have however used in practice travel time residuals from a reference model. The advantage of using travel time residuals is the resolution in the feature of the travel time-distance curve. In this study we have used Jeffreys' model (or equivalently Jeffreys-Bullen times, 1940) as the reference model for P/PcP travel times and a proper combination of US26 model (Anderson and Julian, 1969) and Gutenberg's S velocity model for S/ScS travel times.

2.3.2 Correction due to ellipticity of the earth

Corrections to the travel times for the ellipticity of the earth are in general higher than the reading error and must be taken into account. In fact, for our data, the maximum correction for this source of error was found to be ±1 second for P and PcP travel time data and ±2 seconds

for S and ScS travel time data. These corrections were evaluated from the tables prepared by Bullen (1937a,b; 1938a) for surface focus events. Changes in those tables were found to be insignificant for deep focus earthquakes (Bullen, 1938b) or in light of recent earth models (Bullen and Haddon, 1973).

2.3.3 Correction for mislocation using an inaccurate travel time curve

To locate a hypocenter from teleseismic data, one generally makes use of the existing P wave travel time tables (see Appendix A for details) and thus can run into mislocation if the travel time curves are inaccurate. The corrections to these travel time curves can be divided into two parts - one is the correction to the shape of the curve and the other to the base line value of this curve. Sengupta (1972) evaluated these two parts of correction for the Jeffreys-Bullen (J-B) tables (1940) of P wave for focal depth of 550 km (see Appendix K for details). Correction to the shape of J-B times was determined within ±0.2-0.3 seconds whereas baseline correction was uncertain by as much as ±1 second. For relocation of 14 deep earthquakes of this study, we utilized the correction to the shape of J-B times but omitted the baseline correction because of its uncertainty.

So, listed origin times (Table 2-1) are supposedly earlier than actual by about 1.3±1.0 second corresponding to the determination of base line error in J-B times. To remove network bias in relocation, P wave travel times were also corrected for lateral variation of velocity beneath the stations or "station anomalies" as determined previously by Sengupta (1972) (see Appendix K). In addition, depths were constrained to the values obtained from depth phases.

Bulletin parameters and relocated parameters (Table 2-1) show on the average a difference of ±10 km in depth, ±0.05° (±5 km) in latitude and ±0.1° (±10 km) in longitude. On the basis of computed standard deviation in the relocation parameters, the reliability of these hypocenters is such that on the average, origin times were determined within ±0.2 seconds (barring a d.c. error of approximately -1.3 seconds), depths of focii within ±15 km and epicenter latitudes and longitudes within ±5 km. Such small errors in the computed hypocenters may sound illusive but Mitronovas and Isacks (1971) obtained a similar result after an extensive study on the reliability of location parameters of deep focus earthquakes at the Tonga Arc.

Apart from the d.c. errors in origin times of the events, other estimated errors in the hypocenters do have little effect on the calculated travel times. Table 2-2

lists the values of $\partial T/\partial \Delta$ and $\partial T/\partial h$ related to this problem. It is at once seen that epicentral mislocation will cause a maximum error of only about ±0.8 seconds for S wave travel times at distance of 30°. For P wave, the error will be half this value. On the other hand, constancy of $\partial T/\partial h$ over the entire distance range suggests that error in depth determination affects the calculated travel times mostly in their baselines and those errors are likely to be compensated to a great extent by corresponding d.c. error in the origin times. At any rate, any appreciable error in locating the hypocenters will affect the calculation of P and S travel times more at small distances (say, at less than 60°) than at large distances such as beyond 70°.

2.3.4 Corrections for station anomalies

These corrections arise due to the fact that all receivers are not situated over identical structure of the earth - some of them may be located over geologic structure with higher velocity than that of the average earth model whereas others may be situated at places where velocity is lower than the average. Examples of the first kind are the stations on the Canadian Shield and central and eastern parts of the U.S. whereas the stations in the Basin and Range province fall under the second category.

Theoretically, each ray towards a station should have different station anomaly values depending on the angle and direction of approach. Because of limited quantity in data, such an evaluation of station anomalies is not feasible. Instead, we averaged the travel time residuals at a station to obtain an estimate of station anomaly. This station anomaly can be thought to be due to a statistical average of the velocity anomalies (from the average earth model) beneath the stations as sampled by our data. The error due to ignoring azimuthal variation in velocity anomaly has been estimated to be a very small fraction of the average value of residuals at the station (see section 2.5 in this chapter).

For P waves, Sengupta (1972) evaluated the station anomalies in the above way from a very large set of P wave travel time data (see Appendix K for details). Those station anomalies, (listed under Appendix L) were used in this study to correct for P and PcP travel times. For S waves, station anomalies also were obtained in the similar fashion from an average of S, ScS and SKS travel times residuals at a station. Those residuals were computed from US26 (Anderson and Julian, 1969) model plus Gutenberg's S velocity model (Press, 1966) after using the same hypocenters as determined from P wave data.

Prior to the evaluation of S wave station anomalies, corrections were made to the travel time residuals for the errors in the starting S wave velocity model. In this respect also, we have followed the same approach as for P wave travel time residuals (Appendix K). Reliability and interpretation of the P and S wave station anomalies will be discussed in detail in Chap. 5 with regard to lateral variation in the upper mantle.

Once we have relocated the deep focus earthquakes using the correct travel time curves and made corrections to the observed travel times for the ellipticity of the earth and station anomalies, we have practically eliminated almost all possibilities of systematic errors (except for lateral heterogeneity in deep mantle) in the absolute travel times of respective phases. Using these data one can then determine the average travel time-distance curve for inversion of radial variation of velocity. This part of the topic will be discussed in detail in Chap. 3.

2.4 DETERMINATION OF AVERAGE AMPLITUDE-DISTANCE CURVE

For the same reasons as travel time data, one must remove all systematic errors in the observed body wave amplitudes prior to the determination of the average amplitude-

distance curve corresponding to radial variation in elastic and anelastic properties of the earth. The corrections for amplitude data are more in number as compared to the travel time data and also more complicated for evaluation. These corrections are mostly frequency dependent. Some frequency independent corrections we did consider were the correction for the radiation pattern at the source (in the framework of double-couple point source) and the effect of reflection/transmission at major discontinuities of the earth's upper mantle. Among the frequency dependent corrections were the correction for instrument response, correction for station anomaly and correction for source spectrum. For the sake of convenience, we analyzed only the amplitudes of P and S waves. All the correction factors were determined in the same way for P amplitudes and SV and SH components of S amplitudes. The derivation of SV and SH amplitudes from measurements of S amplitudes has been discussed separately in Appendix D.

Among all the corrections for amplitudes, the first and foremost is possibly the correction due to instrument response in order to obtain actual ground displacement from the measurement of amplitude on the record. All WWSSN stations have identical instrument response, so the instrument response correction at the period of observed amplitude was computed using a general calibration curve

for these instruments (see Appendix B).

To analyze the body wave amplitudes corresponding to the structure in the lower mantle, one should eliminate also the anomalous effects of the upper mantle as far as possible from the observed data. Therefore we have corrected our amplitudes (see Appendix C for details) for the effect of reflection/transmission at the three major sharp discontinuities of the crust and upper mantle - free surface, Moho and 650 km discontinuity (Whitcomb, 1973). Such corrections also were needed to compute correctly S wave polarization angles which were used to determine fault plane solutions.

An important systematic correction to amplitudes (in terms of magnitude) is the correction for the azimuth dependent radiation pattern at the source. We have determined such corrections in light of double couple point source theory. Nodal planes in this connection were determined from both P and S wave first motion data (see Appendix E for details). Parameters of these nodal planes for 14 deep earthquakes have been listed in Table 2-3. As a number of nodal planes could not be constrained very well, we deleted all data requiring large radiation correction. In fact, all amplitude data requiring more than a factor of 3.0 as radiation correction

were deleted. Thus 34% of P and 24% SV amplitude data were rejected from our final analysis. For SH amplitudes, we had to raise the threshold from 3.0 to 5.0, in order to keep a reasonable number of data in the analysis.

Apart from correction due to azimuth dependent radiation pattern at the source, we need to consider also the frequency dependent radiation pattern at the source. It is known that far field displacement spectra from a seismic source have a corner (or peak) frequency (see for example Aki, 1972). Below the corner frequency, displacement spectrum is flat and is proportional to the seismic moment. Above the corner frequency, displacement spectrum decays following one or more power laws. A study of Wyss and Molnar (1972) shows that P and S wave corner periods for deep focus earthquakes at the Tonga Arc lie roughly in the range of 3.0-5.0 seconds. So, short period amplitudes (period <3 seconds) are likely to be lower than those at longer periods (period >5 seconds). Source equalization then beomces important for the analysis of amplitudes where it is necessary to treat short period and long period data separately in order to detect any period dependence of path or station anomalies. It is generally observed that frequency range is small for P and S first motion signals recorded either on short period or long period seismograms. Hence, source-equalization of the short period and long period amplitudes of a single

event were obtained merely by multiplying the observed short period amplitudes by a normalizing factor. This factor was computed by averaging the ratios of long period to short period amplitudes for that event as recorded by different stations. Note that this procedure of source-equalization is independent of corner period for the event. Amplitude equalization with respect to size of events was done prior to the process of source spectrum equalization by reducing the average level of long period amplitudes of each event to a standard value. This standard value was chosen to be the average of all long period amplitudes from all 14 events. In case corner periods of these 14 events lie between the periods observed on short period and long period seismograms, the chosen standard value will correspond to the average moment of those events.

2.4.1 Correction for station anomalies

For correction of station anomalies, we have used $\log_{10}$ amplitude data instead of their absolute values. If 'A' is the observed amplitude (in microns), corrected for the sources of errors described in the previous section, and 'C' is the correction factor to this observed amplitude for station anomaly, then amplitude corrected for station anomaly, 'A_C', can be represented by the following relation:

$$A_C = A.C \tag{2.1}$$

or
$$\log_{10}A_C = \log_{10}A + \log_{10}C \tag{2.2}$$

Note that this expression (2.2) is analogous to the station anomaly correction for travel time data. So, we evaluatedsimilarly the station anomalies for amplitude data from an average of amplitude residuals at a station. With direct analogy to the travel time residuals, the amplitude residual, R_A was defined by:

$$R_A = \log_{10}A - \log_{10}A_{\overline{E}} \tag{2.3}$$

where $A_{\overline{E}}$ is the amplitude for the average earth. The values of $\log_{10}A_{\overline{E}}$ were obtained by fitting a smooth curve through the average of $\log_{10}A$'s in 2° cells of distance.

With the evaluation of these major systematic errors in the observed amplitude data, it is possible now to determine an unbiased amplitude-distance curve. Construction and analysis of this amplitude-distance curve with respect to radial variation of velocity and Q in the lower mantle will be discussed in detail in Chap. 4. Station anomalies of the amplitude data will be taken up separately in Chap. 5 with regard to lateral variation in the upper mantle.

2.5 LIMITATIONS IN THE METHOD

Our method, as it has been emphasized in the beginning of this chapter concentrates on constructing average travel time-distance and amplitude-distance curves appropriate for the lower mantle velocity (and Q) model. Limitations in this method arise then mainly from our inability to take into account the effect of source anomaly, azimuth dependent station anomaly and source dimensions and rupture propagation (for the amplitude data). The effect of these factors has been evaluated as shown in Table 2-4 for P wave data under various assumptions. For S wave data, estimated errors will be two to four fold higher than those shown on the table. The basis of computing these errors deserves some discussion:

a) Source anomaly: as already mentioned in Section 2.1 that P wave velocity inside a typical 'long slab' (Fig. 2-3) is about 5% higher than the surrounding mantle at a depth of 500 km. This velocity anomaly gradually decreases downward and ultimately vanishes at about 600 km. 50-100 km long ray paths through the lowermost part of the slab, as appropriate for deep focus earthquake data, will experience an average velocity anomaly on the order of 2% which will in turn cause a travel time anomaly only on the order of -0.2 to -0.3 seconds. It is of utmost difficulty to obtain

any observational support for this estimate of source anomaly as it lies hidden behind the mislocation of hypocenters. A plot of travel time residuals on the focal spheres of 14 deep events (see Appendix A) has failed to reveal characteristically large residuals which are taken as evidence of source anomalies for shallow earthquakes at island arcs (see for example Toksöz et al., 1974). So, source anomalies, if present at all on deep focus travel time data, can safely be ignored.

The velocity anomaly inside the slab causes focusing, defocussing and multipathing effect on rays (see for example, Ward, 1971, Davies and Julian, 1972). Their effect on teleseismic amplitudes cannot be evaluated from ray theory, but observations of amplitudes from intermediate earthquakes in Tonga, Kermadec and Kuril slab by Sleep (1973) indicate that amplitude anomaly due to velocity heterogeneity around deep focus sources would be small.

The downgoing slab also has about ten-times higher Q than the surrounding mantle (Oliver and Isacks, 1967). But for 50-100 km long ray path in the lowermost part of the slab, the effect of this lateral heterogeneity in Q is shown in Table 2-4 to be small even for $\log_{10}$ amplitude data of short period.

b) Azimuthal variation of station anomaly: estimation of error for this source of anomaly is difficult to come by. It may be reasonable to assume that P wave velocity beneath a station does not vary by more than 1% and Q by more than a factor of two. On this assumption, it can be easily shown that relative azimuthal variation in velocity and Q anomaly, p_v and p_Q in Table 2-4, are roughly 30% and 50% respectively of their averages. This causes an error in the average station anomalies of the order of ±0.3 second for travel time data and ±0.5 for $\log_{10}$ amplitude (microns) data. Notably, these estimates are comparable to reading errors of travel times and amplitude data. For some stations, azimuthal variation in station anomaly may be significant. As for example, travel time anomalies at coastal stations in the western U.S. showed remarkably sinusoidal variation with azimuth (Bolt and Nuttli, 1966; Nuttli and Bolt, 1969). Herrin and Taggart (1968) and Lilwall and Douglas (1970), therefore, incorporated sinusoidal azimuthal variation in their estimation of station anomalies. For our travel time data, however, introduction of sinusoidal azimuthal variation was found to be not very effective in reducing the standard error of estimate of the residuals (Appendix K). Moreover, sinusoidal azimuthal variations of station anomalies as estimated separately by Herrin and Taggart (1968) and

Lilwall and Douglas (1970) were found to be largely inconsistent with each other except for stations on island arcs (Julian, personal communication). This result further shadows the merits of using sinusoidal azimuthal variation terms in representing station anomalies.

c) Source finiteness and rupture propagation: the effect of rupture propagation on far-field first motion amplitude (at distances from the fault plane which are large compared to the dimensions of the fault) has been shown in Table 2-4 in terms of its functional dependence on the position of the observer (r_o, θ_o, ϕ_o), the velocity of the wave observed (c) and the velocity of the rupture (v_r). This dependence can be neglected provided $v_r/c \ll 1$. In fact, by estimating rupture velocities from a theoretical point of view (Mansinha, 1964) or from observations for large deep earthquakes (Chandra, 1973; Fukao, 1972, 1973) it is seen that $v_r/c < 1$. Possibly the most reliable measurement of rupture velocity has been made by Fukao (1972) for a deep focus earthquake at western Brazil and for this determination $v_r/\beta \simeq 0.4$, β being shear velocity. On this basis, it may be safe to assume $v_r/c \ll 1$ and to ignore the effect of rupture propagation on our amplitude data, especially for those of P wave.

d) Variation in focal depths: in this study we have used travel time and amplitude data from deep earthquakes in the depth range of 510 to 625 km with the exception of two earthquakes at depths of 150 and 280 km. The mean of these focal depths is about 530 km and median about 590 km. Generally we have ignored correction to the observed travel time residual for variation in focal depth, except that distances were properly changed to correspond to a depth of 550 km. Distance corrections are very small compared to the distances themselves and slight variation in these corrections because of variation in adopted velocity model will not change our conclusions. On the other hand, variation of travel time residuals against distance or along different ray paths is very crucial to our study. For proper depth equalization of these travel time residuals we need a correct velocity model for both the upper and lower mantle of the earth. Unfortunately, however, we do not have proper data to resolve the velocity models above the depth of roughly 700 km. At any rate, the magnitude of the correction to travel time residuals for variation in focal depth should not exceed $\pm$0.2 seconds. Formally, we have assigned a focal depth of 550 km to the average travel time distance curve as this value falls between the

mean and median of our depth samples. Precise choice of representative depth was also not necessary for amplitude data as variation in focal depth by as much as 50 km was found to have no effect on the shape of the amplitude-distance curve except for its base line.

2.5.1 Insufficiency of data

A major problem in this study is the limited distribution of the deep hypocenters (depth > 450 km) originating at the bottom of different Benioff zones around the world. With our data from 14 deep earthquakes, we have not been able to sample well the deep mantle beneath all oceans except for the regions beneath the Pacific and North Atlantic oceans and the Carribean Sea. To some extent, the deep mantle below the South Atlantic and the Indian Ocean was also covered. Among the continents, the deep mantle under Africa was the major blank area. Lack of stations on the ocean bottom did not allow for good sampling of oceanic upper mantle though continental upper mantle has been sampled to a great extent by receivers in those regions. Bias for this kind of sampling of the upper mantle will be discussed in the next chapter.

Table 2-1

List of Earthquakes Used in This Study

Event Number	Source Region	Bulletin* Magnitude (M_b)	Date	Bulletin* Parameters	Relocation Parameters	Confidence ellipse area in relocation (km^2)
1	2	3	4	5	6	7
1	West Tonga	5.6 (on 20 obs)	7/21/66	18h3om 15.0±0.33S 17.85±0.026°S 178.56±0.027°W 589±4.6 km 1.07S on 115 obs	18h30m 15.2±0.10S 17.83±0.02°S 178.51 0.02°W 596.0±7.0 km 0.83S on 87 obs	100
2	South Fiji	5.9 (on 24 obs)	3/17/66	15h50m 32.3±0.26S 21.08±0.024°S 179.15±0.026°W 627±3.6 km 1.01S on 119 obs	15h50m 31.8±0.09S 21.06±0.018°S 179.07±0.019°W 622.0±5.0 km 0.75S on 84 obs	83
3	Colombia	6.5 (on 34 obs)	7/31/70	17h8m 5.4±0.22S 1.46±0.016°S 72.56±0.019°W 653±3.0 km 0.97S on 244 obs	17h8m 3.8±0.12S 1.53±0.021°S 72.62±0.031°W 626±11 km 1.11S on 113 obs.	152
4	Peru/Brazil	5.9 (on 48 obs)	11/3/65	1h39m 3.2±0.09S 9.04±0.022°S 71.32±0.032°W 587±4.4 km 1.23S on 196 obs	1h39m 2.9±0.07S 9.12±0.012°S 71.39±0.020°W 586±6 km 0.66S on 125 obs.	56
5	Argentina	5.8 (on 38 obs)	12/20/66	12h26m 53.6±0.29S 26.06±0.024°S 63.10±0.032°W 571±3.8 km 1.02S on 167 obs	12h26m 54.1±0.07S 26.13±0.013°S 63.22±0.017°W 580±4 km 0.66S on 118 obs	54

Table 2-1 (cont'd)

1	2	3	4	5	6	7
6	Java Sea	6.0 (on 28 obs.)	1/30/68	3h44m 24.8±0.39S 6.10±0.020°S 113.36±0.022°W 599±5.2 km 1.00S on 169 obs.	3h44m 23.9±0.09S 6.10±0.021°S 113.30±0.020°W 585±6 km 0.59S on 42 obs	98
7	Banda Sea	5.5 (on 17 obs.)	8/17/66	19h54m 11.1±0.60S 5.01±0.025°S 125.15±0.033°E 555±8.1 km 1.09S on 90 obs.	19h54m 11.1±0.08S 5.02±0.014°S 125.12±0.018°E 553±8 km 0.54S on 56 obs.	56
8	Sea of Okhotsk	6.5 (on 30 obs.)	8/30/70	17h46m 8.9±0.18S 52.36±0.013°N 151.64±0.020°E 643±2.7 km 1.01S on 395 obs.	17h46m 7.8±0.05S 52.36±0.01°N 151.73±0.019°E 625±12 km 0.70S on 213 obs.	43
9	E. Russian border	5.2 (on 43 obs.)	4/10/69	14h54m 3.7±0.16S 42.10±0.017°N 131.06±0.025°E 547±2.6 km 1.12S on 254 obs.	14h54m 5.0±0.11S 42.02±0.022°N 131.07±0.033°E 564±7 km 0.78S on 48 obs.	177
10	South Marianas	5.4 (on 34 obs.)	5/10/70	20h5m 16.3±0.30S 18.56±0.016°N 145.28±0.021°E 606±4.2 km 0.95S on 186 obs.	20h5m 15.1±0.09S 18.62±0.019°N 145.41±0.023°E 587±3 km 0.66S on 53 obs.	105
11	Solomon Is.	5.6 (on 21 obs.)	7/6/65	18h36m 47.3±0.09S 4.48±0.019°S 155.07±0.022°E 509±4.3 km 0.97S on 131 obs.	18h36m 47.4±0.07S 4.48±0.013°S 155.10±0.016°E 511±1 km 0.63S on 89 obs.	49

Table 2-1 (cont'd)

1	2	3	4	5	6	7
12	New Hebrides	5.8 (on 30 obs.)	11/04/68	9h7m 39.6S±0.24S 14.20±0.021°S 172.02±0.021°E 596±3.6 km 1.05S on 162 obs.	9h7m 38.7±0.09S 14.23±0.019°S 172.17±0.017°E 587±9 km 0.51S on 40 obs.	77
13	Hindukush	5.7 (on 42 obs.)	1/25/67	1h50m 19.4±0.19S 36.71±0.016°N 71.60±0.017°E 275±2 km 1.05S on 242 obs.	1h50m 19.9±0.1S 36.67±0.02°N 71.66±0.02°E 280±8 km 0.57S on 36 obs.	168
14	Greece	5.7 (on 37 obs.)	7/17/64	2h34m 26.7±0.09S 38.05±0.020°N 23.63±0.022°E 155±2.5 km 1.28S on 216 obs.	2h34m 26.3±0.14S 38.14±0.031°N 23.92±0.040°E 151±1 km 0.78S on 37 obs.	358

*Bulletin parameters are taken from the bulletins of the International Seismological Center.

Parameters are shown in order (top to bottom) of origin time, latitude, longitude, depth of hypocenter and std. error of estimate of P wave travel time residuals.

h = hour, m = minute, s = second

Table 2-2

Values of $\frac{\partial T}{\partial \Delta}$ and $\frac{\partial T}{\partial h}$ from Jeffreys-Bullen tables (1940)

Distance (Δ) (degrees)	$\sim \frac{\partial T}{\partial \Delta}\Big\vert_{h = 550\ km}$ (sec/degree)				$\sim \frac{\partial T}{\partial h}\Big\vert_{h = 550\ km}$ (sec/km)			
	P	PcP	S	ScS	P	PcP	S	ScS
30.0	8.64	2.67	15.59	4.96	-0.05	-0.09	-0.09	-0.17
60.0	6.56	4.06	12.36	7.59	-0.07	-0.09	-0.13	-0.16
90.0	4.58	4.44	9.12	8.37	-0.09	-0.09	-0.16	-0.16

Table 2-3 Focal mechanism solution of deep earthquakes used in our study

No.	Location*	Pole of 1st Nodal Plane		Pole of 2nd Nodal Plane		Pressure Axis		Tension Axis		Null Axis		Reference
		Plunge+	Trend+	Plunge+	Trend+	Plunge+	Trend+	Plunge+	Trend+	Plunge+	Trend+	
1	West Tonga	14	230	24	326	28	276	7	9	62	112	Isacks et al. (1969)
2	South Fiji	20	304	70	110	65	311	25	121	4	213	-DO-
3	Colombia	58	255	32	58	75	32	12	244	8	153	Mendiguren (1972)
4	Peru/Brazil	50	259	40	79	85	79	5	259	0	169	Isacks & Molnar (1971)
5	Argentina	68	216	18	73	60	92	26	243	12	340	-DO-
6	Java Sea	33	194	50	333	66	244	10	356	20	90	This study
7	Banda Sea	64	256	26	76	20	256	71	68	1	176	-DO-
8	Sea of Okhotsk	40	310	50	130	85	310	5	130	0	42	-DO-
9	E. Russian Border	10	226	36	324	32	268	17	10	52	122	-DO-
10	South Marianas	36	61	44	274	66	4	4	261	23	169	-DO-
11	Solomon Is.	21	175	66	23	64	157	24	4	10	269	Isacks & Molnar (1971)
12	New Hebrides	32	106	52	250	69	152	10	271	18	5	-DO-
13	Hindukush	20	236	72	48	27	54	63	240	4	145	This study
14	Greece	40	166	18	60	15	206	42	102	44	312	-DO-

*For details of location see table 2-1.

+Plunge is measured in degrees downward from horizontal plane; trend is measured in degrees clockwise from North.

Table 2-4

Error Analysis for P wave Travel time and Amplitude Data of Deep Focus Earthquakes

Source of error	Basis of error approximation	Adopted parametric values	Estimated error
(1)	(2)	(3)	(4)
1. Source anomaly for downgoing slab			
a) Velocity anomaly	$\Delta t = -(\frac{L}{V})\ \frac{\Delta V}{V}$	$L = 100$ km $V = 9.75$ km/sec $\frac{\Delta V}{V} = 2\%$	$\Delta t = -0.2$ sec
b) Q-anomaly	$\Delta(\log_{10} a) = \pi f t^* (\frac{r-1}{r})$ where $t^* = \frac{L}{VQ}$ $r = \frac{Q'}{Q}$	$f = 1$ Hz $t^* = 0.02$ second [with $L = 100$ km $V = 9.75$ km/sec $Q = 500$] $r = 10$	$\Delta \log_{10} a \simeq 0.06$
2. Azimuthal variation of station anomaly			
a) Velocity anomaly	$\Delta t = -(\frac{L}{V})(\frac{\overline{\Delta V}}{V}) \cdot p_V$ $= \overline{\Delta T} \cdot p_V$ where $p_V = \frac{\Delta V}{\overline{\Delta V}} - 1$	$\overline{\Delta T} = \pm 1$ second $p_V = 30\%$ (see text)	$\Delta t = \pm 0.3$ sec

Table 2-4 (cont'd)

(1)	(2)	(3)	(4)
b) Q-anomaly	$\Delta(\log_{10}a) = \overline{\Delta(\log_{10}A)} \cdot p_Q$	$\overline{\Delta(\log_{10}A)} = \pm 1.0$	$\Delta(\log_{10}a) = \pm 0.5$
	where $p_Q = \frac{\Delta(\log_{10}Q)}{\overline{\Delta(\log_{10}Q)}} - 1$	$p_Q = 50\%$ (see text)	
3. Rupture propagation			
a) Unilateral	$A \propto \frac{1}{[1-(v_r/c)\cos\psi]}$ (Savage, 1965)	$\frac{v_r}{c} \ll 1$ (see text)	$A \propto 1$
b) Bilateral	$A \propto \frac{1}{[1-(v_r/c)^2\cos^2\psi]}$ (Savage, 1965)	$\frac{v_r}{c} \ll 1$ (see text)	$A \propto 1$
c) Radial	$A \propto \int_{\text{fault surface}} \frac{d\phi'}{[1-(v_r/c)\sin\theta_o\cos(\phi'-\phi_o)]^2}$ (Savage, 1966)	$\frac{v_r}{c} \ll 1$ (see text)	$A \propto 1$

Δt: travel time error; $\Delta(\log_{10}a)$: error in $\log_{10}$ amplitude; A:amplitude; f:wave frequency
L: length of ray path; V:normal wave velocity; Q:quality factor
ΔV: Velocity anomaly; $\Delta(\log_{10}Q)$: anomaly in $\log_{10}Q$

$\overline{\Delta T}$: average station anomaly for travel time; $\overline{\Delta(\log_{10}A)}$: average station anomaly for amplitude
v_r: rupture velocity, ψ: angle between direction of rupture propagation and point of observation (r_o, θ_o, ϕ_o)
(r', ϕ'): polar coordinate of rupture front on the fault surface; c:velocity of the observed wave

Figure Captions

Figure 2-1. Comparison of body wave signals from one deep focus earthquake (3/17/66, 15h 50m 32.3 sec, H = 627 km; M_b = 5.9) and two shallow focus earthquakes (8/20/65, 21h 21m 50.0 sec, H = 65 km, M_b = 5.9; 4/2/70, 11h 11m 42.2 sec, H = 33 km, M_b = 5.6) at the Tonga Arc. Note the attenuation of signals in shallow earthquakes compared to deep focus earthquakes.

Figure 2-2. (2 plates) Examples of good quality short period S wave signals (shown by arrows) from deep focus earthquakes whose locations are given in Table 2-1, Δ: epicentral distance in degrees. Note that enrichment of short period S wave energy is found throughout the distance range of 30°-90°.

Figure 2-3. Theoretical temperature and velocity contours (at the interval of 250°C and 0.25 km/sec respectively) in a "typical" long slab that has penetrated up to 700 km depth. This figure has been reproduced from a paper by Sleep (1973). Note that velocity contrast between the slab and the surrounding mantle disappeared at a depth of about 625 km.

Figure 2-4. Distribution of 14 epicenters (shown by crosses) on the earth's surface. Excepting the earthquakes at Hindukush (depth = 280 km) and at Greece (depth = 150 km), all other earthquakes are very deep, depths exceeding 500 km.

Figure 2-5. Distribution of stations recording the body wave phases from the 14 deep focus earthquakes in the distance range of 30°-100°. Triangles are part of the World Wide Standard Seismograph Network (WWSSN), data from which have been read personally. Data from other stations (only the P wave arrival times) have been collected through bulletins of ISC and of USCGS/NOAA.

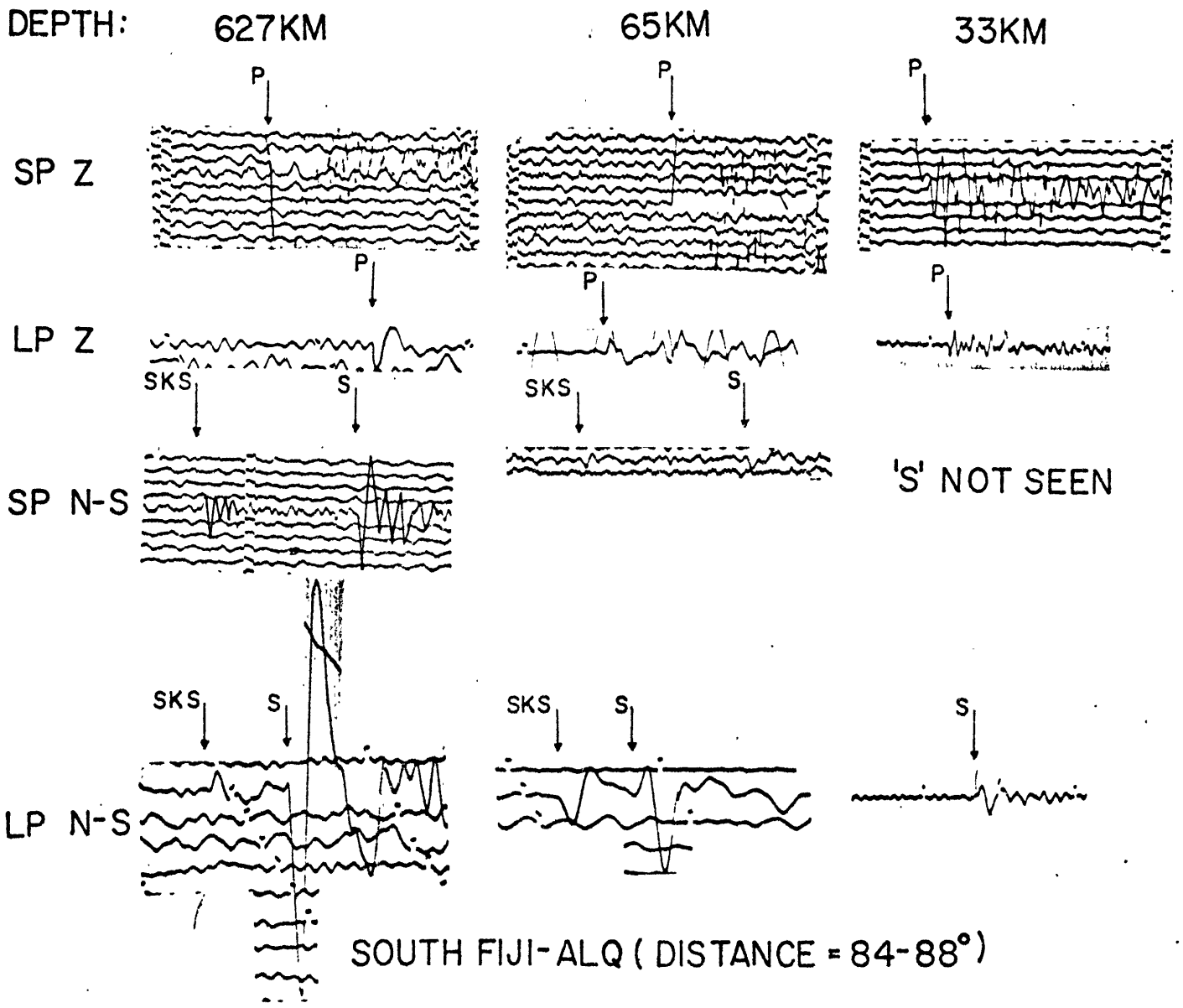

DEPTH:
627KM
65KM
33KM
P
SP Z
LP Z
SKS
S
SP N-S
'S' NOT SEEN
LP N-S
SOUTH FIJI-ALQ (DISTANCE = 84-88°)

Fig. 2-1

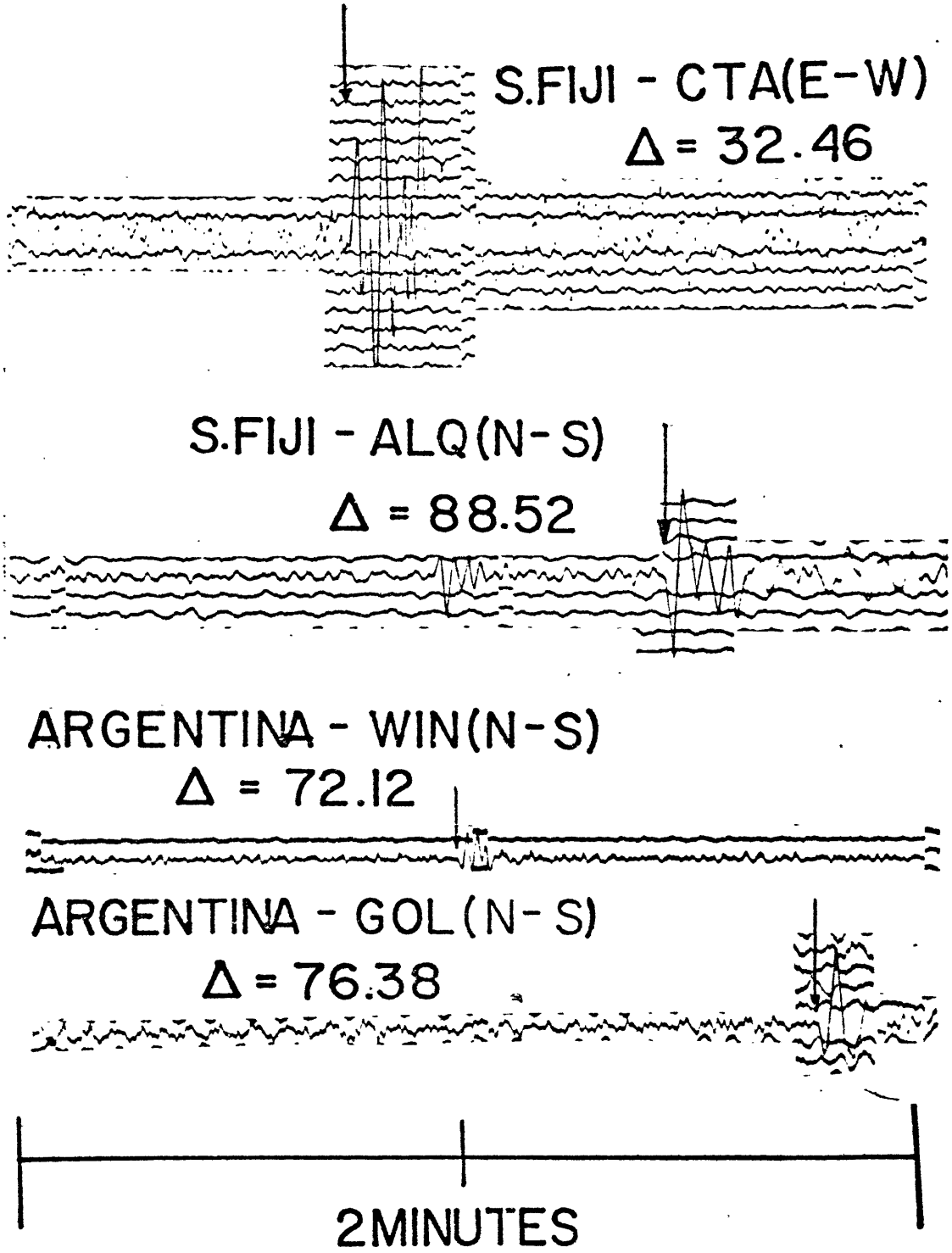

S.FIJI - CTA(E-W)
Δ = 32.46
S.FIJI - ALQ(N-S)
Δ = 88.52
ARGENTINA - WIN(N-S)
Δ = 72.12
ARGENTINA - GOL(N-S)
Δ = 76.38
2MINUTES

Fig. 2-2

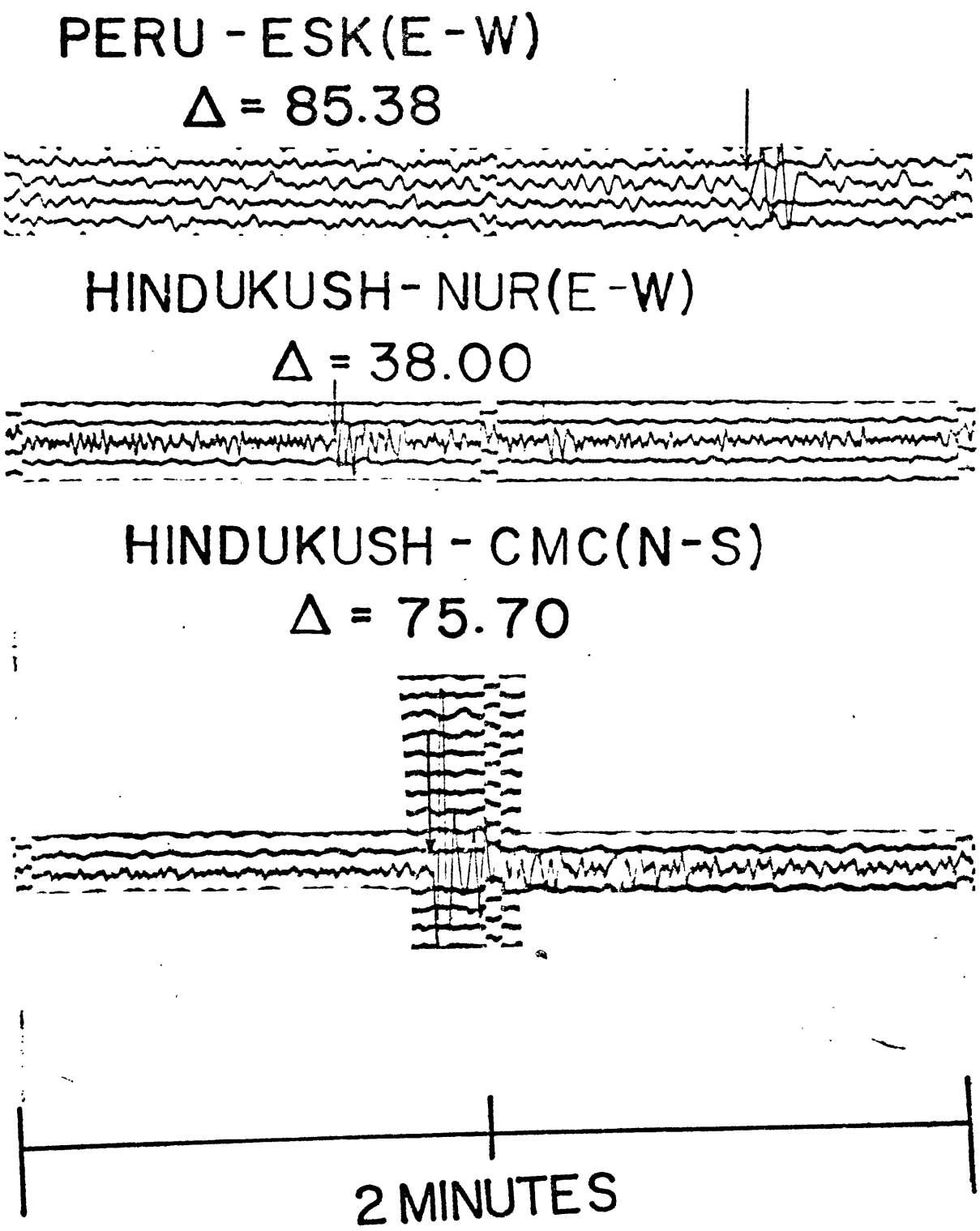

PERU - ESK(E-W)
Δ = 85.38
HINDUKUSH - NUR(E-W)
Δ = 38.00
HINDUKUSH - CMC(N-S)
Δ = 75.70
2 MINUTES

Fig. 2-2 (cont'd)

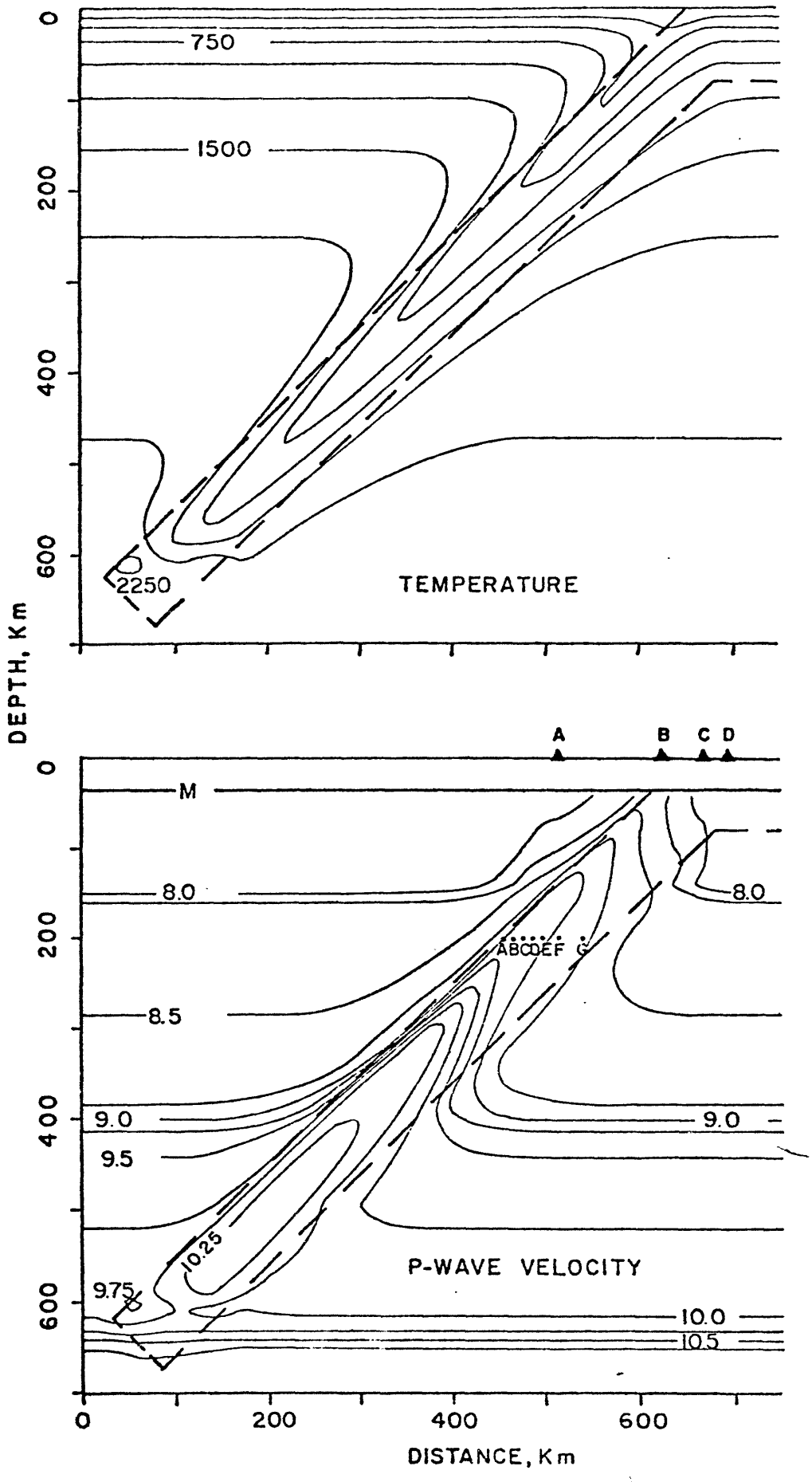
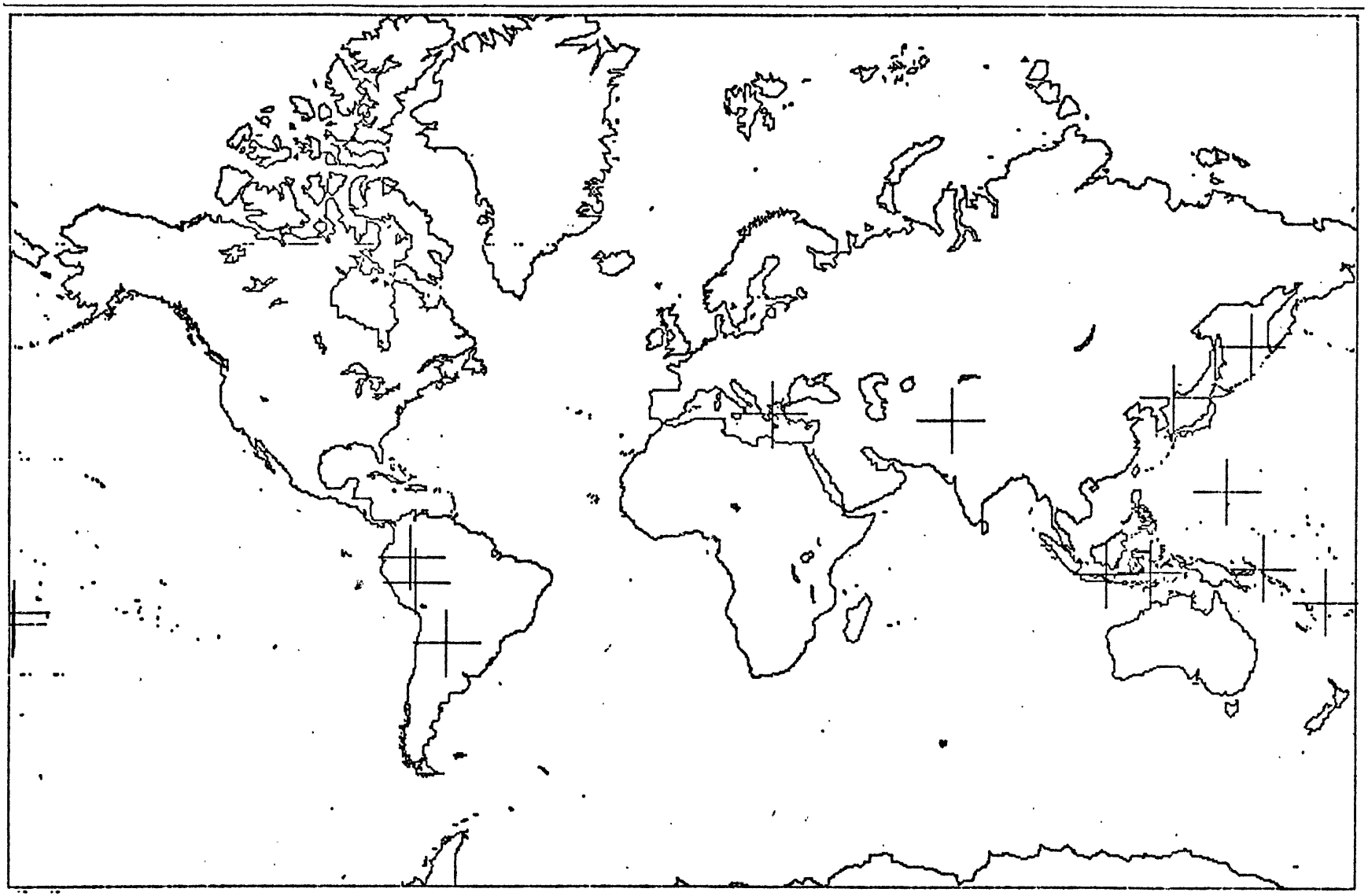

0
200
400
600
750
1500
2250
TEMPERATURE
DEPTH, Km
A
B
C
D
M
8.0
8.0
ABCDEF G
8.5
9.0
9.0
9.5
10.25
9.75
P-WAVE VELOCITY
10.0
10.5
0
200
400
600
DISTANCE, Km

Fig. 2-3



DISTRIBUTION OF EPICENTERS USED IN THIS STUDY

Fig. 2-4

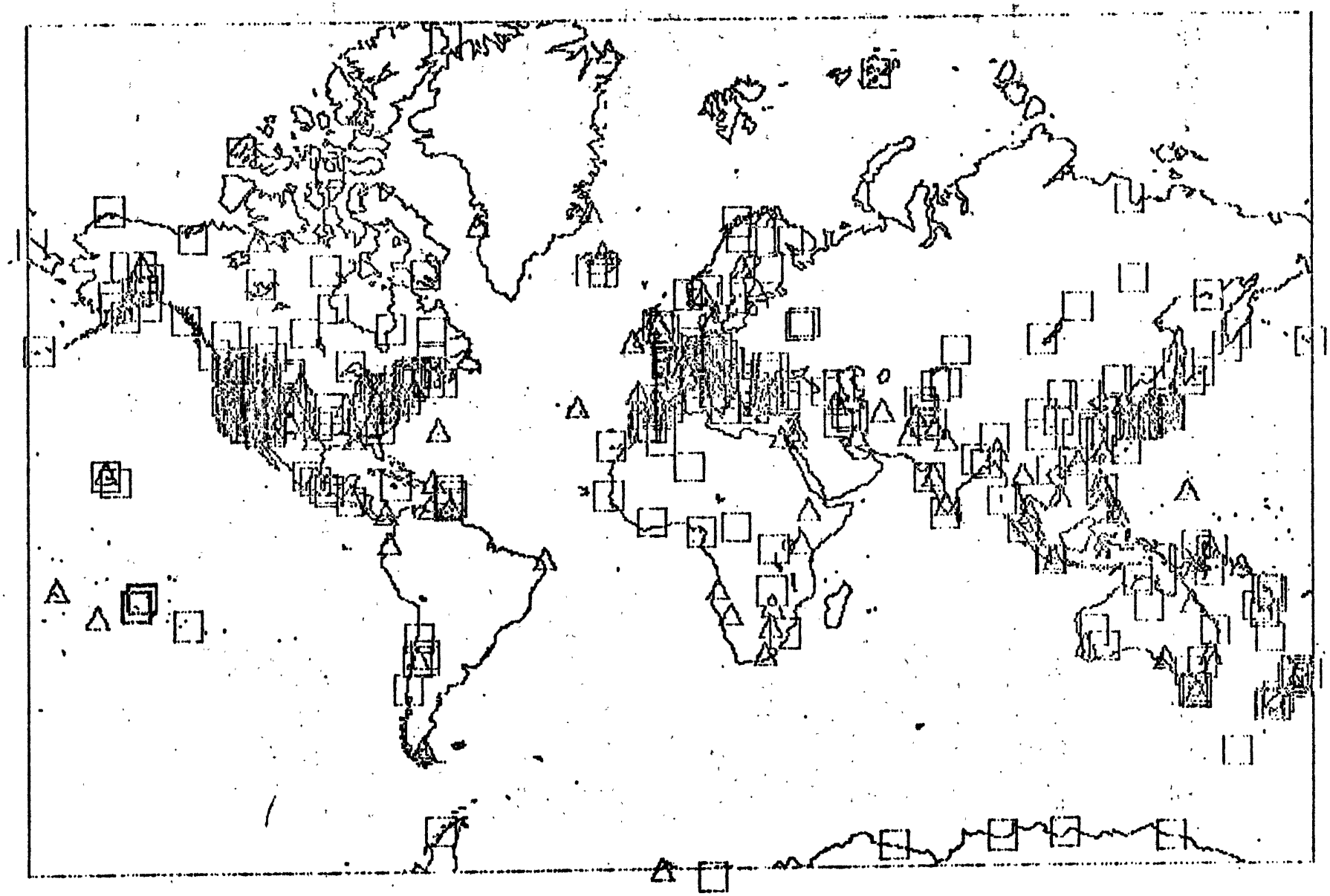


Fig. 2-5

CHAPTER 3

RADIAL VARIATION OF COMPRESSIONAL AND SHEAR VELOCITIES IN THE MONOPOLE (AVERAGE) EARTH

Introduction

From seismic observations on the surface of the earth, our aim is to uncover the properties of the interior of the earth. Given a point source in a spherically symmetric earth, the well-known Herglotz-Weichert formula relates the velocity-depth function with the observed travel time-distance curve (Bullen, 1963, p. 119). But 'real earth' is not spherically symmetric as can be seen from comparison of travel times along different ray paths. So one has to reduce, if possible, the observed travel times along different ray paths in the form of "gross earth data" (Backus and Gilbert, 1968) as if they are related to an earth model whose property (i.e. seismic velocity in this case) varies with radius only. This model of the earth is called monopole (or average) earth. Lateral variation in real earth is characterized by using this average earth model as a reference frame. Proper evaluation of radial inhomogeneities are therefore absolutely essential at this stage in order to assess correctly, at least not to overestimate, the lateral variation in the lower mantle.

In this chapter the features of the 'gross earth' P and S travel time data from deep-focus earthquakes will be discussed in the beginning. We will then describe properties of average velocity models, inverted from these data; also we will characterize the non-uniqueness in those velocity models.

3.1 "AVERAGE EARTH" MODEL AND AVERAGING THEOREM FOR TRAVEL TIME DATA

If $V(r, \theta, \phi)$ is the velocity distribution in the real earth expressed in spherical coordinates with origin at the earth's center, then the "average earth model" is given by the spherically symmetric distributions as follows

$$\bar{V}(r) = 1/4\pi \int_0^{2\pi} \int_0^{\pi} V(r, \theta, \phi) \sin\theta d\theta d\phi \qquad (3.1)$$

$\bar{V}(r)$ has been termed to be 'terrestrial monopole' by Gilbert (1971). The actual velocity distribution in the "real" earth can be represented as

$$V(r,\theta,\phi) = \bar{V}(r) + \delta V(r,\theta,\phi) \qquad (3.2)$$

where 'δV' is the velocity anomaly due to lateral heterogeneity and will average to zero on spheres of

constant radius 'r'.

In practice, travel time data are averaged for different ray paths and then they are inverted to obtain a velocity model of the earth, say, $\bar{V}_o(r)$. Jordan (1973) proved an averaging theorem for the travel times (see Appendix J) by which under some restrictions on observations, $\bar{V}_o(r)$ becomes identical to $\bar{V}(r)$, as defined in (3.1). Our velocity models for the monopole earth are based on the concept of this averaging theorem.

3.2 "GROSS EARTH" TRAVEL TIME DATA FROM DEEP EARTHQUAKES

Observed travel times from the selected deep earthquakes corrected for different sources of systematic bias (see Chap. 2), were transformed into gross earth data by averaging over 2° cells in the distance range of 20°-100° for P and 30°-100° for S. The cell interval was found to be adequate on two grounds. On one hand, this interval is sufficiently small for good resolution in the mean travel time distance curve and on the other hand each interval contained a good number of ray paths (see Tables 3-1 and 3-3) on the average, thus reducing to a large extent the bias of lateral heterogeneity in the mean travel times. A base line correction of -1.3 seconds was added to the mean travel times of all phases. Those mean

travel time data were then inverted for radial variation in velocity in the monopole earth.

Figs. 3-1 and 3-2 show deep focus gross earth travel time data for phases like P, PcP and S, ScS. These data were shown conventionally as "residuals" from Jeffreys-Bullen (J-B) times (1940) which had been 'standard' for the last 35 years. Table 3-1 thru Table 3-4 tabulates the corresponding J-B residuals in different distance cells. In those tables, we have also shown the distribution of ray paths in each distance cell. In doing so, we grouped the corresponding seismic rays in 10° cells of azimuth measured from each hypocenter. The total number of cells which were filled by at least a single ray has been presented in the table. These tables show that between the distance range of 46°-98°, our gross earth P travel times have been very well determined in terms of distribution of rays paths involved and the standard error of the mean. For S, the distribution of ray paths was comparatively poor but still standard errors of the mean were almost always within ±1 second in the whole distance range. More scatter is, noticed, however, for ScS data. Pronounced lateral heterogeneity near the core mantle boundary may very likely be the cause of it. Few PcP data can either confirm or reject this hypothesis.

3.2.1 Characteristic features of deep focus travel time data in relation to those from shallow earthquakes

The usefulness of deep earthquakes in relation to the determination of gross earth data has been shown in Tables 3-5 and 3-6 respectively for P times and S times. In those tables, we have compared the "standard deviation" of J-B residuals in our study with those determined by data from surface focus events. Note that standard deviation of surface focus travel times is in general higher than that of deep focus travel times. Thus instead of using a larger set of surface focus travel time data, one can utilize fewer travel time data from deep events, to determine the mean travel times equally well (in terms of the standard error of mean). The higher standard deviation in the surface focus travel times is very likely due to lateral heterogeneity in the upper mantle near the source region. Incorporating then a 'source correction' for the surface focus travel times can reduce the standard deviation of surface focus travel times. This can explain why the P wave travel time data of Cleary and Hales (1966) show less scatter (see Table 3-5) than those of Herrin et al. (1968). In their analysis of surface focus P times, Cleary and Hales introduced a source correction (a "constant" for each event) and thus obtained a scatter comparable to the deep event data of ours. Lateral

heterogeneity in the upper mantle near the source region is likely to affect S times more than P times and a constant source correction for an event may not suffice for S wave travel time data of surface focus events - one may need to invoke a distance (and/or azimuth) dependent source correction. That is possibly why Doyle and Hales (1967) were not very successful (cf. Table 3-6) in reducing the standard deviation in their S tavel times although they used a method for source correction which was similar to the one used by Cleary and Hales (1966) for P times. Note that standard deviation in our deep focus P travel times is twice as small as that of Herrin et al. (1968) and for S times, the difference in standard deviation is even more between our times and times of Randall (1971) or Doyle and Hales (1967).*

In order to test whether or not we could explain the smallness in the observed standard deviation of deep focus travel times by their limited sample size as compared to the large number of observations for surface focus travel times, a statistical evaluation was undertaken. We have assumed that the population of the travel times in any distance range and for any focal depth is normally distributed as justified

*Note that Hales and Roberts (1970a) did not publish the standard deviations of their S wave travel times; but they are likely to be similar to those of Doyle and Hales (1967).

from the Kolmogorov-Smirnov test on some large samples of deep focus P and S wave travel times (Fig. 3-3 and Tables 3-7 and 3-8). On this assumption, it can be easily shown that if two samples of sizes 15 and 150 (typical of deep focus data and surface focus data respectively) are drawn from two separate populations with identical variance, then at 95% confidence level,

$$0.67 \leq S_{150}/S_{15} \leq 1.83 \qquad (3.3)$$

where S_N is the computed standard deviation for sample of size N. But, if we assume that the deep focus times come from a population which has 4 times smaller variance (due to the smaller effect of near source heterogeneity in the upper mantle), than the population of corresponding surface focus times, then the inequality (3.3) reduces to

$$1.34 \leq S_{150}/S_{15} \leq 3.66 \qquad (3.4)$$

The inequality (3.4) rather than (3.3) better explains the tabulated standard deviations on Tables 3-5 and 3-6. Thus deep focus travel times have about 4 times smaller variance (or standard deviation twice as small) as that of surface focus times.

3.2.2 Some anomalous features for deep focus travel time data

Plotting the mean travel time data in the form of reduced travel time curves (Fig. 3-4) can reveal the anomalous velocity gradient in the lower mantle. The reduced travel time curve for S wave shows in fact some sharp bends at distances of 48°, 60°, and 71° which may correspond to rapid increases in velocity gradient. Hales and Roberts (1970a) suggested a rapid increase of shear velocity between 900-1000 km corresponding to a discontinuity in the slope of the travel time curve around 42°. Fairborn (1969) found an anomalous steep slope in the $dT/d\Delta$ vs. distance curve for S wave in the distance range of 65°-75°. Significantly, Johnson (1969) found evidence of offsets in his $dT/d\Delta$ data for P wave also around the epicentral distance of 49.5, 59.5 and 70.5°. The offsets around 49.5 and 59.5 degrees were large and well-defined whereas the other offset at 70.5° was small and poorly defined. The nature of these offsets seems to correspond well to the nature of sharpness in the bending of our reduced S wave travel time distance curve at similar distances. Though this coincidence is very striking, there may still be an effect of bias in S wave travel time data at those distances due to lateral heterogeneity. In fact, the path distributions for those data are very

limited and the standard deviations are also very large (see Table 3-3), which provided the basis of our suspicion (see also section 5.2.2 in Chap. 5). Note that we do not see any corresponding bend in the reduced travel times of P wave (Fig. 3-4, below). The reason may be the path distribution involved for P wave data (see Table 3-1). It is worth mentioning, however, that offsets in P wave $dT/d\Delta$ values as observed by Johnson (1969), do not produce any sharp bend in the travel time-distance curve as those observed for the reduced S times (Fig. 3-4, top).

3.2.3 Baseline difference in deep focus travel time data with respect to other earth models

We must stress at the outset that for calculation of observed travel times for any phase (P, S, ScS or PcP), we have used the location parameters (including the origin times) determined solely from P wave travel time data with the help of J-B Tables. So, the base line values of our observed travel times for those phases are linearly related to our choice of -1.3 seconds for the base line correction of J-B times of P wave for focal depth of 550 km (see Appendix K for details). With this correction

of -1.3 seconds to our observed travel times of S and ScS phase the computed mean of J-B residuals are as follows: -0.9 seconds for S wave and 0.2 seconds for ScS. Note that relative difference in mean J-B residuals for P and S phases are close to each other. Jeffreys and Bullen (1940) also used the travel time data from deep earthquakes especially for small distances and therefore it is expected that the base line correction to the deep focus J-B times for P and S phases would be similar.

Tables3-9 and 3-10 show the base line difference in P and S times of different velocity models with reference to Jeffreys-Bullen times. The disagreement in the base line values of different models is more pronounced for S times than P times. Particularly the models derived from the inversion of normal mode data have a base line difference of more than 4 seconds in S times as compared to the models derived from travel time data. Consider for example, B1 model of Jordan and Anderson (1974). Note that this model was obtained by inversion of a data set of which 81% were free oscillation eigenperiods. Travel times computed from the B1 model for focal depth of 550 km, show the following average differences from our observed times for deep earthquakes: -0.3 seconds for P, -6.4 seconds for S and -5.7 seconds for ScS, our times being always

smaller than the computed times for B1 model (see Figs. 3-1 and 3-2). These average differences may have an error of ±1.0 seconds because of possible error in our base line correction of J-B times of P wave (see Appendix K). Even taking into account this error, the average difference between our observed S times and computed S times from B1 model is still large. This B1 model was used in our inversion process (section 3.3), so the cause of this large base line difference deserves some discussion. There are at least three possibilities which could cause a base line difference between our observed S times and those from B1 model:

1. It was suggested by Jordan and Anderson (1974) and Sipkin and Jordan (1974) that there may be continental bias in the observed S travel times whereas models derived from normal mode data represent world average upper mantle. It is known that average shear velocity of the continental upper mantle (especially in the shield region) is higher than that of the oceanic upper mantle (see Chap. 1, section 1.2). But to cause a base line difference of about 5 seconds between the S times observed at continental stations and S times from a model satisfying free oscillation data, oceanic upper mantle (which comprises 2/3 of the world in terms of surface

area) must have a delay on the order of 7.5 seconds in shear wave vertical travel times as compared to that for continental upper mantle. We should also add about 2 seconds to this value because of the delay in the observed "station anomaly" for oceanic stations compared to continental stations (see Chap. 5). There is no evidence at present to the effect that shear wave travel times for oceanic upper mantle have a delay of 9.5 seconds compared to those of continental upper mantle. Pure path dispersion data suggest that oceanic upper mantle has vertical shear wave travel times which are only 1-3 seconds larger than that for the shield upper mantle (Toksöz et al., 1967; Dziewonski, 1971). Setting up of ocean bottom seismographs (OBS) may further resolve this issue in the future.

2. It was pointed out by Gilbert and Dziewonski (1974) that there is a lack of suitable modal data to constrain well the shear velocity structure in the upper mantle whereas modes sampling mainly the lower mantle have been well represented. The similarity of the base line difference between our times and times from B1 model with respect to both S and ScS phase (see Fig. 3-2) also suggests that absolute level of shear velocity structure may not have been constrained well in the upper mantle of B1 model. Hales (1974) also mentioned some of the drawbacks in the method of Jordan and Anderson (1974) for correct

determination of the "world average" crust and upper mantle structure from normal mode data.

3. Noting the discrepancy between the absolute S times and modal data, it was suggested by Gilbert and Dziewonski (1974) that the model derived from ray data may be fundamentally in disagreement with the model derived from modal data. They pointed out that the major discontinuities in the earth are those places where normal mode theory and classical ray theory diverge. Incompatibility between those two types of models is likely to arise therefore in the earth's upper mantle which has three major discontinuities, namely Mohorovicic discontinuity, 400 km discontinuity and the 650 km discontinuity. Adequate application of dynamical theory for travel times can reduce then the disagreement in the base line difference of shear wave travel times between the models.

An evidence for incompatibility of normal mode theory and ray theory for the earth's upper mantle comes from a study of Brune and Gilbert (1974) who obtained the SH overtone ($_nT_\ell$) dispersion data by analyzing the phase spectrum of body waves of S and SS observed mostly on continental stations. These overtone data were found to be in agreement with other observed modal data, though the model inverted from this data had a mean delay of 4.0±0.9 seconds with respect to S times of Hales and Roberts (1970a).

This difference in base line is not due to the continental bias in observed S travel times. Also, this base line difference would not arise if normal mode theory were compatible with ray theory. So one cannot rule out flatly the possible incompatibility in the upper mantle part of the models derived from modal data and ray data.

Of all these three possibilities we would stick to the second possibility mainly for internal consistency with our use of body wave travel times as observed on continental stations. Hence, upper mantle (0-670 km) of B1 model would be modified to be consistent with the base line of our observed travel times.

3.3 INVERSION OF DEEP FOCUS TRAVEL TIME DATA TO OBTAIN THE VELOCITY MODELS

In this study, 40 data for P wave average travel times along with 5 data for PcP times (Tables 3-1 and 3-2) were inverted to obtain P velocity variation in the average earth whereas for S velocity variation we had 35 data of average S wave travel times and 10 for ScS times (Tables 3-3 and 3-4). All these data were inverted by the principles of first order perturbation technique

(see for example, Julian and Anderson, 1968; Archambeau et al., 1969; Johnson and Gilbert, 1972). In this method, the starting model is revised by solving a set of linear equations relating small perturbations in the model parameters with changes in the predicted travel times of the model (see Appendix F for details). Such a method has advantages over the conventional Herglotz-Weichert method (Bullen, 1963, p. 119) for inversion of travel time data in the sense that through choice of starting model one can put a constraint on the inverted earth model, in agreement with other geophysical data. Starting models in our linearization-iteration scheme of inversion were chosen to be the models which satisfy the free oscillation data as they are better gross earth data than travel times. One such model is the B1 model of Jordan and Anderson (1974). This model not only satisfied the available normal mode data but also fitted some selected differential travel times including ScS-S and PcP-P times. The 219 basic data that were used to derive this model include 178 normal mode periods, 39 differential travel times and the mass and moment of inertia of the earth. Model B1 fits these data as well as can be expected: 77 percent of the eigenperiods computed from the B1 model differ from the observed by less than one part in one

thousand. We perturbed this B1 model to satisfy our average travel time-distance curve. Knowing that in every cell of the distance range (30°-100°) we did not have adequate distribution of ray paths to remove the effect of lateral heterogeneity in the lower mantle, we sought for minimal perturbations in the B1 model required for a statistically acceptable fit to our data. In other words, we did not force the final fit to pass through every single data point of ours.

Before we present the velocity distribution in our earth model, we would first like to discuss assumptions relating to two features of this model - one involving the choice of radius of the outer core (or depth of discontinuity at the core-mantle boundary) and the other involving the choice of velocity distribution in the upper mantle (depth $\leq$ 670 km).

3.3.1 Choice of radius of the earth's outer core

The radius of the earth's core has been fixed in our inversion algorithm for the following reasons. From a set of P or S travel time data alone, one cannot determine reliably both the velocity structure near the core mantle boundary and the radius of the core. There is a trade off between the two, i.e. one can increase the velocity near the core-mantle boundary and decrease the core radius or

vice versa to satisfy the observed travel times of P or S. Using PcP or ScS times, one can however reduce this trade off between the velocity distribution near the core-mantle boundary and the radius of the earth's core.

In this study, we fixed the radius of the earth's core at 3485 km. This value corresponds to the result obtained by Jordan and Anderson (1974) from PcP-P data and is also in agreement with the value of 3486.1±4.6 km obtained by Hales and Roberts (1970b) using their ScS-S times and the shear velocity distribution of their SLUTD2 model. Very recently Engdahl and Johnson (1974) made another determination of the radius of the outer core from a different set of PcP-P data. Particular care was taken in this study to correct the observed PcP-P times for the lateral heterogeneities near the source region and to minimize (within the limitations of the data) the error due to trade off between the velocity near the core-mantle boundary and the radius of the core. In their study, the radius of the core was estimated to be also in the range of 3484-3486 km. It is worth pointing out that Gilbert, Dziewonski and Brune (1973) also obtained a value of core radius between 3482-3485 km from inversion of a large set of normal mode and travel time (P, S, PKP, SKS and SKKS

but not PcP or ScS) data. Error in our adopted value of core radius is, therefore, expected not to exceed 2-3 km. Note however that even a small error in core radius can cause a large error in velocity. For example, error in core radius of the order of 2-3 km can cause as much as 10% error in the velocity variation in the 25 km thick layer above the core mantle boundary of the B1 model of Jordan and Anderson (1974).

3.3.2 Choice of velocity variation in the upper mantle

As mentioned in section 3.2, internal consistency between our observed data and the sought earth model required a modification in the upper mantle of the B1 model (Jordan and Anderson, 1974) to be consistent with the baseline of our observed travel times. Figure 3-5 shows ad hoc changes in the B1 model in this respect (see also Figs. 3-1 and 3-2 for the nature of baseline agreement). Henceforth the velocity models, incorporating such changes in the upper mantle but retaining the P and S wave velocity variation of the B1 model in the lower mantle, will be referred to as the MKS1P-Ø model for P wave velocity and MKS1S-Ø model for S wave velocity. As our travel time data in the distance range of 20°-100° for P wave and 30°-100° for S wave do not provide resolution for the velocity variation in the upper mantle, MKS1P-Ø

and MKS1S-Ø models, strictly speaking, should not be characterized by the description of velocity variation as shown on Fig. 3-5. Instead, it is only proper to specify the vertical travel time of a one way ray path through those models. The vertical travel time of P wave given by the MKS1P-Ø model is 76.7 seconds for sampling up to a depth of 670 km, this time being only 0.3 seconds smaller than the B1 model. For the MKS1S-Ø model, on the other hand, the vertical travel time of S wave up to a detph of 670 km is 136.2 seconds which is as much as 5.4 seconds smaller than the B1 model. Other proposed models for shear wave velocity variation in the upper mantle also show (see Table 3-11) that for a ray path through this region, shear wave vertical times are in general smaller than the B1 model. Vertical travel times computed from our upper mantle P velocity model of MKS1P-Ø comes closest (within 0.2 seconds) to that computed from the model of Herrin et al. (1968); for shear wave velocity, agreement is the best with Jeffreys' model (Jeffreys , 1970, p. 149) - vertical travel times computed from the upper mantle of Jeffreys' model are only 2.5 seconds larger than that predicted from our model. Note that Jeffreys' upper mantle model also was determined from deep focus travel times. In fact, determination of vertical travel times from deep focus earthquakes should serve as an

independent powerful constraint on the world average velocity models of the upper mantle as these vertical travel times were determined in general from a good quality of data and almost without any assumptions on the nature of velocity variations in the upper mantle.

3.3.3 Determination of P and S velocity variation in the lower mantle and their fit to the observed data

We have seen in the previous section that the baseline difference in our observed times and times from the B1 model (Jordan and Anderson, 1974) has been conveniently explained by ad hoc changes in the upper mantle. Can the remaining difference also be fitted by suitable additional changes in the upper mantle of the B1 model? To answer this question, we present in Fig. 3-6 the data kernels (i.e. $\partial T/\partial V$, partials of travel time with respect to velocity in each layer) of the MKS1S-Ø model for S and ScS data in the distance range of 30°-90°. Note that in the whole distance range the partials, $\partial T/\partial V$, for the upper mantle remain unchanged. This implies that velocity variation in the upper mantle controls only the baseline of deep focus travel times in the distance range of 30°-90° whereas the velocity variation in the lower mantle (depth > 670 km) controls the "shape" of the travel time curve. So the only sensitive way to fit the remaining difference in our observed times and times computed from

the B1 model, is to perturb the velocity variation in the lower mantle of the B1 model.

It is also worth mentioning that data kernels for our deep focus data are almost independent of the upper mantle model. For example, using the same data as in Fig. 3-6, we present, in Fig. 3-7 the similar data kernels for the shear velocity variation in the B1 model. Note in this connection that the MKS1S-Ø model has higher upper mantle shear velocity than the B1 model; in particular between 21 to 420 km, shear velocity of the MKS1S-Ø model is 0.37 km/sec higher than that for the B1 model (see Fig. 3-5). But the data kernels in Fig. 3-6 and Fig. 3-7 appear almost identical for the same data. This result has an important bearing in our inversion of travel time data. It implies that lower mantle velocity variation, inverted to fit the "shape" of deep focus travel time residuals from the B1 model would be independent of the choice of upper mantle models. The resolving kernels (see section 3.4.1) computed for the lower mantle velocity model would also remain unaffected.

The linearization-iteration scheme of inversion for our travel time data by perturbing the velocity variation in the lower mantle (depth > 670 km) of the B1 model converged within only 2-3 cycles. This rapid convergence was obtained through some constraints on the magnitude of

perturbation as well as on the gradient and curvature of the solution model (see Appendix F for details). Total perturbations of P and S wave velocity in the B1 model as required to fit our data are shown in Fig. 3-8. Note that shear velocity in the lower mantle of the B1 model is likely to be more constrained than P velocity because this model was obtained primarily through the fit of normal mode data. That is possibly why we see that required perturbations in the B1 model are large and erratic for P wave velocity whereas perturbation in shear velocity is smaller and more systematic. Final velocity models which differ from the B1 model in both upper mantle and lower mantle portions will be referred subsequently as the MKS1P-A model for P velocity and the MKS1S-A model for S velocity (Fig. 3-9). Fit of our travel time data by these velocity models is shown in Fig. 3-1 and 3-2. Note that observed S wave travel times beyond 97° of epicentral distances were not fitted by the MKS1S-A model because of geometrical shadow. Implications of this failure will be discussed later in this chapter.

A statistical measure of the goodness of fit is given by the 'statistic' χ^2 which is computed as follows (Mathews and Walker, 1964, p. 365).

$$\chi^2 = \sum_{i=1}^{N} (x_i/s_i)^2 \qquad (3.5)$$

where χ_i is the difference between the observed mean travel time and the model time at a distance, s_i is the standard error in the mean travel time, and N is the number of data. Tables 3-12 and 3-13 list respectively the observed P and S times against the travel times computed from the models, MKS1P-A and MKS1S-A. Contributions to the χ^2 statistic by individual data are also shown in these tables. Thus in all, 40 P travel time data give the χ^2 statistic of 23.9 whereas for 33 S travel time data, the computed χ^2 statistic has a value of 45.3. Degrees of freedom for this χ^2 statistic, as applicable to our inversion algorithm are given by the rank (Jackson, 1972) of the square coefficient matrix in the least square normal equation (see Appendix F). On this basis there are 32 degrees of freedom for P data and 31 for S data. The critical value of the χ^2 statistic at 95% confidence level and with 32 degrees of freedom is 46.2 and with 31 degrees of freedom it is 45.0. So the fit to P data by model MKS1P-A is highly satisfactory whereas the fit to S data by the MKS1S-A model can be considered marginal. Note however from Table 3-13 that large contributions of 12.4 and 5.1 to the χ^2 statistic for S travel time data come from two data points at 47 and 49 degrees of epicentral distance. At that distance range, we pointed out in section 3.2.2 that shear wave travel times

appear to be affected either by the bias due to lateral heterogeneity (most likely) or by anomalous velocity gradient in the lower mantle. Smooth velocity variation as in the MKS1S-A model may not be applicable to those data. Deleting those two data points, the χ^2 statistic is reduced to 27.9 and model MKS1S-A then fits the rest of S wave travel time data as well as can be expected.

3.4 NON-UNIQUENESS IN THE DERIVED VELOCITY MODELS

Non-uniqueness in our travel time inversion problem arises primarily for two reasons. First, data kernels (i.e. the partials $\partial T/\partial V$) for a certain portion of the travel time curve behave non-linearly with respect to the changes in the velocity model. This causes the inverted velocity model to be dependent on the starting model. Second, actual radial variation in velocity in real earth is in fact piecewise continuous whereas the number of observations are finite and have observational errors. Backus and Gilbert (1967) have shown that a collection of earth models which fit a finite amount of gross earth data is either empty or infinite dimensional. As one velocity model can always be constructed by the Herglotz-Weichert method (Bullen, 1963, p. 119), restrictions of this method being almost always satisfied in a set of travel time data, it follows therefore that infinite models can be constructed

to satisfy the finite amount of travel time data.

In the framework of the Herglotz-Weichert integral, methods have been developed to formulate the non-uniqueness of velocity models in the form of uncertainty bounds for the velocity model at each depth (Wiggins et al., 1973; Bessenova et al., 1974). These methods have the advantage of taking into account the non-linearity in the inversion of travel time data. Jackson (1973) proposed also a "edgehog method" for description of non-uniqueness in the non-linear inversion problem. In a completely different approach, the "Monte Carlo Method" (see for example, Keilis-Borok and Yanovskaya, 1967; Press, 1970) describes the non-uniqueness in the velocity models by a suitable envelope after random generation of models to satisfy the observed data. But all these methods have certain disadvantages in common. Characterization of resolvability of the features in the inverted velocity model is descriptive. For example, in the framework of those methods, one cannot answer quantitatively a pertinent question such as whether each layer in the parameterized earth model has the required resolution along with a desirable level of uncertainty in the velocity. In this sense, the resolving power approach of Backus and Gilbert (1970) is excellent for the linear inverse problem using finite and inaccurate gross earth

data. In the framework of linearized perturbation theory, their approach is also applicable to non-linear problems like inversion of travel time data. The primary condition of the applicability is that the range of linearity around the velocity model should be beyond the proposed uncertainty in the model. Müller and Alsop (1974) have recently checked the range of linearity for various models and concluded that prediction of travel times - based on linear perturbation theory - is mostly successful even with large perturbation, excepting over the parts of the travel time curve corresponding to a low velocity zone or firsr order discontinuities or zones with high velocity gradients in the models involved. In our velocity models MKS1P-A and MKS1S-A, the earth's lower mantle seems to be largely devoid of any such anomalous feature. So the resolving kernel approach of Backus and Gilbert (1970) is expected to be successful at least for this part of the mantle. For the same reason, we would also be ignoring the first reason of non-uniqueness as stated in the beginning of the section. We will assume that our velocity models for the lower mantle are linearly close to the sought representation of the earth model.

We should mention that another class of linearization-iteration inverse theory is "stochastic inversion"

(Franklin, 1970; Jordan and Anderson, 1974) which adds a level of sophistication in characterizing the non-uniqueness by using the statistical properties of both the model and observations. A priori knowledge of model property (e.g. autocorrelation function) may, however, be difficult to obtain in practice.

3.4.1 Application of Backus and Gilbert method of resolving kernels to our velocity models

In the framework of Backus and Gilbert theory, the degree of non-uniqueness in the velocity model can be described in terms of error bars along both the velocity axis and depth axis (or radius axis) for a spherically symmetric earth model (see Fig. 3-9). Physical interpretation of these error bars can be made as follows. With a finite amount of data it is naturally impossible to resolve the details of arbitrarily small scale. Therefore, one can estimate only the true value of the model at any particular radius $r = r_o$, that is in some sense a smoothed or averaged version of the structure in a small interval around that radius. The averaging kernel may be a distribution in r defined by $A(r, r_o)$. Ideally we would like $A(r, r_o) = \delta(r-r_o)$ where δ is the Dirac delta function. From a finite number of observations, however, one cannot hope to obtain the averaging kernel 'A' which is so localized; the best average one can hope to obtain near radius r_o will be that

weighted average which emphasizes points close to r_o and gives very little weight to distant points. The width of the averaging kernel that contains the heavily weighted values of the velocity model has been termed "spread" (Johnson and Gilbert, 1972). A quantitative measure of this spread has been given in Appendix G, assuming a linear process in evaluating the local average of velocity at radius $r = r_o$. Vertical error bars shown on our velocity profiles in Fig. 3-9 represent the "spread". Arbitrarily we made equal division of the spread on both sides of the depth for which the spread was calculated. Horizontal error bars in the same figure, on the other hand, represent the uncertainty in the velocity arising due to the following reasons. First, the mean travel time distance curve could not be determined exactly because of the reading error and the error due to lateral heterogeneity in the earth. So, each data point on the mean travel time distance curve has standard error associated with it, showing its reliability in the presence of those two errors. The uncertainty in the mean travel time-distance curve causes corresponding uncertainty in the inverted velocity model. Second, a contribution to the uncertainty in this velocity profile also comes from the inadequacy of the inverted velocity model for its failure to fit exactly all of our data. In Appendix G

we have described methods to quantify the standard error of velocity in our earth models arising from those two causes.

We should note that the two error bars (horizontal and vertical) in the velocity profile are not independent of each other. Backus and Gilbert (1970) showed that only their linear combination can be determined by the available data through the minimization process. Consider the linear combination in the form of $S \cos \theta + \rho^2 \sin \theta$ where S is the spread and ρ^2 is the variance of the model error one makes in calculating the velocity profile from erroneous and finite data and θ is a parameter which runs from 0 to $\pi/2$. Backus and Gilbert (1970) proved that as θ goes from 0 to $\pi/2$, the curve ρ^2 against S, called the "trade off curve", is a monotonically decreasing function of S, i.e. one can lower the uncertainty in the determination of velocity profile by willingness to accept a larger spread. The effect of varying 'θ' on the averaging kernels and on the values of spread and standard error of velocity for an interface in our model has been shown in Fig. 3-10. Note that sharpness in the shapes of the averaging kernels (or the values of spread) gradually deteriorates with the increasing values of 'θ' whereas standard error of velocity becomes smaller and smaller. Strictly speaking, the choice of 'θ' to specify the errors in inverted velocity model depends on the algorithm used for inversion, i.e. every

inversion method has a corresponding point on the "trade off curve". We are, however, interested in finding the optimum values of the two parameters - spread and standard error of velocity at each interface - as required to satisfy our observed data. These optimum values, given by the knee of trade off curves, usually occur around $\theta = 45°$. For simplicity therefore, we have chosen all averaging kernels at $\theta = 45°$. The selected kernels of our P wave and S wave velocity models are shown in Fig. 3-11 and Fig. 3-12 and the trade off curves in Figs. 3-13 and 3-14 respectively. Some of the properties of these averaging kernels and trade off curves will be discussed in the following two sections. For convenience, the P and S wave velocity models along with the values of spread and standard error for each interface at $\theta = 45°$, have been tabulated in Tables 3-14 and 3-15.

3.4.2 Some properties of the averaging kernels and their usefulness related to this study

The perturbation δv_j from a velocity model for j^{th} interface should satisfy the following relation (Johnson and Gilbert, 1972) in order to be consistent with observed travel time data,

$$\langle \delta v_j \rangle = \sum_{K=1}^{N} C_K(j) \gamma_K = \sum_{i=1}^{M} A_i(j)\ \delta v_i \qquad (3.6)$$

where $\langle \delta v_j \rangle$ is the linear average perturbation, C_K's are some constants so chosen that resolving kernel is localized at j^{th} layer, γ_K's are the observed travel time residuals from the model, N is the number of data, M is the number of interfaces in the earth's model, $A_i(j)$'s are the contribution of each layer to the resolving kernel calculated for j^{th} interface and δv_i's are the required perturbations in the velocity model to fit the observed residual. Backus and Gilbert (1968) have shown that real earth (spherically symmetric) will have the same linear average velocity as our model if our model is linearly close to the real earth model (which is a fundamental assumption in this study). If, now,

$$A_i(j) = \begin{cases} 1 & \text{for } i = j \\ 0 & \text{for } i \neq j \end{cases} \qquad (3.7)$$

then from (3.6),

$$\langle \delta v_j \rangle = \delta v_j \qquad (3.8)$$

In other words, velocity for that interface is determined uniquely. Otherwise there may be a trade off from the other layers of the model. The magnitude of this trade off being governed by the values of A_i's, the averaging kernels

shown on Figs. 3-11 and 3-12 are helpful in this respect, especially in gaining insight into the trade off between the velocity variations in the lower mantle and the ad hoc upper mantle model of ours (Fig. 3-5). Note that in the plots of the averaging kernels, the whole upper mantle was treated as a 670 km thick single layer such that it satisfies the usual velocity law $V = ar^b$, and preserves the characteristics of total vertical travel time and sum total of partials $\sum_i \partial T/\partial V_i$ contributed by "hypothetical" velocity variation in different layers of the upper mantle. Such a reduction helps to better visualize the trade off for velocity between the upper and the lower mantle of our earth models. For further improving visualization of the trade off between different interfaces of the model, ordinates of the averaging kernel for each layer have been normalized so that the kernel assumes the value of 1.0 at that interface. Save for this normalizing factor, $A_i(j)$'s in (3.6) satisfy the following relation (see Appendix G)

$$\sum_i A_i(j) = 1 \qquad (3.9)$$

It is at once seen from the plots of averaging kernels (Fig. 3-11 and 3-12) that the error in the vertical travel times of our upper mantle models

should not affect the velocity variation in the lower mantle below 1000 km depth. Such a result is also consistent with the construction of model envelopes by 'extremal inversion' (Wiggins et al., 1973) in that uncertainty in the crust and upper mantle model affects the width of the envelope of the lower mantle only up to a depth of about 1200 km. The possibility of error in the vertical travel times of our upper mantle models arises from non-equalization of focal depths of the events and error in depth determination (see Chap. 2, sections 2.5 and 2.3.3).

3.4.3 Some properties of the trade off curves and their usefulness related to this study

The trade off curves (i.e. spread vs. standard error of velocity) for our P and S velocity models in Figs. 3-13 and 3-14 supplement the quantitative aspects of non-uniqueness given by the averaging kernels. For example, our S velocity model below 1100 km is characterized by average resolving length (which would be defined by 'spread/2') of about 70 km and average standard error of velocity by 0.018 km/sec. Thickness of each layer is also 70 km on the average. So these layers are reasonably resolved.* We can then pose a

*Note that discreteness in the velocity model does not allow the minimum value of spread, as computed in Appendix G, to be much less than the thickness of the layers though for perfect resolution one may require the resolving length to be half the thickness of the layer.

question - can one parameterize the lower mantle with layers of less thickness, say, on the order of 50 km? From extrapolation of the trade off curves, it was seen that on the average 50 km thick layers would be resolvable if one were willing to accept a larger standard error of 0.03 km/sec in S wave velocity. This standard error of S wave velocity would produce a standard error on the order of 2.8 seconds in computed vertical travel time of the ScS wave through the 2000 km thick lower mantle. On the other hand, 70 km thick layers with standard error in S velocity on the order of 0.018 km/sec, would result in a magnitude of 1.6 seconds for the similar error. While the standard error of 2.8 seconds in the computed vertical travel time of ScS is too high, a standard error of 1.6 seconds may be acceptable as the observed mean travel times of ScS waves also have a standard error on the order of 0.6-1.0 seconds or even slightly higher. On this basis, we would conclude that parameterization of lower mantle S wave velocity variation by 70 km thick layers may be considered just appropriate for our data whereas 50 km thick layers would have highly unreasonable error in the calculated travel times. Note that we could have reduced the standard error in the calculated ScS times by parameterizing the lower mantle S wave velocity model with thicker layers (thickness >70 km), but then we might have lost some features in the velocity

model which could have been resolved by our data.

Similarly 70 km thick layers in the P velocity model for the lower mantle also seem to be justified as they compromise well the resolution and error. This model has average resolving length on the order of 60 km with a standard error of 0.02 km/sec and thus produces a standard error on the order of 0.8 seconds in the calculated vertical travel time of PcP waves through the lower mantle. This value of the error is not high compared to the standard error in the observed PcP times.

3.4.4 Summary of resolvability of our P and S velocity models for the lower mantle

Resolution of the mantle structure between 670 to 1000 km for the S wave velocity model and between 670 to 850 km for the P wave velocity model is not possible from our data. Resolving length for this part of the lower mantle is on the order of 140 km for S velocity and 80 km for P velocity and it is much greater than the thickness of the layers which is on the order of 50 km; uncertainty in velocity structure also has a large magnitude on the order of 0.05 km/sec in both P and S velocity. Such a poor resolution of the velocity structure in these depth intervals primarily reflects its dependence on the structure of the upper mantle (see the averaging kernels in Figs. 3-11 and 3-12). Between 1000-2860 km, our velocity models have the

proper resolution. The 25 km thick layer immediately adjacent to the core-mantle boundary has, however, very poor resolution; resolving length is about 2-3 times larger than the thickness of this layer, standard error of velocity is also high - on the order of 0.03-0.05 km/sec.

3.5 COMPARISON OF OUR EARTH MODELS (FOR P AND S VELOCITY VARIATIONS IN THE LOWER MANTLE) WITH OTHER EARTH MODELS IN LITERATURE

In this comparison, logically we would first check the similarity in the shapes of our velocity models with other reliable models in literature. But because of non-uniqueness in any earth model inverted from finite geophysical data, it is more proper to compare the data predicted from a model against the data observed on the real earth. Observable data relevant to our earth model, include travel times, ray parameters ($dT/d\Delta$) and amplitudes of P and S waves. Amplitude data will be considered separately in the next chapter. Though periods of normal modes are also valuable data in this connection, they have been excluded as computation of these eigenperiods requires knowledge of density variation as well.

3.5.1 Comparison of the shapes of velocity models

In this discussion we would compare the velocity models in three separate groups - (1) those derived from travel time data, (2) those derived from ray parameter ($dT/d\Delta$) data and finally, (3) those derived from normal mode data. While the first group of models are more sensitive to absolute values of velocity than to velocity gradients, the characteristics of the second group of models are exactly opposite - supposedly they have better resolution for the anomalies in velocity gradients than the models in the first group. Velocity variations derived from normal mode data, on the other hand, are possibly the best possible world average models. Resolving length inherent in these free oscillation models may not, however, be as good as in body wave models. Also, the P wave velocity of free oscillation models may not be as reliable as S wave velocity because of a deficiency in compressional energy of the observed modes.

Fig. 3-15 compares our P wave velocity model against the classical and recent models derived from P wave travel time data. Remarkably our model comes quite close (except for its long wavelength wiggles) to the model of Herrin et al., (1968) between the depth range of 1000-2400 km. Note that Herrin et al. derived their model from the

largest collection of P wave travel time data than ever before. In the same depth range, Jeffreys' (1970, p. 149) model shows relatively lower velocity than ours whereas the model of Hales et al. (1968) shows higher velocity. Buchbinder (1971) adopted the model of Herrin et al. in this depth range for his Model 132 and it is no surprise that his model also shows remarkable agreement with our model. Below a depth of 2400 km, our model shows some anomalous velocity gradients which are not found in the other four models. These anomalous velocity gradients will be tested against the observed $dT/d\Delta$ data in section 3.5.3. Also note that our model shows only a mild reversal in velocity near the core-mantle boundary whereas model 132 of Buchbinder (1971) among others (see section 3.6.1) advocates a pronounced velocity reversal in this region.

Figure 3-16 compares our P wave velocity against two models derived from $dT/d\Delta$ data - the 'MIT 77' model of Chinnery and Toksöz (1967) and the 'CIT 208' model of Johnson (1969), and two other models derived predominantly from normal mode data - the 'B1 model' of Jordan and Anderson (1968) and the '1066B model' of Gilbert and

Dziewonski (1974). Agreement of our model with any one of these four models is not as good as that found with the model of Herrin et al. (1968). P wave velocity in models derived from free oscillation data may not be as reliable as S wave velocity as mentioned earlier in this section. Not too surprisingly, models derived from $dT/d\Delta$ data also showed disagreement with our model even in the velocity gradient. It is quite likely that models derived from averaging $dT/d\Delta$ data may not be consistent with those derived from averaging travel time data as the earth's velocity structure gets averaged in different fashions by the above two processes. It may therefore be more reasonable to compare the predicted $dT/d\Delta$ data of our model with observed data (see section 3.5.3). Another reason for such a discrepancy may be the strong regional dependence of the observed $dT/d\Delta$ anomaly (Hales and Herrin, 1972; Wright and Cleary, 1972; Wiggins et al., 1973) which arises partly due to limited azimuthal sampling of the earth by the array data and partly due to sensitivity of $dT/d\Delta$ data over the crust and mantle structure beneath the arrays.

Fig. 3-17 compares our shear wave velocity distribution in the lower mantle with the models derived from travel time data. As the other models were derived from shallow

focus data, the large reading error and strong effect of near source heterogeneity in those data may have caused the pronounced disagreement of those models with our model. Notice that our shear wave velocity model unlike others (e.g. Randall, 1971) does not show any velocity reversal near the core-mantle boundary, though a possibility of mild reversal cannot be refuted (see section 3.6.1).

Fig. 3-18 compares our S wave velocity model with two models derived from $dT/d\Delta$ data - e.g. the model of Fairborn (1969) and the REDDOG2 model of Robinson and Kovach (1972), and two other models derived from free oscillation data - e.g. the B1 model of Jordan and Anderson (1974) and the 1066B model of Gilbert and Dziewonski (1974). For the same reasons as mentioned earlier for P wave, the observed discrepancy between our model and the models derived from $dT/d\Delta$ data is not unusual. Discrepancy is found to be larger for S wave velocity than for P wave velocity mainly because of the large reading error of $dT/d\Delta$ data for S wave. In contrast to discrepancy with models derived from both travel time and $dT/d\Delta$ data, notice that below about 1600 km, our S wave velocity model agrees very well (except for long wavelength wiggles in our model) with

that of the 1066B model of Gilbert and Dziewonski (1974). Significantly, the 1066B model was derived from 1064 free oscillation eigenperiods which are the largest collection so far for such data. Modes sampling the lower mantle were well represented by this collection (Gilbert and Dziewonski, 1974). This agreement between our model and the 1066B model may also dispel the fear of violating normal mode data because of the observed small but systematic difference in our S wave velocity variation with respect to the B1 model of Jordan and Anderson (1974) (Fig. 3-8).

3.5.2 Comparison of predicted travel times against observed travel times

At the present time, there is no other set of gross earth travel time data of P and S wave available for deep focus earthquakes.* Mean travel time data are available, however, for surface focus earthquakes. But those data, as already mentioned in Chap. 2 (section 2.1), are likely to be biased by the upper mantle heterogeneity near the source region. Any test with those data may not be very useful. Under the circumstances, we can test only whether predicted times from any other presently available and reliable model can satisfactorily fit our deep focus

*Gross earth data of differential travel times from deep focus earthquakes are, however, available (Jordan, 1973; Jordan and Lynn, 1974).

travel time data within their standard errors. Measure of fit has been given in Tables 3-16 and 3-17 by computing the corresponding χ^2 statistics. It is at once seen from Tables 3-16 and 3-17 that none of the presently available models can fit our deep focus travel time data satisfactorily. For fit at 95% confidence level with 35 degrees of freedom, value of the χ^2 statistic should be less than 49.8. Except for a baseline difference, the model (other than ours) which comes the closest to our P wave travel time data is the model of Herrin et al. (1968) and for S wave times it is the 1066B model of Gilbert and Dziewonski (1974). This agreement confirms our conclusions in the previous section as to the similarity of velocity variation in our models with those two models.

Fig. 3-19A compares the "shape" of predicted deep focus (focal depth of 550 km) travel times of P and S wave as computed from different models. For almost all compressional velocity models, there is a broad agreement in the shape of the travel time curves, namely a trough around 25° of epicentral distance, peak at 40°, followed by a broad trough at 55° and another peak at 80°. Only beyond 80°, the travel time curve of our model is comparatively

earlier than other models including that of Herrin et al. (1968). Observed travel time data from explosions at Marshall Islands also show early arrivals in this distance range (Kogan, 1960; Gogna, 1967).

For S wave travel times there is less agreement between the shapes of travel times computed from different models. But all models show that Jeffreys-Bullen S times (1940) are very early for distances greater than 80°.

It is worth noting that both P and S wave travel times computed respectively from the P wave velocity model of Hales et al. (1968) and the S wave velocity model - SLUTD2 of Hales and Roberts (1970b), reveal a "tilt" with respect to our travel times curves. Similar tilt was observed between P wave travel times of Cleary and Hales (1966) and those of Herrin et al. (1968), which started a series of debates over its origin (see for example Herrin and Taggart, 1968; Cleary and Hales, 1968; Cleary and Muirhead, 1969; Muirhead and Cleary, 1969). Ultimately it was concluded (Hales and Herrin, 1972) that explanation of the tilt may lie in the effect of near source heterogeneity along the Alaska-Aleutian Arc biasing the travel times of Cleary and Hales (1966). This conclusion is confirmed from this study of deep focus travel times which are mostly free of the source bias.

3.5.3 Comparison of the predicted dT/dΔ data against the observed data

In section 3.5.1 we mentioned that models derived from dT/dΔ data did not agree with our models, especially with respect to velocity gradients. In this section we directly compare the observed dT/dΔ data against the predicted values from our models. Fig. 3-19B shows the predicted values of dT/dΔ from our models including those for late arrivals. Roughness in velocity gradients of our models (see section 3.6.2) has caused dT/dΔ values to fluctuate from a smooth curve such as that given by the B1 model (Jordan and Anderson, 1974). Particularly, anomalous velocity gradients in our P velocity model around 2400 km depth (Fig. 3-16) showed a comparatively large anomaly in the predicted dT/dΔ values around 80° distance. Though no anomalous velocity gradient was observed at the same depth for models derived from dT/dΔ data (Fig. 3-16), values of P wave dT/dΔ data measured for example by Johnson (1969) at the TFSO array in the U.S., by Husebye et al. (1971) from stations distributed in Scandinavia, and by Wright and Cleary (1972) at the WRA array in Australia, were found to have similar anomaly at 80° distance as predicted from our model (Fig. 3-20). Such evidences of anomaly are, however, not striking among the dT/dΔ values measured at LASA (Chinnery and Toksöz, 1967;

Chinnery, 1969). With the accumulation of data, Chinnery (1969) mentioned only a possibility of a small anomaly in velocity gradient around 2500 km depth by comparing his velocity with Jeffreys' model. At any rate, remarkable agreement is found between predicted values of $dT/d\Delta$ from our model and those observed by Johnson (1969). Large deviations in the observed $dT/d\Delta$ values (e.g. Husebye et al., 1971; Wright and Cleary, 1972) from the predicted ones at distance below 30° are likely to be due to error in the details of ad hoc velocity distribution in our upper mantle model. Also note that correction of the $dT/d\Delta$ data for focal depth has a strong effect on correctly determining the features of ray parameter vs. distance curve and apparently in most of the studies, such correction was not adequate (all $dT/d\Delta$ shown in Fig. 3-20, were supposedly corrected for focal depth).

Compared to P wave data, observed values of $dT/d\Delta$ for S wave show large deviations from the values predicted from our model (Fig. 3-21). This may be due to the difficulty in measuring $dT/d\Delta$ values for S wave because of its long wavelength. $dT/d\Delta$ values measured by Fairborn (1969) are systematically smaller than the predicted values for above 60° of distance but larger than predicted below this distance (Fig. 3-21). This has resulted in a corresponding

systematic difference in our model with that of Fairborn (Fig. 3-18). But no such systematic difference has been observed either with the measured $dT/d\Delta$ values or with the velocity model of Robinson and Kovach (1972) (Fig. 3-18 and Fig. 3-21).

3.6 SUMMARY AND DISCUSSIONS ON THE SIGNIFICANT FEATURES OF OUR P AND S WAVE VELOCITY MODELS FOR THE LOWER MANTLE

In view of the resolution of our data (section 3.4.4 in this chapter), it is proper to discuss the features in our velocity models only below 1000 km of depth. In this depth range, general features of our models can be seen from Fig. 3-22. Seismic parameter, ϕ ($= V_p^2 - 4/3\ V_s^2$) and Poisson ratio, $\sigma \left[= \frac{V_p^2 - 2V_s^2}{2(V_p^2 - V_s^2)} \right]$ are seen to show a tendency to increase with depth (Fig. 3-22a and b), of these two parameters near the core-mantle boundary are subject to some uncertainty as discussed in the following section. Because of increase of the Poisson ratio with depth, S wave (first arrival) is found to bottom at

100-200 km shallower depth than P wave (first arrival) for similar epicentral distance beyond 40° (Fig. 3-22d). Note especially that in our model, velocity gradients, with depth show considerably more fluctuation (Fig. 3-22c) than the B1 model of Jordan and Anderson (1974). This type of fluctuation in the velocity gradient has a geophysical significance. Another feature of geophysical significance is the presence of small velocity reversal in our model (P wave) near the core-mantle boundary. We discuss these two features below.

3.6.1 Small velocity reversal near the core-mantle boundary

Several independent observations (Ergin, 1967; Buchbinder, 1971; Adam, 1972; Bolt, 1972) seem to support a pronounced P wave velocity inversion at a depth of 2750-2800 km (see for example P wave velocity model of Buchbinder (1971) in Fig. 3-15). There are other classes of models, for instance the 1066B model of Gilbert and Dziewonski (1974) which does not require such velocity inversion to satisfy the observed data, (i.e. free oscillation eigenperiods in this case). Our P wave velocity model, MKS1P-A in Fig. 3-9 falls between these two classes of models ; it shows a small velocity reversal at depth of 2821 km where velocity starts to decrease from a value of 13.72 km/sec and reaches a value of 13.64 km/sec at a depth of 2886 km. The velocity gradient is less

than critical so that there is no shadow zone associated with this decrease. Observed P wave amplitudes also seem to support a small velocity reversal near the core-mantle boundary rather than a large one (see next chapter).

There are also suggestions from several observations about a shear velocity decrease above the core mantle boundary (Cleary, 1969; Bolt, et al., 1970; Randall, 1971; Robinson and Kovach, 1972). Contradicting suggestions were made, however, by Mitchell and Helmberger (1973) who favored a velocity increase at the base of the mantle from their observations of amplitude ratios of transversely polarized shear waves ScSH/SH. We noticed that unlike our P wave velocity model, the MKS1S-A model for S wave velocity in Fig. 3-9 does not show a velocity reversal near the core-mantle boundary. But this model does not fit cbserved S wave travel times beyond 97° of epicentral distance because of geometrical shadow (see Fig. 3-2 and Table 3-13). Those unfitted data may not represent diffracted S waves as we had several short period S wave readings in that distance range. One may be inclined then towards small shear velocity inversion near the core-mantle boundary, similar to our P velocity model. This velocity inversion would move the shadow boundary up in the epicentral distance. We will show in the next chapter that there are also indications from S wave

amplitude data about such a velocity inversion. These P and S wave velocity reversals may result from the effect of high temperature and/or composition such as high Fe/Mg ratio near the core-mantle boundary.

We should however mention that the applicability of geometrical ray theory for wave propagation at this region of the core-mantle boundary is of considerable doubt. For example, Johnson (1969) found that the presence of core has a significant diffraction effect upon the measured values of ray parameter ($dT/d\Delta$) beyond an epicentral distance of about 90°. When this effect was removed from the data, the evidence for a complicated velocity structure near the core-mantle boundary was also removed. Richards (1973) also has suggested that the high values of the ray parameter measured along the AB branch of P4KP (see for example, Adams, 1972) may be due to tunelling of mantle rays into the core and can thus be explained even by a Jeffreys' type velocity structure without invoking velocity inversion above the core-mantle boundary. In light of the conflict of geometrical ray theory and wave theory just above the core-mantle boundary, the question of reliability of velocity inversion in this region remains open and it applies as well to our compressional velocity model MKS1P-A too. That is why we did not attempt to

find a corresponding shear velocity inversion above the core-mantle boundary which may be required to fit the observed travel time data beyond 97° of distance.

3.6.2 Wiggly variation in the velocity gradient

During the comparison of our P and S wave velocity model with other models available in the literature, we noted the "wiggly" appearance in our model in contrast with others. Among these wiggles, the most pronounced ones are present in P wave velocity gradient around 1600, 2400 and 2600 km depth (Fig. 3-22c), causing small "triplication" around 57°, 79° and 86° of epicentral distance (Fig. 3-19B). These anomalies in P wave velocity gradients were more or less confirmed by the corresponding anomalies in observed $dT/d\Delta$ data (section 3.5.3, Fig. 3-20). Furthermore, it can be shown that those pronounced wiggles in P wave velocity gradient were not an artifact of variation in path distribution from one distance cell to another. For example in the depth range of 2371-2521 km, the P wave velocity gradient (Fig. 3-22c) goes through rapid changes though the P wave travel time data bottoming in the same depth interval (Fig. 3-22d) came from a single distance cell of 78°-80°. Table 3-18 shows the similarity in path distribution for P wave travel time data in this distance cell and in the two neighboring cells. So, we may

safely say that it is not the variation in path distribution which caused rapid changes of P wave velocity gradient in the depth interval 2371-2521 km. Changes in composition (such as variation in Fe/Mg ratio) and/or phase changes may then be the underlying source of these anomalies in the velocity gradient.

In addition to the pronounced rapid changes with depth, P wave velocity gradient in our model also shows small sinusoidal variation (Fig. 3-22c). A similar wavy variation in P wave velocity gradient in the lower mantle has been noted previously by Vinnick et al. (1972) from measurements of $dT/d\Delta$ by small arrays in the U.S.S.R. However, in light of the uncertainty in our velocity model on the order of ±0.02 km/sec, the observed small-scale sinusoidal variations may not be very reliable. A similar opinion may be held against the sinusoidal variation found also in the S wave velocity model (Fig. 3-22c). It is still worth noting that the P wave velocity gradient in our model shows considerably more fluctuation than that for S wave. Gilbert and Dziewonski (1974) also noted that their P wave velocity model is more wiggly than their S wave velocity model. Consistent with these observations for radial variation in velocity, we will show in Chap. 5 that even for lateral variation, P wave velocity in deep mantle shows greater fluctuation (i.e. larger r.m.s. perturbation) than S wave

velocity. Such a consistency may favor (though not certain at this stage of resolution) a common cause such as variation in the Fe/Mg ratio for observed radial and lateral inhomogeneity in the earth's interior especially near the core-mantle boundary (see also Chap. 5, section 5.4).

Very recently Dziewonski et al. (1975) found a parametrically simple earth model (PEM) which is characterized by very smooth variation (up to third order in polynomial) of velocity with depth in the lower mantle. This PEM model was found to satisfy reasonably the normal mode data and even some selected sets of travel time data. It remains then to be seen whether a parametrically simple earth model can be constructed by satisfying also our deep focus travel time data.

Table 3 - 1

Mean Jeffreys - Bullen residuals* for P times in 2° distance cells (focal depth ~ 550 km)

Distance cell (degrees)	No. of data	No. of † paths	Mean Residual (seconds)	Std. deviation of residual (seconds)	Std. error of mean (seconds)
20-22	15	10	0.09	1.21	0.31
22-24	12	9	-0.60	0.75	0.22
24-26	15	10	-0.59	0.78	0.20
26-28	13	13	-0.14	0.50	0.14
28-30	11	11	-0.48	0.50	0.15
30-32	9	9	0.18	0.57	0.19
32-34	14	12	0.14	0.75	0.20
34-36	15	15	0.23	0.59	0.15
36-38	19	15	0.35	0.71	0.16
38-40	20	14	0.48	0.74	0.17
40-42	14	13	0.10	0.81	0.22
42-44	20	18	-0.08	0.96	0.21
44-46	19	17	-0.10	0.93	0.21
46-48	29	22	-0.18	0.51	0.09
48-50	23	16	-0.49	0.80	0.17
50-52	18	12	-0.59	0.61	0.14
52-54	24	21	-0.46	0.62	0.13
54-56	28	24	-0.67	0.58	0.11
56-58	29	27	-0.34	0.61	0.11
58-60	28	18	-0.42	0.64	0.12
60-62	31	21	-0.48	0.69	0.12
62-64	30	17	-0.38	0.48	0.09
64-66	31	26	-0.30	0.53	0.10
66-68	22	18	0.02	0.49	0.10
68-70	33	24	-0.11	0.59	0.10
70-72	36	23	0.03	0.64	0.11
72-74	39	28	0.04	0.70	0.11
74-76	37	30	0.29	0.58	0.10
76-78	43	29	0.37	0.52	0.08
78-80	34	26	0.50	0.54	0.09

Table 3 - 1 cont.

Distance cell (degrees)	No. of data	No. of † paths	Mean Residual (seconds)	Std. deviation of residual (sedonds)	Std. error of mean (seconds)
80-82	39	25	0.60	0.60	0.10
82-84	37	30	0.21	0.48	0.08
84-86	59	38	0.45	0.75	0.10
86-88	55	32	0.34	0.65	0.09
88-90	40	29	0.16	0.55	0.09
90-92	31	26	0.29	0.67	0.12
92-94	33	25	-0.16	0.83	0.15
94-96	32	23	0.03	0.83	0.15
96-98	24	21	0.11	0.58	0.12
98-100	12	9	0.08	0.94	0.27

* Without a base line correction of -1.3 seconds.

† Each 10° cell in azimuth from the hypocenter is considered to represent a single path when one or more data lie within that cell.

Table 3 - 2

Mean Jeffreys Bullen residuals* for PcP times in 5° distance cells (focal depth ≃ 550 km)

Distance cell (degrees)	No. of data	No. of † paths	Mean Residual (seconds)	Std. deviation of residual (seconds)	Std. error of mean (seconds)
30-35	4	2	-0.55	0.50	0.25
35-40	1	1	-1.11	0.0	0.0
40-45	1	1	0.45	0.0	0.0
45-50	7	3	-0.37	0.33	0.13
50-55	5	3	-0.98	1.57	0.70

* Without a base line correction of -1.3 seconds.

† Each 10° cell in azimuth from the hypocenter is considered to represent a single path when one or more data lie within that cell.

Table 3 - 3

Mean Jeffreys - Bullen residuals* for S times in 2° distance cells (focal depth ≃ 550 km)

Distance cell (degrees)	No. of data	No. of † paths	Mean Residual (seconds)	Std. deviation of residual (seconds)	Std. error of mean (seconds)
30-32	2	1	-3.99	0.0	0.0
32-34	14	7	-1.63	1.67	0.45
34-36	18	8	-0.95	2.02	0.48
36-38	18	12	-0.90	4.09	0.96
38-40	18	6	-0.68	1.02	0.24
40-42	7	5	-0.45	4.20	1.59
42-44	11	5	-1.03	1.04	0.31
44-46	23	11	-1.31	1.76	0.37
46-48	17	11	0.40	1.96	0.48
48-50	10	6	0.87	2.74	0.87
50-52	6	3	-1.33	1.61	0.66
52-54	10	7	-1.90	2.40	0.76
54-56	14	5	-0.64	2.09	0.56
56-58	10	5	-1.34	2.20	0.70
58-60	10	4	0.16	0.59	0.19
60-62	12	7	0.64	3.27	0.94
62-64	9	6	-0.21	0.92	0.31
64-66	24	11	-0.13	1.90	0.39
66-68	21	12	-0.30	2.72	0.59
68-70	21	10	1.27	2.70	0.59
70-72	13	6	2.23	3.73	1.04
72-74	29	15	0.32	2.13	0.40
74-76	19	13	1.21	1.67	0.38
76-78	21	12	0.52	1.28	0.28
78-80	29	12	0.69	1.61	0.30
80-82	22	10	0.59	2.30	0.49
82-84	16	8	0.92	2.51	0.63
84-86	10	7	1.71	2.26	0.71
86-88	23	12	3.52	2.22	0.46

Table 3 - 3 cont.

Distance cell (degrees)	No. of data	No. of † paths	Mean Residual (seconds)	Std. deviation of residual (seconds)	Std. error of mean (seconds)
88-90	16	12	2.69	3.41	0.85
90-92	9	6	4.01	3.52	1.17
92-94	6	3	4.34	1.34	0.55
94-96	14	8	5.80	2.05	0.55
96-98	9	7	5.12	4.22	1.41
98-100	1	1	7.40	0.0	0.0

* Without base line correction of -1.3 seconds.

† Each 10° cell in azimuth from the hypocenter is considered to represent a single path when one or more data lie within that cell.

Table 3 - 4

Mean Jeffreys Bullen residuals* for ScS times in 5° distance cells (focal depth ≃ 550 km)

Distance cell (degrees)	No. of data	No. of † paths	Mean Residual (seconds)	Std. deviation of residual (seconds)	Std. error of mean (seconds)
30-35	6	5	1.90	2.46	1.01
35-40	7	4	1.39	1.04	0.39
40-45	9	5	0.92	1.41	0.47
45-50	12	8	0.12	2.18	0.63
50-55	8	4	0.59	1.66	0.59
55-60	8	4	-0.21	1.32	0.47
60-65	7	6	3.64	3.21	1.21
65-70	7	6	2.40	1.88	0.71
70-75	3	3	3.60	4.01	2.32
75-80	1	1	2.87	0.0	0.0

* Without a base line correction of -1.3 seconds.

† Each 10° cell in azimuth from the hypocenter is considered to represent a single path when one or more data lie within that cell.

Table 3-5

Distance (degrees)	Standard deviation (seconds) for single observation of P travel times (corrected for station and/or source anomaly) [Number of observations are shown in brackets]		
	This study	Herrin et al. (1968)	Cleary and Hales (1966)
30	0.57 (9)	1.108 (165)	
35	0.59 (15)	1.286 (162)	0.81 (29)
40	0.77 (20)	1.268 (191)	0.75 (27)
45	0.93 (19)	1.160 (193)	0.86 (38)
50	0.70 (20)	1.227 (257)	0.80 (33)
55	0.58 (28)	1.210 (204)	0.83 (41)
60	0.66 (29)	0.949 (270)	0.83 (43)
65	0.53 (31)	0.961 (275)	0.91 (57)
70	0.61 (34)	0.973 (269)	0.81 (43)
75	0.58 (37)	0.960 (280)	0.85 (50)
80	0.57 (37)	1.071 (356)	0.81 (46)
85	0.75 (59)	1.074 (275)	0.80 (44)
90	0.61 (40)	1.157 (215)	0.72 (36)
95	0.83 (32)	1.113 (168)	0.59 (18)
100	0.94 (12)	1.122 (81)	

Table 3-6

Distance	Standard deviation (seconds) for single observation of S travel time (corrected for station and/or source anomaly) [Number of observations are shown in brackets]		
	This study	Doyle and Hales (1967)	Randall* (1971)
35	2.02 (18)	3.54 (4)	8.04 (115)
41	4.20 (7)	4.41 (8)	8.30 (168)
45	1.76 (23)	5.32 (16)	6.96 (139)
51	1.61 (6)	5.07 (15)	6.48 (139)
55	2.09 (14)	5.28 (17)	7.81 (149)
61	3.27 (12)	6.15 (25)	6.74 (145)
65	1.90 (24)	5.63 (22)	5.90 (180)
71	3.73 (13)	4.69 (13)	5.46 (186)
75	1.67 (19)	4.95 (17)	5.68 (212)
81	2.30 (22)		
85	2.26 (10)		
91	3.52 (9)		
95	2.05 (14)		

[*No station or source correction was determined in this work]

Table 3-7

Test of normal distribution of deep focus P travel time residuals:

Distance range: 86-88 degrees
Sample size: 55
Mean residual: 0.21 seconds
Standard deviation: 0.69 seconds
Kolmogorov-Smirnov statistic, $D_{0.05} \simeq 0.18$

Residual range (sec.)	Cumulative fractional observation (a)	Cumulative frequency for normal distribution (b)	Difference (D = a-b)	Maximum difference (D_{max})
$\leq$ -1.6	0.02	0.00	0.02	
-1.4	0.02	0.01	0.01	
-1.2	0.04	0.01	0.03	
-1.0	0.05	0.03	0.02	
-0.8	0.07	0.05	0.02	
-0.6	0.13	0.09	0.04	
-0.4	0.18	0.15	0.03	0.09
-0.2	0.27	0.23	0.04	
0.0	0.36	0.33	0.03	
0.2	0.53	0.44	0.09	
0.4	0.58	0.55	0.03	
0.6	0.65	0.67	-0.02	
0.8	0.76	0.76	0.0	
1.0	0.87	0.84	0.03	
1.2	0.93	0.90	0.03	
1.4	0.98	0.94	0.04	
1.6	1.00	0.97	0.03	

Table 3-8

Test of normal distribution of deep focus S travel time residuals

Distance range: 72-74 degrees
Sample size: 29
Mean residual: -4.78 seconds
Standard deviation: 1.67 seconds
Kolmogorov-Smirnov statistic, $D_{0.05} \simeq 0.24$

Residual range (sec)	Cumulative fractional observation (a)	Cumulative frequency for normal distribution (b)	Difference (D = a-b)	Maximum difference (D_{max})
-7.5	0.03	0.04	-0.01	
-7.0	0.10	0.07	0.03	
-6.5	0.17	0.12	0.05	
-6.0	0.31	0.19	0.12	
-5.5	0.34	0.28	0.06	
-5.0	0.45	0.39	0.06	0.12
-4.5	0.52	0.51	0.01	
-4.0	0.72	0.62	0.10	
-3.5	0.76	0.73	0.03	
-3.0	0.86	0.82	0.04	
-2.5	0.90	0.89	0.01	
-2.0	0.93	0.93	0.00	
-1.5	1.00	0.97	0.03	

Table 3-9

Base line difference in P times of different models with reference to P times of Jeffreys-Bullen (1940) (Between 20°-100° of epicentral distance)

Model	Baseline difference (seconds)	
	focal depth = 0 km	focal depth = 550 km
1. Herrin et al. (1968)	-2.6	-1.4
2. Hales et al. (1968)		
a) with upper mantle model of NTS1 (Green & Hales, 1968)	-0.14	-0.98
b) with upper mantle model of ER1 (Green & Hales, 1968)	-3.40	-2.58
	-1.8 (average)	-1.8 (average)
3. CIT 208 (Johnson, 1969)	-2.5	-1.7
4. B1 (Jordan & Anderson, 1974)	-1.8	-1.0
5. 1066B (Dziewonski & Gilbert, 1974)	-0.8	-0.2
6. MKS1P-A (This study)	-2.4?	-1.3

Table 3-10

Baseline difference of S times of different models with reference to S times of Jeffreys-Bullen (1940). (Between 30°-100° of epicentral distance)

Models	Baseline difference (seconds)	
	focal depth = 0 km	focal depth = 550 km
1. SLUTD2 (Hales & Roberts, 1970b)	2.0	3.3
2. Randall (1971)	0.9	-0.9
3. B1 (Jordan & Anderson, 1974)	6.6	5.4
4. 1066B (Dziewonski & Gilbert, 1974)	5.6	4.0
5. MKSJS-A (this study)	-0.2 ?	-0.9

Table 3 - 11

Vertical travel time difference of S wave with B1 model of Jordan and Anderson (1974) as reference:

Model	Vertical travel time difference (second) (One Way)					
	Between 0 - 550 km of depth	Average	Between 550 - 670 km of depth	Average	Between 670 - 2900 km of depth	Average
Class A (models determined from travel time/dT/dΔ data)						
1. Jeffreys (1970)	-1.2		-1.9		1.5	
2. Ibrahim and Nuttli (1967)	-0.8		-0.6		-	
3. SLUTD2 (Hales and Roberts 1970b)	-2.1	-0.5	-0.6	-1.3	0.6	1.3
4. Randall (1971)	0.3		-1.7		2.0	
5. SHR 14 (Helmberger and Engen, 1974)	0.3		-1.4		-	
6. REDDOG2 (Average) Robinson and Kovach, 1972)	0.6		-1.3		1.1	
Class B (shield models determined from surface wave data)						
1. CANSD (Brune and Dorman, 1963)	-1.3		-		-	

Table 3 - 11 cont.

Model	Vertical travel time difference (second) (One Way)					
	Between 0 - 550 km of depth	Average	Between 550 - 670 km of depth	Average	Between 670 - 2900 km of depth	Average
2. S1 (Dziewonski, 1971)	-1.1		-0.8		-	
3. S2 (Dziewonski, 1971)	-1.1	-1.6	-0.6	-0.7	-	
4. CANSD (Massé, 1973)	-2.8 (up to 470 km)		-		-	
Class C (oceanic models from surface wave data)						
1. CIT11 (Anderson and Toksöz, 1963)	-0.5		-0.7		-	
2. 5.08M (Kanamori, 1970; Press, 1970)	-1.3	-0.8	-1.0	-0.8	-	
3. O1 (Dziewonski, 1971)	-0.5		-0.6		-	

Table 3 - 11 cont.

Model	Vertical travel time difference (second) (One Way)					
	Between 0 - 550 km of depth	Average	Between 550 - 670 km of depth	Average	Between 670 - 2900 km of depth	Average
Class D (models determined from free oscillation data)						
1. HB1 (Haddon and Bullen, 1969)	0.7		-1.4		-1.0	
2. OC1 (Mizutani and Abe, 1972)	-0.1	0.3	-0.5	-0.8	-1.2	-0.1
3. 1066B (Gilbert and Dziewonski, 1974)	0.3		-0.6		1.9	
N.B.						
Vertical travel time of the B1 model (Jordan & Anderson, 1974)	118.6		23.0		326.2	

Table 3-12

Fit of P Wave Travel Time Data By MKS1P-A Model

No.	Distance (Degrees)	Observed Time* (Sec.) (a)	Model Time (Sec.) (b)	Difference (Sec.) (a-b)	Standard Error (Sec.)	Contributic to χ^2
1	21.0	244.89	244.66	0.23	0.31	0.54
2	23.0	262.30	262.48	-0.18	0.21	0.70
3	25.0	280.21	280.30	-0.09	0.20	0.20
4	27.0	298.26	298.06	0.20	0.14	2.07
5	29.0	315.32	315.50	-0.18	0.15	1.40
6	31.0	333.08	332.78	0.30	0.19	2.49
7	33.0	349.84	349.90	-0.06	0.20	0.09
8	35.0	366.63	366.67	-0.04	0.15	0.07
9	37.0	383.25	383.24	0.01	0.16	0.00
10	39.0	399.58	399.53	0.05	0.17	0.09
11	41.0	415.30	415.35	-0.05	0.22	0.05
12	43.0	430.92	431.03	-0.11	0.21	0.26
13	45.0	446.50	446.51	-0.01	0.21	0.00
14	47.0	461.72	461.76	-0.04	0.10	0.18
15	49.0	476.51	476.51	0.00	0.17	0.00
16	51.0	491.11	491.16	-0.05	0.14	0.12
17	53.0	505.64	505.54	0.10	0.13	0.63
18	55.0	519.43	519.59	-0.16	0.11	2.12
19	57.0	533.56	533.56	0.00	0.11	0.00
20	59.0	546.98	547.03	-0.05	0.12	0.17
21	61.0	560.12	560.17	-0.05	0.12	0.16
22	63.0	573.12	573.14	-0.02	0.09	0.05
23	65.0	585.90	585.93	-0.03	0.10	0.10
24	67.0	598.62	598.56	0.06	0.11	0.33
25	69.0	610.59	610.61	-0.02	0.10	0.04
26	71.0	622.53	622.44	0.09	0.11	0.71
27	73.0	634.04	634.06	-0.02	0.11	0.03
28	75.0	645.39	645.45	-0.06	0.10	0.40
29	77.0	656.47	656.46	0.01	0.08	0.02
30	79.0	667.20	667.26	-0.06	0.09	0.42
31	81.0	677.70	677.60	0.10	0.10	1.08
32	83.0	687.41	687.54	-0.13	0.08	2.71
33	85.0	697.45	697.43	0.02	0.10	0.04
34	87.0	706.84	706.91	-0.07	0.09	0.63
35	89.0	716.06	716.14	-0.08	0.09	0.87
36	91.0	725.39	725.30	0.09	0.12	0.55
37	93.0	734.14	734.33	-0.19	0.14	1.72
38	95.0	743.43	743.39	0.04	0.15	0.08
39	97.0	752.61	752.42	0.19	0.12	2.55
40	99.0	761.58	761.44	0.14	0.27	0.27

$\Sigma\chi^2 = 23.93$

Total No. of Data = 40

* With baseline correction of -1.3 seconds.

Table 3-13

Fit of S Wave Travel Time Data By MKS1S-A Model

No.	Distance (Degrees)	Observed Time* (Sec.) (a)	Model Time (Sec.) (b)	Difference (Sec.) (a-b)	Standard Error (Sec.)	Contribution to χ^2
1	31.0	596.02	598.01	-1.99	1.50	1.76
2	33.0	628.98	629.06	-0.08	0.45	0.03
3	35.0	659.95	659.87	0.08	0.48	0.03
4	37.0	689.81	689.98	-0.17	0.96	0.03
5	39.0	719.34	718.93	0.41	0.24	2.94
6	41.0	748.38	747.43	0.95	1.59	0.36
7	43.0	776.32	775.81	0.51	0.31	2.62
8	45.0	804.11	804.01	0.10	0.37	0.07
9	47.0	833.60	831.93	1.67	0.48	12.37
10	49.0	861.37	859.42	1.95	0.87	5.08
11	51.0	886.17	886.30	-0.13	0.66	0.04
12	53.0	912.18	912.99	-0.81	0.76	1.13
13	55.0	939.75	939.51	0.24	0.56	0.18
14	57.0	964.84	965.76	-0.92	0.70	1.74
15	59.0	991.84	991.55	0.29	0.19	2.42
16	61.0	1017.14	1016.54	0.60	0.94	0.40
17	63.0	1040.76	1040.99	-0.23	0.30	0.55
18	65.0	1064.96	1065.10	-0.14	0.39	0.12
19	67.0	1088.39	1088.97	-0.58	0.59	0.96
20	69.0	1113.09	1112.43	0.66	0.59	1.25
21	71.0	1136.64	1135.15	1.49	1.03	2.08
22	73.0	1157.00	1157.48	-0.48	0.40	1.49
23	75.0	1179.51	1179.15	0.36	0.38	0.90
24	77.0	1200.23	1200.29	-0.06	0.28	0.05
25	79.0	1221.03	1221.11	-0.08	0.30	0.08
26	81.0	1241.47	1241.52	-0.05	0.49	0.01
27	83.0	1261.23	1261.62	-0.39	0.63	0.39
28	85.0	1281.21	1281.48	-0.27	0.71	0.15
29	87.0	1301.62	1300.91	0.71	0.40	3.12
30	89.0	1318.88	1319.60	-0.72	0.85	0.71
31	91.0	1337.81	1337.83	-0.02	1.17	0.00
32	93.0	1355.44	1355.71	-0.27	0.55	0.25
33	95.0	1373.80	1373.09	0.71	0.50	2.02
34	97.0	1389.92			1.40	
35	99.0	1409.05			1.50	

$\Sigma\chi^2 = 45.33$

Total No. of Data = 33

*With baseline correction of -1.3 seconds.

Table 3-14

P wave velocity model: MKS1P-A

Depth (km)	Velocity (km/sec)	Spread/2.0 (km)	Standard Error (km/sec)
671.0	10.934	49.	0.103
721.0	11.046	101.	0.054
771.0	11.063	56.	0.048
821.0	11.174	85.	0.043
871.0	11.229	72.	0.040
946.0	11.364	71.	0.034
1021.0	11.468	79.	0.034
1096.0	11.630	69.	0.032
1171.0	11.728	55.	0.032
1246.0	11.823	59.	0.029
1321.0	11.964	53.	0.026
1396.0	12.038	72.	0.026
1471.0	12.162	59.	0.021
1546.0	12.210	67.	0.025
1621.0	12.348	61.	0.023
1696.0	12.454	51.	0.026
1771.0	12.533	48.	0.021
1846.0	12.582	76.	0.019
1921.0	12.691	72.	0.017
1996.0	12.800	48.	0.021
2071.0	12.879	52.	0.020
2146.0	12.954	52.	0.019
2221.0	13.031	79.	0.015
2296.0	13.136	56.	0.019
2371.0	13.173	95.	0.021
2446.0	13.275	84.	0.015
2521.0	13.460	72.	0.015
2596.0	13.483	60.	0.025
2671.0	13.584	76.	0.017
2746.0	13.687	63.	0.018
2821.0	13.715	35.	0.019
2861.0	13.652	27.	0.024
2886.0	13.638	45.	0.031

Table 3-15

S wave velocity model: MKS1S-A

Depth (km)	Velocity (km/sec)	Spread/2.0 (km)	Standard Error (km/sec)
671.0	6.111	195.	0.071
721.0	6.153	163.	0.049
771.0	6.184	141.	0.050
821.0	6.213	144.	0.048
871.0	6.232	127.	0.040
946.0	6.281	133.	0.033
1021.0	6.366	125.	0.026
1096.0	6.458	80.	0.023
1171.0	6.490	65.	0.021
1246.0	6.531	87.	0.018
1321.0	6.584	68.	0.018
1396.0	6.604	64.	0.020
1471.0	6.634	58.	0.016
1546.0	6.668	86.	0.016
1621.0	6.727	65.	0.016
1696.0	6.764	55.	0.018
1771.0	6.788	68.	0.016
1846.0	6.821	65.	0.016
1921.0	6.864	75.	0.014
1996.0	6.898	62.	0.014
2071.0	6.938	58.	0.015
2146.0	6.982	50.	0.015
2221.0	7.011	46.	0.016
2296.0	7.043	48.	0.017
2371.0	7.061	56.	0.019
2446.0	7.079	72.	0.011
2521.0	7.115	73.	0.012
2596.0	7.148	68.	0.015
2671.0	7.177	61.	0.015
2746.0	7.199	75.	0.015
2821.0	7.229	54.	0.018
2861.0	7.236	45.	0.023
2886.0	7.247	73.	0.049

Table 3-16

Fit of deep focus P travel time data by different models

Model	χ^2 statistic*		
	Baseline difference not corrected	Baseline difference corrected	Number of data (=degree of freedom)
1. MKS1P-A (this study)	23.7	23.7	40
2. Herrin et al. (1968)	145.0	105.6	38
3. Jeffreys (1970, p. 149)	4943.4	351.1	40
4. Hales et al. (1968)			
a) with upper mantle model of ER1 (Green & Hales, 1968)	4990.4	270.3	35
b) with upper mantle model of NTS1 (Green & Hales, 1968)	424.2	422.6	35
5. CIT208 (Johnson, 1969)	1186.0	1010.1	37
6. MIT77 (Toksöz, Chinnery & Anderson, 1967)	2377.2	1368.1	38
7. B1 (Jordan and Anderson, 1974)	492.1	237.6	38
8. 1066B (Gilbert & Dziewonski, 1974)	4216.9	550.4	38

* $\chi^2 = \sum_{i=1}^{N} (x_i/S_i)^2$, (Mathews & Walker, 1964), where $x_i = (O_i - C_i)$

or, observed − calculated mean travel time

S_i = Std. error of mean

N = No. of data

Table 3-17

Fit of deep focus S travel time data by different models

Model	χ^2 statistic*		
	Baseline difference not corrected	Baseline difference corrected	Number of data (=degree of freedom)
1. MKS1S-A (this study)	45.3	45.3	35
2. Randall (1971)	160.1	132.8	30
3. Jeffreys (1970; p. 149)	674.0	468.1	35
4. SLUTD2 (Hales & Roberts, 1970b)	3612.1	267.9	33
5. Fairborn (1969) (with upper mantle model of Gutenberg)	9030.9	2720.4	32
6. REDDOG-2 (average) (Robinson and Kovach, 1972)	4507.1	294.7	33
7. B1 (Jordan and Anderson, 1974)	7514.3	223.9	34
8. 1066B (Gilbert and Dziewonski, 1974)	4372.0	63.6	35

*for definition of χ^2, see table 3-16.

Table 3-18

Paths and path anomalies for P wave travel times (sec.)

Distance cell 76°-78°			Distance cell 78°-80°			Distance cell 80°-82°		
path		path anomaly*	path		path anomaly*	path		path anomaly*
West Tonga	- ARC	0.26	West Tonga	- JAS	0.58	West Tonga	- PHC	0.25
"	- BKS	0.85	"	- ORV	0.93	"	- COR	0.20
"	- PRI	1.04	"	- MIN	0.77	"	- TUM	0.35
"	- MHC	0.90	South Fiji	- PRI	1.01	"	- BCN	0.82
"	- SLD	0.61	"	- MHC	1.16	"	- EUR	0.39
"	- PAS	0.69	"	- SLD	0.97	"	- TUC	1.27
"	- NHA	-0.30	"	- NHA	-0.73	South Fiji	- PAS	0.86
South Fiji	- SEO	-0.08	"	- VLA	0.42	"	- CED	0.42
"	- YSS	0.00	Colombia	- KTG	-0.48	"	- JAS	0.84
Colombia	- SID	-0.27	"	- FLN	0.30	"	- ORV	1.10
"	- AKU	-0.29	"	- GRR	0.27	"	- MIN	1.14
"	- ALI	-0.18	Peru/Brazil	- GDH	0.43	"	- MAW	0.97
"	- TVO	1.12	"	- TOL	0.29	Colombia	- ESK	-0.11
"	- PPN	-0.37	"	- NVL	0.71	"	- DUR	-0.07
"	- PPT	-0.03	"	- YKC	0.01	"	- SSC	0.27
"	- PAE	1.02	Argentina	- AVE	0.24	"	- MFP	-0.01
"	- AFR	1.02	"	- PPT	0.63	Peru/Brazil	- VAL	0.80
"	- SIT	-0.66	"	- UBO	0.53	Argentina	- RBA	0.67
"	- RES	-1.41	"	- RCD	-0.78	"	- TNP	0.71

Table 3-18 (cont'd)

Peru/Brazil	- PTO	-0.61	Java Sea	- CNG	0.25	Argentina	- DUG	0.43
"	- IFR	0.59	Sea of Okhotsk	- SCP	0.30	"	- EUR	0.22
"	- FSJ	0.29	"	- MRG	0.55	"	- SCH	0.77
Argentina	- GOL	0.08	"	- WES	0.24	Banda Sea	- HVO	0.87
"	- GCA	0.96	"	- PAL	-0.45	Sea of Okhotsk	- NHB	0.52
"	- SIC	0.36	"	- CPO	0.53	"	- NLM	0.62
Java Sea	- NAI	0.25	"	- ORT	0.83	"	- GEO	0.38
"	- TAB	0.35	"	- BRS	0.21	East Russia	- UBO	0.72
Banda Sea	- TIK	-0.33	"	- ATH	0.47	"	- TOO	1.46
"	- SHI	0.53	East Russia	- EUR	1.21	So. Marianas	- NTI	0.43
Sea of Okhotsk	- CLE	0.60	So. Marianas	- RES	0.41	"	- NEW	0.53
"	- BNH	0.05	"	- NOR	0.86	"	- SLD	0.61
"	- TRI	-0.50	Solomon Is.	- KOD	1.43	Solomon Is.	- COL	-0.90
"	- FLN	0.65	Hindukush	- MUN	0.00	New Hebrides	- OLC	0.71
"	- SSC	0.91	Greece	- ANP	0.28	"	- BKS	1.18
"	- GRR	0.91				"	- SLD	1.24
East Russia	- SLD	0.43				"	- JAS	1.01
So. Marianas	- VIC	0.48				"	- PAS	1.03
Solomon Is.	- TIK	0.57				Greece	- ATL	0.93
Hindukush	- WIN	0.30				"	- FLO	1.61
Greece	- NHA	0.29						
Greece	- TRN	1.98						

*Plus sign for late arrival and minus sign for early arrival; corrected for only station anomaly.

Figure Captions

Figure 3-1. Average P (top) and PcP (below) travel time residuals from Jeffreys-Bullen times (1940) roughly for focal depth of 550 km. Averaging was done over 2° distance cell in the 20°-100° range for P and over 5° distance cell in the 30°-100° range for PcP. Standard errors in the average residuals are shown as vertical bars. Note that a base line correction of -1.3 seconds has been added to these data. For comparison, we show also the J-B residuals (focal depth = 550 km) for B1 model (Jordan and Anderson, 1974) which was used as a starting model for inversion of our data. For a description of MKS1P-A and MKS1P-Ø model, see text.

Figure 3-2. Average S (top) and ScS (below) travel time residuals from Jeffreys-Bullen times (1940) roughly for focal depth of 550 km. A baseline correction of -1.3 seconds was added to the observed times. Averaging was done over 2° distance cell for S and over 5° distance cell for ScS in the distance range of 30°-100°. Standard errors in the average residuals are shown as vertical bars. For comparison, we also show J-B residuals (focal depth = 550 km) for B1 model (Jordan and Anderson, 1974). Notice a baseline difference of about 5.5 seconds between our times and

and times computed from the B1 model for both S and ScS phases. For a description of MKS1S-A and MKS1S-Ø model, see text.

Figure 3-3. Histogram of P wave (top) and S wave (below) travel time residuals respectively in the distance range of 86-88 degrees and 72-74 degrees. P wave travel time residuals were computed from Jeffreys' model and S wave residuals from a combination of US26 model (Anderson and Julian, 1969) and Guterberg's model. The smooth curve is the normal distribution having the same mean and standard deviation as those computed for the histograms. Kolmogorov-Smirnov statistics showed that these normal distributions could fit the observed histograms.

Figure 3-4. Reduced travel times of S wave (top) and P wave (below) as computed from average times in 2° distance cells. Standard errors of those average travel times are shown as vertical bars. Note the sharp bends in reduced travel times of S wave in the distance range of 48°, 60° and 71° and comparatively large values of standard error of mean associated with these distances. Reduced travel times of P wave, on the other hand, do not reveal any such anomaly.

Figure 3-5. Ad hoc P and S wave velocity variation in the upper mantle of our earth models - MKS1P-A and MKS1S-A respectively for P- and S- wave velocity. Note that MKS1P-Ø and MKS1S-Ø models (see text) have the same variation in velocity in the upper mantle as shown in the figure. For comparison we show the velocity variation for B1 model (Jordan and Anderson, 1974). The tentative differences from the B1 model satisfy the base line difference between our observed times and times computed from the B1 model (see Figs. 3-1 and 3-2). For S wave velocity, we show also another hypothetical upper mantle model, MKS1S-1, which has the same vertical travel times as MKS1S-Ø (or MKS1S-A) model but may be more realistic. This MKS1S-1 model follows roughly the trend of CIT12 model of Toksöz et al. (1967). The large difference between the MKS1S-1 model and the B1 model at the base of the mantle (depth = 670 km) may not have a significant effect on the fit of normal mode data as S wave velocity in the 1066B model of Gilbert and Dziewonski (1974) is also as large as 5.478 km/sec at this depth.

Figure 3-6. Data kernels ($\partial T/\partial V$) of the MKS1S-Ø model (see text) for S and ScS data in the selected distances, shown at the top. These kernels, given in units of 0.2 sec/(km/sec), have been normalized for

unit thickness in the layers. The anomalous kink around 670 km is due to a numerical problem for sharp velocity discontinuity at that interface. Note that between the depth interval of 0 to 670 km, all data kernels in the distance range of 30°-90° are identical.

Figure 3-7. Same as Fig. 3-6 except that the velocity model in this case is the B1 model of Jordan and Anderson, 1974. Note the similarity of data kernels of Figs. 3-6 and 3-7 in spite of the difference between the B1 model and the MKS1S-Ø model in the upper mantle (Fig. 3-5).

Figure 3-8. Minimal perturbations to P wave velocity (top) and S wave velocity (below) in the lower mantle of the B1 model (Jordan and Anderson, 1974) as required for statistically acceptable fit to our travel time data. Note the large and erratic perturbations to P wave velocity variation as compared to small and more systematic perturbations to S wave velocity variations of the B1 model.

Figure 3-9. Our P wave and S wave velocity models (MKS1P-A and MKS1S-A) for the lower mantle. Horizontal and vertical error bars have been explained in the text.

Figure 3-10 (two plates). Averaging kernels at various values of θ (see text) on the trade-off curve. Four figures associated with each averaging kernel represent

from top - the depth of interface, spread, standard error in velocity and values of θ on the trade-off curves. The MKS1S-A model for S wave velocity was used for the computation of these kernels. For convenience, the whole upper mantle of that model was treated as a 670 km-thick layer. Note that sharpness in averaging kernels (or, the values of spread) gradually deteriorates with increasing 'θ' whereas standard error of velocity improves simultaneously. Our choice of averaging kernels was made for θ = 45° (see text).

Figure 3-11. Averaging kernels at various depths in our P wave velocity model for the lower mantle. For explanation of the four numbers associated with each kernel, see caption in Fig. 3-10. To aid in visualization of the trade-off effect by different layers, kernels have been normalized to the value of 1.0 at depths of concern. For convenience in comparison, kernels at θ = 45° (see text) only are shown. Note that effect of the upper mantle has been diminished below a depth of about 1000 km.

Figure 3-12. Same as in Fig. 3-11 except the kernels in this case are for S wave velocity distribution in the lower mantle. Notice that here, too, velocity distribution in the lower mantle below 1000 km seems

to be unaffected by the upper mantle model.

Figure 3-13. Trade-off curves - spread (km) vs. standard error of velocity (km/sec) - for the same interfaces as in Fig. 3-11 for the P wave velocity model of the lower mantle. Depths of the interfaces are shown in rectangular boxes. Nine points computed for each trade-off curve represent (from left to right) θ = 10°, 20°, 30°, 40°, 45°, 50°, 60°, 70°, 80° (see text). Note the monotonic decrease in standard error of velocity with increasing values of spread.

Figure 3-14. Same as Fig. 3-13 except that these trade-off curves are for S wave velocity distribution in the lower mantle.

Figure 3-15. Comparison of our P wave velocity model for the lower mantle against other models derived also from travel time data. Note a remarkable agreement between our model (except for its long wavelength wiggles) and the model of Herrin et al. (1968) between the depth range of 1000 to 2400 km. Also notice that our model shows only a mild velocity reversal near the core-mantle boundary whereas 'Model 132' of Buchbinder (1971), among others, favors a large velocity reversal.

Figure 3-16. Comparison of our P wave velocity model for the lower mantle against other modesl derived from

dT/dΔ data (e.g. MIT77 model of Chinnery and Toksöz, 1967; CIT208 model of Johnson, 1969) and models derived from free oscillation data (e.g. the B1 model of Jordan and Anderson, 1974; and 1066B model of Gilbert and Dziewonski, 1974). Note that none of these models shows as good agreement with our model as that of Herrin et al. (1968) (Fig. 3-15).

Figure 3-17. Comparison of our S wave velocity model against other models, derived from travel time data of shallow focus earthquakes. Notice a large discrepancy between those models and our model. Large velocity reversal near the core-mantle boundary (e.g. Randall, 1971) is also not required in our model.

Figure 3-18. Comparison of our S wave velocity model with two models derived from dT/dΔ data (e.g. model of Fairborn, 1969, and REDDOG2 model of Robinson and Kovach, 1972) and two other models derived from free oscillation data (e.g. the B1 model of Jordan and Anderson, 1974 and 1066B model of Dziewonski and Gilbert, 1974). Notice a large disagreement of our model with those from dT/dΔ data but a close agreement with models derived from normal mode data. Below 1600 km of depth, the 1066B model of Gilbert and Dziewonski is almost similar to our model except for long wavelength wiggles in our S wave velocity.

Figure 3-19A. Comparison of the "shapes" of travel time curves predicted from different models for a focal depth of 550 km. Conveniently, these travel time curves are represented by residuals from Jeffreys-Bullen times (1940). Curves were adjusted vertically to have the same baseline as Jeffreys-Bullen times.

(top) P wave travel time curves. Note a similarity between our travel time curve and the curve of Herrin et al. (1968) below 80° of distance. On the other hand, there is a tilt between our curve and the curve of Hales et al. (1968).

(below) S wave travel time curves. Note here that our curve is the most similar to that of Gilbert and Dziewonski (1974). A tilt is also found between our curve and that of Hales and Roberts (1970).

Figure 3-19B. Predicted values of $dT/d\Delta$ (including late arrivals) from P wave velocity model and S wave velocity model of this study. Note a small triplication in the predicted $dT/d\Delta$ values of P wave around 56°, 79°, and 86° of distance. For comparison we show the smooth $dT/d\Delta$ values predicted from the B1 model of Jordan and Anderson (1974).

Figure 3-20. Comparison of predicted values of $dT/d\Delta$ (only first arrival) with observed values for P wave. The predicted values are computed from our P wave velocity model (MKS1P-A) for focal depths of 0 to 550 km. In case of overlapping, the number of observed data has been thinned somewhat to show clearly the trend of data. Note a remarkable agreement between the predicted values of $dT/d\Delta$ and the observed ones by Johnson (1969). Effect of focal depth for determining correctly the features of ray parameter vs. distance curve is also noteworthy.

Figure 3-21. Comparison of predicted values of $dT/d\Delta$ (only first arrival) and observed ones by Fairborn (1969) and Robinson and Kovach (1972). The predicted values are computed for our S wave velocity model, MKS1S-A for focal depths of 0 and 550 km. Note a systematic difference of observed $dT/d\Delta$ values of Fairborn (1969) with predicted values, which is not found however among the observed data of Robinson and Kovach (1972).

Figure 3-22. Variation of (a) seismic parameter, $\phi (= V_p^2 - 4/3\ V_s^2)$, (b) Poisson ratio $\sigma \left[= \frac{V_p^2 - 2V_s^2}{2(V_p^2 - V_s^2)} \right]$ and (c) P- and S- wave velocity gradient with depth as computed from our models (Fig. 3-9). Bottoming depths of first arrivals of P and S waves in these models are

shown in (d) as a function of epicentral distance. Note that S wave bottoms at about 100-200 km shallower depth than P ray at similar distances beyond 40°.

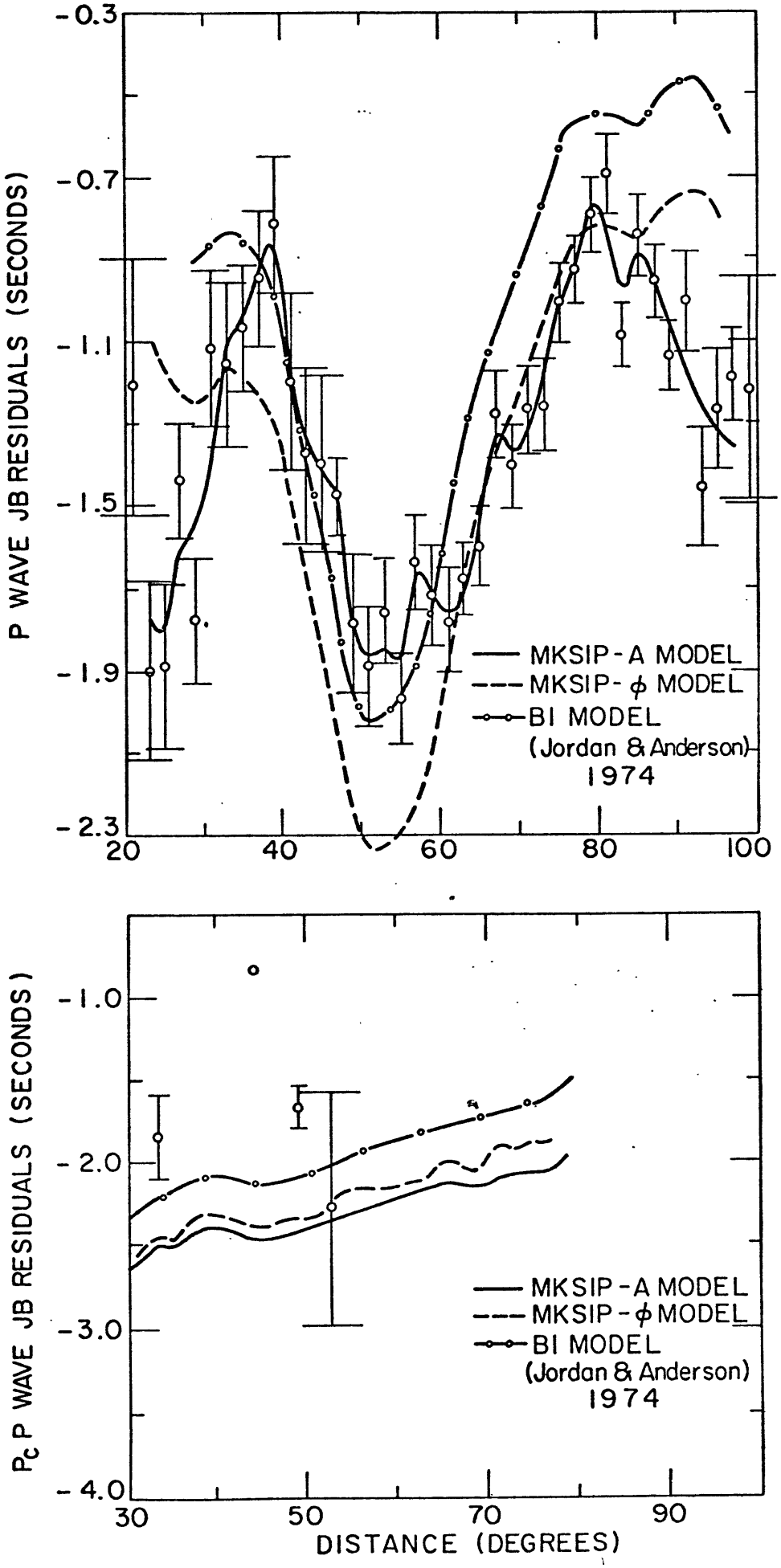

P WAVE JB RESIDUALS (SECONDS)
-0.3
-0.7
-1.1
-1.5
-1.9
-2.3
20
40
60
80
100
MKSIP-A MODEL
MKSIP-φ MODEL
BI MODEL
(Jordan & Anderson)
1974
Pc P WAVE JB RESIDUALS (SECONDS)
-1.0
-2.0
-3.0
-4.0
30
50
70
90
DISTANCE (DEGREES)
MKSIP-A MODEL
MKSIP-φ MODEL
BI MODEL
(Jordan & Anderson)
1974

Fig. 3-1

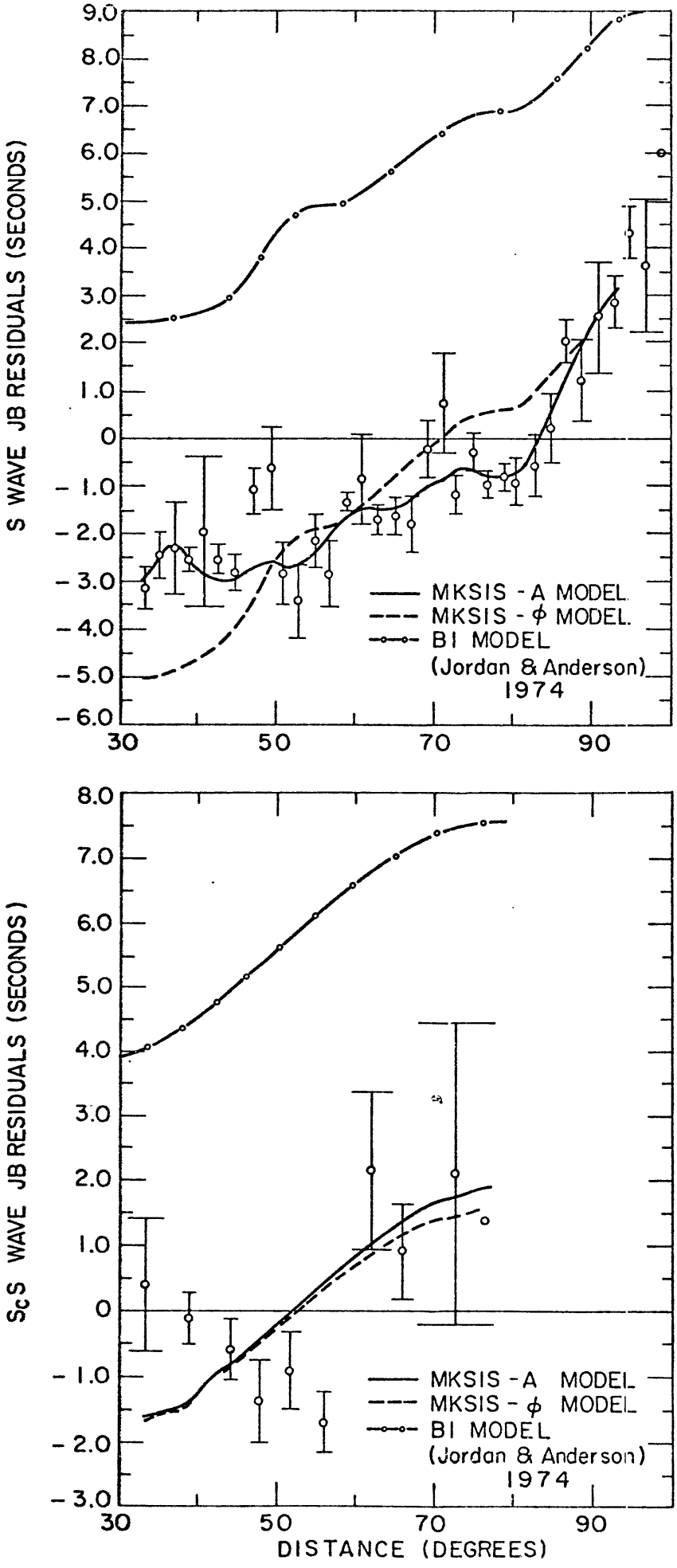

S WAVE JB RESIDUALS (SECONDS)
9.0
8.0
7.0
6.0
5.0
4.0
3.0
2.0
1.0
0
-1.0
-2.0
-3.0
-4.0
-5.0
-6.0
30
50
70
90
MKSIS - A MODEL
MKSIS - φ MODEL
BI MODEL
(Jordan & Anderson)
1974
ScS WAVE JB RESIDUALS (SECONDS)
8.0
7.0
6.0
5.0
4.0
3.0
2.0
1.0
0
-1.0
-2.0
-3.0
30
50
70
90
DISTANCE (DEGREES)
MKSIS - A MODEL
MKSIS - φ MODEL
BI MODEL
(Jordan & Anderson)
1974

Fig. 3-2

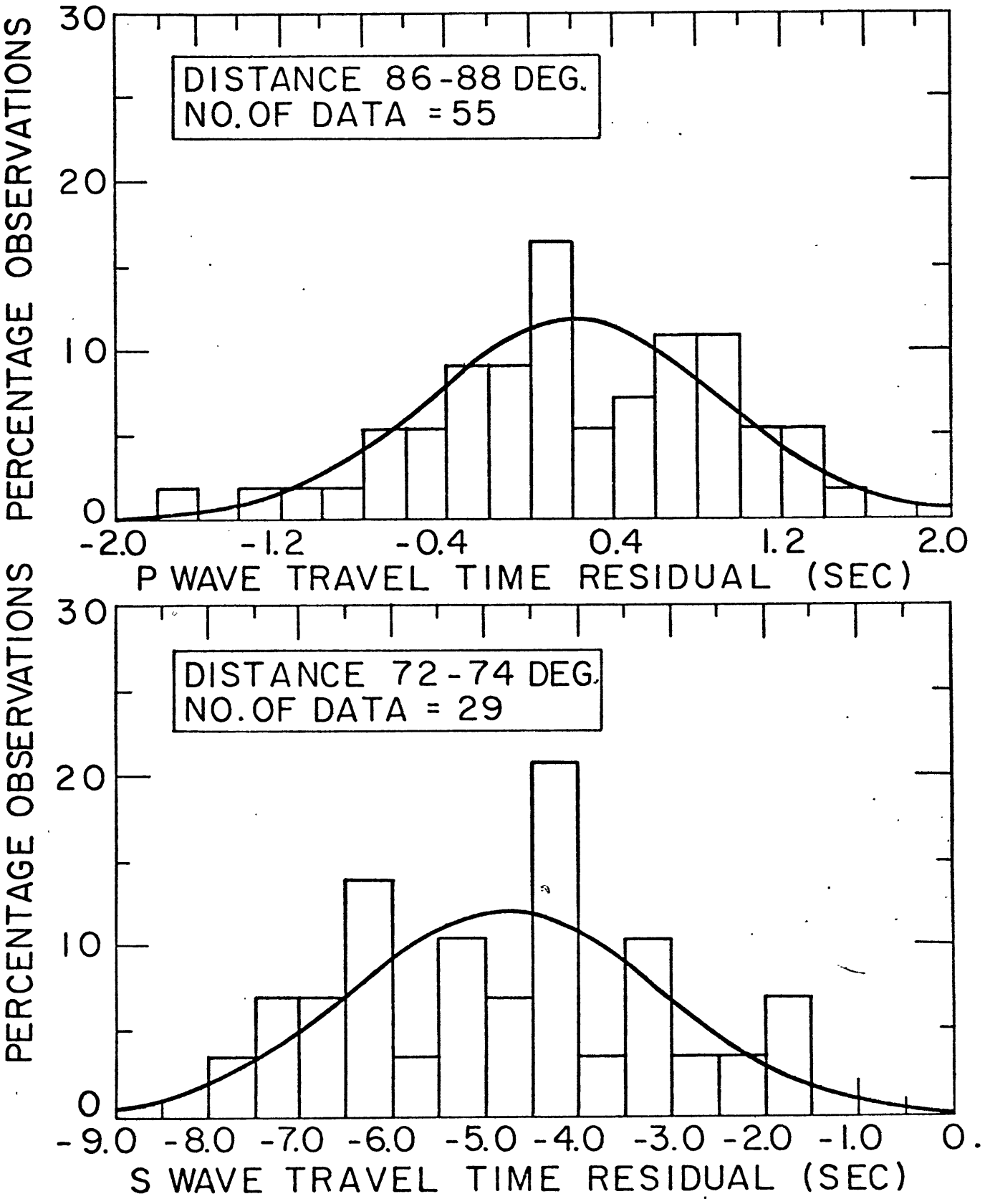

DISTANCE 86-88 DEG.
NO. OF DATA = 55
PERCENTAGE OBSERVATIONS
30
20
10
0
-2.0
-1.2
-0.4
0.4
1.2
2.0
P WAVE TRAVEL TIME RESIDUAL (SEC)
DISTANCE 72-74 DEG.
NO. OF DATA = 29
PERCENTAGE OBSERVATIONS
30
20
10
0
-9.0 -8.0 -7.0 -6.0 -5.0 -4.0 -3.0 -2.0 -1.0 0.
S WAVE TRAVEL TIME RESIDUAL (SEC)

Fig. 3-3

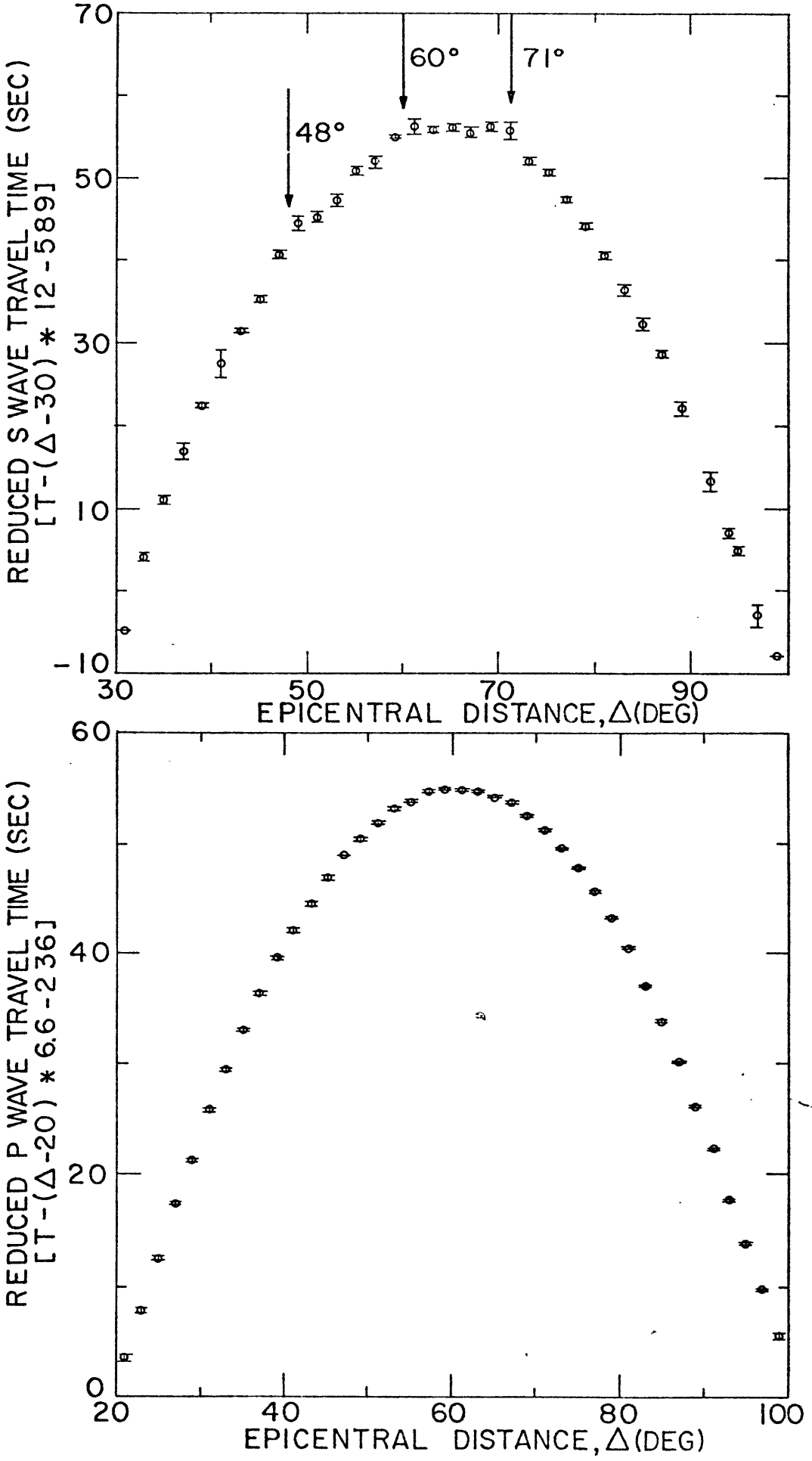

70
50
30
10
-10
60°
71°
48°
REDUCED S WAVE TRAVEL TIME (SEC)
[T-(Δ-30) * 12-589]
30
50
70
90
EPICENTRAL DISTANCE, Δ(DEG)
60
40
20
0
REDUCED P WAVE TRAVEL TIME (SEC)
[T-(Δ-20) * 6.6-236]
20
40
60
80
100
EPICENTRAL DISTANCE, Δ(DEG)

Fig. 3-4

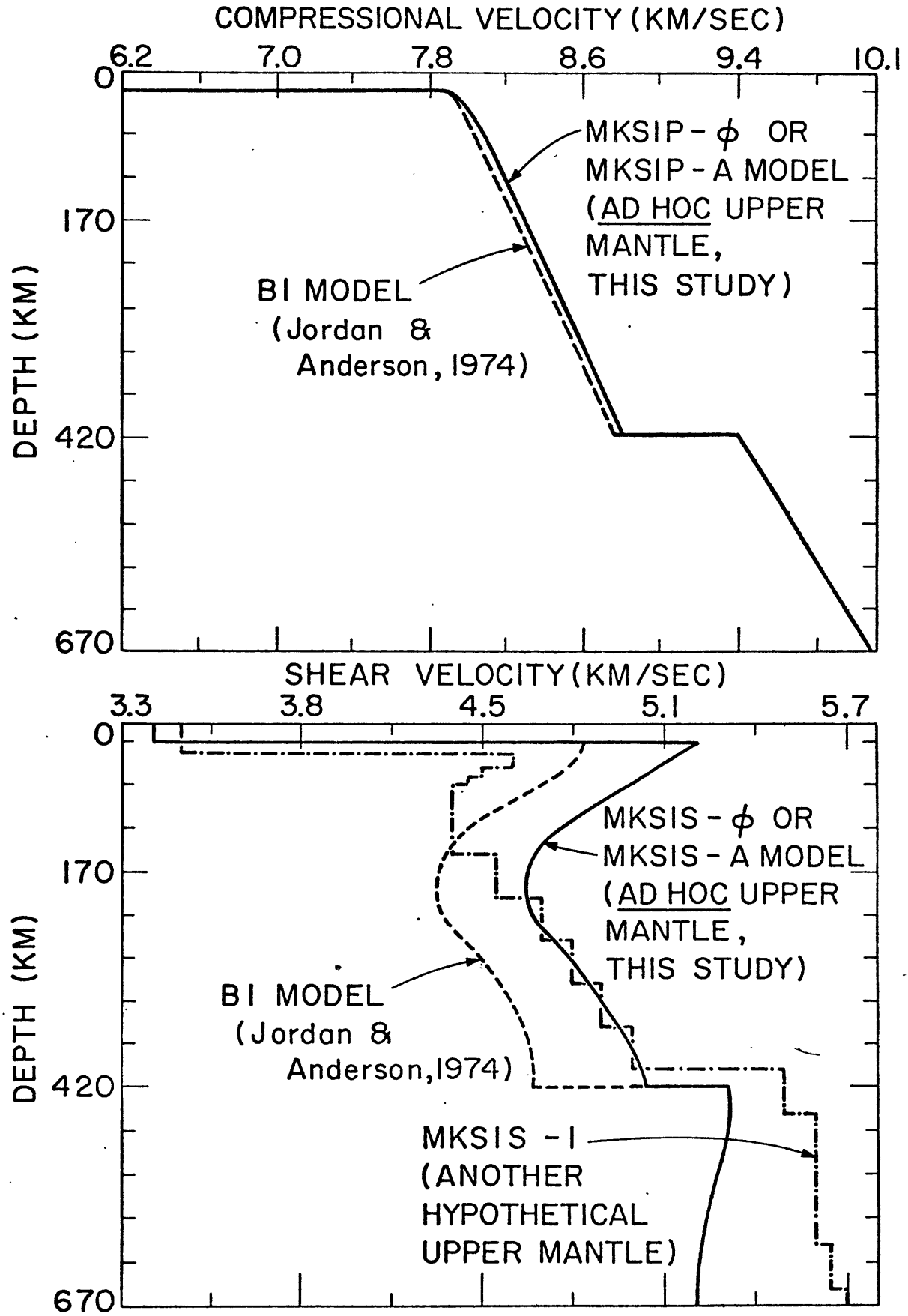
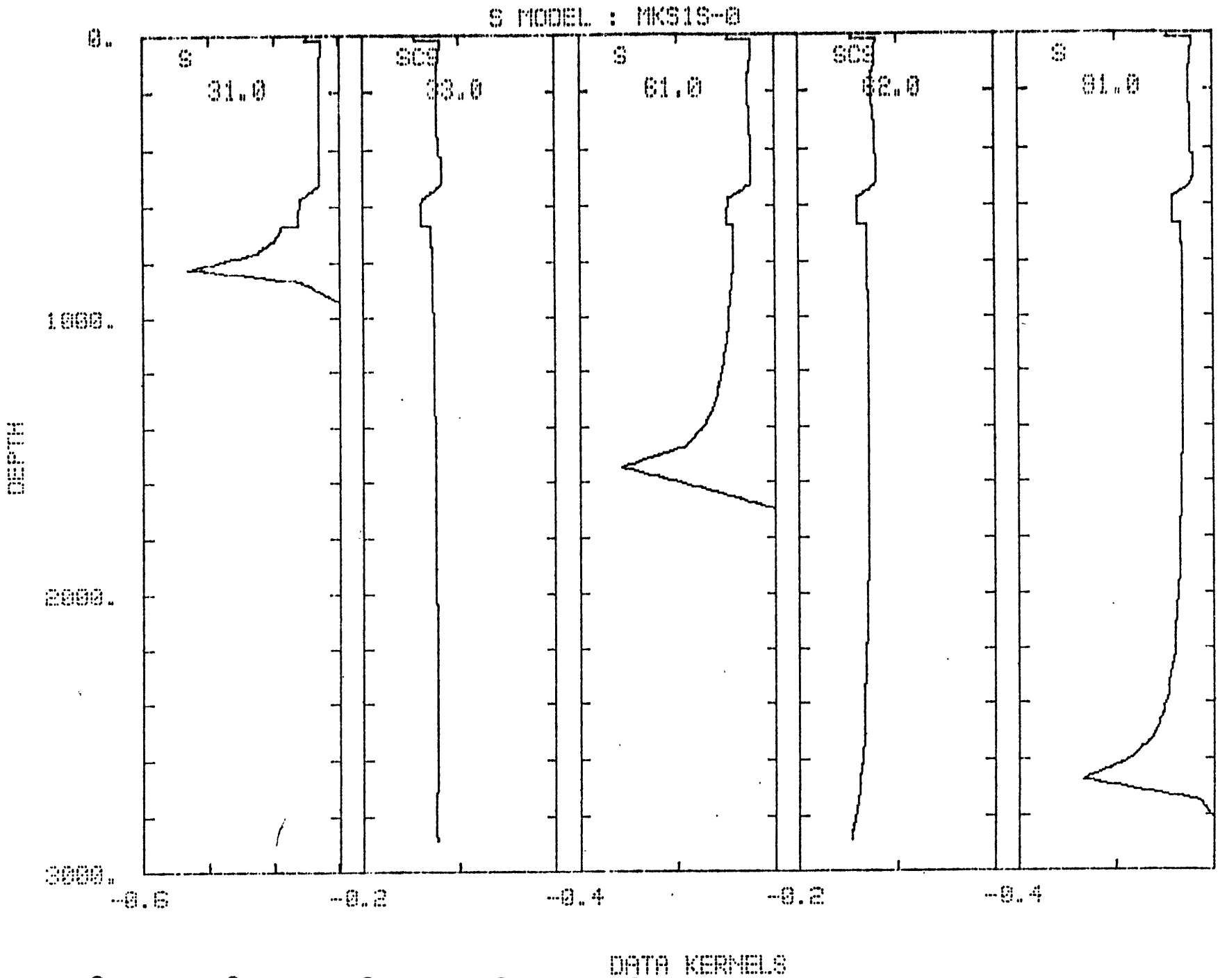

COMPRESSIONAL VELOCITY (KM/SEC)
6.2
7.0
7.8
8.6
9.4
10.1
0
170
420
670
DEPTH (KM)
MKSIP - φ OR
MKSIP - A MODEL
(AD HOC UPPER
MANTLE,
THIS STUDY)
BI MODEL
(Jordan &
Anderson, 1974)
SHEAR VELOCITY (KM/SEC)
3.3
3.8
4.5
5.1
5.7
0
170
420
670
DEPTH (KM)
MKSIS - φ OR
MKSIS - A MODEL
(AD HOC UPPER
MANTLE,
THIS STUDY)
BI MODEL
(Jordan &
Anderson, 1974)
MKSIS - I
(ANOTHER
HYPOTHETICAL
UPPER MANTLE)

Fig. 3-5


S MODEL : MKS1S-0
0.
1000.
2000.
3000.
DEPTH
S
31.0
SCS
33.0
S
61.0
SCS
62.0
S
61.0
-0.6
-0.2
-0.4
-0.2
-0.4
DATA KERNELS

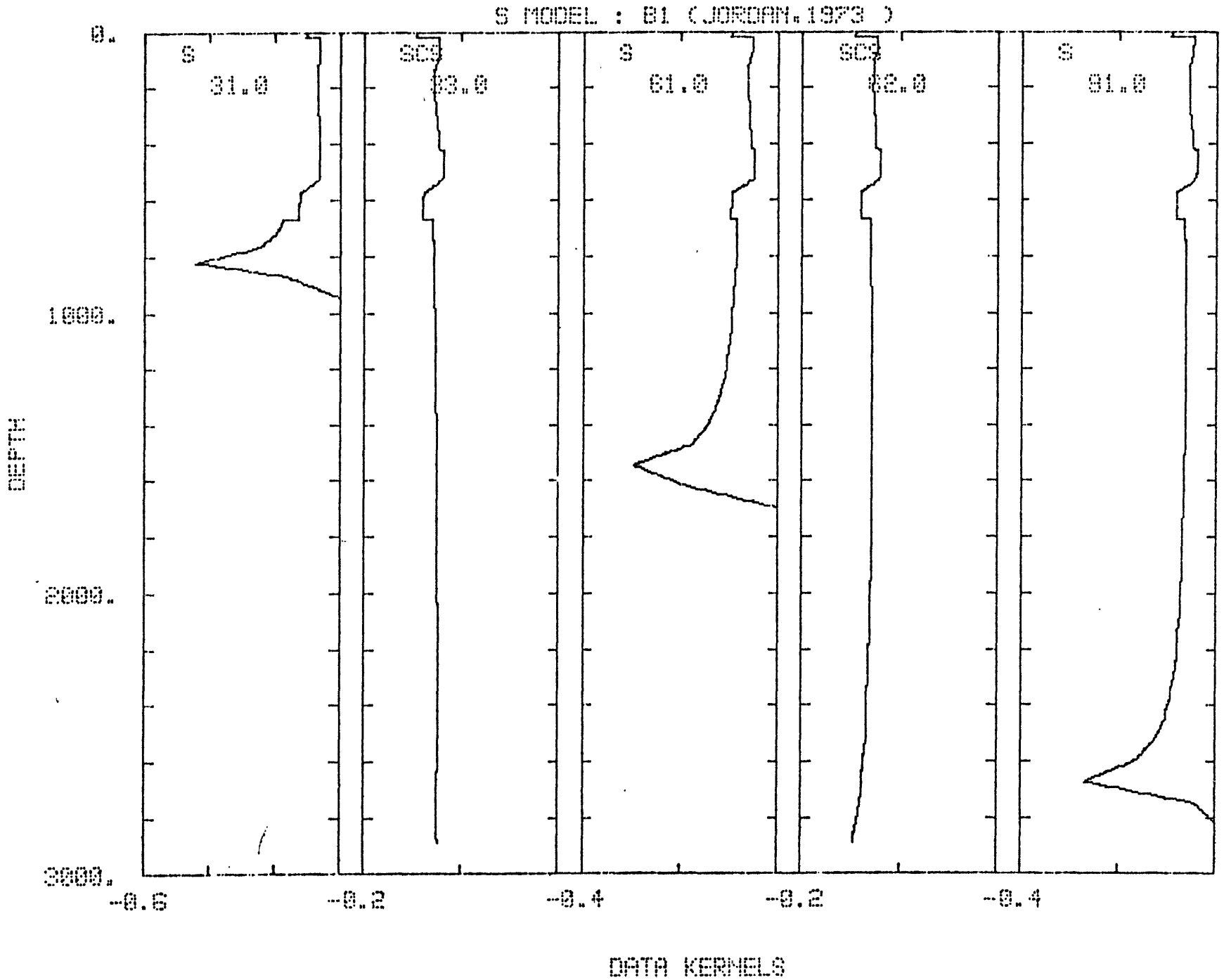
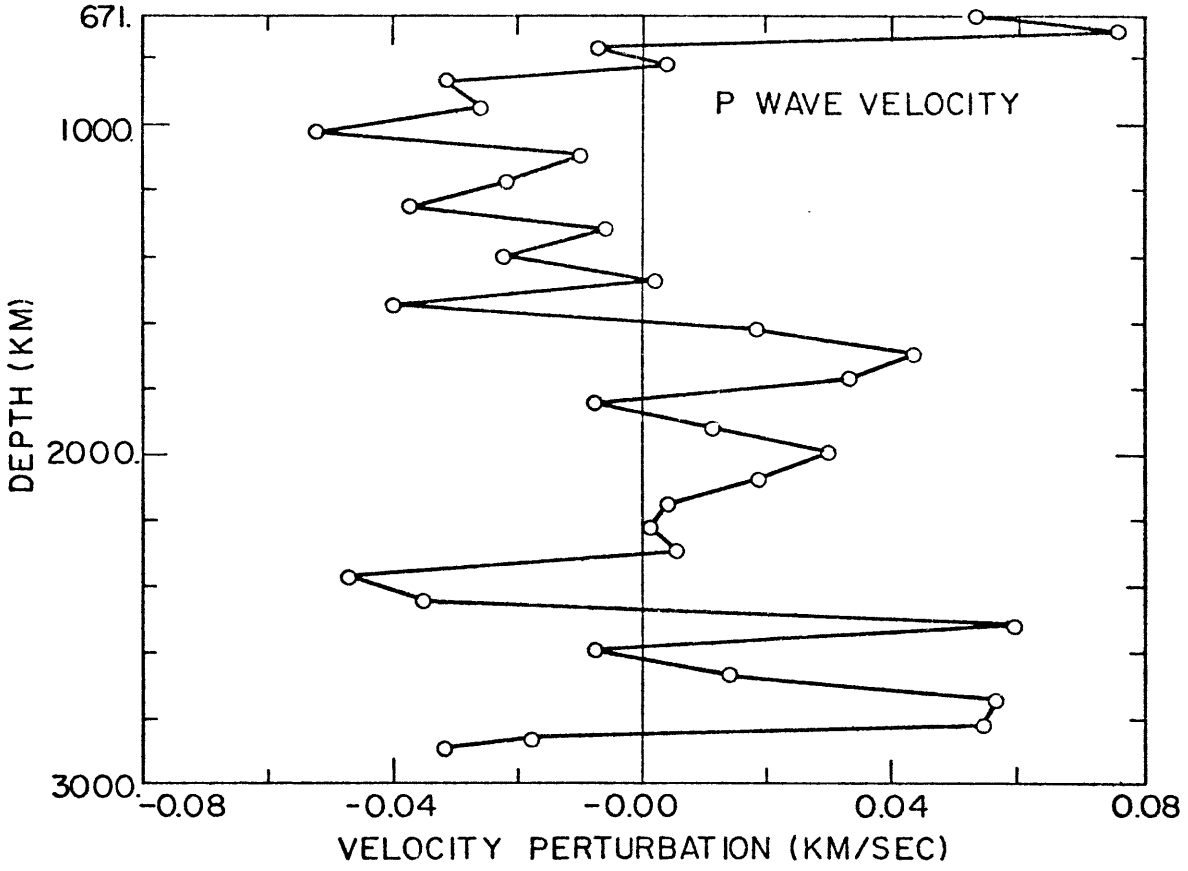

S MODEL : B1 (JORDAN,1973)
0.
1000.
2000.
3000.
DEPTH
S
31.0
SCS
63.0
S
61.0
SCS
92.0
S
91.0
-0.6
-0.2
-0.4
-0.2
-0.4
DATA KERNELS

Fig. 3-7


671.
1000.
2000.
3000.
DEPTH (KM)
P WAVE VELOCITY
-0.08
-0.04
-0.00
0.04
0.08
VELOCITY PERTURBATION (KM/SEC)

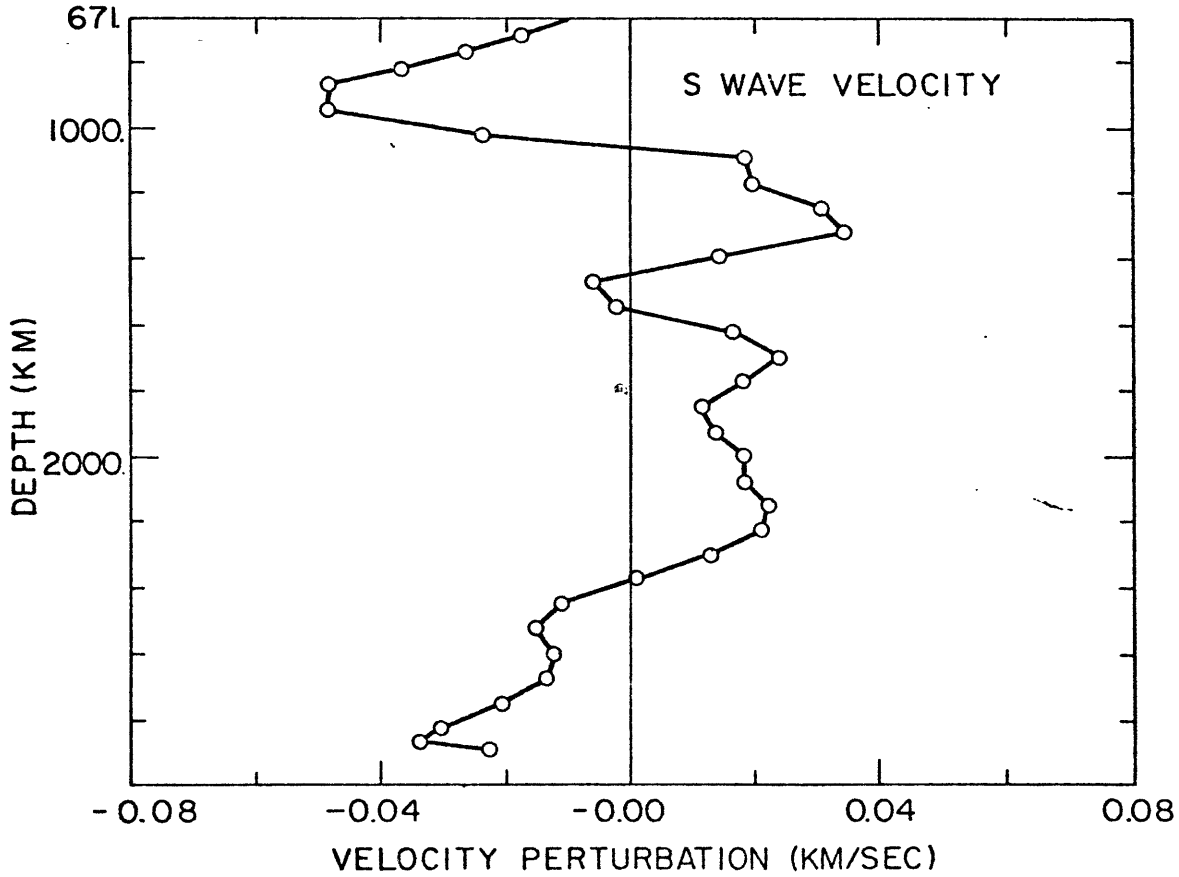

671.
1000.
2000.
DEPTH (KM)
S WAVE VELOCITY
-0.08
-0.04
-0.00
0.04
0.08
VELOCITY PERTURBATION (KM/SEC)

Fig. 3-8

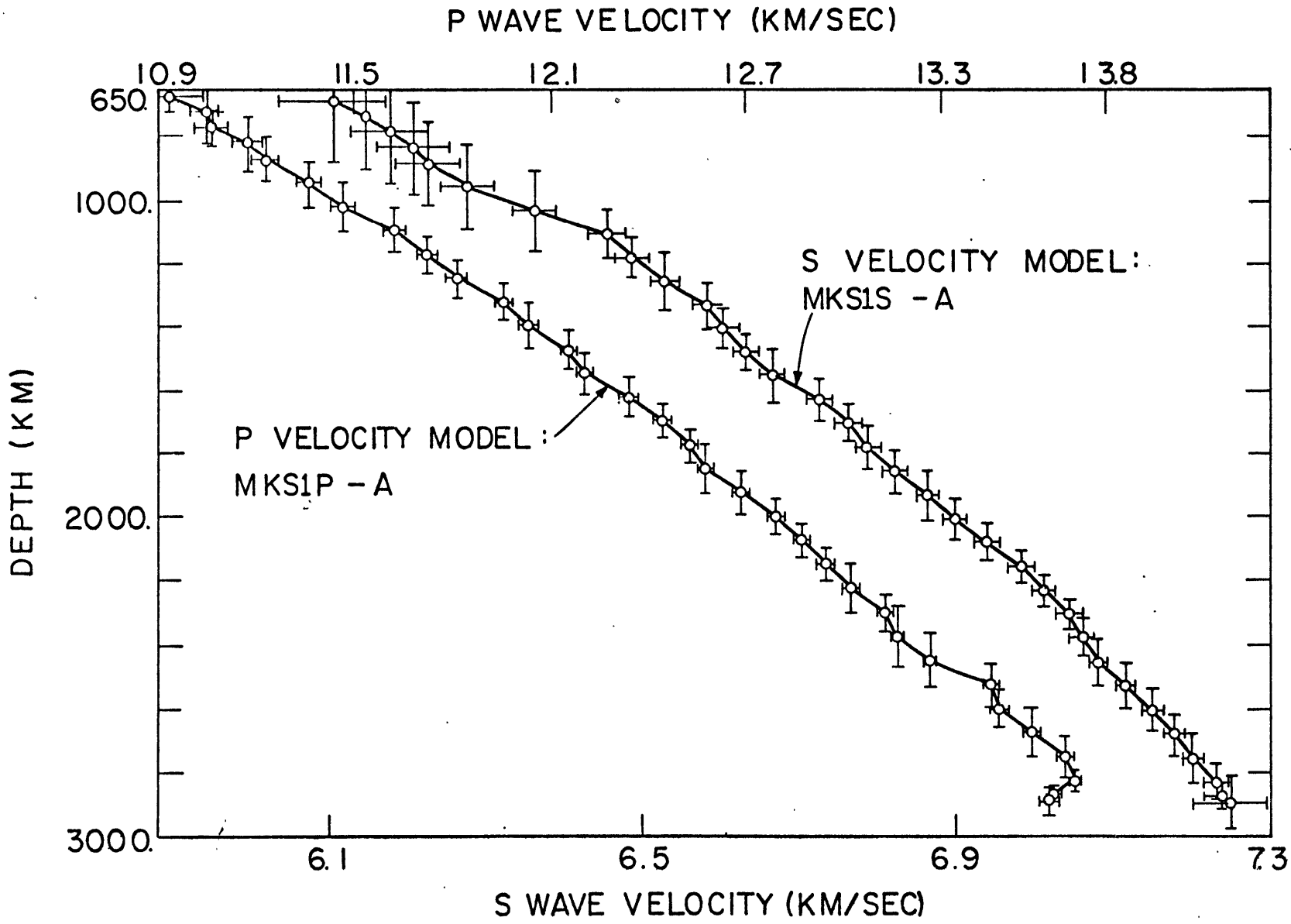

P WAVE VELOCITY (KM/SEC)
10.9
11.5
12.1
12.7
13.3
13.8
650.
1000.
2000.
3000.
DEPTH (KM)
S VELOCITY MODEL:
MKS1S - A
P VELOCITY MODEL:
MKS1P - A
6.1
6.5
6.9
7.3
S WAVE VELOCITY (KM/SEC)

Fig. 3-9

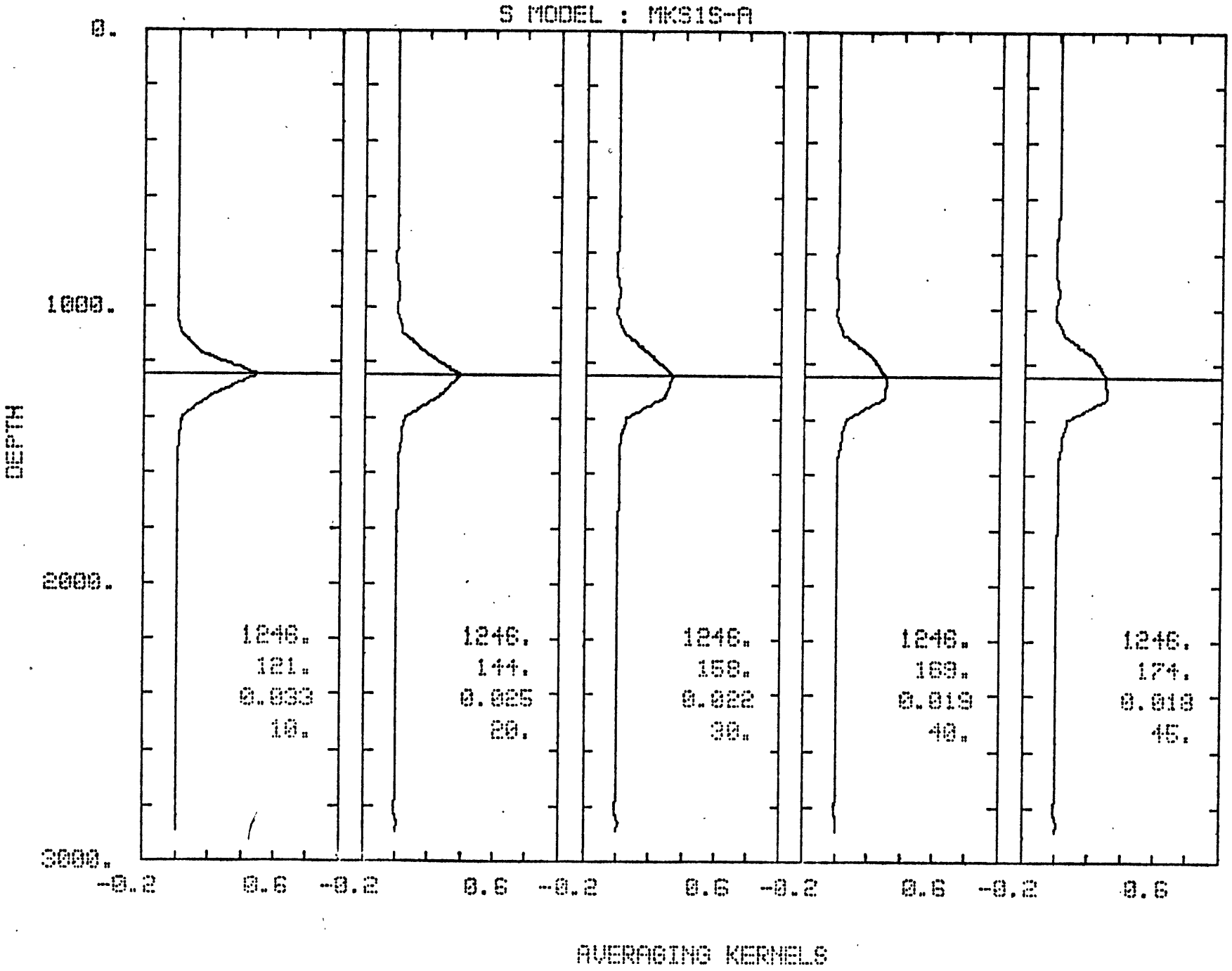

S MODEL : MKS1S-A
0.
1000.
2000.
3000.
DEPTH
1246.
121.
0.033
10.
1246.
144.
0.025
20.
1246.
158.
0.022
30.
1246.
169.
0.019
40.
1246.
174.
0.018
45.
-0.2
0.6
-0.2
0.6
-0.2
0.6
-0.2
0.6
-0.2
0.6
AVERAGING KERNELS

Fig. 2.10

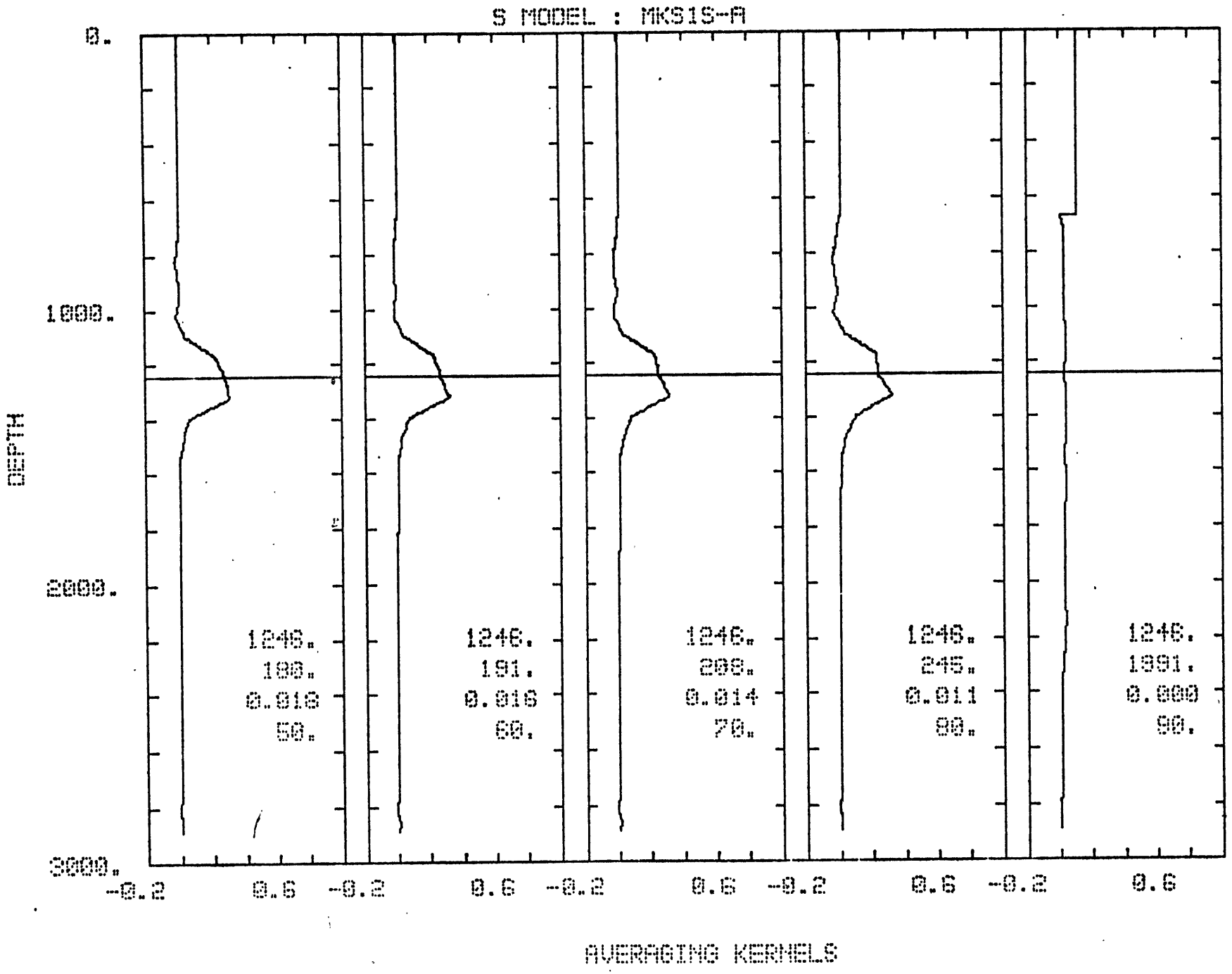

S MODEL : MKS1S-A
0.
1000.
2000.
3000.
DEPTH
1246.
100.
0.010
50.
1246.
191.
0.010
60.
1246.
208.
0.014
70.
1246.
245.
0.011
80.
1246.
1991.
0.000
90.
-0.2
0.6
-0.2
0.6
-0.2
0.6
-0.2
0.6
-0.2
0.6
AVERAGING KERNELS

Fig. 3-10 (cont)

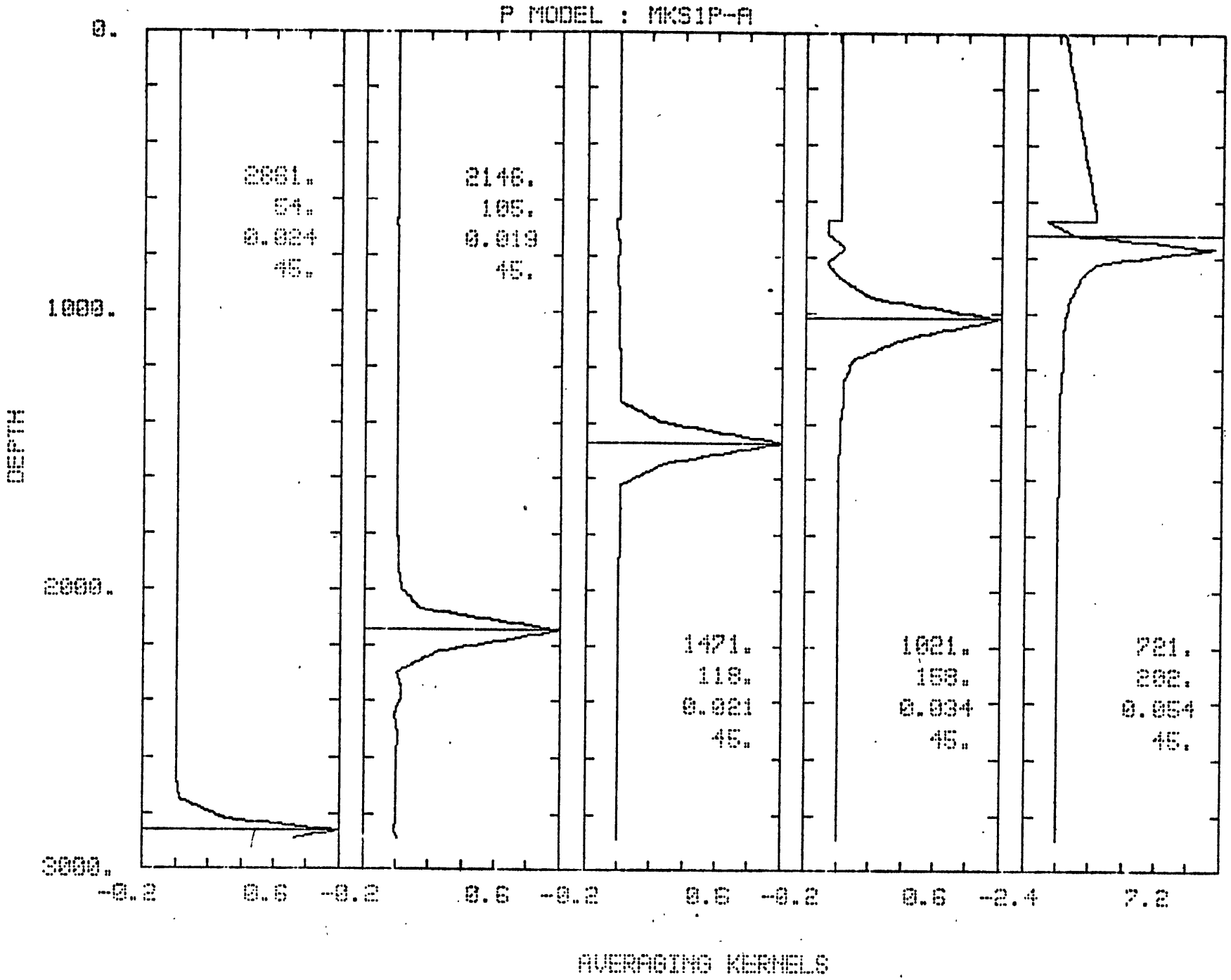

P MODEL : MKS1P-A
0.
1000.
2000.
3000.
DEPTH
2661.
54.
0.024
45.
2146.
105.
0.019
45.
1471.
118.
0.021
45.
1021.
158.
0.034
45.
721.
282.
0.054
45.
-0.2
0.6
-0.2
0.6
-0.2
0.6
-0.2
0.6
-2.4
7.2
AVERAGING KERNELS

Fig. 3-11

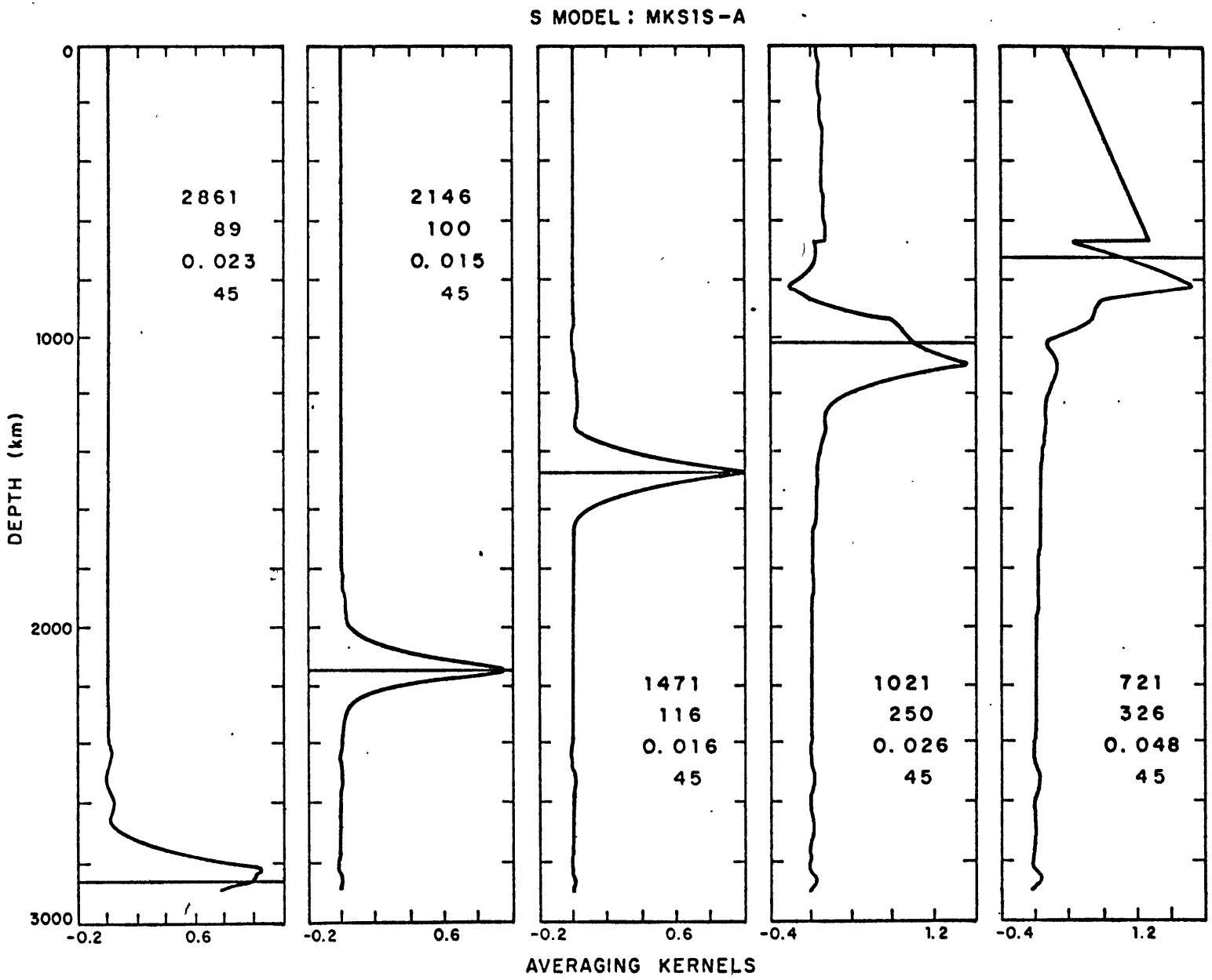

S MODEL : MKS1S-A
0
1000
2000
3000
DEPTH (km)
2861
89
0.023
45
2146
100
0.015
45
1471
116
0.016
45
1021
250
0.026
45
721
326
0.048
45
-0.2
0.6
-0.2
0.6
-0.2
0.6
-0.4
1.2
-0.4
1.2
AVERAGING KERNELS

Fig. 3-12

P MODEL : MKS1P-A

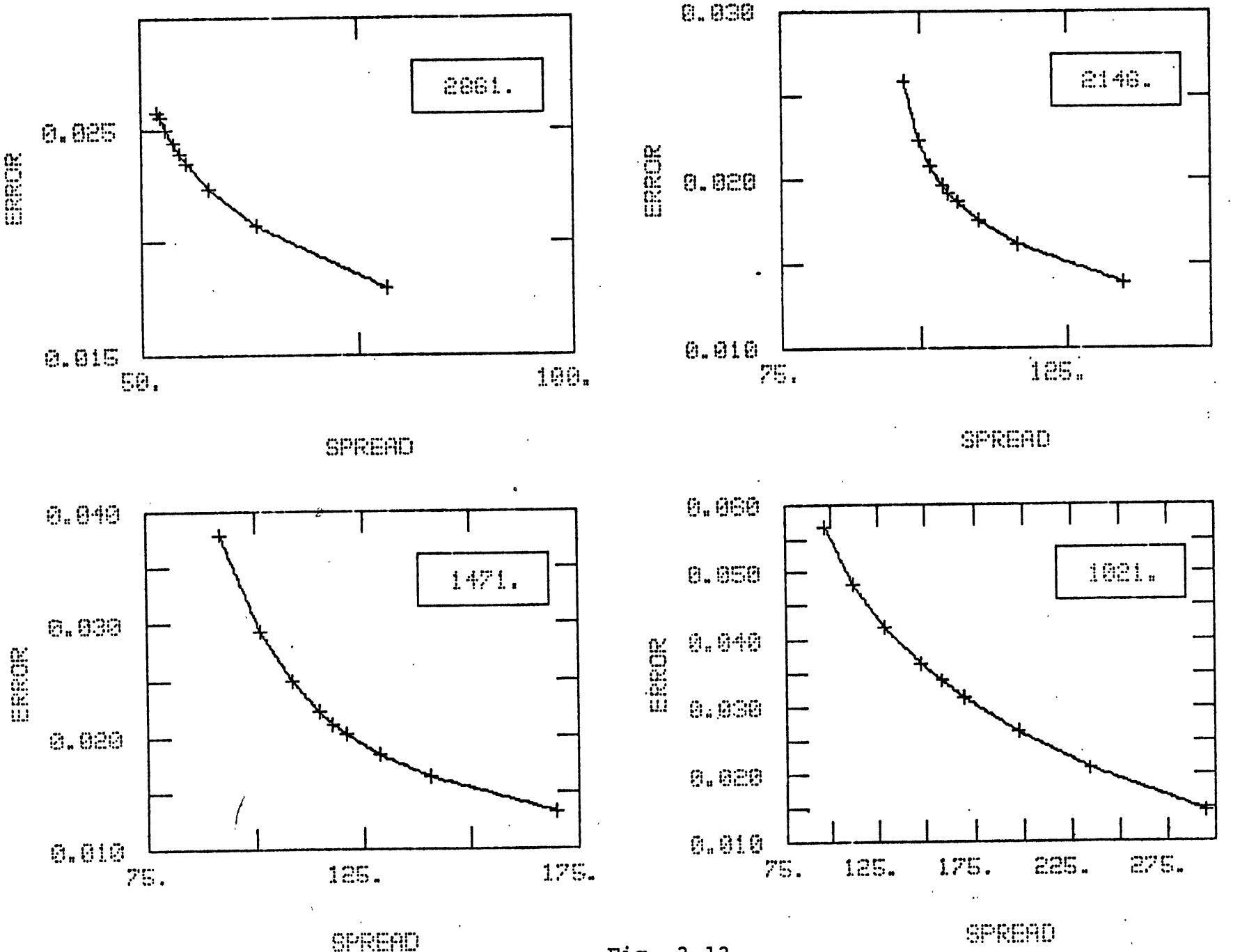


Fig. 3-13

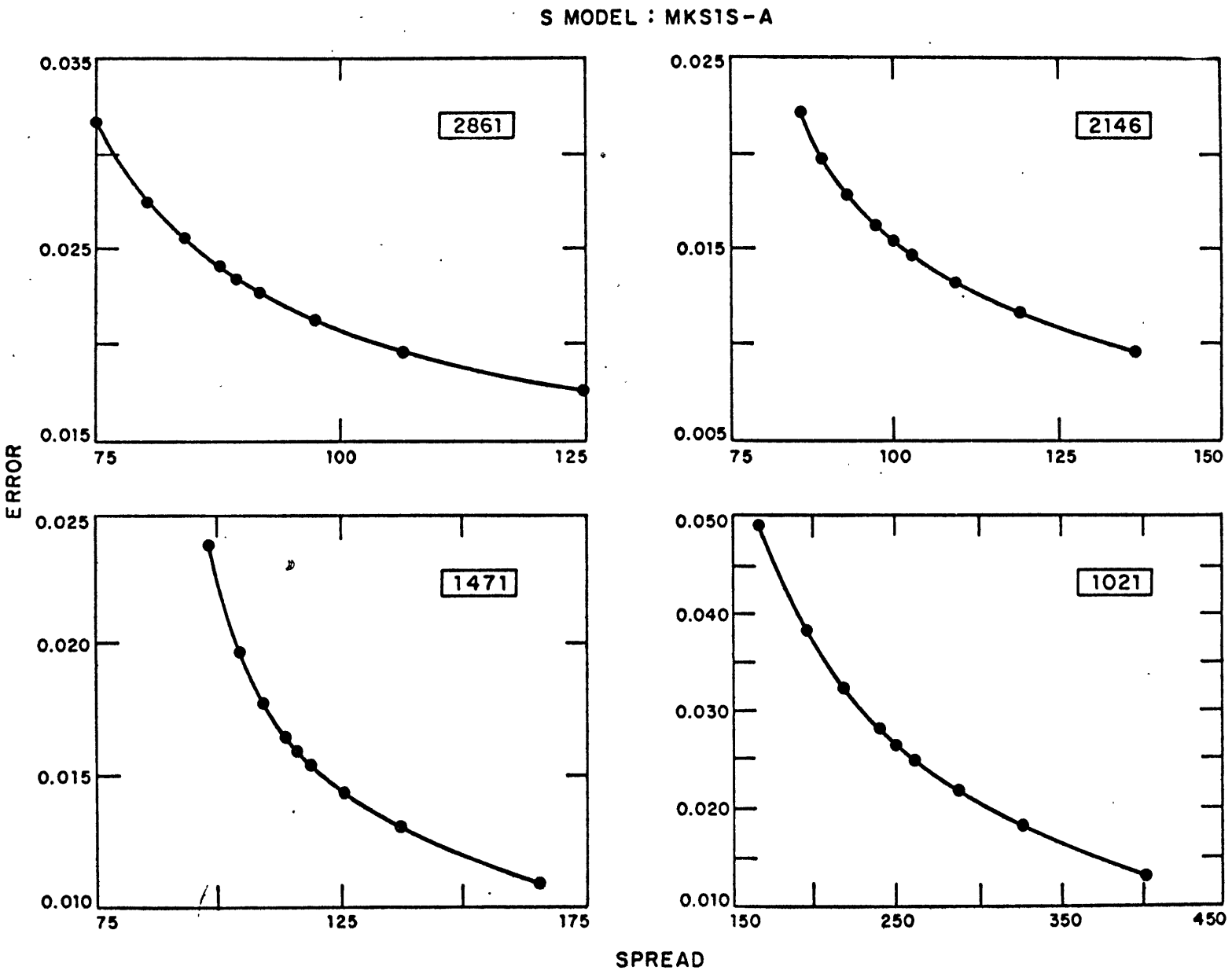

S MODEL : MKS1S-A
ERROR
SPREAD
2861
2146
1471
1021
0.035
0.025
0.015
0.025
0.015
0.005
0.025
0.020
0.015
0.010
0.050
0.040
0.030
0.020
0.010
75
100
125
150
175
250
350
450

Fig. 3-14

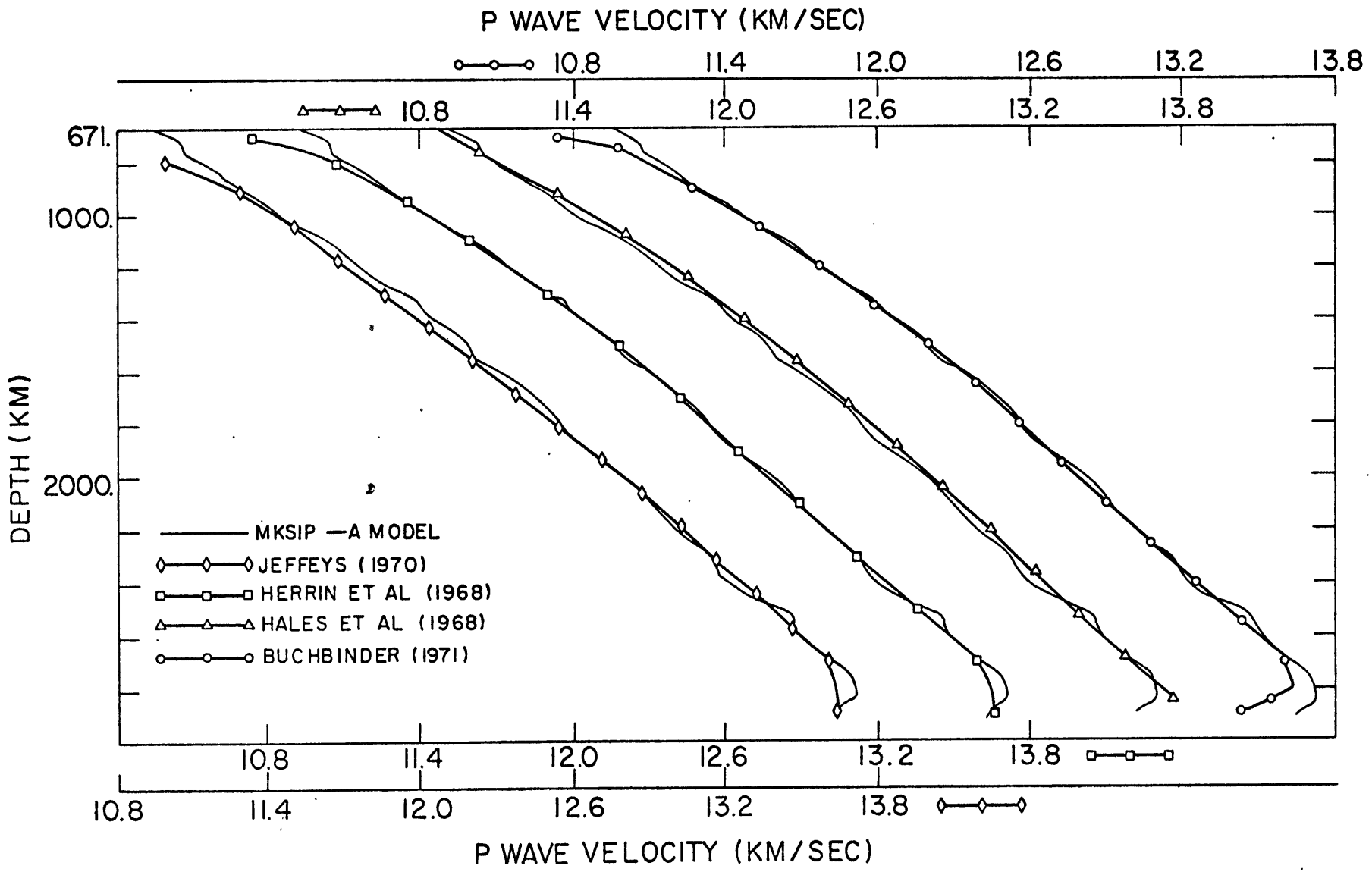

P WAVE VELOCITY (KM/SEC)
10.8
11.4
12.0
12.6
13.2
13.8
671.
1000.
2000.
DEPTH (KM)
MKSIP —A MODEL
JEFFEYS (1970)
HERRIN ET AL (1968)
HALES ET AL (1968)
BUCHBINDER (1971)
P WAVE VELOCITY (KM/SEC)

Fig. 3-15

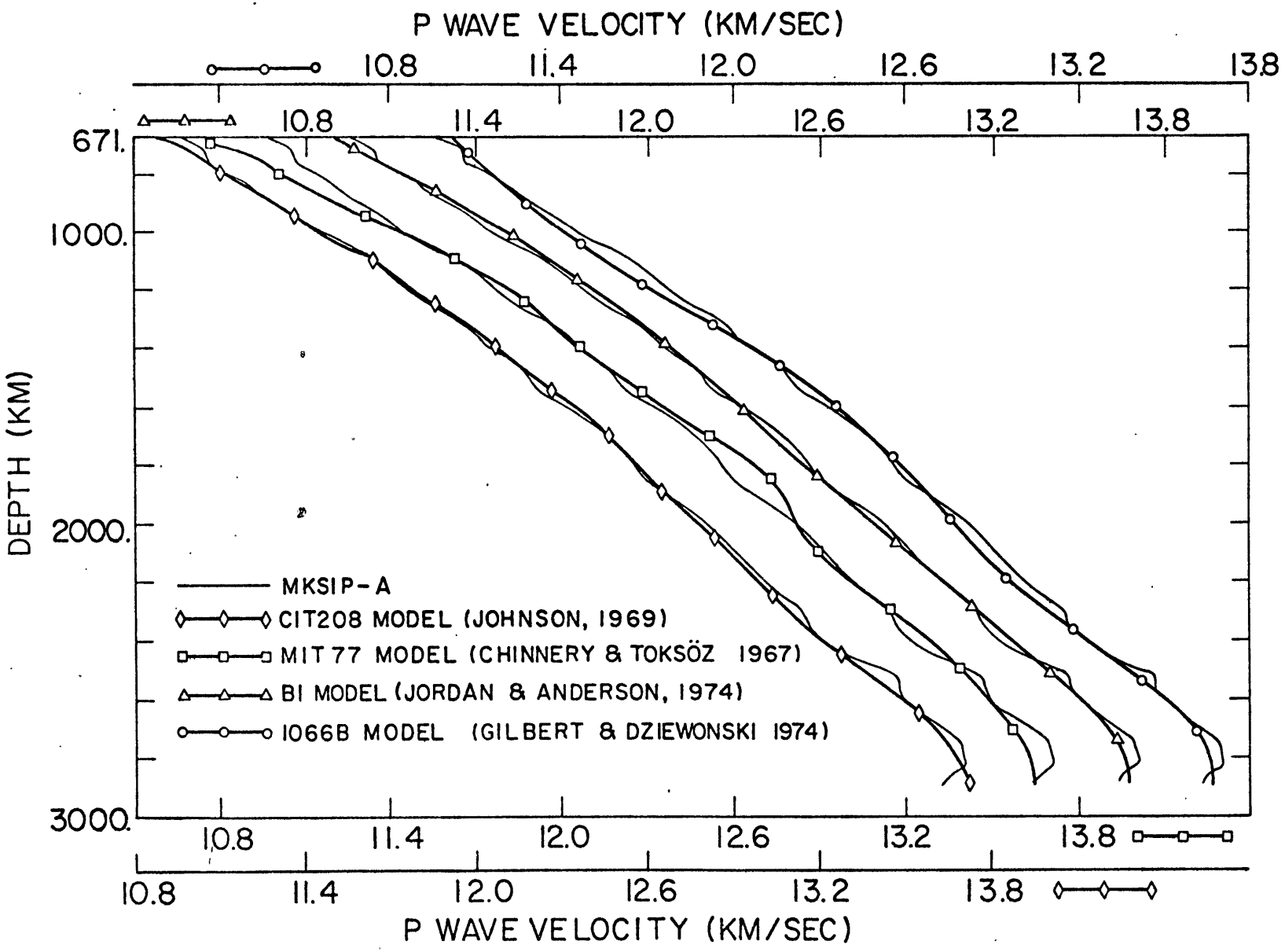

P WAVE VELOCITY (KM/SEC)
10.8
11.4
12.0
12.6
13.2
13.8
671.
1000.
2000.
3000.
DEPTH (KM)
MKSIP-A
CIT208 MODEL (JOHNSON, 1969)
MIT 77 MODEL (CHINNERY & TOKSÖZ 1967)
BI MODEL (JORDAN & ANDERSON, 1974)
1066B MODEL (GILBERT & DZIEWONSKI 1974)
P WAVE VELOCITY (KM/SEC)

Fig. 3-16

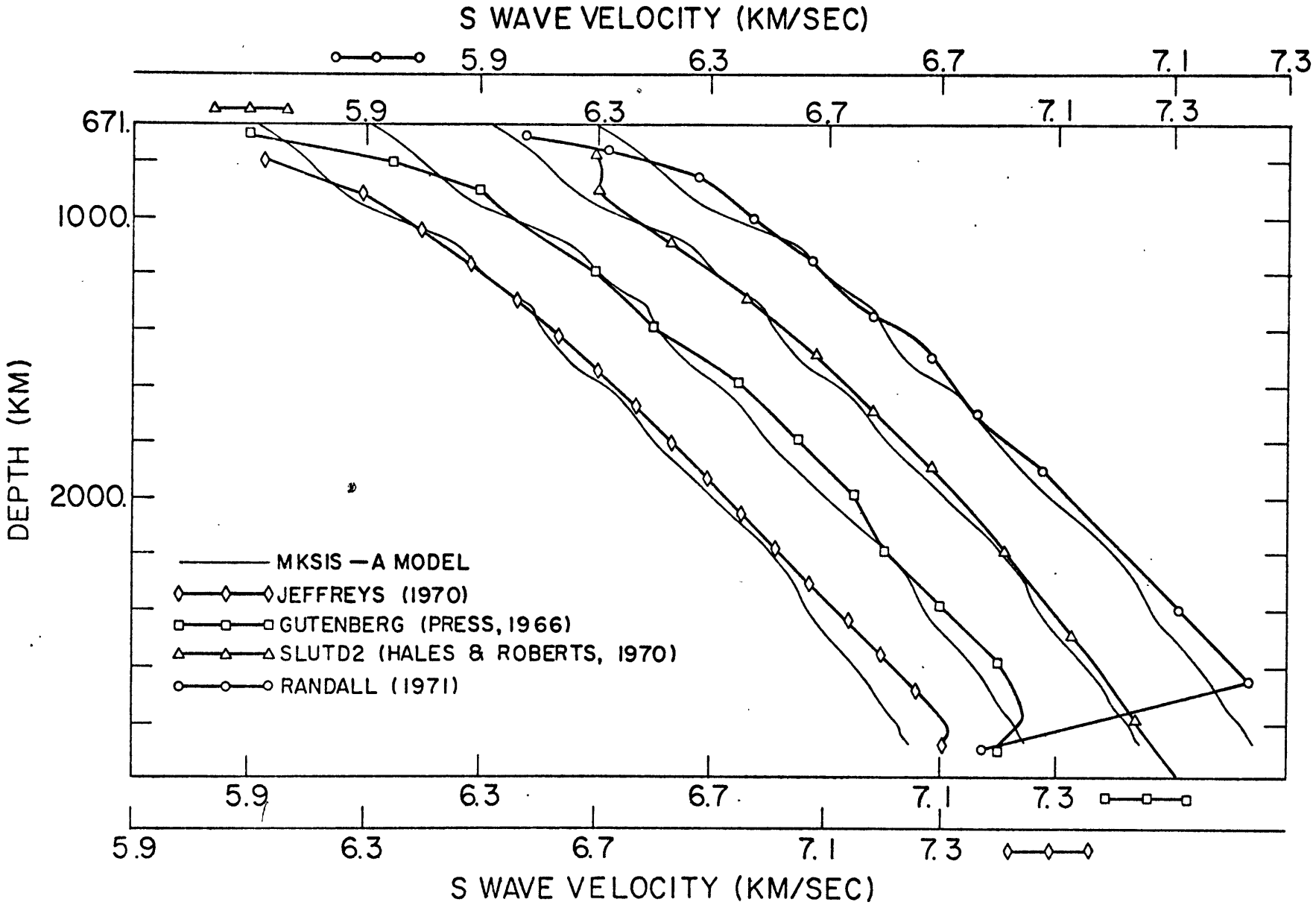

S WAVE VELOCITY (KM/SEC)
5.9
6.3
6.7
7.1
7.3
671.
1000.
2000.
DEPTH (KM)
MKSIS — A MODEL
JEFFREYS (1970)
GUTENBERG (PRESS, 1966)
SLUTD2 (HALES & ROBERTS, 1970)
RANDALL (1971)
S WAVE VELOCITY (KM/SEC)

Fig. 3-17

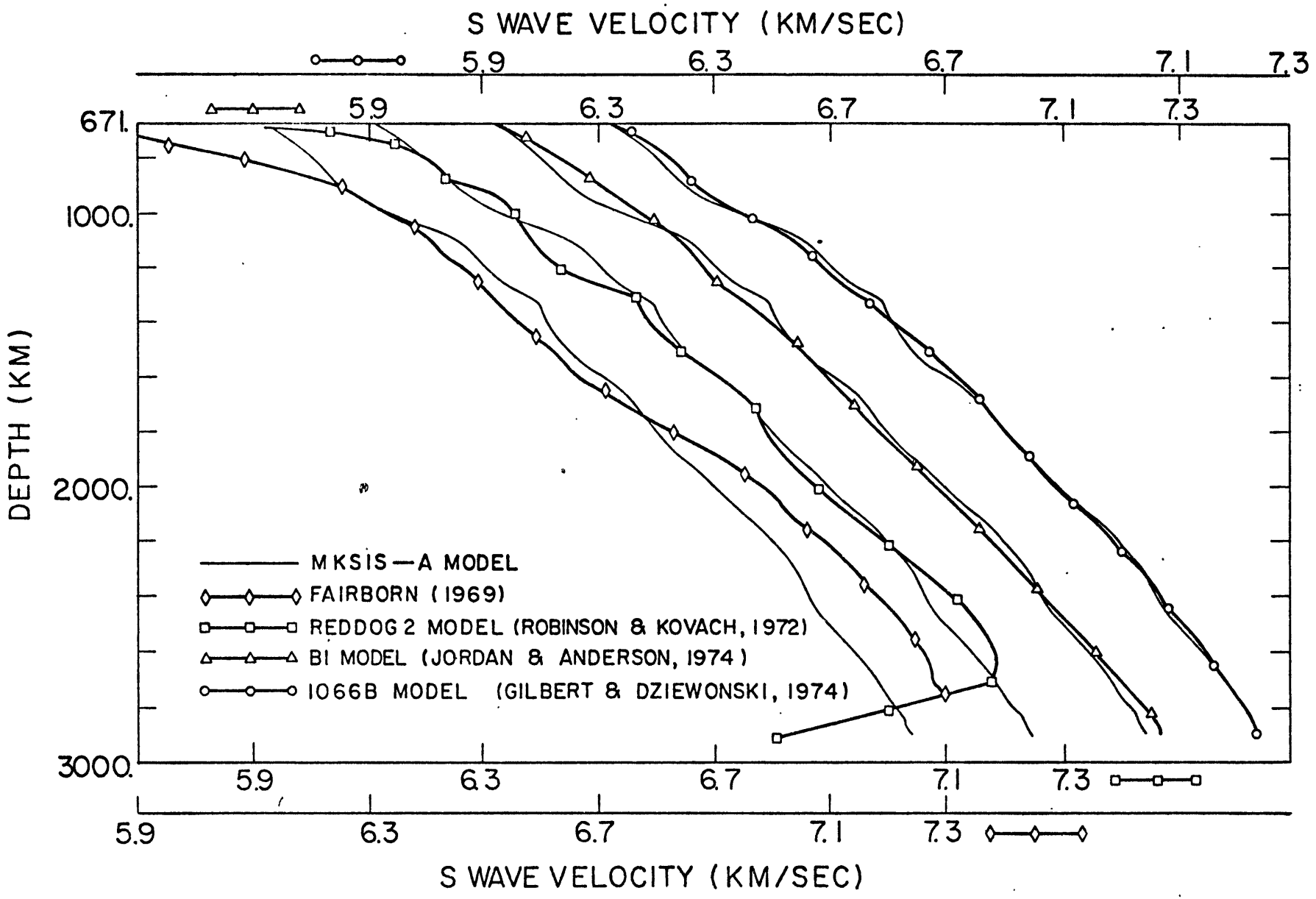
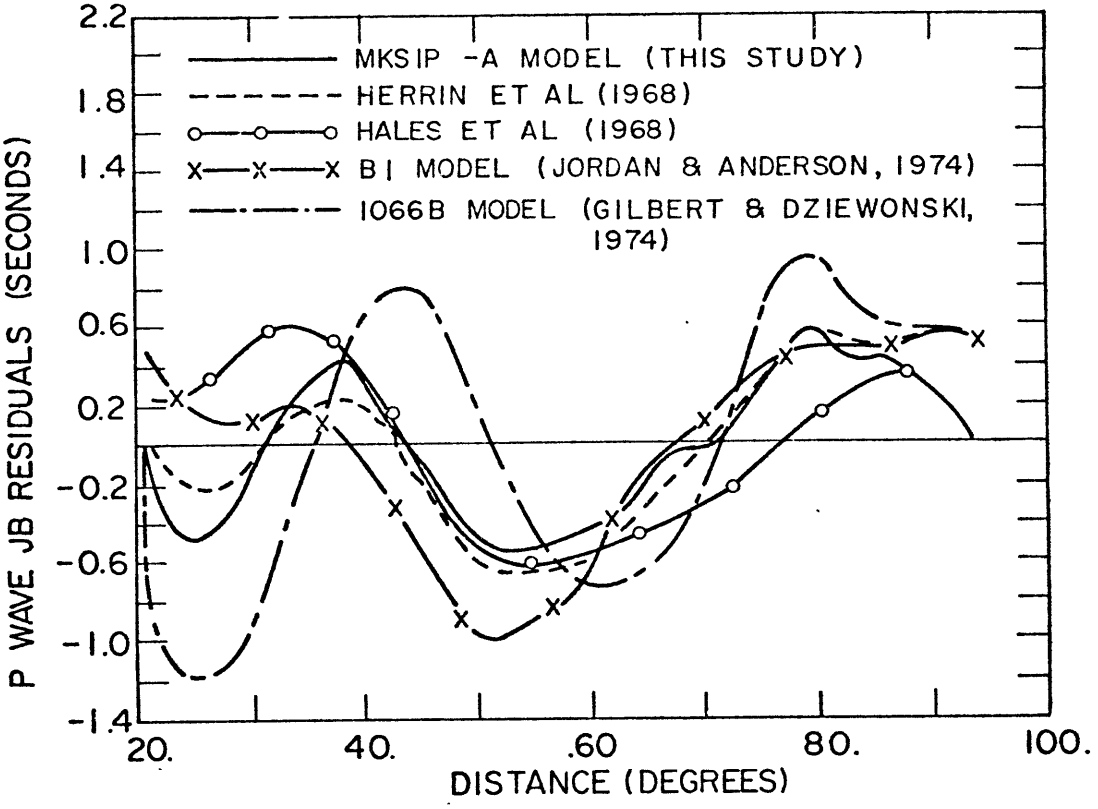

S WAVE VELOCITY (KM/SEC)
5.9
6.3
6.7
7.1
7.3
671.
1000.
2000.
3000.
DEPTH (KM)
MKSIS—A MODEL
FAIRBORN (1969)
REDDOG 2 MODEL (ROBINSON & KOVACH, 1972)
BI MODEL (JORDAN & ANDERSON, 1974)
1066B MODEL (GILBERT & DZIEWONSKI, 1974)
S WAVE VELOCITY (KM/SEC)

Fig. 3-18


MKSIP -A MODEL (THIS STUDY)
HERRIN ET AL (1968)
HALES ET AL (1968)
BI MODEL (JORDAN & ANDERSON, 1974)
1066B MODEL (GILBERT & DZIEWONSKI, 1974)
P WAVE JB RESIDUALS (SECONDS)
2.2
1.8
1.4
1.0
0.6
0.2
-0.2
-0.6
-1.0
-1.4
20.
40.
60.
80.
100.
DISTANCE (DEGREES)

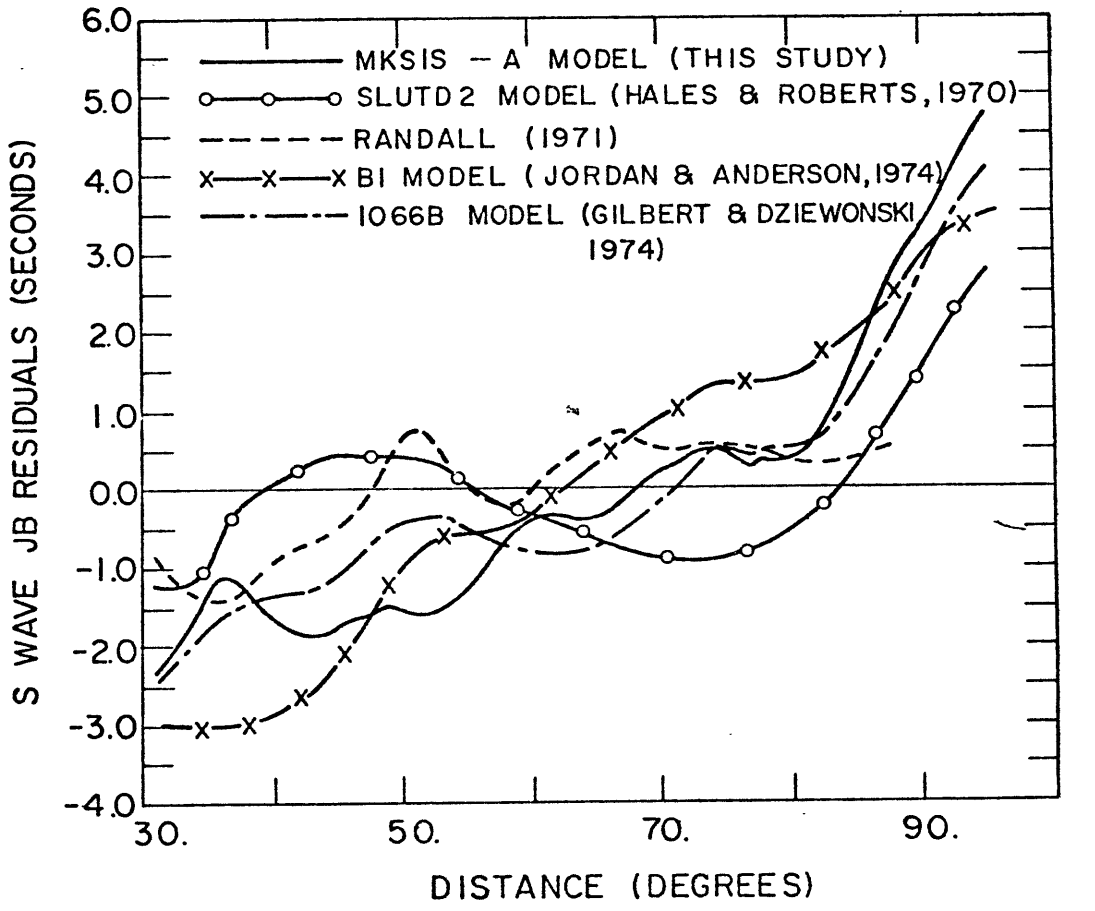
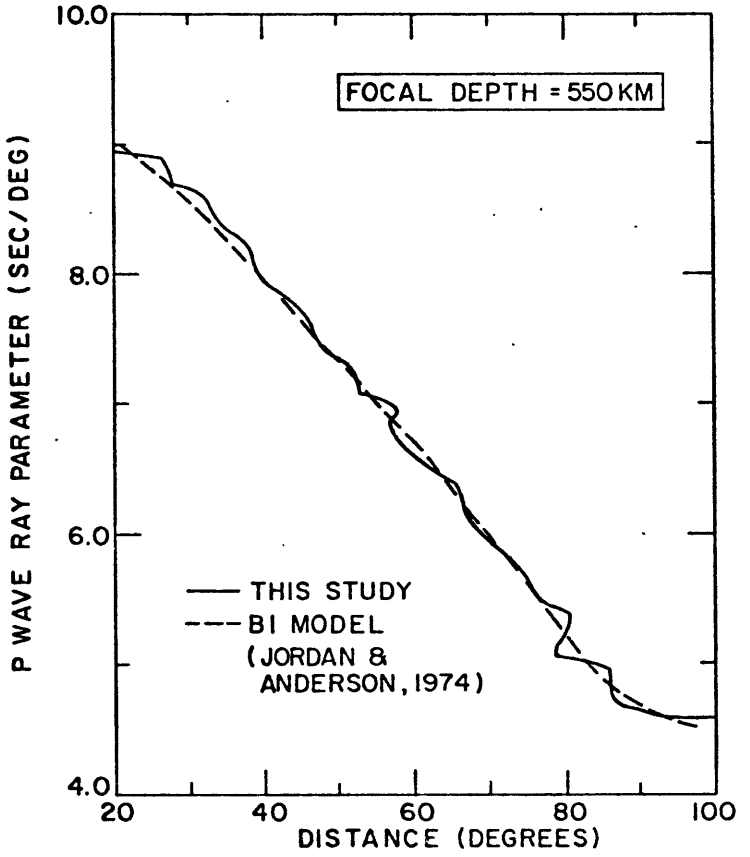

MKSIS - A MODEL (THIS STUDY)
SLUTD2 MODEL (HALES & ROBERTS, 1970)
RANDALL (1971)
BI MODEL (JORDAN & ANDERSON, 1974)
1066B MODEL (GILBERT & DZIEWONSKI, 1974)
S WAVE JB RESIDUALS (SECONDS)
6.0
5.0
4.0
3.0
2.0
1.0
0.0
-1.0
-2.0
-3.0
-4.0
30.
50.
70.
90.
DISTANCE (DEGREES)

Fig. 3-19A


10.0
8.0
6.0
4.0
FOCAL DEPTH = 550 KM
P WAVE RAY PARAMETER (SEC/DEG)
THIS STUDY
BI MODEL
(JORDAN & ANDERSON, 1974)
20
40
60
80
100
DISTANCE (DEGREES)

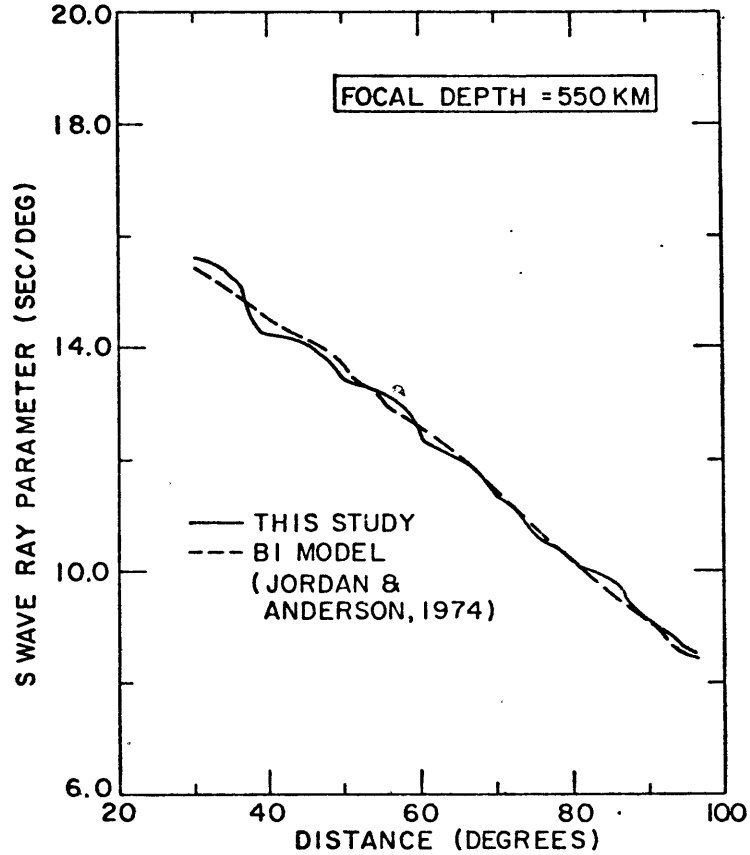

20.0
18.0
14.0
10.0
6.0
FOCAL DEPTH = 550 KM
S WAVE RAY PARAMETER (SEC/DEG)
THIS STUDY
BI MODEL
(JORDAN & ANDERSON, 1974)
20
40
60
80
100
DISTANCE (DEGREES)

Fig. 3-19B

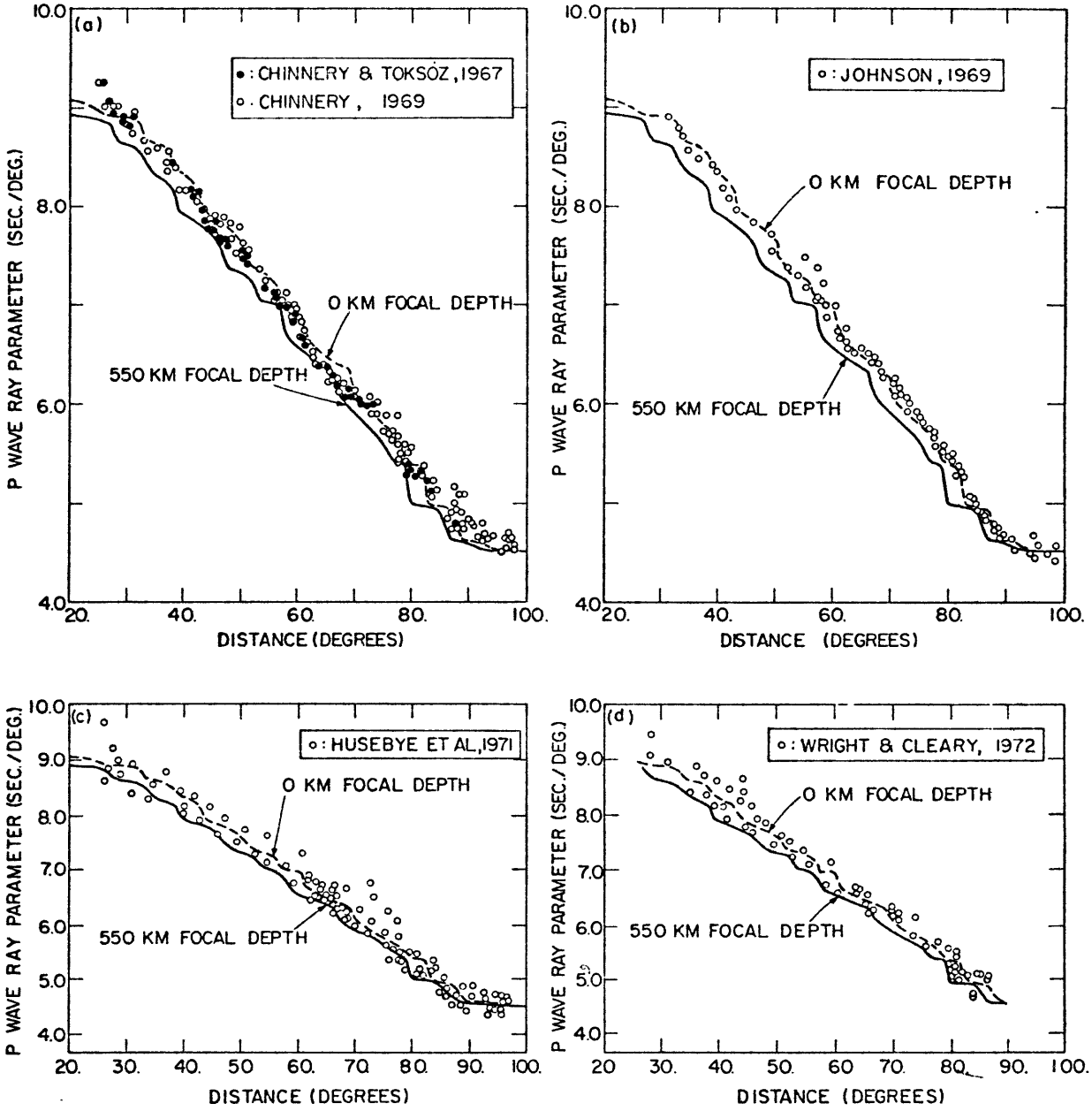

(a)
•: CHINNERY & TOKSÓZ, 1967
○: CHINNERY, 1969
0 KM FOCAL DEPTH
550 KM FOCAL DEPTH
P WAVE RAY PARAMETER (SEC./DEG.)
DISTANCE (DEGREES)
(b)
○: JOHNSON, 1969
0 KM FOCAL DEPTH
550 KM FOCAL DEPTH
P WAVE RAY PARAMETER (SEC./DEG.)
DISTANCE (DEGREES)
(c)
○: HUSEBYE ET AL, 1971
0 KM FOCAL DEPTH
550 KM FOCAL DEPTH
P WAVE RAY PARAMETER (SEC./DEG.)
DISTANCE (DEGREES)
(d)
○: WRIGHT & CLEARY, 1972
0 KM FOCAL DEPTH
550 KM FOCAL DEPTH
P WAVE RAY PARAMETER (SEC./DEG.)
DISTANCE (DEGREES)

Fig. 3-20

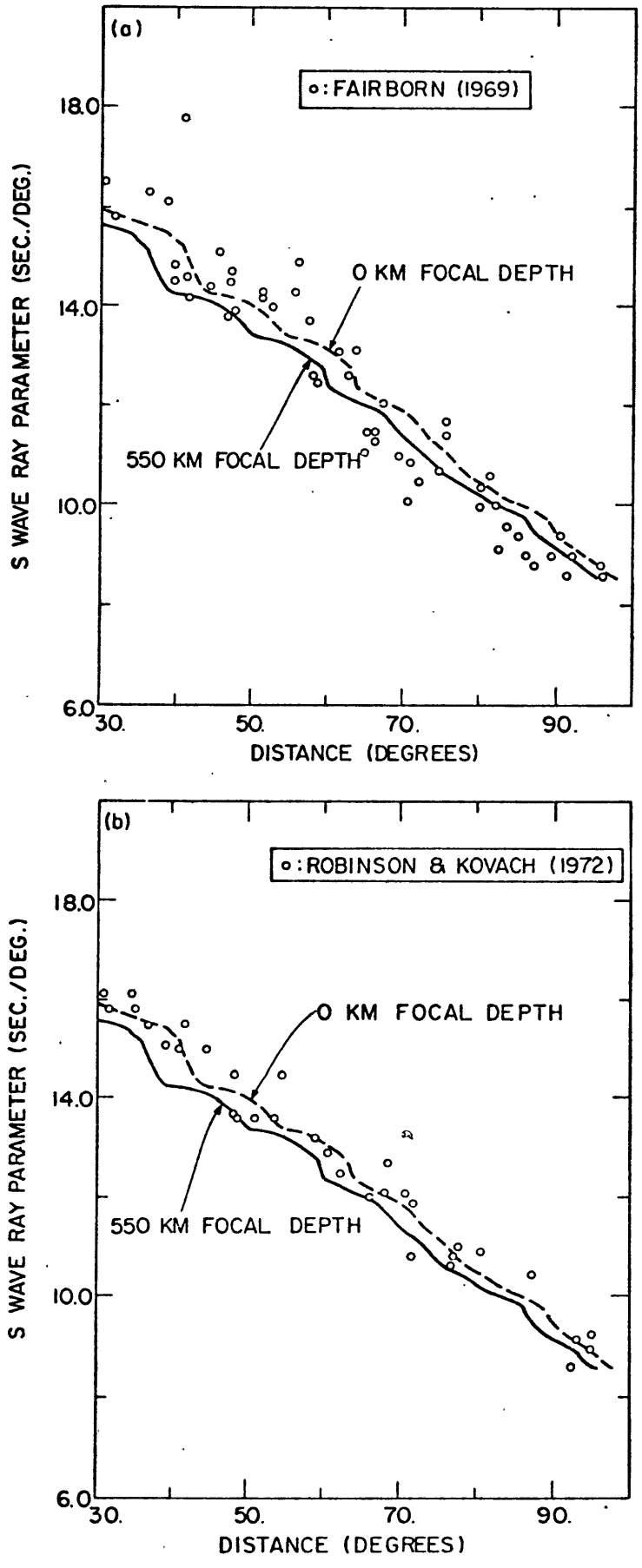

(a)
o: FAIRBORN (1969)
0 KM FOCAL DEPTH
550 KM FOCAL DEPTH
S WAVE RAY PARAMETER (SEC./DEG.)
18.0
14.0
10.0
6.0
30.
50.
70.
90.
DISTANCE (DEGREES)
(b)
o: ROBINSON & KOVACH (1972)
0 KM FOCAL DEPTH
550 KM FOCAL DEPTH
S WAVE RAY PARAMETER (SEC./DEG.)
18.0
14.0
10.0
6.0
30.
50.
70.
90.
DISTANCE (DEGREES)

Fig. 3-21

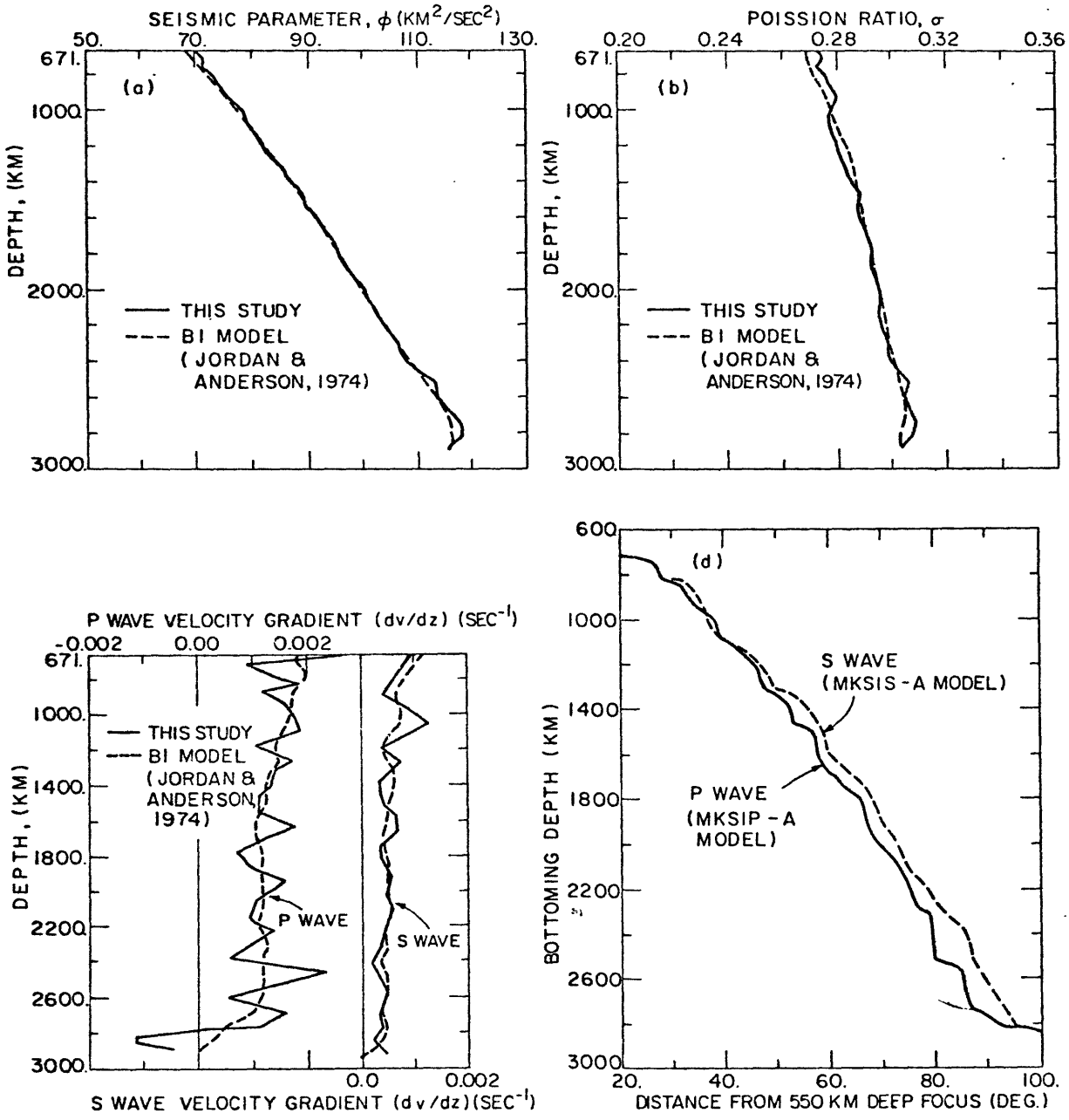

SEISMIC PARAMETER, ϕ (KM^2/SEC^2)
50.
70.
90.
110.
130.
671.
1000.
2000.
3000.
DEPTH, (KM)
(a)
THIS STUDY
BI MODEL
(JORDAN & ANDERSON, 1974)
POISSION RATIO, σ
0.20
0.24
0.28
0.32
0.36
(b)
P WAVE VELOCITY GRADIENT (dv/dz) (SEC^{-1})
-0.002
0.00
0.002
1400.
1800.
2200.
2600.
P WAVE
S WAVE
0.0
S WAVE VELOCITY GRADIENT (dv/dz)(SEC^{-1})
600
(d)
BOTTOMING DEPTH (KM)
S WAVE
(MKSIS-A MODEL)
P WAVE
(MKSIP-A MODEL)
20.
40.
60.
80.
100.
DISTANCE FROM 550 KM DEEP FOCUS (DEG.)

Fig. 3-22

CHAPTER 4

INVESTIGATION OF ELASTIC AND ANELASTIC PROPERTIES OF THE EARTH'S MANTLE BY USE OF DEEP FOCUS EARTHQUAKE AMPLITUDE DATA

Introduction

Seismic wave propagation through the earth's interior can be characterized well by two parameters - one, seismic velocity and the other the dimensionless specific dissipation function (whose inverse is the commonly known quality factor, Q). Body wave amplitudes are controlled by both elastic and anelastic properties of the earth's interior and thereby on one hand can narrow down the range of non-uniqueness in the seismic velocity models inverted from body wave travel time data, and on the other can provide constraints on the Q-model in the frequency range of 0.05 Hz to 1 Hz.

In this chapter we will discuss first the salient features of our short period and long period amplitude data of P and S waves from deep earthquakes. Later we will utilize those features to test our velocity models determined in the previous chapter and also to constrain the Q-models of the lower mantle. Based on our amplitude-data, we will also provide a set of corrections for the determination of body wave magnitudes and show their effect.

4.1 BODY WAVE AMPLITUDE-DISTANCE DATA FOR DEEP FOCUS EARTHQUAKES

Observed deep focus amplitudes of P and S waves in the distance range of 30°-100° were corrected first for various factors including correction for instrument response, radiation pattern at the source and also for the effect of crustal and upper mantle discontinuities and station anomalies (see Chap. 2). In order to study the radial variation in the earth's structure, the $\log_{10}$-amplitude data, as observed on different ray paths, were averaged like travel time data for each 2° cells of distance. To analyze the effects for the frequency dependency as mentioned in Chap. 2, these amplitude data were divided into two groups - short period (with period <3 second) and long period (period >5 second), both groups being normalized to the same level. The average period of our short period amplitude data is 1.5 seconds for P wave and 2.0 seconds for S wave, and the average period of long period data is 9.5 seconds for P and 12.0 seconds for S wave. The average short period and long period amplitudes in each 2° distance cell have been tabulated in Tables 4-1 thru 4-3 respectively for P, SV and SH waves and are shown in Figs. 4-1 thru 4-6.

4.1.1 Characteristic features of deep focus P wave amplitudes

In terms of the number of selected data and ray paths

involved (see Tables 4-1a and 4-1b) short period P wave average amplitude data appear to be better determined than long period data and also show more features (cf. data in Figs. 4-1 and 4-2). Short period amplitudes (Fig. 4-1) have a peak at 30°, followed by a trough at about 60° and another peak at about 75° of epicentral distance. Starting at about 88°, these short period amplitudes start to fall off rapidly and continuously. In contrast to these behaviors, long period amplitudes (Fig. 4-2) are fairly constant up to about 85° of epicentral distance. Signature of trough at 60° and a peak for 75° is present at best vaguely among the long period data. Compared to short period amplitudes, the long period amplitudes begin to fall off at a smaller distance (from about 85°) and at a slower rate.

The difference in the behavior of short period and long period P wave amplitudes up to 80° of epicentral distance is very likely due to variation of Q in the lower mantle (see section 4.4). On the other hand, the difference in the decay rate of short period and long period P wave amplitudes beyond 85° is possibly due to "diffraction" reducing short period amplitudes more than the long period ones (see for example, Phinney and Cathles, 1969; Willey et al., 1970) and/or due to the difference in short period and long period response of the "transition zone" (D" region; Bullen, 1963, p. 238) in the lowest 200 km of the

mantle (see section 4.3).

4.1.2 Comparison of deep focus P wave amplitude data with other studies

There are several amplitude-distance curves for P waves which exist in literature (Carpenter et al., 1967; Cleary, 1967; Evernden and Clark, 1970; Kaula, 1970; Willey et al., 1970; Nuttli, 1972; Veith and Clawson, 1972; Booth et al., 1974) including the classical work by Gutenberg (Richter, 1958). A selected few of them have been compared with our P wave amplitude data (Fig. 4-1 and 4-2) in their respective period range. Because of arbitrary normalization with respect to source size, the baseline of the amplitude-distance curve is also arbitrary. So, we adjusted vertically other published amplitude-distance curves to fit with our data as well as possible. In comparing our data with those curves one should also keep in mind (1) that our data apply to roughly the focal depth of 550 km whereas the published curves were derived either from shallow earthquakes or explosions (with the exception of the Gutenberg curve which is shown for 550 km depth); thereby features in those curves may be displaced towards a little larger epicentral distance by about 3-4 degrees; (2) that with the exception of the amplitude-distance curves given by Carpenter et al. (1967) and Cleary (1967) which were determined from $\log_{10}$-amplitude

data like ours, all other curves were derived from $\log_{10}$ (amplitude/period) data. Allowing for the discrepancy to arise from the above reasons, we find that our short period P wave amplitude data agree best with the amplitude-distance curve of Carpenter et al. (1967) and long period data with that of Nuttli (1972).

It is worth mentioning that our data as shown in Figs. 4-1 and 4-2 are actually the absolute amplitudes of P wave after correcting the observed vertical component P wave amplitudes also for the effect of reflection/transmission at free surface, Moho and 650 km discontinuity (Appendix C). As mentioned in Chap. 2, we introduced these corrections to study properly the amplitudes for ray paths through the lower mantle after removing the anomalous effects of the upper mantle. But, for the comparison of amplitude-distance curves which are conventionally given for the vertical component of P wave amplitudes, it may be more fitting to use similar measurements for deep focus amplitudes. With this end in view, Fig. 4-3 compares the vertical components of our P wave amplitudes with the amplitude-distance curve of Carpenter et al. (1967) for short period data and with that of Nuttli (1972) for long period data. Our amplitude data as shown in this figure were corrected for the usual factors like instrument response, radiation

pattern and event size. The only significant difference between our vertical component P wave amplitude data in Fig. 4-3 and absolute amplitudes in Figs. 4-1 and 4-2 is in the baseline. Vertical component P wave amplitude data fit the curve of Carpenter et al. (1967) and Nuttli (1972) almost the same, or a little better than absolute amplitudes of P wave.

It is worth noting that the amplitude-distance curves of Carpenter et al. (1967) and Nuttli (1972) were determined from explosion data. Signals of teleseismic P waves from explosions are as good as those of deep focus earthquakes and moreover, correction to P wave amplitudes of explosions for the radiation pattern at the source is likely to be not as severe as those from shallow earthquakes which were used in other curves we show in Figs. 4-1 and 4-2. The strong indication of a large peak around epicentral distance of 75° in the short period P wave amplitude data from explosions (Carpenter et al., 1967) which did not have any counterpart in the amplitude data from shallow earthquakes (see for example, Cleary, 1967; Booth et al., 1974), is, however, more or less confirmed from our amplitude data. It is also worth mentioning that the commonly used

amplitude-distance curve of Gutenberg (Richter, 1958) does not satisfy our amplitude data well. For short period data, agreement is good only beyond 70° of epicentral distance. The "peak" in Gutenberg's curve around 60° has a counterpart of "trough" in both short and long period amplitude data of ours. In fact, our long period amplitude data show poorer fit with Gutenberg's curve. The misfit of Gutenberg's curve with recent observation of long period amplitude data has also been noted by Willey et al. (1970) and Nuttli (1972).

4.1.3 Characteristic features of deep focus S wave amplitudes

As seen from Tables 4-2 and 4-3, our deep focus S wave amplitude data, especially the short period ones are very limited in number. This is because short period S waves were not recorded as frequently as long period S waves. Also, in many cases short period S waves were discernible on only one horizontal component of the seismogram and therefore were not used in the present analysis for the reduction of SV and SH components of S wave amplitudes (see Appendix D). As a consequence of the limited sample size, average amplitudes of short period SV and SH components (Fig. 4-4) show more pronounced scattering than those of long period SV and SH components (Fig. 4-5). In order to reduce the

scattering for any possible error in determining the radiation correction (Appendix E), it was preferred to unify the average amplitudes of SV and SH components into average amplitudes of S waves. We used the following relation

$$\left.\begin{aligned} \bar{A}_S &= \sqrt{\bar{A}_{SV}^2 + \bar{A}_{SH}^2} \\ E_S &= \sqrt{\sigma_{SV}^2 + \sigma_{SH}^2} \;/\; \sqrt{N_{SV} + N_{SH}} \end{aligned}\right\} \quad (4.1)$$

where $\bar{A}$ is the mean amplitude in a particular distance cell, σ^2 the variance of the mean amplitude, N the number of data to compute the mean amplitude, and E the standard error in the mean amplitude of S wave. Reduced S wave amplitude data are shown in Fig. 4-6 separately for short period and long period range. From Fig. 4-6, it appears at best that short period S wave amplitudes have a sharp peak around 40°, are fairly constant between 55-75° and have a relative peak around 80°. Beyond 85°, there are ambiguous signs for a fall off in the amplitudes. Long period S wave amplitudes on the other hand also show a peak around 40° and between 50°-80° they decay slowly but beyond about 80°, fall off in the amplitudes is relatively fast. The large peak in S wave amplitudes around 80° found from short period data is practically missing among the

long period data. This discrepancy may very well be related to the Q-model (see section 4.4). The well established trend in the fall off of long period S wave amplitudes beyond 80°, is possibly due to "diffraction" around the core-mantle boundary. The rate of fall off may also suggest a mild velocity reversal near the core-mantle boundary (see section 4.3).

4.1.4 Comparison of deep focus S wave amplitude data with other works

The most reliable amplitude-distance curve for S waves available in literature is possibly that of Gutenberg (Richter, 1958). His curve, computed for a focal depth of 550 km, has been compared in Fig. 4-6 with our short period and long period S wave amplitude data. Again, because of arbitrary normalization of amplitudes with respect to source size, we needed a vertical adjustment in the Gutenberg curve to fit with our data as well as possible. One should keep in mind also (1) that the Gutenberg curve was derived from $\log_{10}$ (amplitude/period) data, rather than $\log_{10}$ (amplitude) data like ours and (2) that the Gutenberg curve is valid for the horizontal component of S waves (to be distinguished from the SH component) as deduced from the recorded amplitudes on N-S and E-W components of seismograms whereas

our data were derived from the absolute amplitudes of S waves also taking into consideration the effect of reflection/transmission at free surface, Moho and 650 km discontinuity. At any rate, the Gutenberg curve fits our long period data as well as can be expected within the above sources of discrepancy. Fit to short period data is poor.

4.2 ON THE COMPUTATION OF THEORETICAL AMPLITUDE-DISTANCE CURVES FOR BODY WAVES

Given a velocity and Q model, the forward problem of calculating body wave amplitudes as a function of epicentral distance has been solved to date at best to a good approximation. Frequency-dependent wave response for the proposed models can be calculated from the generalized ray theory (see for example Helmberger, 1974) or from the reflectivity method (Fuchs and Müller, 1971). The computation is, however, complex and expensive to be applied to our mean amplitude data. The technique of quantized ray theory (Wiggins and Mädrid, 1974) shortcuts the generalized ray theory through an empirical approximation to make the calculations relatively simple and inexpensive. But there is no guarantee that the empirical relationship will hold good for any proposed velocity model. For these reasons we computed the frequency-independent amplitudes from

approximation of geometrical ray theory (henceforth called ray theoretical amplitudes) to interpret our deep focus amplitude-distance data.

From geometrical ray theory, the amplitude of the emerging wave is determined by 'geometric spreading' as given by (Julian and Anderson, 1968)

$$E/I = \frac{V(r)\ \tan i(r)}{R^2 r\ \sin\Delta\ \cos i(R)} \left|\frac{d^2T}{d\Delta^2}\right| \qquad (4.2)$$

where E = power/unit area of the wavefront at the earth's surface

I = power/unit solid angle at source

R = radius of the earth

r = radial coordinate of hypocenter

i = angle between ray and vertical

Δ = epicentral distance between the hypocenter and the station

V = seismic velocity

T = travel time of seismic waves

Amplitude A is related to power E by

$$E = (1/2)\ \rho V(R)\ \omega^2 A^2 \qquad (4.3)$$

where ρ = density at the earth's surface

ω = angular frequency

Among the parameters in (4.3) we have assumed crustal velocity to be 6.2 km/sec for P waves and 3.4 km/sec for S waves and crustal density, to be 2.79 gm cm^{-3} in accordance with the B1 model of Jordan and Anderson (1974). The effect of attenuation is to reduce the amplitude A in the wave by the factor

$$e^{-\pi f \int_{ray} dT/Q} \qquad (4.4)$$

where Q = dimensionless quality factor and the integral is evaluated along the ray path. Based on (4.2), (4.3) and (4.4), ray theoretical amplitudes were calculated at one degree distance interval by a program written by Dr. Bruce Julian of M.I.T., Lincoln Laboratory. P and S wave velocity models obtained in Chap. 3 and different Q models (section 4.4) were used for such computation. In this program velocity in each layer was interpolated by the Mohorovicić law $V = ar^b$, a and b being constants. A focal depth of 550 km was chosen to compute the ray theoretical amplitudes for comparison with our data. Varying the focal depth by as much as 50 km did not change the trend in the computed ray theoretical amplitude-distance curve. Note that during the computation of ray theoretical amplitudes, source size [i.e. 'I' in (4.2)]

was left as free parameters so that the computed curve for $\log_{10}$ amplitude vs. epicentral distance could be adjusted vertically to fit with the observed $\log_{10}$-amplitude data which have been normalized arbitrarily with respect to source size.

It is also worth mentioning that ray theoretical amplitudes, though simple to compute, are very unstable because of their sensitivity to the roughness in the velocity model through the parameter $|d^2T/d\Delta^2|$ in (4.2). Smoothness in the velocity model is controlled in turn by the way the velocity-depth profile is parameterized and on the technique of interpolation of velocity from the parameterized models. That is why the occurrence of zeroes and infinities in the slope of the ray-parameter, p (= $dT/d\Delta$) vs. distance (Δ) curve is often encountered in practice and gives a sawtooth appearance in the ray theoretical amplitudes (see Fig. 4-7 for example). The fact that geometrical ray theory predicts infinite amplitudes at the caustics is certainly not a valid representation of the actual body wave behavior. By finding a smooth functional representation of V(r), and numerical integration, one can eliminate many of the points at which $|d^2T/d\Delta|^2$ becomes infinite (see for example,

Chapman, 1971). We preferred, however to smooth the ray theoretical amplitudes by hand (see Fig. 4-7).

Amplitudes from geometrical ray theory are only high frequency approximations. Estimated errors in applying this approximation to the period range of our data are about 3% for short period P wave and 20% for long period P wave data (see Archambeau et al., 1969). Similar error is expected for ray theoretical amplitudes of S waves. Observed amplitudes, however, have measurement errors much larger than the above estimates (see Chap. 2, section 2.2.1). So it is reasonable to compare even the long period amplitude data with the ray theoretical amplitudes.

4.3 USE OF AMPLITUDE DATA FOR THE VERIFICATION OF SEISMIC VELOCITY PROFILES

In Chap. 3 (section 3.3) we inverted the deep focus travel time data to obtain the seismic velocity models for P and S waves; also we described the range of non-uniqueness in our velocity models (section 3.4). Amplitude data are sensitive to velocity gradient and can theoretically serve as a constraint on the velocity profile (see for example Asbel et al., 1966; Archambeau et al., 1969; Helmberger and Wiggins, 1971; Wiggins and Helmberger, 1973). On the other hand, it is very likely that averaging the amplitudes along different ray paths does not average the velocity distribution

of the earth's interior in roughly the same way as averaging the travel time data along the same paths. That is why we did not attempt to use the average amplitude data during inversion of velocity models from average travel time data. But in this section average amplitude data will be put to use to narrow the range of non-uniqueness in those models. With this end in view, we have compared our average amplitude-distance data with the variation of geometric spreading factor as computed for our velocity models.

Fig. 4-7 shows the short period and long period P wave amplitude data in comparison with the computed geometric spreading factors. As already mentioned in section 4.2, the computed curves could be adjusted vertically and were so adjusted, to suit our observed data. Along with the zig-zag computed curves, we also show a hand-smoothed version. Relatively rapid increases in P wave velocity gradient around 1600 km, 2400 km and 2600 km depth (Fig. 3-22C in Chap. 3) of our model produce very small triplication (within a spread of 1-2 degrees) in the travel time-distance curves of 550 km focal depth around 57°, 79° and 86° of the epicentral distance. At these distances, two other late arrivals come within only one tenth of a second from the first arrival. The theoretical amplitudes

of these late arrivals are however drastically different compared to the first arrival as shown in Fig. 4-7. The hand-smoothed curves for the geometric spreading factors were drawn through the average amplitudes of all those arrivals - first and late.

The major discrepancy between the theoretical geometrical spreading factor and the observed average amplitude data of P waves is seen around epicentral distance of 80° where both short period and long period observed amplitudes are higher than the predicted curve. In addition to this difference, short period data also appear to disagree with the smoothed geometric spreading curve around 60° and 75° whereas long period data differ from that curve, only in the trend of the fall-off in the amplitudes beyond 85° of the epicentral distance. All those amplitude data showing anomaly with the predicted values do not come from a single event so that anomaly could not be explained by the error in radiation correction. The discrepancies observed in the short period P wave amplitude data around 60° and 75° are likely to be related to the Q model (see section 4.4) rather than the velocity model because such discrepancies are not pronounced among long period data. The cause of anomaly for both short period and long period P wave amplitudes around 80° may be more complicated in nature.

Amplitude data at these distance ranges come from data whose rays bottom at a depth of 2300-2600 km. At those depths, our P velocity model (see Fig. 3-22 in Chap. 3) has anomalous velocity gradients which satisfy our P wave travel time data from deep earthquakes as well as $dT/d\Delta$ data measured by others (see Chap. 3, section 3.5.3). The apprehension that average amplitude data and average travel time data do not average the velocity structure in the same way may come true for this distance range. Alternately, within the range of uncertainty in our P velocity model, one can possibly modify the model very slightly to satisfy both travel time and amplitude data.

It is remarkable that beyond 85° of epicentral distance the computed geometric spreading factor agrees well with short period P wave amplitude data whereas long period amplitude data show a slower rate of fall-off than computed. Part of the difference in the behavior of short period and long period P wave amplitude data in this distance range can certainly be due to diffraction around the core-mantle boundary (Phinney and Cathles, 1969; and Willey et al., 1970). But it is unlikely that such diffraction can be responsible for the fall-off in the short period P wave amplitudes in the distance range of 85°-93° which is more than 3° short of the shadow boundary (Cleary, 1974).

The match of computed geometric spreading factor with the fall-off in the observed short period amplitudes in this distance range confirms the reversal in P wave velocity gradient as shown in our model near the core-mantle boundary (see Fig. 3-22C in Chap. 3).

Fig. 4-8 compares our S wave amplitude data with the geometric spreading curve (vertically adjusted and handsmoothed) computed from our S wave velocity model (Fig. 3-9 in Chap. 3). Due to the scattering in short period S wave amplitudes, it is difficult to judge the quality of fit. At any rate the major misfit for short period data occurs around 80° of distance but such a misfit at this distance is not seen among the long period data. So S wave velocity model does not seem to be related to this anomaly. Those short period S wave amplitude collected from different events, likely reflect the effects of Q variation at the corresponding depth (see section 4.4). On the other hand, fit of long period amplitude data with the computed geometric spreading factor is satisfactory. Beyond about 85°, fall-off in the observed long period S wave amplitudes is comparable or even faster than the computed geometric spreading factor. This trend is virtually impossible because of the known diffraction

effect around the core-mantle boundary (see for example, Phinney and Cathles, 1969; Willey et al., 1970; also compare Fig. 4-7 with Fig. 4-8 for long period data). In other words, there is an indirect suggestion of reversal in S wave velocity gradient near the core-mantle boundary such that fall-off in the computed geometric spreading factor is faster than observed fall-off in long period S wave amplitudes. Significantly, this suggestion from the long period S wave amplitude data is consistent with our earlier conclusion from S wave travel time data (see section 3.6.1).

The fit of our short period and long period amplitude data especially for P waves with the computed geometric spreading factor alone is as good as can be expected. This leads us to conclude that the Q model for the earth's lower mantle is such that the integral $\int_{ray} dT/Q$ $(=t^*)$ in (4.4) is virtually constant in the distance range of 30°-100°. A consequence of t^* = constant in the entire distance range is that Q in the lower mantle should be increasing with depth (see for example Fig. 10 in the paper of Mikumo and Kurita, 1968; also see next section). This result is also in accordance with the general opinion that anelastic attenuation is small for teleseismic P waves with periods of 1 second or greater (Duda, 1971; Nuttli, 1972).

4.4 WORKING Q(r) MODELS FOR P AND S WAVES

As our amplitude data are not adequate to obtain a quantitative Q-model, a working Q(r) model as a function of radius, r, was found by a selection process of the available Q-models in literature. The selection was based on suitability of the Q-model to fit our short period amplitude data. It is obvious from (4.4) that short period amplitude data (period <3 seconds) will be more sensitive to the Q(r) model than long period amplitude data with period >5 seconds. Note that our amplitude data are available only in the distance range of 30°-100° for a focal depth of roughly 550 km. So these amplitude data will not be able to resolve any Q-model above about 700 km depth.

Among existing Q models in literature for P waves, given for depths below 700 km, we have chosen the following ones:

a) Q_α model of Archambeau *et al.* (1969): this model is applicable to the western United States and it was obtained from P wave spectral amplitude data of explosions. In this model, Q_α is about 1900 at a depth of 670 km and then increases step by step to 8000 at a depth of 1800 km. Below that depth, we assumed Q_α to be 10,000.

b) Q_α model of Teng (1968): this model on the other hand was derived from the spectral amplitude data of P waves

from two deep South American earthquakes and using stations throughout the world. Out of eight possible models given by the author, we chose only the G-type model (see Table 4 in his paper) as it appears to fit his data best. In this model, Q_α in the lower mantle increases step by step from 75 at a depth of 670 km to 1000 at a depth of 1875 km. From this depth onwards, Q_α decreases step by step to 100 at the core-mantle boundary.

c) MM8 Q_α models of Anderson et al. (1965): in contrast to the Q-models given in (a) and (b), this Q-model was determined from amplitude decay data of Love and Rayleigh waves in the period range of 50 to 300 sec. In this model also, Q_α increases step by step from the value of 562.5 at the depth of 670 km to the value of 1350 at the depth of 1000 km. Below that depth we assumed Q_α for this model to be 5175 after Ibrahim (1971).

d) Q_α model of Kanamori (1967): this model is essentially a slight modification of the MM8 Q_β model (Anderson et al., 1965) for shear waves which was obtained from the same data as described in (c). In this model, Q values increase step by step from the value of 250 at a depth of 670 km to the value of 2300 at the core-mantle boundary. This model will be referred to later also as MM8' Q_β model following the nomenclature of Kanamori (1967).

All these four (a through d) Q_α models thus have their own characteristic and provide also fair representation of the range of Q_α values by other investigators. Note in particular that Teng's (1968) model as described in (c) incorporates low values of Q near the core-mantle boundary which was also suggested by Mikumo and Kurita (1968). In our selection for the Q model of shear waves, we have used also all these four models of which only one i.e., MM8' Q_β model as described in (d) was originally derived for shear waves.

The ray theoretical amplitudes as computed from (4.2), (4.3) and (4.4) for these four Q-models and P and S velocity models of ours (Fig. 3-9 in Chap. 3), were adjusted vertically to fit with our amplitude data. Based on the fit (Fig. 4-9) we found that our P wave short period amplitude data do not support Teng's (1968) Q_α model where Q decreases towards the core-mantle boundary. Rather, three other models where Q increases gradually with depth fitted our data much better. All those models have high Q-values for the lower mantle and it is difficult to select out any one of them by the fit of data beyond 40° of distance. But the Q_α model of Archambeau et al. (1969) had a better fit for the data at less than 40° of distance (see Fig. 4-10). So this Q-model was chosen for short period P wave amplitude data and it fits as well our long period amplitude data except for those

beyond 85°, which were presumably affected by diffraction around the core-mantle boundary (see previous section).

The Q-model of Archambeau et al. (1969) and Teng (1968) has been shown in Fig. 4-11 along with the values of t* as computed in conjunction with our P wave velocity model (Fig. 3-9 in Chap. 3). As our amplitude data require t* to be roughly constant over the distance range of 30°-100° (see previous section), it is clearly seen then why Teng's Q model failed to satisfy our amplitude data whereas the Q model of Archambeau et al. provided satisfactory fit to those data.

It may be worth mentioning that the possibility of Q-decreasing near the core-mantle boundary is not eliminated altogether from the fit of short period P wave amplitude data by models where Q monotonically increases with depth. We can possibly introduce smaller reversal in velocity gradient near the core-mantle boundary than shown for our P velocity model (Fig. 3-22c, in Chap. 3). This change may not seriously violate P wave travel time data (Fig. 3-1 in Chap. 3) but fit better the long period P wave amplitude data (Fig. 4-10). The misfit to short period P wave amplitude data caused by the required change in P velocity model can be removed by lowering Q values appropriately near the core-mantle boundary. This adjustment might have placed our P wave velocity model

and Q-model in harmony to each other with respect to the reversal near the core-mantle boundary, but the effect of diffraction complicated this adjustment.

Short period P wave amplitude data around 60° and 75° also tend to suggest that Q-values of the fitted model should be relatively lowered around a depth of 1500-1700 km and increased at a depth of about 2100-2300 km. Corresponding to a given Q-anomaly, the anomlay in the $\log_{10}$-amplitude of long period P wave is about six times smaller than that of short period P wave because of the difference in their periods. That is why possibly no Q-anomalies are very evident around 60° and 75° for the observed long period P wave amplitude data. The selected Q_α-model of Archambeau et al. (1969), however, was not changed to fit exactly with the short period P wave amplitudes. It may be premature to change the Q_α-model pending further evidence especially when the errors associated with those data are also large. One cannot rule out again the possibility of a frequency-dependent Q-model (see for example, Solomon, 1972).

In similar fashion to the fit of P wave amplitude data, we found that except for Teng's (1968) Q model, the other three Q models fitted our short period and long period S wave amplitude data more or less well, a slightly better fit (Fig. 4-12) being obtained by the MM8' Q_β model

of Kanamori (1967). This Q model is shown in Fig. 4-11. In contrast to the fit by this model, Teng's Q-model showed very poor fit to the S wave amplitude data between 50-70 degrees for short period waves. Significantly the MM8' Q model failed to fit the short period S wave amplitudes around 80° of distance and predicted smaller ray theoretical amplitudes at this distance. Those amplitude data are associated with rays bottoming at depths of about 2200-2400 km. Note especially that the P waves also show similar anomalies in short period amplitudes (around 75°) for rays bottoming almost in the same depth interval.

In summary, Q in the lower mantle should be increasing with depth for both P and S waves. A possibility of 'Q-reversal' at the base of the mantle is not refuted however.

4.5 ON THE DETERMINATION OF BODY WAVE MAGNITUDE

Body wave magnitude is possibly the only parameter related to the source size which can be computed from the observed seismograms. Conventionally one uses

the amplitude and period of P waves recorded on the vertical component of seismograms (short period). Body wave magnitudes (M_b) are then computed by employing a relationship like

$$M_b = \log_{10} (A/T) + B + S \qquad (4.5)$$

where A is the amplitude, T is the period, B is the correction factor to take into account the geometric spreading and attenuation in a spherically symmetric earth and S is the station correction due to departure of real earth from the spherical symmetry.

Our study on the variation of P wave amplitudes with distance indicates that the combined effect of geometric spreading and attenuation on P wave amplitudes is different for short period and long period P waves (see Fig. 4-10), so also the station corrections (see Appendix M). Retaining the same baseline as the B-values of Gutenberg (Richter, 1958), we have derived separately the B-values for short period and long period P waves (see Tables 4-4 and 4-5) from our average amplitude-distance data (Figs. 4-1 and 4-2). Figs. 4-13 and 4-14 show how these B values and station corrections for amplitude data (Appendix M) have affected determinations of short period and long period body wave

magnitudes, M_b and M_B respectively. For the computation of magnitudes, we used vertical component P wave amplitudes from deep events of this study. The result also has been tabulated in Table 4-6. Several features in these figures and the table are worth mentioning:

(1) Note that average deviation between calculated magnitude and bulletin magnitude remains the same whether we use Gutenberg's B values or our B values. This assures us that we correctly adjusted the baseline of magnitude determination similar to that of Gutenberg. To date, all body wave magnitudes are given in general with respect to Gutenberg's amplitude-distance curve. It is appropriate then to retain the same baseline of his curve while improving the shape of the curve.

Magnitudes calculated from our amplitude-distance curve were found, however, to be systematically higher (on the average by 0.2 magnitude units) than those reported in the ISC (International Seismological Center) bulletin. Comparing body wave magnitudes reported in the ISC and USCGS/NOAA bulletins (see Table 4-7), we find that magnitudes reported in the USCGS/NOAA bulletins are also in general higher than those reported in the ISC bulletin. The cause of this difference may lie in the operational procedures such as correction for instrument response, use of station

corrections, the exact form of amplitude-distance curve, etc.

(2) Average deviation of calculated magnitude and the bulletin magnitude is the same whether we use the short period amplitude data (Fig. 4-13) or long period amplitude data (Fig. 4-14) along with our B-Values (B-part of the figures). In other words, on the average, short period P wave magnitude (M_b) is the same as long period magnitude (M_B) even though P wave amplitudes were not corrected for the frequency-dependent source spectrum during the computation. This implies that the shape of the amplitude spectrum over the range of about 0.1-0.7 Hz is proportional to f^{-1} (i.e. A/T values constant between periods of 1.5 to 9.5 seconds approximately). Similar results were obtained by Nuttli (1972) from P wave amplitude data of explosions in the frequency range of 0.3-1 Hz.

(3) Standard deviation in the multi-station determination of M_b or M_B (short period or long period body wave magnitude) is insensitive to whether we used Gutenberg's B-values or our set of B-values in the computation. Even after correcting the P wave amplitudes for radiation pattern at the source (Appendix E), there was almost no change in the standard deviation (C-part in the figures), though average magnitude changed in some instances by 0.1-0.2 magnitude units (see Table 4-6).

Standard deviations of magnitudes, however, were somewhat reduced through the application of station corrections for the amplitudes (see D-part in the figures). This result is in line with the study of Ward and Toksöz (1971) and Evernden and Filson (1971) who attributed much of the variation in short period P wave magnitudes to lateral variation in attenuation within the upper mantle. Wave propagation through an anelastic medium not only attenuates seismic energy but also lengthens the period of travelling wave, so that period measurement is also affected (Kurita, 1966). This latter effect may also contribute significantly to the variation in the body wave magnitudes especially those determined from long period P waves.

Table 4-1a

Amplitudes (in microns) for short period (period <3 second)
P wave in 2° distance cells (focal depth ≈ 550 km)

Distance cell (degrees)	No. of data	No. of paths *	Mean of $\log_{10}$ (amplitude)	Std. deviation of $\log_{10}$ (amplitude)	Std. error of mean
1.	2.	3.	4.	5.	6.
30-32	2	2	1.25	0.16	0.11
32-34	6	6	1.07	0.27	0.11
34-36	4	4	0.89	0.18	0.09
36-38	2	2	1.06	0.09	0.07
38-40	3	3	0.89	0.14	0.08
40-42	6	6	0.94	0.10	0.04
42-44	5	5	0.88	0.24	0.11
44-46	6	6	0.85	0.10	0.04
46-48	3	3	0.77	0.18	0.11
48-50	3	3	0.63	0.65	0.38
50-52	5	5	0.87	0.26	0.12
52-54	3	3	0.79	0.19	0.11
54-56	6	6	0.59	0.21	0.08
56-58	3	3	0.51	0.32	0.18
58-60	2	2	0.62	0.14	0.10

Table 4-1a (Continued)

1.	2.	3.	4.	5.	6.
60-62	4	4	0.45	0.46	0.23
62-64	4	4	0.44	0.58	0.29
64-66	3	3	0.59	0.09	0.05
66-68	3	3	0.75	0.45	0.26
68-70	3	3	0.84	0.32	0.18
70-72	5	4	0.79	0.19	0.08
72-74	6	6	1.09	0.53	0.22
74-76	4	4	1.20	0.42	0.21
76-78	7	7	0.76	0.33	0.12
78-80	12	11	0.83	0.37	0.11
80-82	5	5	0.82	0.28	0.12
82-84	8	8	0.75	0.29	0.10
84-86	8	8	0.84	0.34	0.12
86-88	7	7	0.76	0.29	0.11
88-90	6	6	0.33	0.31	0.13
90-92	6	6	0.43	0.54	0.22
92-94	7	7	0.32	0.28	0.10

Table 4-1a (Continued)

1.	2.	3.	4.	5.	6.
94-96	10	9	0.10	0.46	0.15
96-98	6	6	0.06	0.33	0.14
98-100	2	2	0.15	0.21	0.15

*: Each 10° cell in azimuth from the hypocenter is considered to represent a single path when one or more data lie within that cell.

Table 4-1b

Amplitudes (in microns) for long period (period >5 second)
P wave in 2° distance cells (focal depth ≈ 550 km)

Distance cell (degrees)	No. of data	No. of* paths	Mean of $\log_{10}$ (amplitude)	Std. deviation of $\log_{10}$ (amplitude)	Std. error of mean
30-32	2	2	0.77	0.04	0.03
32-34	5	5	0.76	0.06	0.03
34-36	5	5	0.78	0.08	0.04
36-38	2	2	0.72	0.12	0.08
38-40	2	2	0.72	0.18	0.12
40-42	4	4	0.76	0.06	0.03
42-44	4	4	0.67	0.26	0.13
44-46	5	5	0.80	0.15	0.07
46-48	1	1	0.68	0.00	0.00
48-50	2	2	0.69	0.10	0.07
50-52	4	4	0.67	0.04	0.02
52-54	3	3	0.60	0.21	0.12
54-56	2	2	0.64	0.19	0.14
56-58	3	3	0.54	0.18	0.11
58-60	3	3	0.59	0.02	0.01
60-62	3	3	0.55	0.10	0.06

Table 4-1b (Continued)

1.	2.	3.	4.	5.	6.
62-64	1	1	0.59	0.00	0.00
64-66	2	2	0.59	0.22	0.16
66-68	4	4	0.68	0.12	0.06
68-70	4	4	0.60	0.03	0.02
70-72	5	5	0.59	0.09	0.04
72-74	7	7	0.58	0.15	0.06
74-76	7	7	0.66	0.13	0.05
76-78	7	7	0.52	0.08	0.03
78-80	7	6	0.52	0.08	0.03
80-82	9	7	0.51	0.07	0.02
82-84	7	7	0.52	0.10	0.04
84-86	5	5	0.51	0.10	0.04
86-88	7	7	0.37	0.12	0.05
88-90	8	8	0.32	0.11	0.04
90-92	3	3	0.26	0.09	0.05
92-94	2	2	0.29	0.16	0.11
94-96	9	8	0.14	0.09	0.03
96-98	4	4	0.06	0.12	0.06
98-100	2	2	0.01	0.01	0.01

*: Each 10° cell in azimuth from the hypocenter is considered to represent a single path when one or more data lie within that cell.

Table 4-2a

Amplitudes (in microns) for short period (period <3 second) SV wave in 2° distance cells (focal depth ≈ 550 km)

Distance cell (degrees)	No. of data	No. of * paths	Mean of $\log_{10}$ (amplitude)	Std. deviation of $\log_{10}$ (amplitude)	Std. error of mean
30-32	-	-	-	-	-
32-34	2	2	0.59	0.39	0.27
34-36	6	6	0.95	0.30	0.12
36-38	3	3	0.59	0.63	0.36
38-40	2	2	1.52	0.77	0.54
40-42	-	-	-	-	-
42-44	-	-	-	-	-
44-46	4	4	1.00	0.02	0.01
46-48	2	2	0.98	0.00	0.00
48-50	1	1	0.69	0.00	0.00
50-52	1	1	0.96	0.0	0.0
52-54	1	1	1.02	0.0	0.0
54-56	1	1	0.67	0.0	0.0
56-58	2	2	0.71	0.64	0.45
58-60	-	-	-	-	-
60-62	2	2	0.69	0.16	0.11

Table 4-2a (Continued)

1.	2.	3.	4.	5.	6.
62-64	2	2	1.02	0.32	0.22
64-66	3	3	0.74	0.13	0.08
66-68	3	3	1.00	0.27	0.16
68-70	1	1	0.86	0.0	0.0
70-72	4	4	0.71	0.29	0.14
72-74	-	-	-	-	-
74-76	4	4	0.54	0.44	0.22
76-78	2	2	1.18	0.08	0.06
78-80	5	5	1.15	0.25	0.11
80-82	2	2	1.28	0.12	0.09
82-84	1	1	1.19	0.0	0.0
84-86	3	3	1.26	0.38	0.22
86-88	4	4	1.09	0.02	0.01
88-90	1	1	1.68	0.0	0.0
90-92	1	1	0.76	0.0	0.0
92-94	2	2	1.25	0.65	0.46
94-96	2	2	0.11	0.16	0.11

*: Each 10° cell in azimuth from the hypocenter is considered to represent a single path when one or more data lie within that cell.

Table 4-2b

Amplitudes (in microns) for long period (period > 5 second)
SV wave in 2° distance cells (focal depth ≈ 550 km)

Distance cell (degrees)	No. of data	No. of * paths	Mean of $\log_{10}$ (amplitude)	Std. deviation of $\log_{10}$ (amplitude)	Std. error of mean
30-32	-	-	-	-	-
32-34	4	4	1.04	0.20	0.10
34-36	6	6	1.20	0.10	0.04
36-38	6	6	1.25	0.25	0.10
38-40	3	3	1.21	0.04	0.02
40-42	4	4	1.11	0.13	0.07
42-44	3	3	1.00	0.15	0.09
44-46	3	3	0.99	0.14	0.08
46-48	9	9	0.98	0.23	0.08
48-50	-	-	-	-	-
50-52	3	3	1.01	0.13	0.08
52-54	3	3	0.78	0.24	0.14
54-56	3	3	0.95	0.08	0.04
56-58	4	4	0.81	0.36	0.18
58-60	2	2	0.81	0.35	0.25
60-62	1	1	0.68	0.00	0.00

Table 4-2b (Continued)

1.	2.	3.	4.	5.	6.
62-64	4	4	1.04	0.25	0.12
64-66	4	4	0.75	0.04	0.02
66-68	5	5	0.63	0.09	0.04
68-70	6	5	0.70	0.36	0.15
70-72	4	4	0.70	0.06	0.03
72-74	4	4	0.62	0.22	0.11
74-76	6	6	0.70	0.38	0.16
76-78	5	5	0.71	0.20	0.09
78-80	4	4	0.68	0.06	0.03
80-82	4	4	0.65	0.14	0.07
82-84	2	2	0.83	0.23	0.17
84-86	2	2	0.58	0.00	0.00
86-88	8	7	0.64	0.23	0.08
88-90	7	7	0.51	0.27	0.10
90-92	-	-	-	-	-
92-94	1	1	0.33	0.00	0.00
94-96	5	5	0.32	0.20	0.09
96-98	4	4	0.01	0.01	0.01

*: Each 10° cell in azimuth from the hypocenter is considered to represent a single path when one or more data lie within that cell.

Table 4-3a

Amplitudes (in microns) for short period (period <3 second)
SH wave in 2° distance cells (focal depth ≈ 550 km)

Distance cell (degrees)	No. of data	No. of * paths	Mean of $\log_{10}$ (amplitude)	Std. deviation of $\log_{10}$ (amplitude)	Std. error of mean
30-32	-	-	-	-	-
32-34	-	-	-	-	-
34-36	1	1	0.95	0.00	0.00
36-38	2	2	1.00	0.01	0.01
38-40	3	2	1.04	0.01	0.00
40-42	-	-	-	-	-
42-44	-	-	-	-	-
44-46	2	2	1.10	0.0	0.0
46-48	2	2	1.08	0.0	0.0
48-50	-	-	-	-	-
50-52	-	-	-	-	-
52-54	1	1	1.28	0.0	0.0
54-56	1	1	0.93	0.0	0.0
56-58	2	2	0.59	0.14	0.10
58-60	-	-	-	-	-
60-62	2	2	0.84	0.09	0.07

Table 4-3a (Continued)

1.	2.	3.	4.	5.	6.
62-64	2	2	1.13	0.34	0.24
64-66	3	3	0.75	0.27	0.15
66-68	2	2	0.81	0.02	0.01
68-70	-	-	-	-	-
70-72	3	3	0.92	0.19	0.11
72-74	-	-	-	-	-
74-76	2	2	0.84	0.22	0.15
76-78	1	1	1.01	0.0	0.0
78-80	3	3	1.16	0.28	0.16
80-82	1	1	0.96	0.0	0.0
82-84	-	-	-	-	-
84-86	1	1	0.63	0.0	0.0
86-88	2	2	0.76	0.03	0.02
88-90	1	1	0.63	0.0	0.0
90-92	1	1	0.41	0.0	0.0
92-94	2	2	0.53	0.07	0.05
94-96	2	2	0.07	0.10	0.07

* :Each 10° cell in azimuth from the hypocenter is considered to represent a single path when one or more data lie within that cell.

Table 4-3b

Amplitudes (in microns) for long period (period >5 second) SH wave in 2° distance cells (focal depth ≈ 550 km)

Distance cell (degrees)	No. of data	No. of* paths	Mean of $\log_{10}$ (amplitude)	Std. deviation of $\log_{10}$ (amplitude)	Std. error of mean
30-32	1	1	1.32	0.0	0.0
32-34	-	-	-	-	-
34-36	3	3	1.07	0.11	0.06
36-38	5	5	0.84	0.27	0.12
38-40	3	3	0.96	0.18	0.10
40-42	3	3	0.93	0.06	0.04
42-44	1	1	0.90	0.00	0.00
44-46	1	1	1.02	0.0	0.0
46-48	5	5	0.95	0.31	0.14
48-50	-	-	-	-	-
50-52	1	1	0.98	0.0	0.0
52-54	2	2	0.69	0.28	0.19
54-56	3	3	0.74	0.17	0.10
56-58	3	3	0.96	0.22	0.13
58-60	2	2	0.98	0.01	0.61
60-62	1	1	0.96	0.00	0.00

Table 4-3b (Continued)

1.	2.	3.	4.	5.	6.
62-64	4	4	1.04	0.23	0.11
64-66	5	5	0.84	0.13	0.06
66-68	4	4	0.90	0.04	0.02
68-70	5	4	0.81	0.53	0.24
70-72	4	4	0.86	0.01	0.01
72-74	2	2	0.91	0.21	0.15
74-76	3	3	0.89	0.06	0.04
76-78	3	3	0.35	0.57	0.33
78-80	1	1	0.28	0.00	0.00
80-82	3	3	0.73	0.16	0.09
82-84	1	1	0.50	0.00	0.00
84-86	1	1	0.52	0.00	0.00
86-88	7	6	0.57	0.31	0.12
88-90	4	4	0.63	0.17	0.08
90-92	-	-	-	-	-
92-94	1	1	0.55	0.00	0.00
94-96	3	3	0.56	0.18	0.11
96-98	2	2	0.00	0.00	0.00

*: Each 10° cell in azimuth from the hypocenter is considered to represent a single path when one or more data lie within that cell.

TABLE 4-4

Amplitude-distance curve and the reduced B-values for short period P wave (focal depth $\simeq$ 550 km)

Distance (degrees)	Log_{10} amplitude (A) [Amplitude in microns]	B-values of this study †	Gutenberg's B values (focal depth = 550 km)
30	1.02	6.08	6.40
35	1.00	6.10	6.40
40	0.94	6.16	6.40
45	0.86	6.24	6.30
50	0.77	6.33	6.20
55	0.65	6.45	6.10
60	0.58	6.52	6.10
65	0.69	6.41	6.30
70	0.86	6.24	6.30
75	0.91	6.19	6.20
80	0.84	6.26	6.20
85	0.69	6.41	6.40
90	0.44	6.66	6.70
95	0.13	6.97	7.00
100	-0.13	7.23	7.20

† $B = M_b - \log_{10} (A/T)$

where $M_b = 6.9$ (see Fig. 4-1)

$T = 1.5$ second (see text, Section 4.1)

TABLE 4-5

Amplitude-distance curve and the reduced B-values for long period P wave (focal depth $\simeq$ 550 km)

Distance (degrees)	Log_{10} amplitude (A) [Amplitude in microns]	B-values of this study †	Gutenberg's B values (focal depth = 550 km)
30	0.78	6.12	6.40
35	0.78	6.12	6.40
40	0.77	6.13	6.40
45	0.74	6.16	6.30
50	0.68	6.22	6.20
55	0.62	6.28	6.10
60	0.60	6.30	6.10
65	0.59	6.31	6.30
70	0.59	6.31	6.30
75	0.57	6.33	6.20
80	0.52	6.38	6.20
85	0.43	6.47	6.40
90	0.28	6.62	6.70
95	0.11	6.79	7.00
100	0.00	6.90	7.20

† $B = M_B - \log_{10} A/T$

where $M_B = 5.9$ (see Figure 4-2)

$T = 9.5$ second (see text, section 4.1)

TABLE 4-6

Short period(SP) and Long period(LP) body wave magnitudes (M_b and M_B respectively)

Event location†	Bulletin †† magnitude (body wave)	A	B	C	D	Period range
W. Tonga	5.6 (20)*	6.1±0.4 (7)*	6.1±0.4 (7)*	6.2±0.3(6)*	6.4±0.2(8)*	SP
		5.9±0.2 (4)	5.9±0.0 (4)	6.0±0.1(4)	5.9±0.1(4)	LP
S. Fiji	5.9 (24)	6.0±0.3 (16)	6.0±0.3 (16)	6.3±0.4(16)	6.2±0.3(16)	SP
		6.1±0.2 (17)	6.1±0.3 (17)	6.3±0.3(17)	6.2±0.2(17)	LP
Colombia	6.5(34)	6.7±0.5 (14)	6.7±0.5 (14)	6.7±0.6(16)	6.5±0.4(16)	SP
		7.0±0.3 (20)	6.9±0.3 (20)	7.0±0.1(19)	6.9±0.2(21)	LP
Peru - Brazil	5.9(48)	5.8±0.3 (25)	5.9±0.3 (25)	6.1±0.3(25)	6.0±0.2(25)	SP
		6.2±0.3 (24)	6.3±0.2 (24)	6.5±0.2(23)	6.3±0.1(24)	LP
Argentina	5.8 (38)	6.1±0.2 (6)	6.1±0.2 (6)	6.2±0.2(6)	6.2±0.1(6)	SP
		6.0±0.1 (5)	6.1±0.1 (5)	6.2±0.2(5)	6.1±0.1(5)	LP
Java Sea	6.0 (28)	6.1±0.3 (13)	6.0±0.4 (13)	6.3±0.3(13)	6.4±0.4(13)	SP
		5.8±0.0 (1)	5.9±0.0 (1)	5.9±0.0 (1)	5.9±0.0(1)	LP

TABLE 4 - 6 (CONTINUED)

Event location	Bulletin magnitude (body wave)	A	B	C	D	Period range
Sea of Okhotsk	6.5(30)*	6.5±0.2(13)*	6.6±0.3(13)*	6.3±0.3(13)*	6.8±0.2(13)*	SP
		6.5±0.2(39)	6.5±0.2(39)	6.8±0.2(39)	6.7±0.1(39)	LP
E. Russia	5.2(43)	5.6±0.2(16)	5.7±0.2(16)	5.9±0.2(14)	5.9±0.2(14)	SP
		5.2±0.0 (1)	5.3±0.0(1)	5.3±0.0(1)	5.3±0.0(1)	LP
S. Marianas	5.4(34)	5,6±0.4(14)	5.6±0.4(14)	5.8±0.4(13)	5.8±0.2(14)	SP
		5.4±0.0 (2)	5.4±0.1(2)	5.5±0.2(2)	5.6±0.1(2)	LP
Solomon Islands	5.6(21)	5.9±0.3(6)	5.8±0.4(7)	6.0±0.3(6)	6.1±0.2(7)	SP
		6.0±0.1(5)	5.7±0.1 (5)	6.0±0.1(5)	6.0±0.1(5)	LP
New Hebrides	5.8(30)	6.3±0.4(12)	6.3±0.4(13)	6.4±0.3(9)	6.4±0.3(12)	SP
		6.2±0.2(9)	6.1±0.1(9)	6.4±0.2(9)	6.3±0.1(9)	LP
Hindu Kush	5.7(42)	5.9±0.3(19)	5.8±0.3(19)	6.0±0.3(18)	6.0±0.2(19)	SP
		5.8±0.2(14)	5.7±0.2(14)	5.8±0.2(13)	5.8±0.2(14)	LP
Greece	5.7(37)	5.3±0.1(2)	5.2±0.1(2)	5.2±0.2(2)	5.6±0.2(2)	SP
		5.9±0.1(6)	5.9±0.1(6)	6.0±0.2(6)	5.9±0.2(6)	LP

† For details of location parameters, see table 2-1 (Ch. 2)

†† International Seismic Center (ISC) bulletin.

* Number of data used is shown in brackets; also the standard deviation of computed maagnitude whenever available.

A: event magnitude using Gutenberg's B values (see table 4-4).

B: event magnitude using our B-values (table 4-4 and 4-5). Note these B-values are also used in C and D.

C: event magnitude after correcting the observed amplitude for radiation pattern.

D: event magnitude after correcting the observed amplitude for station anomaly in addition to correction for radiation pattern.

Table 4-7

Difference in ISC & USCGS/NOAA reported short period body wave magnitude (M_b)

Event location+	ISC (a)	USCGS/NOAA (b)	This study (c)	(c-a)	(b-a)	(c-b)
West Tonga	5.6(20)*	5.6(10)*	6.4(8)*	0.8	0.0	0.8
South Fiji	5.9(24)	6.2(11)	6.2(16)	0.3	0.3	0.0
Colombia	6.5(34)	7.1(13)	6.5(16)	0.0	0.6	-0.6
Peru-Brazil	5.9(48)	6.2(19)	6.0(25)	0.1	0.3	-0.2
Argentina	5.8(38)	5.7(17)	6.2(6)	0.4	-0.1	0.5
Java Sea	6.0(28)	6.2(10)	6.4(13)	0.4	0.2	0.2
Sea of Okhotsk	6.5(30)	6.6(22)	6.8(13)	0.3	0.1	0.2
East Russia	5.2(43)	5.6(18)	5.9(14)	0.7	0.4	0.3
South Marianas	5.4(34)	5.6(19)	5.8(14)	0.4	0.2	0.2
Solomon Is.	5.6(21)	6.5(4)	6.1(7)	0.5	0.9	-0.4
New Hebrides	5.8(30)	5.8(23)	6.4(12)	0.6	0.0	0.6
Hindukush	5.7(42)	5.7(18)	6.0(19)	0.3	0.0	0.3
Greece	5.7(37)	5.4(4)	5.6(2)	-0.1	-0.3	0.2

+For details of location parameters see table 2-1 in chap. 2.

*Number of data used in the computation is shown in the bracket.

Figure Captions

Figure 4-1. (top) Short period P wave amplitude-distance curve of this study (solid line) is shown against the mostly used standard curve of Gutenberg. Absolute P wave amplitudes of deep focus earthquakes, averaged over 2° distance cells are shown as circles and standard errors of the mean as vertical error bars. These amplitudes were corrected for (i) instrument response, (ii) radiation pattern, (iii) event size, (iv) frequency dependent source spectrum, (v) crust and upper mantle discontinuities and (vi) station anomaly (see text). Smoothed ray theoretical amplitudes computed from our P wave velocity model (Chap. 3) and Q-model of Archambeau et al. (1969) are also shown for comparison.

(below) Same data in comparison with amplitude-distance curve of Carpenter et al. (1967), Cleary (1967), Booth et al. (1974). Those curves were displaced vertically to fit our data as well as possible. Notice that our data agrees well with the curve of Carpenter et al. which was derived from short period vertical component amplitude data from explosions.

Figure 4-2. (top) Same as in Fig. 4-1 except that we show here long period amplitude-distance curve of this study.

(below) Absolute long period amplitude data of deep focus earthquakes are shown against the amplitude-distance curves of Nuttli (1972) and Booth et al. (1974), which were displaced vertically to fit our data as well as possible. Notice that our amplitude data agrees well with the curve of Nuttli which was derived from long period vertical component amplitudes from explosions.

Figure 4-3. Vertical component P wave amplitudes of deep focus earthquakes, as averaged over 2° distance cells. These amplitudes were corrected for the same factors as described under the caption of Fig. 4-1 except for discontinuities in the upper mantle. Notice that difference between absolute amplitudes (Figs. 4-1 and 4-2) and the vertical component amplitudes is primarily in the baseline. Short period vertical component amplitudes (top) have been compared against the amplitude-distance curve of Carpenter et al. (1967) and long period ones (below) against the amplitude-distance curve of Nuttli (1972). Those two curves, derived from vertical component amplitudes of explosions,

fitted the absolute amplitudes (Fig. 4-1, 4-2) better than other available curves.

Figure 4-4. Short period SH and SV amplitude data of deep earthquakes. These amplitudes were corrected for various factors (see the caption in Fig. 4-1) and averaged over 2° distance cells. Vertical bars are the standard errors of mean. Values without bars (0) represent single measurements in a 2° distance cell.

Figure 4-5. Long period SH and SV amplitudes of deep earthquakes. See also caption in Fig. 4-4 for further description.

Figure 4-6. Short period and long period S wave amplitudes as reduced from the observed amplitudes of SH and SV component (Figs. 4-4 and 4-5) (see also text). These amplitudes are compared against the amplitude-distance curve of Gutenberg (Richter, 1958).

Figure 4-7. Comparison of observed short period (top) and long period (below) P wave amplitude data against the geometric spreading factor computed from our P wave velocity model (see Chap. 3). Note that predicted late arrivals due to rapid increase in our P wave velocity gradient (Fig. 3-22 in Chap. 3) come only within one tenth of a second from the first arrival, but their amplitudes are drastically different from the first arrival.

Figure 4-8. Comparison of observed short period (top) and long period (below) S wave amplitude data with the geometric spreading factor computed from our S wave velocity model (see Chap. 3).

Figure 4-9. Comparison of short period P wave amplitude data against the ray theoretical amplitudes computed from our P velocity model (see Fig. 3-9 in Chap. 3) and Q-model of Teng (1968) (see Fig. 4-11).

Figure 4-10. Comparison of P wave amplitudes against ray theoretical amplitudes computed from the P wave velocity model (Fig. 3-9 in Chap. 3) and Q-model of Archambeau et al. (1969) (Fig. 4-11). Notice that short period amplitudes around 60° and 75° are not satisfied by the ray theoretical amplitudes.

Figure 4-11. (top) Q-model of Teng (1968), Archambeau et al. (1969) and Kanamori (1967).

(below) t^* ($= \int_{ray} dT/Q$) values as computed from above three Q-models and our P and S velocity models (Fig. 3-9 in Chap. 3). Note that t^* values computed from Teng's model varies with epicentral distance whereas values from the other two models are relatively constant over the entire distance range.

Figure 4-12. Comparison of our S wave amplitude data with the ray theoretical amplitudes computed from our S wave velocity model (Fig. 3-9 in Chap. 3) and the MM8'Q_β model of Kanamori (1967). Notice that short period amplitudes around 80° are not satisfied by the ray theoretical amplitudes.

Figure 4-13. Short period body wave magnitude (M_b) determination of deep events (Table 4-6) from measurement of P wave amplitudes and periods on the short period vertical component of the seismograms. These magnitudes are compared against those reported in International Seismological Center (ISC) bulletins. X, shown inside the rectangular boxes, represent the average of (calculated M_b - bulletin M_b) whereas S is the r.m.s. deviation between calculated M_b and bulletin M_b. Standard deviations of computed magnitudes (represented by circles) are shown as the vertical error bars.

Part A in the figure corresponds to computation of M_b using Gutenberg's B-values.

Part B corresponds to computation of M_b using our B-values (Table 4-4).

Part C corresponds to computation of M_b using our B-values and radiation correction for amplitudes.

Part D corresponds to computation of M_b from our B-values using correction for station anomalies of amplitudes (Appendix M) in addition to radiation corrections.

Figure 4-14. Long period body wave magnitude (M_B) determination of deep events (Table 4-6) from measurement of P wave amplitudes and periods on the long period vertical component of the seismograms. Long period B-values for this computation have been tabulated in Table 4-5. See also caption in Fig. 4-13.

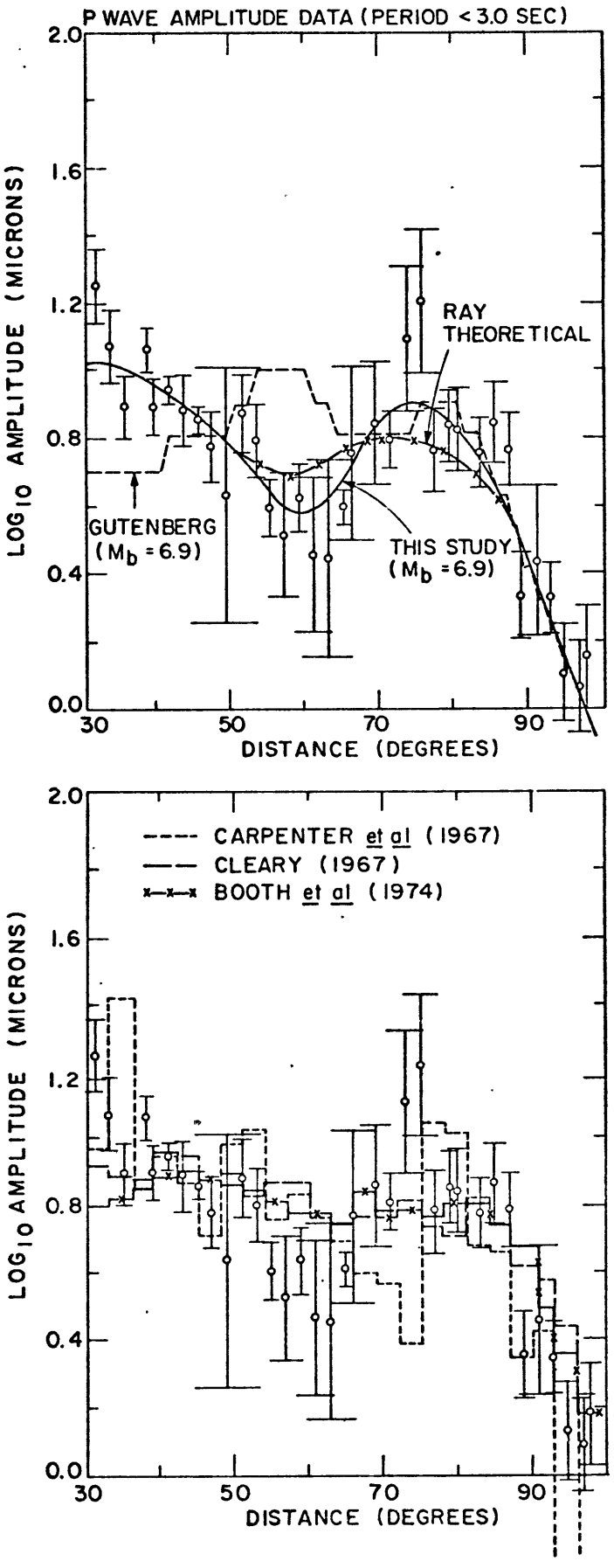

P WAVE AMPLITUDE DATA (PERIOD < 3.0 SEC)
LOG10 AMPLITUDE (MICRONS)
2.0
1.6
1.2
0.8
0.4
0.0
30
50
70
90
DISTANCE (DEGREES)
RAY THEORETICAL
GUTENBERG (Mb = 6.9)
THIS STUDY (Mb = 6.9)
CARPENTER et al (1967)
CLEARY (1967)
BOOTH et al (1974)

Fig. 4-1

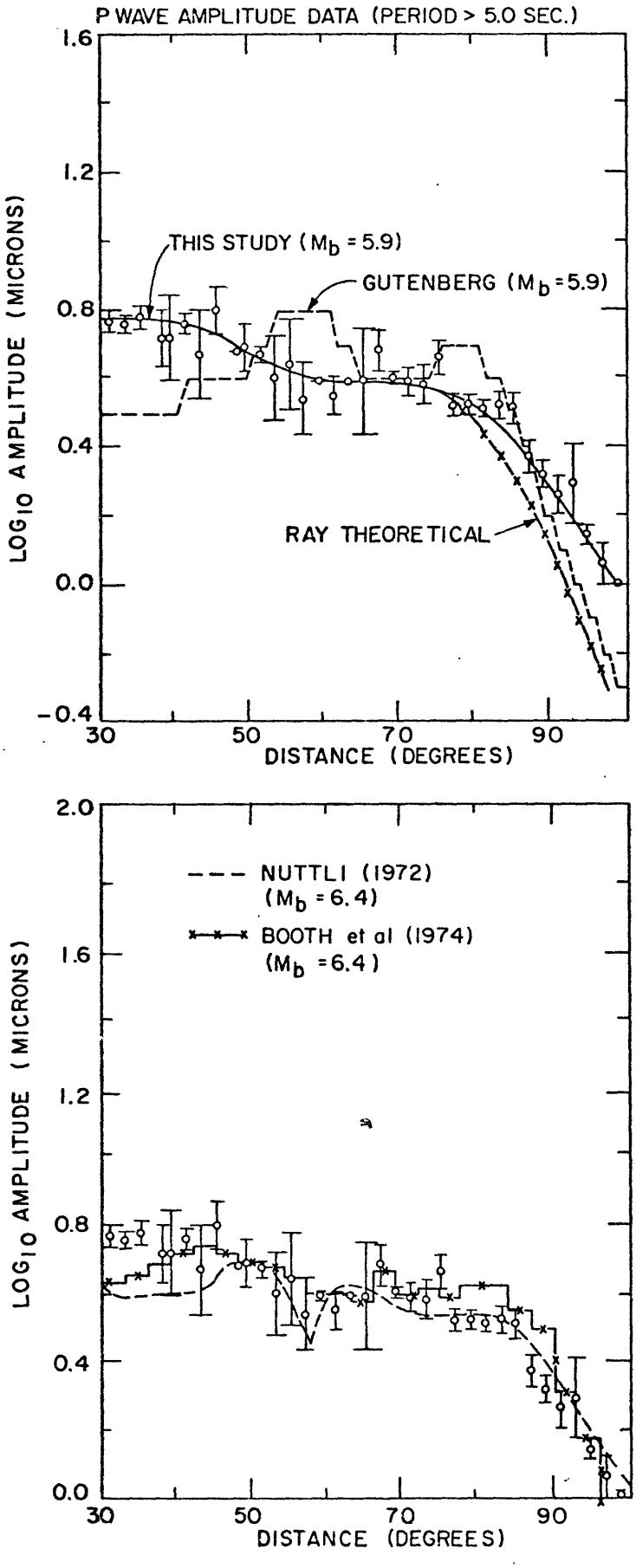

P WAVE AMPLITUDE DATA (PERIOD > 5.0 SEC.)
LOG10 AMPLITUDE (MICRONS)
1.6
1.2
0.8
0.4
0.0
-0.4
THIS STUDY (Mb = 5.9)
GUTENBERG (Mb = 5.9)
RAY THEORETICAL
30
50
70
90
DISTANCE (DEGREES)
2.0
1.6
1.2
0.8
0.4
0.0
NUTTLI (1972)
(Mb = 6.4)
BOOTH et al (1974)
(Mb = 6.4)
LOG10 AMPLITUDE (MICRONS)
30
50
70
90
DISTANCE (DEGREES)

Fig. 4-2

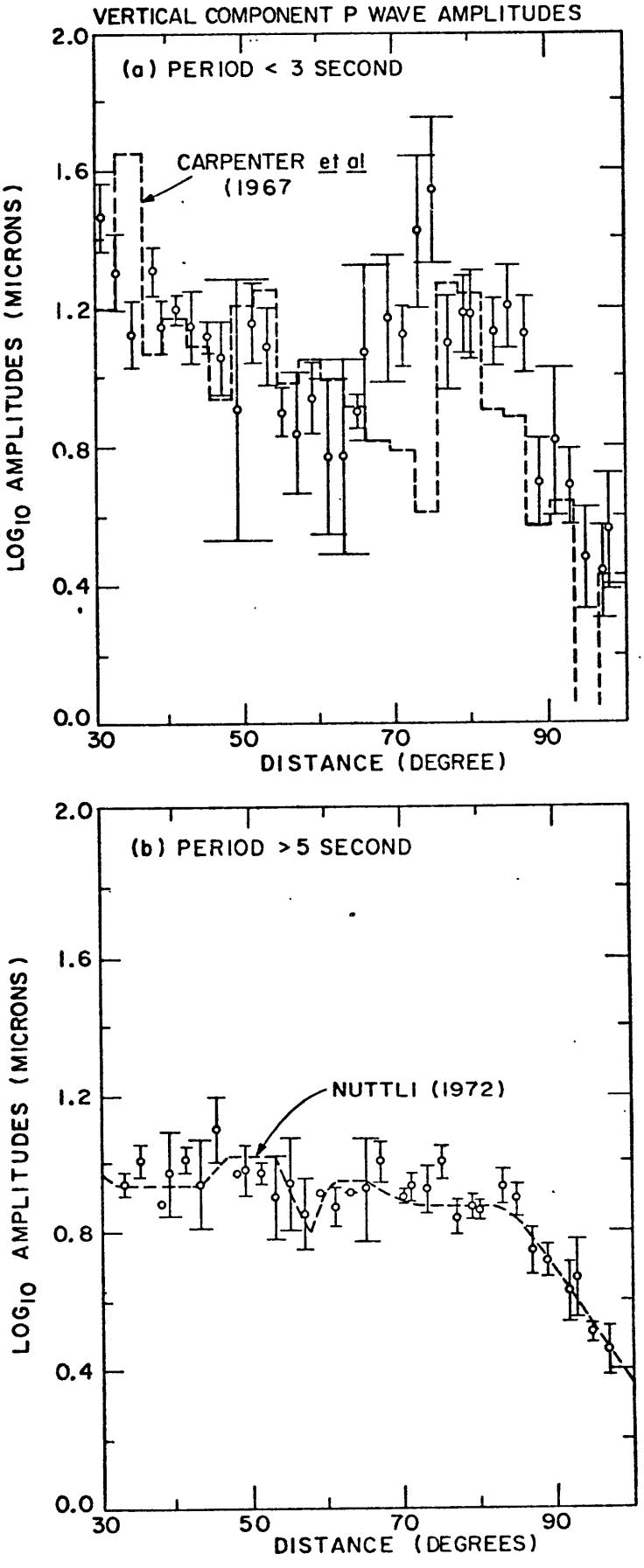

VERTICAL COMPONENT P WAVE AMPLITUDES
(a) PERIOD < 3 SECOND
CARPENTER et al (1967
LOG10 AMPLITUDES (MICRONS)
2.0
1.6
1.2
0.8
0.4
0.0
30
50
70
90
DISTANCE (DEGREE)
(b) PERIOD >5 SECOND
NUTTLI (1972)
LOG10 AMPLITUDES (MICRONS)
DISTANCE (DEGREES)

Fig. 4-3

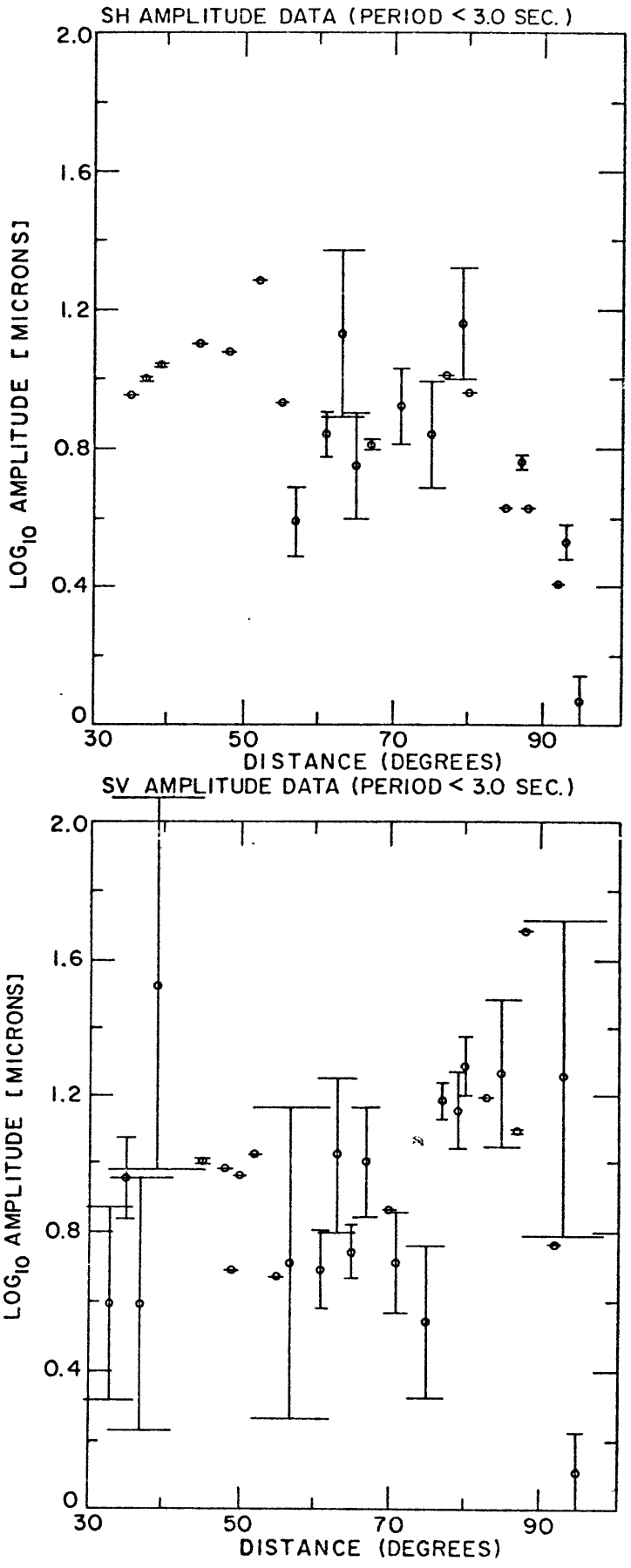
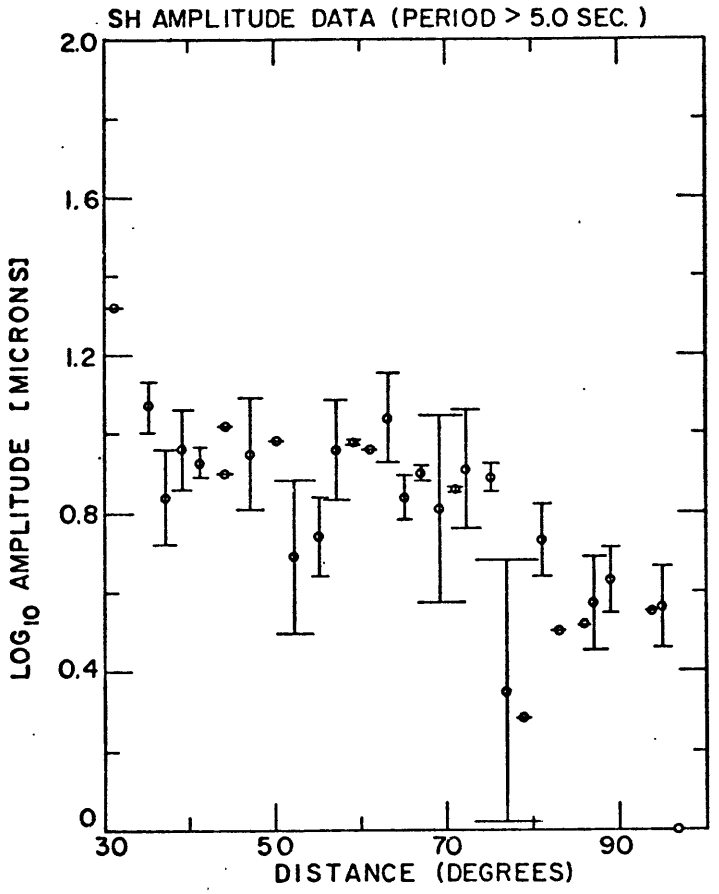

SH AMPLITUDE DATA (PERIOD < 3.0 SEC.)
LOG10 AMPLITUDE [MICRONS]
2.0
1.6
1.2
0.8
0.4
0
30
50
70
90
DISTANCE (DEGREES)
SV AMPLITUDE DATA (PERIOD < 3.0 SEC.)
LOG10 AMPLITUDE [MICRONS]
2.0
1.6
1.2
0.8
0.4
0
30
50
70
90
DISTANCE (DEGREES)

Fig. 4-4


SH AMPLITUDE DATA (PERIOD > 5.0 SEC.)
2.0
1.6
1.2
0.8
0.4
0
LOG10 AMPLITUDE [MICRONS]
30
50
70
90
DISTANCE (DEGREES)

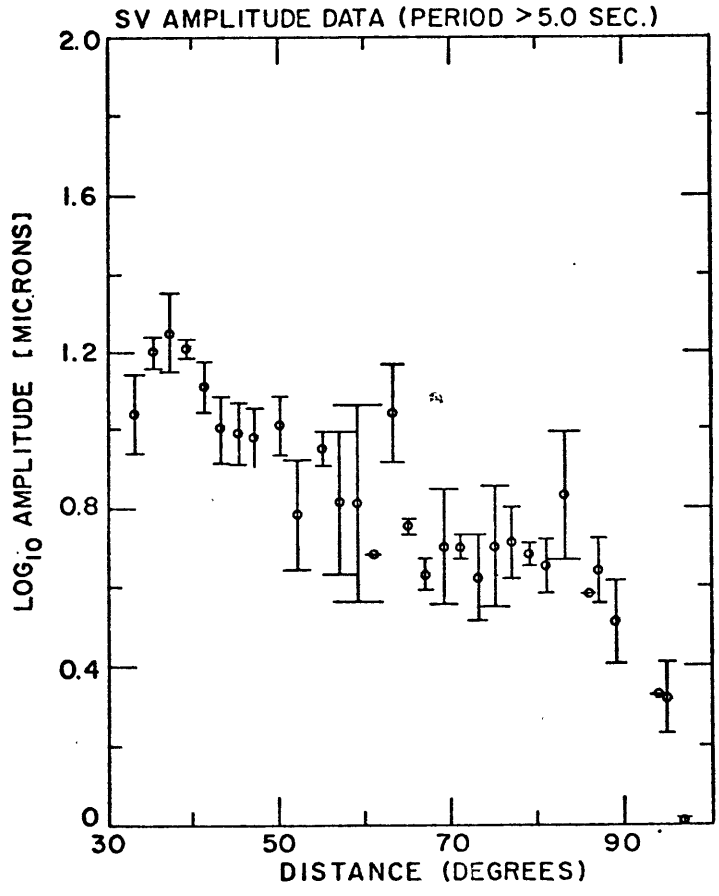
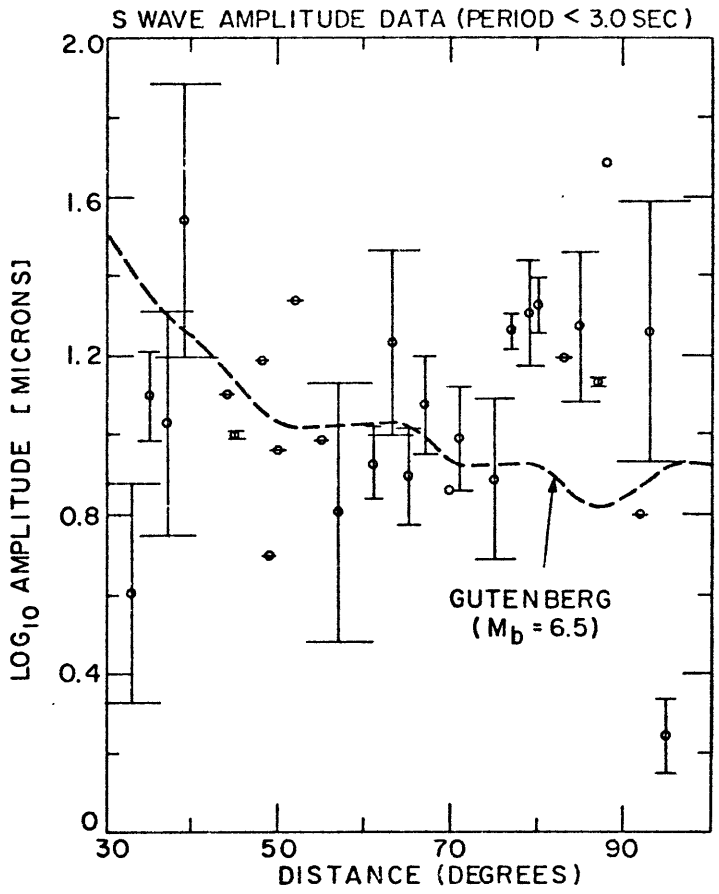

SV AMPLITUDE DATA (PERIOD >5.0 SEC.)
2.0
1.6
1.2
0.8
0.4
0
LOG10 AMPLITUDE [MICRONS]
30
50
70
90
DISTANCE (DEGREES)

Fig. 4-5


S WAVE AMPLITUDE DATA (PERIOD < 3.0 SEC)
LOG10 AMPLITUDE [MICRONS]
2.0
1.6
1.2
0.8
0.4
0
30
50
70
90
DISTANCE (DEGREES)
GUTENBERG
(Mb = 6.5)

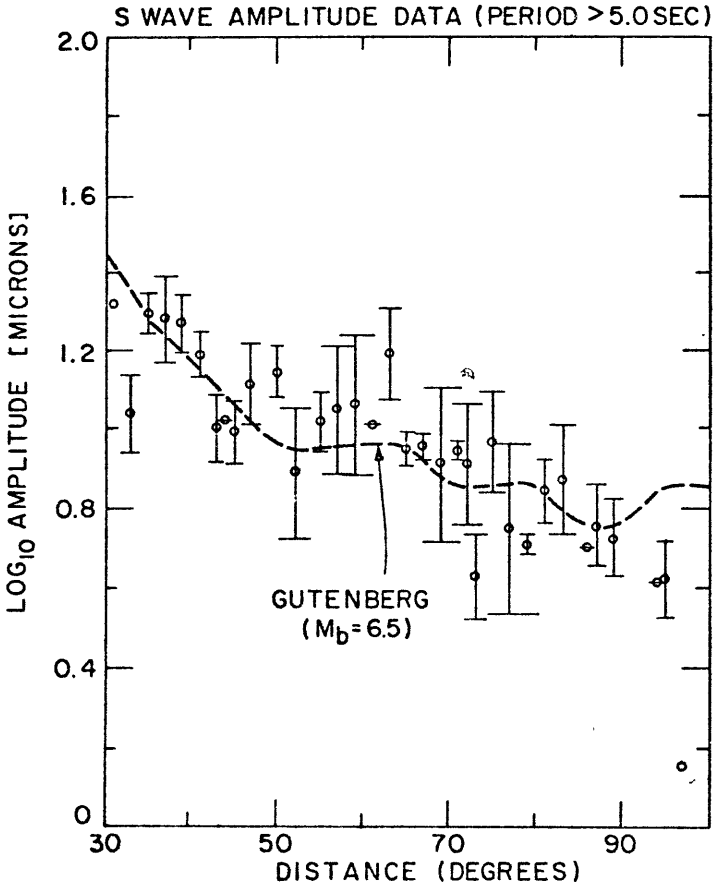

S WAVE AMPLITUDE DATA (PERIOD > 5.0 SEC)
LOG10 AMPLITUDE [MICRONS]
2.0
1.6
1.2
0.8
0.4
0
30
50
70
90
DISTANCE (DEGREES)
GUTENBERG
(Mb = 6.5)

Fig. 4-6

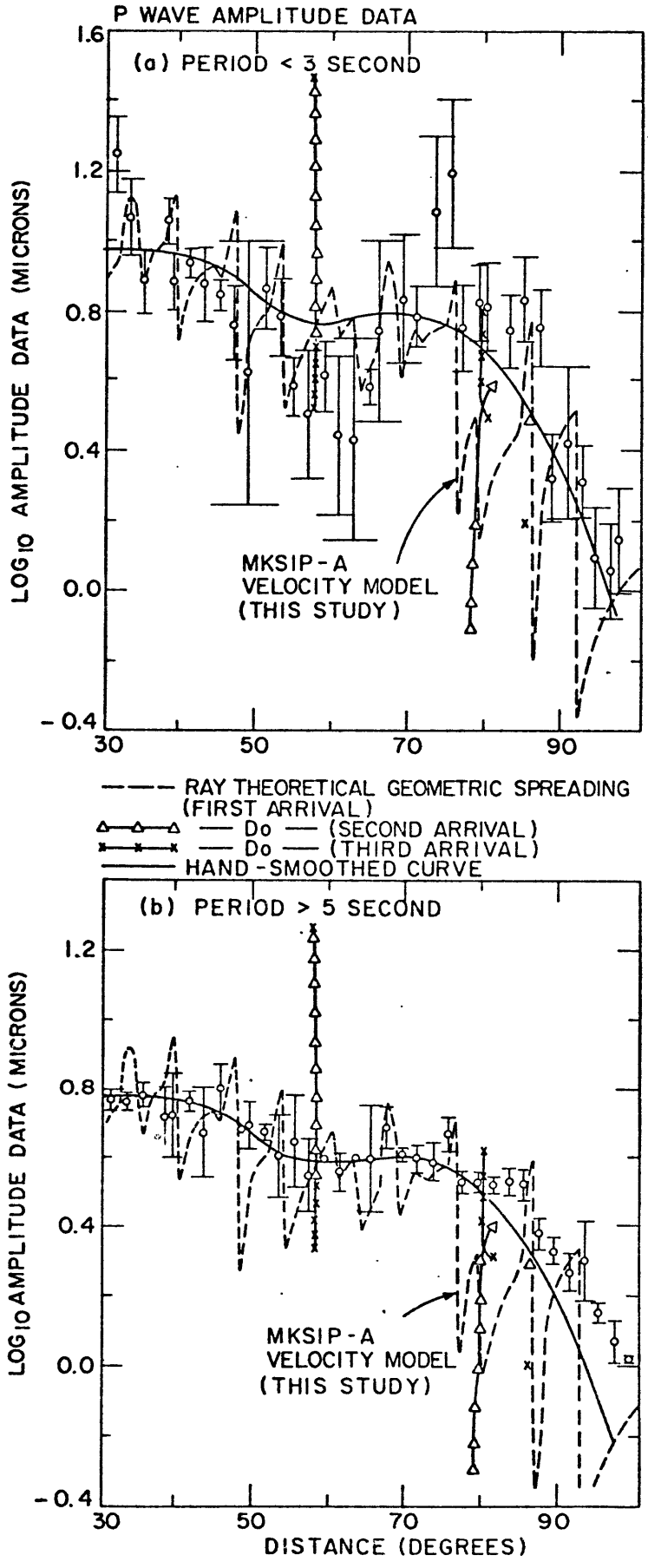

P WAVE AMPLITUDE DATA
(a) PERIOD < 3 SECOND
LOG10 AMPLITUDE DATA (MICRONS)
1.6
1.2
0.8
0.4
0.0
-0.4
30
50
70
90
MKSIP-A
VELOCITY MODEL
(THIS STUDY)
RAY THEORETICAL GEOMETRIC SPREADING
(FIRST ARRIVAL)
Do (SECOND ARRIVAL)
Do (THIRD ARRIVAL)
HAND-SMOOTHED CURVE
(b) PERIOD > 5 SECOND
LOG10 AMPLITUDE DATA (MICRONS)
1.2
0.8
0.4
0.0
-0.4
30
50
70
90
DISTANCE (DEGREES)
MKSIP-A
VELOCITY MODEL
(THIS STUDY)

Fig. 4-7

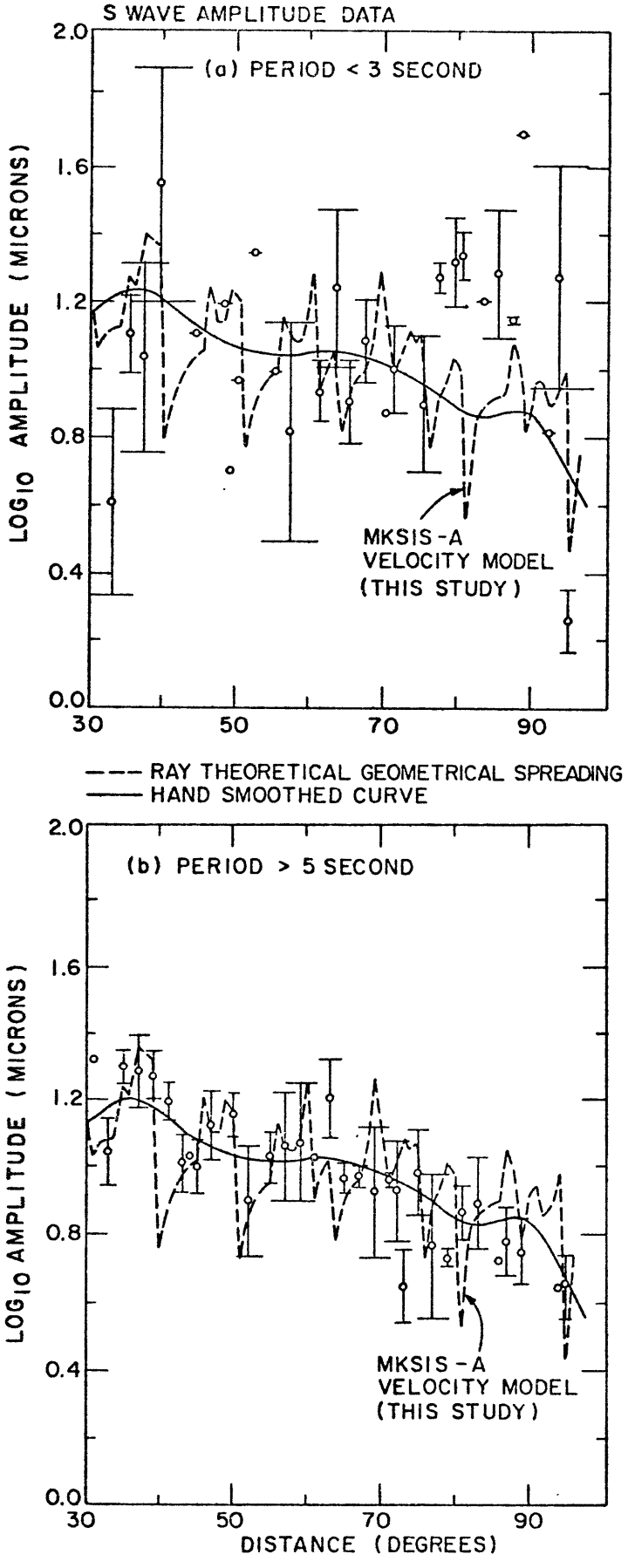

S WAVE AMPLITUDE DATA
(a) PERIOD < 3 SECOND
LOG10 AMPLITUDE (MICRONS)
2.0
1.6
1.2
0.8
0.4
0.0
30
50
70
90
MKSIS-A
VELOCITY MODEL
(THIS STUDY)
--- RAY THEORETICAL GEOMETRICAL SPREADING
—— HAND SMOOTHED CURVE
(b) PERIOD > 5 SECOND
LOG10 AMPLITUDE (MICRONS)
2.0
1.6
1.2
0.8
0.4
0.0
30
50
70
90
MKSIS-A
VELOCITY MODEL
(THIS STUDY)
DISTANCE (DEGREES)

Fig. 4-8

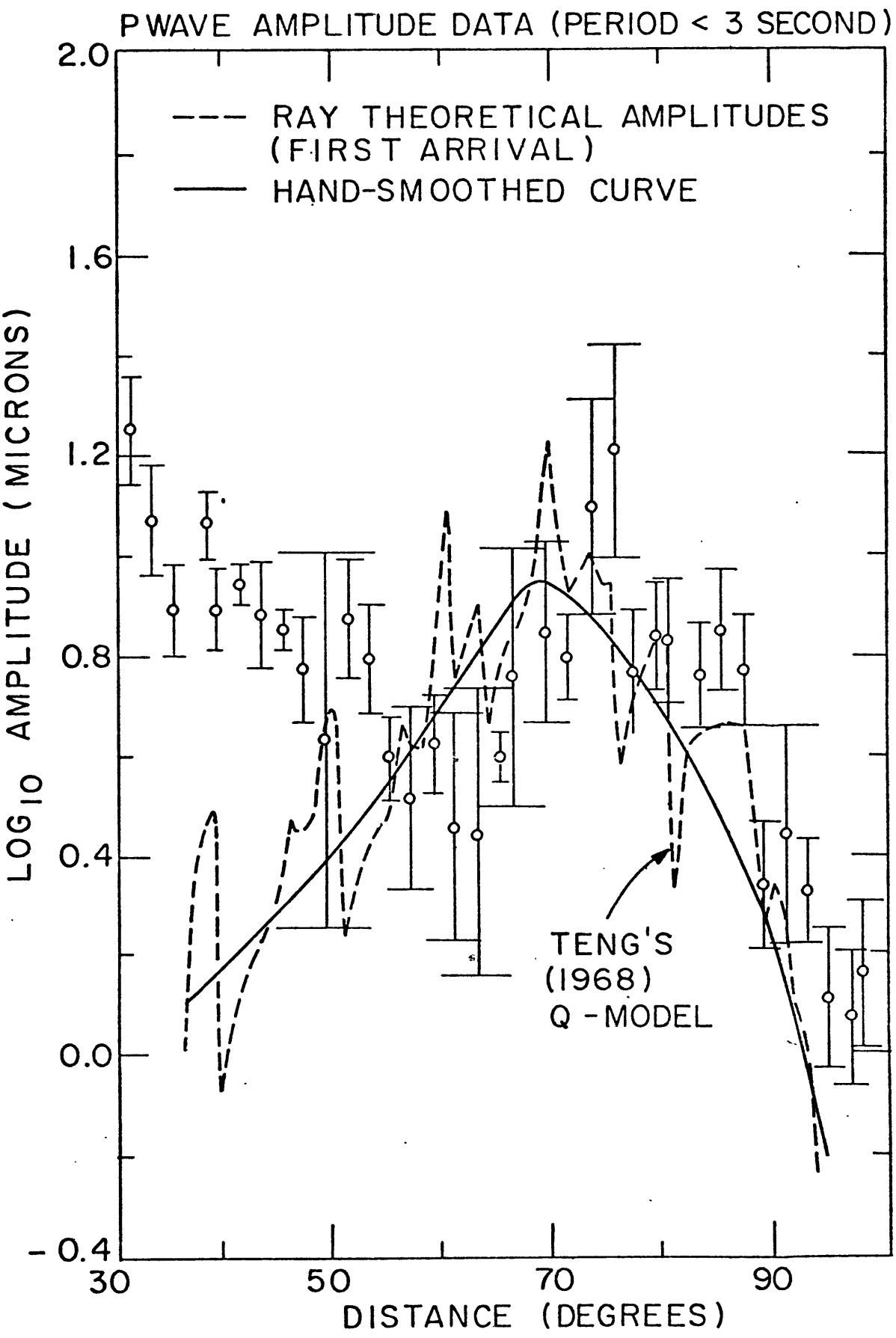

PWAVE AMPLITUDE DATA (PERIOD < 3 SECOND)
RAY THEORETICAL AMPLITUDES
(FIRST ARRIVAL)
HAND-SMOOTHED CURVE
TENG'S
(1968)
Q - MODEL
LOG10 AMPLITUDE (MICRONS)
DISTANCE (DEGREES)
2.0
1.6
1.2
0.8
0.4
0.0
- 0.4
30
50
70
90

Fig. 4-9

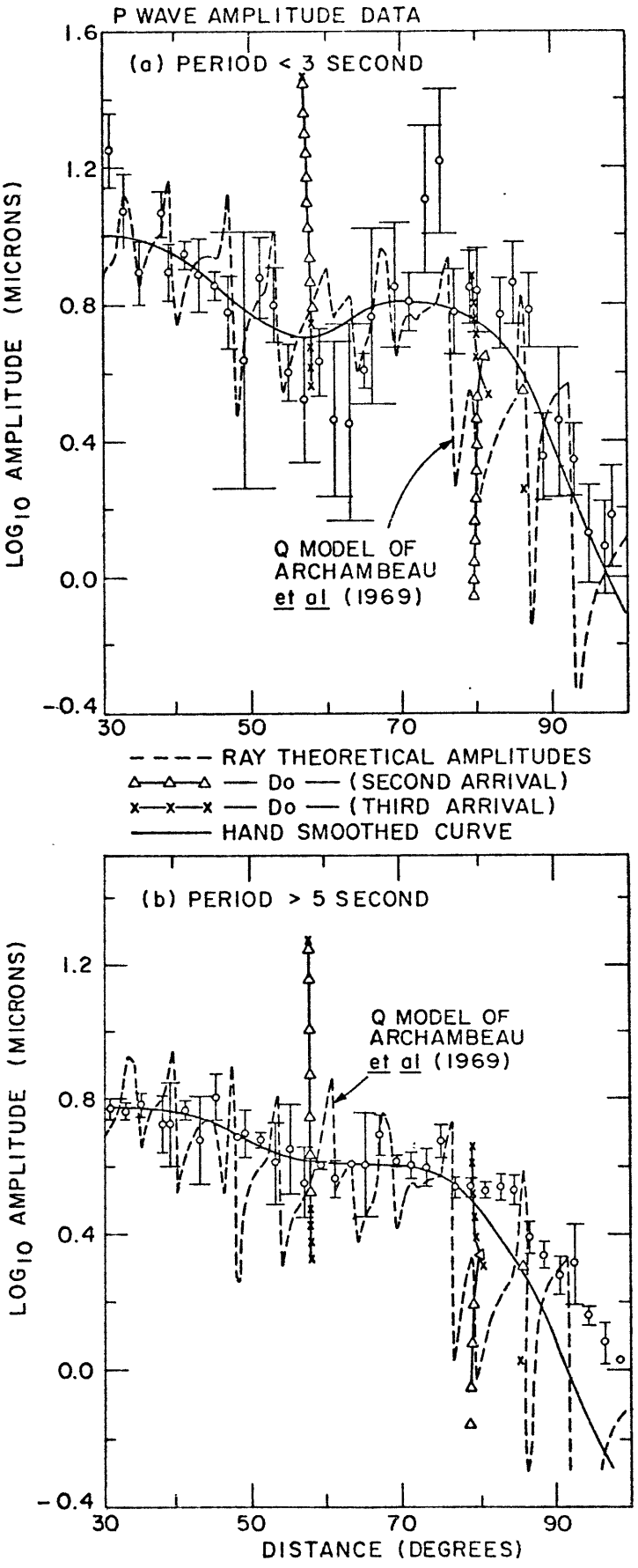

P WAVE AMPLITUDE DATA
(a) PERIOD < 3 SECOND
LOG10 AMPLITUDE (MICRONS)
1.6
1.2
0.8
0.4
0.0
-0.4
30
50
70
90
Q MODEL OF ARCHAMBEAU et al (1969)
RAY THEORETICAL AMPLITUDES
Do (SECOND ARRIVAL)
Do (THIRD ARRIVAL)
HAND SMOOTHED CURVE
(b) PERIOD > 5 SECOND
LOG10 AMPLITUDE (MICRONS)
1.2
0.8
0.4
0.0
-0.4
30
50
70
90
Q MODEL OF ARCHAMBEAU et al (1969)
DISTANCE (DEGREES)

Fig. 4-10

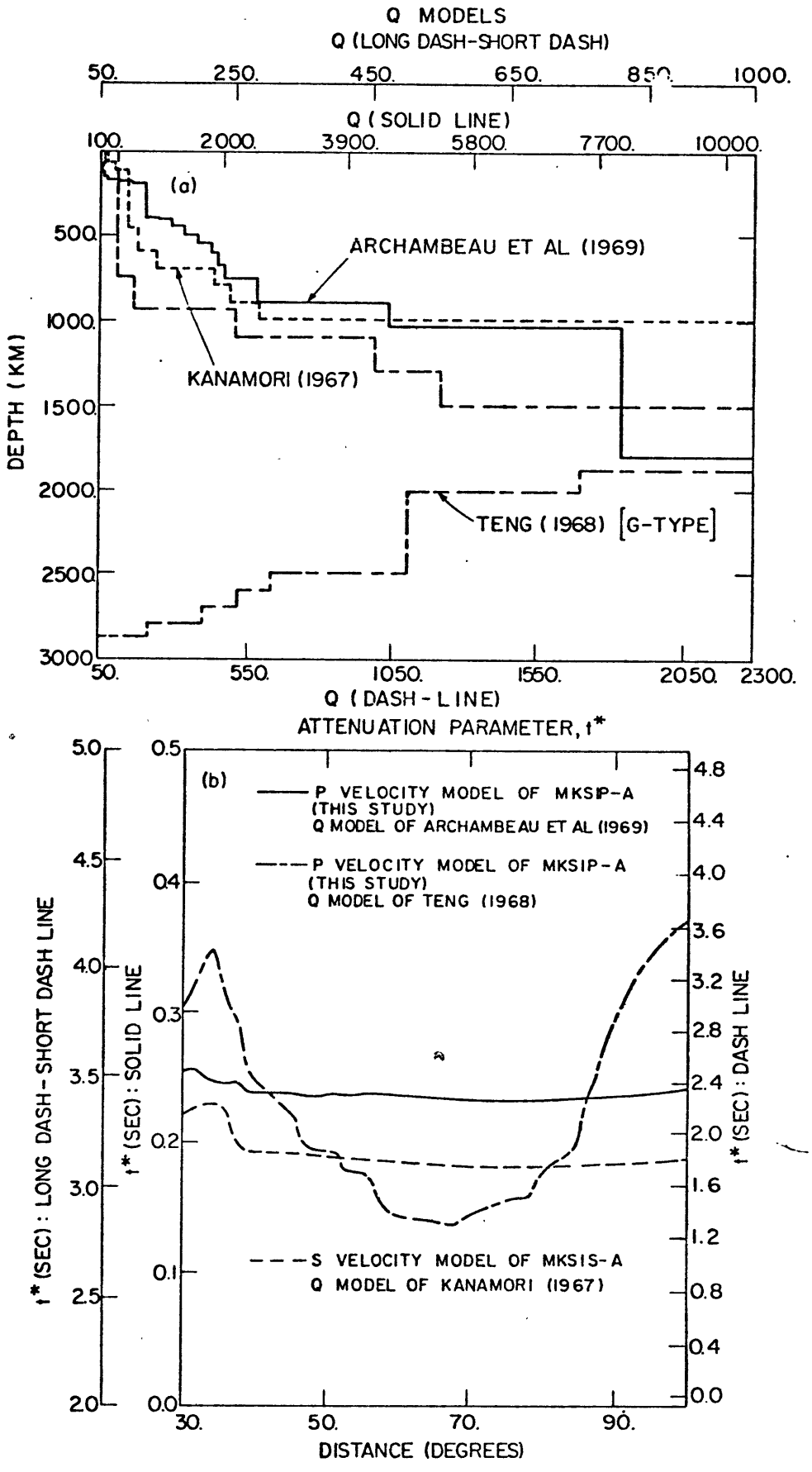

Q MODELS
Q (LONG DASH-SHORT DASH)
50. 250. 450. 650. 850. 1000.
Q (SOLID LINE)
100. 2000. 3900. 5800. 7700. 10000.
(a)
ARCHAMBEAU ET AL (1969)
KANAMORI (1967)
TENG (1968) [G-TYPE]
DEPTH (KM)
500.
1000.
1500.
2000.
2500.
3000.
50. 550. 1050. 1550. 2050. 2300.
Q (DASH-LINE)
ATTENUATION PARAMETER, t*
(b)
P VELOCITY MODEL OF MKSIP-A
(THIS STUDY)
Q MODEL OF ARCHAMBEAU ET AL (1969)
P VELOCITY MODEL OF MKSIP-A
(THIS STUDY)
Q MODEL OF TENG (1968)
S VELOCITY MODEL OF MKSIS-A
Q MODEL OF KANAMORI (1967)
t* (SEC): LONG DASH-SHORT DASH LINE
5.0 4.5 4.0 3.5 3.0 2.5 2.0
t* (SEC): SOLID LINE
0.5 0.4 0.3 0.2 0.1 0.0
t* (SEC): DASH LINE
4.8 4.4 4.0 3.6 3.2 2.8 2.4 2.0 1.6 1.2 0.8 0.4 0.0
30. 50. 70. 90.
DISTANCE (DEGREES)

Fig. 4-11

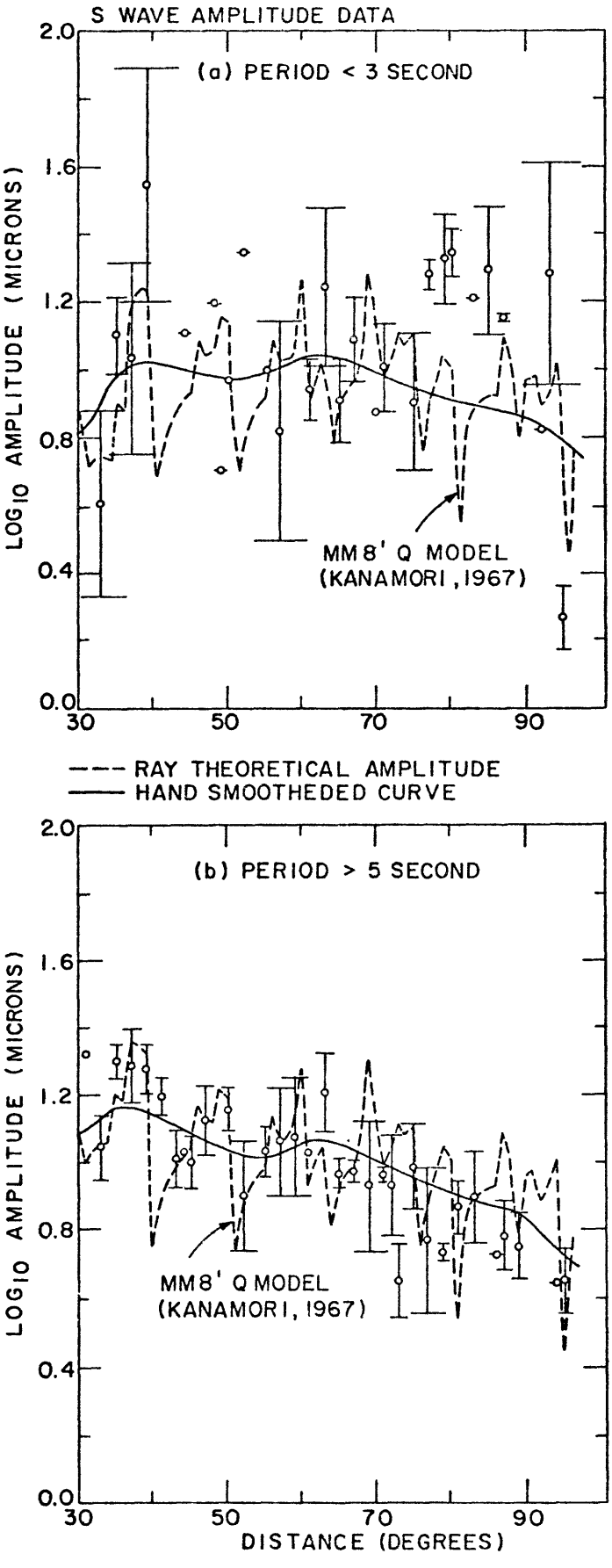

S WAVE AMPLITUDE DATA
(a) PERIOD < 3 SECOND
LOG10 AMPLITUDE (MICRONS)
2.0
1.6
1.2
0.8
0.4
0.0
30
50
70
90
MM8' Q MODEL
(KANAMORI, 1967)
--- RAY THEORETICAL AMPLITUDE
—— HAND SMOOTHEDED CURVE
(b) PERIOD > 5 SECOND
MM8' Q MODEL
(KANAMORI, 1967)
DISTANCE (DEGREES)

Fig. 4-12

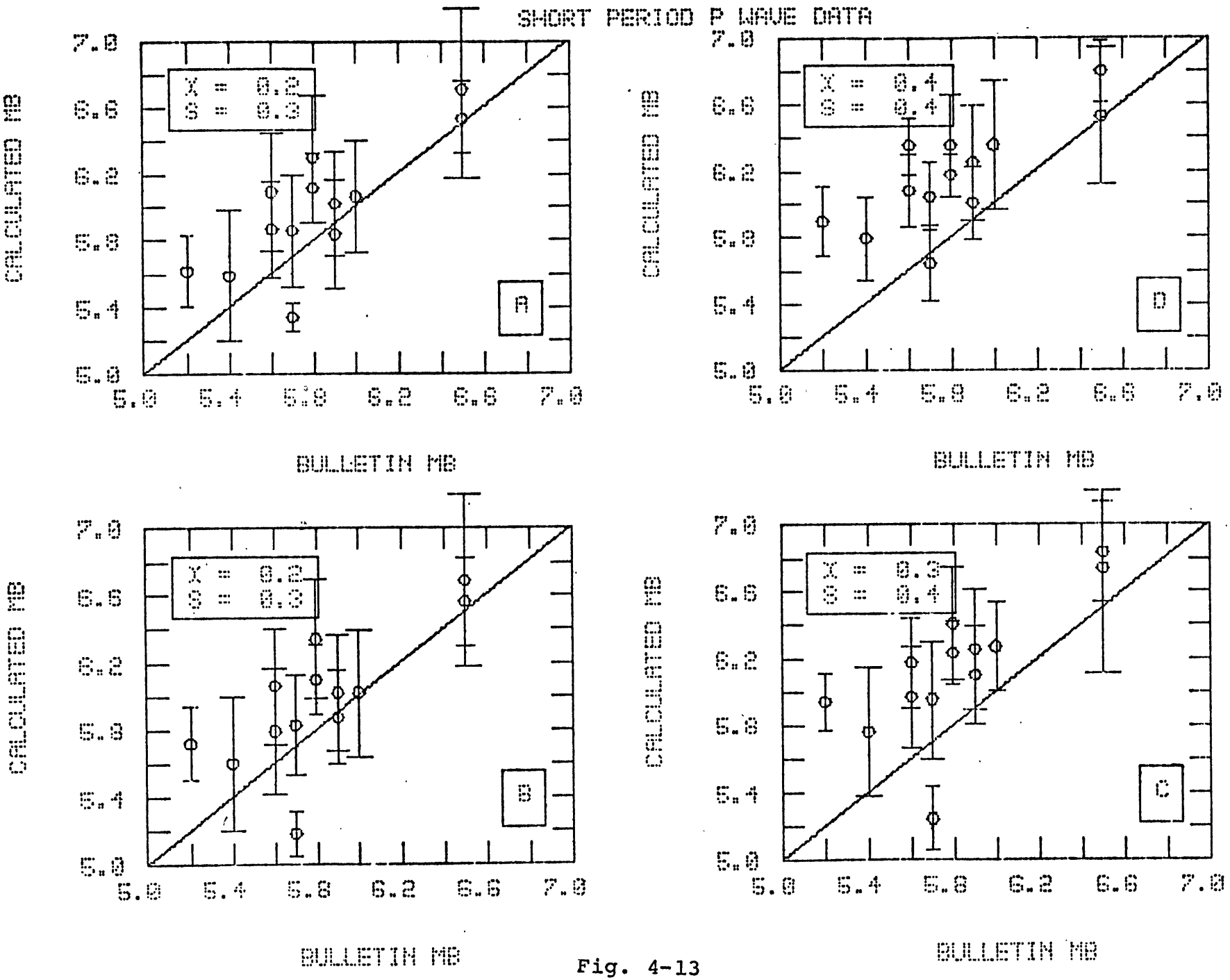

SHORT PERIOD P WAVE DATA
CALCULATED MB
BULLETIN MB
X = 0.2
S = 0.3
A
X = 0.4
S = 0.4
D
B
X = 0.3
S = 0.4
C
5.0
5.4
5.8
6.2
6.6
7.0

Fig. 4-13

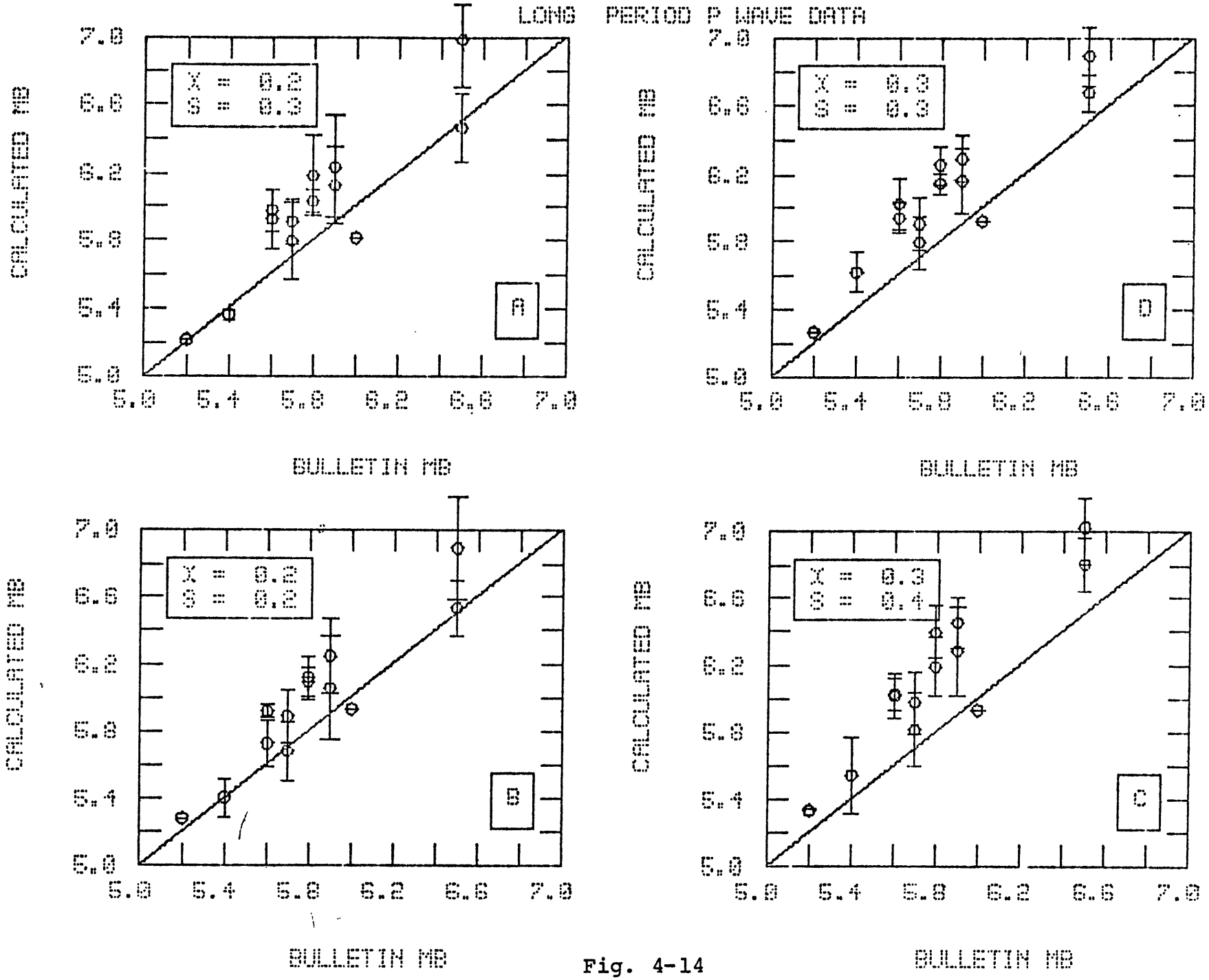

LONG PERIOD P WAVE DATA
CALCULATED MB
BULLETIN MB
X = 0.2
S = 0.3
A
X = 0.3
S = 0.3
D
X = 0.2
S = 0.2
B
X = 0.3
S = 0.4
C
5.0
5.4
5.8
6.2
6.6
7.0

Fig. 4-14

CHAPTER 5

LATERAL VARIATION IN THE STRUCTURE OF THE EARTH'S MANTLE

Introduction

With the increasing data and growing evidence for lateral variation in seismic velocities, one dimensional earth models present an oversimplified picture of the real earth. On the other hand, lateral variations are not large in terms of percentage, so that one dimensional models can be appropriately used as a reference frame for the description of lateral inhomogeneities.

In this chapter we start by presenting evidence for lateral variation in the earth's mantle from body wave travel time and amplitude data from deep earthquakes. First, we look at variations in the crust and upper mantle, and then go deeper giving evidence for lateral inhomogeneity in the lower mantle. In the third part of this chapter we describe our scheme and results of inversion of body wave travel time data to obtain three dimensional earth models of seismic velocity. From such three dimensional models we draw our conclusions about the state of the lower mantle, especially with reference to its interactions with the observed lateral variations in the earth's upper mantle.

5.1 EVIDENCE OF LATERAL VARIATION IN THE EARTH'S UPPER MANTLE

There are a variety of methods for studying the lateral inhomogeneity in the earth's upper mantle (see for example, Toksöz et al., 1967; Knopoff, 1971a). One such method is to find the difference in the travel time (or amplitude) of body waves along vertical paths beneath the stations or equivalently to determine "station anomalies" (see Chap. 2) with reference to the average structure of the earth. At present, this method cannot give a complete picture of lateral variation in the earth's upper mantle as there are no stations on ocean bottoms. In fact, lateral variation between oceanic and continental upper mantle contributes to most of the lateral inhomogeneity (Toksöz, et al., 1967; Dziewonski, 1971). But, on the other hand, this method has perhaps the greatest resolving power for lateral variations within the continental upper mantle.

In the past, Cleary and Hales (1966), Herrin and Taggart (1968), Lilwall and Douglas (1970) among others have studied the regional variation in the earth's structure by using station anomalies for travel time data. Herrin and Taggart (1968) have further shown a correlation of P wave travel time station anomalies of North American stations with lateral

variation in Pn velocity beneath this continent, thus suggesting that origin of these station anomalies lies within the upper mantle (see also Hales, 1972). A part of these station anomalies can certainly originate due to lateral variation in crustal structure (Press and Biehler, 1964). Carpenter et al. (1967) and Booth et al. (1974) carried out a similar study of station anomalies with amplitude data. But all previous authors used data primarily from shallow focus earthquakes or explosions. In this study we redetermine the station anomalies of travel times and amplitude data exclusively from deep focus earthquakes and thereby remove the spurious effect, if any, of contamination of station anomalies by the effect of near source heterogeneity in the upper mantle.

5.1.1 Station anomalies for deep focus travel time data

In this study we have found that the standard deviation of travel time residuals at a station is larger for the surface focus times than that for deep focus times though the average values of the residuals are comparable to each other. Figures 5-1 and 5-2 compare the histograms of the standard deviations of P and S wave station anomalies of this study against those determined by others using surface focus travel times. The average standard deviation of P station anomalies determined from deep

focus data in this study is about 0.57 seconds whereas for similar stations (124 in all), use of surface focus travel time data gives the following values: 0.96 seconds for the data set of Herrin and Taggart (1968), 0.93 seconds for the data set of Lilwall and Douglass (1970) and 0.70 seconds for the data set of Cleary and Hales (1966). In other words, the average standard deviation of P station anomalies determined from deep focus travel time data is about twice as small as that from surface focus data. The effectiveness of deep focus data becomes more significant when we notice that Herrin and Taggart (1968) and Lilwall and Douglas (1970) had more free parameters (incorporating sinusoidal azimuthal variation of station anomaly) than we had to fit the travel time residuals at a station. Standard deviations of S wave station anomalies also show a trend similar to P wave data. Only 15 WWSSN stations on the North American continent for which Doyle and Hales (1967) also tabulated the standard deviation of S wave station anomalies, have been used for this comparison (see Fig. 5-2). Average standard deviation of 2.45 seconds for S wave station anomalies determined in this study can be compared against the value of 4.35 seconds for the data set of Doyle and Hales (1967). Note that limited azimuthal sampling of deep focus travel time data cannot explain such a two-fold

reduction in the standard deviation of station anomalies as compared to surface focus data. We have already shown in Chap. 2 (section 2.5) that with reasonable assumptions, the azimuthal variation of velocity beneath a station can cause a scatter of only ±0.3 seconds for the observed P wave travel time residuals at a station and a scatter of about ±0.6 seconds for S wave residuals. These estimates of scatter comprise only 15-30% of the observed standard deviations of station anomalies determined from surface focus travel time data, whereas reduction in those standard deviations by using deep focus data is more than 50%. Smallness in the standard deviation of station anomalies from deep focus data can be explained, on the other hand, by the elimination of scatter due to upper mantle heterogeneity near the source region.

Next, we have compared the average station anomalies determined by different authors using various methods and distinct sets of travel time data. If these average station anomalies are found to be compatible to one another, we can attach then much physical significance to their values. This comparison of average station anomalies has been shown in Fig. 5-3 using a common set of stations in North America - 42 stations for comparison of P wave station anomalies and 15 WWSSN stations

for comparison of S wave station anomalies. Because of moderately good distribution of deep events from these stations, station anomalies of this study are likely to be better determined for these stations than those in other parts of the world. Note that r.m.s. deviations of station anomalies of other studies with respect to ours are smaller than average standard deviation of station anomalies. Hence a physical interpretation of these station anomalies is justified.

5.1.1A Interpretation of station anomalies for travel times

Lateral variations in the upper mantle of North America are well documented in the literature (see for example, Herrin, 1969; Archambeau et al., 1969; Solomon and Toksöz, 1970; Biswas and Knopoff, 1974). P and S wave station anomalies for this continent have been shown in Fig. 5-4 and Fig. 5-5 (a complete list of the station anomalies is given in Appendix L). Those station anomalies agree with our present knowledge that compressional and shear velocities under the central and eastern part of North America are higher than those in the Basin and Range province. Attenuating stations like ALQ and TUC (Solomon and Toksöz, 1970) also show positive station anomalies (or late arrivals) indicating a correlation between low velocity and high attenuation. A high

correlation also exists between S and P wave station anomalies (Fig. 5-6) with a ratio of S to P station anomaly in the range of 3.0-4.0. Doyle and Hales (1967) and Hales and Roberts (1970a) also arrived at similar conclusions from entirely different sets of data.

For interpretation of lateral variation on a global scale we have classified the stations as shown on Table 5-1 after Sipkin and Jordan (1974). Statistics of P and S wave station anomalies for each group of stations are tabulated in Table 5-2. This table along with Fig. 5-7 clearly shows that even on a global scale there is a variation in P and S wave station anomalies similar to those observed for stations on North America. For example, stations on stable continents and shield areas, such as northern Europe, Canadian shield, South African shield, Indian shield, eastern and central U.S.A., are marked with early arrivals or negative station anomalies whereas stations on continental rift zones like eastern Africa and Basin and Range province in U.S.A. show significantly late arrivals (or positive station anomalies). There may also be a difference in the ratio of S to P station anomalies between these two groups of stations. It appears that for stations on stable continents and shield areas (including eastern and central U.S.A.) this ratio may be smaller (in the range of 2.0-4.0) as compared

to stations on continental rift zones where this ratio may be as large as 4.0-6.0 (Fig. 5-7). To investigate the implications for the ratio of S to P station anomaly, we write that ratio as follows

$$\frac{\delta t_s}{\delta t_p} = \left(\frac{\delta\beta}{\delta\alpha}\right) \cdot \left(\frac{\alpha^2}{\beta^2}\right) \qquad (5.1)$$

where α and β are the P and S wave velocities for the upper mantle in the average earth and $\delta\alpha$, $\delta\beta$ are the velocity anomalies in the real earth. It may be reasonable to assume that the upper mantle of the average earth has a Poisson ratio close to 0.28 (see, for example, Jordan and Anderson, 1974; Gilbert and Dziewonski, 1974). On this assumption,

$$\frac{\alpha}{\beta} = 1.81 \qquad (5.2)$$

Then, equation (5.1) can be rewritten as:

$$\left(\frac{\delta\beta}{\delta\alpha}\right) \cdot \left(\frac{\alpha}{\beta}\right) = 0.55 \ \frac{\delta t_s}{\delta t_p} \qquad (5.3)$$

For stable continent and shield areas, $\frac{\delta t_s}{\delta t_p} \simeq 3.0$

so that from (5.3)

$$\left(\frac{\delta\beta}{\delta\alpha}\right)\left(\frac{\alpha}{\beta}\right) = 1.66 \qquad (5.4)$$

For continental rift zones, $\frac{\delta t_s}{\delta t_p} \simeq 5.0$, which gives

$$\left(\frac{\delta\beta}{\delta\alpha}\right) \cdot \left(\frac{\alpha}{\beta}\right) = 2.75 \qquad (5.5)$$

From the limited measurements of the temperature coefficients of the velocities for the upper mantle constituents (Table 5-3), it may appear that mere temperature difference (with respect to average earth) cannot satisfy either (5.4) of (5.5). All laboratory measurements of $\left(\frac{\delta\beta}{\delta\alpha}\right).\left(\frac{\alpha}{\beta}\right)$ for temperature dependence fall short of values derived from our seismic observation. In addition to temperature excess from the average earth, one may have to introduce partial melting to explain the high ratio of S to P station anomalies. Such a suggestion was also made by Hales and Doyle (1967) and Hales and Herrin (1972). In fact, Walsh's (1969) theoretical model for velocity in partially melted material also predicts a high ratio of S to P station anomaly. A large decrease in ridigity but relatively negligible decrease in bulk modulus are the features of Walsh's model. From the viewpoint of attenuation, this model was verified for the upper mantle of western North America by Solomon and

Toksöz (1970) and Solomon (1972).

Another significance in our determination of P and S station anomalies is to confirm that overall P and S wave velocity under normal continents may be faster than that under normal oceans. Travel times to normal oceanic stations are late compared to normal continental stations by about 1 and 2 seconds respectively for P and S waves (Table 5-2). Extreme differences in S wave station anomalies between oceanic and continental stations are no more than 3 seconds (Table 5-4). The observed difference in S wave station anomalies is found to be compatible with the difference in the vertical travel times of shield and oceanic upper mantle models (Fig. 5-8) as determined from surface wave dispersion data. These models suggest a difference between shield and oceanic structure up to only 200-300 km of depth. Whether or not lateral variation between these two structures extends up to a depth of about 700 km (Sipkin and Jordan, 1974) is an open question but such conclusions are not required by our data.

5.1.2 Station anomalies for amplitudes of P, SV and SH wave

Like travel time data, station anomalies for amplitude data also originate due to lateral heterogeneity beneath the stations. But unlike their counterparts, amplitude

station anomalies are not only controlled by velocity anomalies beneath the station, but also by anomalous attenuation (Teng, 1968; Mikumo and Kurita, 1968; Solomon and Toksöz, 1970), acoustic impedance of the layers near the recording site (see for example Murphy et al., 1971; Booth et al., 1974) and possible mode conversion. Those effects are likely to be frequency dependent. So, corresponding to our amplitude-distance curves, station anomalies were divided into two categories - short period station anomaly (for waves with period <3.0 second) and long period station anomaly (for waves with period >5.0 second). Values of amplitude station anomalies for various WWSSN stations throughout the world have been listed in Tables I and II of Appendix M respectively for short period and long period amplitude data. Note that positive station anomalies in that list mean larger amplitudes compared to that of average earth and negative station anomalies stand for smaller amplitudes. On the whole, station anomalies of $\log_{10}$-amplitudes (in microns) for P and S (SH and SV) waves range from about -1.0 to +1.0. Short period station anomalies have a larger range of variation than long period station anomalies by a factor of two or more. This is expected as short period amplitudes are likely to be more affected

by the fine structure in the crust and the upper mantle and/or by the Q-anomaly.

It is also worth mentioning that there is a major discrepancy between amplitude station anomalies and travel time station anomalies in the sense that amplitude station anomalies for S waves are not 3-4 times larger than those of P waves, but the values are comparable to each other. It merely suggests that crustal layering affects P wave amplitudes more than amplitudes of S waves because of smaller wavelengths for P wave whereas the effect of anelastic attenuation is stronger for S waves compared to P waves.

Fig. 5-9 compares our short period P wave amplitude station anomalies with those of Carpenter et al. (1967). Their amplitude station anomalies are possibly the best available so far in literature. However, there appears to be little agreement (correlation coefficient = -0.01) between these two sets of station anomalies. Note that Carpenter et al. determined their station anomalies from explosion data whereas we used deep focus amplitude data. It is quite likely that station anomalies determined from explosion data are contaminated by the effect of near source heterogeneity in the upper mantle. Such a contamination is likely to be more pronounced for amplitude data than travel time data from shallow

earthquakes/explosions. In spite of the disagreement in station anomalies, it is not surprising to note a good agreement between our amplitude-distance curve and that of Carpenter et al. (see Chap. 4); the effect of near source heterogeneity is likely to be averaged out by the large data set used in the determination of the amplitude-distance curve.

Fig. 5-10 shows the short and long period P wave amplitude station anomalies for WWSSN stations on the North American continent. Comparison of these amplitude station anomalies with relative attenuation (Solomon and Toksöz, 1970) or with travel time station anomalies (previous section) does not reveal any simple correlation.

5.2 EVIDENCE OF LATERAL VARIATION IN THE DEEP MANTLE

The very presence of lateral heterogeneity in the earth's upper mantle and crust creates a severe problem of resolution in the study of lateral variation in the earth's deep mantle. The resolution has been improved in this study to a great extent by the use of data from deep focus earthquakes, and the correction of these data for lateral inhomogeneity in the upper mantle by station corrections (see previous section) and taking into account the radial inhomogeneity with the help of improved spherically symmetric velocity models (see Chap. 3). We

present here two pieces of evidence for lateral inhomogeneity in the deep mantle by studying the variation of P wave travel times, and S wave travel times along different paths through the lower mantle. Because of the meager quantity of data, evidence from S wave times may not be convincing as to the presence of lateral inhomogeneity in the deep mantle but collectively with those of P times, they endorse our conclusion in that respect.

5.2.1 Evidence from P wave travel time data

In the course of a study (similar to this) of P wave travel times from deep focus earthquakes using about 3300 arrival time data reported in bulletins (Sengupta, 1972; also see Appendix K), it was found that the observed times show a striking dependence upon the ray path (Fig. 5-11). That this regional dependence is not due to any gross error in the bulletin data has been subsequently checked by comparing the data reported in bulletins with the data read personally from the seismograms. The variation in the travel times is seen to be more pronounced beyond about 80° of epicentral distance. In this distance range, for example, there is a variation of about 1.5 seconds in the P wave travel times between paths from the Kuril Arc to Spain-Morocco-Algeria with a mean delay of -1.1 seconds

and paths from South America to northwestern Europe with an average delay of 0.4 seconds. This distance-dependent variation of P wave travel times is best summarized in Fig. 5-12 showing the standard deviations of P wave travel time associated with gross earth data for each 2° distance cell (Table 3-1, in Chap. 3). Notice the trend that standard deviation of P wave travel times increases beyond about 80° of distance.

Possible causes of a regional dependence of P wave travel times are velocity variations in the upper mantle near the source or receiver regions or in the lower mantle, and mislocation of the events (caused by uneven station distribution and so on). Event mislocation is the least likely because it would be expected to cause larger variation in P wave travel times at smaller distances than at larger ones and therefore cannot explain the increase of scatter beyond 80°. The effect of structure beneath the receiver region upon the observed times was largely removed by station corrections (see section 5.1.1) represented by the average of travel time anomalies at each station. Azimuthal variation in this anomaly was not taken into account in our analysis and such variation could possibly be responsible for the large scatter at smaller distances (say at distances of 40°) as those seen

on Fig. 5-12. Barring a problem of non-uniform sampling of stations in the whole distance range of 20°-100°, one does not expect in general the larger scatter beyond 80° to be caused by the azimuthal variation in station anomaly alone as the magnitude of this azimuthal variation is in general small - within ±0.3 seconds (see Table 2-4 in Chap. 2). It is conceivable that structure in the source regions could produce a distance dependent regional variation of this kind, if the velocity anomalies were systematically located relative to the earthquake hypocenters (as indeed they are beneath island arcs). In that case the variations would have to be localized in a very small region beneath the hypocenters, because a distance interval of 80°-100° maps into about 5° difference in angle at the focus at a depth of 550 km. Even if the anomalous regions are as deep as 1000 km, the velocity change must occur over a horizontal distance of only 60 km or so. This possibility may be ruled out because all the earthquakes in each source region yielded a similar pattern of travel time residuals, even though the epicenter locations in each region (see Table K-1 in Appendix K) were typically distributed over as much as 200 km. Velocity variations near the focus are further ruled out because pronounced early arrivals beyond 80° such as those from the event at the Sea of Okhotsk (Fig. 5-11ℓ) are not restricted to observations

of deep earthquakes; they also occur, for example, in the data from nuclear explosions in the Marshall Islands (Fig. 5-13) along paths toward western North America (BOU, FAY, KLC, RCD, RES, TUC), India-Pakistan (POO, QUE), Sweden (KIR) and Antarctica (BYR) (see also Carder et al., 1966).

The arguments for a deep mantle origin of these systematic variations in observed P wave travel times became stronger when Julian and Sengupta (1973) calculated the average travel time residual for each of a number of "bundles" of rays following nearly identical paths from a seismic region to a group of stations thus reducing the possibility of the introduction of bias by the azimuthal variation of station anomalies. Table 5-5 summarizes the travel time data for all paths for which 9 or more observations were available. For each path a student's t-test was used to evaluate the hypothesis that the mean travel time (after station corrections have been applied) is the value given by the smooth curve shown in Fig. 5-11 and that deviations from this curve can be attributed to random measuring errors. Those ray paths for which the hypothesis could be rejected at the 99.5% confidence level are indicated in Table 5-5. For observations at distances beyond 70°, 16 paths (out of 35 tested) showed significant variations from the average curve, whereas for smaller

distances (less than 70°) only 3 anomalous paths (out of 22) were found. This strongly suggests that most of the systematic variations in observed P times originate in the deep mantle (depth >2000 km).

5.2.2 Evidence from S wave travel time data

Observations of S wave travel times from deep earthquakes corroborate the inferences obtained in the previous section. For example, Fig. 5-14 shows that observed S times also have similar striking dependence upon the ray paths as P wave data (Fig. 5-11). Around 80° of distance, the variation in S times is as large as 7 seconds between paths from the Tonga Arc to western North America with a mean delay of 4.4 seconds and paths from the Kuril Arc to eastern North America with a mean delay of -2.8 seconds. The standard deviations of S times (Fig. 5-12) associated with gross earth data for each 2° distance cell (see Table 3-3 in Chap. 3) reveal the largeness in the variation of S times also in the distance range of 85°-100°. Significantly, large standard deviations are found at epicentral distances of 48°, 60° and 70° where we observed earlier sharp bends in the reduced S times (see Chap. 3, section 3.2.2). These peaks in variation of S times have their counterpart in the standard deviation of P times at least for the distance ranges of

48°-50° and 60°-62°. Tables 5-6A and 5-6B list the paths corresponding to data in those two distance ranges. It is clear from the tables that the large standard deviations in these distance ranges are due to systematic variation of travel times and amplitudes along different groups of paths. Some of these paths, for example, the path from the Kuril Arc to northwestern North America and the path from Japan to Alaska were found earlier (see Table 5-5) to have significant variation in the P travel times from the average curve. It is safe, then, to say that the sharp bends observed for average S wave travel times (Fig. 3-4 in Chap. 3) at least in the distance ranges of 48°-50° and 60°-62° are caused mainly by sampling bias and that is why one does not see any corresponding bends in the average P wave travel times which sampled more paths than S wave data.

Table 5-7 lists the means and standard deviations of S wave travel time anomalies for several paths for which five or more data were available. These anomalies were computed for the data shown on Fig. 5-14 with respect to the solid line in that figure. Fig. 5-15 shows comparison between P and S wave travel time anomalies along these paths. The ratios of average S to P anomalies along these paths are apparently very large and may be an artifact of the difference in sample sizes of

P and S wave data (cf. Table 5-5 and Table 5-7). Otherwise, the paths which were found to be significantly early or late for P wave travel time (i.e. path 1-4, 2-4, and 2-5) are also seen to be correspondingly early or late for S wave travel times. The exceptions found for paths 1-6, 2-6, and 2-7 in Fig. 5-15 are not too surprising as the scatter associated with these paths compared to the average value of travel time anomaly is in general larger than for paths 1-4, 2-4, and 2-5. The paths 3-2, 3-3, 4-2 and 4-5 which did not show any significant variation in the P wave travel time residuals from the average curve, also have large scatter in the S travel time anomalies compared to the mean values. Also, when the paths are most similar to each other like paths 1-4 and 2-4, 2-6 and 3-3, 1-6 and 2-7, 3-2 and 4-2 (see Table 5-7), <u>average</u> P and S wave travel time anomalies do not differ much from each other in any of these pairs (Fig. 5-15). Correlation coefficients between P and S wave travel time anomalies are also shown on Fig. 5-15 and Table 5-7. These correlation coefficients were found to be erratic in general. The reason may be that for a given source-station pair beyond 40° of epicentral distance, the S wave does not follow the same path as the corresponding P wave but bottoms at about 100-200 km shallower depth than the P wave (see Fig. 3-22d, Chap. 3).

5.3 METHOD OF ESTIMATING LATERAL VARIATION OF VELOCITY IN THE EARTH'S MANTLE

Estimation of lateral variation of velocity is intimately related to the size of the regions within which the travel time anomalies originate. There are indications (Haddon & Cleary, 1974) that the size of lateral heterogeneities is less than 100 km. With this scale length of heterogeneity a deterministic earth model may not be reliably obtained from our limited quantity of travel time data. On the other hand assuming arbitrarily that travel time anomalies along different ray bundles originate at central 30° of each path, Julian and Sengupta (1973) showed that one can obtain a self-consistent picture for the distribution of velocity anomaly along different paths. The size of inhomogeneity they inferred this way was about 1000 km or less in horizontal dimension and a few hundred km in radial dimension. Corresponding to this scale of heterogeneity, available P wave travel time data may be just sufficient to obtain a three dimensional velocity model of the earth (we will comment later in this chapter on the insufficiency of available S wave travel time data in this respect). With this end in view, the mantle (including the crust) has been divided into blocks of size 10° in longitude, 10° in latitude and 500 km in depth; thus one has altogether 36 x 18 x 6 (=3888) blocks to

consider. Many of these blocks (40% for P wave travel times and 60% for S wave travel times) remained unsampled by our data and so a complete description of a three dimensional velocity model for the earth is not possible at this stage. For the remaining blocks, sampled by our data, the perturbation of velocity from a spherically symmetric earth model has been estimated by a method of successive approximation. Like any other inversion of finite and inaccurate geophysical data, these estimates of velocity anomalies are subject to limitations in resolution and errors due to uncertainty (Backus and Gilbert, 1970). Another limitation of our method is to assume a uniform relative perturbation in velocity ($\delta V/V$) for each block.

If we represent the observed travel time anomaly for the i^{th} earthquake and j^{th} station as ΔT_{ij}^{obs} then we can express the travel time anomalies in terms of relative perturbation of velocity (p_m) in each block as follows:

$$\Delta T_{ij}^{obs} = \sum_m K_{ijm}\, p_m \qquad (5.6)$$

where the index m is summed over the blocks the corresponding ray traverses during its journey from source to receiver and the K_{ijm}'s are the 'data kernels'. A direct least square solution for the p_m's in the above equation

involves inversion of a matrix of size (m x m) where m is of the order of 2000. Even utilizing the symmetric properties of this matrix, this process involves an enormous amount of computer storage space and computation time, so we resorted to the brute-force technique of "successive approximation" of velocity anomaly in each block.

In our method of successive approximation, the r^{th} approximation of the velocity perturbation in the m^{th} block (= p_m^r) is given by the weighted least square solution of the system of n linear equations of the form:

$$\Delta T_{ij}^{obs} + C_{ij}^r = K_{ijm}^r \, p_m^r \qquad (5.7)$$

where n is the number of ray paths passing through the m^{th} block, C_{ij}^r is the r^{th} approximation of the correction to ΔT_{ij}^{obs} for the perturbation of velocity in other blocks, K_{ijm}^r is the r^{th} approximation of "data kernel" of the m^{th} block corresponding to ΔT_{ij}^{obs}. If we use a sign convention such that positive value of p_m^r corresponds to higher velocities than those of the spherically symmetric earth model and negative value of p_m^r to lower velocities, then the K_{ijm}^r's are given by:

$$K_{ijm}^r = - T_{ijm}^r \qquad (5.8)$$

where T^r_{ijm} is the r^{th} approximation for the calculated travel time of the corresponding ray in the m^{th} block. The perturbation of the velocity in each block will in fact change the ray path, but the effect of this change in ray path on the calculated travel time can be neglected for computation correct to the first order in the perturbation. T^r_{ijm} in (5.8) is then simply given by

$$T^r_{ijm} = T^o_{ijm} \, (1 - p^{r-1}_m) \tag{5.9}$$

where T^o_{ijm} is the time the corresponding ray spends in the m^{th} block in a spherically symmetric earth model. Obtaining K^r_{ijm} from (5.8) and (5.9), the least square solution for p^r_m from the n equations in (5.7) can be evaluated as follows:

$$\tilde{p}^r_m = \frac{\sum_n K^r_{ijm} \, W_{ijm} \, (\Delta T^{obs}_{ijm} + C^r_{ij})}{\sum_n (K^r_{ijm} \cdot W_{ijm} \cdot K^r_{ijm} + \alpha)} \tag{5.10}$$

where W_{ijm} are the weights given to each datum according to the fraction of the total travel time the ray spends in the m^{th} block, and α is a parameter whose value one may assign to constrain the magnitude of velocity perturbation in that block. In practice, we did not allow the magnitude of the perturbation ($|\tilde{p}^r_m - \tilde{p}^{r-1}_m|$) to exceed 5% (or 1% if

there was only one datum) in any individual cycle of iteration. Note that in choosing the weights, we have assumed that observed travel time anomalies for a ray can be proportioned in different blocks according to the fractions of the total travel time the ray spends in those blocks. In the absence of such weights, perturbation in a block could be biased by the large travel time anomalies of a ray which spends hardly any time in that block.

The convergence in the process of successive approximation was tested by computing for each iteration the fractional reduction (x^r) in the variance of observed minus calculated times as follows:

$$x^r = \left[1 - \frac{\sum_i \sum_j (\Delta T_{ij} + C_{ij}^r)^2}{\sum_i \sum_j (\Delta T_{ij})^2}\right] \qquad (5.11)$$

For the criterion of convergence we adopted the following relation

$$\left| x^r - x^{r-1} \right| < 0.1 \qquad (5.12)$$

Through actual experiment one can easily find then whether the solution converges or not.

The advantages of successive approximation lie in the fact that in a very convenient way, one can obtain a

large size solution vector like ours, and also that one can constrain individual elements of this vector in any way one wishes. These advantages however are somewhat undermined by the possibility of bias in the solution vector depending on the sequence in which the respective blocks are chosen during the inversion. Such a bias can be removed possibly by randomizing the sequence.

Non-uniqueness in such three dimensional velocities models is not as easy to study from quantitative viewpoints as for one dimensional models. The large size of the matrix involved makes it extremely difficult to construct resolving kernels and trade-off curves (Backus and Gilbert, 1970), similar to those for one dimensional models (Appendix G). Qualitatively, however, we have studied the non-uniqueness by comparing the solution vectors obtained through using different sequences of blocks during inversion (see next section).

5.3.1 Inversion procedures and results for laterally heterogeneous earth models

1490 P and PcP data and 314 S and ScS travel time anomalies along different ray paths were used in the inversion for the lateral variation of velocity. 1056 P travel time anomaly data in our collection came from a selection of bulletin data (see Chap. 2 and Appendix K)

and the rest of the P/PcP and S/ScS data were obtained through our own readings of the seismograms. Travel time anomalies along different ray paths were calculated through ray-tracing in a spherically symmetric earth model of seismic velocity described in Chap. 3. In this connection we used a computer program written originally by Dr. Bruce Julian of M.I.T. Lincoln Laboratory and later modified by the author to suit the requirement of the inversion. From the ray tracing output, one obtains the time, T^{o}_{ijm} in equation (5.9), that the ray spends in each block. To ensure that the ray does not overshoot the block boundaries by a large margin while calculating these travel times, we interpolated the velocity model at every 5 km of depth using a cubic spline function and then determined the coordinates of the rays at each interface. In this process, overshoot was less than 0.1° in both latitude and longitude and less than 5 km in depth.

Travel time anomalies calculated for different ray paths were corrected for station anomalies (section 5.1.1) before being used for inversion through equation (5.10). These station anomalies, as we have seen in section 5.1.1 often vary rapidly within 1000 km of distance. For example, COR and LON, separated by approximately 300 km, differ by about 1 second in their

P wave station anomalies and about 3 seconds in their S wave station anomalies. These station anomalies, represented by the average of travel time residuals at each station, reflect the average velocity anomalies in crust and upper mantle beneath the stations. Unless these station anomalies were corrected beforehand from the calculated travel time anomalies along all ray paths, one may end up overestimating the lateral variation of velocity in the deep mantle by the present inversion scheme. On the other hand, in the presence of lateral heterogeneity in the deep mantle, there is a possibility that those average station anomalies may not have been very correctly estimated. The inverted velocity perturbations in the blocks of the surface layer (0-500 km) will then reflect the errors in estimating these average station anomalies plus the errors in ignoring the azimuthal variation of those station anomalies (see Chap. 2, section 2.5). We will show in section 5.6 that these errors in general are smaller than and uncorrelated with our estimated station anomalies (Figs. 5-18 and 5-19; Tables 5-10 and 5-11).

The bias in the inversion caused by the sequence in which the blocks were chosen was checked by using three different sequences. In the first trial (later to be referred to as 'MODEL 1'), the blocks were sequenced in

an ordered way starting from the core-mantle boundary and terminating on the free surface; in the second trial ('MODEL 2'), the above sequence was reversed. Finally in 'MODEL 3', the blocks were sequenced randomly. All three models were found (unfortunately) to have similar r.m.s. perturbations (1.3 to 1.5% for P wave velocity and about 1.3% for S wave velocity) from the spherically symmetric earth model and thus selection of one model is not possible on the basis of minimum r.m.s. perturbation. All three sequences resulted in similarly fast convergence in the inversion within three iterations. The percentage drop in the r.m.s. residual at each iteration step was 46%, 71% and 77% for the P velocity model and 71%, 96% and 99% for the S wave velocity model. Figs. 5-16 and 5-17 show some of the P and S wave travel time anomalies before and after correction for lateral inhomogeneity. In the presence of reading error, the extremely good fit of the S wave travel time anomalies is an artifact produced by the small quantity of data in comparison with the rather large number of free parameters in the three dimensional model.

To summarize the effectiveness of our earth models we plotted the histograms of travel time residuals of P and S waves (Fig. 5-18 and 5-19) obtained at different stages of construction of those models. In this context,

we have preferred to choose MODEL 3, which was obtained through random sequencing of blocks. Notice that the correction for lateral heterogeneity in the deep mantle has the largest effect on the travel time residuals in terms of factorial reduction of the r.m.s. values. To check whether the remaining travel time residuals, after fit through the three dimensional earth model, can be explained by reading error, we have compared the histogram of those residuals with the theoretical distribution curves assuming that the reading errors are normally distributed with zero mean and standard deviations of 0.36 and 0.75 seconds respectively for P and S wave travel time data. Note that those two values of standard deviations correspond closely to our estimates of reading error for P and S wave travel times (Appendix H). Apparently travel time residuals have been somewhat "overfitted" by three dimensional earth models. The Kolmogorov-Smirnov test (Hoel, 1962; p. 345) showed that fit of observed histograms by the normal distribution curves is not acceptable at 95% confidence level. The discrepancy is not, however, large for P wave travel times.

5.4 ON THE ASPECT OF MAGNITUDE AND CAUSES OF LATERAL HETEROGENEITY IN THE EARTH'S MANTLE

The most significant feature of our three dimensional earth model is shown in Fig. 5-20, where we plotted for

each 500 km depth interval the r.m.s. perturbation of velocity from the spherically symmetric earth model. In calculating the r.m.s. perturbation for the surface layer (0-500 km) we have added a contribution corresponding to the average ($\overline{\Delta T}$) of station anomalies in each block. The relative velocity perturbation for adjustment of station anomalies was simply given by

$$\frac{\Delta V}{V} = \frac{\overline{\Delta T}}{T_v} \qquad (5.13)$$

where 'T_v' is the vertical travel time computed from the spherically symmetric velocity models in the depth interval of 0 to 500 km. Notice that all three earth models (Model 1, Model 2 and Model 3) show a relative maximum in r.m.s. perturbation occurring for the surface layer (0-500 km) and the layer near the core-mantle boundary (2500-3000 km) indicating that these two layers have the largest lateral heterogeneity. The exception in Model 2 for S wave velocity reflects the stronger influence of sequence of blocks on the result because of the limited number of S wave travel time data. That the increase in r.m.s. perturbation for the surface layer and near the core-mantle boundary is not an artifact of a few scattered large perturbations can be easily seen from the histograms of the velocity perturbations (Figs. 5-21 and 5-22) for Model 3.

ADDENDUM TO THESIS

Table 5-7A shows, however, the presence of another systematic bias in the inversion - there seems to be a systematic decrease in the velocity perturbation with the increasing sampling of the blocks. We are not sure at this stage whether this systematic decrease is solely due to the artifact of the inversion scheme or also reflects the fact that the scale length of heterogeneity in the 'real earth' is less than 500 km. Under both circumstances, perturbation in a large block when reasonably sampled by a good number of data is expected to be small. More work needs to be done in the future in determining the actual scale length of heterogeneity in the lower mantle. Also, additional numerical experiments need to be conducted to understand the "artifacts" of the inversion. Until these are completed, my results should be interpreted only qualitatively. It is worth mentioning also that perturbations in blocks with hist $\geq$ 20 are not in fact independent of the perturbations in the rest of the blocks. So it may not be meaningful to restrict ourselves only to blocks with hit $\geq$ 20 without paying attention to the perturbations in other blocks, especially when the numbers of blocks with hit $\geq$ 20 are so small compared to the total number of blocks sampled by the data at any depth interval. Velocity perturbations in blocks with only one hit have been, however, somewhat artificially constrained in the inversion - not exceeding 1% at any iteration and not exceeding 5% in the total. The blocks with one or a few (<5) hits are most likely to be affected by the above limitations. Even after deleting the blocks with few (<5)

data we find from Table 5-7A that there is a trend that r.m.s. velocity perturbation tends to increase with depth but this is a weak indication at best.

The range of variation in relative velocity perturbation (which is about twice the r.m.s. value) is approximately 4% in P wave velocity and 5% in S wave velocity for the surface layer (0-500 km) as seen in Model 3 (see Fig. 5-20). These estimates of variation in P and S wave velocity, applicable within the continental upper mantle of the receiver regions agree very well with our present knowledge of lateral variation of Pn and Sn velocity under the continents (see for example, Herrin, 1969; Helmberger and Engen, 1974; Huestis et al., 1974). Lateral variations near the core-mantle boundary, on the other hand, may not be similarly pronounced as the range of variation in P and S wave velocity near the core-mantle boundary is found to be less than that in the surface layer by factors of 1.1 and 1.6, respectively, for Model 3. More importantly, however, the r.m.s. perturbation for S wave velocity near the core-mantle boundary is almost the same or even less than that for P wave velocity. This latter result may not be the artifact of a small number of S wave data for the following reasons: first, smaller r.m.s. perturbation of S wave velocity near the core-mantle boundary is also found for Model 1 and second, in all three earth models, the r.m.s. perturbation of S wave velocity for the surface layer (0-500 km) is larger, as expected, than that of P wave velocity even though the

number of blocks sampled by S wave data were twice as small as those sampled by P wave data. So, we will not ignore the possibility that the variations in S wave velocity near the core-mantle boundary may be really smaller as compared to the variations in P wave velocity.

Variation in temperature and partial melt in the upper mantle environment (Toksöz, et al., 1967; Hales and Doyle, 1967) is known to cause larger variation in S wave velocity than in P wave velocity (see also section 5.1.1A). This conclusion is primarily supported by the laboratory measurements (see Table 5-3). Limited measurements for temperature coefficients of compressional and shear velocities are also available for simple dense oxides which are probable constituents of lower mantle composition (Anderson et al., 1972; Press and Siever, 1974). However, the ratio of relative variation in shear velocity to compressional velocity ranges very widely from about 0.8 to 1.7 between these measurements (Anderson et al., 1968; Manghani, 1969; Spetzler, 1970; Wang and Simmons, 1973). The maximum value of 1.7 was obtained by Spetzler (1970) from a measurement on Mgo and this measurement may be considered more appropriate for the lower mantle environment than others. On this basis, temperature variation does not seem to explain the characteristics of observed lateral heterogeneity near the core-mantle boundary. The possibility

that lateral variations near the core-mantle boundary are caused by undulations on the core-mantle topography, is very remote. Observations of travel times for PcP (Johnson, 1969; Jordan, 1973; Engdahl and Johnson, 1974) and ScS (Hales and Roberts, 1970b) and multiple core phases like PmKP with m = 3 to 9 (Buchbinder, 1972) require the bumps not to exceed even 5 km unless present knowledge of seismic velocity near the core-mantle boundary is grossly wrong. Such small bumps cannot cause the observed lateral heterogeneity near the core-mantle boundary. We are left with the alternative that this lateral heterogeneity must be due to lateral variation in composition, such as variation in the FeO/(FeO+MgO) ratio which is a key parameter in lower mantle composition (see for example, Press 1970; Anderson et al., 1972; Ringwood, 1972). Velocity-density systematics of Liebermann (1970) also indicate that substitution of iron may cause a relatively larger change in compressional velocity than in shear velocity. Observed properties of both radial and lateral variation in seismic velocity near the core-mantle boundary can thus be fitted with radial and lateral variation in the Fe/Mg ratio (see also Chap. 3, section 3.6.2).

5.5 DESCRIPTION OF THE THREE DIMENSIONAL VELOCITY MODELS

For the description of our three dimensional velocity models for the earth's mantle, we consider only Model 3

which was obtained by inversion with random sequencing of blocks and thus presumably is free of most of the systematic biases inherent in our inversion scheme. The P and S wave velocities for this model are shown in Figs. 5-23 and 5-24, respectively (see also Appendix N). Tables 5-8 thru 5-12 show various correlation coefficients computed for this model. First, we calculated the correlation coefficients between the velocity perturbations of Model 3 and those of Model 1 and Model 2 (see section 5.3.1), and these coefficients are shown in Tables 5-8 and 5-9. Judging from the correlation coefficients (in excess of 0.5) one can attach confidence to the P velocity of Model 3 in the depth intervals 0-500 km, 2000-2500 km and 2500-3000 km, whereas for S velocity we can rely on Model 3 only for the surface layer (0-500 km). In subsequent discussion, emphasis will be placed on the velocities of Model 3 in these depth intervals only. Though there exists more doubt about the uniqueness of Model 3 for other depth intervals, the velocities in those intervals are not necessarily wrong. Next, Tables 5-10 and 5-11 show the correlation coefficients between perturbations at different depth intervals for P wave and S wave velocities of Model 3. As the cross-correlation coefficients in these tables are

low (less than 0.3), it is expected (though not certain) that there exists to a first approximation, fair resolution of overall velocity perturbations at different depth intervals. Finally, Table 5-12 shows the correlation coefficients between P and S wave velocity perturbations of Model 3. It is worth mentioning that though the correlation coefficient between overall P and S wave velocity perturbations at any depth interval is small, regionally there may be significant correlation, for example, in the surface layer (0-500 km) beneath North America. Also, we must caution again that S wave velocity perturbations are not very reliable because of the meager quantity of data.

It is worth mentioning that Julian and Sengupta (1973) also tentatively sketched regions in the earth's lower mantle thought to be fast or slow based on P wave travel time anomalies from a similar data-base to the one used in this study. Arbitrarily they assumed that travel time anomalies originate mostly in the central 30° of ray paths. Because of this assumption, there is some disagreement between their tentative model and Model 3 of this study. A pronounced difference occurs, for example, in the bottoming regions of path 1-5 (i.e. middle America) which was shown in the tentative model to be "fast" in contrast to MODEL 3 in the depth interval of 2500-3000 km. Note that

the path 1-5 (Argentina to western North America) also passes through an extensive region of high velocity to the north and the observed travel time anomalies therefore cannot be satisfied without a comparatively low velocity region beneath middle America.

5.5.1 Comparison of existing studies of lateral variation in the earth's upper mantle

During the era of the Upper Mantle Project (UMP), various geophysical data have been collected and interpretations have been made related to lateral variation in the upper mantle. Because of the abundance of quality data and interpretation, we will limit ourselves primarily to seismological evidence in this regard and compare them with our P and S velocity variations as shown in Figs. 5-23 and 5-24. Agreement for the P wave velocity model was found to be better than that for the S wave velocity model, possibly because of the larger quantity of data used in the inversion for the P wave model. Magnitudes of velocity perturbation at times were somewhat smaller than those in other studies because we assumed the velocity anomaly to occur uniformly over a depth interval of 500 km whereas in reality those anomalies probably occur over a smaller depth interval. There is also a possibility of an error in the

baseline of our inverted velocity perturbations arising from the uncertainty in the baseline of the observed travel times (Appendix K). But this error, at any rate, should not exceed more than ±0.5% in terms of relative velocity perturbation. With a background of these limitations, we would like to mention some of the areas of agreement between our model and contemporary evidence of lateral variation in the earth's upper mantle.

It is well documented in the literature (see Herrin, 1969) that western North America is underlain by comparatively slow upper mantle and eastern North America by comparatively fast upper mantle. Our model is in harmony with this documentation. Comparatively slow upper mantle beneath Hawaii and Iceland, as seen from our model (especially for P waves) is again to be expected from the volcanic activity associated with these regions Stauder (1973) and Isacks and Barazangi (1973) have shown evidence of subduction of a part of the Nazca plate under the coast of western South America from a study of general seismicity of the region, earthquake focal mechanisms and S wave signal characteristics. Our earth model for lateral variation in the western coast of South America is consistent with their studies along with another study by Molnar and Oliver (1969) who found efficient transmission of Sn waves off the coast of western South America in

contrast to inefficient transmission inside the continent. Lateral variation of velocity in the African continent with relatively fast velocities on the South African shield area and slow velocities beneath rift zones as predicted by our model, agrees well with the study of regional variation of Sn wave propagation across the continent by Gumper and Pomeroy (1970). Comparatively higher compressional velocity beneath Scandinavia and western Russia also has been noted by Massé and Alexander (1974). Study of Sn wave propagation by Molnar and Oliver (1969) and Huestis et al. (1973) suggests the presence of a relatively low velocity region beneath the Northern Himalayas and high velocities beneath India. Both of these studies agree with our model. From a study of travel time anomalies from local deep earthquakes, Ishida (1970) revised the "thick" (≈200 km) plate-like structure beneath the area of Japan as given by Utsu (1967) to a "thin" (≈70 km) plate structure. In his revision, Ishida also proposed a low velocity region, 70 km thick, running parallel to the plate on the underside. On the continental side, a thick (≈250 km) low velocity region (asthenosphere) lies above the plate. Except for low velocity regions beneath the plate, this structure is similar to the model proposed by Kanamori (1968) to explain the travel time residuals to Japanese stations

from the Longshot explosion. At any rate, teleseismic body waves to stations in south Japan have longer paths through the overlying low velocity region than those to the stations in north Japan. Effective upper mantle velocity should be relatively lower in south Japan compared to north Japan. Ishida's velocity model determined from local earthquake data is thus compatible with our earth model determined from global teleseismic data. Also, our model of lateral variation of velocity beneath the Australian continent fits remarkably well with the station anomalies determined by Cleary (1967b) from travel time data for explosions. The abrupt decrease in velocity in the middle of the northern territory of this continent as shown in our model, could be confirmed (see Denham et al., 1972) by the relatively large travel times to the field stations of DOR, SBL, AIL compared to that for WRA which lies further north. Those field stations were set up in that region to record two chemical explosions in Northern Australia during 1970 and 1971. Comparatively high heat flow ($\simeq$2.3 μcal/cm^2) in this region has been reported by Howard and Sass (1964). Finally, lateral variation beneath New Zealand has been studied by Mooney (1970a, and b) and Hatherton (1970) by examining variations in frequency characteristics and travel time anomalies of seismic

arrivals along with variation in geology, heat flow and gravity values over the continent. Both of them have indicated that a comparatively low-velocity, high-attenuation region underlies a portion of North Island, especially the northwest half of it. Their result is in very good agreement with our model, especially for S waves.

In essence, our three dimensional velocity model is successful in faithfully representing the lateral variation within the receiver regions of continental upper mantle, as known to date.

5.5.2 Comparisons of other studies of lateral variation in the deep mantle

Until recently, studies relating to lateral heterogeneity in the deep mantle were very few and far between. Alexander and Phinney (1966) showed for the first time convincing seismological evidence of lateral variation in the properties of the core-mantle boundary by measuring the spectral attenuation coefficient of diffracted P waves. Lateral changes were found to be very gradual between four distinctly different paths beneath the Pacific, one of them being underneath the Hawaiian Island chain. However, a path under the Atlantic off northern Africa showed a distinctly different spectrum from the paths in the Pacific. Remarkably, our P wave velocity model (Fig. 5-24) also shows small lateral variation near the core-mantle boundary beneath the central Pacific region.

Unfortunately we have not sampled with our P wave travel time data the same region under the Atlantic and north Africa that Alexander and Phinney did.

The difference in the spectral attenuation coefficient as measured by Alexander and Phinney was attributed non-uniquely to the difference in velocity gradient at the base of the mantle (Phinney and Alexander, 1969). The deep mantle beneath the Pacific was required to have a higher velocity gradient (velocity increasing downward) than the mantle beneath the Atlantic. Measurements of $dT/d\Delta$ also are very sensitive to the velocity gradients near the bottoming points of rays. From a recent collection of measurements of $dT/d\Delta$ and azimuth at the Large Aperture Seismic Array (LASA), Montana (USA), Davies and Sheppard (1972) noted that the rays which bottom within 300 km of the core-mantle boundary beneath the Hawaiian Islands show an azimuth anomaly of at least +5° (towards East) whereas measured $dT/d\Delta$ values were only slightly larger (<0.1 sec/deg) than those predicted from the J-B Tables. This azimuth anomaly took place only within a 5° window in azimuth, implying that structure beneath the array is unlikely to be the cause. Moreover, this azimuth anomaly was found to be too large (by at least a factor of two) to be accounted for by near source heterogeneity in the

upper mantle. So, they tentatively interpreted the observed azimuth anomaly to be due to a 200 km radius low velocity zone beneath Hawaii with 6% velocity contrast. Their conclusion does not agree with the interpretation of velocity gradient under Hawaii given by Phinney and Alexander (1969) as noted earlier. This conflict rose to a peak when Kanasewich et al. (1973) measured phase velocities of P waves (inverse of $dT/d\Delta$) from events at Tonga and the Samoan Islands using arrays of seismic stations at western Canada and also LASA. They reported 15% higher phase velocities than predicted from the J-B Tables but surprisingly small azimuth anomalies, of the order of 2-3°. This high phase velocity was interpreted in terms of radial heterogeneity with P velocity as high as 14.7 km/sec between 2861 and 2898 km beneath Hawaii. Contrary to this observation, Wright (1973) measured phase velocities at the Yellowknife array for P waves bottoming slightly northwest of Hawaii and reported phase velocities only about 2% higher than predicted from the J-B Tables and equally small azimuth anomaly of the order of +2°. These differences in measurements of velocity gradient suggest to us that in all probability there exists a lateral variation in the deep mantle in the immediate vicinity of Hawaii. Allowing then the size of the inhomogeneity to be as large as 1000 km, our P wave velocity

model appears to represent well the nature of this lateral variation.

Classical seismological evidence of lateral inhomogeneity in the deep mantle based on observed $dT/d\Delta$ values was on the other hand given by Toksöz et al. (1967) and later by Greenfield and Sheppard (1969). They observed that P waves from the South American events in the distance range of 70°-85° and along an azimuth of 140°-160° from LASA have relatively low $dT/d\Delta$ values compared to the events in a similar distance range along an azimuth of 300°-320°. Rays in the first group bottom under Central America in the depth interval of 2000-2500 km whereas the bottoming regions of the second group lies beneath the northeast Siberian Peninsula. Remarkably, our earth model in the similar depth interval shows relatively high velocities beneath Central America and low velocities beneath the northeast Siberian Peninsula. Relatively low velocities beneath Central America and pronounced lateral variation beneath Arctic-Northwest USSR as shown by our P wave velocity model near the core-mantle boundary also have their counterparts respectively in the observations of relatively high $dT/d\Delta$ values at the Yellowknife Array by Wright (1973) [see his Fig. 5] and in the observations of broad and large $dT/d\Delta$ and

azimuth anomalies at LASA in the azimuth range of 340° to 10° and for $dT/d\Delta$ value less than 5.0 sec/deg (Davies and Sheppard, 1972; see Fig. 4 in their paper). Encouraging agreement in the interpretation of $dT/d\Delta$ data and our earth model suggests that in the future joint inversion of travel time and $dT/d\Delta$ data may improve the resolution of structural details in the lateral variation of the lower mantle.

The seismic travel time evidence for lateral inhomogeneity in the deep mantle includes the recent studies of Niazi (1973), Jordan and Lynn (1974), and of Julian and Sengupta, (1973) which has already been described in section 5.2.1 and 5.5. Niazi used SH wave travel times along paths from Iran and Turkey to western North American stations and concluded that below a depth of 2500 km, the mantle beneath the North Pole is slower than that under Iceland. Unfortunately we have not sampled the North Pole region with our S wave travel time data, but indications from our P wave velocity model in the same depth range support his conclusions. Jordan and Lynn (1974) on the other hand, studied ScS-S and PcP-P travel-time anomalies from two deep Peru-Brazil earthquakes recorded by North American stations and reached a conclusion that mantle beneath the Caribbean region may

be faster in the approximate depth interval of 600-1400 km. Revising their depths estimates to 1000-1500 km in accordance with ray tracing in our spherically symmetric earth model, we find a very good agreement between their conclusion and both of our P and S wave velocity models. Finally, precursors to PKIKP waves have been explained recently (see for example, Haddon and Cleary, 1974) in terms of lateral heterogeneity in a 200 km thick layer near the core-mantle boundary. Their laterally heterogeneous earth model is, however, stochastic in nature with correlation distances of about 30 km, whereas our earth model is deterministic in nature with the minimum size of heterogeneities being 1000 km. Their model thus reveals the fine scale structure of this heterogeneity in contrast to the broad scale lateral variations shown in our three dimensional velocity models.

Apart from seismology, other disciplines in the earth sciences have produced evidence of the presence of large scale lateral heterogeneity in the deep mantle. For example, gravity anomalies also suggested lateral variation in the deep mantle (Kaula, 1972; Allan 1972). Lack of correlation between gravitational potential and crustal thickness for spherical harmonic coefficients up to sixth degree (Toksöz et al., 1969) together with

positive correlation of gravity and topography at higher harmonics (Kaula, 1972) have led to the idea that broad variations in gravity represented by low-degree harmonics (features more than 4000 km extent) are produced in the mantle. In fact, from a statistical test of the hypothesis that gravity anomalies arise from density variations at a single radius, Allan (1972) has shown that the effective depth corresponding to the gravity field of low-degree (up to sixth) spherical harmonic is about 1700 km whereas the effective depth is in the range of 200-300 km for higher degree harmonics. Contours of geopotential for the low degree harmonics have been shown by Toksöz et al. (1967). The coefficients they used, at least the larger ones excluding the second zonal harmonic, do not differ by more than 5% from the recent determination by Gaposchkin (1974). At any rate, their computed contours in geopotential have broad minima (i.e. negative values) over most of North America (excluding the Alaskan region) and over India and central Asia. On the other hand, broad maxima (i.e. positive geopotential) are found over western Europe, the Peru-Bolivia region and over the New Guinea-Australia-western Pacific area where maximum was relatively sharp. There appears to be some correlation between these variations in geopotential and lateral velocity variation

in our model which also seems to suggest that deep mantle (depth >1500 km) on the whole appears to be fast beneath North America (excluding Alaska), India and central Asia and slow under the regions of New Guinea, Australia and the western Pacific, western Europe and Peru and Bolivia. This correlation may be explained by lateral variation in density (e.g. by variation in Fe/Mg ratio) causing variation in both gravitational potential and seismic velocity. We may not rule out, however, that a part of lateral variation in geopotential may be caused by undulations (not more than 2-5 km) in core-mantle topography (Hide and Horai, 1968; Hide and Malin, 1970).

In addition to evidence from gravity anomaly data, geomagnetic data in a single instance also appear to lend support to our laterally heterogeneous earth model for the deep mantle. Doell and Cox (1972) suggested that lateral heterogeneity in the lower mantle beneath the central Pacific may be responsible for attenuation of geomagnetic spectrum in the period range of 200 to 2000 years and cause a subdued non-dipole field (<4000 gammas) and small secular variation (<30 gammas/year) in this area. Notably, in our P velocity model near the core-mantle boundary (2500-3000 km), the central Pacific region stands out as having small variation in velocity (within ±0.5%) compared to our spherically symmetric earth model. It is

difficult to relate the lateral variation in seismic velocity to the findings from geomagnetic data though both kinds of data support a laterally homogeneous small anomaly under the central Pacific. Gravity potentials in this region as computed by Toksöz et al. (1967) are also small.

At least for P wave velocity, we can conclude that features in our three dimensional model for the deep mantle are not altogether artifacts of the inversion procedure as they seem to be consistent with other studies using various geophysical data. It is then worth mentioning that comparison of the P wave velocity variations in the surface layer (0-500 km depth) of this three dimensional earth model with those near the core-mantle boundary reveals no relationship between the surface tectonics and the structure of the deep mantle.

Table 5-1

Classification of WWSSN stations related to Table 5-2

Class 1	Normal continental stations
	AAM, ADE, ATL, BLA, BUL, CMC, COL, COP, CTA, ESK, GDH, GEO, KEV, KOD, KON, KTG, LUB, MUN, NOR, NUR, OXF, POO, PRE, PTO, SDB, SHI, SHL, TAU, TRN, UME, VAL, WES, WIN (33 in all)
Class 2	Normal oceanic stations
	AFI, KIP, RAR (3 in all)
Class 3	Stations on continental rift zones
	AAE, ALQ, DUG, GSC, NAI, TUC (6 in all)
Class 4	Stations on oceanic rift zones
	AKU, GIE (2 in all)
Class 5	Stations on continental subduction zone
	ANP, ANT, BAG, DAV, LEM, MAN, NNA, SHK (8 in all)
Class 6	Stations on oceanic subduction zone
	GUA, HNR, RAB, SJG (4 in all)
Class 7A	North American stations
	AAM, ALQ, ATL, BKS, BLA, CMC, COL, COR, DUG, GDH, GEO, GOL, GSC, JCT, LON, LUB, OXF, RCD, TUC, WES (20 in all)
Class 7B	Only Central and Eastern North American stations
	AAM, ATL, BLA, CMC, GEO, OXF, WES (7 in all)
Class 8	All WWSSN stations
	AAE, AAM, ADE, AFI, ALQ, ANP, ANT, ATL, BAG, BKS, BLA, BUL, CHG, CMC, COL, COP, COR, CTA, DAV, DUG, ESK, GDH, GEO, GOL, GSC, GUA, HKC, HNR, IST, JCT, JER, KEV, KIP, KOD, KON, KTG, LEM, LON, LPS, LUB, MAN, MSH, MUN, NAI, NDI, NHA, NNA, NOR, NUR, OXF, PMG, POO, PRE, PTO, QUE, RAB, RAR, RCD, RIV, SBA, SDB, SEO, SHI, SHK, SHL, SJG, SPA, TAB, TAU, TOL, TRN, TUC, UME, VAL, WEL, WES, WIN (77 in all)

Table 5-2

	Subgroup* of WWSSN Stations	P Stn. anomaly (sec.)† Mean ($\bar{x}$)	P Stn. anomaly (sec.)† S.D. (s_x)	P Stn. anomaly (sec.)† N	S Stn. anomaly (sec.)† Mean ($\bar{y}$)	S Stn. anomaly (sec.)† S.D. (s_y)	S Stn. anomaly (sec.)† N	Correlation Co-efficient (r) between x's and y's	Slope (b)‡ of regression line y = bx
1.	Normal continental stations	-0.41	0.37	33	-1.65	1.24	33	0.41	1.37
2.	Normal oceanic stations	0.47	0.45	3	0.47	1.66	3	0.25	0.92
3.	Stations on continental rift zones	0.72	0.29	6	3.43	2.06	6	0.84	5.97
4.	Stations on oceanic rift zones	-	-	-	-		-	-	-
5.	Stations on continental subduction zones	0.05	0.69	8	0.52	1.76	8	0.34	0.87
6.	Stations on oceanic subduction zones	-0.71	0.37	4	-1.68	1.15	4	0.64	1.99
7A.	North American stations	-0.01	0.60	20	0.02	2.01	20	0.84	2.81
7B.	Central and Eastern North American stations	-0.49	0.44	7	-1.84	0.90	7	0.69	1.43
8.	All WWSSN stations	-0.07	0.66	77	-0.38	2.27	77	0.73	2.50

* See Table 5-1

† Used are the stations with at least 3 data.

‡ $b = \frac{s_y}{s_x} \cdot r$ (Draper and Smith, 1966, p. 35).

Table 5-3

Temperature coefficients for P and S wave velocities of probable constituents of the upper mantle

Structure	Compound	$1/\alpha(\partial\alpha/\partial T)_P$ ($deg^{-1}x10^{-4}$)	$1/\beta(\partial\beta/\partial T)_P$ ($deg^{-1}x10^{-4}$)	$(\partial\beta/\partial\alpha).(\alpha/\beta)$	References
Olivine	Mg_2SiO_4	-0.56	-0.68	1.21	Kumazawa and Anderson (1969
	$(Mg_{0.93}Fe_{0.07})_2SiO_4$	-0.58	-0.70	1.21	-DO-
	Fe_2SiO_4	-0.57	-0.79	1.39	Chung (1971)
Pyroxene	$(Mg_{0.8}Fe_{0.2})SiO_3$	-1.17	-1.03	0.88	Frissilo and Barsch (1972)
Garnet	Almandite-pyrope	-0.46	-0.46	1.0	Anderson et al (1968)
Spinel	$MgO.2.6\ Al_2O_3$	-0.34	-0.39	1.15	-DO-
	$NiFe_2O_4$	-0.37	-0.35	0.95	Liebermann (1972)

α: compressional velocity

β: shear velocity

P: pressure

T: temperure

Table 5-4

Station anomaly of normal oceanic and continental stations for S wave.

[Number of data (in brackets) and standard errors also are shown]

a) Normal Oceanic Stations

Station	Station Anomaly (seconds)	Mean Delay (seconds)
AFI	-0.88 ± 0.16 (4)	
KIP	2.33 ± 1.43 (6)	0.47
RAR	-0.03 ± 0.75 (9)	

b) Normal Continental Stations

Station	Station Anomaly (seconds)	Mean Delay (seconds)
ADE	-2.19 ± 0.23 (13)	
ATL	-2.49 ± 0.13 (14)	
GDH	-2.37 ± 0.18 (9)	
KEV	-3.90 ± 0.63 (7)	
MUN	-2.31 ± 0.60 (8)	-2.85
NDI	-3.47 ± 0.51 (15)	
NUR	-4.36 ± 0.45 (8)	
OXF	-3.08 ± 0.30 (11)	
POO	-2.59 ± 0.38 (12)	
SCP	-2.20 ± 0.66 (12)	
SHL	-2.26 ± 0.16 (18)	
WEL	-2.93 ± 0.53 (7)	

TABLE 5-5

Travel Time Statistics for Mantle P Wave Paths

IDENT. NO.	N	$\bar{x}$	s	t	$t_{99.5}$	PATH
(a) $85° < \Delta < 100°$						
1-1 *	17	0.46	0.43	4.41	3.25	Japan - USA
1-2	12	-0.11	0.56	-2.15	3.50	Bonin and Marianas Arc - USA
1-3 *	15	-0.76	0.48	-6.13	3.33	Tonga Arc - Alaska
1-4 *	90	0.23	0.50	4.37	2.89	Tonga Arc - Western North America
1-5 *	29	-0.34	0.57	-3.21	3.05	Argentina - Western North America
1-6 *	40	0.37	0.70	3.34	2.97	South America - Northwestern Europe
1-7 *	84	0.38	0.79	4.40	2.89	South America - Southern Europe
1-8	11	0.06	0.56	0.36	3.58	South America - Southern Africa
1-9 *	13	-1.09	0.91	-4.31	3.43	Kuril Arc - Spain, Morocco and Algeria
1-10	16	-0.36	0.58	-2.48	3.29	Bonin Arc - Europe
1-11	42	-0.19	0.65	-1.90	2.97	Indonesia and Philippine Is. - Central and Northern Europe
1-12	14	0.16	0.48	1.25	3.37	Indonesia and Philippine Is. - Middle East and Balkans
1-13	13	0.47	0.96	1.77	3.43	Indonesia and Philippine Is. - Central and Southern Africa
1-14	10	-0.12	0.56	-0.68	3.69	Tonga Arc - Siberia and China
1-15	9	-0.24	0.28	-2.57	3.83	Indonesia - Alaska
1-16 *	56	0.34	0.61	4.17	2.92	Solomon Is. - Western USA
1-17	29	0.04	0.33	0.65	3.05	New Hebrides - Western North America
(b) $70° < \Delta < 85°$						
2-1	57	-0.12	0.45	-2.02	2.92	Japan - USA
2-2 *	12	-0.51	0.36	-4.90	3.45	Japan - Southwestern USA
2-3 *	34	-0.38	0.37	-5.99	3.01	Bonin Arc - Western USA
2-4 *	122	0.16	0.40	4.38	2.86	Tonga Arc - Western North America
2-5 *	27	-0.27	0.39	-3.60	3.07	Kuril Arc - Eastern North America
2-6 *	76	-0.19	0.45	-3.68	2.90	Argentina and Bolivia - Central and Western USA
2-7 *	30	0.25	0.44	3.11	3.04	South America - Spain and Northern Africa
2-8	20	-0.09	0.45	-0.89	3.17	South America - Central and Southern Africa

TABLE 5-5 Continued

IDENT. NO.	N	$\bar{x}$	s	t	$t_{99.5}$	PATH
2-9 *	58	0.19	0.43	3.36	2.92	Kuril Arc - Western Europe
2-10 *	69	-0.33	0.52	-5.28	2.91	Japan - Western Europe
2-11	22	0.02	0.36	0.26	3.14	New Hebrides - Western North America
2-12	20	-0.06	0.47	-0.57	3.17	Indonesia and Philippine Is. - Middle East
2-13	30	-0.09	0.52	-0.95	3.04	Bonin and Marianas Arcs - Scandinavia and Western Russia
2-14	23	0.14	0.38	1.77	3.12	Japan and Kuril Arc - Australia
2-15	11	-0.06	0.54	-0.37	3.58	Kuril Arc - Middle East
2-16	12	-0.39	0.56	-2.41	3.50	Indonesia - Antarctica
2-17	10	-0.22	0.25	-2.78	3.69	Marianas Arc - Western USA
2-18	12	-0.22	0.69	-1.10	3.50	Japan - Middle East
(c) $55° < \Delta < 70°$						
3-1 *	93	0.23	0.38	5.84	2.89	Kuril Arc - Western USA
3-2	45	0.12	0.40	2.01	2.96	Northern South America - Western USA
3-3	42	0.06	0.49	0.79	2.97	Bolivia and Argentina - Central USA
3-4	93	-0.05	0.54	-0.89	2.89	Kuril Arc and Sea of Japan - Northern and Eastern Europe and Middle East
3-5	30	-0.09	0.41	-1.20	3.03	Indonesia andPhilippine Is. - Southwestern Asia
3-6	15	0.18	0.62	1.12	3.33	Japan and Kuril Arc - Melanesia
3-7	12	-0.04	0.41	-0.34	3.43	Tonga Arc - Western Australia
3-8	10	-0.28	0.45	-1.97	3.58	Japan and Kuril Arc - Australia
3-9	9	-0.19	0.55	-1.04	3.69	New Hebrides - China and Siberia
3-10	8	0.13	0.78	0.47	4.03	Solomon Is. - Japan
3-11	15	0.26	0.47	2.14	3.29	Tonga Arc - Antarctica
3-12	9	0.22	0.58	1.14	3.69	Indonesia - New Zealand
3-13	10	0.15	0.59	0.80	3.58	Indonesia - Antarctica

TABLE 5-5 Continued

IDENT. NO.		N	$\bar{x}$	s	t	$t_{99.5}$	PATH
(d) $40° < \Delta < 55°$							
4-1	*	23	0.41	0.48	4.10	3.12	Kuril Arc - Northwestern North America
4-2		44	-0.18	0.48	-2.49	2.97	Northern South America - USA
4-3		15	0.35	0.41	3.31	3.33	Kuril Arc - Northern Europe
4-4		34	0.16	0.43	2.17	3.01	Japan - Southwestern Asia
4-5		17	-0.25	0.51	-2.02	3.22	Indonesia - India and Pakistan
4-6	*	17	0.82	0.56	6.03	3.25	Japan - Alaska
4-7		13	-0.51	0.65	-2.82	3.37	Indonesia - Japan and Korea
4-8		40	0.02	0.55	0.23	2.97	Indonesia - Southeastern Australia and Tasmania
4-9		20	-0.06	0.58	-0.46	3.15	Solomon Is. - Japan, Korea, and Eastern China

N = number of observations

$\bar{x}$ = mean travel time residual after station correction (sec)

s = standard deviation of residuals (sec)

$$t = \frac{\bar{x}}{s/\sqrt{N}}$$

$t_{99.5}$ = 99.5% confidence limit for $|t|$ if true mean is zero

* - Indicates paths with mean significantly different from zero.

Table 5-6A

Paths and path anomalies in the distance range of 48°-50°

P wave travel times (sec)			S wave travel times (sec)		
path		path anomaly*	path		path anomaly*
West Tonga	- GUA	0.58	West Tonga	- GUA	5.90
Colombia	- SFA	-0.31	South Fiji	- GUA	5.84
"	- ALQ	-1.15	Peru/Brazil	- GEO	
"	- TUC	-0.95	Java Sea	- NDI	-1.93
Peru/Brazil	- JCT	0.85	Banda Sea	- KOD	3.31
"	- GEO	-0.63	East Russia	- RAB	5.15
"	- WSC	-0.13			
"	- MRG	-0.26			
Java Sea	- KYS	-1.84			
"	- DDR	-0.58			
"	- TSK	-1.35			
"	- NDI	-0.39			
Banda Sea	- KOD	0.04			
East Russia	- COL	1.59			
"	- PJD	1.60			
"	- PMR	0.60			
"	- KDC	0.13			
"	- RAB	1.26			
Solomon Is.	- MCQ	0.20			
"	- TNG	-0.65			
"	- CNT	0.51			
"	- NAN	1.42			
New Hebrides	- KLG	-0.45			

*Plus sign for late arrival and minus sign for early arrival; corrected for only station anomaly

Table 5-6B

Paths and path anomalies in the distance range of 60°-62°

P wave travel times (sec)			S wave travel times (sec)		
path		path anomaly*	path		path anomaly*
West Tonga	- SBA	0.25	West Tonga	- DAV	-3.04
"	- MUN	0.14	Colombia	- BKS	-0.73
"	- DAV	-1.31	Peru/Brazil	- RCD	-1.69
South Fiji	- DAV	-0.87	Banda Sea	- LAH	-0.06
Colombia	- BKS	0.16	East Russia	- NUR	-0.47
"	- BMO	-1.09	New Hebrides	- SHK	1.91
"	- HHM	-0.73	Greece	- PRE	3.45
"	- SES	-0.34			
Peru/Brazil	- CED	-0.03			
"	- UBO	-0.20			
"	- BCN	-0.45			
"	- RCD	-0.54			
"	- MBO	0.0			
"	- LNM	0.0			
Banda Sea	- LAH	0.11			
Sea of Okhotsk	- FBC	-0.06			
"	- CRC	0.41			
"	- MHC	0.75			
"	- HCC	0.31			
"	- JAS	1.33			
"	- BMN	0.82			
"	- CBC	0.28			
"	- STC	0.43			
"	- PRI	1.01			
"	- EUR	1.22			
"	- OBN	-0.20			
"	- NUR	0.15			
East Russia	- NUR	-0.21			
South Marianas	- SAV	-0.32			
Solomon Is.	- PAO	-0.17			
Greece	- PRE	0.84			

*Plus sign for late arrival and minus sign for early arrival; corrected for only station anomaly

TABLE 5-7A

Dependence of velocity perturbation on the sampling of the blocks.

MODEL 1 (Sequence going up from core mantle boundary)

Depth interval (km)	Rms velocity perturbation (%) for ≥1	≥5	≥20 (hits/block)
500-1000	1.60(343)*	0.64(182)*	0.45(62)*
1000-1500	1.18(404)	0.77(218)	0.49(84)
1500-2000	1.21(448)	0.86(246)	0.40(71)
2000-2500	1.46(470)	1.06(248)	0.61(73)
2500-3000	2.02(387)	1.46(181)	0.57(32)

MODEL 2 (Sequence going down from core mantle boundary)

500-1000	1.49(343)	0.66(182)	0.39(62)
1000-1500	1.09(404)	0.71(218)	0.48(84)
1500-2000	1.25(448)	0.81(246)	0.38(71)
2000-2500	1.50(470)	0.91(248)	0.45(73)
2500-3000	1.59(387)	0.69(181)	0.39(32)

MODEL 3 (Random sequence)

500-1000	1.24(343)	0.55(182)	0.40(62)
1000-1500	0.96(404)	0.60(218)	0.44(84)
1500-2000	1.14(448)	0.87(246)	0.43(71)
2000-2500	1.33(470)	0.97(248)	0.46(73)
2500-3000	1.73(387)	1.03(181)	0.45(32)

*Number of blocks are shown in parentheses.

Depth interval 0-500 km was deleted as station anomalies were to be added.

Table 5-7

Statistics for S wave travel time anomalies along different paths through lower mantle.

Path+	Path description	S wave travel time anomaly (seconds) No.	Mean	Std. deviation	Correlation coefficient between P and S wave travel time anomalies
1-4	Tonga Arc - Western North America	8	4.4	1.5	-0.12
1-6	South America - North Western Europe	6	0.0	2.0	0.84
2-4	Tonga Arc - Western North America	5	4.2	1.1	-0.80
2-5	Kuril Arc - Eastern North America	6	-2.8	1.1	0.34
2-6	Argentina - Central and Western USA	5	0.8	2.3	0.86
2-7	South America - Spain, North Africa	5	-0.3	2.4	0.39
3-2	Northern South America - Western USA	7	-1.4	2.0	0.53
3-3	Argentina - Central USA	5	1.1	3.3	0.89
4-2	Northern South America -	9	0.1	1.2	0.37
4-5	Indonesia - India and Pakistan	5	0.3	2.0	0.84

+Path number corresponds to those shown on Table 5-5

Table 5-8

Correlation matrix of P wave velocity perturbations of three earth models

(a)

MODEL 1 \ MODEL 3	0-500 km*	500-1000 km	1000-1500 km	1500-2000 km	2000-2500 km	2500-3000 km
0-500 km*	0.75	0.07	0.00	0.02	-0.12	-0.03
500-1000 km	0.07	0.57	-0.01	0.03	0.05	-0.15
1000-1500 km	0.05	0.06	0.28	-0.01	0.02	0.01
1500-2000 km	0.05	0.07	-0.09	0.28	0.06	-0.07
2000-2500 km	-0.02	-0.03	0.03	-0.04	0.60	0.00
2500-3000 km	0.01	-0.08	-0.02	-0.02	0.05	0.57

(b)

MODEL 2 \ MODEL 3	0-500 km*	500-1000 km	1000-1500 km	1500-2000 km	2000-2500 km	2500-3000 km
0-500 km*	0.84	0.07	0.03	0.04	-0.02	-0.03
500-1000 km	-0.05	0.36	0.02	0.05	0.00	0.09
1000-1500 km	-0.03	-0.05	0.51	0.03	-0.01	0.02
1500-2000 km	0.01	-0.05	0.01	0.56	-0.01	0.02
2000-2500 km	-0.03	0.00	-0.03	-0.03	0.65	0.01
2500-3000 km	0.02	-0.03	0.05	-0.04	0.01	0.67

* station anomaly removed from the travel time residual data

Table 5-9

Correlation matrix of S wave velocity perturbation of three earth models

(a)

MODEL 1 \ MODEL 3	0-500 km*	500-1000 km	1000-1500 km	1500-2000 km	2000-2500 km	2500-3000 km
0-500 km*	0.64	-0.01	0.20	0.03	-0.04	-0.02
500-1000 km	0.07	0.16	-0.07	-0.05	-0.05	-0.00
1000-1500 km	0.19	0.12	0.43	-0.03	0.17	0.28
1500-2000 km	-0.01	-0.06	-0.01	0.40	-0.02	0.16
2000-2500 km	0.10	-0.09	0.09	0.07	0.34	0.16
2500-3000 km	0.05	-0.01	0.20	0.09	0.09	0.41

(b)

MODEL 2 \ MODEL 3	0-500 km*	500-1000 km	1000-1500 km	1500-2000 km	2000-2500 km	2500-3000 km
0-500 km*	0.55	-0.01	0.15	0.01	0.03	0.00
500-1000 km	0.07	0.28	-0.04	-0.07	0.02	0.05
1000-1500 km	0.14	0.02	0.34	-0.04	-0.03	0.06
1500-2000 km	0.08	0.07	0.04	0.50	-0.06	0.20
2000-2500 km	0.28	0.15	0.15	-0.08	0.51	0.08
2500-3000 km	-0.12	0.05	-0.04	0.11	-0.16	0.23

* station anomaly removed from travel time residual data

Table 5-10

Correlation matrix of P wave velocity perturbations of Model 3 for different depth intervals

	Stn. anomaly (a)	0-500 km (b)	(a)+(b)	500-1000 km	1000-1500 km	1500-2000 km	2000-2500 km	2500-3000 km
Stn. anomaly (a)	1.00	0.04	0.78	0.06	0.10	-0.17	0.05	0.01
0-500 km (b)		1.00	0.86	0.09	-0.00	0.03	-0.05	0.02
(a)+(b)			1.00	0.09	0.04	-0.04	-0.02	0.02
500-1000 km				1.00	-0.12	0.01	0.02	-0.14
1000-1500 km					1.00	0.09	-0.00	0.02
1500-2000 km						1.00	-0.01	-0.01
2000-2500 km							1.00	-0.00
2500-3000 km								1.00

Table 5-11

Correlation matrix of S wave velocity perturbations of Model 3 for different depth intervals

	Stn. anomaly (a)	0-500 km (b)	(a)+(b)	500-1000 km	1000-1500 km	1500-2000 km	2000-2500 km	2500-3000 km
Stn. anomaly (a)	1.00	-0.22	0.91	-0.23	0.13	-0.10	0.24	0.03
0-500 km (b)		1.00	0.80	0.07	0.19	0.03	0.19	-0.10
(a)+(b)			1.00	-0.05	0.23	0.00	0.27	-0.08
500-1000 km				1.00	0.02	-0.00	-0.02	0.07
1000-1500 km					1.00	-0.20	0.05	0.24
1500-2000 km						1.00	-0.01	0.06
2000-2500 km							1.00	0.07
2500-3000 km								1.00

Table 5-12

Correlation matrix of P and S wave velocity perturbations of Model 3

P wave velocity perturbation

S wave velocity perturbation	Stn. anomaly (a)	0-500 km (b)	(a)+(b)	500-1000 km	1000-1500 km	1500-2000 km	2000-2500 km	2500-3000 km
Stn. anomaly (a)	0.70	0.03	0.65	0.04	0.03	-0.28	-0.06	-0.05
0-500 km (b)	-0.20	-0.04	-0.12	-0.07	0.12	0.03	0.13	0.17
(a)+(b)	0.32	-0.01	0.14	-0.03	0.11	-0.12	0.08	0.14
500-1000 km	-0.16	-0.10	-0.14	0.01	0.08	0.02	-0.10	-0.09
1000-1500 km	0.03	-0.06	-0.04	-0.06	-0.03	-0.02	0.07	0.04
1500-2000 km	0.11	-0.14	-0.08	0.01	-0.07	0.09	0.03	-0.05
2000-2500 km	-0.06	0.03	-0.00	-0.11	0.06	-0.02	0.06	0.04
2500-3000 km	0.17	0.02	-0.05	-0.02	-0.04	0.06	-0.06	-0.11

Figure Captions

Figure 5-1. Comparison of standard deviations of P wave station anomalies determined from deep focus travel time data (this study) with those from surface focus data. A common group of 124 stations distributed all over the world was used for this comparison. Note that average standard deviation of station anomalies of this study is about twice as small as those from other studies.

Figure 5-2. Comparison of standard deviation of S wave station anomalies determined from deep focus travel time data (this study) with those from surface focus data (Doyle and Hales, 1967). A common group of 15 WWSSN stations on North America was used in this comparison. Note that average standard deviation of station anomalies of this study is smaller than those of Doyle and Hales by more than a factor of two.

Figure 5-3. Comparison of average $\hat{P}$ and S wave station anomalies determined from deep focus travel time data (this study) and those from surface focus travel time data. A common group of 42 and 15 stations on North America were used respectively for P and S wave data. N in the rectangular box shows the number of stations,

R the correlation coefficient, S the r.m.s. difference, T the average difference. Note the r.m.s. difference is less than average standard deviation of station anomalies (Figs. 5-1 and 5-2).

Figure 5-4. P wave station anomalies of travel time data (taken from Sengupta, 1972) for stations on the North American continent. Note that stations other than WWSSN are also included.

Figure 5-5. S wave station anomalies of travel time data (this study) for stations on the North American continent. All stations shown here are part of WWSSN.

Figure 5-6. Linear correlation in S and P wave station anomalies of travel time data (this study) for WWSSN stations on North America. Horizontal and vertical bars represent standard errors of the average station anomalies. Theoretical regression lines with ratio of S to P station anomalies as 2.0, 3.0, 4.0, and 5.0 are also shown. Notice that stations from both eastern and western North America were included in the plot.

Figure 5-7. Correlation of S and P wave station anomalies of travel time data (this study) for WWSSN stations on (a) stable continents and shield areas (top) and (b) continental rift zones (below). For classification of the stations see Table 5-1. Horizontal and vertical bars are the standard errors of the mean station anomalies. N in

the square box shows the number of stations used and R the correlation coefficient. Theoretical regression lines with ratio of S to P station anomalies as 1.0, 2.0, 4.0 and 6.0 are also shown. Notice that ratio of S to P station anomaly may be higher for stations on continental rift zones than for stations on stable continent and shield areas.

Figure 5-8. Difference in the vertical travel times between shield and ocean structure determined from surface wave dispersion data. Note that difference in the vertical travel time remains almost constant beyond 200 km depth with the exception of CANSD model of Massé (1973).

Figure 5-9. Comparison of short period P wave station anomalies for $\log_{10}$-amplitude (microns) data with those determined by Carpenter et al. (1967). WWSSN stations throughout the world were used in this comparison. N is the number of stations used, R the correlation coefficient, S the r.m.s. difference, T the average difference.

Figure 5-10. Short period (top) and long period (below) station anomalies of P waves for $\log_{10}$-amplitude (microns) data. All stations shown are part of WWSSN. Note that positive station anomalies mean anomalously large amplitudes and negative station anomalies imply anomalously small amplitudes.

Figure 5-11 (two plates) P wave travel time residuals vs. distance, shown separately for each of 18 deep seismic zones. Data are from bulletins collected by Sengupta (1972). Travel time residuals were computed from Jeffreys-Bullen times (1940) and were corrected for station anomalies (Appendix L). Solid line is the hand smoothed curve determined from all data averaged over 2° distance cell (see Appendix K). Notice that deviations of travel time residuals from this smooth curve are very pronounced beyond about 80° of distance.

Figure 5-12 (top) Standard deviation of P wave travel time residuals associated with gross earth data for each 2° distance cell (see Chap. 3). Notice the large standard deviation around 20°, 45° and the trend that standard deviation increases beyond about 80° of distance.

(below) Standard deviation of S wave travel time residuals associated with gross earth data for each 2° distance cell (see Chap. 3). Notice relative peaks around 40°, 48°, 60° and 70° (see text for their implications). The standard deviations around 80° are also large.

Figure 5-13. P wave travel time residuals from explosions at Marshall Islands. Data are from Carder (1964). These residuals were computed from Jeffreys-Bullen times (1940) and were corrected for station anomalies (Appendix L). Notice the pronounced early arrivals beyond 80° (see also text).

Figure 5-14. S wave travel time residuals vs. distance, shown separately for each of 14 source regions used in this study. Data are from WWSSN stations only, arrival times being read personally from the seismograms. Travel time residuals were computed from a combination of Gutenberg's model for the lower mantle and US26 model (Anderson and Julian, 1969) for the upper mantle. These residuals were corrected for station anomalies (Appendix L). Solid line is the travel time curve computed from our S wave velocity model (Chap. 3). Note that there is a large variation of S wave travel times around 80° of distance.

Figure 5-15. Comparison of average P and S wave travel time anomalies along different paths. These anomalies for P and S wave travel times were computed for data shown respectively on Figs. 5-11 and 5-14, and with respect to the solid lines shown on those figures. Paths are numbered like 1-4, 2-4, etc. and descriptions

are given in Table 5-5. Paths for which average P wave travel time residuals were found to be statistically significant (Table 5-5) have been distinguished by "filled circles" in contrast to "open circles" otherwise. Horizontal and vertical bars represent standard deviation of P and S wave travel time residuals respectively along these paths. Correlation coefficient between P and S wave travel time residuals are shown in the brackets.

Figure 5-16. P wave travel time residuals before (left) and after (right) fit by our three dimensional velocity model (MODEL 3). These two source zones were chosen because of the pronounced difference in the observed travel times (left- figures) from the solid line which represents the times predicted from our one dimensional P wave velocity model (see Chap. 3). Note that P wave travel time residuals were calculated in the same way as those in Fig. 5-11.

Figure 5-17. Same as Fig. 5-16, except that data here are for S wave travel time residuals, and solid line is for the times predicted from our one dimensional S wave velocity model (see Chap. 3). The travel time residuals were computed in the same way as those in Fig. 5-14. Note that three dimensional velocity model (MODEL 3) in this case "overfits" the data.

Figure 5-18. Histograms of P wave travel time residuals at different stages of construction of three dimensional velocity model. N in the rectangular box represents the number of observations, R is the r.m.s. value of travel time residuals.

Part (a): travel time residuals computed from Jeffreys-Bullen times (1940) with correction for ellipticity in earth.

Part (b): travel time residuals computed from our one dimensional velocity model (Chap. 3) with correction for ellipticity in the earth.

Part (c): residuals from (b) corrected for station anomalies.

Part (d): residuals from (c) corrected for our three dimensional velocity variation (MODEL 3). Smooth curve is the normal distribution with zero mean and standard deviation of 0.36 seconds. Note that factorial reduction in the r.m.s. residual is the largest after introducing three dimensional velocity perturbations.

Figure 5-19. Same as Fig. 5-18 except that data here are for S wave travel time residuals. Starting travel time residuals (part a) were computed from a combination of Gutenberg's S velocity model in the lower mantle and US26 model (Anderson and Julian, 1969) in the upper mantle. Smooth curve in part (d) of this figure corresponds to a normal distribution with zero mean and standard deviation of 0.75 seconds. Note that three dimensional velocity perturbations of MODEL 3 have "overfitted" data (see also Fig. 5-17).

Figure 5-20. R.m.s. relative perturbations (in percent) of P and S wave velocity for each 500 km depth interval up to the core-mantle boundary. Notice a minimum in r.m.s. perturbation for the middle mantle in all three sequencing of blocks during inversion (except for one sequencing for S velocity model). Also note the r.m.s. perturbation for S velocity is larger than that for P velocity in the upper mantle, but smaller (or, comparable) near the core-mantle boundary.

Figure 5-21. Histogram of relative velocity perturbation (in percent) of P wave velocity for each 500 km depth interval up to the core-mantle boundary. Only the results of inversion from random sequencing of blocks (MODEL 3) are shown. N in the rectangular box refers to the number of blocks sampled by our data, R, the

r.m.s. perturbation (in percent, H the depth interval. We also show the histograms for relative perturbations corresponding to the average of station anomalies in each block. Note that relative perturbation corresponding to station anomalies are in general larger than those obtained by inversion for 0-500 km depth.

Figure 5-22. Same as Fig. 5-21 except this figure is for S wave velocity perturbation.

Figure 5-23. (7 plates) Three dimensional P wave velocity model. Only the results of inversion from random sequencing of blocks (MODEL 3) are shown. Each color represents a range in relative velocity perturbation, the legend of which is given in the first plate. The positive values in relative velocity perturbation correspond to higher velocity than the spherically symmetric velocity model (Chap. 3) and the negative perturbations to lower velocity. Note that for the surface layer (0-500 km depth), contributions of velocity perturbations corresponding to station anomalies have been added to those obtained by inversion.

Figure 5-24. (6 plates) Same as Fig. 23 except that this figure is for three dimensional velocity model for S wave (MODEL 3).

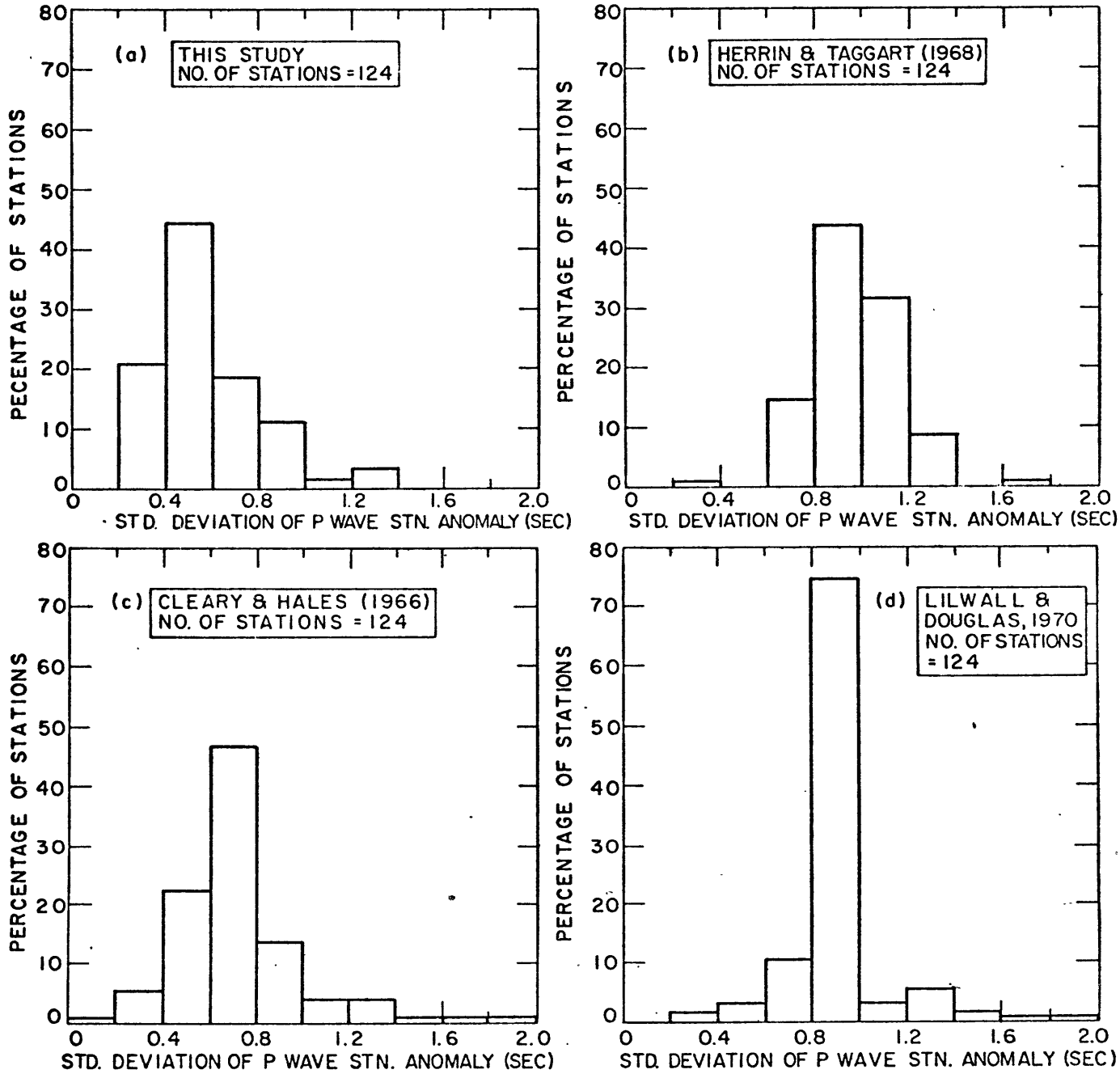

(a) THIS STUDY
NO. OF STATIONS = 124
(b) HERRIN & TAGGART (1968)
NO. OF STATIONS = 124
(c) CLEARY & HALES (1966)
NO. OF STATIONS = 124
(d) LILWALL & DOUGLAS, 1970
NO. OF STATIONS = 124
PECENTAGE OF STATIONS
PERCENTAGE OF STATIONS
0 10 20 30 40 50 60 70 80
0 0.4 0.8 1.2 1.6 2.0
STD. DEVIATION OF P WAVE STN. ANOMALY (SEC)

Fig. 5-1

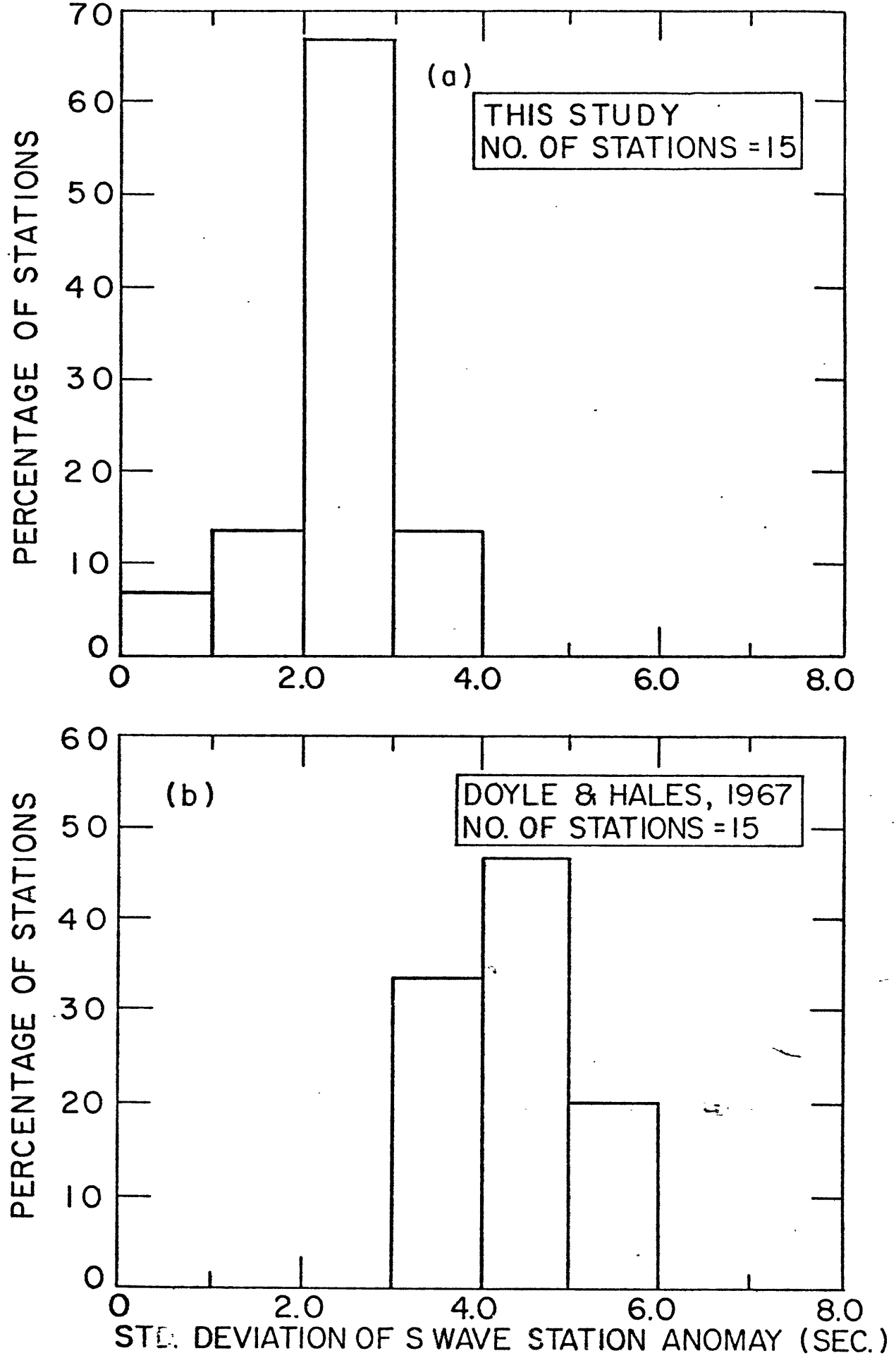

(a)
THIS STUDY
NO. OF STATIONS = 15
PERCENTAGE OF STATIONS
70
60
50
40
30
20
10
0
0
2.0
4.0
6.0
8.0
(b)
DOYLE & HALES, 1967
NO. OF STATIONS = 15
PERCENTAGE OF STATIONS
60
50
40
30
20
10
0
0
2.0
4.0
6.0
8.0
STD. DEVIATION OF S WAVE STATION ANOMAY (SEC.)

Fig. 5-2

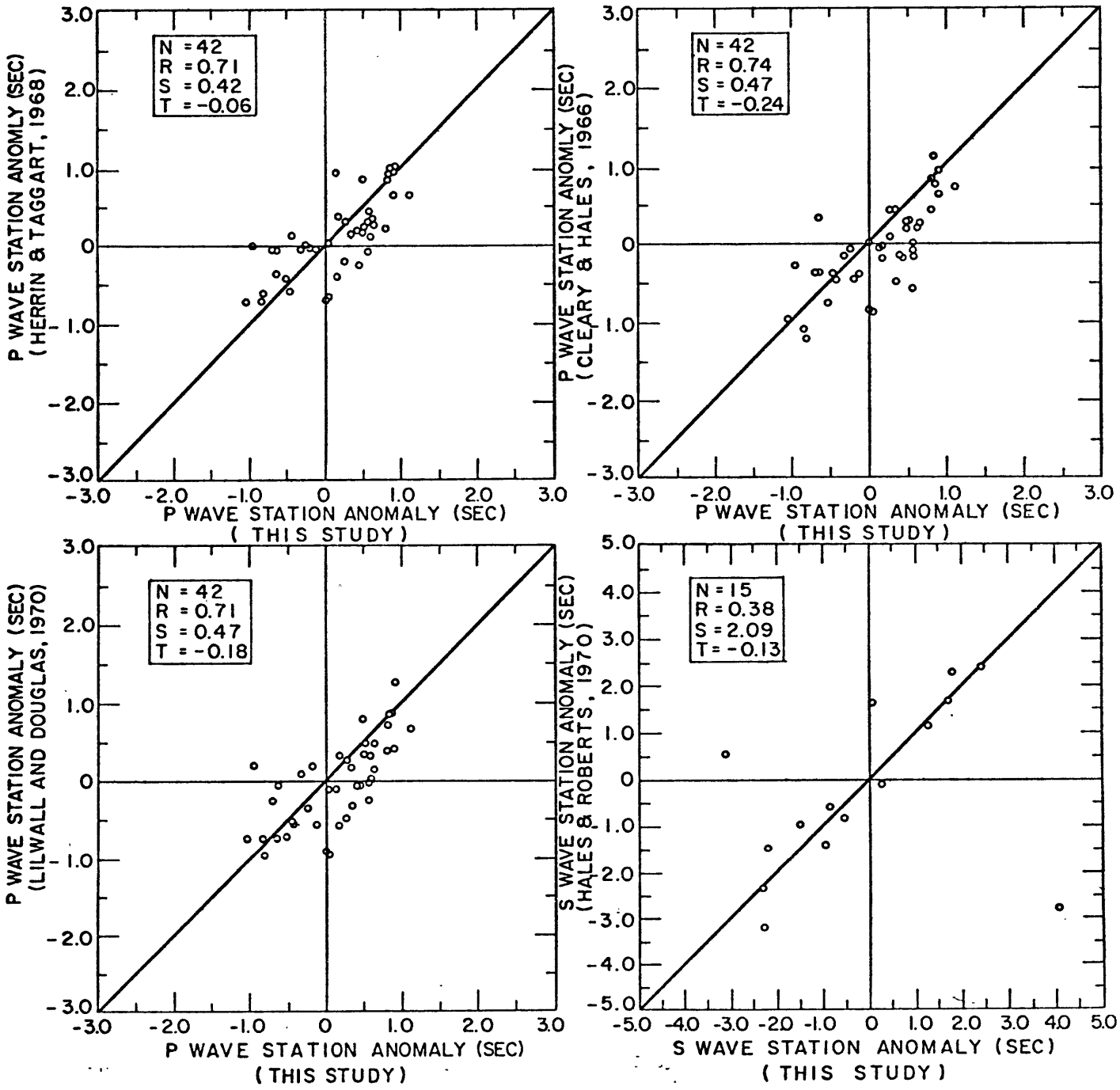

N = 42
R = 0.71
S = 0.42
T = -0.06
P WAVE STATION ANOMLY (SEC)
(HERRIN & TAGGART, 1968)
P WAVE STATION ANOMALY (SEC)
(THIS STUDY)
N = 42
R = 0.74
S = 0.47
T = -0.24
P WAVE STATION ANOMLY (SEC)
(CLEARY & HALES, 1966)
P WAVE STATION ANOMALY (SEC)
(THIS STUDY)
N = 42
R = 0.71
S = 0.47
T = -0.18
P WAVE STATION ANOMALY (SEC)
(LILWALL AND DOUGLAS, 1970)
P WAVE STATION ANOMALY (SEC)
(THIS STUDY)
N = 15
R = 0.38
S = 2.09
T = -0.13
S WAVE STATION ANOMALY (SEC)
(HALES & ROBERTS, 1970)
S WAVE STATION ANOMALY (SEC)
(THIS STUDY)

Fig. 5-3

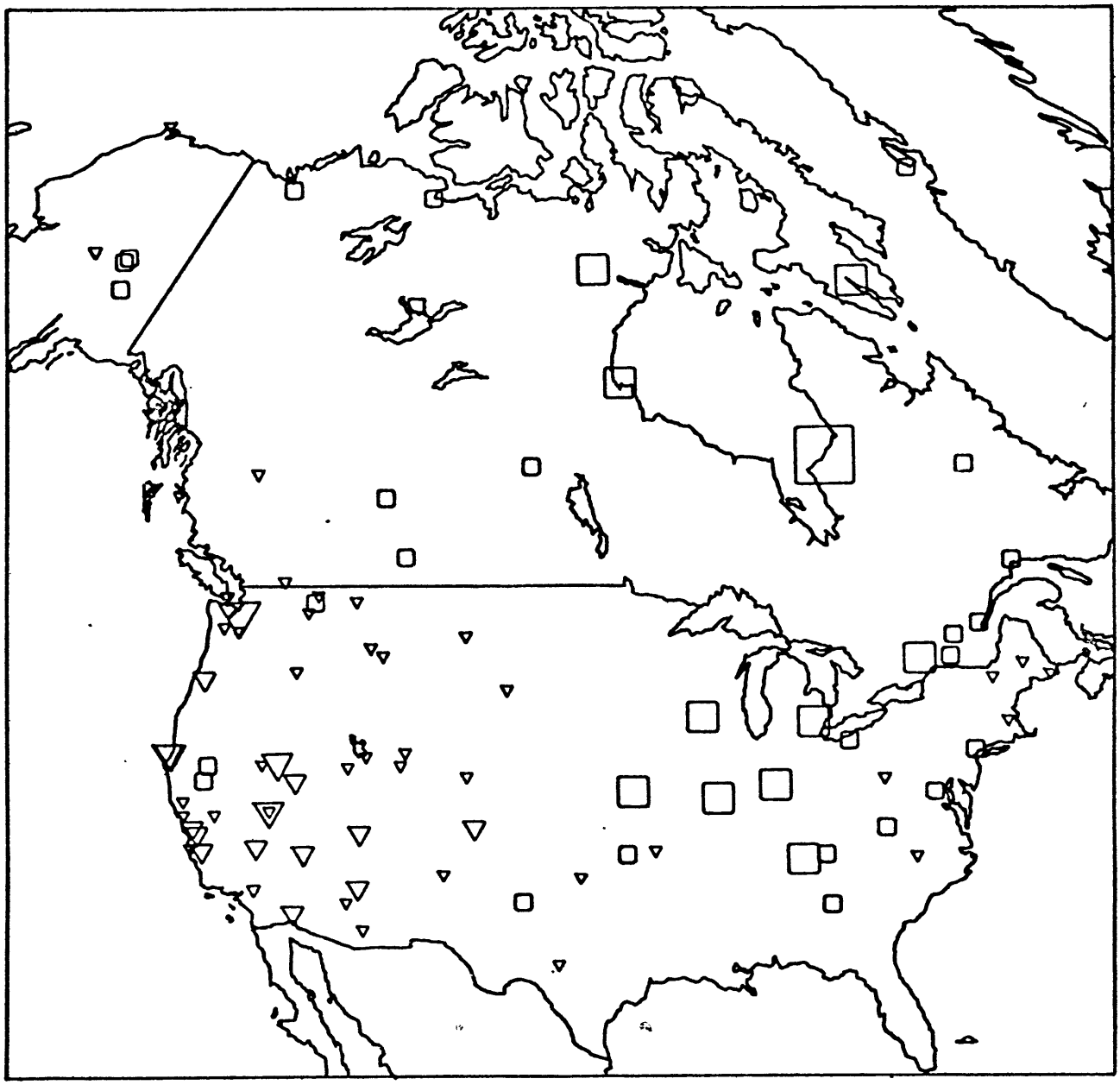


Fig. 5-4

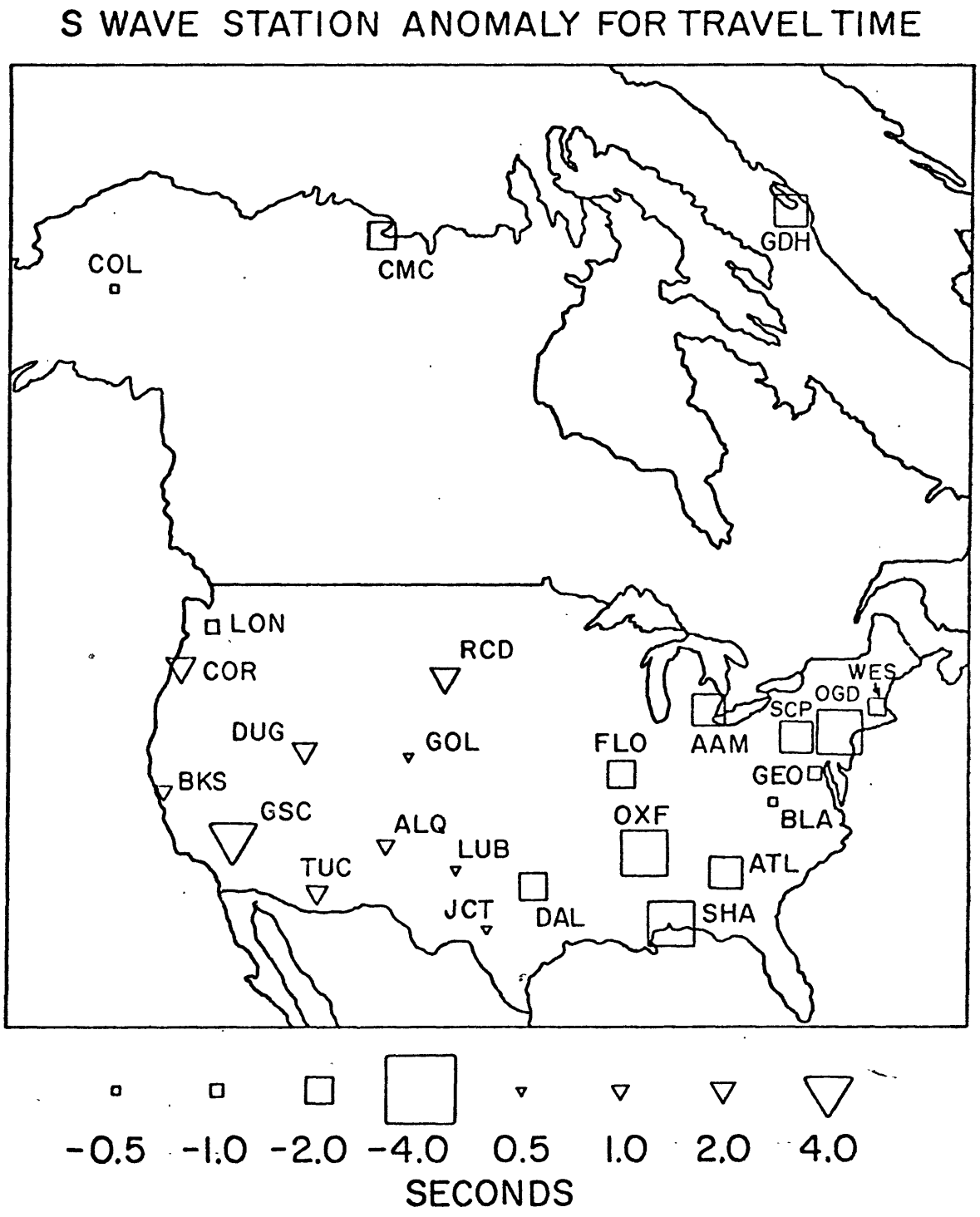

S WAVE STATION ANOMALY FOR TRAVEL TIME
COL
CMC
GDH
LON
COR
RCD
WES
OGD
SCP
DUG
GOL
FLO
AAM
BKS
GEO
GSC
ALQ
OXF
BLA
LUB
TUC
ATL
JCT
DAL
SHA
-0.5 -1.0 -2.0 -4.0 0.5 1.0 2.0 4.0
SECONDS

Fig. 5-5

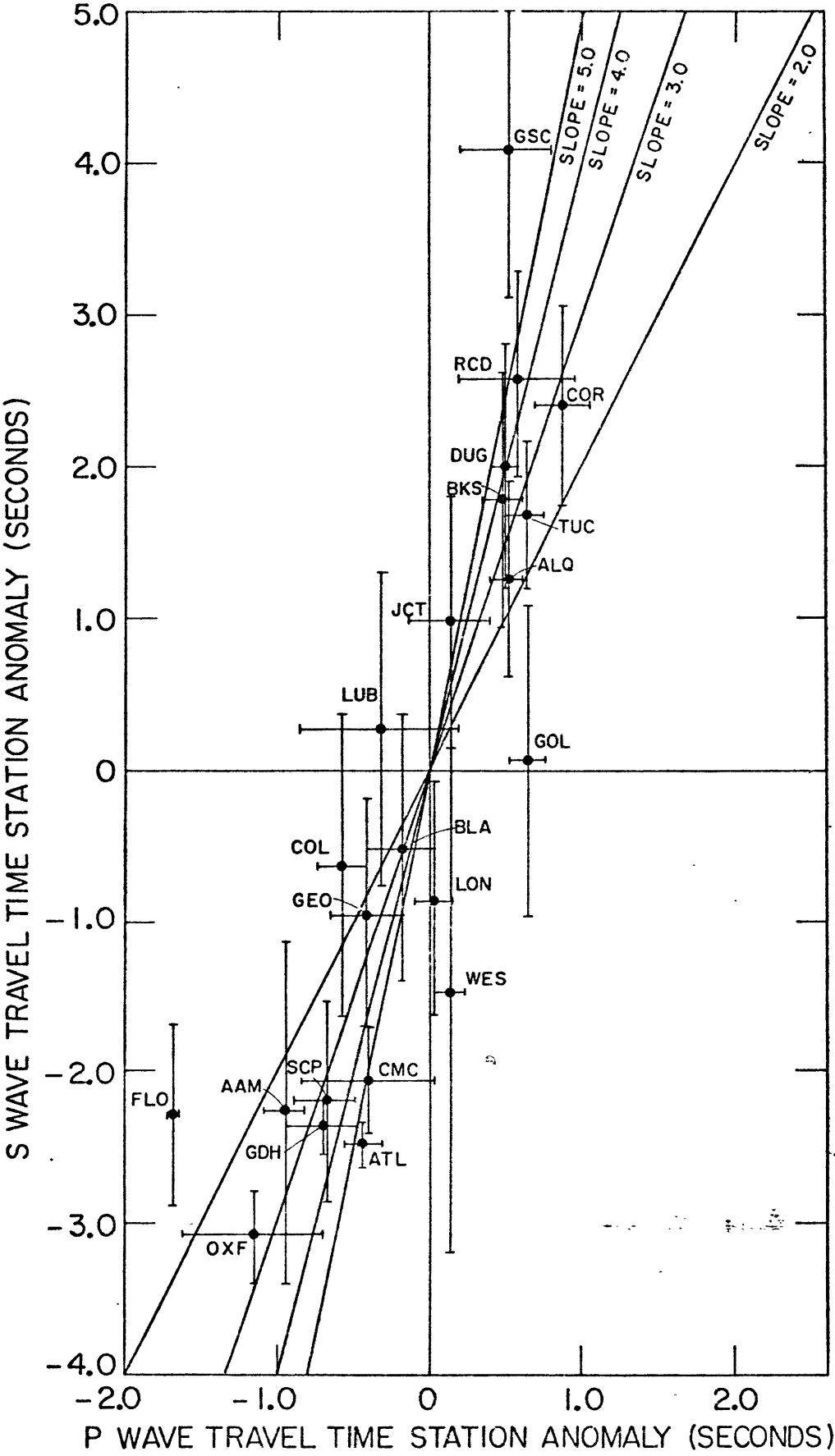
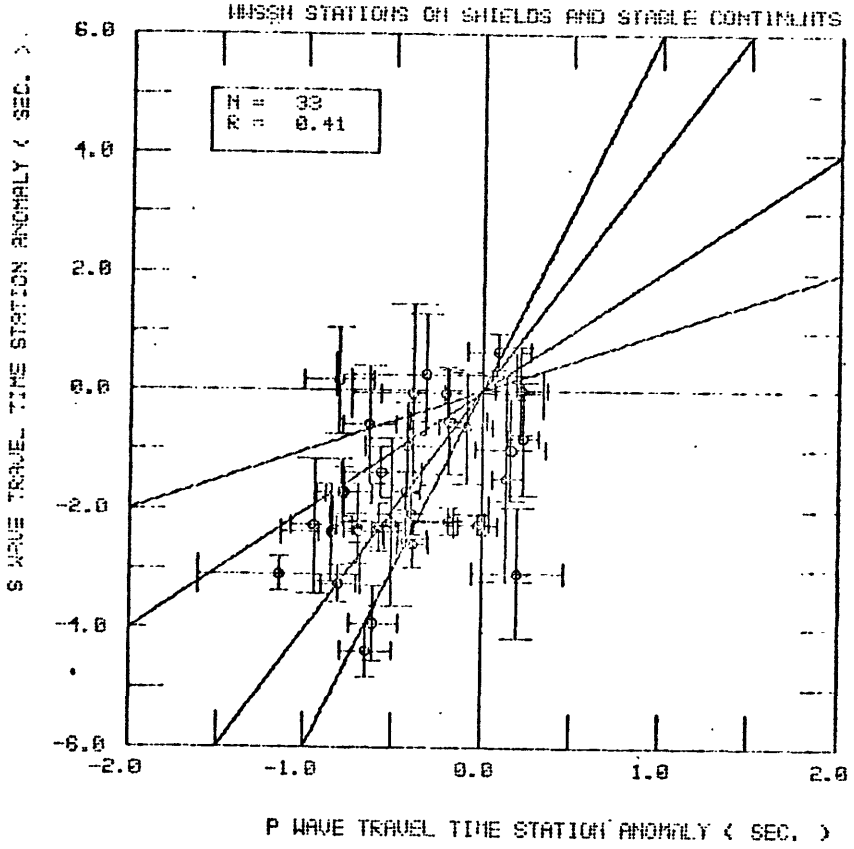

5.0
4.0
3.0
2.0
1.0
0
-1.0
-2.0
-3.0
-4.0
-2.0
-1.0
0
1.0
2.0
S WAVE TRAVEL TIME STATION ANOMALY (SECONDS)
P WAVE TRAVEL TIME STATION ANOMALY (SECONDS)
SLOPE = 5.0
SLOPE = 4.0
SLOPE = 3.0
SLOPE = 2.0
GSC
RCD
COR
DUG
BKS
TUC
ALQ
JCT
LUB
GOL
BLA
COL
LON
GEO
WES
SCP
CMC
AAM
FLO
GDH
ATL
OXF

Fig. 5-6


WWSSN STATIONS ON SHIELDS AND STABLE CONTINENTS
N = 33
R = 0.41
S WAVE TRAVEL TIME STATION ANOMALY (SEC.)
P WAVE TRAVEL TIME STATION ANOMALY (SEC.)
6.0
4.0
2.0
0.0
-2.0
-4.0
-6.0
-2.0
-1.0
0.0
1.0
2.0

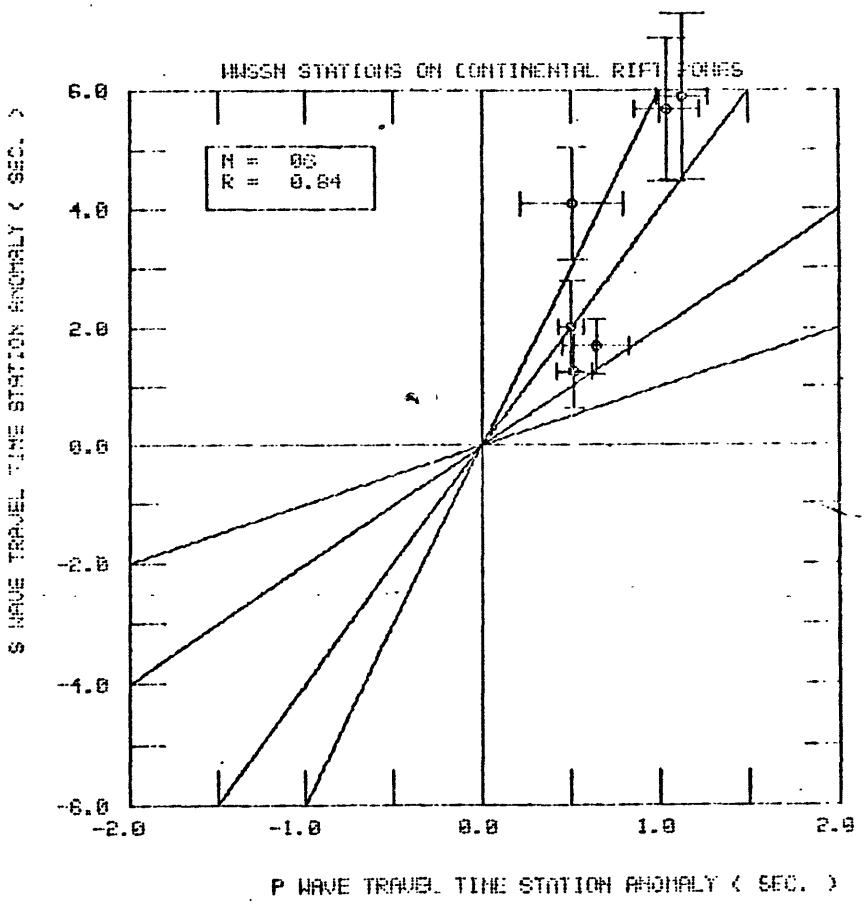

WWSSN STATIONS ON CONTINENTAL RIFT ZONES
N = 96
R = 0.84
S WAVE TRAVEL TIME STATION ANOMALY (SEC.)
P WAVE TRAVEL TIME STATION ANOMALY (SEC.)
6.0
4.0
2.0
0.0
-2.0
-4.0
-6.0
-2.0
-1.0
0.0
1.0
2.0

Fig. 5-7

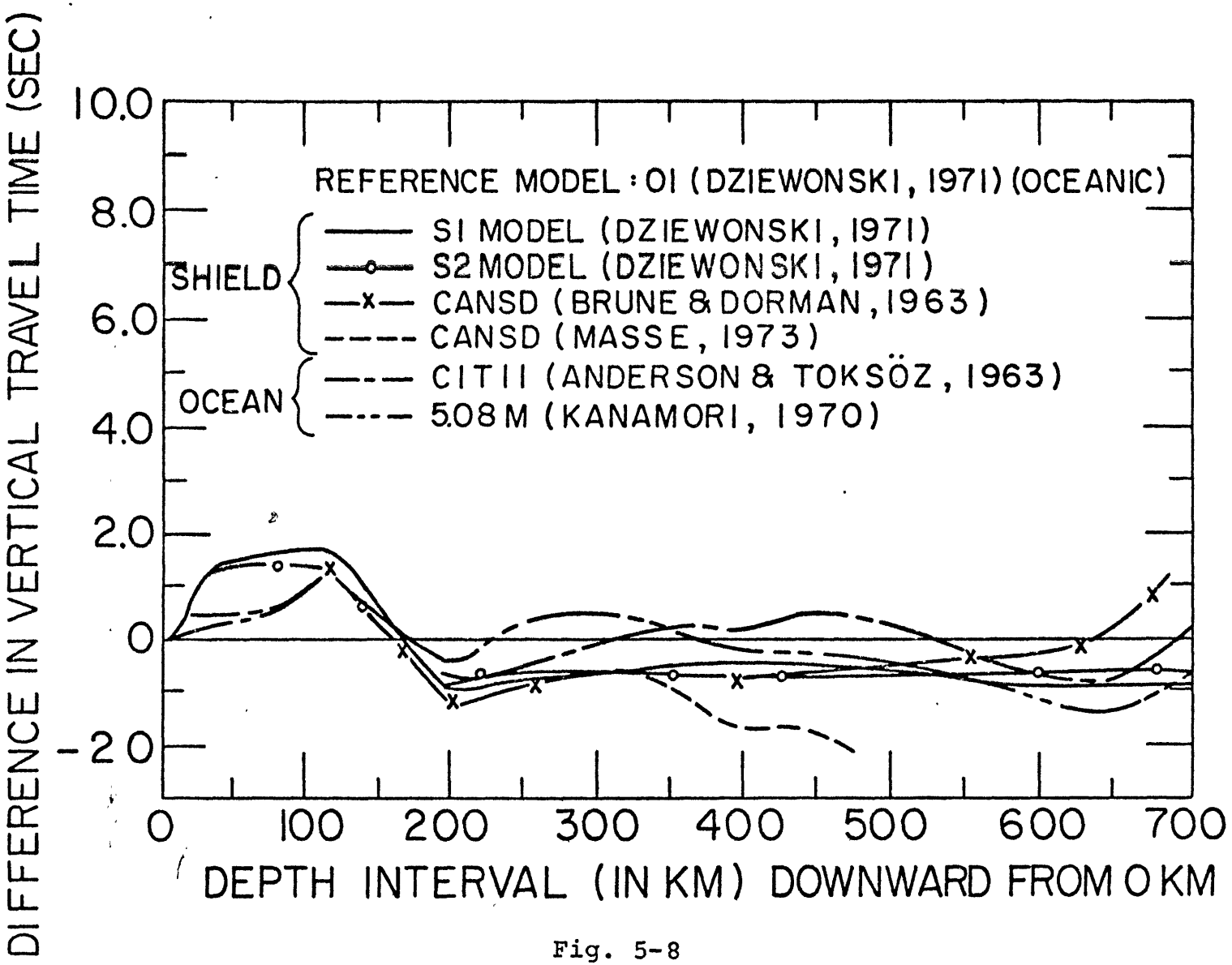

DIFFERENCE IN VERTICAL TRAVEL TIME (SEC)
10.0
8.0
6.0
4.0
2.0
0
-2.0
REFERENCE MODEL : 01 (DZIEWONSKI, 1971) (OCEANIC)
SHIELD
S1 MODEL (DZIEWONSKI, 1971)
S2 MODEL (DZIEWONSKI, 1971)
CANSD (BRUNE & DORMAN, 1963)
CANSD (MASSE, 1973)
OCEAN
CIT11 (ANDERSON & TOKSÖZ, 1963)
5.08M (KANAMORI, 1970)
0
100
200
300
400
500
600
700
DEPTH INTERVAL (IN KM) DOWNWARD FROM 0 KM

Fig. 5-8

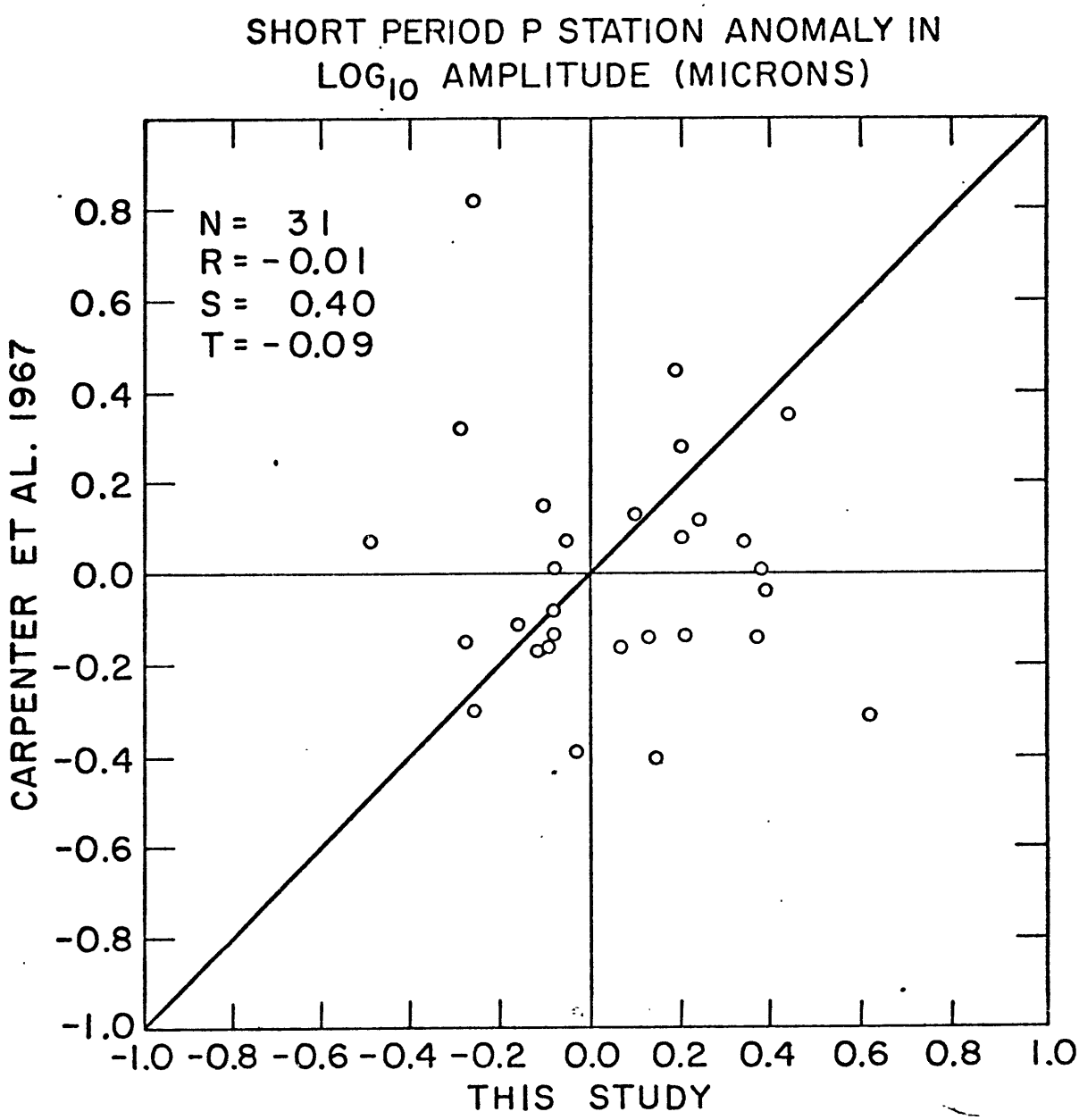
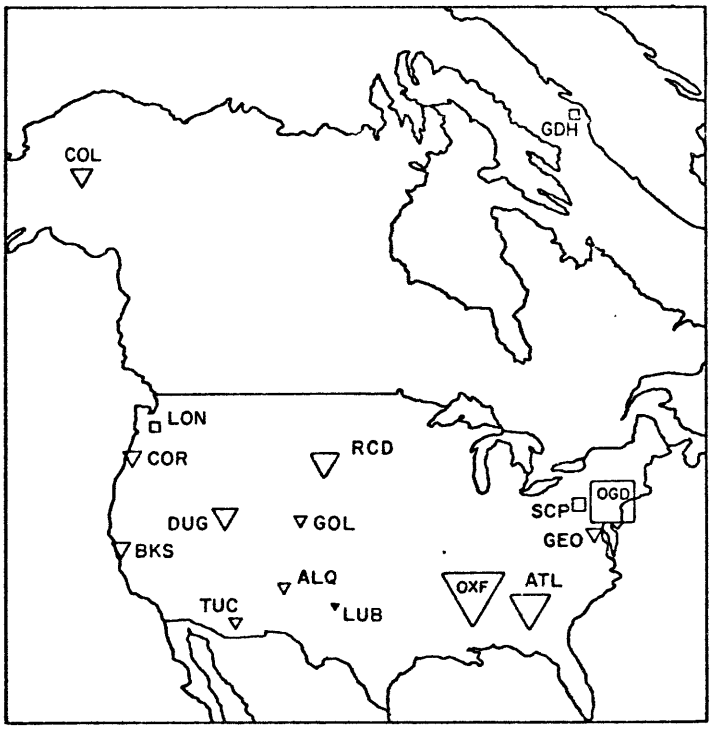
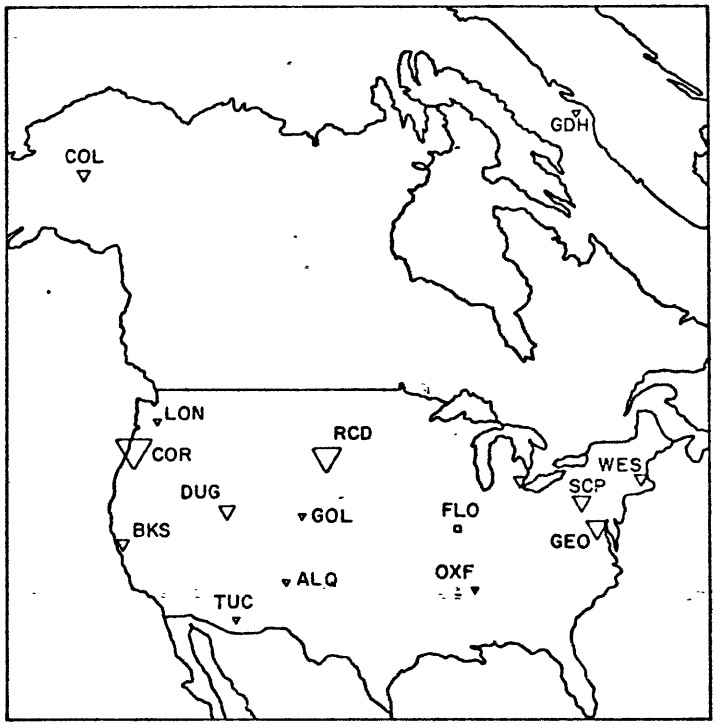

SHORT PERIOD P STATION ANOMALY IN
LOG10 AMPLITUDE (MICRONS)
N = 31
R = -0.01
S = 0.40
T = -0.09
CARPENTER ET AL. 1967
THIS STUDY
0.8
0.6
0.4
0.2
0.0
-0.2
-0.4
-0.6
-0.8
-1.0
-1.0 -0.8 -0.6 -0.4 -0.2 0.0 0.2 0.4 0.6 0.8 1.0

Fig. 5-9

(a) SP STATION ANOMALY FOR LOG_{10} AMPLITUDES (MICRONS) OF PWAVE



(b) LP STATION ANOMALY FOR LOG_{10} AMPLITUDES (MICRONS) OF PWAVE



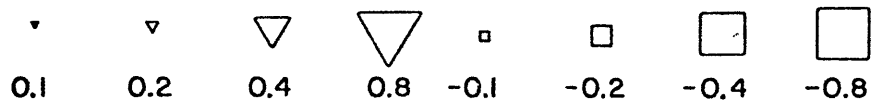


Fig. 5-10

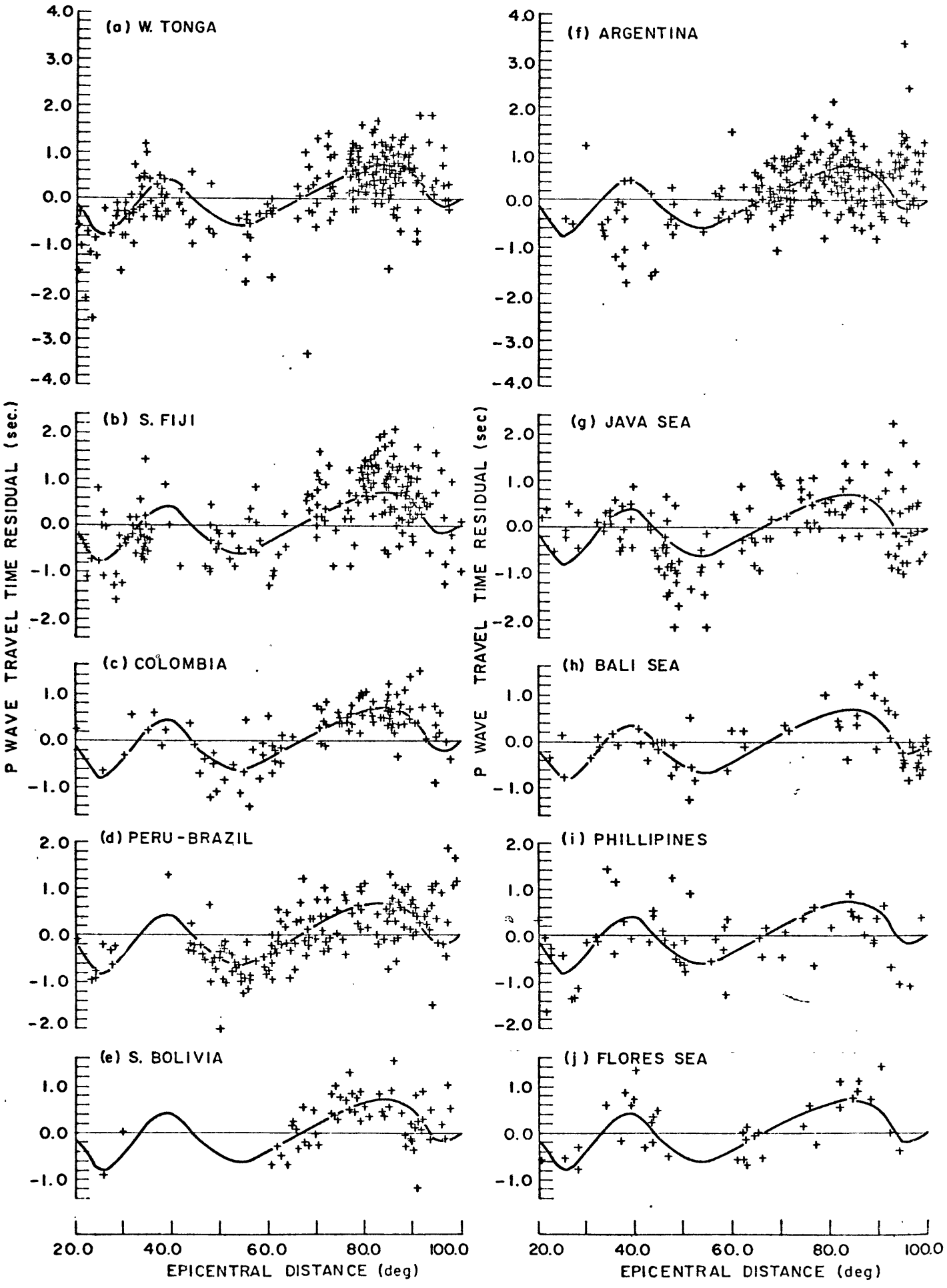

(a) W. TONGA
(b) S. FIJI
(c) COLOMBIA
(d) PERU-BRAZIL
(e) S. BOLIVIA
(f) ARGENTINA
(g) JAVA SEA
(h) BALI SEA
(i) PHILLIPINES
(j) FLORES SEA
P WAVE TRAVEL TIME RESIDUAL (sec.)
EPICENTRAL DISTANCE (deg)
20.0
40.0
60.0
80.0
100.0

Fig. 5-11

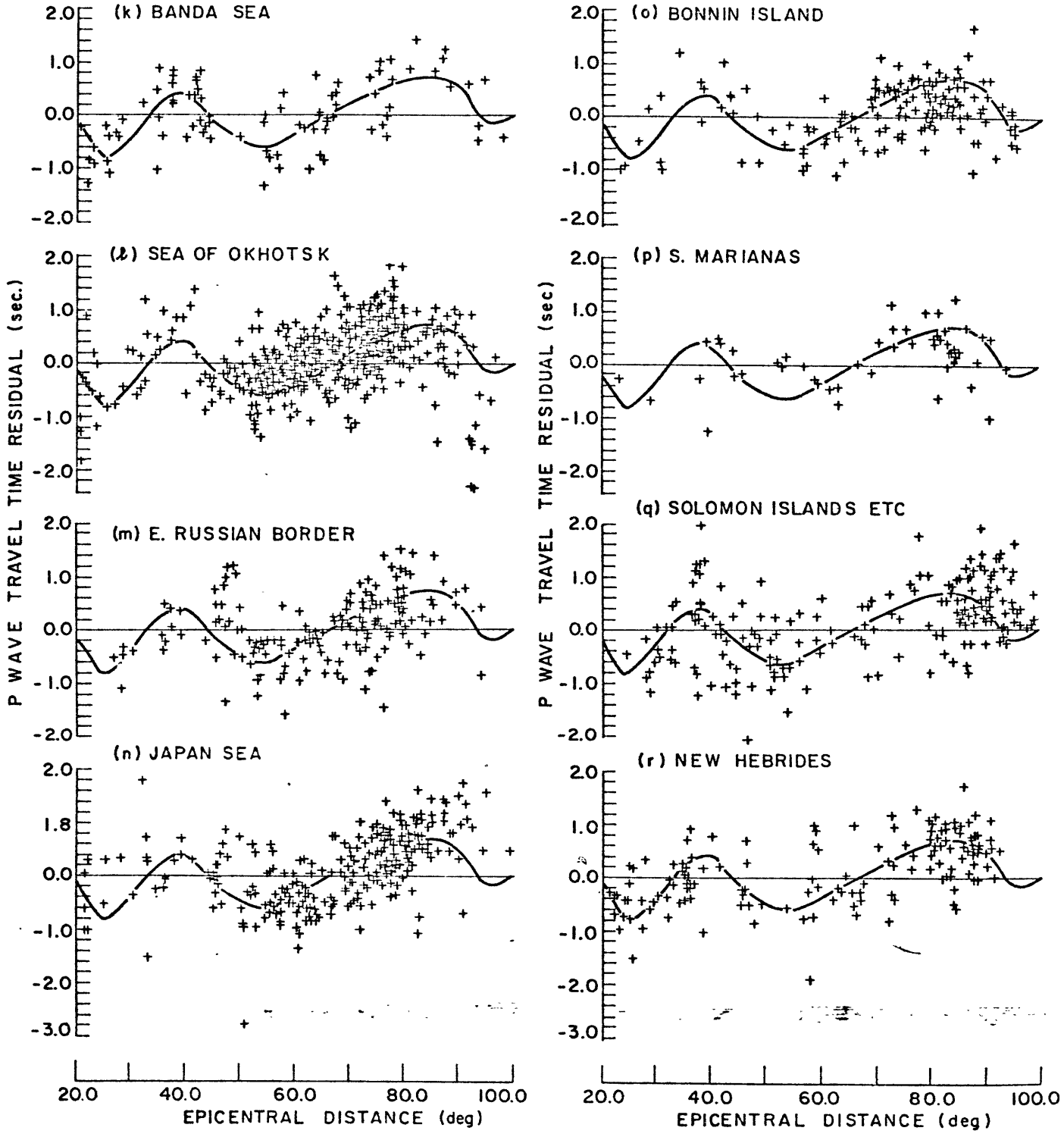
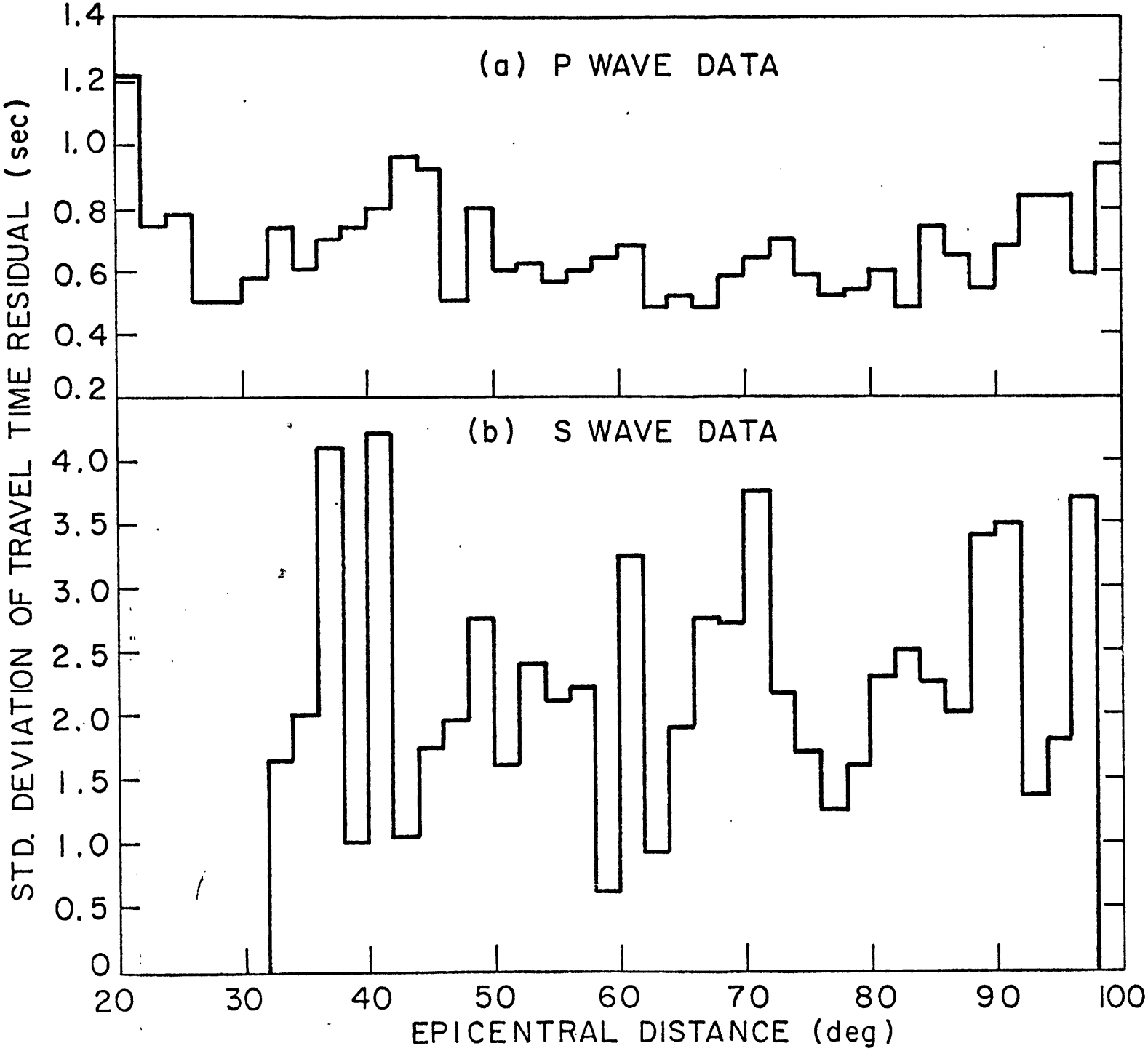


Fig. 5-11 (contd)


(a) P WAVE DATA
(b) S WAVE DATA
STD. DEVIATION OF TRAVEL TIME RESIDUAL (sec)
EPICENTRAL DISTANCE (deg)
1.4
1.2
1.0
0.8
0.6
0.4
0.2
4.0
3.5
3.0
2.5
2.0
1.5
1.0
0.5
0
20
30
40
50
60
70
80
90
100

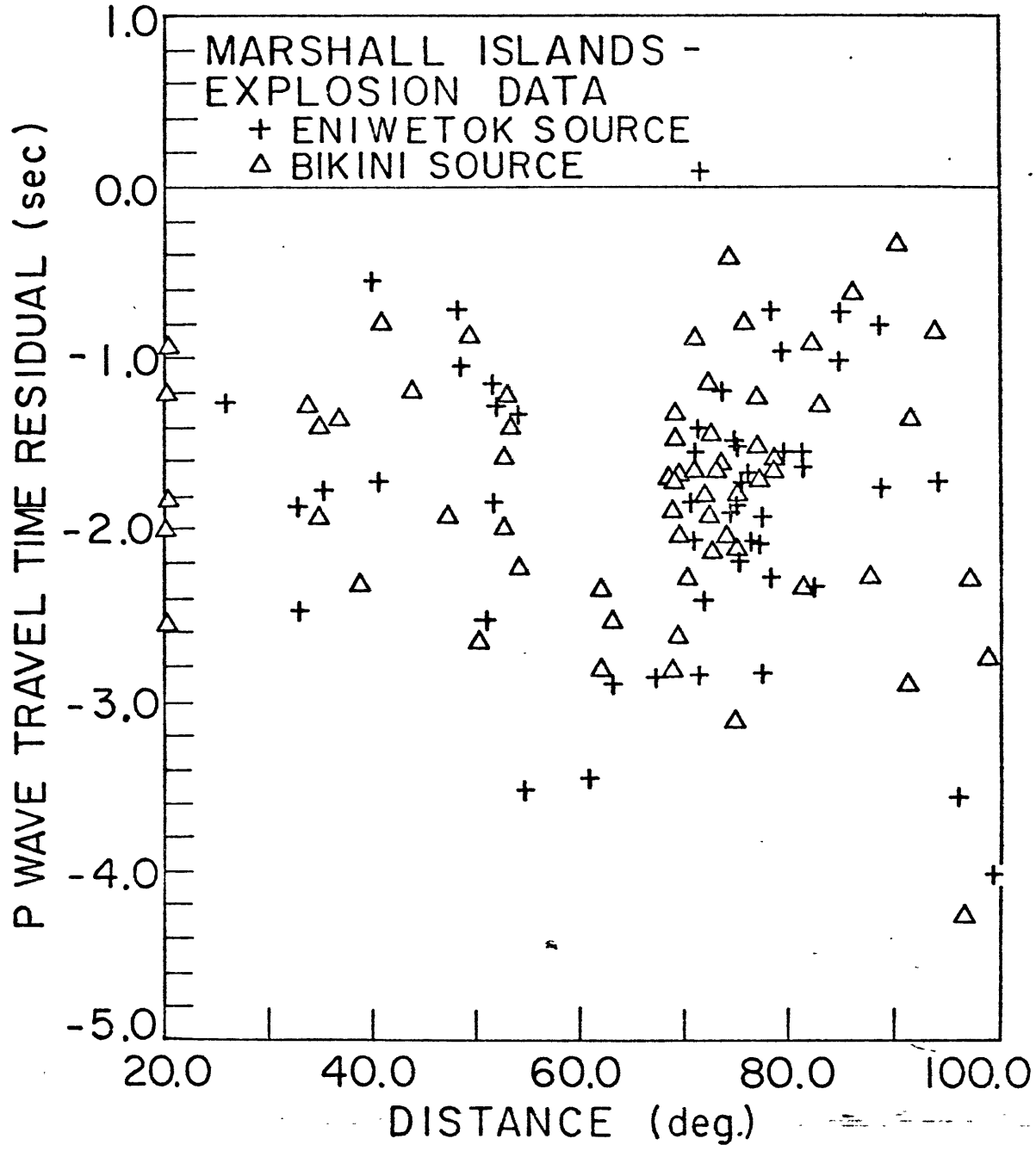
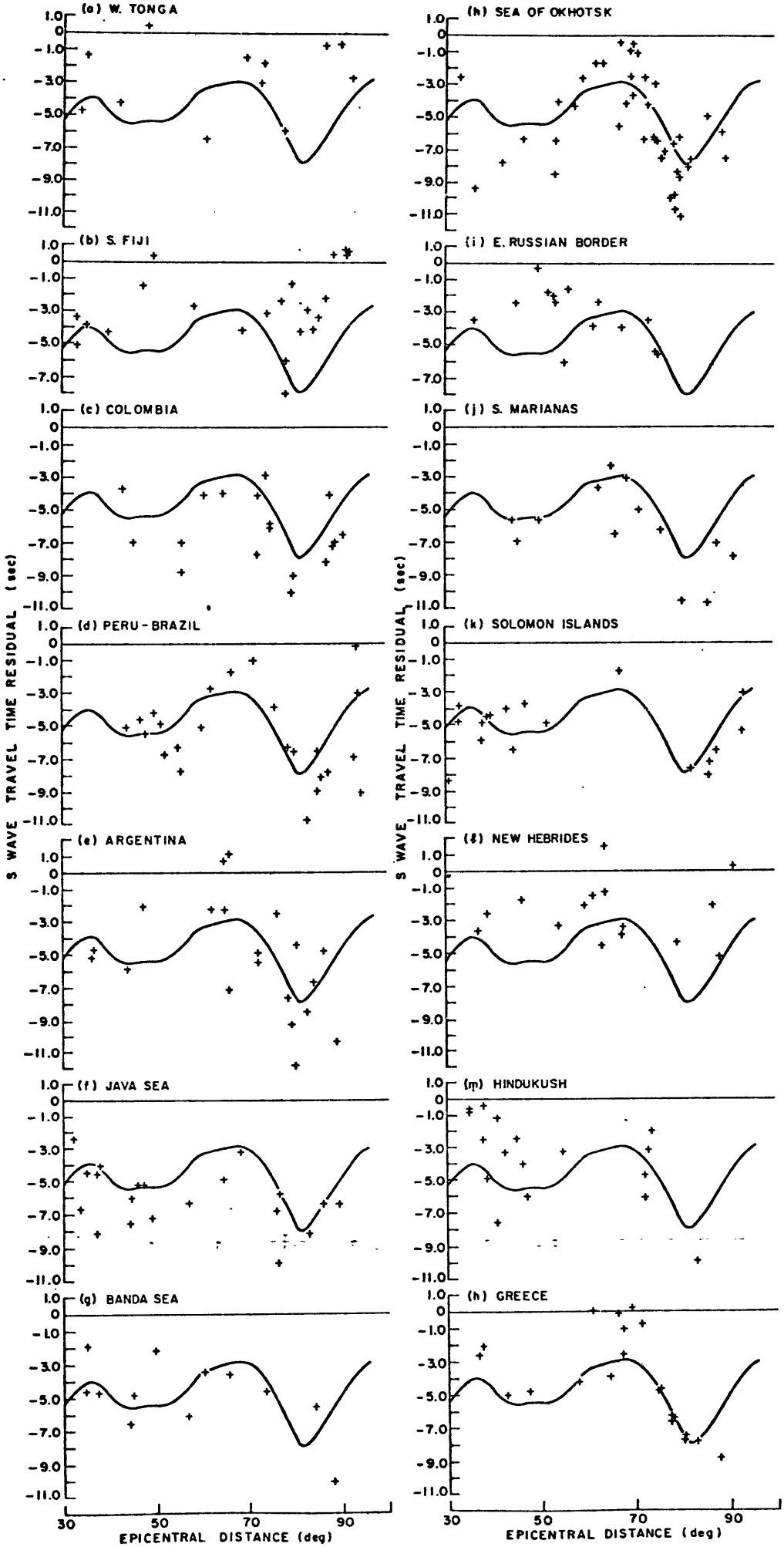

MARSHALL ISLANDS -
EXPLOSION DATA
+ ENIWETOK SOURCE
△ BIKINI SOURCE
P WAVE TRAVEL TIME RESIDUAL (sec)
1.0
0.0
-1.0
-2.0
-3.0
-4.0
-5.0
20.0
40.0
60.0
80.0
100.0
DISTANCE (deg.)

Fig. 5-13


(a) W. TONGA
(b) S. FIJI
(c) COLOMBIA
(d) PERU-BRAZIL
(e) ARGENTINA
(f) JAVA SEA
(g) BANDA SEA
(h) SEA OF OKHOTSK
(i) E. RUSSIAN BORDER
(j) S. MARIANAS
(k) SOLOMON ISLANDS
(l) NEW HEBRIDES
(m) HINDUKUSH
(n) GREECE
S WAVE TRAVEL TIME RESIDUAL (sec)
1.0
0
-1.0
-3.0
-5.0
-7.0
-9.0
-11.0
30
50
70
90
EPICENTRAL DISTANCE (deg)

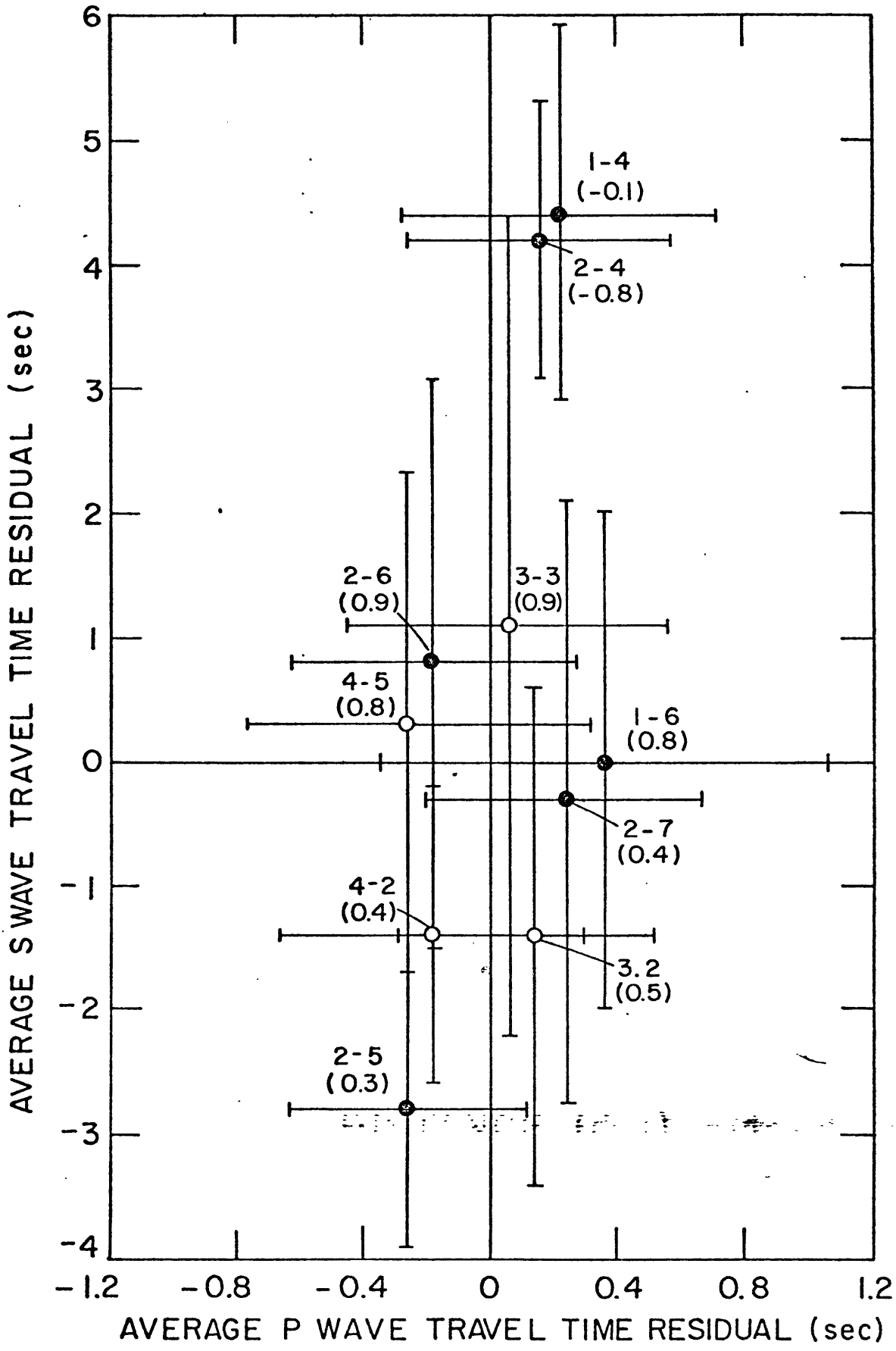

AVERAGE S WAVE TRAVEL TIME RESIDUAL (sec)
AVERAGE P WAVE TRAVEL TIME RESIDUAL (sec)
6
5
4
3
2
1
0
-1
-2
-3
-4
-1.2
-0.8
-0.4
0
0.4
0.8
1.2
1-4
(-0.1)
2-4
(-0.8)
2-6
(0.9)
3-3
(0.9)
4-5
(0.8)
1-6
(0.8)
2-7
(0.4)
4-2
(0.4)
3.2
(0.5)
2-5
(0.3)

Fig. 5-15

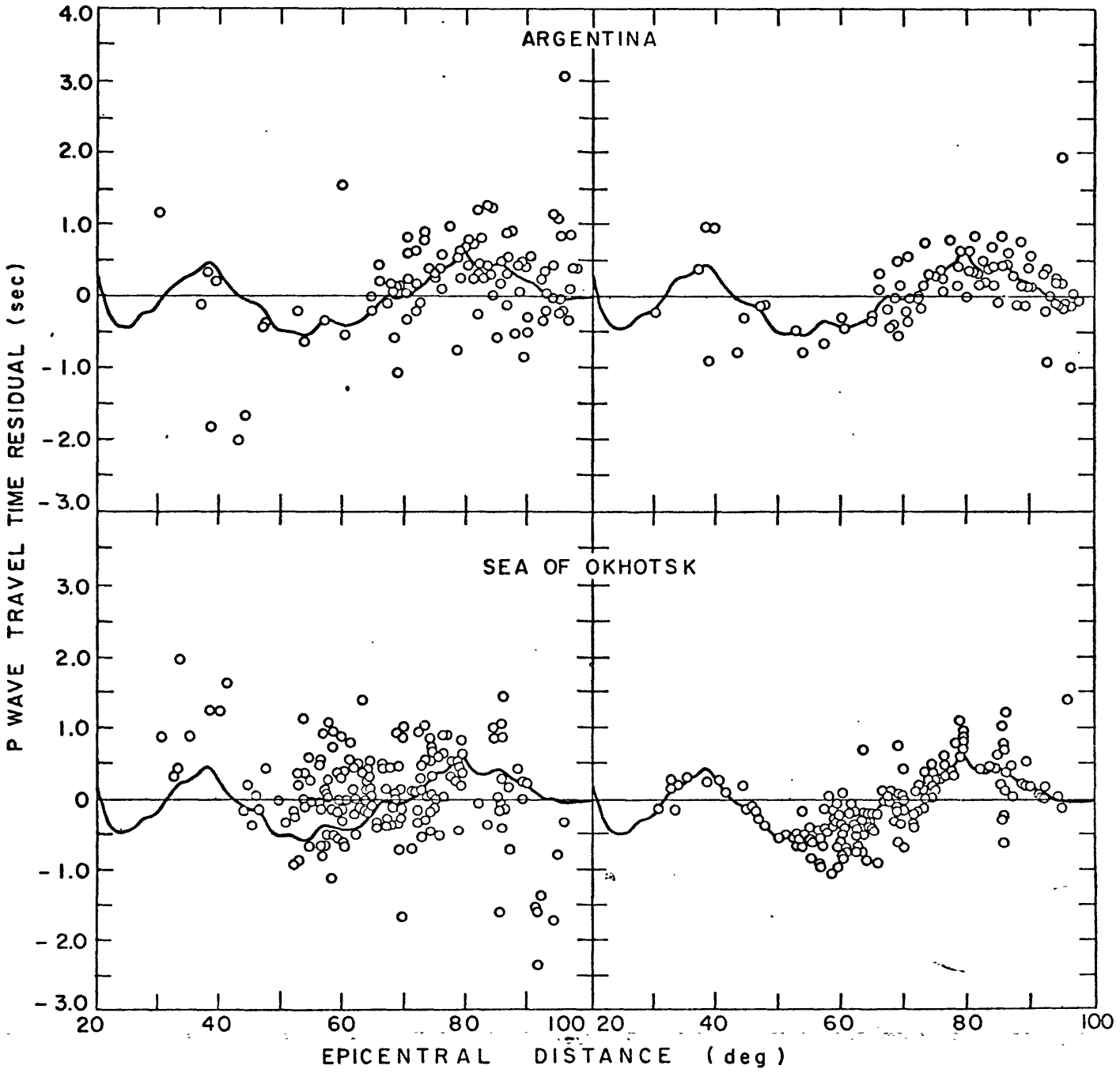

ARGENTINA
SEA OF OKHOTSK
P WAVE TRAVEL TIME RESIDUAL (sec)
4.0
3.0
2.0
1.0
0
-1.0
-2.0
-3.0
20
40
60
80
100
EPICENTRAL DISTANCE (deg)

Fig. 5-16

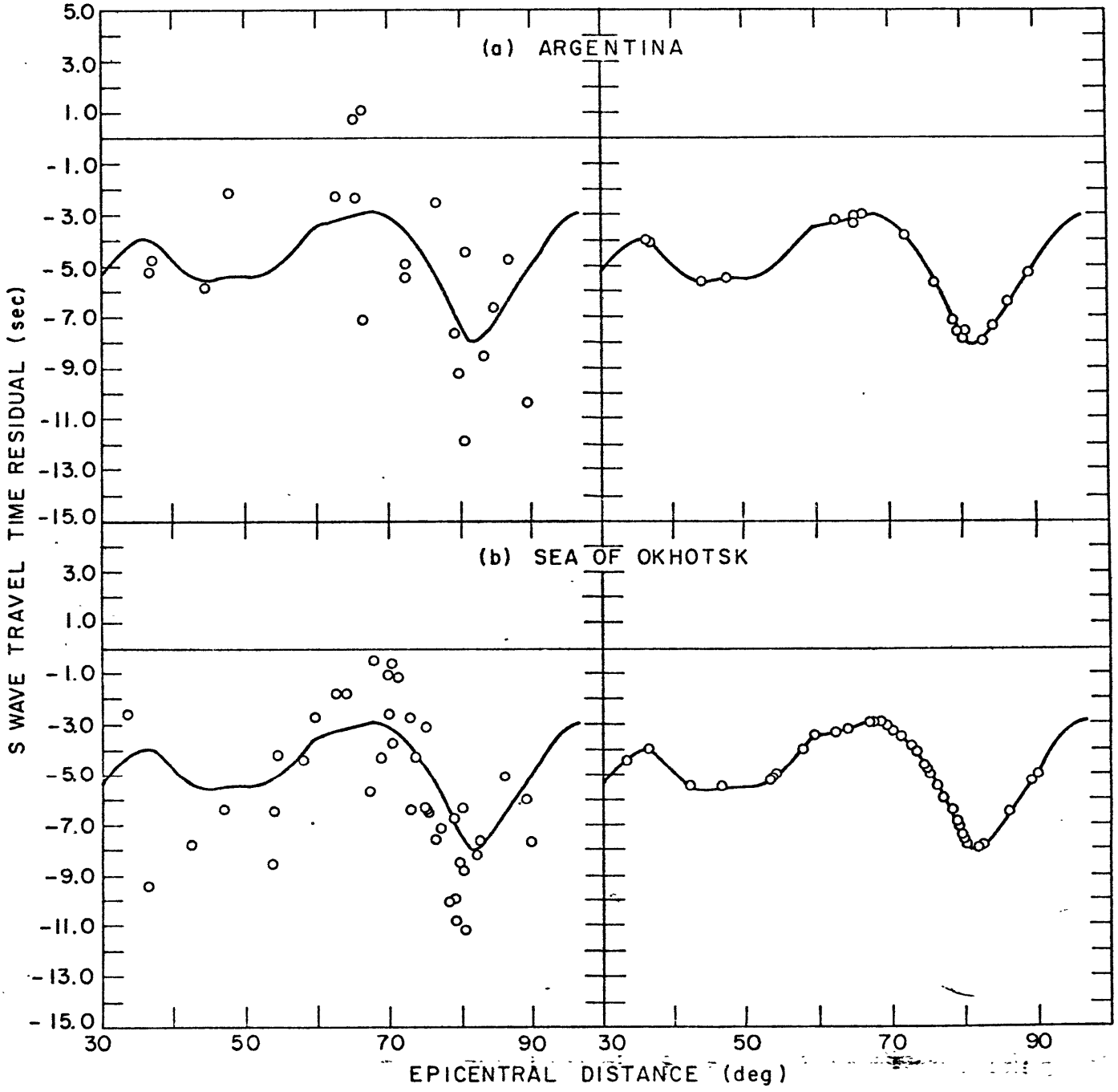

(a) ARGENTINA
(b) SEA OF OKHOTSK
S WAVE TRAVEL TIME RESIDUAL (sec)
5.0
3.0
1.0
-1.0
-3.0
-5.0
-7.0
-9.0
-11.0
-13.0
-15.0
30
50
70
90
EPICENTRAL DISTANCE (deg)

Fig. 5-17

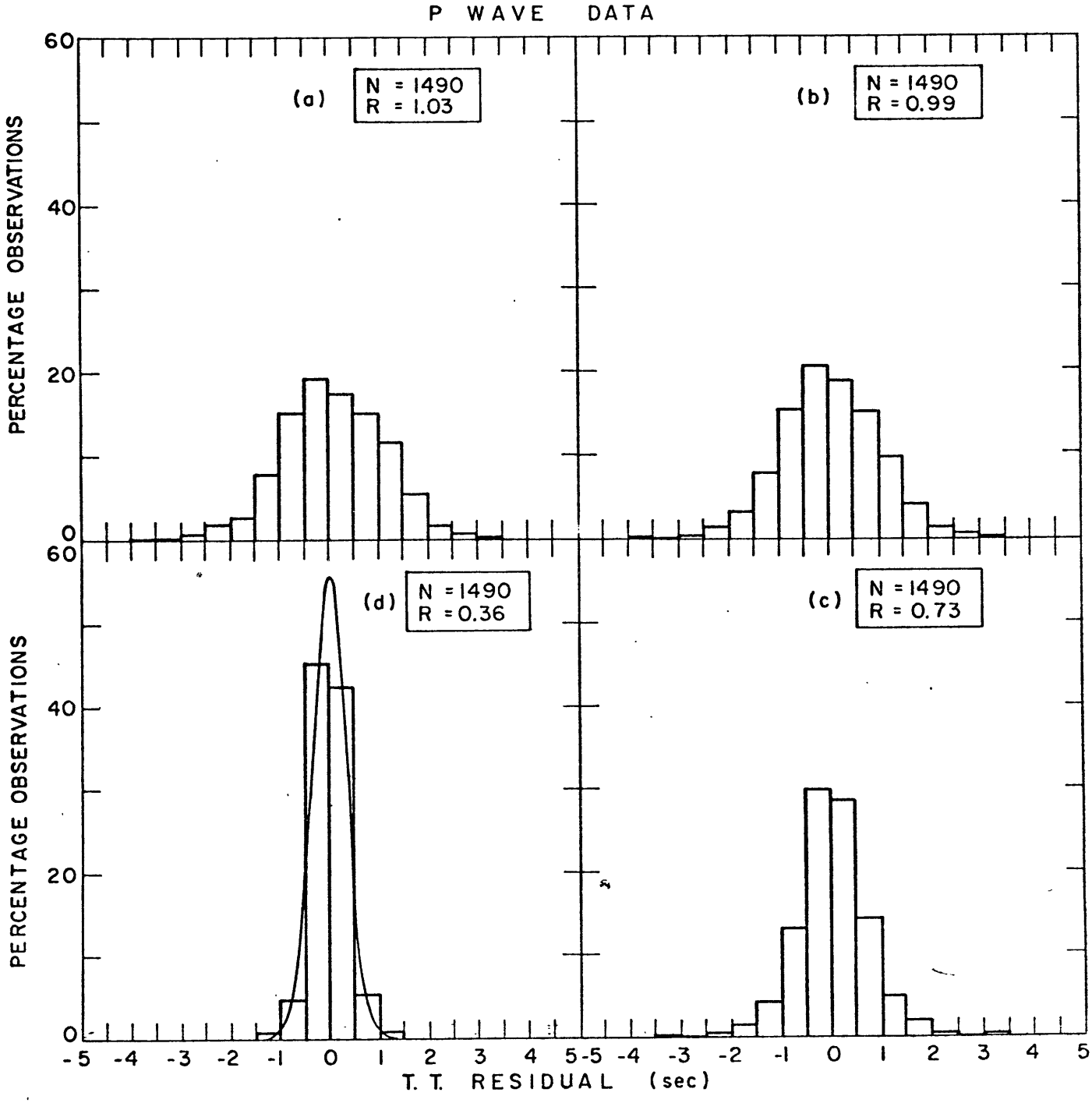

P WAVE DATA
(a)
N = 1490
R = 1.03
(b)
N = 1490
R = 0.99
(d)
N = 1490
R = 0.36
(c)
N = 1490
R = 0.73
PERCENTAGE OBSERVATIONS
PERCENTAGE OBSERVATIONS
0
20
40
60
-5 -4 -3 -2 -1 0 1 2 3 4 5
T. T. RESIDUAL (sec)

Fig. 5-18

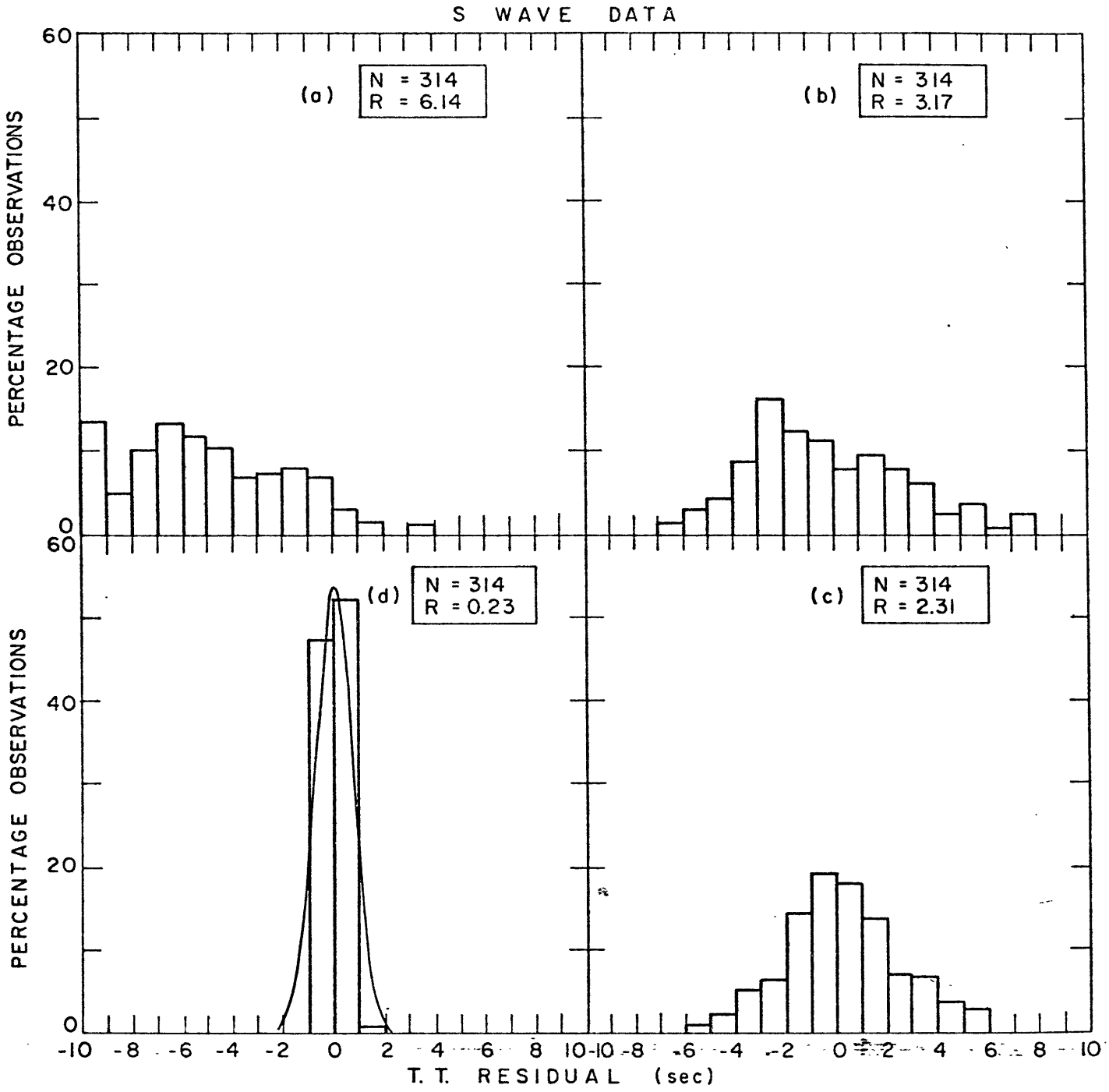
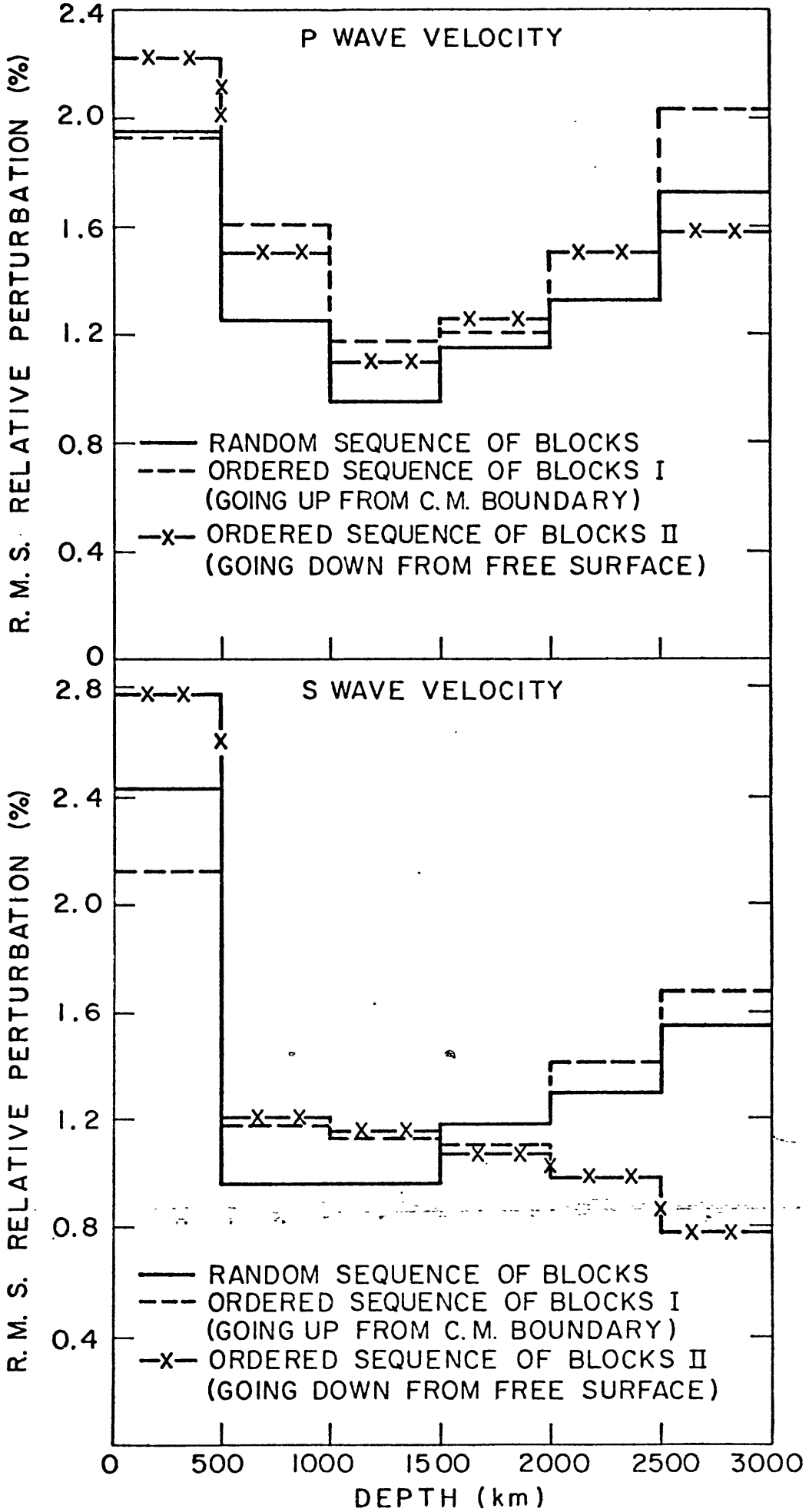

S WAVE DATA
(a)
N = 314
R = 6.14
(b)
N = 314
R = 3.17
(d)
N = 314
R = 0.23
(c)
N = 314
R = 2.31
PERCENTAGE OBSERVATIONS
PERCENTAGE OBSERVATIONS
60
40
20
0
60
40
20
0
-10 -8 -6 -4 -2 0 2 4 6 8 10
-10 -8 -6 -4 -2 0 2 4 6 8 10
T. T. RESIDUAL (sec)

Fig. 5-19


P WAVE VELOCITY
R. M. S. RELATIVE PERTURBATION (%)
2.4
2.0
1.6
1.2
0.8
0.4
0
RANDOM SEQUENCE OF BLOCKS
ORDERED SEQUENCE OF BLOCKS I
(GOING UP FROM C. M. BOUNDARY)
ORDERED SEQUENCE OF BLOCKS II
(GOING DOWN FROM FREE SURFACE)
S WAVE VELOCITY
R. M. S. RELATIVE PERTURBATION (%)
2.8
2.4
2.0
1.6
1.2
0.8
0.4
RANDOM SEQUENCE OF BLOCKS
ORDERED SEQUENCE OF BLOCKS I
(GOING UP FROM C. M. BOUNDARY)
ORDERED SEQUENCE OF BLOCKS II
(GOING DOWN FROM FREE SURFACE)
0
500
1000
1500
2000
2500
3000
DEPTH (km)

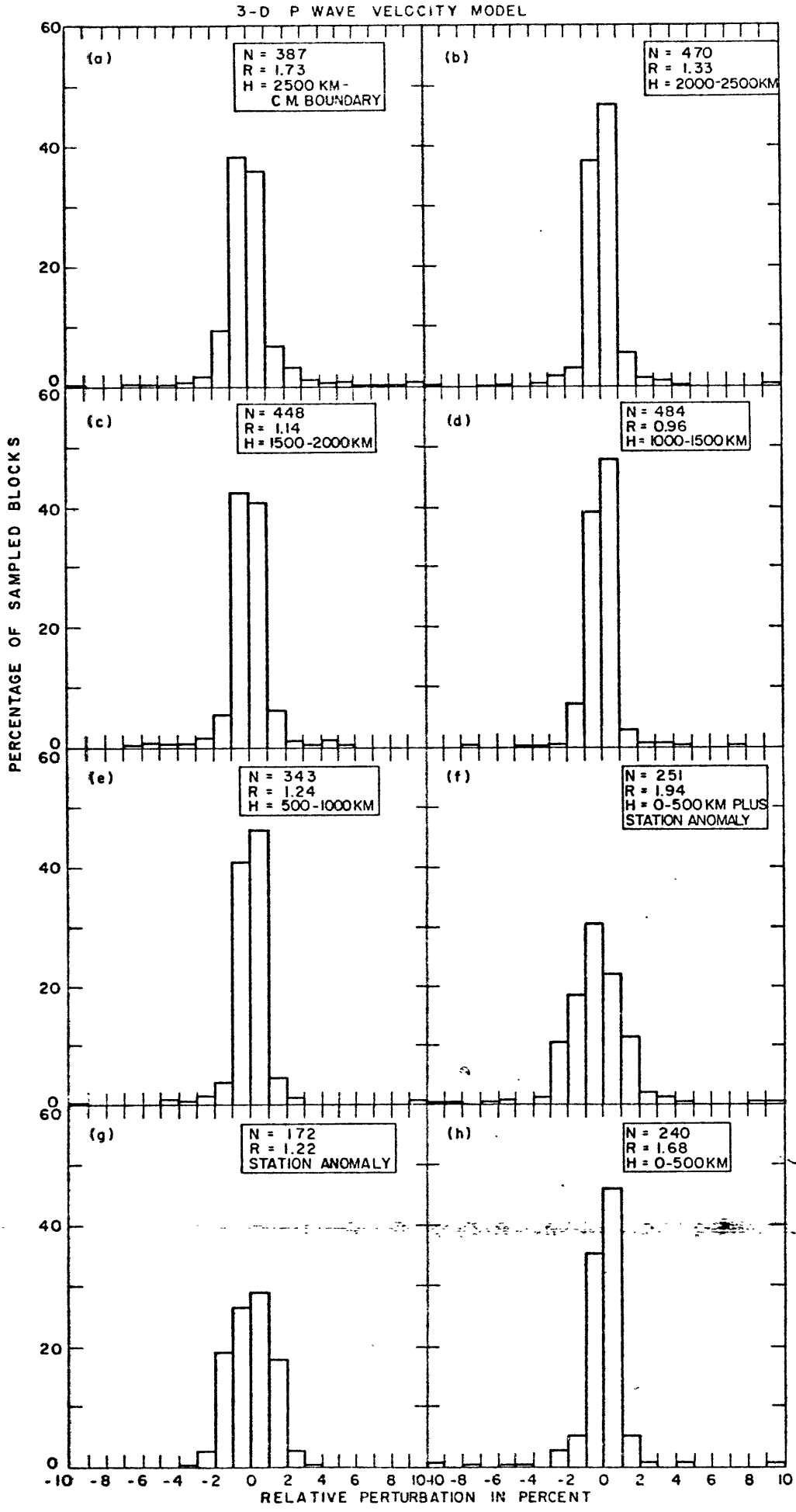

3-D P WAVE VELOCITY MODEL
(a)
N = 387
R = 1.73
H = 2500 KM - C M BOUNDARY
(b)
N = 470
R = 1.33
H = 2000-2500KM
(c)
N = 448
R = 1.14
H = 1500-2000KM
(d)
N = 484
R = 0.96
H = 1000-1500KM
(e)
N = 343
R = 1.24
H = 500-1000KM
(f)
N = 251
R = 1.94
H = 0-500 KM PLUS STATION ANOMALY
(g)
N = 172
R = 1.22
STATION ANOMALY
(h)
N = 240
R = 1.68
H = 0-500KM
PERCENTAGE OF SAMPLED BLOCKS
0
20
40
60
-10 -8 -6 -4 -2 0 2 4 6 8 10
RELATIVE PERTURBATION IN PERCENT

Fig. 5-21

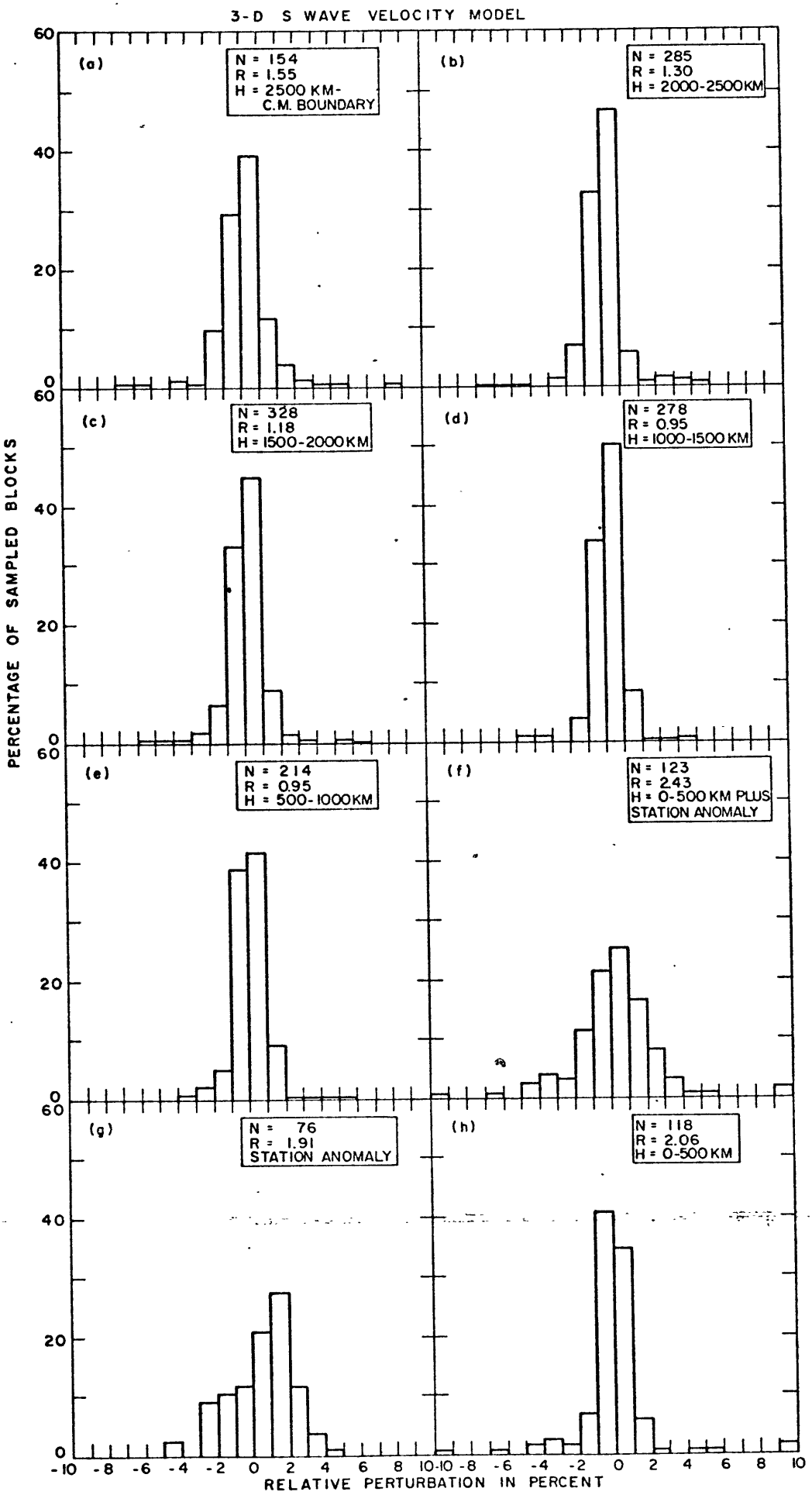

3-D S WAVE VELOCITY MODEL
(a)
N = 154
R = 1.55
H = 2500 KM-
C.M. BOUNDARY
(b)
N = 285
R = 1.30
H = 2000-2500KM
(c)
N = 328
R = 1.18
H = 1500-2000KM
(d)
N = 278
R = 0.95
H = 1000-1500 KM
(e)
N = 214
R = 0.95
H = 500-1000KM
(f)
N = 123
R = 2.43
H = 0-500 KM PLUS
STATION ANOMALY
(g)
N = 76
R = 1.91
STATION ANOMALY
(h)
N = 118
R = 2.06
H = 0-500 KM
PERCENTAGE OF SAMPLED BLOCKS
0
20
40
60
-10 -8 -6 -4 -2 0 2 4 6 8 10
RELATIVE PERTURBATION IN PERCENT

Fig. 5-22

LEGEND

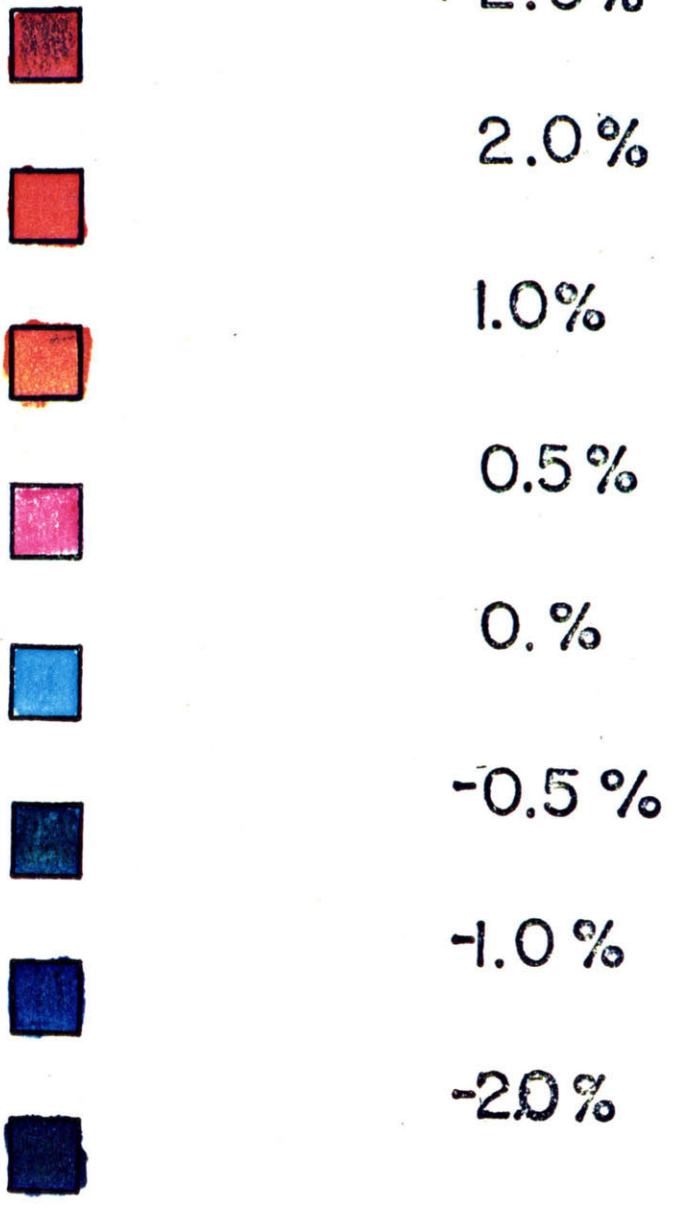


Fig. 5-23

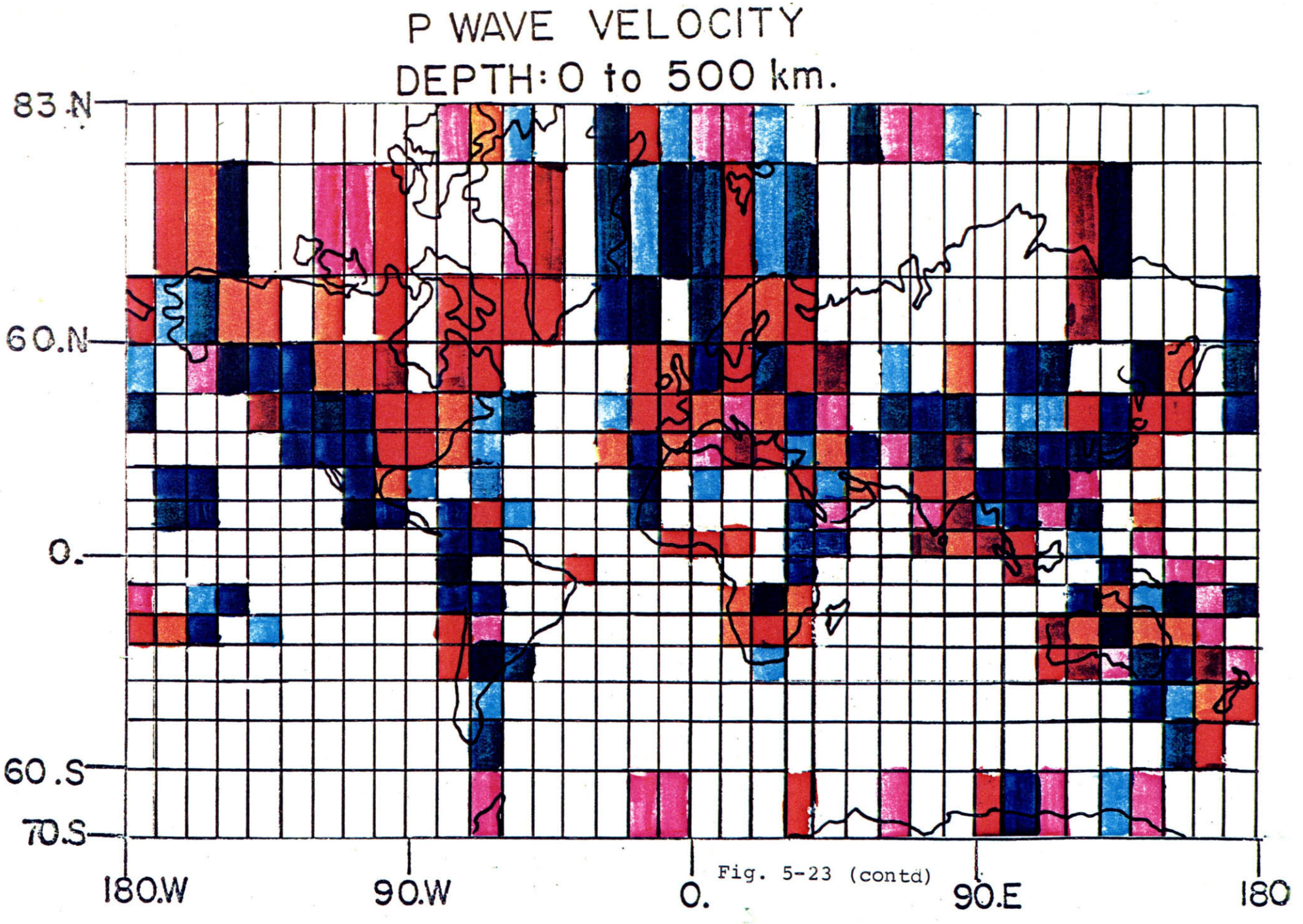


Fig. 5-23 (contd)

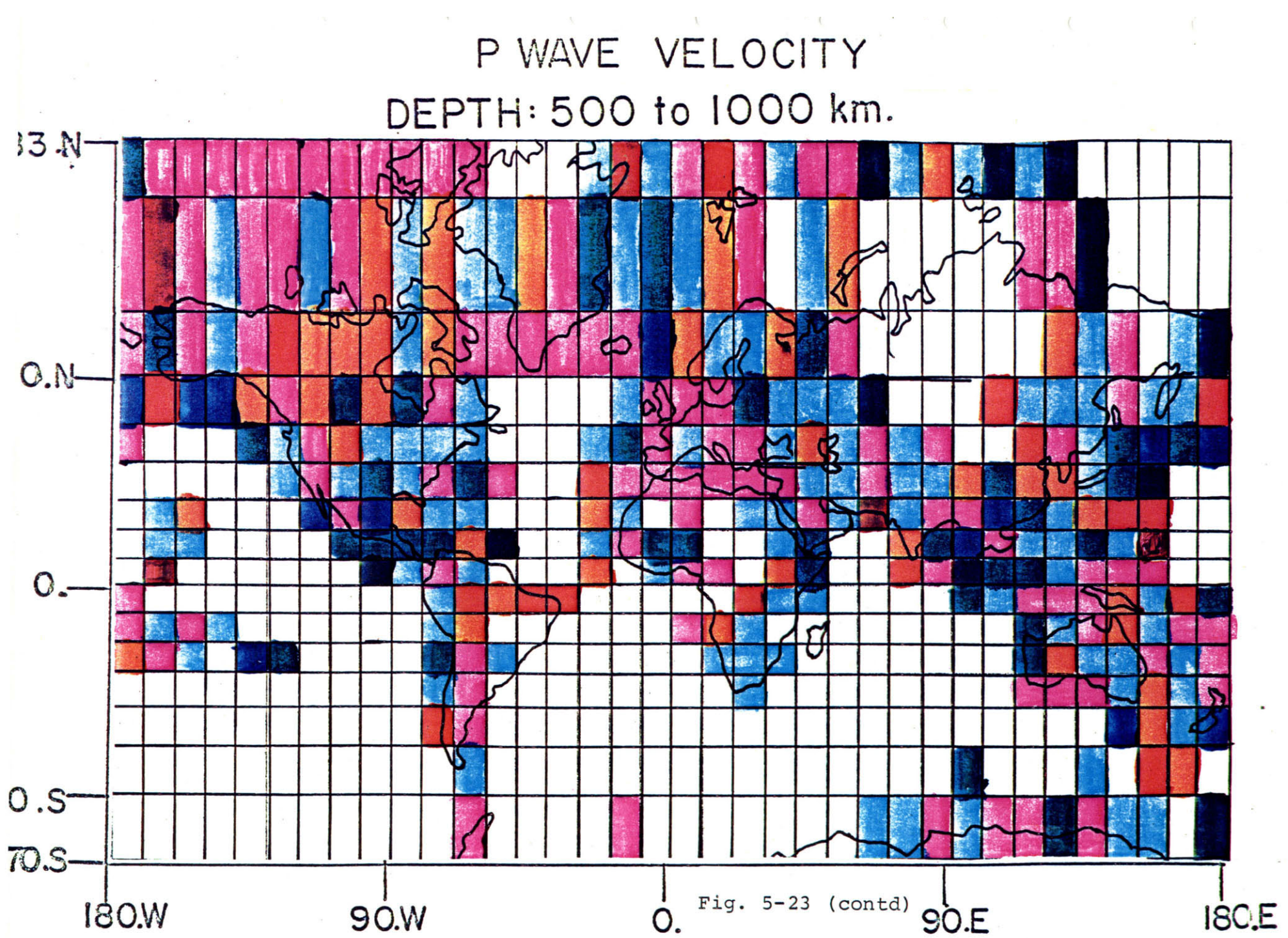


Fig. 5-23 (contd)

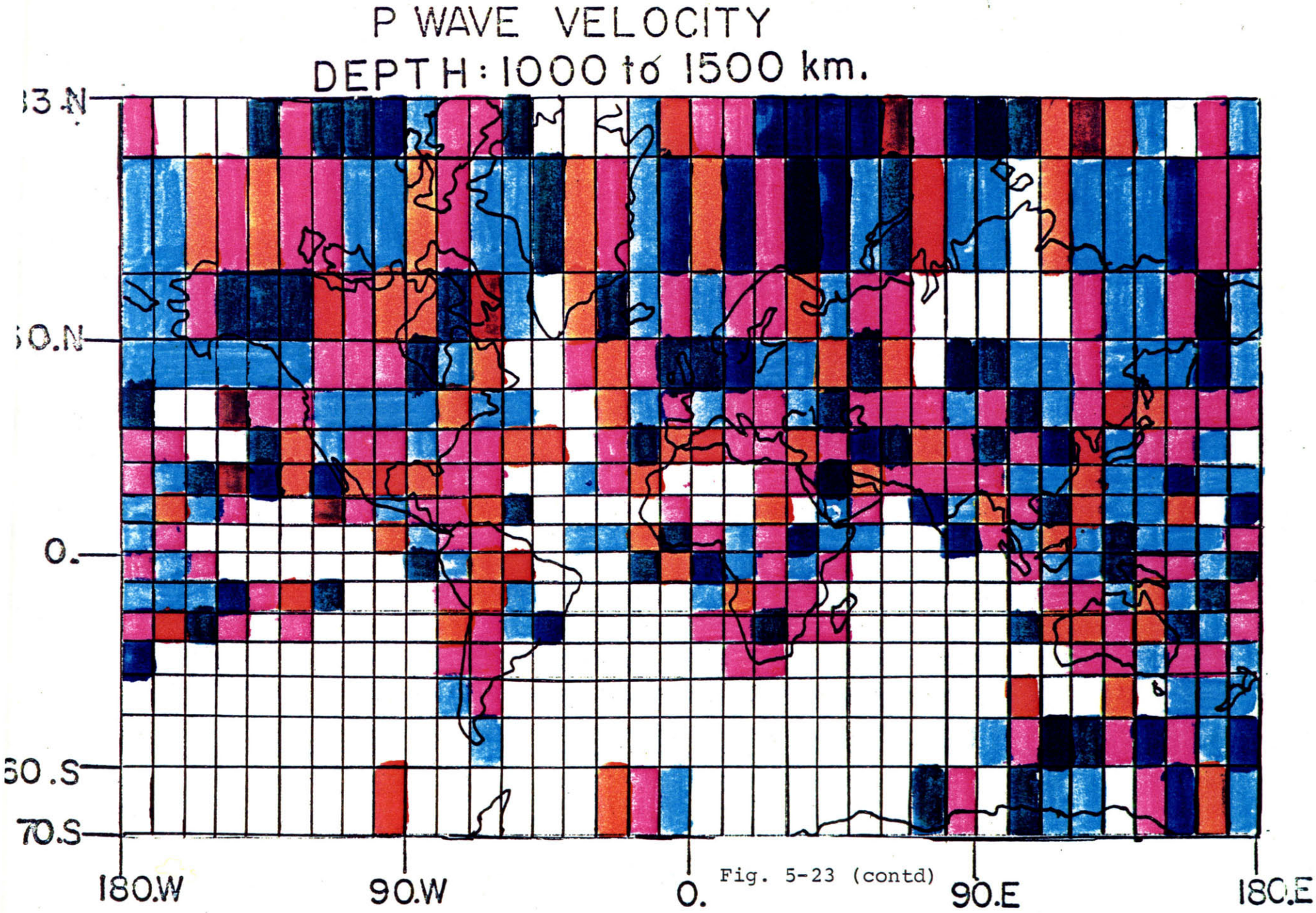


Fig. 5-23 (contd)

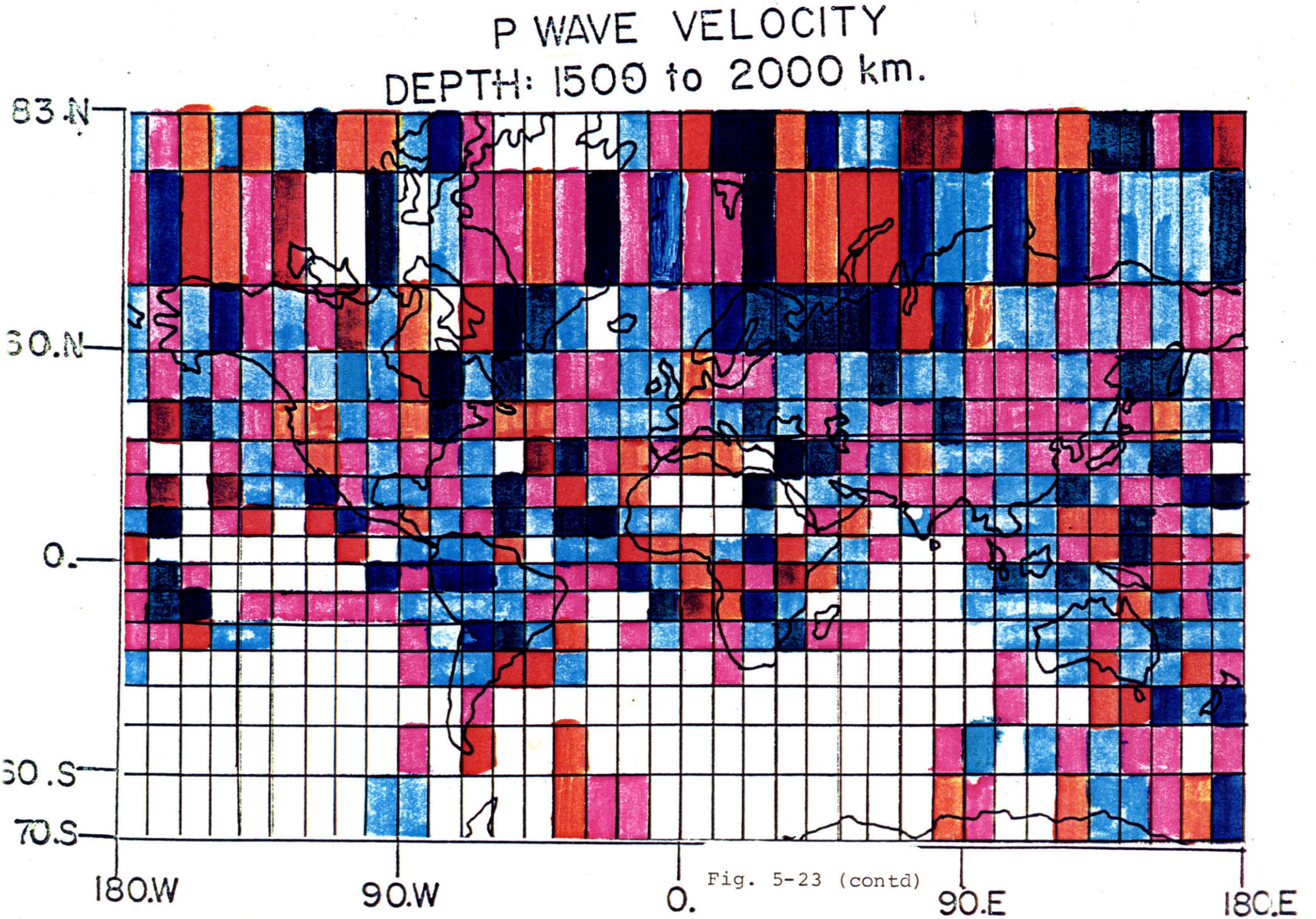


Fig. 5-23 (contd)

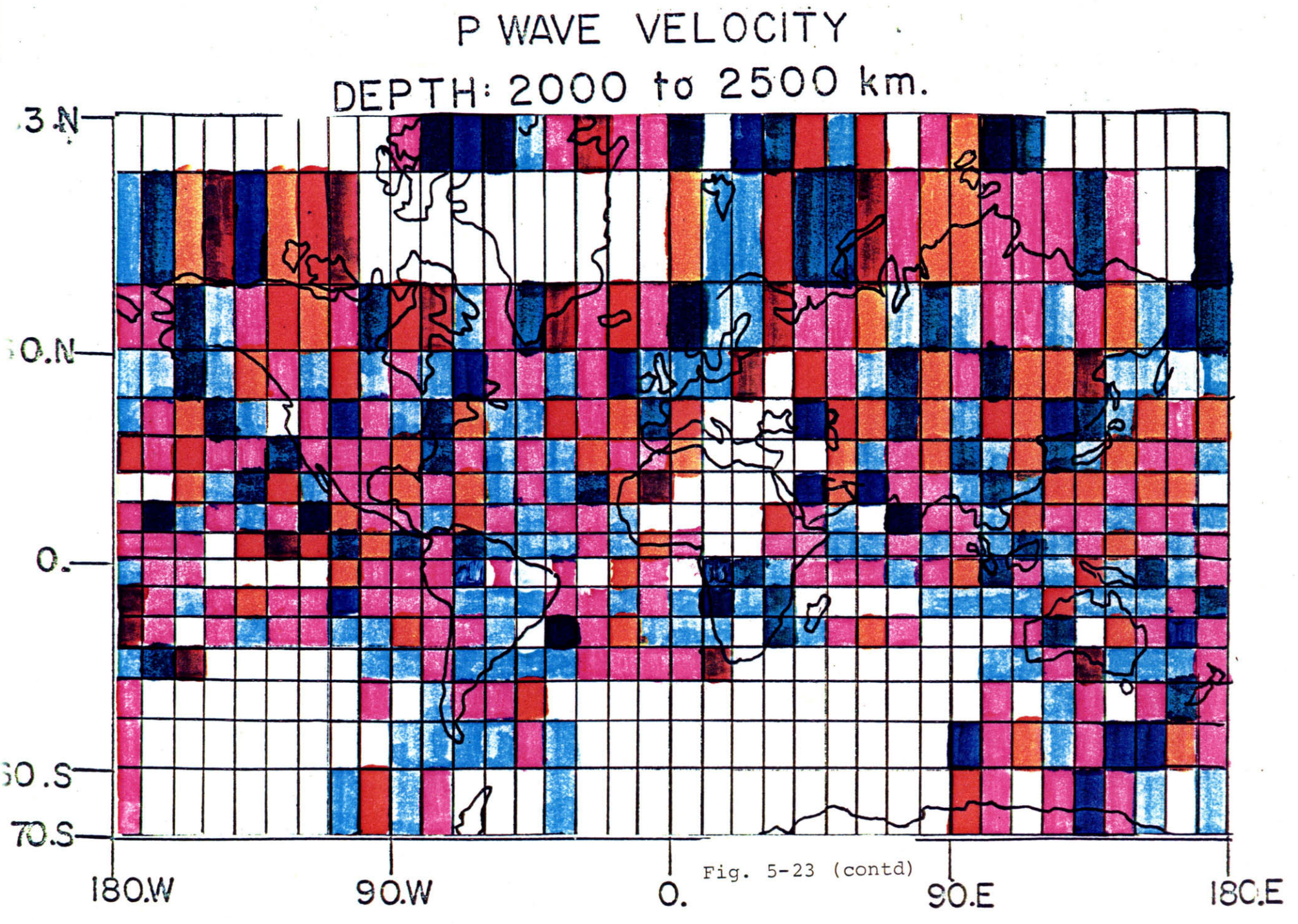


Fig. 5-23 (contd)

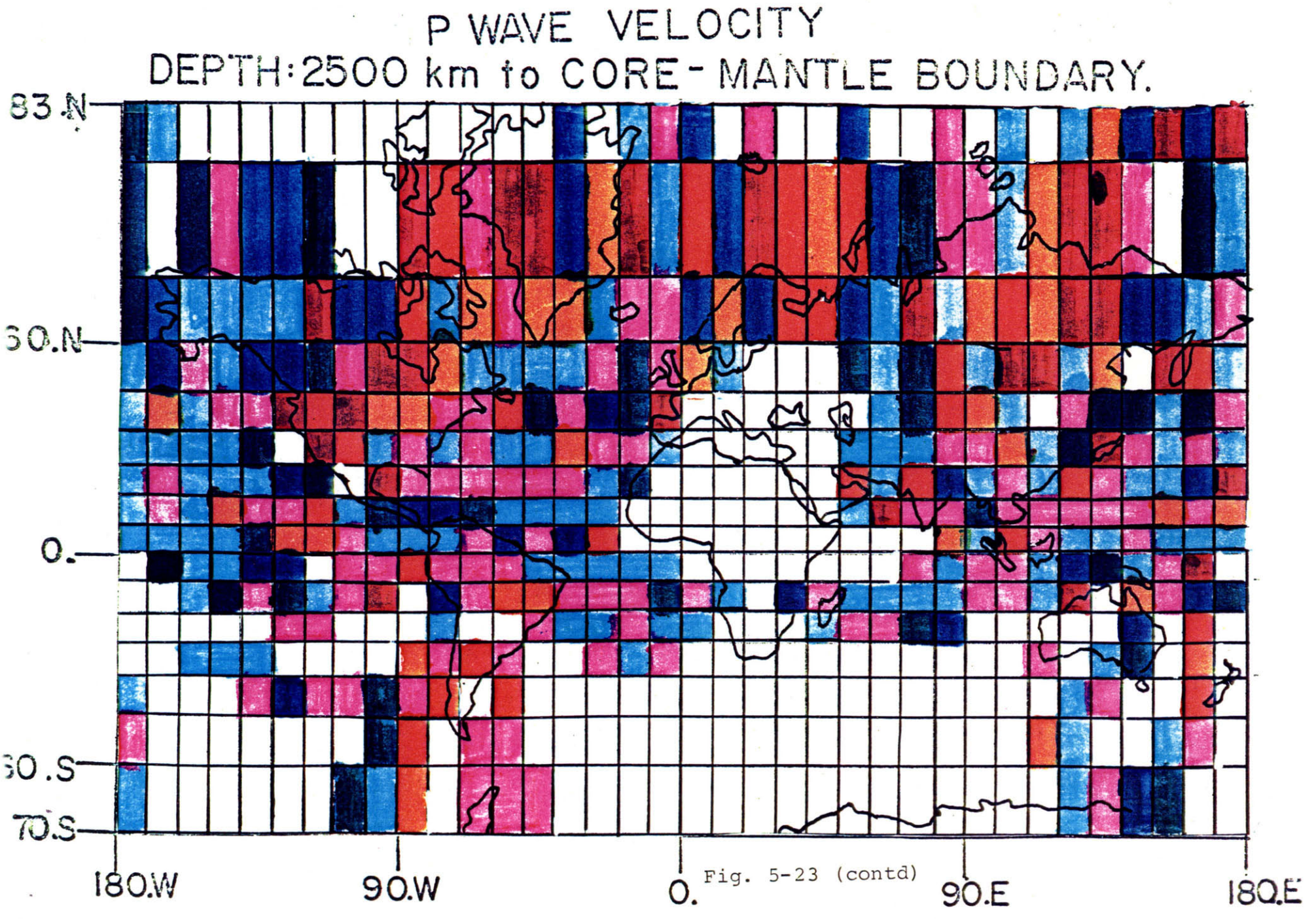


Fig. 5-23 (contd)

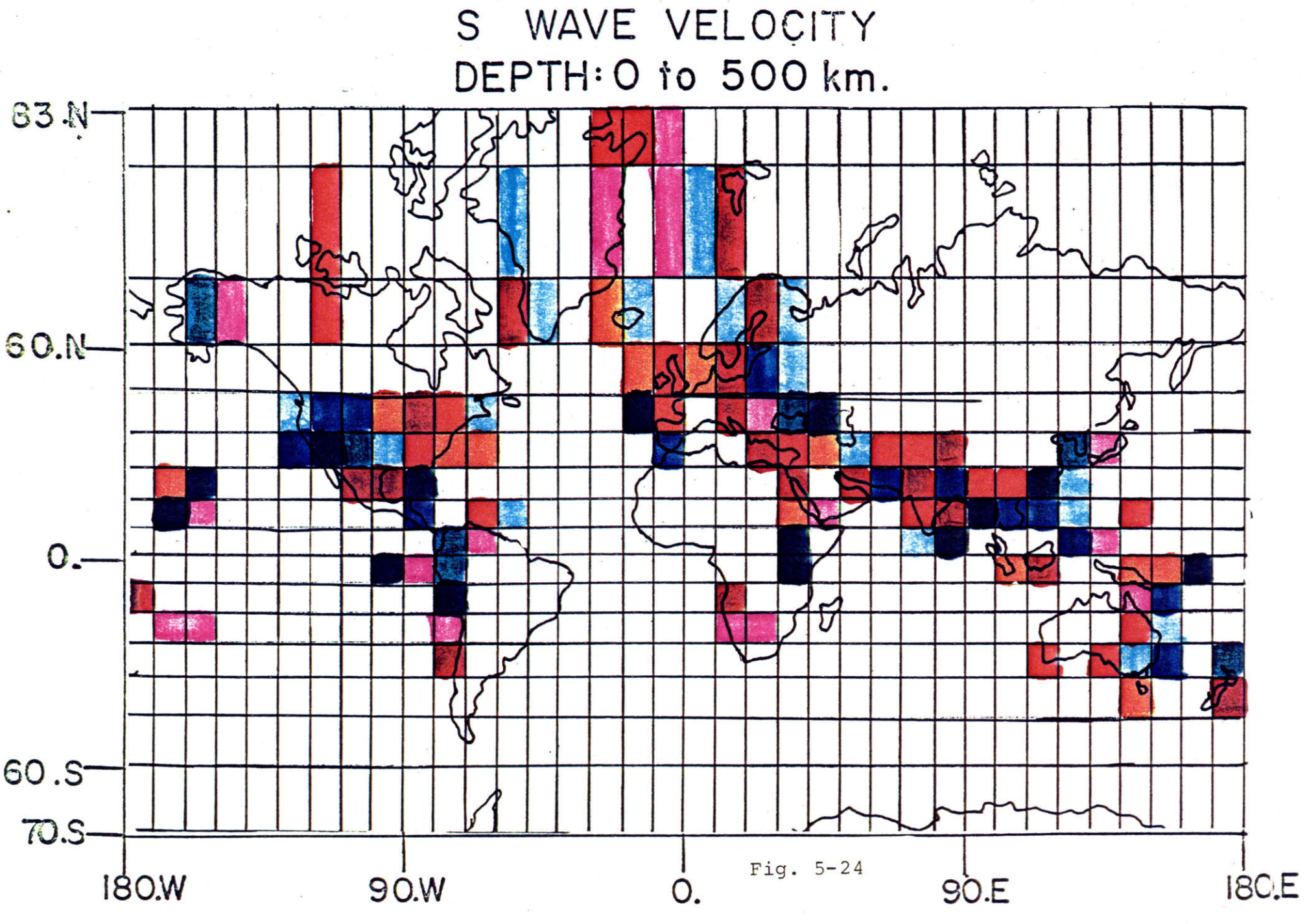

S WAVE VELOCITY
DEPTH: 0 to 500 km.
83.N
60.N
0.
60.S
70.S
180.W
90.W
0.
90.E
180.E

Fig. 5-24

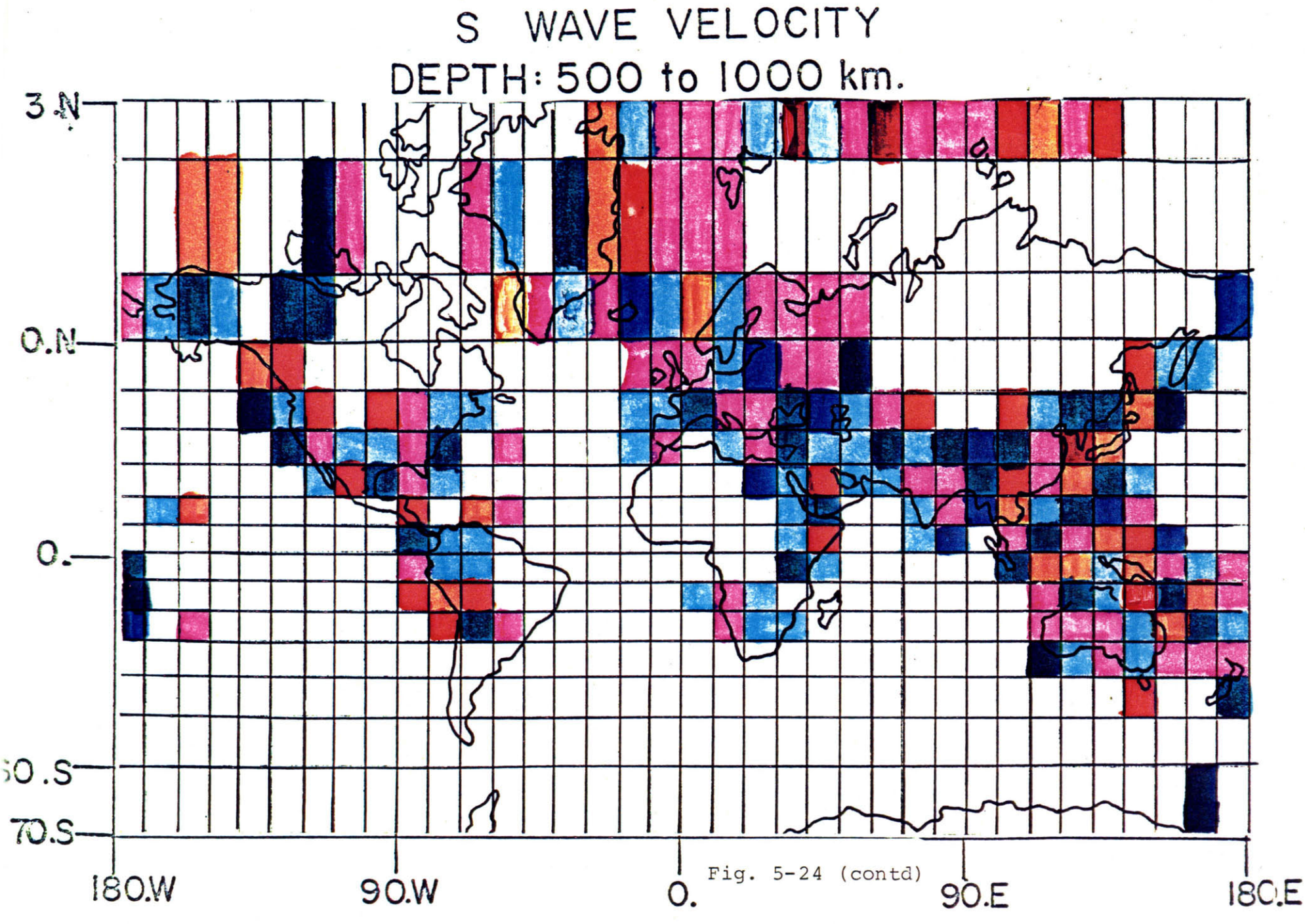


Fig. 5-24 (contd)

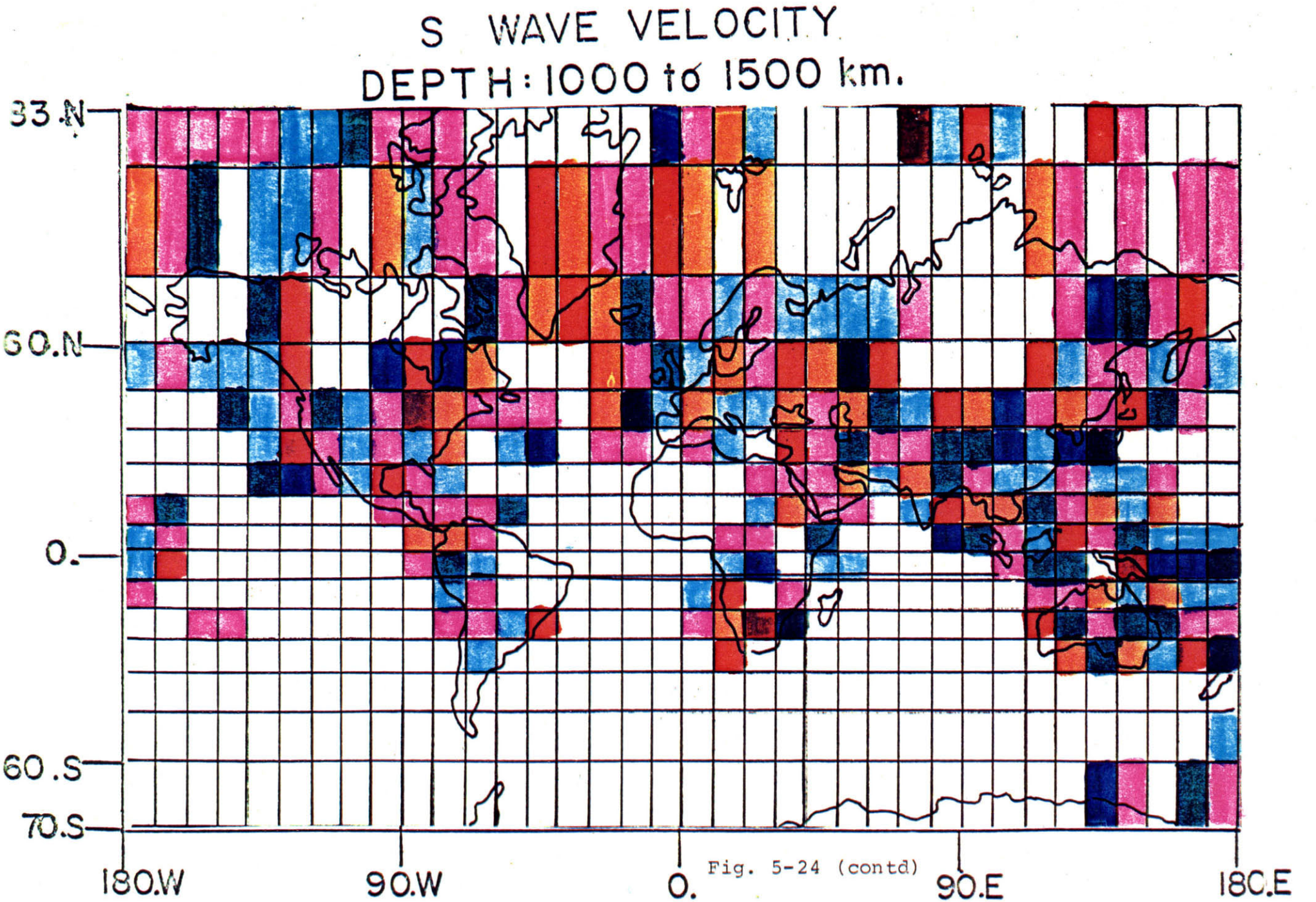


Fig. 5-24 (contd)

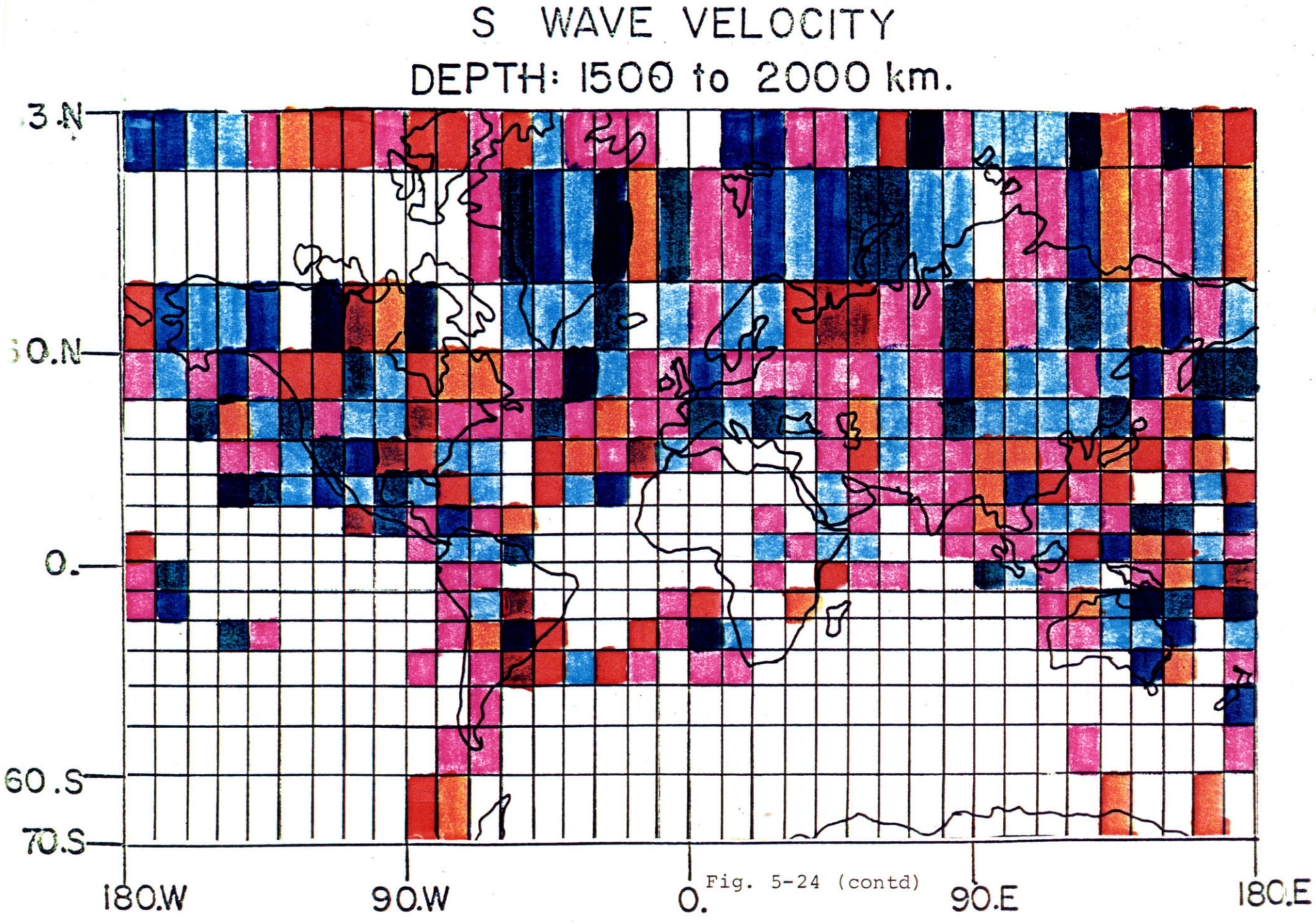


Fig. 5-24 (contd)

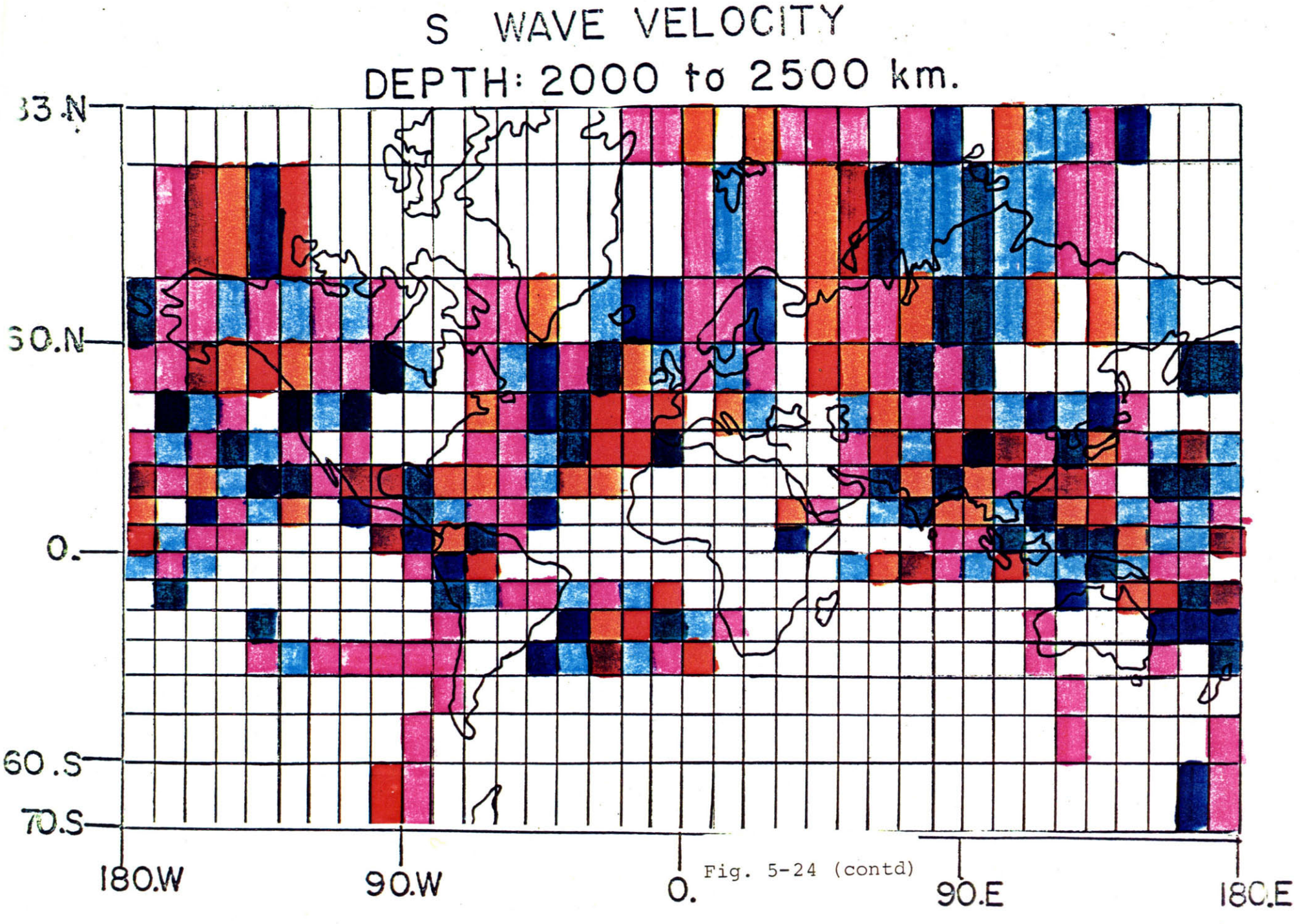


Fig. 5-24 (contd)

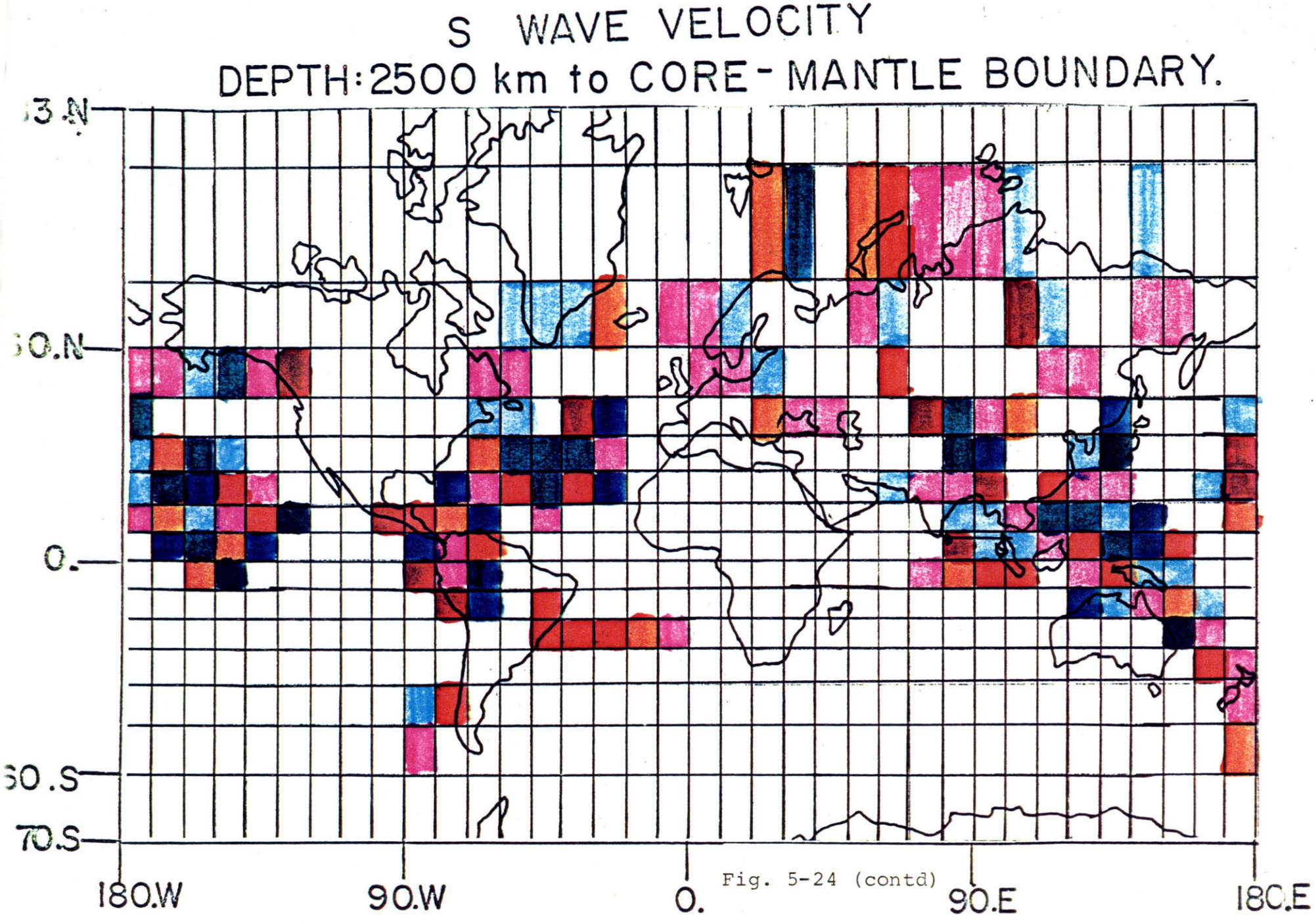


Fig. 5-24 (contd)

CHAPTER 6

CONCLUSIONS

The major conclusions of this study are summarized as follows along with some suggestions for future works:

1. Body wave data from deep focus earthquakes have certain distinct advantages over those from shallow focus earthquakes. The impulsive character of the signals of deep focus earthquakes, enrichment in short period energy, along with the marked absence of surface waves on seismograms, were certainly helpful in improving the precision of readings of arrival times and amplitudes especially for shear waves. Enrichment in short period energy for deep focus earthquakes is likely to be due to less attenuation on the one-way ray path through the upper mantle as opposed to two-way ray paths for shallow focus earthquakes. About 30% of the S wave data have come as a result of readings of short period seismograms. A combined effect of the improved quality of arrival time data and elimination of the effect of near source heterogeneity in the upper mantle has caused a reduction in the standard deviation in average travel times of P and S waves by as much as a factor of two from those determined from shallow focus earthquakes. Statistical analysis showed that a comparatively small number of paths, typical

for deep focus earthquake data, cannot merely cause such systematic two-fold reduction in standard deviation over the entire distance range. In the future however, path distribution in this type of analysis can be greatly enhanced by including the data from "intra-plate" earthquakes (Sykes and Sbar, 1973) which have generally higher Q paths through the upper mantle and smaller source bias than shallow earthquakes in tectonic regions. One can also include the shallow focus earthquakes at "transform faults" of plate boundaries.

2. Free-oscillation models such as B1 of Jordan and Anderson (1974) and 1066B of Gilbert and Dziewonski (1974) showed a 6.3 and 4.9 second delay respectively in the baseline from our S wave travel time data. This difference is too large even for the remote possibility of ± 1 second error in the computed origin times of our events. Through the setting up of ocean bottom seismographs, it remains to be seen in the future whether such a large baseline difference can solely be attributed to the continental bias of the observed travel times (Jordan and Anderson, 1974) as compared to the normal mode data. At this stage it appears, however, that proper average upper mantle has not been or could not be constructed from the available normal mode data (see for example, Hales, 1974; Gilbert and Dziewonski, 1974). We ascribe the observed baseline

difference to this cause. According to our observations, then, vertical travel times through the upper mantle in the depth interval of 0 to 670 km are 136.2 seconds for S wave and 76.7 seconds for P wave. Among all available upper mantle models for S waves, it is Jeffreys' model (Jeffreys, 1970; p. 149) which comes closest (his model being late by about 2 seconds) to our estimation of S wave vertical travel time. Note that vertical travel time through the upper mantle in Jeffreys' model also was derived from travel time data of deep focus earthquakes. On the other hand, for P wave velocity, the upper mantle model of Herrin et al. (1968) produces the same vertical travel time (within 0.2 seconds) as required by our data.

3. One dimensional velocity models, inverted from the average travel time data, show a definite improvement over the existing body wave models especially for S wave velocity. In the scheme of Backus and Gilbert (1970), these velocity models for the lower mantle are characterized by a half spread of about 70 km and standard error in velocity of about 0.02 km/sec. Below about 1000 km depth, features in our parameterized velocity models with 75 km thick layers seem to be satisfactorily resolved in depth.

4. No prominent reversal in P and S wave velocity near the core-mantle boundary is required by our travel

time and amplitude data. A small velocity decrease with gradient less than critical is however not ruled out. Around 1600, 2400 and 2600 km depth (corresponding to epicentral distances of 57°, 79° and 86°), the P wave velocity model shows some anomalous rapid changes in velocity gradient. Evidence from $dT/d\Delta$ data of Johnson (1969), Husebye et al. (1971), and Wright and Cleary (1972) seem to support those anomalies. In addition, both P and S wave models reveal sinusoidal variation in velocity, the significance of which cannot be firmly established at this stage because of uncertainty in our velocity models. In the future, such a problem of resolution in the radial inhomogeneity can be solved if one can combine the measurements of $dT/d\Delta$ from all available arrays taking into account their different sensitivity towards the local crust-mantle structure and also simultaneously develop an 'averaging theorem' for joint inversion of average travel time and $dT/d\Delta$ data. At any rate, our inverted P wave velocity model for the lower mantle comes closest to the model of Herrin et al. (1968) among all existing models. Note that the model of Herrin et al. was determined from the largest collection of P wave travel time data in this century. The major discrepancy between these two models occurs only near a depth of 2400 and 2800 km. Similarly, our S wave velocity model for the lower mantle corresponds closely to

the 1066B model of Gilbert and Dziewonski (1974) which, again, has been derived from the largest collection, so far, of 1064 free oscillation eigenperiods. Below 1600 km of depth, however, our S wave velocity model is more wiggly than the 1066B model.

5. Decay in short period P wave amplitude data follows closely the geometric spreading factor computed from our P velocity model except in the distance range of 60°, 75°, 80-85°. The discrepancy there can possibly be explained by a proper Q-structure. The excellent agreement between the observed and predicted short period amplitudes around 85°-95° of distance, almost rules out the possibility of a large velocity reversal at the base of the mantle as suggested by some authors (see for example Cleary, 1974). Long period P wave amplitude data also are in good agreement with the predicted geometric spreading curve of our velocity model except beyond 80° of distance. In that distance range a lesser gradient in the decay of observed long period amplitudes than in the predicted curve is possibly due to the effect of diffraction for amplitudes in the lit zone (Phinney and Cathles, 1969). Long period S wave amplitude data, on the other hand, are closely followed by the geometric spreading factor even beyond the distance of 80°. This anomalous trend suggests a decrease in gradient of our S velocity model near the

core-mantle boundary. Observed S wave travel times are consistent with amplitude data in this respect as they also seem to require a small decrease in S velocity near the core-mantle boundary for extending the geometrical shadow boundary of the present model from 96° to 100° in distance.

6. Because of good agreement between observed amplitudes and the computed geometric spreading factors from our velocity models, Q in the lower mantle is required to be increasing with depth to satisfy the same amplitude data. This requirement is found to be consistent with the general trend of the Q-model of Archambeau et al. (1969) fitting P wave amplitudes of this study and the MM8' Q model of Kanamori (1967) satisfying S wave amplitudes. This result contradicts the suggestion of Teng (1968) that Q may start to decrease gradually from a depth of 1900 km to the core-mantle boundary. At the lowest 200 km of the mantle, a decrease in Q is not, however, ruled out. Short period P wave amplitudes around 75° distance show a noteworthy difference from the ray theoretical amplitudes. A similar anomaly was observed also for short period S wave amplitudes in the distance range of 80°-85°.

7. Our short period P wave amplitude-distance curve agrees excellently with that of Carpenter et al. (1967) and the long-period curve with that of Nuttli (1972). Note that those two amplitude-distance curves were derived from explosion data whose signals have characteristics similar to deep focus earthquakes. Similarity in short period and long period P wave magnitudes determined from our amplitude-distance curves also suggests that P wave amplitudes are inversely proportional to frequency in the period range of 1-10 seconds. Scatter in multi-station body wave magnitude determinations were found to be fairly insensitive to our revision of the amplitude-distance curve of Gutenberg (Richter, 1958, p. 688) or to correction for radiation at the source. Reduction in the scatter was achieved somewhat, however, by our correction for station anomalies of P wave amplitudes, indicating that source of scatter lies in lateral variation of the crust and upper mantle structure.

8. Station anomalies for P and S travel time data correlate fairly well with our knowledge of surface tectonics in different parts (mainly continents) of the world in that late arrivals are seen in tectonically active areas like western North America, eastern Australia, the African rift zone, the Hawaiian Islands, Iceland, etc. whereas shield areas or stable continents like the Canadian

shield, central and eastern USA, western Australia, South Africa etc. are characterized by early arrivals. These station anomalies are also in good agreement with similar studies such as that of Herrin and Taggart (1968) and Hales and Roberts (1970a). Standard deviation of station anomalies determined from deep focus travel time data are however two-fold smaller than those for shallow focus earthquakes. As azimuthal variation of velocity beneath a station causes only 15-30% of the scatter in the station anomaly for shallow focus earthquake data, a two-fold decrease in standard deviation cannot be caused merely by the limited azimuthal coverage of a station with a comparatively small number of data from deep focus earthquakes. Such a reduction on the other hand shows the effect removal of the near source heterogeneity in the upper mantle by the choice of deep focus data. We also found that S wave station anomalies for travel time data are higher than P wave station anomalies by a factor of 4.0 to 6.0 for stations on continental rift zones and by a factor of 2.0 to 4.0 for stations on shield and stable continental regions. Such a high ratio of S to P station anomalies reflects a variation in temperature and partial melting in the upper mantle beneath those regions as suggested by Toksöz et al. (1967) and Hales and Doyle (1967). Oceanic stations like KIP, RAB and AFI were found to show a mean

delay of 2-3 seconds in their S wave station anomalies as compared to those for stations in shield areas. This difference can be explained by 'slowness' in the oceanic upper mantle compared to structure beneath the shields, the variation extending up to 300 km depth in accordance with surface wave studies (Toksöz, et al., 1967; Dziewonski, 1971). Whether such lateral inhomogeneity extends up to 700 km depth (Sipkin and Jordan, 1974) is an open question, but is certainly not required by our data.

9. Station anomalies for S wave amplitude data, unlike their counterparts in travel time data, are not 3-4 times larger than but comparable to those of P wave data even for the stations in continental rift zones. It suggests that acoustic impedance of the surface layers affects P wave amplitudes more than amplitudes of S waves whereas the effect of anelastic attenuation is stronger for S waves compared to P waves.

10. After correction for the lateral variation in the upper mantle, observed P and S wave travel time anomalies have qualitatively pleaded a case in favor of pronounced lateral inhomogeneity near the core-mantle boundary relative to middle mantle. Quantitative calculation of relative perturbation to velocity of average earth models as computed for blocks of size 10° in longitude and latitude

and 500 km in depth gave strong support to that conclusion. R.m.s. perturbation (in percent) was found to have maxima in the surface layer (0-500 km of depth) and near the core-mantle boundary (2500-3000 km of depth). While r.m.s. values for perturbations in P and S velocity of the surface layer were of the order of 2.0% and 2.5%, being larger for S waves, those for the core-mantle boundary were of the order of 1.6%, being little larger for P waves. Details in three dimensional models, however, may not be reliable, especially for S waves, because of the meager quantity of data. At this point, we can count only on the velocity perturbations in the surface layer (for P and possibly for S velocity) and two layers in the deepest mantle, 2000-2500 km and 2500-3000 km in depth, for P wave velocity. In the future, the number of data can be enhanced immensely by including shallow "intraplate" and "transform fault" earthquakes in this type of analysis, as mentioned earlier. Also, encouraging agreement in the pattern of lateral variation of velocity deduced separately from travel time and $dT/d\Delta$ data suggest that inclusion of $dT/d\Delta$ data in the inversion of the three dimensional velocity model may improve the resolution of structural details. At any rate, we can safely conclude at this stage that velocity perturbations of the surface layer (0-500 km) correlated well with the known knowledge of geology but it appears

at best that there is almost no correlation between the surface tectonics and conditions near the core-mantle boundary as seen through the P wave velocity model. A remarkable region of laterally homogeneous anomaly exists near the core-mantle boundary beneath the central and part of the eastern Pacific region which is characterized by (1) small relative perturbation in P wave velocity, (2) small gravitational potential (Toksöz et al., 1969) for spherical harmonics up to sixth degree, and (3) anomalously small non-dipole intensity (Doell and Cox, 1972) in the earth's magnetic field. Success of the proposed three dimensional velocity model is also remarkable in the sense that 77% of observed P wave travel time residuals can be fitted within the framework of this model and the rest can be explained easily in terms of normal reading error.

11. Last but not least, dear faithful reader,

"There are more things in heaven and earth, Horatio,
Than are dreamt of in your philosophy."

Hamlet (Shakespeare)

REFERENCES

Adams, R.D. (1972) Multiple inner core reflections from a Novaya Zemlaya explosion, Bull. Seismo. Soc. Am., 62, 1063-1071.

Aki, K. (1972) Scaling law of earthquake source time function, Geophys. J. R. astr. Soc., 31, 3-25.

Aki, K., E. Husebye, A. Christoffersson, and C. Powell (1974) Three dimensional seismic velocity anomalies in the crust and upper-mantle under the U.S.G.S. California seismic array, Abs. AGU Fall Meeting, 1974 EOS, 56, 1146.

Aki, K. and F. Press (1961) Upper mantle structure under oceans and continents from Rayleigh waves, Geophys. J. R. astr. Soc., 5, 291-305.

Alexander, S.S. and R.A. Phinney (1966) A study of the core-mantle boundary using P waves diffracted by the earth's core, J. Geophys. Res., 71, 5943-5958.

Allan, R.R. (1972) Depth of sources of gravity anomaly, Nat. Phys. Sci., 236, 22-23.

Anderson, D.L., A. Ben-Menahem and C.B. Archambeau (1965) Attenuation of seismic energy in the upper mantle, J. Geophys. Res., 70, 1441-1448.

Anderson, D.L. and B.R. Julian (1969) Shear velocities and elastic parameters of the mantle, J. Geophys. Res., 74, 3281-3286.

Anderson, D.L., C. Sammis, T. Jordan (1972) Composition of the mantle and core, in: Nature of the Solid Earth, 41-66, ed. by E.C. Robertson, McGraw-Hill Inc., New York, 677 pp.

Anderson, D.L. and M.N. Toksöz (1963) Surface waves on a spherical earth, J. Geophys. Res., 63, 3483-3500.

Anderson, O.L., E. Schreiber, R.C. Liebermann and N. Soga (1968) Some elastic constant data on minerals relevant to geophysics, Rev. Geophys., 6, 491-524.

Archambeau, C.B. and E.A. Flinn and D.G. Lambert (1969) Fine structure of the upper mantle, J. Geophys. Res., 74, 5825-5865.

Asbel, I.Ja, V.I. Keilis-Borok and T.B. Yanovskaja (1966) A technique of a joint interpretation of travel-time and amplitude-distance curves in the upper mantle studies, Geophys. J. R. astr. Soc., 11, 25-55.

Backus, G.E. and J.F. Gilbert (1967) Numerical applications of a formalism for geophysical inverse problems, Geophys. J. R. astr. Soc., 13, 247-276.

Backus, G. and F. Gilbert (1968) The resolving power of gross earth data, Geophys. J. R. astr. Soc., 16, 169-205.

Backus, G. and F. Gilbert (1969) Constructing P-velocity models to fit restricted sets of travel time data, Bull. Seismo. Soc. Am., 59, 1407-1414.

Backus, G. and F. Gilbert (1970) Uniqueness in the inversion of inaccurate gross earth data, Phil. Trans. R. Soc. Lond., 266A, 123-192.

Båth, M. and A.L. Arroyo (1963) Pa and Sa waves under the upper mantle, Rev. Geofisica Pura E Applicata, 56, 67-92.

Bessenova, E.N., O.D. Gotsadze, V.I. Keilis-Borok, I.V. Kirillova, S.D. Kogan, T.I. Kikhtikova, L.N. Malinoskaya, G.I. Pavolva, and A.A. Sorskii (1960) Investigation of the mechanism of earthquakes, Soviet Research in Geophysics, English Translation, 40, American Geophysical Union, New York.

Bessenova, E.N., V.M. Fishman, V.Z., Ryaboyi and G.A. Sitnikova (1974) The tau method of inversion of travel times - I. Deep seismic sounding data, Geophys. J. R. astr. Soc., 36, 377-398.

Biswas, N.N. and L. Knopoff (1974) The structure of the upper mantle under the United States from the dispersion of Rayleigh waves, Geophys. J. R. astr. Soc., 36, 515-539.

Bolt, B.A. (1972) The density distribution near the base of the mantle and near the earth's center, Phys. Earth Planet. Interiors, 5, 301-311.

Bolt, B.A., M. Niazi, and M.R. Somerville (1970) Diffracted ScS and the shear velocity at the core boundary, Geophys. J. R. astr. Soc., 19, 299-305.

Bolt, B.A. and O.W. Nuttli (1966) P wave residuals as a function of azimuth 1. observations, J. Geophys. Res., 71, 5977-5985.

Booth, D., P.D. Marshall and J.B. Young (1974) Long and short period P wave amplitudes from earthquakes in the range of 0°-114°, Geophys. J. R. astr. Soc., 39, 523-527.

Brune, J.N. (1969) Surface waves and crustal structure, in: The Earth's Crust and Upper Mantle, pp. 230-242, ed. by P.J. Hart, AGU Monograph no. 13, 776 pp.

Brune, J.N. and J. Dorman (1963) Seismic waves and earth structure in the Canadian shield, Bull. Seismo. Soc. Am., 53, 167-210.

Brune, J.N. and F. Gilbert (1974) Torsional overtone dispersion from correlations of S waves to SS waves, Bull. Seismo. Soc. Am., 64, 313-329.

Buchbinder, G.A.R. (1971) A velocity structure of the earth's core, Bull. Seismo. Soc. Am., 61, 429-456.

Buchbinder, G.A.R. (1972) Travel times and velocities in the outer core from PmKP, Earth Plan. Sci. Letters, 14, 161-168.

Bullen, K.E. (1937) The ellipticity correction to travel times of P and S earthquake waves, Monthly Notice R. Astron. Soc., Geophys. Suppl., 4, 143-157.

Bullen, K.E. (1937)b A suggested new "seismological" latitude, Monthly Notice R. Astron. Soc., Geophys. Suppl., 4, 158-164.

Bullen, K.E. (1938)a Ellipticity correction to earthquake waves reflected at the central core, Monthly Notice R. Astr. Soc., Geophys. Suppl., 4, 332-335.

Bullen, K.E. (1938)b The ellipticity correction and deep focus earthquakes, Monthly Notice R. Astr. Soc., Geophys. Suppl., 4, 469-471.

Bullen, K.E. (1963) An Introduction to the Theory of Seismology, Cambridge Univ. Press, London, 381 pp.

Bullen, K.E. and R.A.W. Haddon (1973) The ellipticities of surfaces of equal density inside the earth, Phys. Earth and Plan. Int., 7, 179-202.

Carder, D.S. (1964) Travel times from central Pacific nuclear explosions and inferred mantle structure, Bull. Seismo. Soc. Am., 54, 2271-2294.

Carder, D.S., D.W. Gordon and J.N. Jordan (1966) Analysis of surface-foci travel times, Bull. Seismo. Soc. Am., 56, 815-840.

Carpenter, E.W., P.D. Marshall, and A. Douglas (1967) The amplitude-distance curve for short period teleseismic P waves, Geophys. J. R. astr. Soc., 13, 61-70.

Chandra, U. (1973) Source processes of a large deep-focus earthquake and its tectonic implications - the Western Brazil earthquake of 1963: Comments, Phys. Earth and

Plan. Interiors, 7, 115-121.

Chapman, C.H. (1971) On the computation of seismic ray travel times and amplitudes, Bull. Seismo. Soc. Am., 61, 1267-1274.

Chinnery, M.A. (1969) Velocity anomalies in the lower mantle, Phys. Earth Planet. Interiors, 2, 1-10.

Chinnery, M.A. and M.N. Toksöz (1967) P wave velocities in the mantle below 700 km, Bull. Seismo. Soc. Am., 57, 199-226.

Chung, D.H. (1971) Elasticity and equations of state of olivines in the Mg_2SiO_4-Fe_2SiO_4 system, Geophys. J. R. astr. Soc., 25, 511-538.

Cleary, J. (1967a) Analysis of the amplitudes of short period P waves recorded by Long Range Seismic Measurements stations in the distance range 30° to 102°, J. Geophys. Res., 72, 4705-4712.

Cleary, J. (1967b) P times to Australian stations from nuclear explosions, Bull. Seismo. Soc. Am., 57, 773-781.

Cleary, J. (1967c) Azimuthal variation of the Longshot source term, Earth and Planet. Sci. Letters, 3, 29-37.

Cleary, J. (1969) The S velocity at the core-mantle boundary, from observations of diffracted S, Bull. Seismo. Soc. Am., 59, 1399-1405.

Cleary, J. (1974) The D" region, Phys. Earth Planet. Interiors, 9, 13-27.

Cleary, J. and A.L. Hales (1966) An analysis of the travel times of P waves to North American stations, in the distance range 32° to 100°, Bull. Seismo. Soc. Am., 56, 467-489.

Cleary, J. and A.L. Hales (1968) P times from the nuclear explosion "Greely", Earth and Planet. Sci. Letters, 4, 305-309.

Cleary, J. and K.J. Muirhead (1969) Comparison of the 1968 P tables with times from nuclear explosions (1) Longshot and Greely, Earth and Planet. Sci. Letters, 7, 119-124.

Davies, D. and B.R. Julian (1972) A study of short period P wave signals from Longshot, Geophys. J. R. astr. Soc. 29, 185-202.

Davies, D. and D.P. McKenzie (1969) Seismic travel time residuals and plates, Geophys. J. R. astr. Soc., 18, 51-63.

Davies, D. and R.M. Sheppard (1972) Lateral heterogeneity in the earth's mantle, Nature, 239, 318-323.

Denham, D. (1969) Distribution of earthquakes in the New Guinea-Solomon Islands region, J. Geophys. Res., 74, 4290-4299.

Denham, D., D.W. Simpson, P.J. Gregson, and D.J. Sutton (1972) Travel times and amplitudes from explosions in Northern Australia, Geophys. J. R. astr. Soc., 28, 225-235.

Doell, R.R. and A. Cox (1972) The Pacific geomagnetic secular variation anomaly and the question of lateral uniformity in the lower mantle, in: Nature of Solid Earth, ed. by E.C. Robertson, pp. 245-284, McGraw-Hill, New York, 677 pp.

Doornbos, D.J. and N.J. Vlaar (1973) Regions of seismic wave scattering in the earth's mantle and precursors to PKP, Nature Phys. Sci., 243, 58-61.

Doyle, H.A. and A.L. Hales (1967) An analysis of the travel times of S waves to North American stations, in the distance range 28° to 82°, Bull. Seismo. Soc. Am., 57, 761-771.

Draper, N.R. and H. Smith (1966) Applied regression analysis, John Wiley and Sons, Inc., New York, 407 pp.

Duda, S.J. (1971) Travel times and body wave magnitude, Pure and Applied Geophysics, 87, 13-37.

Dziewonski, A.M. (1971) Upper mantle models from 'Pure Path' dispersion data, J. Geophys. Res., 76, 2587-2601.

Dziewonski, A.M., A.L. Hales, and E.R. Lapwood (1975) Parametrically simple earth models consistent with geophysical data, submitted to Phys. Earth and Planet. Int..

Engdahl, E.R. and L.E. Johnson (1974) Differential PcP travel times and the radius of the core, Geophys. J. R. astr. Soc., 39, 435-456.

Ergin, K. (1967) Seismic evidence for a new layered structure of the earth's core, J. Geophys. Res., 72, 3669-3687.

Espinosa, A.F., G.H. Sutton and H.J. Miller (1965) VESIAC Spec. Rep. 4410-106-X, Univ. of Michigan, Ann Arbor.

Evernden, J.F. (1969) Identification of earthquakes and explosions by use of teleseismic data, J. Geophys. Res., 74, 3828-3856.

Evernden, J.F. and D.M. Clark (1970) Study of teleseismic P II - amplitude data, Phys. Earth Planet. Interiors, 4, 24-31.

Evernden, J.F. and J. Filson (1971) Regional dependence of surface-wave versus body wave magnitudes, J. Geophys. Res., 76, 3303-3308.

Fairborn, J.W. (1969) Shear wave velocities in the lower mantle, Bull. Seismo. Soc. Am., 59, 1983-1999.

Fitch, T.J. and P. Molnar (1970) Focal mechanism along inclined earthquake zones in the Indonesia-Philippines region, J. Geophys. Res., 75, 1431-1444.

Flinn, E.A. (1965) Confidence regions and error determinations for seismic event locations, Rev. Geophys., 3, 157-185.

Forsyth, D.W. (1974) Anisotropy and the structural evolution of the oceanic upper mantle, Ph.D. thesis, M.I.T., 255 pp.

Forsyth, D.W. and F. Press (1971) Geophysical tests of petrological models of the spreading lithosphere, J. Geophys. Res., 76, 7963-7979.

Franklin, J.N. (1970) Well-posed stochastic extension of ill-posed linear problems, J. Math. Anal. Appl., 31, 682-716.

Frasier, C.W. (1970) Discrete time solution of plane P-SV waves in a plane layered medium, Geophysics, 35, 197-219.

Frissilo, A.L. and G.R. Barsch (1972) Measurement of single-crystal elastic constants of Brozite as a function of pressure and temperature, J. Geophys. Res., 77, 6360-6384.

Fuchs, K. and G. Müller (1971) Computation of synthetic seismograms with the reflectivity method and comparison with observations, Geophys. J. R. astr. Soc., 23, 417-433.

Fukao, Y. (1972) Source process of a large deep-focus earthquake and its tectonic implications - the western Brazil earthquake of 1963, Phys. Earth Planet. Interiors, 5, 61-76.

Fukao, Y. (1973) Source processes of a large deep-focus earthquake and its tectonic implications - the western Brazil earthquake of 1963: Reply, Phys. Earth Planet. Interiors, 7, 115-121.

Gaposchkin, E.M. (1974) Earth's gravity field to the eighteenth degree and geocentric coordinates for 104 stations from satellite and terrestrial data, J. Geophys. Res., 79, 5377-5411.

Gilbert, F. (1971) The diagonal sum rule and averaged eigen frequencies, Geophys. J. R. astr. Soc., 23, 119-123.

Gilbert, F., A. Dziewonski, and J.N. Brune (1973) An informative solution to a seismological inverse problem, Proc. Natl. Acad. Sci. U. S., 70, 1410-1413.

Gilbert, F. and A.M. Dziewonski (1974) An application of normal mode theory to the retrieval of structural parameters and source mechanisms for seismic spectra, submitted to Phil. Trans. Roy. Soc. London.

Gogna, M.L. (1967) Travel times from Central Pacific nuclear explosions, Geophys. J. R. astr. Soc., 23, 119-123.

Green, R.W.E. and A.L. Hales (1968) The travel times of P waves to 30° in the central United States and upper mantle structure, Bull. Seismo. Soc. Am., 58, 267-289.

Greenfield, R.J. and R.M. Sheppard (1969) The Moho depth variations under the LASA and their effect on $dT/d\Delta$ measurements, Bull. Seismo. Soc. Am., 59, 409-420.

Gumper, F. and P.W. Pomeroy (1970) Seismic wave velocities and earth structure on the African continent, Bull.

Seismo. Soc. Am., 60, 651-668.

Gutenberg, B. and C.F. Richter (1936) Travel time curves prepared by The Seismological Laboratory, Calif. Inst. of Tech.

Gutenberg, B. and C.F. Richter (1954) Seismicity of the earth and associated phenomena, Princeton Univ. Press, Princeton, New Jersey.

Haddon, R.A.W. and K.E. Bullen (1969) An earth model incorporating free earth oscillation data, Phys. Earth Planet. Interiors, 2, 35-49.

Haddon, R.A.W. and J.R. Cleary (1974) Evidence for scattering on seismic PKP waves near the mantle-core boundary, Phys. Earth and Planet. Sci. Interiors, 8, 211-234.

Hales, A.L. (1972) The travel times of P seismic waves and their relevance to the upper mantle velocity distribution, Tectonophysics, 13, 447-482.

Hales, A.L. (1974) Eigenperiods of earth models and the determination of travel time base lines, J. Geophys. Res., 79, 422-423.

Hales, A.L., J.R. Cleary and J.L. Roberts (1968) Velocity distribution in the lower mantle, Bull. Seismo. Soc. Am., 58, 1975-1989.

Hales, A.L. and H.A. Doyle (1967) P and S travel time anomalies and their interpretation, Geophys. J. R. astr. Soc., 13, 403-415.

Hales, A.L., C.E. Helsley and J.B. Nation (1970) P travel times for an oceanic path, J. Geophys. Res., 75, 7362-7381.

Hales, A.L. and J.L. Roberts (1970a) The travel times of S and SKS, Bull. Seismo. Soc. Am., 60, 461-489.

Hales, A.L. and J.L. Roberts (1970b) Shear velocities in the lower mantle and the radius of the core, Bull. Seismo. Soc. Am., 60, 1427-1436.

Hart, R.S. and F. Press (1973) Sn velocities and the composition of the lithosphere in the regionalized Atlantic, J. Geophys. Res., 78, 407-411.

Hatherton, T. (1970) Upper mantle inhomogeneity beneath New Zealand: surface manifestation, J. Geophys. Res., 75, 269-284.

Helmberger, D.V. (1974) Generalized ray theory for shear dislocations, Bull. Seismo. Soc. Am., 64, 45-64.

Helmberger, D.V. and G.R. Engen (1974) Upper mantle shear structure, J. Geophys. Res., 79, 4017-4028.

Helmberger, D. and R.A. Wiggins (1971) Upper mantle structure of Midwestern United States, J. Geophys. Res., 76, 3229-3245.

Herrin, E. (1969) Regional variations of P wave velocity in the upper mantle beneath North America in: The Earth's Crust and Upper Mantle, ed. by P. Hart, American Geophysical Union, Washington, D.C., 736 pp.

Herrin, E. and J.N. Taggart (1968) Regional variation in P travel times, Bull. Seismo. Soc. Am., 58, 1325-1337.

Herrin, E., W. Tucker, J. Taggart, D.W. Gordon, and J.L. Lobdell (1968) Estimation of surface focus P travel times, Bull. Seismo. Soc. Am., 58, 1273-1291.

Hide, R. and K. Horai (1968) On the topography of the core-mantle interface, Phys. Earth Planet. Interiors, 1, 305-308.

Hide, R.M. and S.R.C. Malin (1970) Novel correlations between global features of the earth's gravitational and magnetic fields, Nature, 225, 605-609.

Hirasawa, T.H. (1966) A least square method for the focal mechanism determination from S wave data, Bull. Earthquake Res. Institute, 44, 901-918.

Hoel, P.G. (1962) Introduction to Mathematical Statistics, Third edition, John Wiley and Sons, Inc., New York.

Howard, L.E. and J.H. Sass (964) Terrestrial heat flow in Australia, J. Geophys. Res., 69, 1617-1626.

Huestis, S., P. Molnar and J. Oliver (1973) Regional Sn velocities and shear velocity in the upper mantle, Bull. Seismo. Soc. Am., 63, 469-475.

Husebye, E.S., R. Karestrom and R. Rud (1971) Observations of vertical and lateral P velocity anomalies in the earth's mantle using the Fennoscandian shield, Geophys. J. R. astr. Soc., 25, 3-16.

Ibrahim, A.K. (1971) The amplitude ratio PcP/P and the core-mantle boundary, Pure and Applied Geophys., 91, 114-133.

Ibrahim, A.K. and O.W. Nuttli (1967) Travel time curves and upper mantle structure from long period S waves, Bull. Seismo. Soc. Am., 57, 1063-1092.

Isacks, B. and P. Molnar (1971) Distribution of stresses in the descending lithosphere from a global survey of focal mechanism solution of mantle earthquakes, Rev. Geophys., 9, 103-174.

Isacks, B., J. Oliver, and L. Sykes (1968) Seismology and the new global tectonics, J. Geophys. Res., 73, 5855-5899.

Isacks, B., L. Sykes, and J. Oliver (1969) Focal mechanism of deep and shallow earthquakes in the Tonga-Kermadec Region and the tectonics of island arcs, Bull. Geol. Soc. Am., 80, 1443-1470.

Isacks, B.L. and M. Barazangi (1973) High frequency shear waves guided by a continuous lithosphere descending beneath western South America, Geophys. J. R. astr. Soc., 33, 129-139.

Ishida, M. (1970) Seismicity and travel time anomaly in and around Japan, Bull. Earthquake Res. Institute, 48, 1023-1051.

Jackson, D.D. (1972) Interpretation of inaccurate, insufficient and inconsistent data, Geophys. J. R. astr. Soc., 28, 97-109.

Jackson, D.D. (1973) Marginal solutions to quasi-linear inverse problems in geophysics: the edgehog method, Geophys. J. R. astr. Soc., 35, 121-136.

Jeffreys, H. (1970) The Earth, Fifth edition, Cambridge Univ. Press, London.

Jeffreys, H. and K.E. Bullen (1940) Seismological Tables, Brit. Assoc. Advancement of Sci., Gray-Milne Trust, London, 1940.

Johnson, L.R. (1967) Array measurements of P velocities in the upper mantle, J. Geophys. Res., 72, 6309-6325.

Johnson, L.R. (1969) Array measurements of P velocities in the lower mantle, Bull. Seismo. Soc. Am., 59, 973-1008.

Johnson, L.E. and F. Gilbert (1972) Inversion and inference for teleseismic ray data, in: Methods in Computational Physics, 12, Academic Press, New York, 231-266.

Jordan, T.H. (1973) Estimation of the radial variation of seismic velocities and density in the earth, Ph.D. thesis, Calif. Instit. of Tech.

Jordan, T.H. and D.L. Anderson (1974) Earth structure from free oscillations and travel times, Geophys. J. R. astr. Soc., 36, 411-459.

Jordan, T.H. and W.S. Lynn (1974) A velocity anomaly in the lower mantle, J. Geophys. Res., 79, 2679-2685.

Julian, B.R. (1970) Regional variations in upper mantle structure beneath North America, Ph.D. thesis, Calif. Inst. of Tech., Pasadena, Calif., 208 p.

Julian, B.R. and D.L. Anderson (1968) Travel times, apparent velocities, and amplitudes of body waves, Bull. Seismo. Soc. Am., 58, 339-366.

Julian, B.R. and M.K. Sengupta (1973) Seismic travel time evidence for lateral inhomogeneity in the deep mantle, Nature, 242, 243-247.

Kaila, K.L. (1970) Decay rate of P wave amplitudes from nuclear explosions and the magnitude relations in the epicentral distance range 1° to 98°, Bull. Seismo. Soc. Am., 60, 447-460.

Kanamori, H. (1967) Spectrum of P and PcP in relation to the mantle-core boundary and attenuation in the mantle, J. Geophys. Res., 72, 559-571.

Kanamori, H. (1968) Travel times to Japanese stations from Longshot and their geophysical explanations, Bull. Earthquake Res. Inst., 46, 841-859.

Kanamori, H. (1970) Velocity and Q of mantle waves, Phys. Earth Planet. Interiors, 2, 259-275.

Kanasewich, E.R., R.M. Ellis, C.H. Chapman and P.R. Kulowski (1973) Seismic array evidence of a core boundary source

for the Hawaiian linear volcanic chain, J. Geophys. Res., 78, 1361-1371.

Kaula, W.M. (1972) Global gravity and mantle convection, Tectonophysics, 13, 341-359.

Kaula, W.M. (1975) Absolute plate motions by boundary velocity minimization, J. Geophys. Res., 80, 244-248.

Katsumata, M. and L.R. Sykes (1969) Seismicity and tectonics of the western Pacific: Izu-Mariana-Caroline and Ryukyu-Taiwan Ridge, J. Geophys. Res., 74, 5923-5948.

Keilis-Borok, V.I. and T.B. Yanovskaja (1917) Inverse problems of seismology (structural review): Geophys. J. R. astro. Soc., 13, 223-234.

King, D.W., R.A.W. Haddon and J.R. Cleary (1973) Evidence for seismic wave scattering in the D" layer, Earth and Planet. Sci. Letters, 20, 353-356.

Knopoff, L. (1971) On the significance of the upper mantle project, United States Program - Final Report, published by U.S. Upper Mantle Committee, 278 pp.

Kogan, S.D. (1960) Travel times of longitudinal and transverse waves calculated from data on nuclear explosions made in the region of the Marshall Islands, Bull. Acad. Sci. USSR (Izvest.), Geophys. Series, 3, 246-253.

Kumazawa, M. and O.L. Anderson (1969) Elastic moduli, pressure derivatives and temperature derivatives of

single-crystal olivine and single-crystal Forsterite, J. Geophys. Res., 74, 5961-5972.

Kurita, T. (1966) Attenuation of long period P waves and Q in the mantle, J. Physics of the Earth, 14, 1-14.

Leeds, A.R., L. Knopoff, and E.G. Kausel (1974) Variations of upper mantle structure under the Pacific Ocean, Science, 186, 141-143.

Liebermann, R.C. (1970) Velocity-density systematics for the olivine and spinel phases of Mg_2SiO_4-Fe_2SiO_4, J. Geophys. Res., 75, 4029-4034.

Liebermann, R.C. (1972) Pressure and temperature dependence of the elastic properties of polycrystalline Trevorite ($NiFe_2O_4$), Phys. Earth Planet. Int., 6, 360-365.

Lilwall, R.C. and A. Douglas (1970) Estimation of P wave travel times using joint epicenter method, Geophys. J. R. Astr. Soc., 19, 165-181.

Manghani, M.H. (1969) Elastic constants of single-crystal Rutile under pressures to 7.5 kilobars, J. Geophys. Res., 74, 4317-4328.

Mansinha, L. (1964) The velocity of shear fracture, Bull. Seismo. Soc. Amer., 54, 369-376.

Massé, R.P. (1973a) Compressional velocity distribution beneath central and eastern North America, Bull. Seismo. Soc. Amer., 63, 911-935.

Massé, R.P. (1973b) Shear velocity distribution beneath the Canadian Shield, J. Geophys. Res., 78, 6943-6950.

Massé, R.P. (1973c) Upper mantle compressional velocity and continental drift rates, Nature Phys. Sci., 245, 134-135.

Massé, R.P. and S.S. Alexander (1974) Compressional velocity distribution beneath Scandinavia and Western Russia, Geophys. J. R. astr. Soc., 39, 587-602.

Massé, R.P., M. Landisman and J.B. Jenkins (1972) An investigation of the upper mantle compressional velocity distribution beneath the Basin and Range province, Geophys. J. R. astr. Soc., 30, 19-36.

Mathews, J. and R.L. Walker (1964) Mathematical methods of physics, published by W.A. Benjamin, Inc., New York.

Mendiguren, J. (1972) Source mechanism of a deep earthquake from analysis of world wide observations of free oscillation, Ph.D. thesis, M.I.T., Cambridge, Mass., 140 pp.

Mikumo, T. and T. Kurita (1968) Q distribution for long period P waves in the mantle, J. Phys. Earth, 16, 11-29.

Minster, J.B., T.H. Jordan, P. Molnar, and E. Haines (1974) Numerical modelling of instantaneous plate tectonics, Geophys. J. R. astr. Soc., 36, 541-576.

Mitchell, B.J. and D.V. Helmberger (1973) Shear velocities at the base of the mantle from observations of S and ScS, J. Geophys. Res., 78, 6009-6020.

Mitronovas, W. and B.L. Isacks (1971) Seismic velocity anomalies in the upper mantle beneath the Tonga-Kermadec island arc, J. Geophys. Res., 76, 7154-7179.

Miyamura, S. (1969) The seismicity of Japan and the surrounding area, Izv., 7, 420-437.

Mizutani, H. and K. Abe (1972) An earth model consistent with free oscillation and surface wave data, Phys. Earth Planet. Int., 5, 345-356.

Molnar, P. and J. Oliver (1969) Lateral variations of attenuation in the upper mantle and discontinuities in the lithosphere, J. Geophys. Res., 74, 2648-2662.

Mooney, H.M. (1970a) Upper mantle inhomogeneity beneath New Zealand: Seismic evidence, J. Geophys. Res., 75, 285-309.

Mooney, H.M. (1970b) Theoretical and observed travel times for New Zealand deep earthquakes, New Zealand Jour. Geol. and Geophys., 13, 703-717.

Muirhead, K.J. and J.R. Cleary (1969) Comparison of 1968 P tables with times from nuclear explosions (II), the Marshall Islands and Sahara series, Earth and Planet. Sci. Letters, 7, 132-136.

Müller, G. and L.E. Alsop (1974) Partial derivatives of travel times, Letter to the Editor, Geophys. J. R. astr. Soc., 36, 239-243.

Murphy, J.R., A.H. Davies and N.L. Weaver (1971) Amplification of seismic body waves by low velocity surface layer, Bull. Seismo. Soc. Am., 61, 109-145.

Niazi, M. (1973) SH travel times and lateral heterogeneities in the lower mantle, Bull. Seismo. Soc. Am., 63, 2035-2046.

Nuttli, O.W. (1964) The determination of S wave polarization angles for an earth model with crustal layering, Bull. Seismo. Soc. Am., 54, 1429-1440.

Nuttli, O.W. (1972) The amplitudes of teleseismic P waves, Bull. Seismo. Soc. Am., 62, 343-356.

Nuttli, O.W. and B.A. Bolt (1969) P wave residuals as a function of azimuth, 2. Undulations of the mantle low velocity layer as an explanation, J. Geophys. Res., 74, 6594-6602.

Nuttli, O.W. and J.D. Whitmore (1962) On the determination of the polarization angle of the S wave, Bull. Seismo. Soc. Am., 52, 95-107.

Oliver, J. and B. Isacks (1967) Deep earthquake zones, anomalous structures in the upper mantle and the lithosphere, J. Geophys. Res., 72, 4259-4275.

Papoulis, A. (1962) The Fourier Integral and Its Applications, McGraw-Hill, New York.

Phinney, R.A. and S.S. Alexander (1969) The effect of velocity gradient at the base of the mantle on diffracted P waves in the shadow, J. Geophys. Res., 74, 4967-4971.

Phinney, R.A. and L.M. Cathles (1969) Diffraction of P by the core: a study of long period amplitudes near the edge of the shadow, J. Geophys. Res., 74, 1556-1574.

Press, F. (1966) Seismic velocities in: Handbook of Physical Constants, ed. S.P. Clark, Jr., published by the Geological Society of America, 587 pp.

Press, F. (1970) Earth models consistent with geophysical data, Phys. Earth Planet. Int., 3, 3-22.

Press, F. and S. Biehler (1964) Inferences on crustal velocities and densities from P wave delays and gravity anomalies, J. Geophys. Res., 69, 2979-2995.

Press, F. and R. Siever (1974) Earth, published by W.H. Freeman and Co., San Francisco, 945 pp.

Randall, M.J. (1971) A revised travel-time table for S, Geophys. J. R. Astr. Soc., 22, 229-234.

Richards, P.G. (1973) Calculation of body waves for caustics and tunnelling in core phases, Geophys. J. R. Astr. Soc., 35, 243-264.

Richter, C.F. (1958) Elementary Seismology, published by W.H. Freeman and Co., San Francisco.

Ringwood, A.E. (1972) Mineralogy of the deep mantle: current status and future developments, in: The Nature of Solid Earth, ed. by E.C. Robertson, published by McGraw-Hill, Inc., New York, 67-92 pp.

Robinson, R. and R.L. Kovach (1972) Shear wave velocities in the earth's mantle, Phys. Earth Planet. Int., 5, 30-44.

Santo, T. (1969) Characteristics of seismicity in South America, Bull. Earthquake Res. Inst., 47, 635-672.

Santo, T. (1970a) Regional study on the characteristic seismicity of the world, Part III: New Hebrides Island region, Bull. Earthquake Res. Inst., 48, 1-18.

Santo, T. (1970b) Regional study on the characteristic seismicity of the world, Part IV New Britain Island region, Bull. Earthquake Res. Inst., 48, 127-143.

Santo, T. (1970c) Regional study on the characteristic seismicity of the world, Part V: Bonin-Marianas Island region, comparative study on the reliability of USCGS seismic data since 1963, Bull. Earthquake Res. Inst., 48, 363-379.

Savage, J.C. (1965) The effect of rupture velocity upon seismic first motion, Bull. Seismo. Soc. Am., 55, 263-275.

Savage, J.C. (1966) Radiation from a realistic model of faulting, Bull. Seismo. Soc. Am., 56, 577-592.

Sengupta, M.K. (1972) A travel time study of P wave using deep-focus earthquakes, S.M. thesis, M.I.T., Cambridge, Mass., 1972.

Shimshoni, M. and C.L. Pekeris (1966) The seismic crustal function of the earth, Geophys. J. R. astr. Soc., vol. II, 1-4.

Simpson, D.W., C. Wright, and J.R. Cleary (1971) Double discontinuity in the upper mantle, Nature Phys. Sci., 231, 201-203.

Sipkin, S.A. and T.H. Jordan (1974) The baseline difference between continents and oceans, EOS Trans. AGU, 55, 350.

Sleep, N. (1973) Teleseismic P wave transmission through slab, Bull. Seismo. Soc. Am., 63, 1349-1373.

Solomon, S.C. (1971) Seismic wave attenuation and the state of the upper mantle, Ph.D. thesis, M.I.T., Cambridge, Mass., 321 pp.

Solomon, S.C. (1972) Seismic wave attenuation and partial melting in the upper mantle of North America, J. Geophys. Res., 77, 1483-1502.

Solomon, S.C. (1973) Shear wave attenuation and melting beneath the mid-Atlantic ridge, J. Geophys. Res., 78, 6044-6059.

Solomon, S.C. and B.R. Julian (1974) Seismic constraints on ocean-ridge mantle structure, Geophys. J. R. astr. Soc., 38, 265-285.

Solomon, S.C. and N.H. Sleep (1974) Some simple physical models for absolute plate motions, J. Geophys. Res., 79, 2557-2567.

Solomon, S.C. and M.N. Toksöz (1970) Lateral variation of attenuation of P and S waves beneath the United States, Bull. Seismo. Soc. Am., 60, 819-838.

Spetzler, H. (1970) Equation of state of polycrystalline and single-crystal Mgo to 8 kilobars and 800°K, J. Geophys. Res., 75, 2073-2087.

Stauder, W. (1962) The focal mechanism of earthquakes, Advan. Geophys., 9, 1-76.

Stauder, W. (1971) Mechanism and spatial distribution of Chilean earthquakes with relation to subduction of the oceanic plate, J. Geophys. Res., 78, 5033-5061.

Sykes, L.R. (1964) Deep focus earthquakes in the New Hebrides region, J. Geophys. Res., 69, 5353-5355.

Sykes, L.R. (1966) The seismicity and deep structure of island arcs, J. Geophys. Res., 71, 12, 2981-3006.

Sykes, L.R., B.L. Isacks and J. Oliver (1969) Spatial distribution of deep and shallow earthquakes of small magnitudes in the Fiji-Tonga region, Bull. Seismo. Soc. Am., 59, 3, 1093-1113.

Sykes, L.R. and M.L. Sbar (1973) Intraplate earthquakes lithospheric stresses and the driving mechanism of plate tectonics, Nature, 245, 298-302.

Teng, T. (1968) Attenuation of body waves and the Q structure of the mantle, J. Geophys. Res., 73, 2195-2208.

Toksöz, M.N., J. Arkani-Hamed and C.A. Knight (1969) Geophysical data and long wave heterogeneities of the earth's mantle, J. Geophys. Res., 74, 3751-3770.

Toksöz, M.N., M.A. Chinnery and D.L. Anderson (1967) Inhomogeneities in the earth's mantle, Geophys. J. R. astr. Soc., 13, 31-59.

Toksöz, M.N., J.W. Minear and B.R. Julian (1971) Temperature field and geophysical effects of a downgoing slab, J. Geophys. Res., 76, 1113-1138.

Toksöz, M.N., N. Sleep, and A. Smith (1973) Evolution of the downgoing lithosphere and the mechanisms of deep focus earthquakes, Geophys. J. R. astr. Soc., 35, 285-310.

Tucker, W., E. Herrin and H. Freedman (1968) Some statistical aspects of the estimation of seismic travel times, Bull. Seismo. Soc. Amer., 58, 1243-1260.

Turcotte, D.L. and E.R. Oxburgh (1973) Mid-plate tectonics, Nature, 244, 337-339.

Utsu, T. (1967) Anomalies in seismic wave velocity and attenuation associated with a deep earthquake zone (I) J. Fac. Sci., Hokkaido Univ., 3, 1-25.

Veith, K.F. and G.E. Clawson (1972) Magnitude from short-period P wave data, Bull. Seismo. Soc. Am., 62, 435-452.

Vinnik, L.P., A.A. Lukk and A.V. Nikolayev, Inhomogeneities in the lower mantle, Phys. Earth Planet. Int., 5, 328-331.

Walsh, J.B. (1969) New analysis of attenuation in partially melted material, J. Geophys. Res., 74, 4333-4337.

Wang, H. and G. Simmons (1973) Elasticity of some mantle crystal structures, 2. Rutile GeO_2, J. Geophys. Res., 78, 1262-1273.

Ward, R. (1971) Synthesis of teleseismic P waves from sources near transition zones, Ph.D. thesis, M.I.T. Cambridge, Mass., 206 pp.

Ward, R.W. and M.N. Toksöz (1971) Causes of regional variation of magnitudes, Bull. Seismo. Soc. Am., 61, 649-670.

Weidner, D.J. (1974) Rayleigh wave phase velocities in the Atlantic ocean, Geophys. J. R. astr. Soc., 36, 105-139.

Whitcomb, J.H. (1973) A study of the velocity structure of the earth by the use of core phase (Part I), Ph.D. thesis, Calif. Inst. of Tech., 443 pp.

Whitcomb, J.H. and D.L. Anderson (1970) Reflection of P'P' seismic waves from discontinuities in the mantle, J. Geophys. Res., 75, 5713-5728.

Wiggins, R.A. and D.V. Helmberger (1973) Upper mantle structure of the western United States, J. Geophys. Res., 78, 1870-1880.

Wiggins, R.A. and J.A. Madrid (1974) Body wave amplitude calculations, Geophys. J. R. astr. Soc., 37, 423-433.

Wiggins, R.A., G.A. McMechan, and M.N. Toksöz (1973) Range of earth structure non-uniqueness implied by body wave observations, Rev. Geophys., 11, 87-113.

Willey, G., J.R. Cleary and P.D. Marshall (1970) Comparison of least squares analyses of long and short period P wave amplitudes, Geophys. J. R. astr. Soc., 19, 439-445.

Wright, C. (1973) Array studies of P phases and the structure of the D" region of the mantle, J. Geophys. Res., 78, 4965-4982.

Wright, C. and J.R. Cleary (1972) P wave travel time gradient measurements for the Warramunga seismic array and lower mantle structure, Phys. Earth Planet. Int., 5, 213-230.

Wright, C. and J.A. Lyons (1975) Seismology, $dT/d\Delta$ and deep mantle convection, Geophys. J. R. astr. Soc., 40, 115-138.

Wyss, M. and P. Molnar (1972) Source parameters of intermediate and deep focus earthquakes in the Tonga arc, Phys. Earth Planet. Int., 6, 279-292.

Yanovskaya, T.B. (1963) Calculation of upper mantle velocity profiles from a seismic wave travel time curve as an inverse mathematical problem, Bull. Acad. Sci. U.S.S.R. Geophys. Ser., 8, 711-714.

Yasar, T. and O.W. Nuttli (1974) Structure of the shear-wave low-velocity channel in the western United States, Geophys. J. R. astr. Soc., 37, 353-364.

APPENDIX A

Relocation of Hypocenters

The main features of our relocation scheme are as follows: a) depths of the events were determined exclusively from pP-P/sP-P times, b) epicenters and origin times were determined from the least square solutions of P wave travel time residuals, c) equal weight was given to each 10° x 10° area in distance and azimuth, d) only those times reported as "i" ("impetus") arrivals in the bulletin and having residuals less than ±4 seconds were used in the relocation, and e) correction for station anomalies and corrections to Jeffreys-Bullen times (1940) (Appendix K) were used to correct the travel times. Elliptic corrections (Bullen, 1937a, 1938b) to the travel times were made as well.

Table A-1 shows the depths of 14 events, determined from pP-P/sP-P times in comparison with the depths reported in the bulletin. The difference in our computed depths and the bulletin depths was often more than 10 km. It may be argued that anomalously higher velocity within the downgoing slabs may reduce the travel time of the upgoing ray of pP or sP from a deep source and thereby cause a shallower depth. This possibility has been tested for the Columbia event where depth calculated from our pP-P times was about 25 km less than that reported in the bulletin.

In Fig. A-1 we show the reflecting points of pP rays along with the calculated values of depth. It is obvious from the figure that source region does not have a systematic bias on the depths determined from the depth phases.

Another source of error in depths calculated from the depth phases is the presence of deep ocean water near the reflecting points of pP/sP. The pP-P/sP-P time obviously will then depend on the fact whether the reflection has occurred on the free surface or at the interface of the water and oceanic crust. For a pure contact between oceanic crust and water (with no transition layer like sand and water etc.), larger reflected amplitude (in the ratio of about 4:1 for normal incidence) is expected from this interface rather than from the free surface. In these types of situations, depths calculated from pP-P times will be less than actual but the difference should not be larger than 5-6 km if only teleseismic data are chosen. In the other cases, when pP undergoes the reflection from free surface, the result will be drastically opposite, i.e. depths determined from pP-P times will exceed the actual depth by about 25 km. We checked the above effect for the events at West Tonga, South Fiji and the New Hebrides. We plotted (Fig. A-2) the different depth values of the events (calculated from depth phases at different stations) against

the water depths at the reflection points of pP/sP and we found no correlation. The water depths have been obtained from a bathymetry map of the southwestern Pacific compiled by Scripps Institute of Oceanography. For the West Tonga event and for the South Fiji event the vague correlation with negative slope may be suggestive of the reflection of depth phases at the bottom of the ocean rather than at its surface.

Due to apparent randomness in the values of the depth of an event calculated from depth phases at different stations, we have preferred to take the average of those values. In this averaging we combined the values from both pP-P and sP-P times as no systematic difference in depth has been noticed between these two groups. We should note also that the calculated values of depth are sensitive to the velocity models (P or S) only above the event depth and for our calculation we used an up-to-date version of average models as compiled by Julian (personal communication). However, velocity model for some source region may be different from the average model. Assuming $x\%$ variation in velocity from the average model above the source depth, there will be an error of $x\%$ in depth when the depths are calculated from the average model.

With depths fixed from depth phases, origin times and epicenters of the events (Table 2-1 in Chap. 2) were determined from a standard least square equation of condition (see for example, Tucker et al., 1968) using corrected J-B times (Appendix K). Starting location parameters were taken from bulletins of ISC and/or USCGS/NOAA. A parameter of judging the reliability of the epicenters is the area of the joint confidence region of the epicentral coordinates. Following a process similar to Flinn's (1965), we have computed the area of the 95% confidence ellipse. Under the ideal condition, this ellipse should mark a boundary within which the actual epicenter will lie at 95% confidence level. But when a systematic bias exists among the observed data or when a wrong travel time table is used for location, such an interpretation of confidence ellipse is not valid any longer. However, the area of such an ellipse, in any case, is a measure of the internal consistency of both the observed data and applied corrections with respect to the computed epicentral coordinates -- the smaller the area, the greater the internal consistency. On the average the area of our confidence ellipse is 100 sq. km (Table 2-1 in Chap. 2). Note in this connection that a location, in general, is considered to be bad when the area of such a confidence ellipse exceeds 1000 sq. km (Herrin et al., 1968).

Table A-1

Depths from the Depth Phases

Event	Depth from pP-P times	Depth from sP-P times	Average depth (km)	Bulletin+ depth (km)
West Tonga	594±8(7)*	600±5(3)*	596±7(10)*	589±4.6
South Fiji	624±5(4)	619±4(4)	622±5(8)	627±3.6
Colombia	626±11(7)	-	626±11(7)	653±3.0
Peru/Brazil	586±6(17)	-	586±6(17)	587±4.4
Argentina	577±5(3)	582±2(3)	580±4(6)	571±3.8
Java Sea	585±6(7)	-	585±6(7)	599±5.2
Banda Sea	553±8(4)	-	553±8(4)	555±8.1
Sea of Okhotsk	632±10(10)	617±7(9)	625±12(19)	643±2.7
East Russia	563±8(4)	566.0±0(1)	564±7(5)	547±2.6
South Marianas	-	587±3(4)	587±3(4)	606±4.2
Solomon Is.	511±1(5)	-	511±1(5)	509±4.3
New Hebrides	581±4(4)	592±10(5)	587±9(9)	596±3.6
Hindukush	282±5(14)	275±11(9)	280±8(23)	275±2
Greece	151±2(8)	151±0(1)	151±1(9)	155±2.5

*Average depth, standard deviation, and number of data (within the bracket) are shown.

+Depth reported in the bulletins of International Seismological Center (ISC)

Figure Captions

Figure A-1. Check for systematic bias in the depth determination from depth phases of Columbian deep event (Table 2-1 in Chap. 2). Solid circles represent the reflecting points of pP phases in distance-azimuth diagram with hypocenter at the center of the plot. Circles are drawn at one degree distance intervals from the hypocenter. Computed depths (in km) and the names of stations recording the pP phases are also shown. Note that there appears no systematic variation in depth with respect to the positions of reflecting points.

Figure A-2. Check for systematic bias in the depth determination from the depth phases of deep events at West Tonga, South Fiji and New Hebrides (Table 2-1 in Chap. 2). Depths computed from the depth phases are shown against the water depths near the reflecting points of the depth phases. Water depths were determined from a bathymetry map prepared by Scripps Institution of Oceanography. Dashed line represents the depths used in this study. Note that a vague correlation between the water depths and the computed hypocentral depths for events at West Tonga and South Fiji, suggests that reflection of those depth phases may occur at ocean bottom rather than at free surface.

Figure A-3. (4 plates) Plot of P wave travel time residuals (after relocation) of 14 deep events (Table 2-1 in Chap. 2) on the equal area projection of unit spheres around the hypocenters. The crosses and circles are for rays leaving the focus downward and the triangles and squares for rays leaving the focus upward.

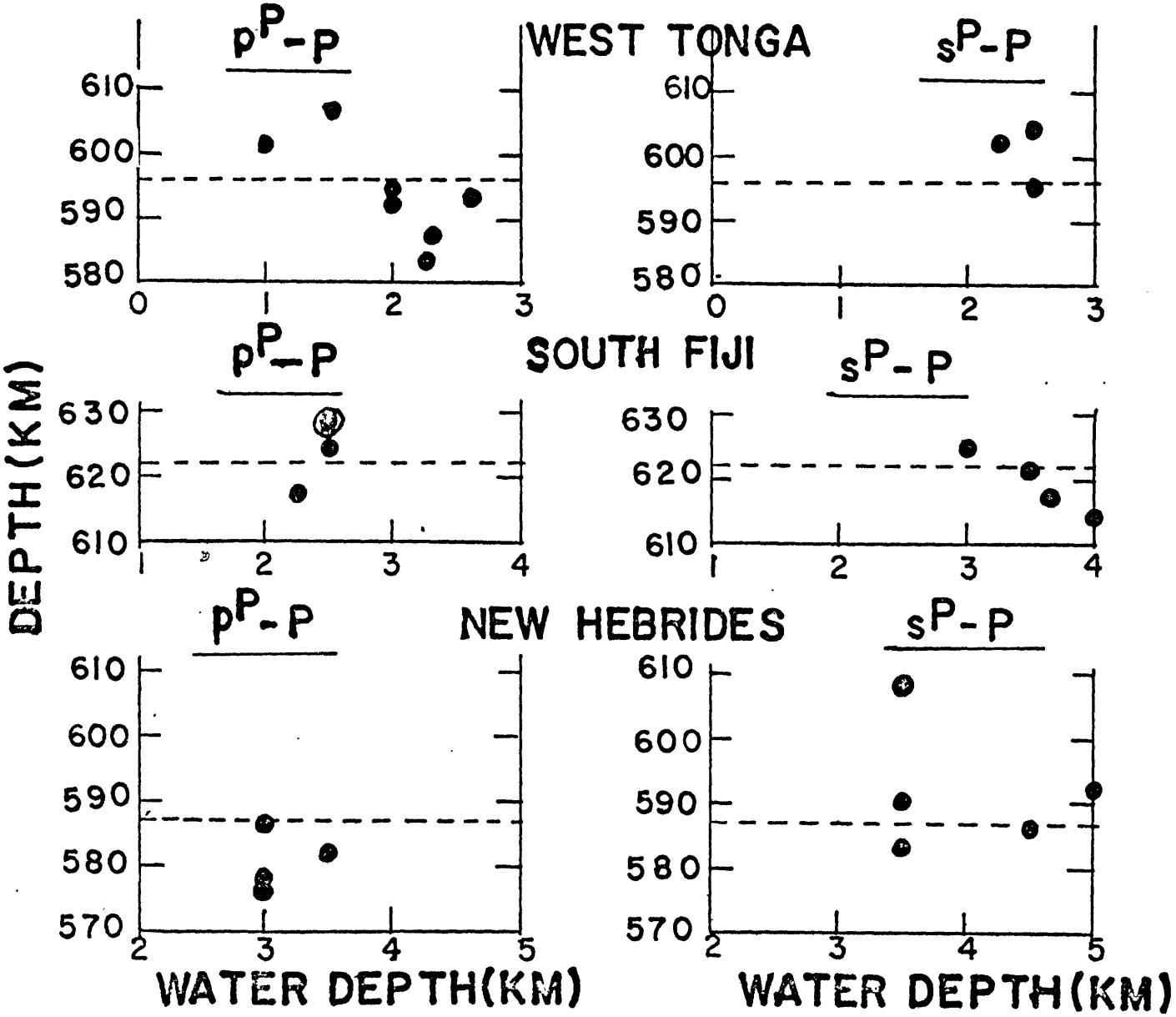

WEST TONGA
SOUTH FIJI
NEW HEBRIDES
pP-P
sP-P
DEPTH(KM)
WATER DEPTH(KM)
WATER DEPTH(KM)

Fig. A-2

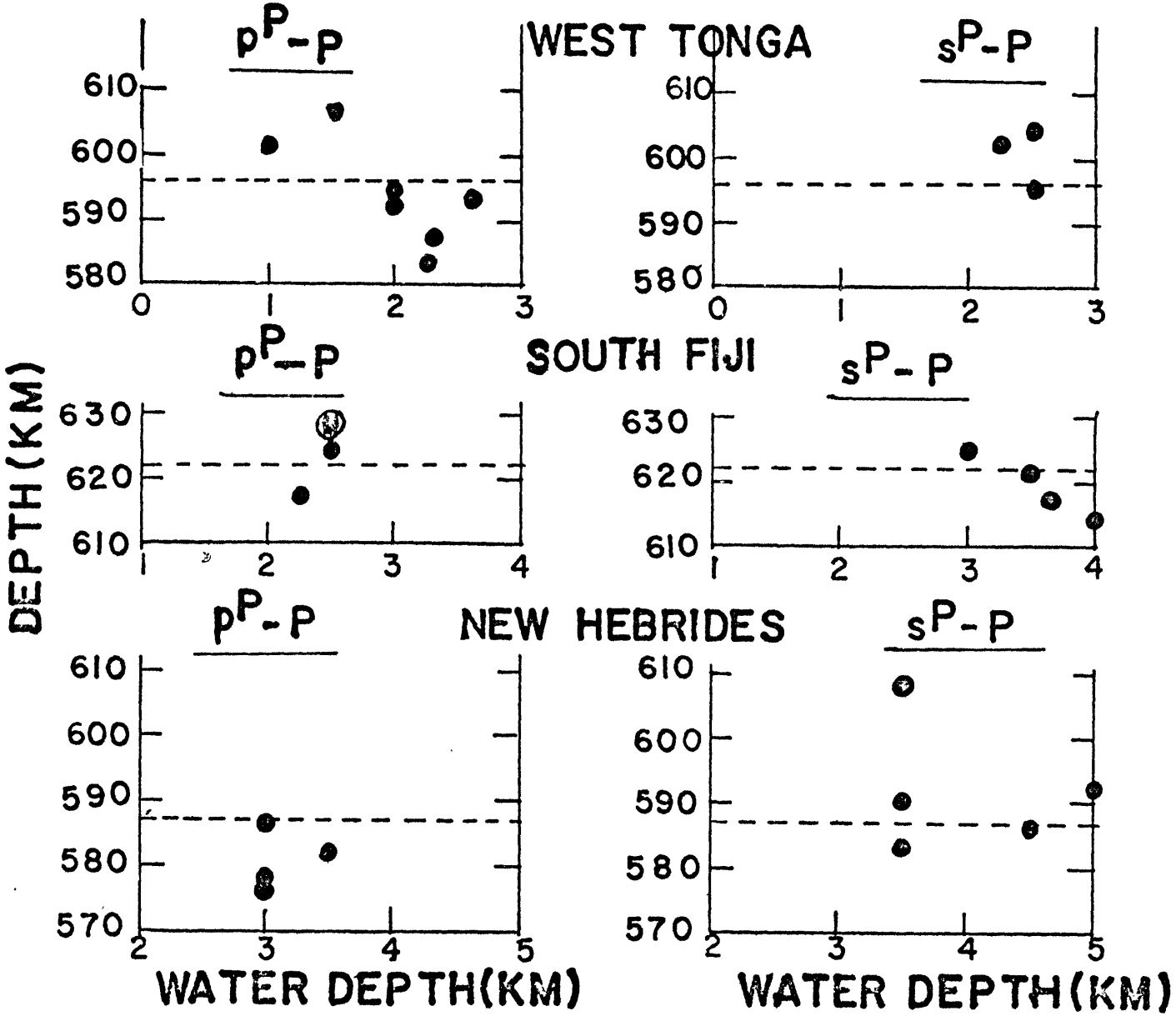

pP-P
WEST TONGA
sP-P
610
600
590
580
0
1
2
3
pP-P
SOUTH FIJI
sP-P
630
620
610
1
2
3
4
DEPTH(KM)
pP-P
NEW HEBRIDES
sP-P
610
600
590
580
570
2
3
4
5
WATER DEPTH(KM)
WATER DEPTH(KM)

Fig. A-2

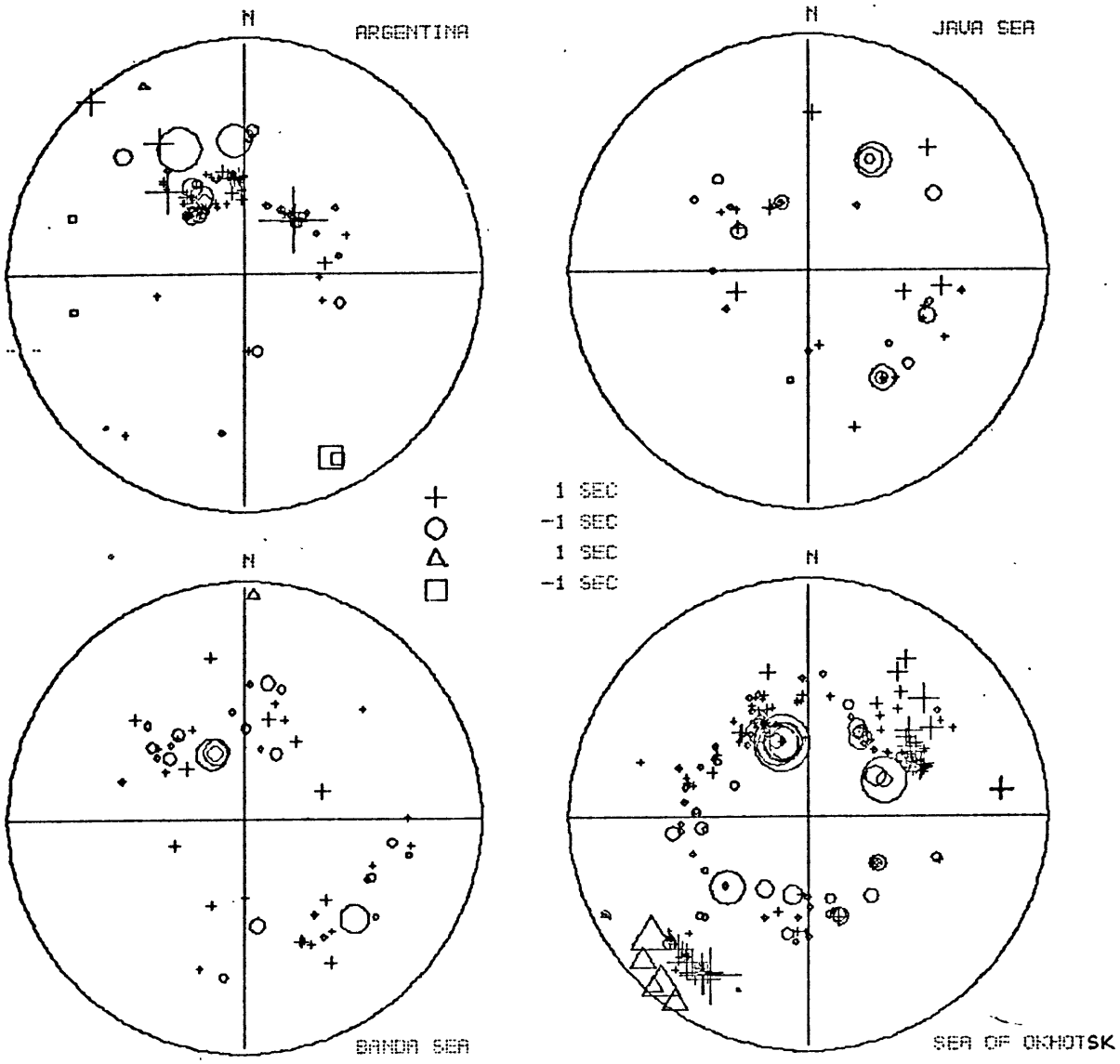

N
ARGENTINA
N
JAVA SEA
1 SEC
-1 SEC
1 SEC
-1 SEC
N
BANDA SEA
N
SEA OF OKHOTSK

Fig. A-3 (contd)

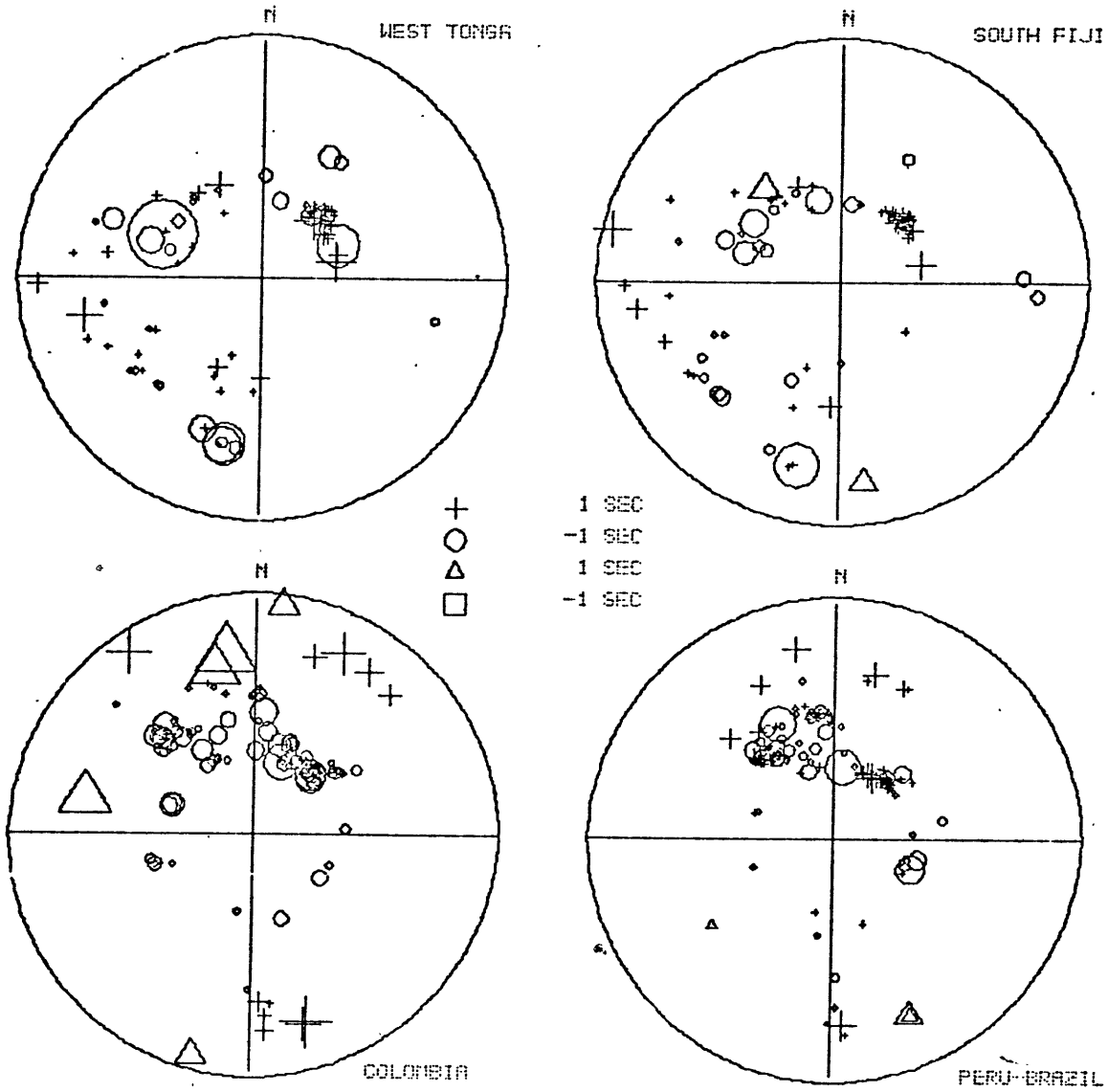

N
WEST TONGA
N
SOUTH FIJI
1 SEC
-1 SEC
1 SEC
-1 SEC
N
COLOMBIA
N
PERU-BRAZIL

Fig. A-3

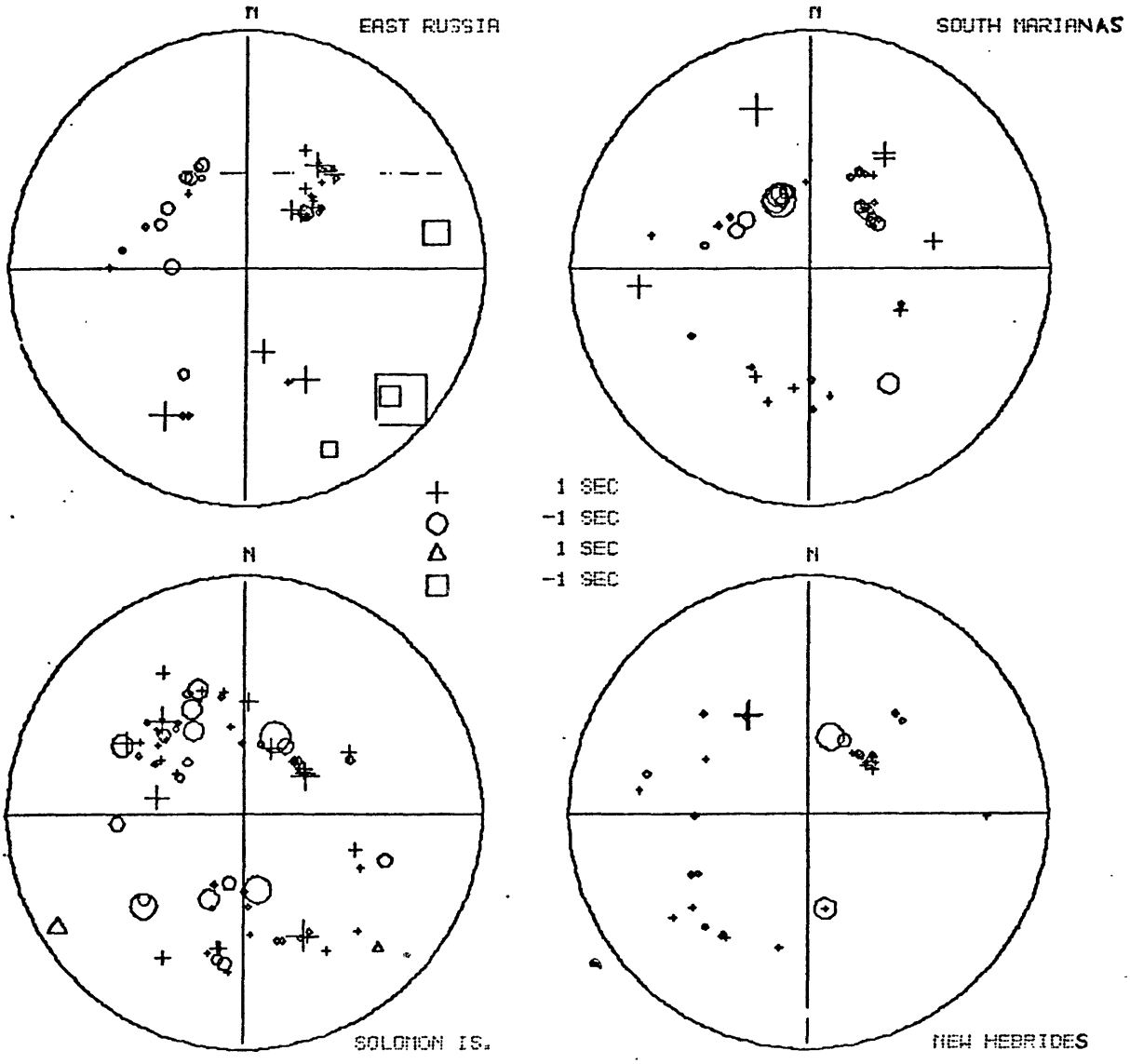

N
EAST RUSSIA
N
SOUTH MARIANAS
1 SEC
-1 SEC
1 SEC
-1 SEC
N
SOLOMON IS.
N
NEW HEBRIDES

Fig. A-3 (contd)

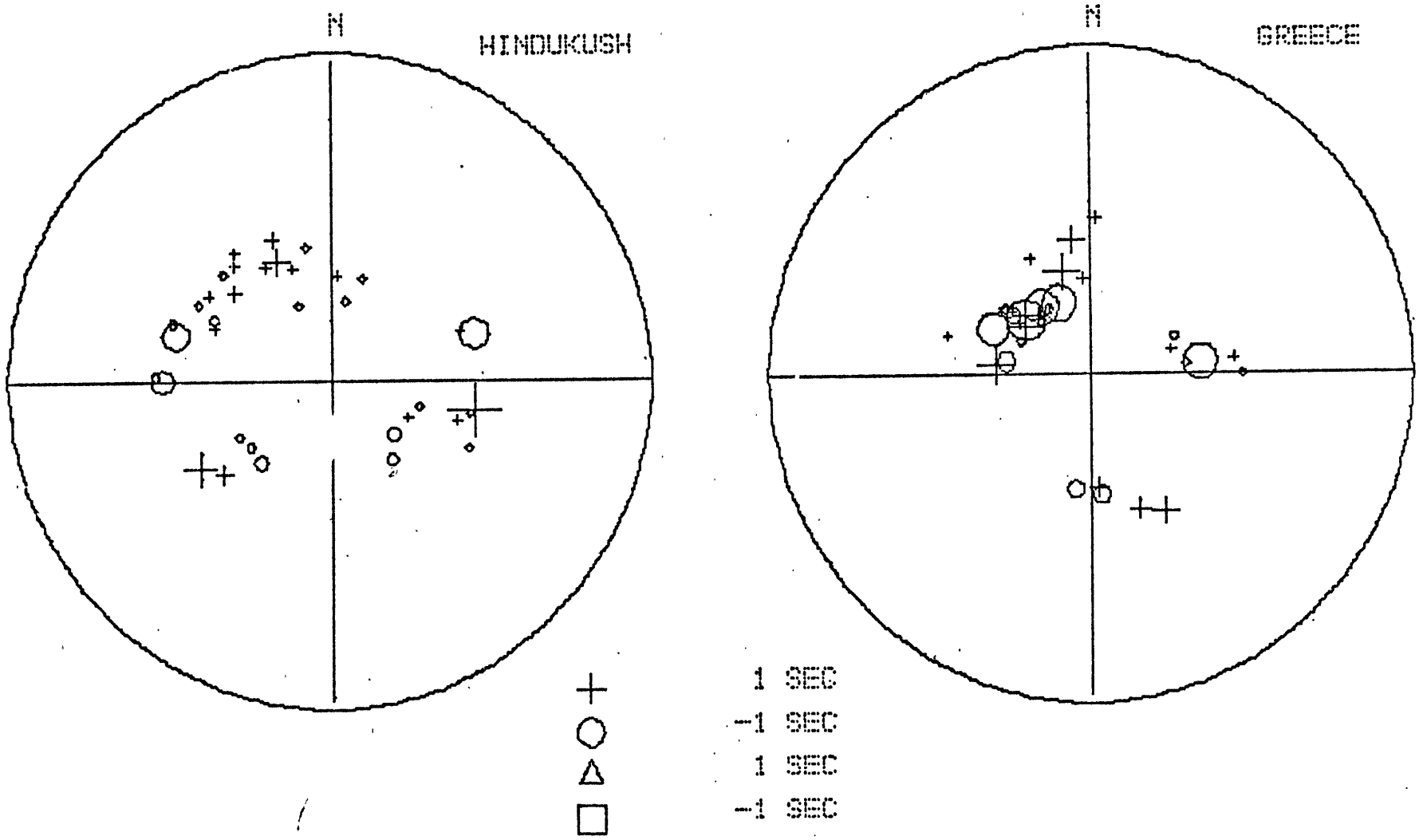


Fig. A-3 (contd)

APPENDIX B

Instrument Response Correction for Observed Amplitudes

Our amplitude data have been read from all six components of the world-wide standard seismograph (WWSS) stations. The precise values of amplitude corrections for the instrument response can only be made from the calibration curves shown on each seismograph. However, as the measurement errors in the amplitudes are normally large (even sometimes on the order of the amplitude itself), we have preferred to avoid that lengthy process. Instead, we have calculated the instrument response correction from the general calibration curves of short and long period system (WWSSN). Fig. B-1 shows the combined response curve of a WWSSN seismograph for the long and short periods. If the peak magnification of the seismograph is M_{Max} (which generally corresponds to 1 second period for the short period seismograph and 15 second period for the long period seismograph) and the relative response of the seismograph at period T_o is $M(T_o)$, then the instrument response correction (IRC) is given by $IRC = 1.0/[M_{Max} \times M(T_o)]$. The peak magnification, M_{Max} has been noted from each seismogram, and the relative magnification, $M(T_o)$ has been found from the interpolation of Table B-1. The period T_o has been directly measured from the seismogram corresponding to each of our amplitude data.

Table B-1

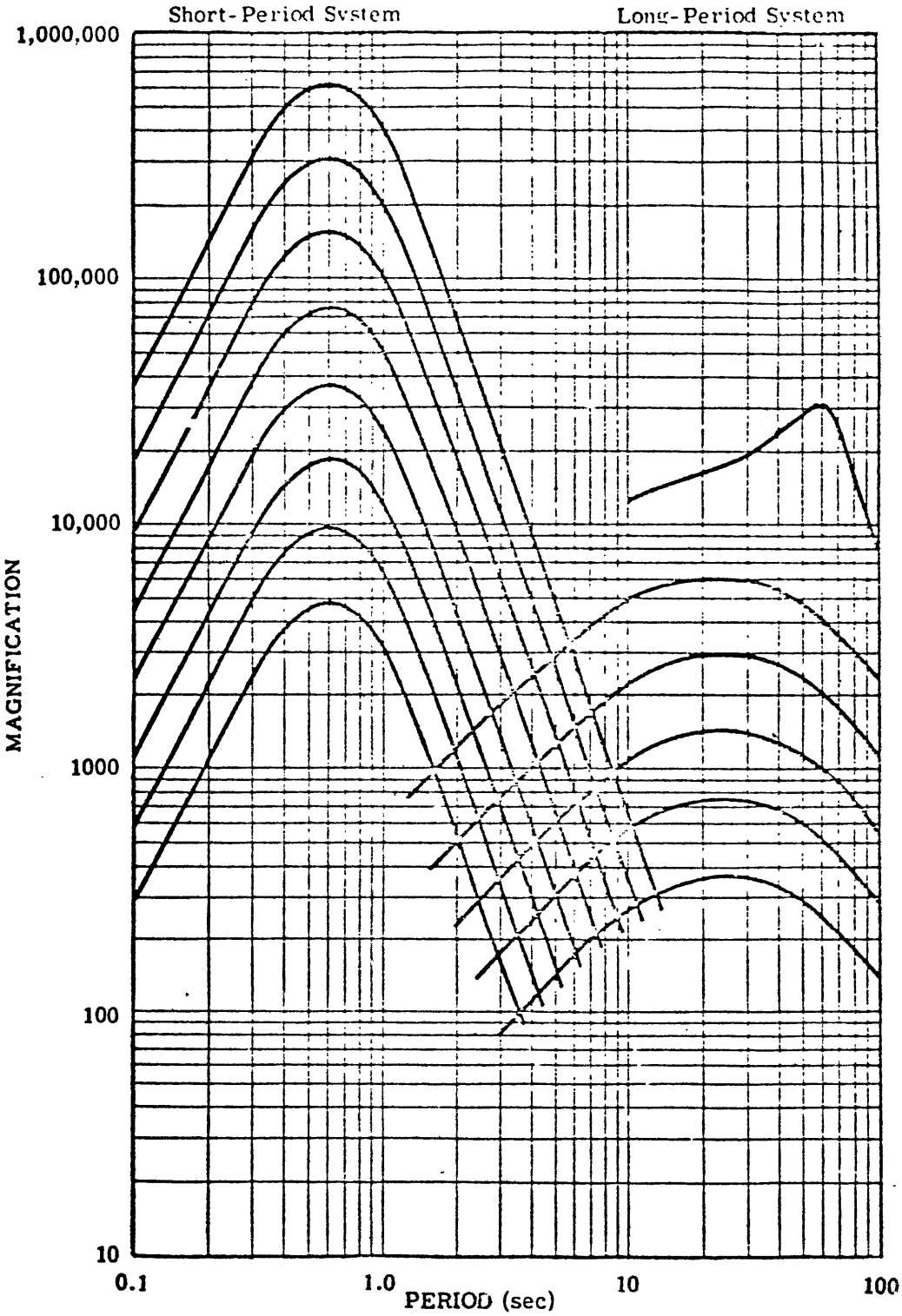
a) Frequency response of displacement in short period WWSSN seismographs (normalizing response to 1.0 at 1 second period)

Period	Response	Period	Response
0.1	0.09	1.6	0.30
0.2	0.36	1.7	0.26
0.3	0.77	1.8	0.22
0.4	1.18	1.9	0.19
0.5	1.42	2.0	0.17
0.6	1.50	2.1	0.15
0.7	1.46	2.2	0.13
0.8	1.34	2.3	0.11
0.9	1.19	2.4	0.10
1.0	1.00	2.5	0.09
1.1	0.79	2.6	0.08
1.2	0.64	2.7	0.07
1.3	0.52	2.8	0.07
1.4	0.43	2.9	0.06
1.5	0.36	3.0	0.05

b) Frequency response of displacement in long period WWSSN seismographs (normalizing response to 1.0 at 15 second period)

Period	Response	Period	Response
1.0	0.42	16.0	0.99
2.0	0.58	17.0	0.98
3.0	0.67	18.0	0.97
4.0	0.74	19.0	0.96
5.0	0.78	20.0	0.94
6.0	0.82	21.0	0.93
7.0	0.85	22.0	0.90
8.0	0.87	23.0	0.88
9.0	0.88	24.0	0.86
10.0	0.90	25.0	0.83
11.0	0.94	26.0	0.82
12.0	0.97	27.0	0.80
13.0	0.98	28.0	0.78
14.0	0.99	29.0	0.75
15.0	1.00	30.0	0.73

Figure B-1. Frequency response of the world wide standard seismograph for the ground motion displacement. This figure has been reproduced from a report by Espinosa et al. (1965).



FREQUENCY RESPONSE OF THE WORLD-WIDE STANDARD SEISMOGRAPH

Fig. B-1

APPENDIX C

Correction of Amplitudes for the Effect of Reflection and Transmission at the Major Discontinuities of the Earth

Among all discontinuities in the velocity structure of the earth's upper mantle and crust, the major sharp ones are possibly the free surface, Moho and 650 km discontinuity. Fig. C-1 shows the seismic velocities and densities related to these discontinuities, as taken from the B1 model of Jordan and Anderson (1974). We have corrected our amplitude data taking into consideration the frequency independent reflection and transmission coefficient at the above mentioned discontinuities for one way teleseismic ray paths (upwards) from the deep hypocenters. Small errors in the modelling of the discontinuities are not expected to introduce any severe bias in the analysis of our amplitude data as we will see later that the correction factors are nearly constant in the range of the epicentral distance of our interest, i.e. between 30° to 100°. It is also worth mentioning that we did not make any correction to the observed amplitudes for the 400 km discontinuity as Whitcomb (1973) reported that the 400 km discontinuity is not as good a reflector as the 650 km discontinuity. The effect of crustal layering, on

the other hand, may have a profound effect especially on the short period P wave amplitudes. But we preferred to incorporate this effect into 'station anomalies' (see Chap. 5) as the crustal structure is known to vary widely from site to site.

In our computation, we have treated each discontinuity as an interface between two homogeneous, elastic and isotropic half spaces. The reflection and transmission coefficients of the displacements of P, SV and SH waves have been computed for plane waves incident to those interfaces at angles corresponding to the ray parameters of our amplitude data. For SH waves, the computation of reflection and transmission coefficients at an interface is simple and straightforward. The expressions are given by Bullen (1963, p. 103, equations 8 and 9). For P and SV waves, the computation is complicated because of the coupling of P and SV waves at a given interface. The reflection and transmission coefficients of these two phases (P and SV) were computed by a program written by Dr. Clint Frasier of M.I.T. Lincoln Laboratory. The program employs the formulae described in a paper by Frasier (1975). We found that in the range of incidence angles of our interest, the phase difference between the reflected (or transmitted) wave and the incident wave at any of the three discontinuities

(Fig. C-1) is either close to 0° or 180°. This may assure some reliability of the corrections for the effect of these discontinuities. The program of Dr. Frasier computes the reflection/transmission coefficient as the ratio of two displacement vectors which are positive in the direction of phase velocity. Following this sign convection, we computed the <u>total</u> correction factor for P and SV amplitude, as measured on the earth's surface, to take into consideration the effect of transmission/reflection at all three discontinuities (Fig. C-1).

If T^2_{SV}, T^3_{SV} are the transmission coefficients of SV waves respectively for the Moho and 650 km discontinuity, R^1_{SV} and α^1_{SV} are respectively the reflection coefficients and the incidence angles of the corresponding SV rays on the free surface, then U_{SV} and W_{SV}, the correction factors respectively for the horizontal and vertical components of SV amplitudes can be easily shown to be equal to

$$U_{SV} = T^3_{SV} \cdot T^2_{SV} \cdot (1 + R^1_{SV}) \cdot \cos \alpha^1_{SV} \qquad (C.1)$$

$$W_{SV} = T^3_{SV} \cdot T^2_{SV} \cdot (1 - R^1_{SV}) \cdot \sin \alpha^1_{SV} \qquad (C.2)$$

Similarly W_p, the correction factors for the vertical component P wave amplitudes are given as follows:

$$W_P = T_P^3 \cdot T_P^2 \cdot (1 - R_P^1) \cdot \cos \alpha_P^1 \qquad (C.3)$$

Using the same type of notation, the correction factors (U_{SH}) for the SH amplitudes are given by

$$U_{SH} = T_{SH}^3 \cdot T_{SH}^2 \cdot (1 + R_{SH}^1) \qquad (C.4)$$

Above, R_{SH}^1, the reflection coefficient of SH wave at the free surface, is equal to 1.0. So,

$$U_{SH} = 2 \cdot T_{SH}^3 \cdot T_{SH}^2 \qquad (C.5)$$

Fig. C-2 shows the values of U_{SV}, W_{SV}, W_p and U_{SH} against the values of incidence angle on the earth's free surface. Those values have also been tabulated in the Tables C-1 and C-2. The observed amplitudes of the vertical component P waves and the horizontal components SV and SH waves were respectively divided by the corresponding factors of W_p, U_{SV} and U_{SH}.

Table C-1

Reduction factors for SV and P amplitudes for the effect of reflection/transmission at all three discontinuities (Fig. C-1)

Incidence angle on the earth's surface (degrees)	Ray parameters (sec/deg)		Reduction factors		
	S wave	P wave	SV (horizontal) (U_{SV})	SV (vertical) (W_{SV})	P (vertical) (W_P)
0.0	0.00	0.00	2.80	0.00	2.59
2.0	1.14	0.63	2.79	0.00	2.58
4.0	2.28	1.25	2.76	0.00	2.57
6.0	3.42	1.87	2.70	0.01	2.54
8.0	4.55	2.50	2.63	0.02	2.51
10.0	5.68	3.11	2.53	0.03	2.47
12.0	6.80	3.73	2.42	0.05	2.42
14.0	7.91	4.34	2.29	0.08	2.36
16.0	9.01	4.94	2.14	0.12	2.29
18.0	10.11	5.54	1.97	0.16	2.21
20.0	11.19	6.13	1.82	0.21	2.13
22.0	12.25	6.72	1.64	0.27	2.04
24.0	13.30	7.29	1.44	0.32	1.94
26.0	14.34	7.86	1.23	0.36	1.83
28.0	15.35	8.42	1.04	0.39	1.71
30.0*	-	8.97	-	-	1.57

*No corresponding P ray exists below the 650 km discontinuity for an angle of incidence more than 30° on the earth's surface given the model of Fig. C-1. For an SV ray, the threshold of angle of incidence is still lower - at 29°.

Table C-2

Reduction factors for SH amplitudes to take into account the effect of reflection/transmission at all three discontinuities in Fig. C-1.

Incidence angle on the earth's surface (degrees)	Ray parameter (sec/deg)	Reduction factor (U_{SH})
0.0	0.00	2.80
2.0	1.14	2.80
4.0	2.28	2.80
6.0	3.42	2.79
8.0	4.55	2.78
10.0	5.68	2.76
12.0	6.80	2.74
14.0	7.91	2.72
16.0	9.01	2.69
18.0	10.11	2.64
20.0	11.19	2.59
22.0	12.25	2.52
24.0	13.30	2.42
26.0	14.34	2.25
28.0	15.35	1.93
29.0*	15.85	1.55

*No corresponding SH ray exists below the 650 km discontinuity for an angle of incidence more than 29° on the earth's surface given the model of Fig. C-1.

Figure C-1. The velocity and density model of the three major sharp discontinuities in the earth's crust and upper mantle. This model was used to correct the observed amplitudes of P, SV and SH wave for the effect of reflection/transmission at these discontinuities. The parameter values of this model were taken from the B1 model of Jordan and Anderson (1974). In this figure, α is the P wave velocity, β, the shear velocity, ρ the density and 'i' the incidence angle.

Figure C-2. Reduction factors for the amplitudes of SH, P (vertical component), and SV (horizontal and vertical component) waves as a function of the incidence angle on the earth's surface. Observed amplitudes are to be divided by these factors to correct for the effect of reflection/transmission at all three discontinuities shown in Fig. C-1.

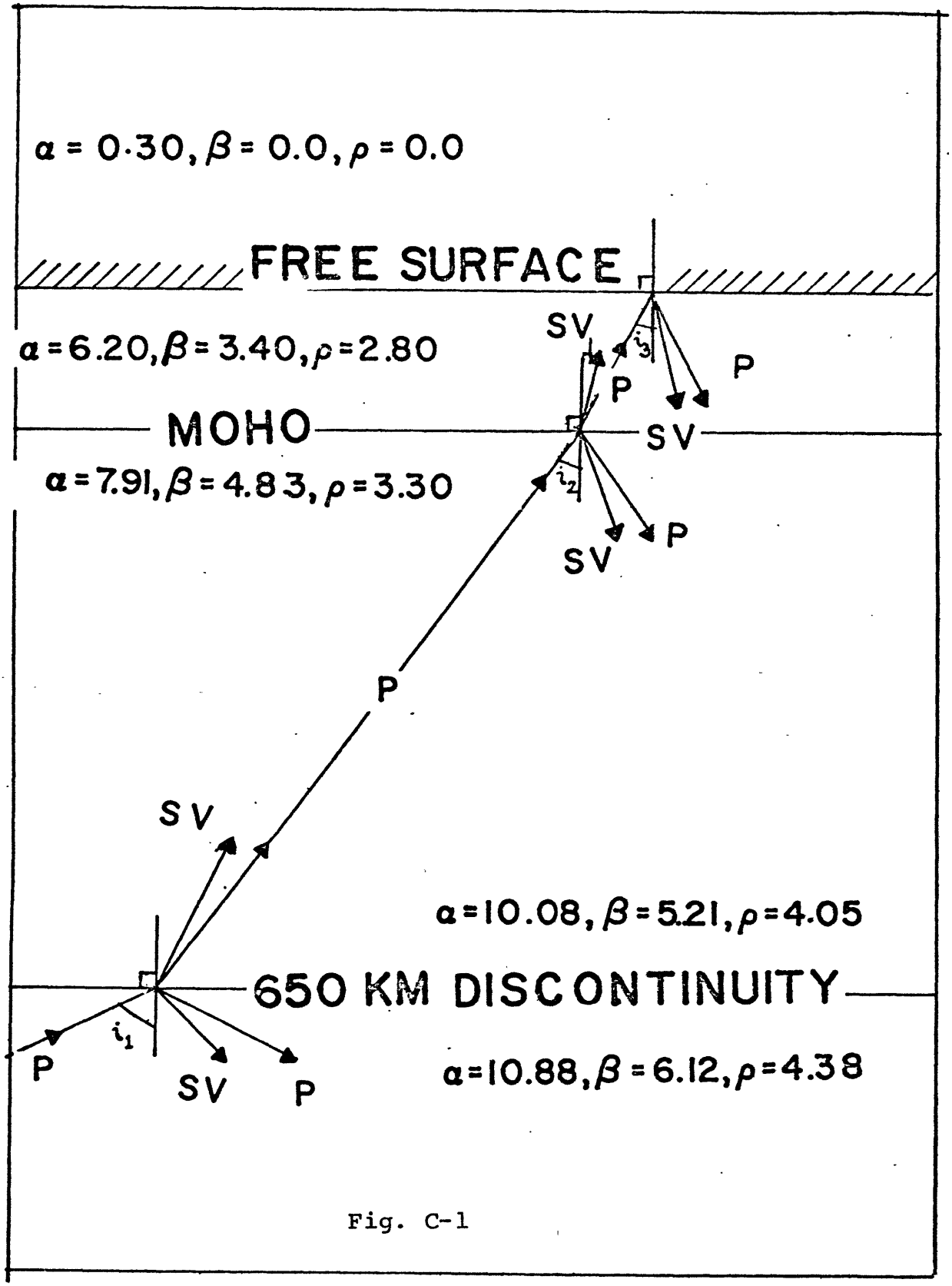

α = 0.30, β = 0.0, ρ = 0.0
FREE SURFACE
α = 6.20, β = 3.40, ρ = 2.80
MOHO
α = 7.91, β = 4.83, ρ = 3.30
α = 10.08, β = 5.21, ρ = 4.05
650 KM DISCONTINUITY
α = 10.88, β = 6.12, ρ = 4.38
SV
P
SV
P
P
SV
P
P
SV
P
SV
P
i1
i2
i3

Fig. C-1

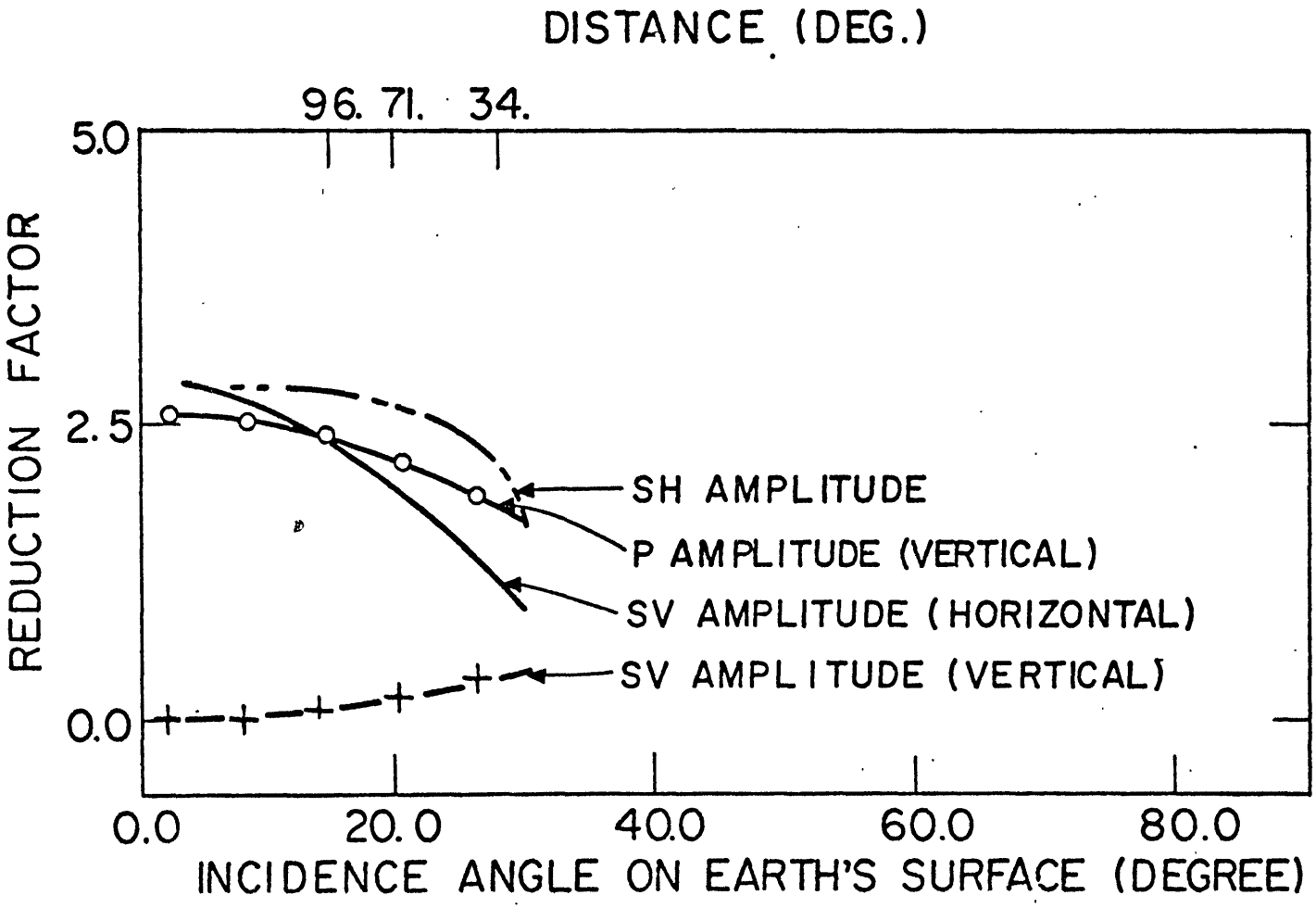

DISTANCE (DEG.)
96. 71. 34.
5.0
2.5
0.0
REDUCTION FACTOR
SH AMPLITUDE
P AMPLITUDE (VERTICAL)
SV AMPLITUDE (HORIZONTAL)
SV AMPLITUDE (VERTICAL)
0.0
20.0
40.0
60.0
80.0
INCIDENCE ANGLE ON EARTH'S SURFACE (DEGREE)

Fig. C-2

APPENDIX D

Determination of SH and SV Amplitudes and Calculation of S-polarization Angles

To determine the SH and SV amplitudes, we computed first the horizontal components of S wave displacements along and perpendicular to the great circle paths, noted below as U_R and U_H respectively. The former was assumed to be positive when directed towards the source as viewed from the station and the latter was assumed to be positive to the left when looking from the station to the source. If 'N' and 'E' represent the S wave displacements respectively, towards the North and East (the recorded amplitudes being already corrected for the instrument response to get the actual ground displacement) and 'α' the azimuth towards the epicenter as measured from the station (positive clockwise), then it can be easily shown that

$$\left.\begin{aligned} U_R &= N\cos\alpha + E\sin\alpha \\ U_H &= N\sin\alpha - E\cos\alpha \end{aligned}\right\} \quad (D.1)$$

Knowing the U_H and U_R, the SH and SV amplitudes can be computed as follows:

$$\left.\begin{aligned} (SH) &= U_H / U_{SH} \\ (SV) &= U_R / U_{SV} \end{aligned}\right\} \quad (D.2)$$

where U_{SH} and U_{SV} are respectively the reduction factors for SH and SV (horizontal component) waves to correct for the effect of propagation through the earth's crust and mantle. SV amplitudes could be determined also from the vertical component displacement, Z, by the following relation

$$(SV) = Z / W_{SV} \qquad (D.3)$$

where W_{SV} is the similar reduction factor as U_{SV} but computed for the vertical component of SV waves. As the vertical component S wave amplitudes were rarely measured and often not very reliable, we have preferred to calculate the SV amplitudes from (D.2) whenever possible.

For determination of the focal mechanism by S wave first motion data (see Appendix E), one must determine the angles of polarization, ϵ as defined by the angles between the S movement and the plane of incidence. Conventionally, 'ϵ' is given by

$$\epsilon = \tan^{-1}\left[(SH)/(SV) \right] \qquad (D.4)$$

or from (D.1) and (D.2)

$$\epsilon = \tan^{-1}\left(\frac{U_H}{U_R} \cdot \frac{U_{SV}}{U_{SH}} \right) \qquad (D.5)$$

To determine correctly ϵ at the focus, the effect of propagation must be taken into account through the reduction factors U_{SV} and U_{SH} in (D.5). The reduction factors U_{SH} and U_{SV} (and W_{SV}) are in general functions of the frequency of S wave, epicentral distance and the layered structure of the earth, especially near the receiving stations. Nuttli (1964) computed these correction factors for different crustal layering, wave periods and epicentral distances to determine correctly the S polarization angles from the S wave particle motion diagrams. However, our data of S wave displacements are very crude in the form of only measurements of peak to peak amplitudes, so we preferred a simpler calculation of the reduction factors of U_{SH}, U_{SV} (and W_{SV}) as described in Appendix C. We should note in this connection that the usual practice among the seismologists is to shortcut the computation of polarization angles from a relationship like

$$\epsilon = \tan^{-1}\left(\frac{U_H}{U_R} \right) \qquad (D.6)$$

instead of using (D.5). In other words, they assume,

$$\frac{U_{SV}}{U_{SH}} \simeq 1 \qquad (D.7)$$

Limitations of the above assumption have been discussed in detail by Nuttli and Whitmore (1962). Our computations of U_{SV} and U_{SH} (Tables C-1 and C-2 in Appendix C) show that the ratio of U_{SV} to U_{SH} is in fact as low as 0.70 around 70° distance and reduces further to 0.54 at 30° distance.

We must emphasize that in equation (D.1), the displacements 'N' and 'E' are assumed to be positive respectively towards the North and East and negative towards the South and West. So, when it is possible to observe the first motions of S wave on the horizontal seismograms (which are often hard to observe), one can correctly obtain the directions of S polarization in addition to the polarization angles as determined from the equation (D.5). If we fail to observe, on the other hand, the first motions of S wave on the N-S and E-W seismograms and read the amplitudes half a period too late, we are still able to determine the S polarization angles correctly though the directions of polarizations will be in error by 180°.

APPENDIX E

Determination of the Focal-mechanisms of the Deep Earthquakes Used in the Study and Calculation of the Radiation Correction

Of the 14 deep events used in this study, reliable focal-mechanisms for 7 events existed already in literature (see Table 2-3 in Chap. 2). For the remaining events, we determined the orientation of nodal planes from both the first motion data of P-wave and the polarization angle data of S wave. These are shown in Fig. E-1 on the equal area projections of the lower half of the focal sphere.

The data of P wave first motions were read from both the long and short period vertical components of WWSSN seismograms. For deep earthquakes, the first motions of P waves could be often picked more reliably from the short period seismograms than the long period ones (Fig. E-2). Some first motion data of P (and pP) waves on the upper half of the focal sphere were also read. By the symmetry of the double couple model, they were included in the projections (Fig. E-1) through "inversion" about the center of the focal sphere. Through visual inspection, two orthogonal planes were drawn in the plane of projection (solid lines of Fig. E-1) to satisfy the first motion data in the framework of the double couple model.

The reliability of P nodal planes was checked by the

S-polarization angles. These S-polarization angles were determined from both short and long period records of WWSSN seismograms. Appendix D elaborates the method of determination of these polarization angles. Those angles were measured counterclockwise at the station with respect to the incidence planes but were plotted clockwise in the projections (Fig. E-1) due to the change of sense of the horizontal component of SV wave during the ray tracing from a station to the source. Note that because of the preceding coda, it was sometimes difficult to observe a small S wave first motion. Instead, the amplitudes were read a half-period too late. That is why some of the observed S wave first motions in Fig. E-1 are 180° out of phase with the ones predicted from the nodal planes determined from P wave first motions. It is worth mentioning also that the assumption of a S-polarization angle remaining constant all along a seismic ray, from the source to a station, is more extreme than the conservation of the polarity of P wave first motions (Stauder, 1962). The change in polarization angles during propagation through the mantle and the crust may be different from what we accounted for in Appendix D. This may explain a part of the difference between the observed and the predicted S-polarization angles in Fig. E-1. Observational errors could obviously be other reasons for such discrepancy. To minimize the effect of the observational errors of S-polarization angles for the

check of reliability of the nodal planes determined from P wave first motions, we inverted the observed S-polarization angles through a least square method (Hirasawa, 1966) to obtain also the dip directions and dip angles of the two P-nodal planes (dotted lines of Fig. E-1). Starting solutions in this least square method were the nodal planes determined from P wave first motion data. With a background of the errors expected in S-polarization angles, agreement between the two sets of P-nodal planes - one from P (and pP) wave first motions and another from S wave first motions, may be considered satisfactory.

Isacks and Molnar (1972) showed previously that for the deep earthquakes a parallelism exists between the stress axes (which were assumed to be 'P' and 'T' axes of the fault plane solution) and the planar geometry of the seismic zones. The deep focus earthquakes are strongly dominated by the down-dip compression whereas the intermediate-depth solutions are more variable and include down-dip compression or extension or neither of the two. Our fault plane solutions mostly confirm their results, indicating down-dip compressions for the deep earthquakes beneath the Java Sea, the Sea of Okhotsk and the South Marianas. The down-dip tension for the deep earthquake beneath the Banda Sea is an exception to this rule but at this end of the Sunda Arc there is a pronounced bending in the descending lithospheric slab. This may change

the usual stress pattern within the slab. Two intermediate focus earthquakes further to the east of this event also had down-dip tension in the study of Isacks and Molnar (1972). However, they did not have data from the deep earthquakes in this region. In our fault plane solutions, another deep event near the eastern border of U.S.S.R. showed exceptionally large strike-slip component (Fig. E-1) than what would be expected for such a deep event. But the parameter of this solution that is the most nearly parallel to the dip of the seismic zone is still the P axis. The two other earthquakes - one at Hindukush and the other in Greece - are of intermediate depth and show down-dip tension. Isacks and Molnar (1972)also found that down-dip extension at intermediate depth is predominant in regions where no deep earthquakes are present.

Radiation correction. For the purpose of expressing the theoretical displacement for a double-couple source, let us choose an x, y, z - coordinate system with origin at the focus and assume that the double couple forces are acting parallel to the x and y axes. Let us further denote K(t) as a time (t) dependent single force of the double couple system. Also, we specify $\bar{x}$, $\bar{y}$, $\bar{z}$ to be the axes of a geographic system whose origin coincides with that of the x, y, z system. The orientation of the observed nodal planes is generally given with respect to the geographic

system where $\bar{x}$ axis is directed to the North, $\bar{y}$ to the East and $\bar{z}$ vertically downward. If we let U_P, U_{SV} and U_{SH} represent the theoretical displacements in P, SV and SH wave at a great distance from the double couple source, then we can express them as follows (Bessenova et al., 1960; Stauder, 1962):

$$\left.\begin{aligned} U_P &= 2xy\, K'(t - R/a)/4\pi\rho a^3 R^3 \\ U_{SV} &= D\, K'(t - R/b)/4\pi\rho b^3 R^3 \\ U_{SH} &= -C\, K'(t - R/b)/4\pi\rho b^3 R^3 \end{aligned}\right\} \quad (E.1)$$

where ρ is the density, a the P wave velocity, b the S wave velocity and K'(t) the time derivative of K(t). 'C' and 'D' in equation (E.1) are given as follows:

$$\left.\begin{aligned} C &= \frac{(\alpha_x y + \alpha_y x)\bar{y} - (\beta_x y + \beta_y x)\bar{x}}{\sin i_h} \\ D &= \frac{2xy\cos^2 i_h - \bar{z}(\gamma_x y + \gamma_y x)}{\sin i_h \cos i_h} \end{aligned}\right\} \quad (E.2)$$

Above, α_q, β_q, γ_q are the direction cosines of q-axis (i.e. x, y or z) with respect to $\bar{x}$, $\bar{y}$, $\bar{z}$ axes respectively

and i_h is the take-off angle of the corresponding seismic ray at the focus measured with respect to the direction from the focus to the center of the earth. Now if ϕ is the azimuth of the ray path at the epicenter towards the station, AZ_x and AZ_y are the azimuths of the poles of the two nodal planes, PL_x and PL_y are the corresponding dip angles (measured from the horizontal) of those poles, then the following expressions can be derived:

$$\left.\begin{aligned} x &= \alpha_x \bar{x} + \beta_x \bar{y} + \gamma_x \bar{z} \\ y &= \alpha_y \bar{x} + \beta_y \bar{y} + \gamma_y \bar{z} \end{aligned}\right\} \quad (E.3)$$

Where,

$$\left.\begin{aligned} \bar{x} &= \cos\phi \cdot \sin i_h \\ \bar{y} &= \sin\phi \cdot \sin i_h \\ \bar{z} &= \cos i_h \end{aligned}\right\} \quad (E.4)$$

and

$$\left.\begin{aligned} \alpha_x &= \cos AZ_x \cdot \cos PL_x \\ \beta_x &= \sin AZ_x \cdot \cos PL_x \\ \gamma_x &= \sin PL_x \\ \alpha_y &= \cos AZ_y \cos PL_y \\ \beta_y &= \sin AZ_y \cos PL_y \\ \gamma_y &= \sin PL_y \end{aligned}\right\} \quad (E.5)$$

Signs of U_P, U_{SH} and U_{SV} calculated from the formulaes in (E.1) correspond to the orientation of the double couple such that (PL_x, AZ_x) and (PL_y, AZ_y) represent the directions of the force vectors. The formulae also make use of a convention that P is positive when directed away from the focus, SH is positive when directed clockwise (to the right as one looks along the azimuth of the ray with back to the focus), and SV is positive when directed upward from the ray in the plane of incidence. All the terms in (E.1) except for 2xy, D and (-C) are constant on the focal sphere. Thus the observed P, SV and SH amplitudes, when divided by 2xy, D and (-C) respectively, are corrected for the radiation pattern at the source.

In Fig. E-3, we show the contours of P, SV and SH displacements computed from (E.1) for pure strike slip and dip slip faults. From these figures it is apparent that the reliable determination of the radiation correction depends critically on how well the nodal planes are constrained. A small error in determining the orientation of nodal planes can cause a large difference in the computed radiation correction.

Figure E-1 (8 plates). Focal mechanisms for seven deep events as determined from data of this study. On the left P and pP first motion data are shown on equal area projection of the lower half of the focal sphere and on the right, the S wave first motion data on the same projection. The first motion data for the upgoing rays are shown in these projections through "inversion" about the center of the focal sphere. For pP first motions, we assumed also a polarity change on reflection at the free surface. Observed S wave polarization angles have been plotted clockwise with respect to the radial lines. Solid great circles are nodal planes determined exclusively from P (and pP) wave first motion data whereas dashed great circles are nodal planes determined exclusively from S wave first motion data. 'T' and 'P' are tension and pressure axes respectively. Legend of the other symbols are given in the very first plate. Note that the predicted S wave first motions are based on the nodal planes determined from P wave first motion data.

Figure E-2. (2 plates). Some examples of P and pP first motion signals of deep events as recorded on the short period and long period vertical (Z) component of WWSSN seismograms. Notice that qualities of the short period P wave first motion data are in general better than those from the long period records. The opposite seems to be

true for the first motion of pP. 'Δ' in the figure represents the epicentral distance in degrees. Locations of the events are shown in Table 2-1 (Chap. 2).

Figure E-3 (3 plates). Contours for the theoretical displacements (0.1, 0.2 and 0.5 units, maximum displacement being 1.0 unit) of P, SV and SH wave for a pure strike-slip (strike = N45°E, dip = 90° from horizontal) and a pure dip-slip (strike = north, dip = 45° from horizontal) fault. Dashed lines are the nodal planes. Thick solid lines are the orientation of the fault plane and the auxiliary plane, when they aren't the nodal planes.

LEGEND

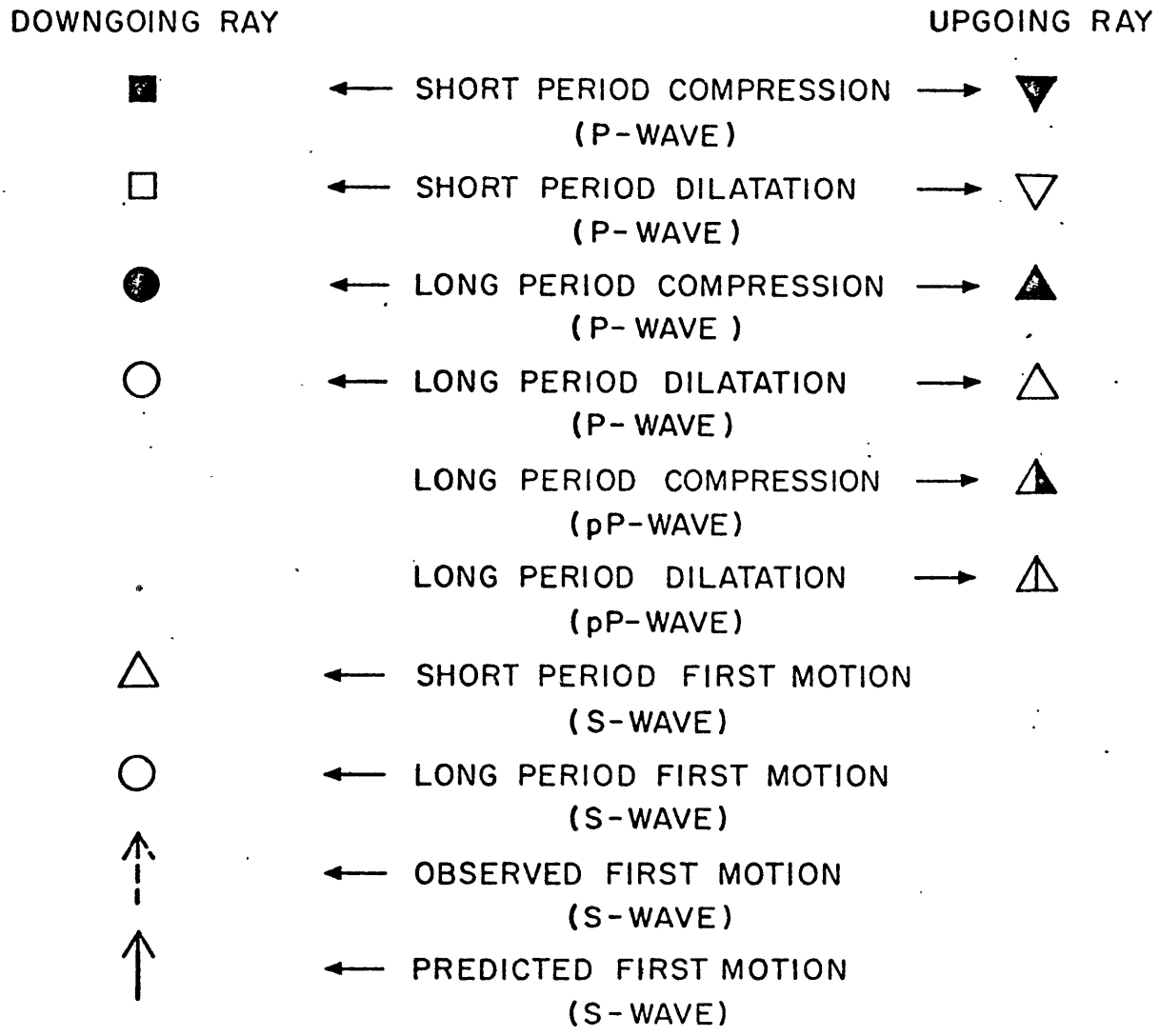


Fig. E-1

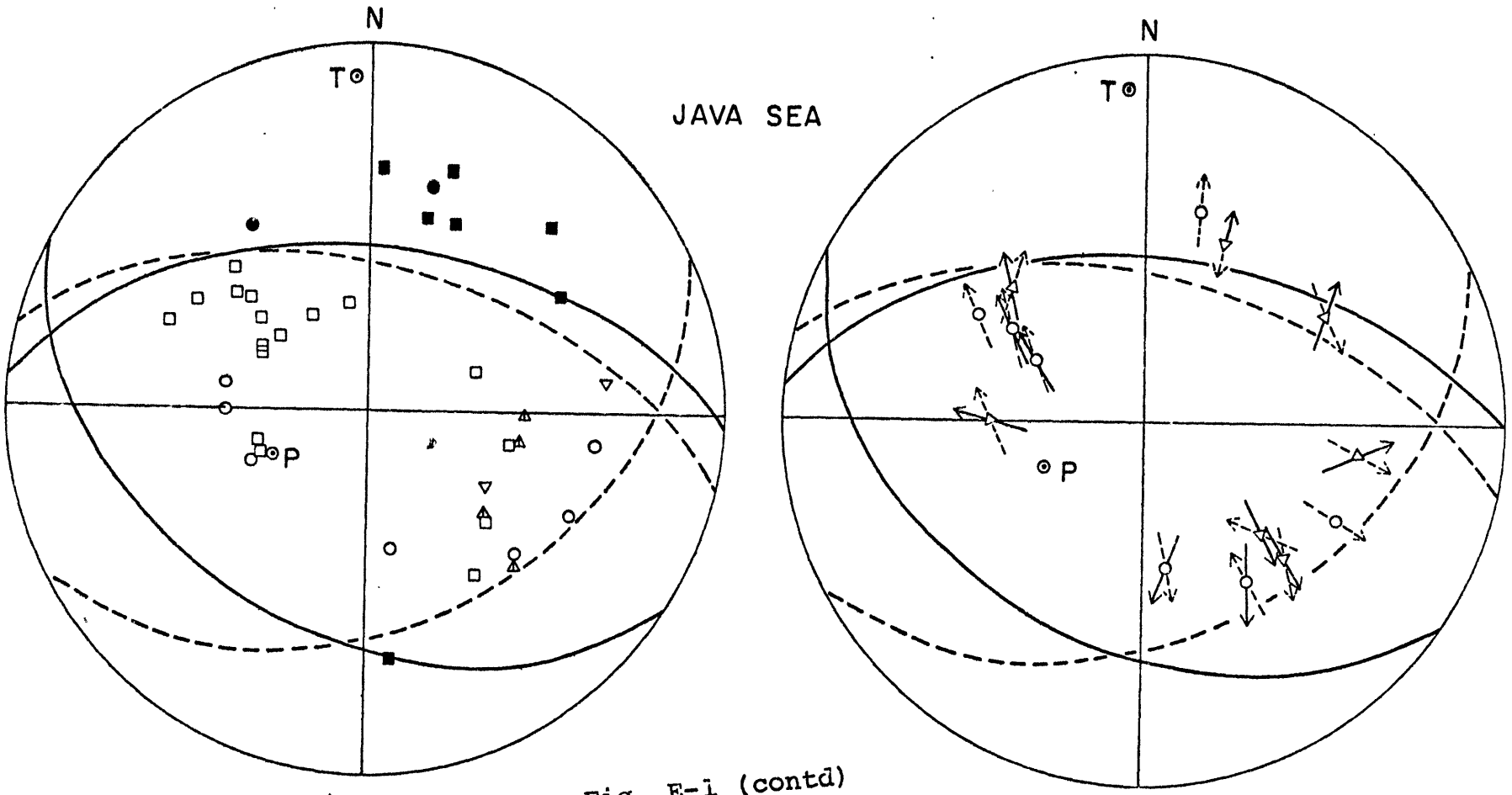


Fig. E-1 (contd)

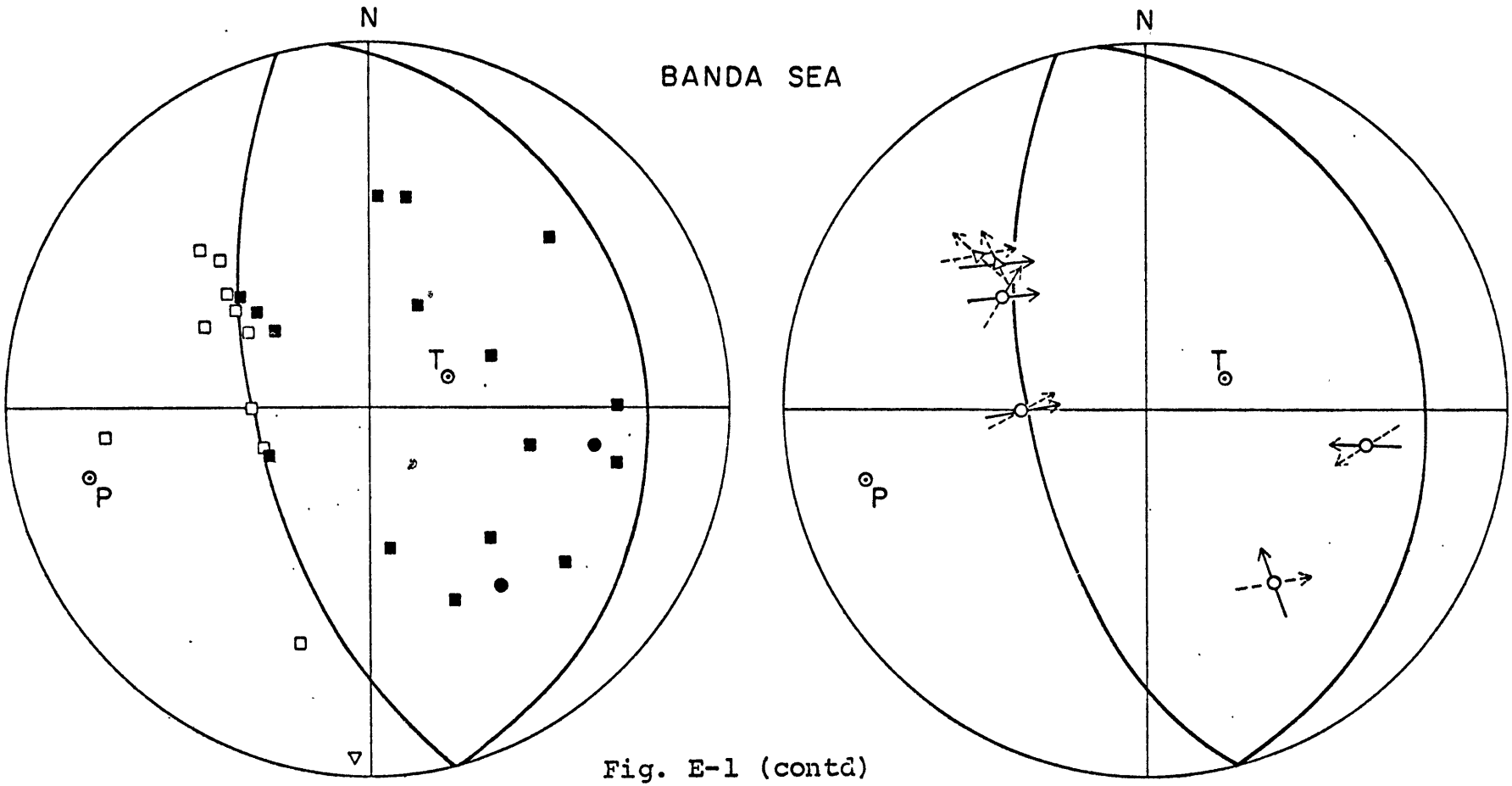


Fig. E-1 (contd)

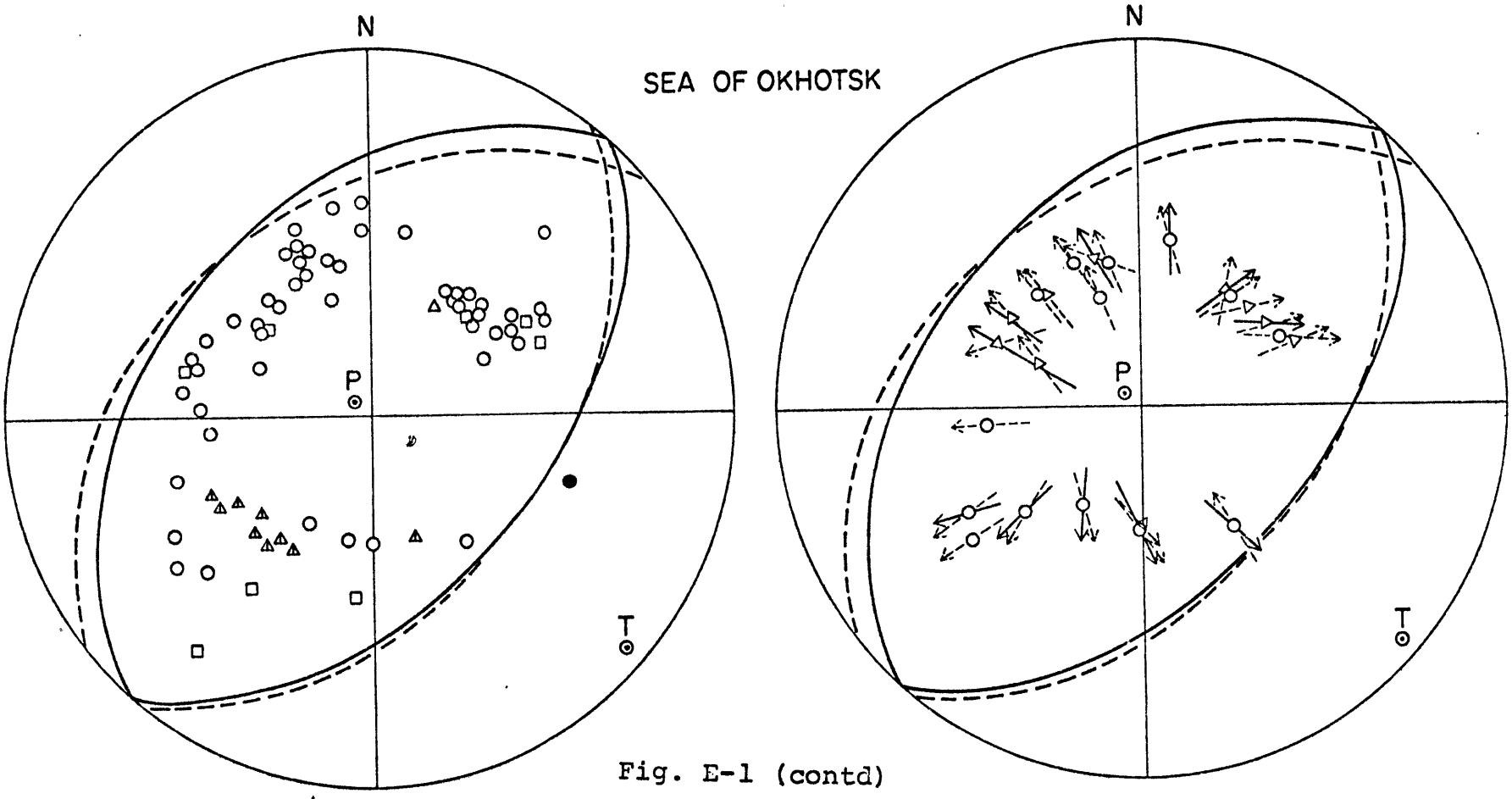


Fig. E-1 (contd)

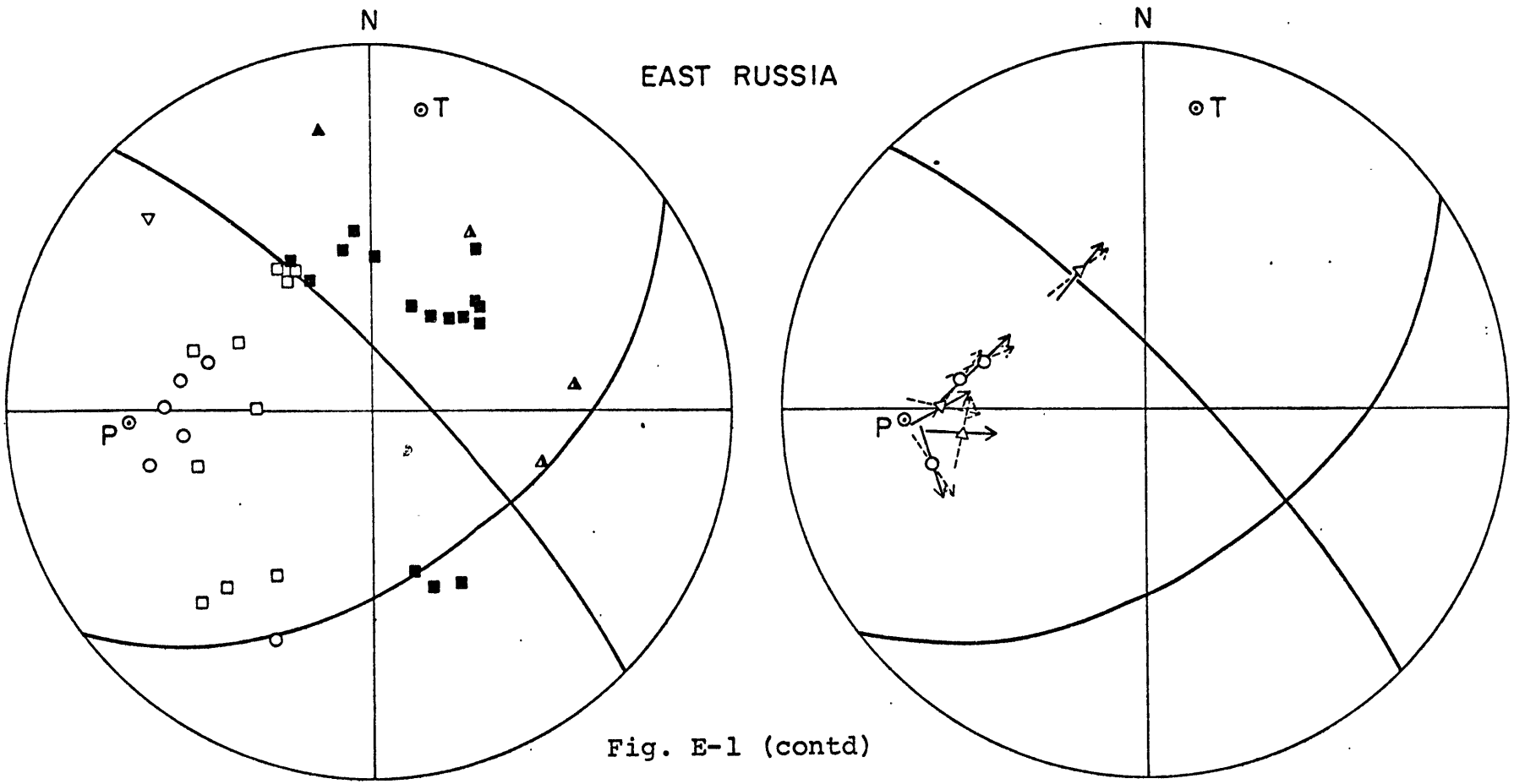


Fig. E-1 (contd)

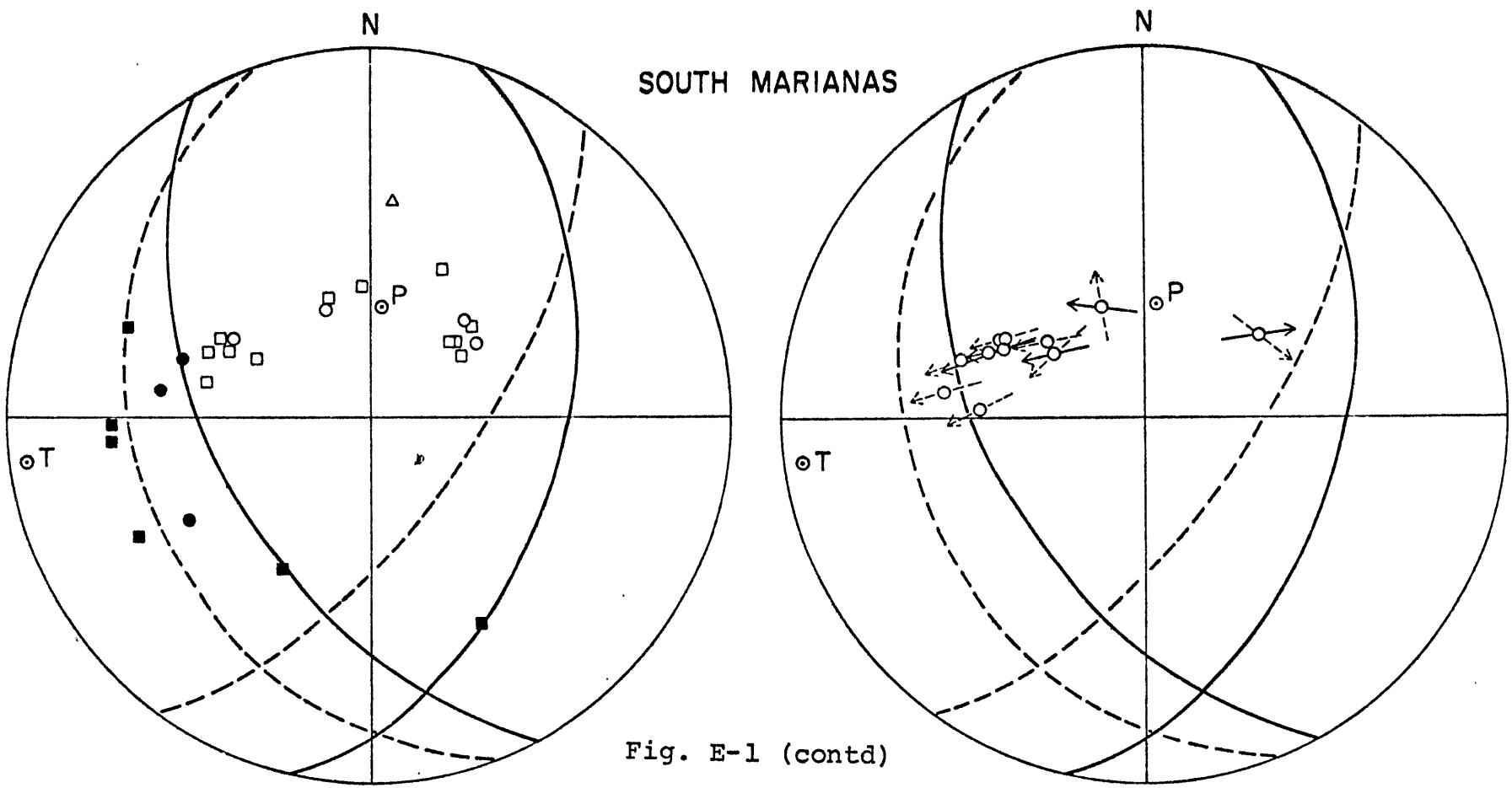


Fig. E-1 (contd)

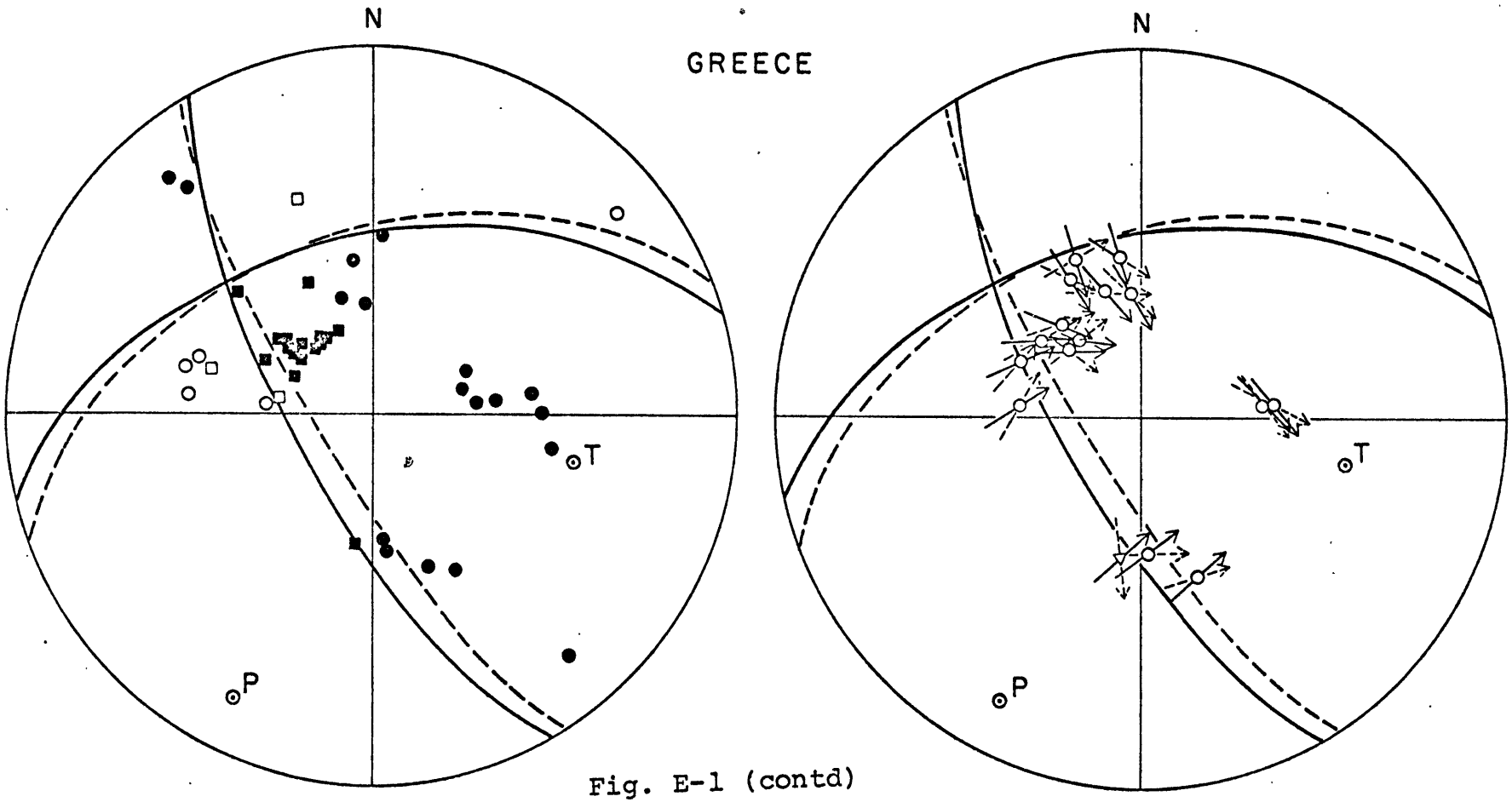


Fig. E-1 (contd)

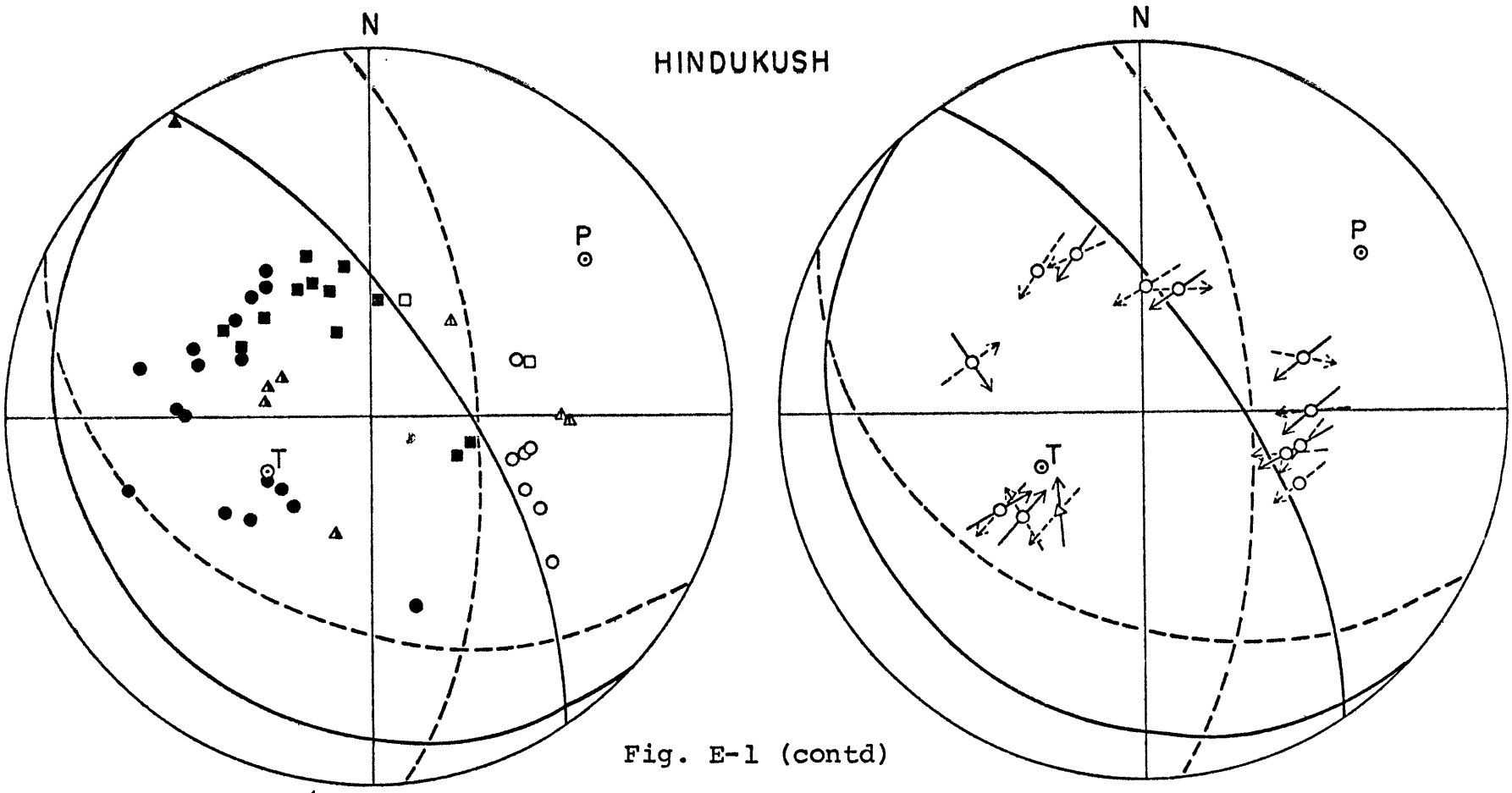


Fig. E-1 (contd)

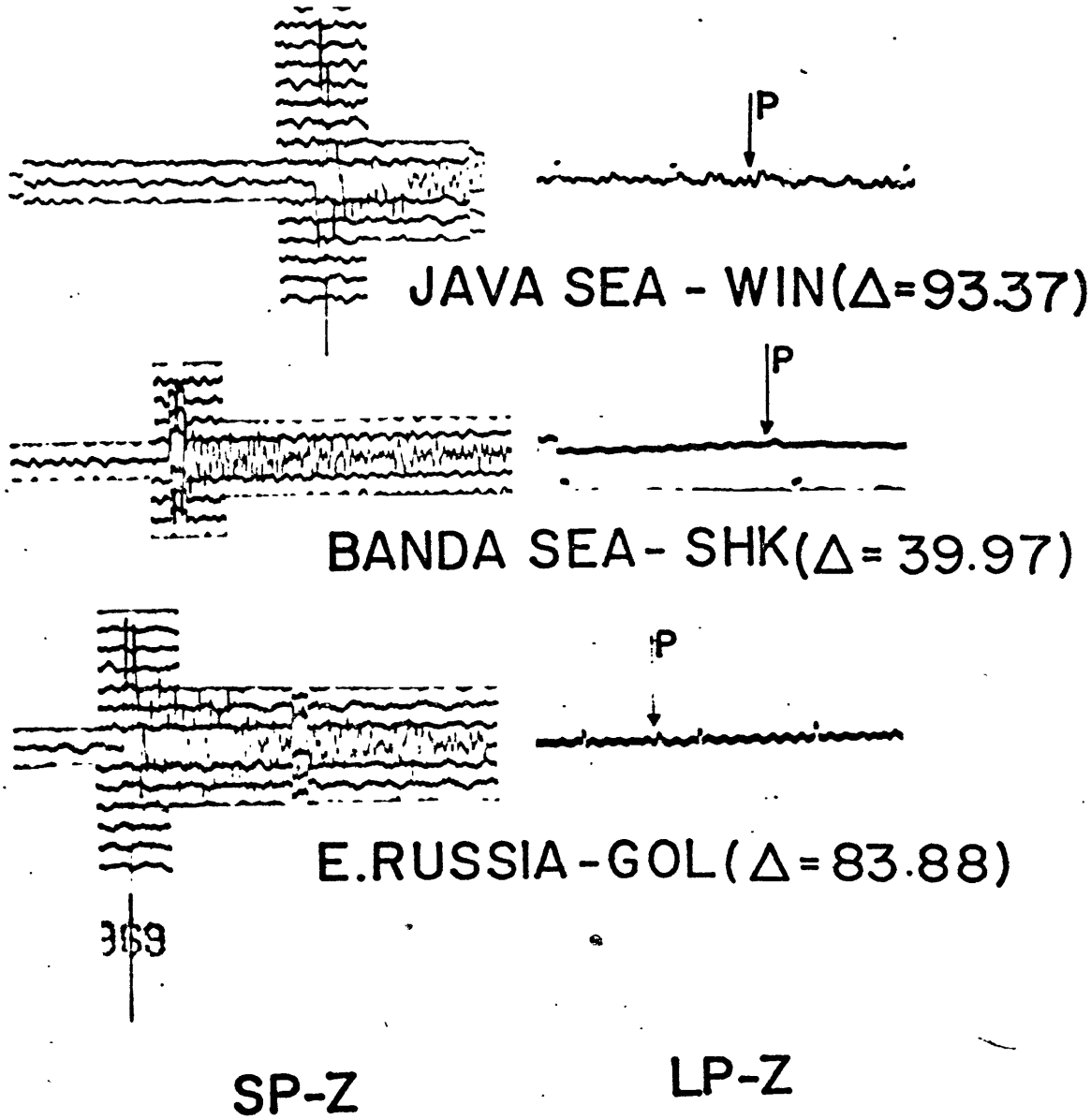

P
JAVA SEA - WIN(Δ=93.37)
P
BANDA SEA- SHK(Δ=39.97)
P
E.RUSSIA-GOL(Δ=83.88)
SP-Z
LP-Z

Fig. E-2

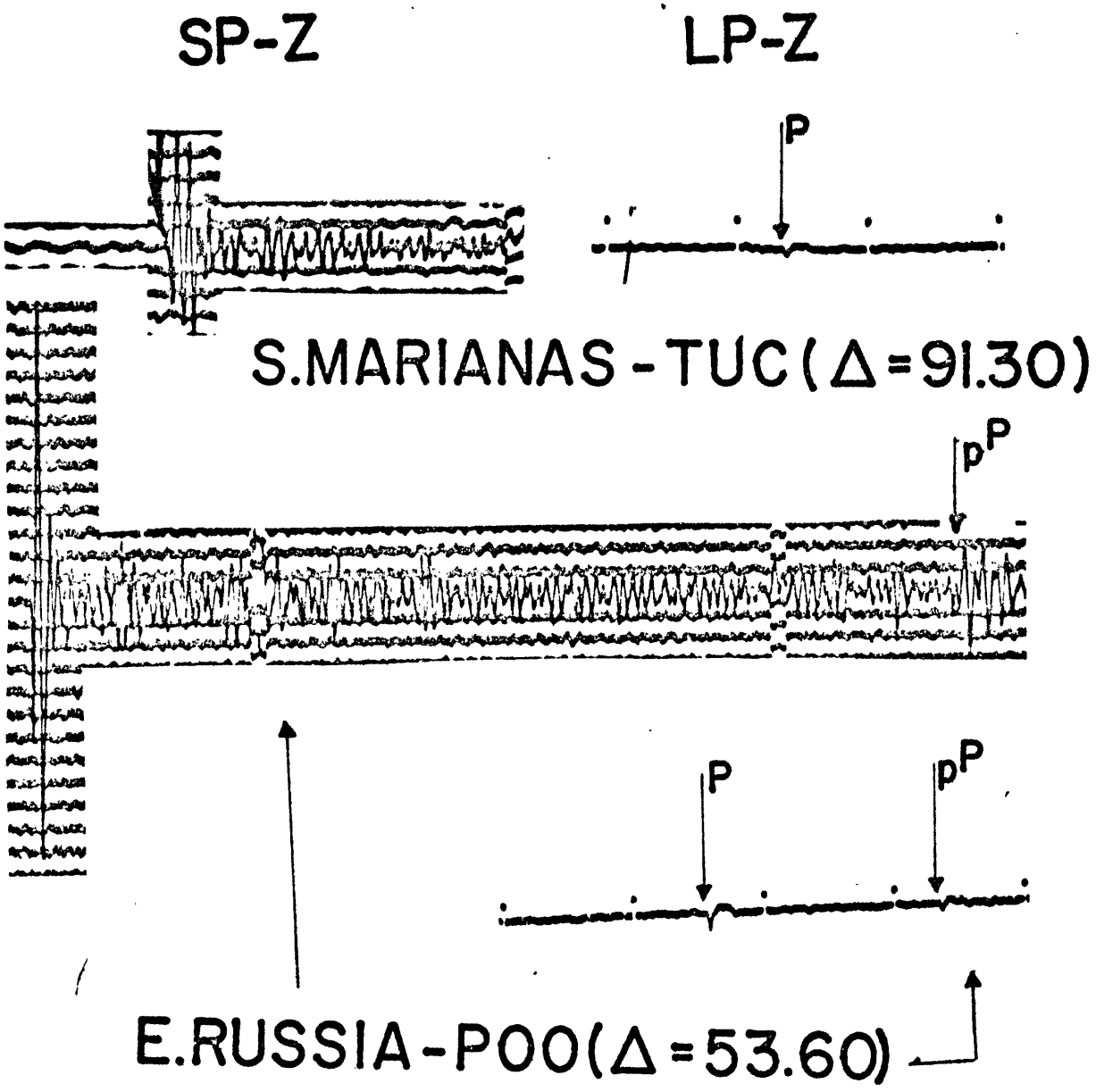


Fig. E-2 (contd)

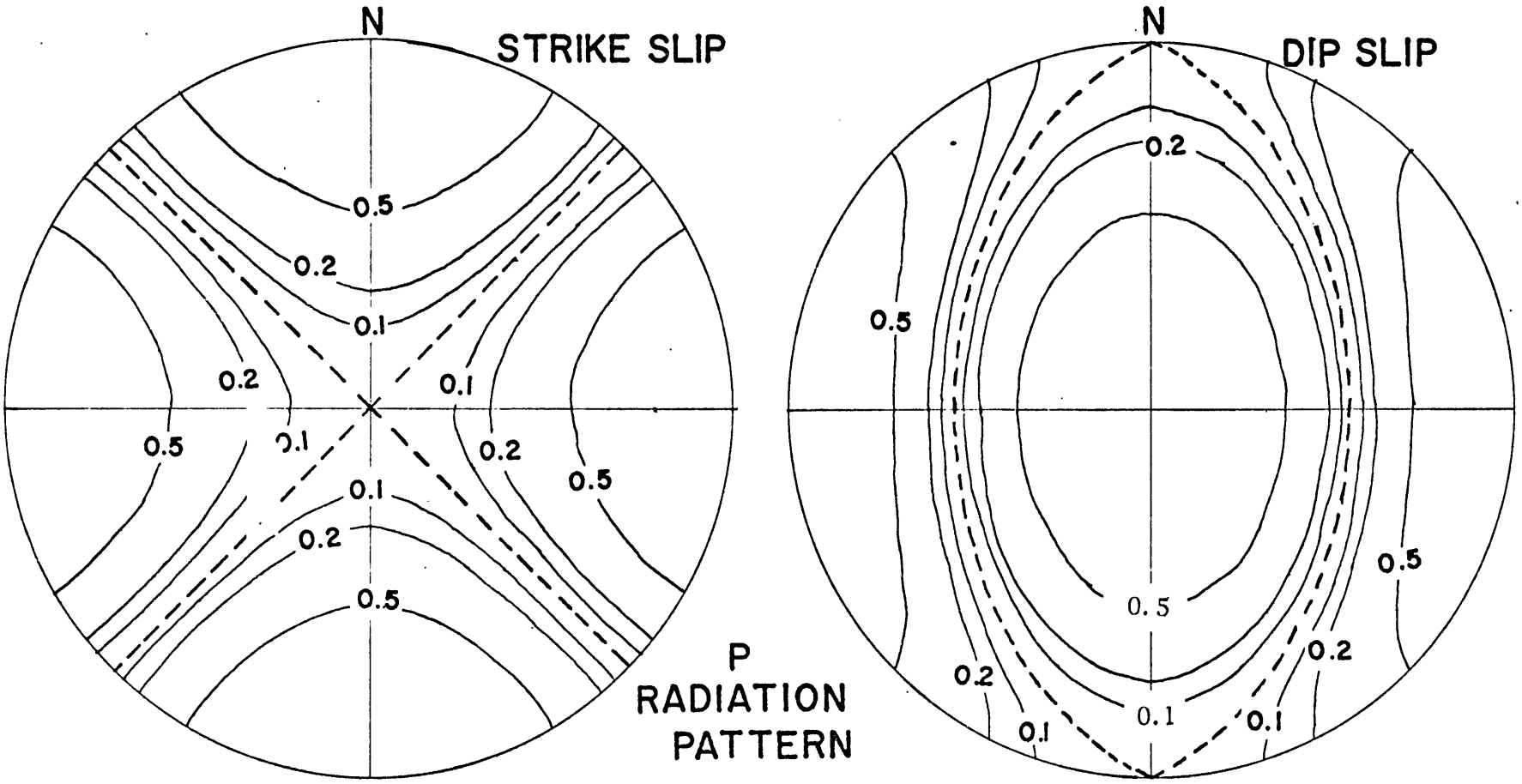

N
STRIKE SLIP
0.5
0.2
0.1
0.2
0.1
0.5
0.1
0.2
0.5
0.1
0.2
0.5
N
DIP SLIP
0.2
0.5
0.5
0.2
0.1
0.1
0.2
0.5
P
RADIATION
PATTERN

Fig. E-3

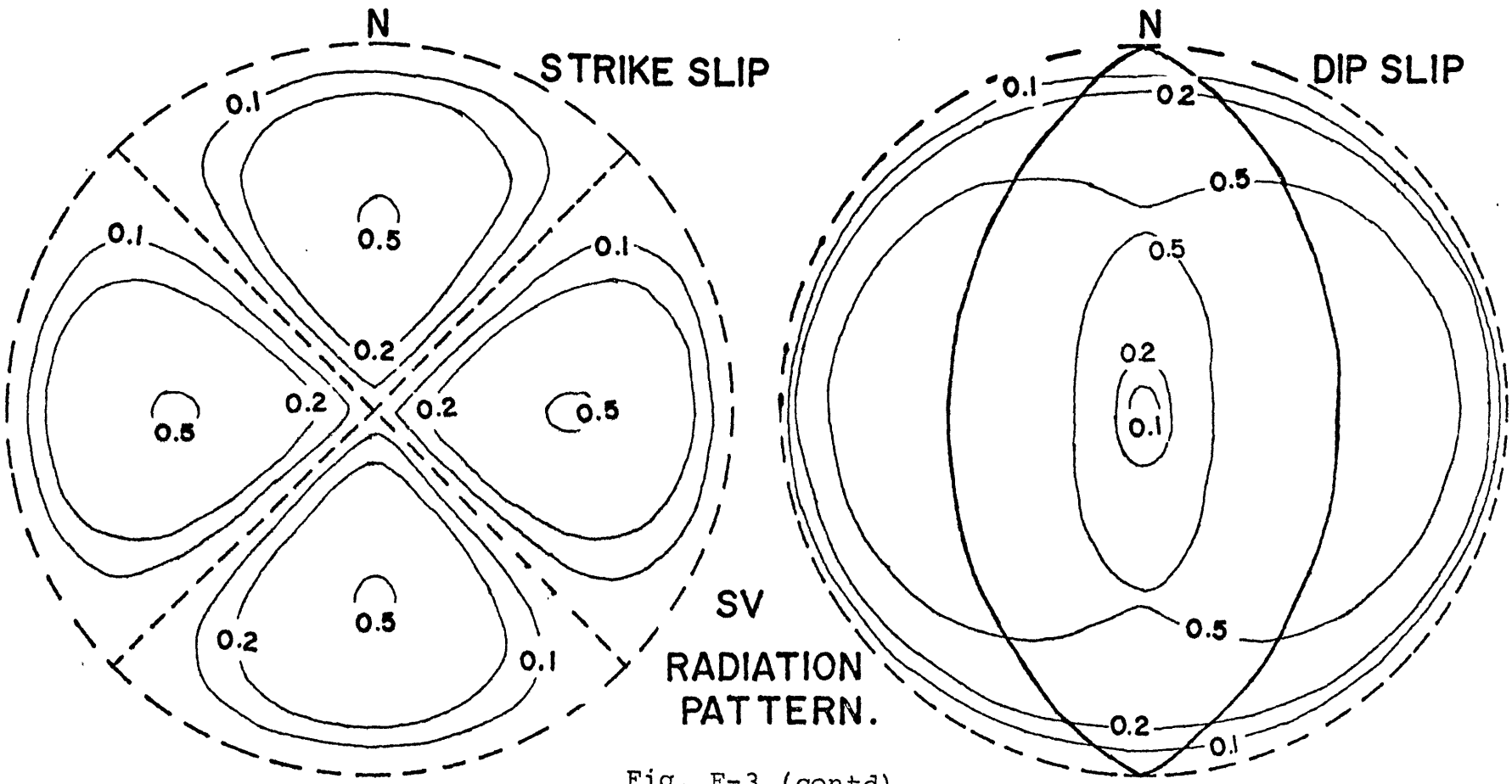

N
STRIKE SLIP
0.1
0.1
0.5
0.1
0.2
0.2
0.2
0.5
0.5
0.2
0.5
0.1
SV
RADIATION
PATTERN.
N
DIP SLIP
0.1
0.2
0.5
0.5
0.2
0.1
0.5
0.2
0.1

Fig. E-3 (contd)

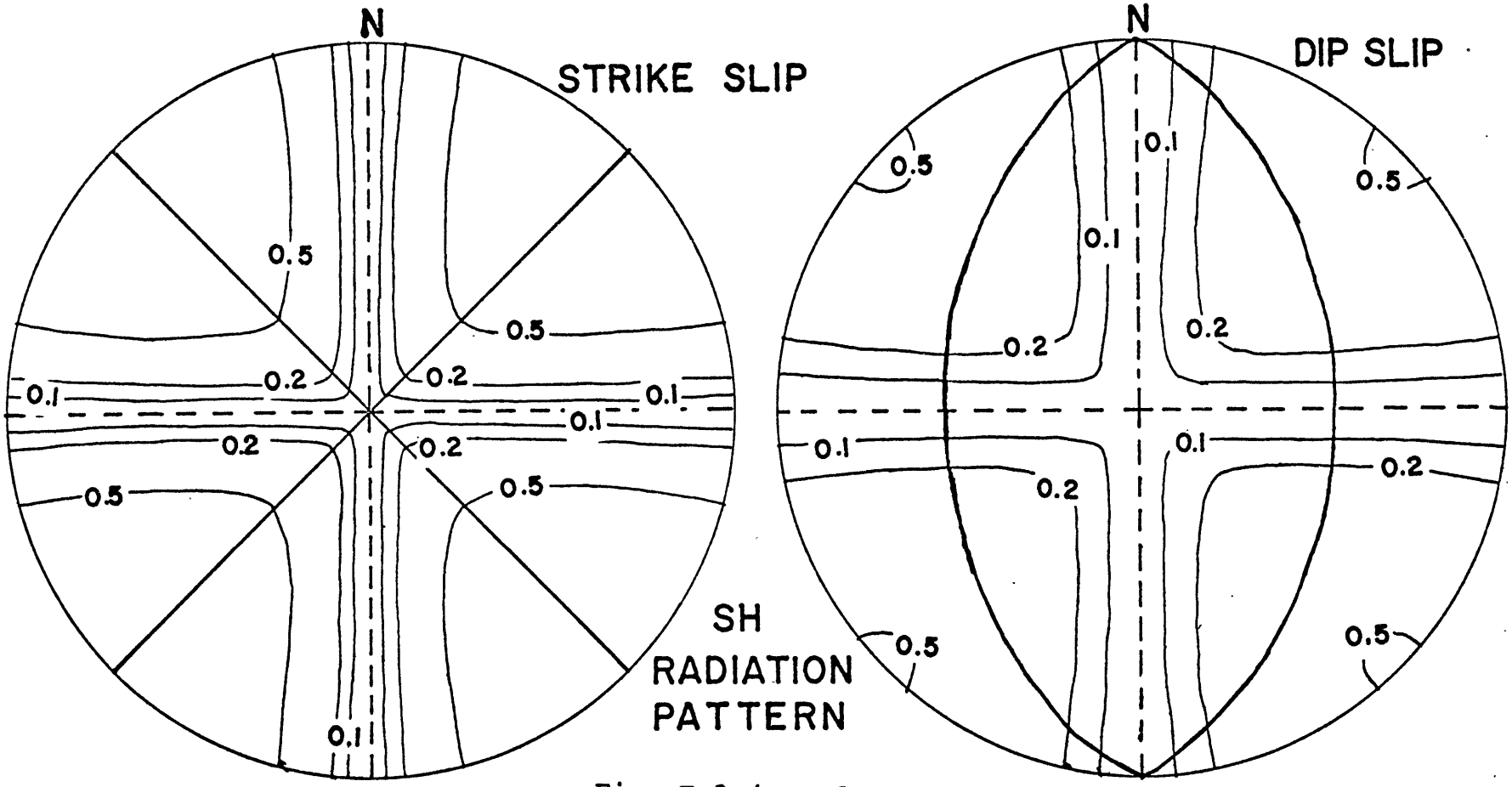

N
STRIKE SLIP
0.5
0.5
0.1
0.2
0.2
0.1
0.1
0.2
0.2
0.5
0.5
0.1
N
DIP SLIP
0.5
0.1
0.5
0.1
0.2
0.2
0.1
0.1
0.2
0.2
0.5
0.5
SH
RADIATION
PATTERN

Fig. E-3 (contd

APPENDIX F

The Method of Inversion of Travel Time Data in a Spherically Symmetric Earth

Given the travel times $T_i (i = 1, N)$ and their standard errors σ_i for N finite values of distances, Δ_i, in a spherically symmetric earth, we wish to obtain the values of seismic velocity V(r) as a continuous function of radius. This is a grossly underdetermined problem which cannot have a resolving length to this scale without a large uncertainty in the inverted velocity model. We would like to then approximate V(r) by a discrete velocity model $V_j = V(r_j)$ for j = 1, M. The choice of M is such that we can determine the seismic velocities at those radii (r_j) with a reasonable uncertainty and without losing any important information on the nature of V(r) except for its fine details. In this appendix, we present a first order perturbation technique of inversion (Julian, personal communication) by which we find the changes in a parameterized velocity model, which are required to fit the observed travel time data. This method is an extension of the usual least square method and overcomes the unstable behavior which may affect the least square fitting.

Travel times are non-linear functionals of the seismic velocity. This causes a problem in computing the partial derivatives of travel time with respect to the changes in

the seismic velocity. To facilitate such a computation we need another approximation. We linearize the problem assuming that "data kernels" vary smoothly, that they may be expanded in a Taylor series about the initial velocity model, and that all higher order derivatives beyond the first one can be ignored. This enables us to calculate to the first order the changes in travel times produced by small changes in the velocity model.

In this inversion of travel time data, we assumed that at each spherical shell ($r_j<r<r_{j+1}$, for j = 1, M-1) the velocity could be given by some analytic function of radius having two free parameters a_j and b_j, e.g. $V(r) = a_j r^{bj}$. The values of a_j's and b_j's are solved from the following equations knowing r_j and $V(r_j)$, r_{j+1} and $V(r_{j+1})$:

$$\left.\begin{aligned} V(r_j) &= a_j r_j^{bj} \\ V(r_{j+1}) &= a_j r_{j+1}^{bj} \end{aligned}\right\} \quad (F.1)$$

Julian and Anderson (1968) presented the expressions for $\left(\frac{\partial T}{\partial V_j}\right)\Big|_\Delta$ for such a piecewise analytic velocity variation (equations 29, 31, and 32 in the appendix of their paper). The subscript 'Δ' indicates that the distance is held fixed for such a computation. Knowing the partial derivatives,

it is easy to find the changes in an initial velocity model in order to fit the observed travel times.

Because of the non-linearity of this inverse problem, an iteration is performed where the newly computed velocity model becomes the initial model. In a given iteration, the changes in the initial model are found through a modified least square technique. The usual least square technique may produce a large velocity perturbation which may cause an instability in the next iteration. So, instead of minimizing simply the sum of the square of the travel time residuals, the following expression was minimized:

$$\left.\sum_{i=1}^{N}\left[T_i+\delta T_i-O_i\right]^2+\alpha\sum_{j=1}^{M}(\delta V_j)^2+\beta\sum_{j=1}^{M}(\delta V_j-\delta V_{j-1})^2+\gamma\sum_{j=0}^{M}(\delta V_{j-1}-2\delta V_j+\delta V_{j+1})^2\right\} \quad \text{(F.2}$$

where $\delta V_k = 0$ for $k<1$ and $k>M$ and α, β, γ are some preassigned constants such that larger is the value of α, smaller is the perturbation in the initial velocity model, larger is the value of β, smaller is the change in the slope of the initial model and larger is the value of γ, smaller is the change in the curvature of the initial model. T_i are the calculated travel times for the initial velocity model, V_j; O_i are the observed travel times and δT_i are the changes in T_i for small perturbations δV_j in the initial model and are given by:

$$\delta T_i \simeq \sum_{j=1}^{M} \left(\frac{\partial T}{\partial V_j}\right)\Big|_{\Delta,\, T=T_i} \delta V_j \qquad (F.3)$$

Under the condition $\alpha=\beta=\gamma=0$, the case is equivalent to the conventional least square fitting. The typical values of α, β, and γ chosen during the inversion of our data were respectively 10, 25 and 50. The condition for minimizing (F.2) is expressed by a system of M simultaneous linear algebraic equations, which are obtained by setting the partial derivatives of (F.2) with respect to ∂V_j (j = 1, M) equal to zero. In matrix form, the system can be expressed as:

$$\left[\tilde{A}^T\tilde{A} + \alpha\tilde{I} + \beta\tilde{J} + \gamma\tilde{K}\right]\bar{x} = \tilde{A}^T\bar{b} \qquad (F.4)$$

The superscript T indicates the transposition of a matrix. The elements of the individual matrices in (F.4) are given as follows:

$$x_j = \delta V_j \,, \quad j = 1, \ldots, M$$

$$A_{ij} = \left(\frac{\partial T}{\partial V_j}\right)\Big|_{\Delta,\, T=T_i} \,; \quad \begin{matrix} i = 1, \ldots, N \\ j = 1, \ldots, M \end{matrix}$$

$$b_i = O_i - T_i \,, \quad i = 1, \ldots, N$$

$\tilde{I}$ is a (M x M) identity matrix, $\tilde{J}$ is also a (M x M) matrix as

given by:

$$\begin{bmatrix} 2 & -1 & 0 & 0 & \cdots & 0 & 0 & 0 & 0 \\ -1 & 2 & -1 & 0 & \cdots & 0 & 0 & 0 & 0 \\ 0 & -1 & 2 & -1 & \cdots & 0 & 0 & 0 & 0 \\ \cdots & \cdots & \cdots & \cdots & \cdots & \cdots & \cdots & \cdots & \cdots \\ \cdots & \cdots & \cdots & \cdots & \cdots & \cdots & \cdots & \cdots & \cdots \\ 0 & 0 & 0 & 0 & \cdots & -1 & 2 & -1 & 0 \\ 0 & 0 & 0 & 0 & \cdots & 0 & -1 & 2 & -1 \\ 0 & 0 & 0 & 0 & \cdots & 0 & 0 & -1 & 2 \end{bmatrix}$$

Similarly, $\tilde{K}$ is a (M x M) matrix given as follows

$$\begin{bmatrix} 6 & -4 & 1 & 0 & 0 & \cdots & 0 & 0 & 0 & 0 & 0 \\ -4 & 6 & -4 & 1 & 0 & \cdots & 0 & 0 & 0 & 0 & 0 \\ 1 & 4 & 6 & 4 & 1 & \cdots & 0 & 0 & 0 & 0 & 0 \\ \cdots & \cdots & \cdots & \cdots & \cdots & \cdots & \cdots & \cdots & \cdots & \cdots & \cdots \\ \cdots & \cdots & \cdots & \cdots & \cdots & \cdots & \cdots & \cdots & \cdots & \cdots & \cdots \\ 0 & 0 & 0 & 0 & 0 & \cdots & 1 & -4 & 6 & -4 & 1 \\ 0 & 0 & 0 & 0 & 0 & \cdots & 0 & 1 & -4 & 6 & -4 \\ 0 & 0 & 0 & 0 & 0 & \cdots & 0 & 0 & 1 & -4 & 6 \end{bmatrix}$$

In practice, we gave each travel time datum a weight inversely proportional to its variance. In this case, (F.4) is modified as follows

$$\left[\tilde{A}^T \tilde{W} \tilde{A} + \alpha \tilde{I} + \beta \tilde{J} + \gamma \tilde{K}\right] \bar{x} = \tilde{A}^T W \bar{b} \qquad (F.5)$$

where W is a (N x N) diagonal matrix whose elements are given by

$$W_i = 1/\sigma_i^2 \quad , \quad i = 1, \cdots, N .$$

We solved the expression (F.5) for the solution vector $\bar{x}$ and added these velocity perturbations to the initial model to start the next iteration where T_i's and $\left(\frac{\partial I}{\partial v_j}\right)\Big|_{A, T=T_i}$ were calculated from the new model.

One drawback of the present inversion method is that the final model can be biased by the initial velocity model if there is a local minimum in (F.2). But, if we start with an up-to-date velocity model which incorporates all present-day information about the earth's structure, we can reasonably ignore the above-mentioned drawback.

APPENDIX G

Backus-Gilbert Method of Calculating the Averaging Kernels and the Trade-off Curves for the Inversion of Travel Time Data in a Spherically Symmetric Earth

In this appendix we assume that a velocity model which fits the travel time data, has already been obtained after inversion through a method described in Appendix F. We present now the method of Backus and Gilbert (1970) for calculating the averaging kernels and trade-off curves as a measure of non-uniqueness for the inverted model. We modified their method slightly to add another contribution in the variance of the model error having arisen due to inadequacy of the model in addition to the observational error in data. Lack of exact fit to the travel time data by the inverted velocity model is the source of this model inadequacy. Also, we incorporated the discreteness in the velocity model, $V(r_j)$, as opposed to continuous radial variation in velocity $V(r)$ which is generally used in their papers (see for example, Backus and Gilbert, 1968; Backus and Gilbert, 1970; Johnson and Gilbert, 1972). So our expressions will be in the form of a matrix notation instead of the analytic expressions involving integration.

In the matrix notation, we adopted the following convention:

(1) repeated index indicates summation over that index unless specified otherwise.

(2) $\tilde{A}$ is a rectangular matrix with elements (A_{ij}).

(3) $\bar{X}$ is a column vector with elements x_j.

(4) Superscript "T" denotes the transpose of a matrix.

Let us assume that we have N data for the observed travel times, T_i, (i = 1, ..., N) at epicentral distances Δ_i for a spherically symmetric earth. Let us also assume for the time being that these travel time data are free from any observational error. To the first order in the small perturbation of velocity, corresponding changes in the travel times $\delta T_i'$ will be further assumed to be well-defined linear functionals and could be represented by

$$\delta T_i' = K_{ij}\, \delta V_j \quad , \quad j = 1, \cdots, M \qquad (G.1)$$

where K_{ij}'s are the data kernels given by

$$K_{ij} = \left.\frac{\partial T}{\partial V_j}\right|_{\Delta_i} \qquad (G.1a)$$

These data kernels were obtained in practice from the relationships given by Julian and Anderson (1968) assuming a velocity function of the form $V = ar^b$ in each layer of our model. Computing data kernels this way avoids the integrable singularity in the analytic expression corresponding to (G.1)

for the continuous velocity function V(r) (Johnson and Gilbert, 1972). In the framework of the linearized perturbation theory, our model is given by

$$m_j = \delta v_j \qquad (G.1b)$$

and corresponding changes in computed travel times (T_i') by

$$\gamma_i = T_i - T_i' = \delta T_i' \qquad (G.1c)$$

So, (G.1) is now rewritten as

$$\gamma_i = K_{ij}\, m_j \qquad (G.2)$$

or

$$\bar{\gamma} = \tilde{K} \cdot \bar{m} \qquad (G.2a)$$

To consider linear averages of velocity V_L around depth h_L, we would have,

$$\left.\begin{aligned} \sum_{i=1}^{N} a_i(L)\,\gamma_i &= \sum_{j=1}^{M} m_j \left(\sum_{i=1}^{N} a_i(L)\, K_{ij} \right) \\ &= \sum_{j=1}^{M} A_j(L)\, m_j \\ &= \langle \bar{A}(L), m \rangle \end{aligned}\right\} \qquad (G.3)$$

where $A_j(L)$'s define the averaging kernel for the L^{th} interface in the model and is given by

$$A_j(L) = \sum_{i=1}^{N} a_i(L)\, K_{ij} \qquad (G.4)$$

Above, $a_i(L)$'s are some constants properly chosen to make $A_j(L)$'s resemble a Dirac-delta function centered on the L^{th} interface, $\langle \bar{A}(L), m \rangle$ is the linear average velocity perturbation for the L^{th} interface and is given by

$$\langle \bar{A}(L), m \rangle = \sum_{i=1}^{N} a_i \gamma_i \qquad (G.5)$$

Approximation of averaging kernels to Dirac-delta function can be measured by the so-called 'δ-ness' criteria of Backus and Gilbert (1968, 1970). One such criterion of Backus and Gilbert, suitably modified for our discrete velocity model is given by the following expressions,

$$S(L) = 9 \cdot \left[\bar{A}(L)\right]^T \cdot \tilde{R}(L) \cdot \left[\bar{A}(L)\right] + \left(|h_{L+1} - h_{L-1}|/2 \right) \qquad (G.6)$$

subject to constraint that

$$\sum_{j=1}^{M} A_j(L) = 1 \qquad (G.7)$$

where $\tilde{R}$ is a diagonal matrix given by

$$R_{jj}(L) = \left(|h_j - h_L|^2 / |h_{L+1} - h_{L-1}| \right) \qquad (G.8)$$

From (G.4), the constraint (G.7) can be rewritten as

$$\left[\bar{a}(L) \right]^T \cdot \bar{g} = 1 \qquad (G.9)$$

where

$$g_i = \sum_{j=1}^{M} K_{ij} \qquad (G.10)$$

Note that if the averaging kernel, $A_j(L)$'s appear as a "box car" function given by

$$A_j(L) = \begin{cases} \frac{1}{3} & \text{for } |j-L| \leq 1 \\ 0 & \text{for } |j-L| > 1 \end{cases} \qquad (G.11a)$$

then from (G.6)

$$S(L) = |h_{L+1} - h_{L-1}| \qquad (G.11b)$$

S(L), being thus identical to the width of the 'boxcar', is called the 'spread' of the averaging kernel (Johnson and Gilbert, 1972). On the other hand, if the averaging kernel appears as a "triangular" function such that

$$A_j(L) = \begin{cases} 1 & \text{for } j = L \\ 0 & \text{for } j \neq L \end{cases} \qquad (G.12a)$$

then from (G.6)

$$S(L) = \left| h_{L+1} - h_{L-1} \right| / 2 \qquad (G.12b)$$

In our computation of the averaging kernels (see Chap. 3), they appeared most of the times as triangular functions; so the computed spreads should be interpreted as the half-width of the bases of those triangular kernels. The "spread" as given by (G.6) is the one measure of non-uniqueness in the inverted velocity model. The other measure of non-uniqueness, supplementary to the spread is given by the "variance of the model error". As mentioned in the beginning, variance of the model error is caused by both the model inadequacy and the observational error. Inadequacy of the velocity model is due to the lack of exact fit of our travel time data by the inverted model and therefore will cause a non-zero

linear average perturbation to the inverted model. This non-zero linear average perturbation can be considered a "model error", $(\Delta V_L)_1$ of the inverted velocity V_L at the L^{th} interface and is given by

$$(\Delta V_L)_1 = \langle \bar{A}(L), m \rangle = \sum_{i=1}^{N} a_i \gamma_i \quad (6.13)$$

The variance of this model error can be represented by $\lambda^2(L)$ as follows:

$$\lambda^2(L) = [\bar{a}(L)]^T \cdot \tilde{\Gamma} \cdot [\bar{a}(L)] \quad (6.14)$$

where $\tilde{\Gamma}$ is a <u>diagonal</u> matrix given by

$$\tilde{\Gamma}_{ii} = \gamma_i^2 \quad (6.14a)$$

Observational error ΔT_i in the travel time data would cause another independent contribution to the model error, $(\Delta V_L)_2$ at the L^{th} interface:

$$(\Delta V_L)_2 = \Delta \langle \bar{A}(L), m \rangle = \sum_{i=1}^{N} a_i(L) \Delta T_i \quad (6.15)$$

If we assume that the errors in the observed travel time data have zero mean and the finite co-variance matrix represented by $\tilde{E}$, then the variance in the model error due to this source is:

$$\mu^2(L) = [\bar{a}(L)]^T . \tilde{E} . [\bar{a}(L)] \quad (G.16)$$

So, the total variance of the model error, ΔV_L, of the velocity V_L, at the L^{th} interface is

$$\rho^2(L) = \lambda^2(L) + \mu^2(L)$$
$$= [\bar{a}(L)]^T . [\tilde{E} + \tilde{\Gamma}] . [\bar{a}(L)] \quad (G.17)$$

The spread, S(L), and the variance of model error, $\rho^2(L)$ are independent of one another. The linear sum of the two errors can only be minimized to obtain a_i's. Consider the combination

$$q = S\cos\theta + W\rho^2 \sin\theta \quad (G.18)$$

where θ is a parameter which runs from 0 to $\pi/2$. When $\theta = 0$, we are minimizing the spread and when $\theta = \pi/2$ we are minimizing the variance of the model error. Backus and Gilbert (1970) proved that as θ goes from 0 to $\pi/2$, the ρ^2 vs. S curve called the "trade-off" curve, is a monotonically decreasing function of 'S'. In other words,

we can lower the model error by willingness to accept a larger spread.

'W' in (G.18) is a weighting factor and it was introduced because of the difference in the dimensions of variance ρ^2 and spread S. For example, the variance of the model error is typically as low as 0.004 km^2/sec^2 whereas typical values of the spread is 100 km for our velocity model. Without the weighting factor 'W', varying values of θ do not have any effect on the least square minimization of (G.18). Typical values chosen for 'W' were 500 for the P velocity model and 1000 for the S velocity model. Once chosen, the values of W remained the same for all values of θ on the trade-off curves and for all layers in the model.

Minimizing (G.18) subject to (G.9) leads to a solution of a_i's in the form of

$$\bar{a}(L) = \eta(L) \quad \tilde{Q}^{-1}(L) \cdot \bar{g} \qquad (G.19)$$

where

$$\tilde{Q}(L) = g \cos\theta \; \tilde{K} \cdot \tilde{R}(L) \cdot \tilde{K}^T + W \sin\theta \, (\tilde{E} + \tilde{F}) \qquad (G.20)$$

and η is a Lagrange multiplier given by

$$\eta(L) = 1 \Big/ \left[\bar{g}^T \cdot \tilde{Q}^{-1}(L) \cdot \bar{g}\right] \qquad (G.21)$$

So there are different sets of a_i's for different values of θ on the trade-off curves. For each set of a_i's, one can compute the averaging kernels A_j's from (G.4). The spread and the variance of the model error corresponding to a particular value of θ on trade-off can then be computed respectively from (G.6) and (G.17).

APPENDIX H

Reading Errors for the First Arrival Times of P and S Phases

To estimate the reading errors, we have compared our readings for the arrival times of P and S waves with those reported in the International Seismological Center (ISC) bulletin and computed the value of r.m.s. difference. This r.m.s. value should be roughly a measure of error in reading the times of P and S phases. In Figure H-1 we have plotted the difference of bulletin readings from our readings as a function of distance. A striking feature in this plot for S wave data is that there are some large negative differences at a distance of 35°-40° and positive differences at 65°-80° distance. This feature, initially thought to be due to the misidentification of S phases in the bulletin was found out to be due to gross errors in the reported times. Similarly a second check on all P wave readings disagreeing by more than one second reveals also gross errors in the Bulletin times. In computing the r.m.s. deviation in the two sets of the readings, we have eliminated those data with time difference of more than 3 seconds as they reflect unusual error in the reading/printing/punching or identification of the phases. The computed r.m.s. deviation for P waves is 0.45 seconds with a mean of 0.09 seconds. For S waves, the

computed mean and the r.m.s. deviation are respectively 0.2 seconds and 1.09 seconds.

Is there any systematic difference between the arrival times measured from the short period and the long period records? To answer this question we computed the signal front delays (Papoulis, 1962, p. 134) for the short period and the long period WWSSN seismographs. Signal front delay, Δt_s (in seconds), is defined by:

$$\Delta t_s = \lim_{\omega \to \infty} (\phi/\omega) \qquad (H.1)$$

where ϕ/ω is the phase delay (in seconds) in the instrument response of the ground motion and is shown in Figs. H-2 and H-3 respectively for the short period and the long period WWSSN seismographs corresponding to various periods of ground motion. The phase delays were computed from the following expression of frequency response of the WWSSN type seismograph as given by Aki (unpublished):

$$X(\omega) = -C i\omega^3 U e^{i\omega t} \left[\frac{1}{-\omega^2 + 2i\epsilon_1\omega + \omega_1^2}\right] \cdot \left[\frac{1}{-\omega^2 + 2i\epsilon_2\omega + \omega^2}\right] \qquad (H.2)$$

where C is the instrument constant relating to the absolute value of seismograph sensitivity, $u = Ue^{i\omega t}$ is the ground displacement, ϵ_1 and ϵ_2 are respectively the damping constants for the pendulum and the galvanometer. $\omega = 2\lambda/T$, $\omega_1 = 2\lambda/T_1$

and $\omega_2 = 2\lambda/T_2$ where T is the period of the harmonic signal, T_1 and T_2 are respectively the natural periods of the pendulum and the galvanometer. Note that in (H.2), the coupling between the seismometer and the galvanometer was neglected. Putting $X(\omega) = A(\omega)\ e^{i\omega t - i\phi(\omega)}$ where, $A(\omega) = |X(\omega)|$, the phase delay (in radians) is given by $\phi(\omega)$ and the amplitude response by $A(\omega)$. From (H.2) we can obtain the expressions for the amplitude response and the phase delay as follows:

$$A(\omega) = C\,\omega^3\,U\left[\frac{1}{\sqrt{(\omega_1^2-\omega^2)+4\epsilon_1^2\omega^2}}\cdot\frac{1}{\sqrt{(\omega_2^2-\omega^2)+4\epsilon_2^2\omega^2}}\right] \qquad (H.3)$$

$$\phi(\omega) = \pi/2 - \tan^{-1}\left(\frac{2\epsilon_1\omega}{\omega^2-\omega_1^2}\right) - \tan^{-1}\left(\frac{2\epsilon_2\omega}{\omega^2-\omega_2^2}\right) \qquad (H.4)$$

The group delays, Δt_g (in seconds), for the instrument response, also can be computed easily as follows:

$$\Delta t_g(\omega) = \frac{d\phi(\omega)}{d\omega} = \left[\frac{1}{1+A^2}\cdot\frac{2\epsilon_1(\omega_1^2+\omega^2)}{(\omega_1^2-\omega^2)^2} + \frac{1}{1+B^2}\cdot\frac{2\epsilon_2(\omega_2^2+\omega^2)}{(\omega_2^2-\omega^2)^2}\right] \qquad (H.5)$$

where,

$$A = \frac{2\epsilon_1\omega}{\omega^2-\omega_1^2} \quad \text{and} \quad B = \frac{2\epsilon_2\omega}{\omega^2-\omega_2^2}$$

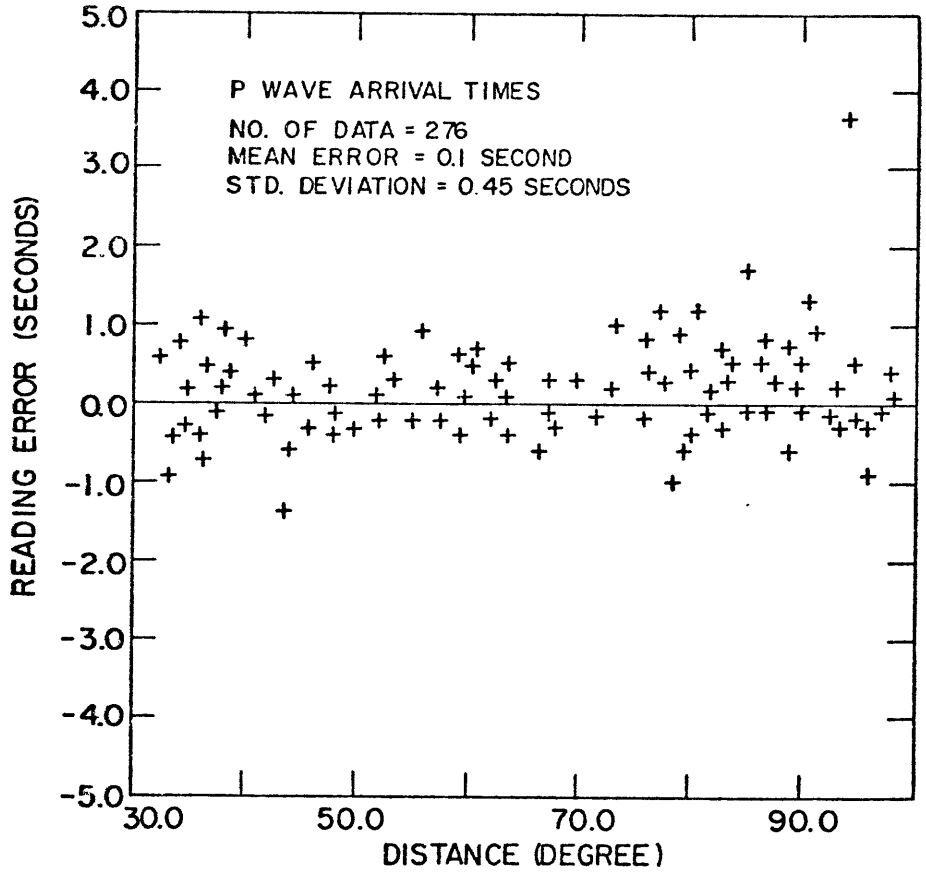
Assuming a critical damping in both the galvanometer and the pendulum, i.e. $\varepsilon_1 = \omega_1$ and $\varepsilon_2 = \omega_2$, we computed the amplitude responses, the phase delays and the group delays for both the short period and the long period WWSSN seismographs (Fig. H-2 and H-3). In those computations, the natural periods of the pendulum and the galvanometer were taken respectively to be 1.0 seconds and 0.75 seconds for the short period WWSSN seismographs and 15 seconds (and 30 seconds for the older type of the WWSSN seismographs) and 100 seconds respectively for the long period seismographs. It is seen that there should be no systematic difference in the signal front delays for the short period and the long period WWSSN seismographs. We found this to be true from observations, also.

Figure H-1. The r.m.s. difference of our own readings of P wave arrival times (top) and S wave arrival times (bottom) with respect to the times reported in the International Seismological Center (ISC) bulletin (the "standard deviation" as labelled on the figure is actually the r.m.s. difference). All data shown in this figure came from the deep events selected in this study. The data have been thinned out somewhat in case of overlapping. Note that the large negative difference for S wave arrival times around 35°-40° and the positive differences around 65°-80° are not due to the misidentification of S phases but gross errors in the reported times.

Figure H-2. Amplitude response (log-log scale), phase and group delays appropriate to the short period WWSSN seismographs. Natural periods of the seismometer (T_o) and of the galvanometer (T_g) are respectively 1 second and 0.75 seconds. Damping is critical.

Figure H-3. Same as Fig. H-2 except that the instrument responses shown here are appropriate for the long period WWSSN seismographs. Note that we have used two values for the natural period of seismometer (T_o) - 15 seconds for the recent types of WWSSN seismographs (top) and 30 seconds for the older types (below). In

both cases, natural period of the Galvanometer (Tg) is taken to be 100 seconds.


P WAVE ARRIVAL TIMES
NO. OF DATA = 276
MEAN ERROR = 0.1 SECOND
STD. DEVIATION = 0.45 SECONDS
READING ERROR (SECONDS)
5.0
4.0
3.0
2.0
1.0
0.0
-1.0
-2.0
-3.0
-4.0
-5.0
30.0
50.0
70.0
90.0
DISTANCE (DEGREE)

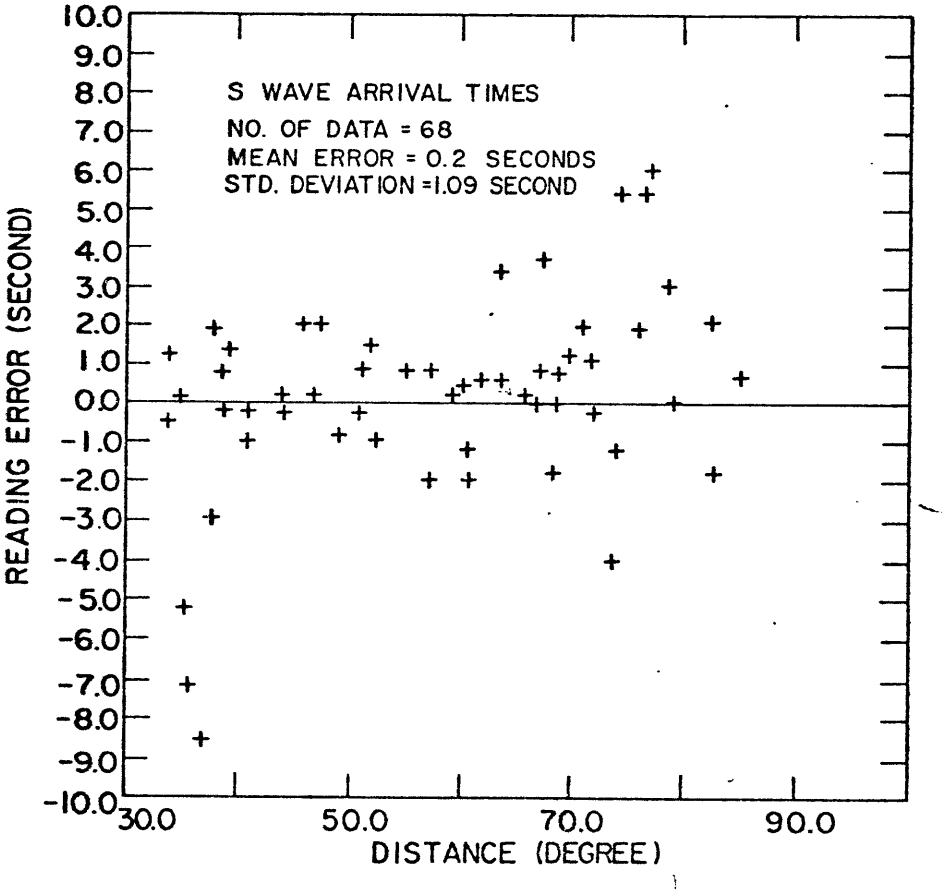

S WAVE ARRIVAL TIMES
NO. OF DATA = 68
MEAN ERROR = 0.2 SECONDS
STD. DEVIATION = 1.09 SECOND
READING ERROR (SECOND)
10.0
9.0
8.0
7.0
6.0
5.0
4.0
3.0
2.0
1.0
0.0
-1.0
-2.0
-3.0
-4.0
-5.0
-6.0
-7.0
-8.0
-9.0
-10.0
30.0
50.0
70.0
90.0
DISTANCE (DEGREE)

Fig. H-1

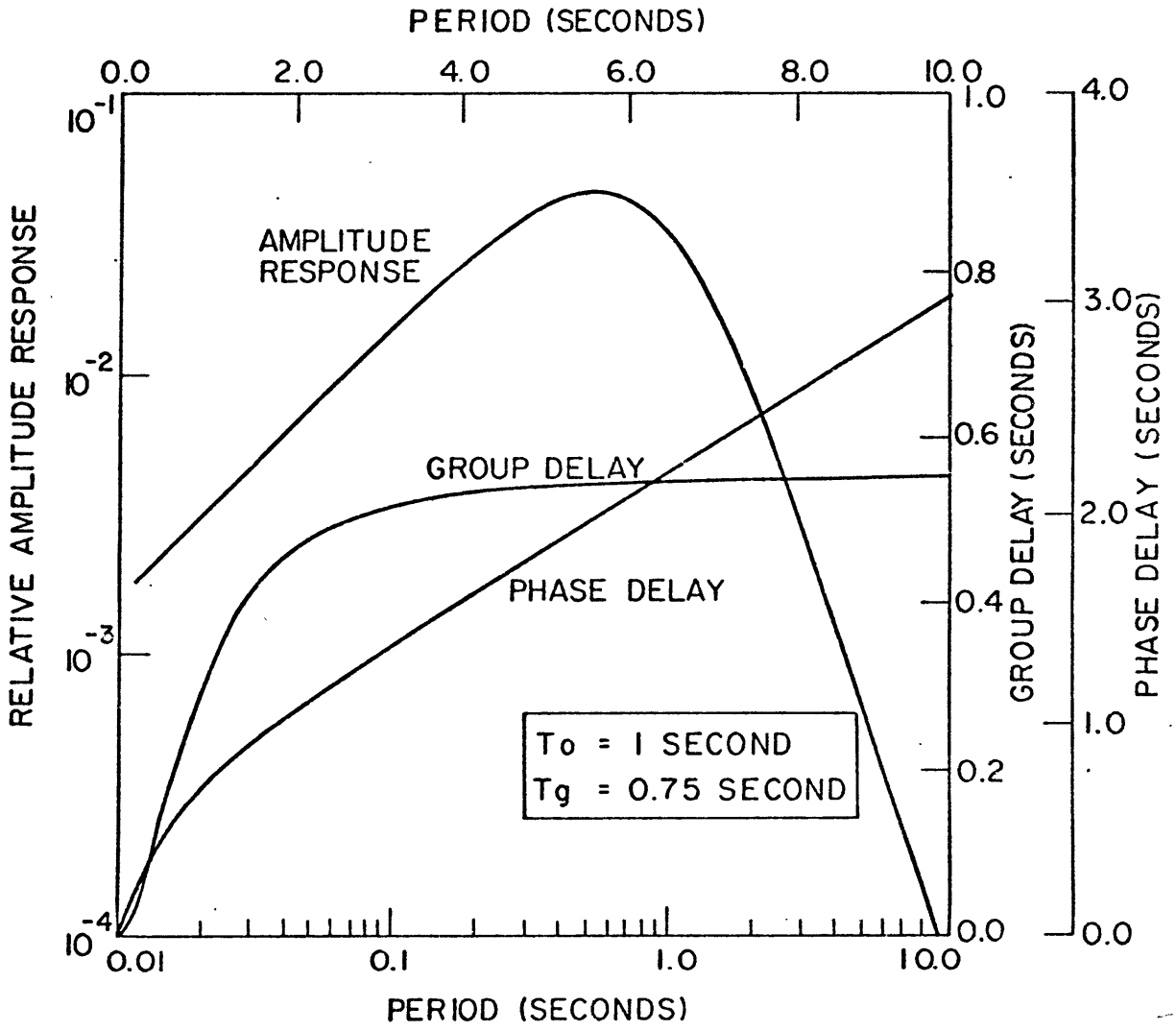
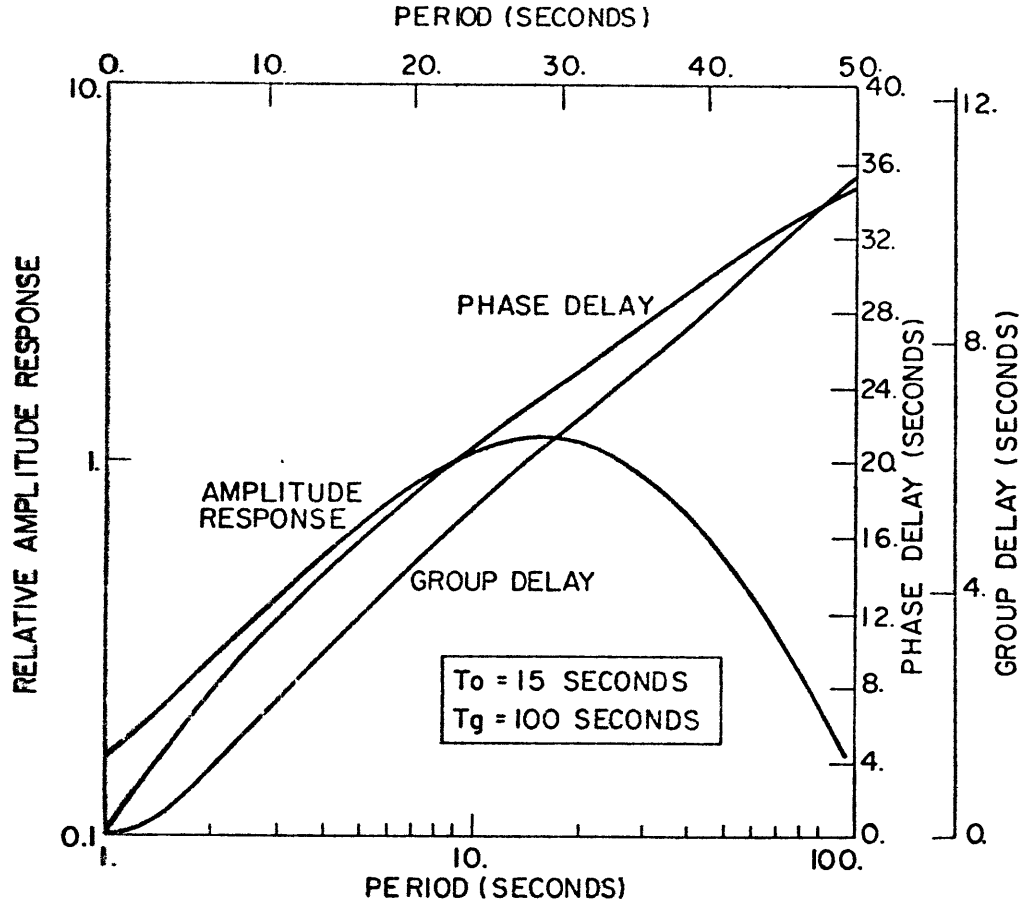

PERIOD (SECONDS)
0.0
2.0
4.0
6.0
8.0
10.0
RELATIVE AMPLITUDE RESPONSE
10^{-1}
10^{-2}
10^{-3}
10^{-4}
AMPLITUDE RESPONSE
GROUP DELAY
PHASE DELAY
To = 1 SECOND
Tg = 0.75 SECOND
1.0
0.8
0.6
0.4
0.2
0.0
GROUP DELAY (SECONDS)
4.0
3.0
2.0
1.0
0.0
PHASE DELAY (SECONDS)
0.01
0.1
1.0
10.0
PERIOD (SECONDS)

Fig. H-2


PERIOD (SECONDS)
0.
10.
20.
30.
40.
50.
10.
1.
0.1
40.
36.
32.
28.
24.
20.
16.
12.
8.
4.
0.
12.
8.
4.
0.
PHASE DELAY
AMPLITUDE RESPONSE
GROUP DELAY
To = 15 SECONDS
Tg = 100 SECONDS
RELATIVE AMPLITUDE RESPONSE
PHASE DELAY (SECONDS)
GROUP DELAY (SECONDS)
1.
10.
100.
PERIOD (SECONDS)

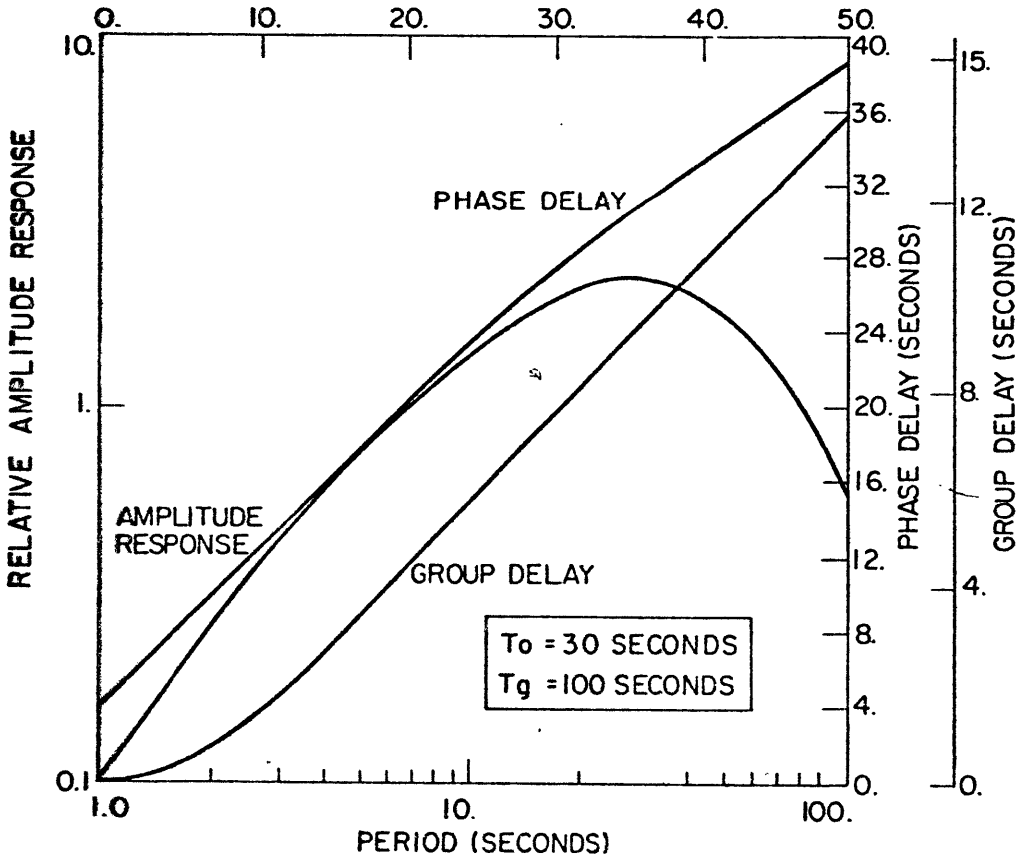

0.
10.
20.
30.
40.
50.
10.
1.
0.1
40.
36.
32.
28.
24.
20.
16.
12.
8.
4.
0.
15.
12.
8.
4.
0.
PHASE DELAY
AMPLITUDE RESPONSE
GROUP DELAY
To = 30 SECONDS
Tg = 100 SECONDS
RELATIVE AMPLITUDE RESPONSE
PHASE DELAY (SECONDS)
GROUP DELAY (SECONDS)
1.0
10.
100.
PERIOD (SECONDS)

Fig. H-3

APPENDIX I

Identification of the Seismic Phases

We are primarily concerned in this study with identification of the phases like P, S, ScS and PcP and also the depth phases pP and sP. In this appendix, we will discuss some of the problems associated with the identification of these phases.

Identification of the P waves generally has no problem as they are the first arriving energy in a sequence of signals. The impulsive nature of the P wave signals from the deep events reduced the problem of identification even further, as those signals appeared very distinct from the background noise. Often however we relied on the short period records for the arrival time and amplitude data of P waves because the long period signal to noise ratio was generally poor.

Identification of the S waves from the deep events has a few major problems, especially around 40° and 80° distances where the phases like PcS and SKS respectively begin to precede the S waves (Fig. I-1) and could be misidentified as S waves. Unless we could clearly associate a signal with S waves, we did not use those data. Some of our identifications of S phases around 80° and 40° distances are shown in Fig. I-2 through I-6. All these identifications were made using the travel time charts of Gutenberg and Richter

(1936). Note in Fig. I-2, the ScS phase is vague and the onset time could not be read. For the signals shown in Fig. I-3, we could only pick the data for S waves. In this figure S waves precede both the SKS and ScS phases by a small interval of time and the amplitudes of SKS and ScS are generally small. The amplitudes of PcS are as large as S when they follow S waves at a distance range of 30°-35° (see Fig. I-4), but are generally smaller than S beyond about 45° when they precede S (Fig. I-5). These amplitudes, however, are also dependent on the radiation pattern at the source and thus nature of their variation cannot be simply generalized. Also note that in Fig. I-4, PcS, being an SV type wave, could be identified easily as it was very predominant on the E-W component of the seismogram (back azimuth = 92°). In Fig. I-5, a large signal (especially in the vertical component), lying between the PcS and the S, remains unexplained. It is worthwhile to note that the SKS signals from the deep earthquakes also could be seen distinctly on the short period records.

Another source of misidentification for the S phases is the presence of precursors (the Sp phases) to S waves (see Fig. I-6, also Fig. I-5). These precursors most likely originate from a S to P conversion at the upper mantle discontinuities (especially Moho). That the precursors were not generated at the source could be checked by examining

the P wave signals (cf. Fig. I-6). The converted phase, Sp, is strongly recorded on the vertical components and usually not seen on the short period seismograms (the example of the short period Sp's in Fig. I-6 is among few exceptional cases which may be related to the unusual crustal structure beneath the Himalayas). Visual correlation of the signals in all six components of the seismograms was used to pick the right onset of the S motion. From the coefficients of SV to P conversion at Moho (Fig. I-7) it is clear that the converted phase, Sp, would be virtually absent on the seismograms beyond about 60° distance.

Observations of the ScS phases as compared to the S phases are very sporadic. Irregularity in the core mantle transition zone may be the cause of it. Also, identification of the ScS phase is troublesome beyond about 70° distance (see Figs. I-2 and I-3). At small distances (around 40°), presence of the surface waves and S waves reflected from the earth's free surface may potentially cause misidentification. But, those signals are generally not seen on the short period records, mainly because of the upper mantle attenuation (see Fig. I-8).

The other core reflected phase PcP could be identified for the deep events beyond 40° distance (Fig. I-9). Below 40°, the pP and PP phases also arrive between the P and PcP phases. But the phases like pP and PP have longer periods

and more distorted shapes on the long period records compared to the PcP phase (Fig. I-9). The total number of observations for the PcP phase is scant and is about 4 times less than that of ScS. This is mainly because the PcP amplitudes from the deep events were found to be large primarily in the distance range of 30°-50° where unfortunately the onsets could not be picked reliably because of the presence of other phases.

Identification of the depth phases from the deep events did not pose any major problem. The amplitudes of pP phase were often large and could be observed both on the short and the long period seismograms. Picking of the onset times of pP was especially easier beyond about 50° distance (Fig. I-1). The onset times of sP could be picked reliably at all distance ranges. The sP signals also were seen to be very large compared to pP on the long period records, though sometimes they were not observed at all on the short period seismograms (see for example the top two seismograms in Fig. I-9). The S waves generally get strongly attenuated during their traverse through the low velocity layer in the upper mantle and that is why the sP phases were not observed as many times as the pP phases from the deep events. The bifurcation of pP signals on the long period vertical seismogram (and a suspected precursor on the short period vertical seismogram) as observed for the Hindukush event may be related to the unusual crustal structure beneath the Himalayas.

Figure I-1. Travel time charts prepared by Gutenberg and Richter (1936) for the seismic phases recorded in the epicentral distance range of 30°-100° and for a focal depth of 550 km.

Figure I-2. An example of identification of the S phase in presence of the preceding SKS phase. Note that no data were read for the ScS phase in this case because of its vague presence. Arrows are shown in this figure (and all subsequent figures) at the same times on all components of the seismograms ('Z' referring to the vertical component) to indicate the expected arrivals. These arrows not necessarily imply our picks of arrival time data. For identification of the seismic phases and to pick their onset times, all six components of the seismograms were always visually scanned in the similar way as shown here.

Figure I-3. An example of identification of the S phase in presence of the following SKS and ScS phases. Note that no data were picked for onsets of the SKS and ScS phases in this case.

Figure I-4. An example of the S and the following PcS phases. Note that the PcS phase, being predominantly SV type, is recorded distinctly on the E-W component (Back azimuth = 92°). The predominance of S on the N-S component indicates on the other hand that the S phase primarily has SH motion in this case.

Figure I-5. More examples of identifying the S phase in presence of the ScP and PcS phases preceding the S phase. Note a precursor to the S phase which is possibly the Sp phase, resulting from a conversion of the S phase to the P phase beneath the receiver region. A large signal between the PcS and the Sp phases, on the long period vertical component seismogram, remains unexplained.

Figure I-6. More examples of the Sp phases due to a conversion from the S to P phases beneath the receiver region. This figure shows one of the few exceptional cases for the short period recordings of the Sp phase, which may very well be related to the unusual crustal structure as expected to be present beneath the Himalayas. That this converted phase cannot be attributed to the source has been checked by inspecting the P wave signals shown at the bottom.

Figure I-7. Coefficients for SV to P and SV to SV transmission at Moho. The model for this discontinuity has been shown in Fig. C-1 in Appendix C. Note that on the basis of these computed coefficients, the converted phase - Sp, should be virtually absent (or unidentifiable) beyond 60° distance.

Figure I-8. An example of identification of the ScS phase at small distance (around 40°). Unlabelled arrows on

the short period seismograms show the times expected for the SS arrivals. Notice a distortion in the shape of the SS phase compared to the ScS phase. On the long period E-W seismogram, the ScS phase seems to be followed by the surface waves as identified from their typical dispersed signals.

Figure I-9. Some examples of the PcP, pP and sP phases. Note that because of the preceding coda, onsets of these phases are more clear on the long period seismograms than on the short period ones. The periods of the sP phases as recorded on the long period components are notably larger than those of the pP signals. Note also a bifurcation in the long period pP signal (and a suspected precursor to the pP on the short period vertical component seismogram) of the Hindukush event in comparison with the simple P wave signal from this event.

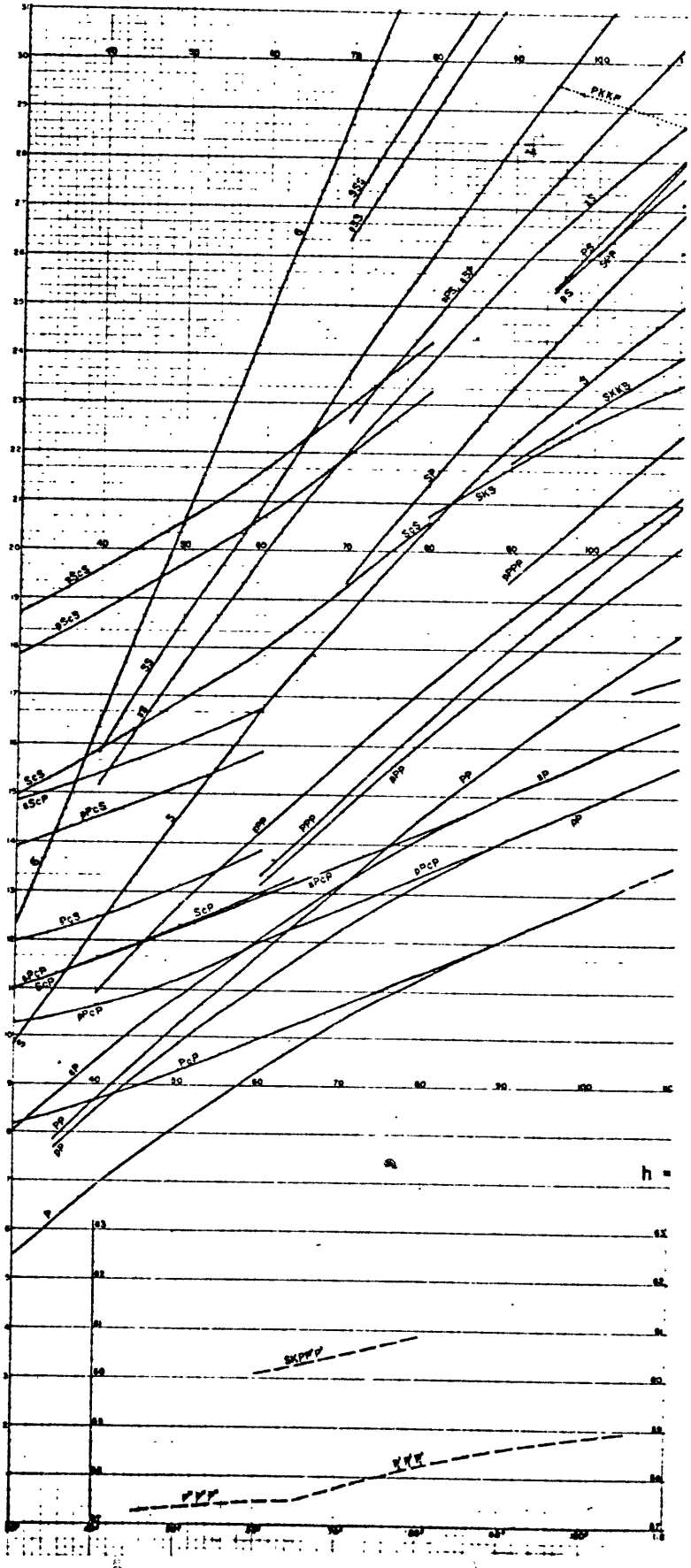

PKKP
SKS
SKP
PKS
SCS
sSCS
pSCS
SCP
sSCP
pPCS
PCS
sPCP
SCP
pPCP
PCP
PP
sPP
pPP
PPP
SKKKP
PKKP
h =

Fig. I-1

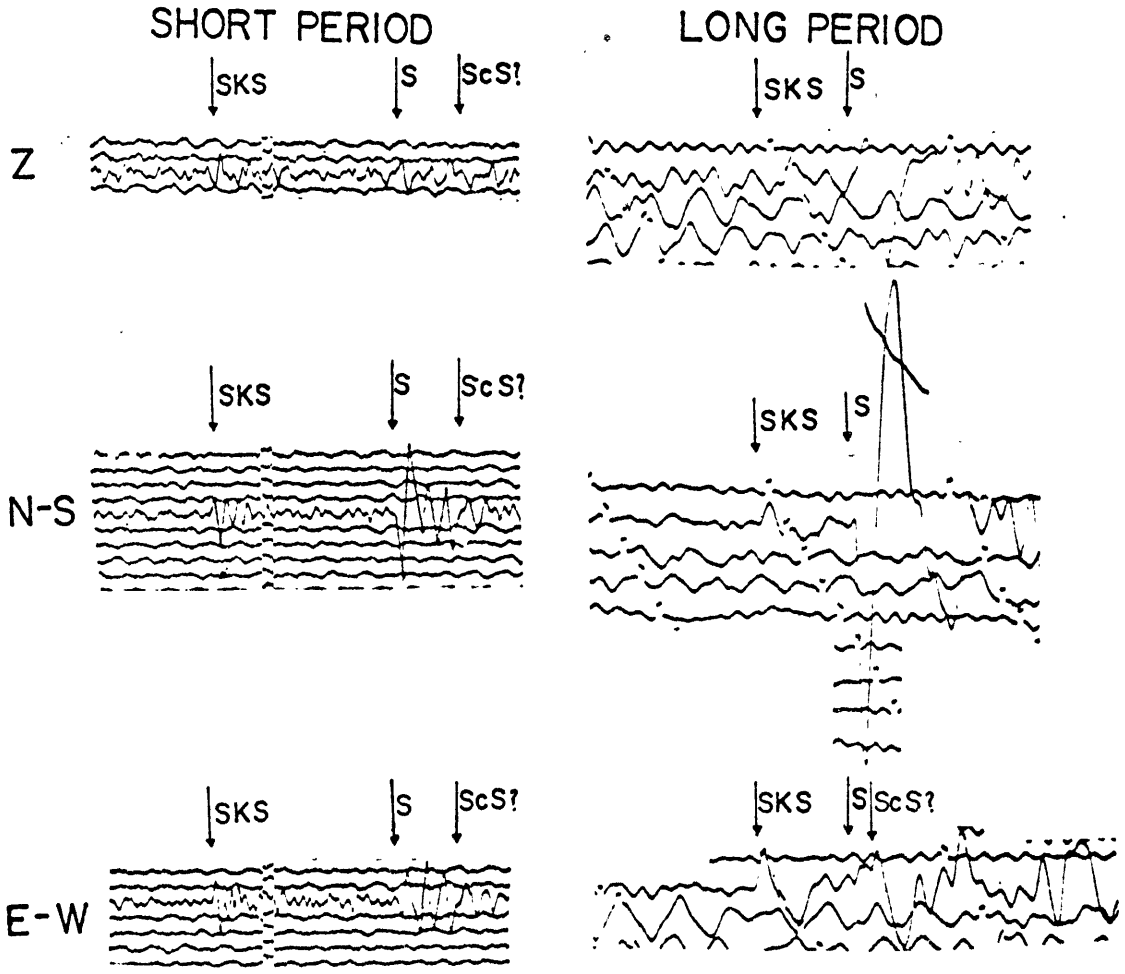
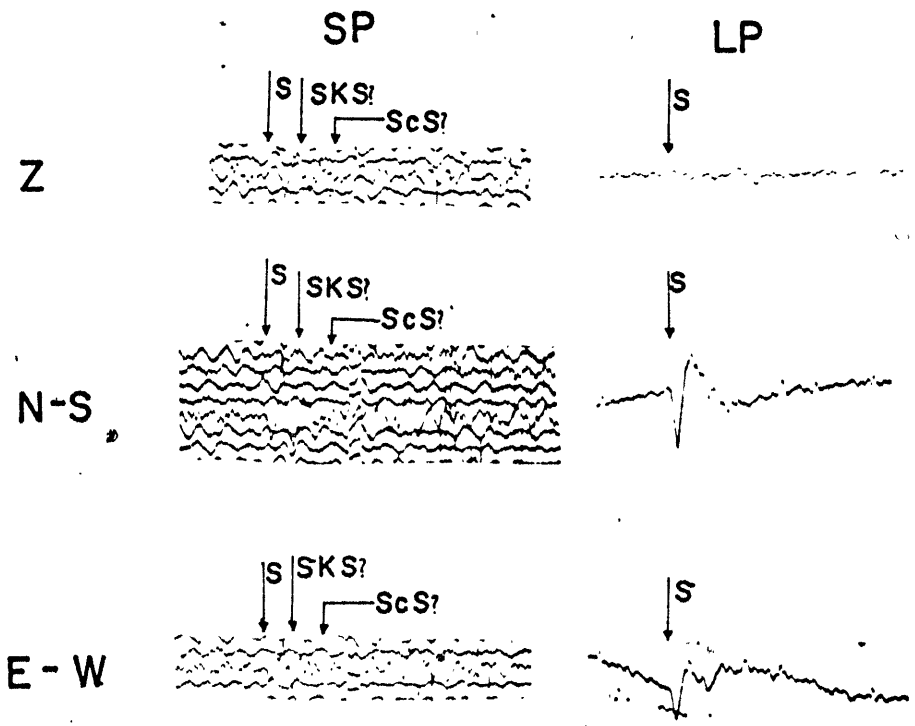

SHORT PERIOD
LONG PERIOD
SKS
S
ScS?
Z
N-S
E-W
S. FIJI - ALQ , DISTANCE = 88.52, BACK AZIMUTH = 243.

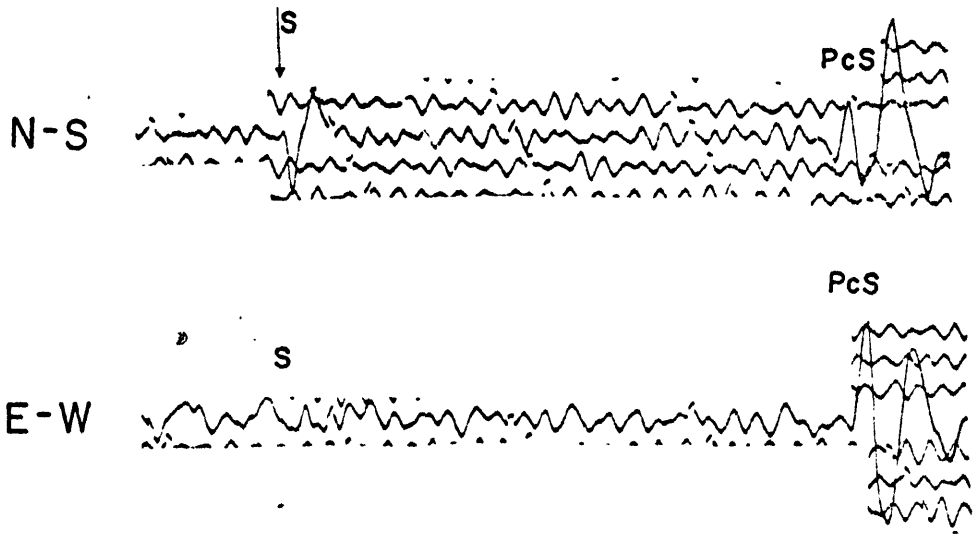
Fig. I-2



ARGENTINA- GOL, DIST.=76.38, AZ(BACK)=142.

Fig. I-3

LONG PERIOD



WEST TONGA CTA, DIST.=33.39, BACK AZ=92.

Fig. I-4

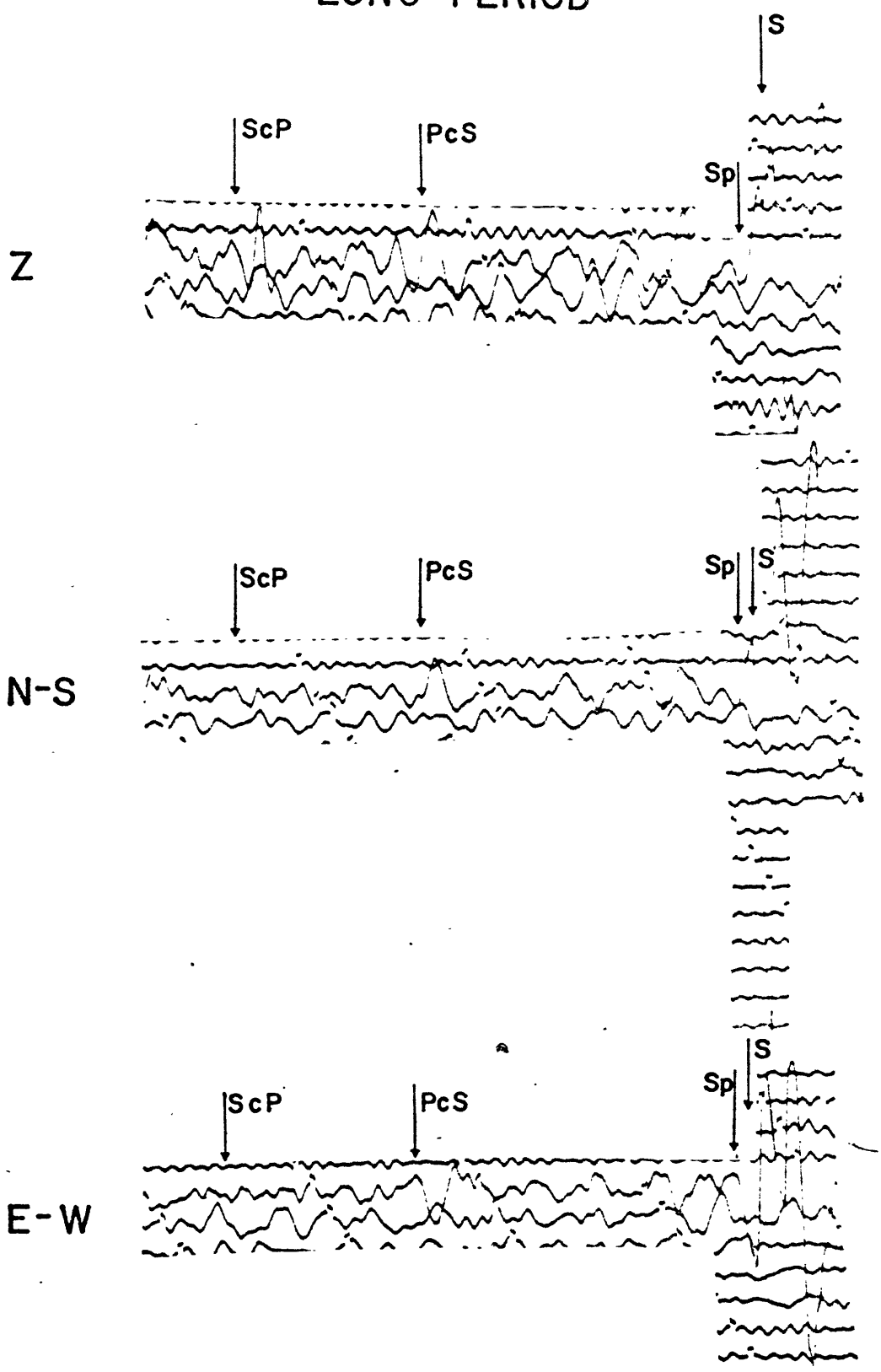
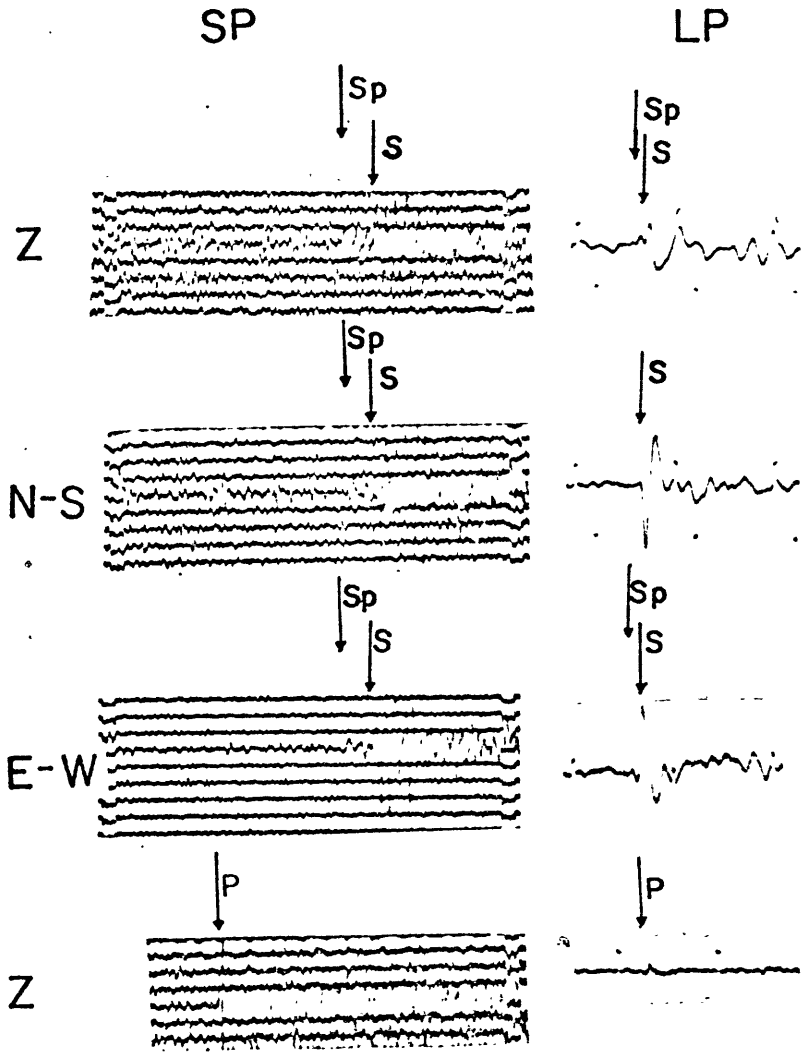

LONG PERIOD
S
ScP
PcS
Sp
Z
ScP
PcS
Sp
S
N-S
S
Sp
ScP
PcS
E-W
PERU-ALQ,DIST.=54.94,BACKAZ=136.

Fig. I-5



S. MARIANAS - SHL, DIST. = 49.81, BACK AZIMUTH = 87.

Fig. I-6

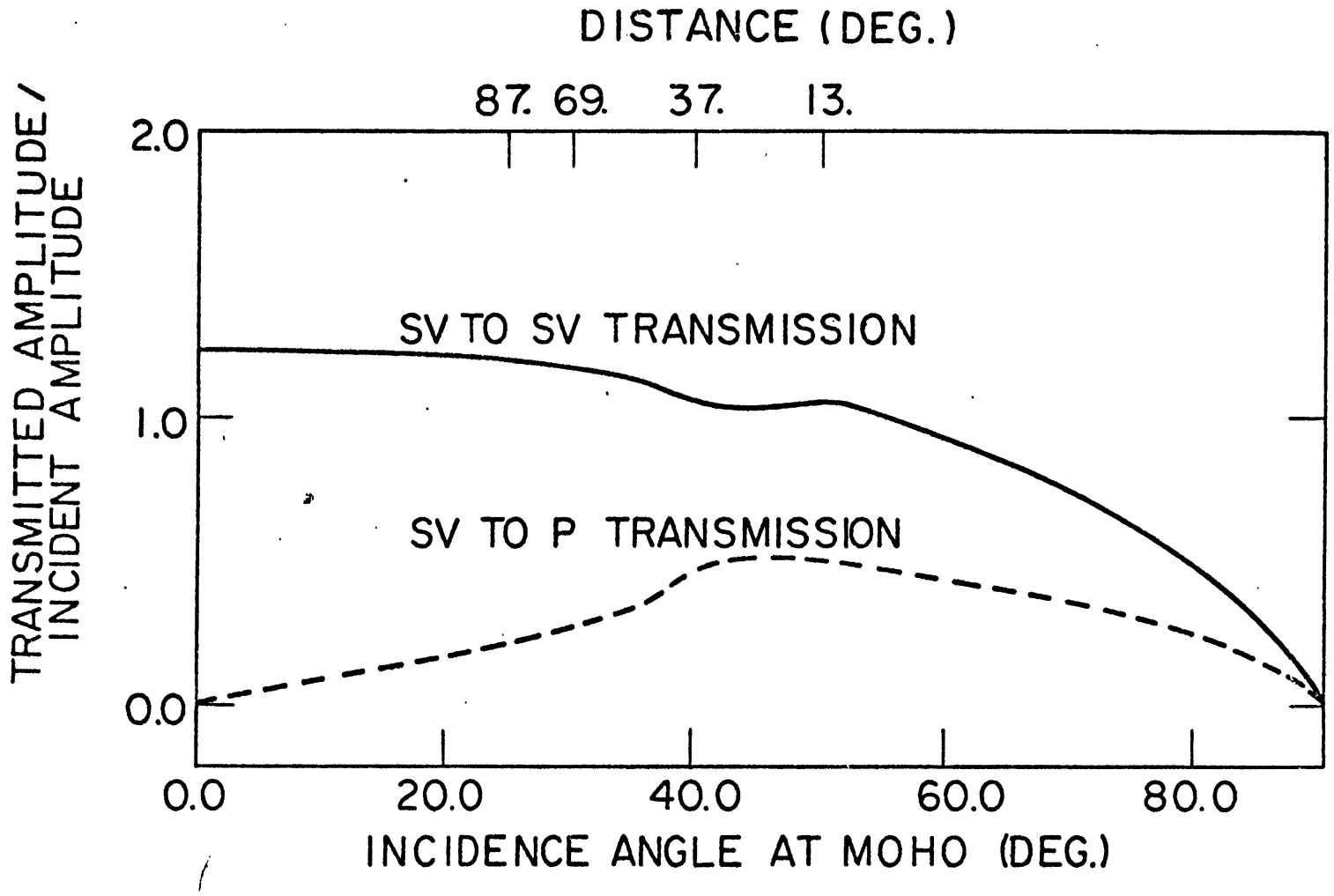
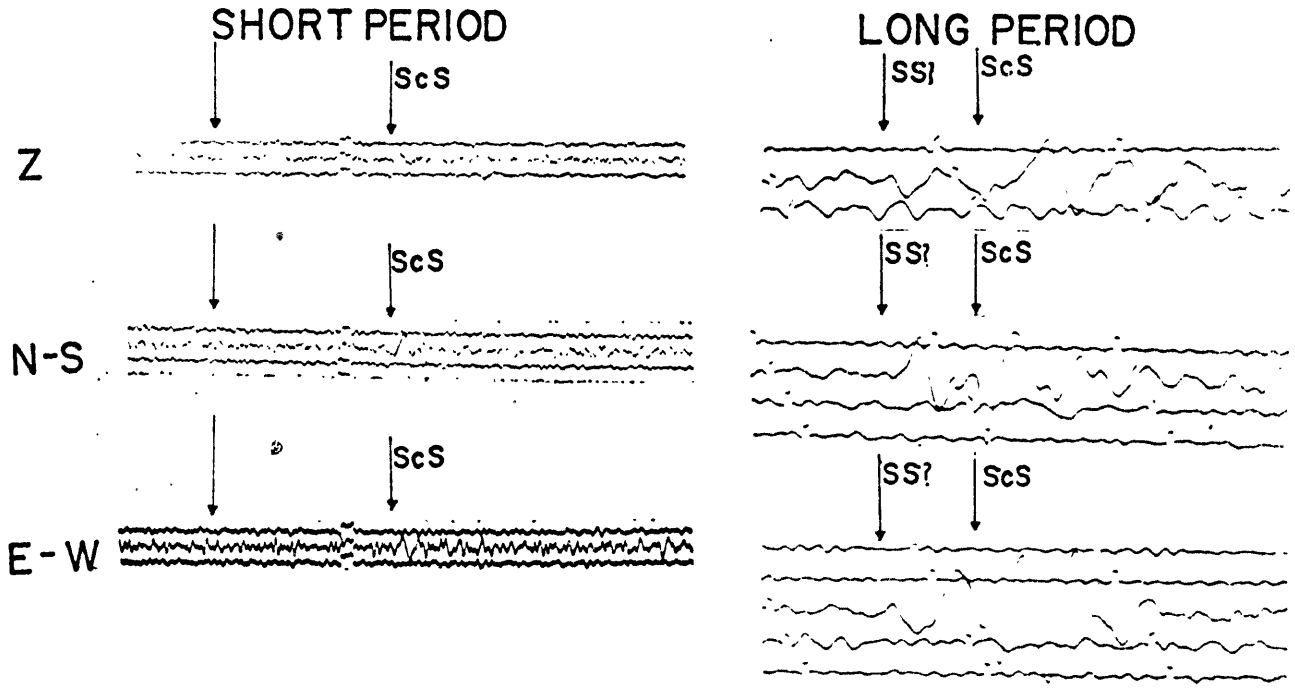

DISTANCE (DEG.)
87. 69. 37. 13.
2.0
1.0
0.0
TRANSMITTED AMPLITUDE / INCIDENT AMPLITUDE
SV TO SV TRANSMISSION
SV TO P TRANSMISSION
0.0
20.0
40.0
60.0
80.0
INCIDENCE ANGLE AT MOHO (DEG.)

Fig. I-7

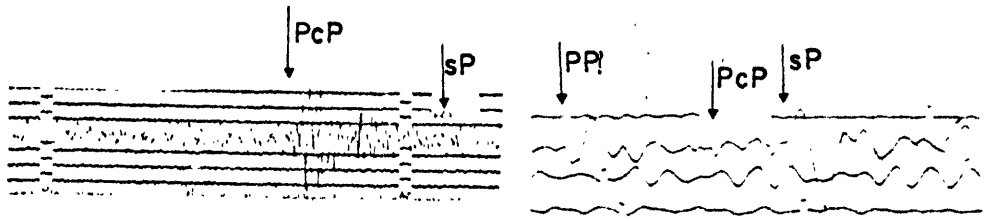


SOUTH FIJI-ADE, DIST. = 39.50, BACK AZ. = 80.67.

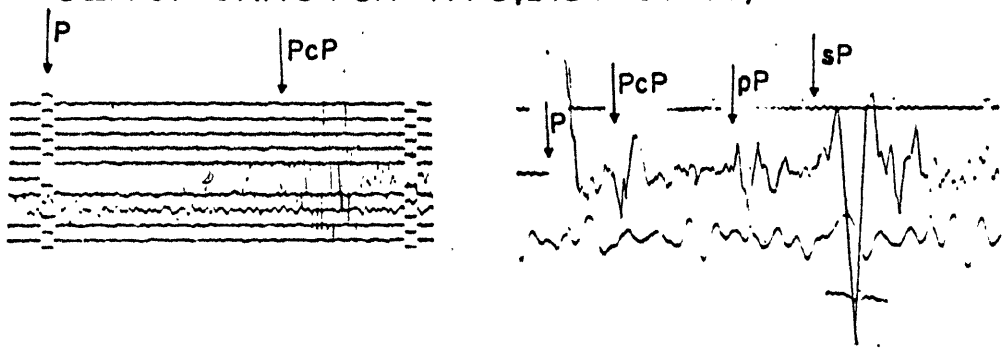
Fig. I-8

SPZ LPZ

S.FIJI-RAB, DIST. =32.60, BACK AZ. =123.



SEA OF OKHOTSK - KTG, DIST.=57.46, BACK AZ=5.



HINDUKUSH - ATU, DIST = 37.82, BACK AZ = 77.

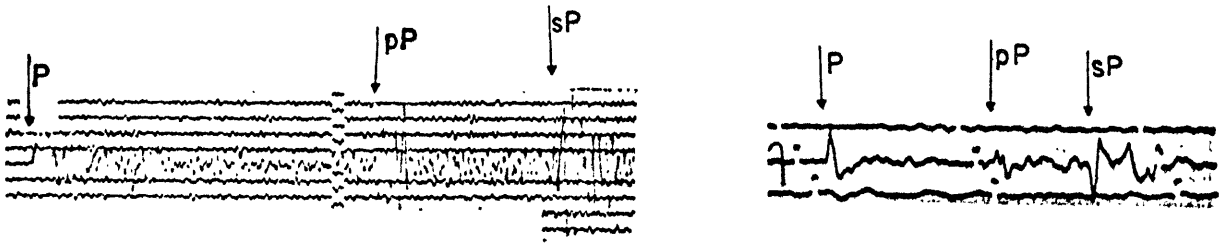


Fig. I-9

APPENDIX J

The Averaging Theorem For Travel Times

Jordan (1973) stated and proved the following averaging theorem for the surface focus travel times.

Statement: To the first order in velocity perturbation, the ray-theoretical surface-focus travel times between the source-receiver pairs at a constant angular distance Δ are distributed with a mean equal to the travel time, T_o at a distance, Δ, through the "Terrestrial Monopole" (Gilbert, 1971) provided the distribution of sources and receivers on the surface of earth is uniform.

Proof: To the first order, the travel time T between a source and a receiver can be written as the sum of two terms

$$T = T_o + \delta T \qquad (J.1)$$

where T_o is the travel time through the spherically symmetric terrestrial monopole, and δT is the first order perturbation in the travel time due to lateral perturbations (δV), in the velocity, V. While T_o, depends only on the angular distance Δ, separating the source and the receiver, the term δT depends on the source position, the angular distance, and the azimuth from source to station. The averaging theorem is proved if one can show that the mean fluctuation, $\overline{\delta T}$ is

zero over a sphere of radius R, the earth's radius. As the distribution of the sources and the receivers is assumed to be "uniform" over the surface of the earth, $\overline{\delta T}$ can be written as

$$\overline{\delta T} \propto \int_{S(R)} \int_0^{2\pi} \delta T(\Omega_0, \phi)\, d\phi\, d\Omega_0 \qquad (J.2)$$

where S(R) specifies the surface of sphere with a radius R; Ω_0, a coordinate on this surface and ϕ the azimuth measured from this coordinate. $\delta T(\Omega_0, \phi)$ to first order in δV, can be written from the Fermat's principle as equal to an integral of the velocity perturbation along the ray path (Backus and Gilbert, 1969):

$$\delta T = \int_{ray} (\delta V / V^2)\, ds \qquad (J.3)$$

One can rewrite (J.2) as follows:

$$\overline{\delta T} \propto \int_0^R \int_{S(r)} \delta V(r, \Omega_0)\, d\Omega_0\, dr \qquad (J.4)$$

By the definition of terrestrial monopole, the lateral perturbations average to zero when integrated over the sphere, i.e.

$$\int_{S(r)} \delta V(r, \Omega_0)\, d\Omega_0 = 0 \qquad (J.5)$$

(J.5) implies that $\overline{\delta T}$ is zero. This proves the averaging theorem for the surface focus travel times.

The extension of this averaging theorem to the deep focus travel times is straightforward. The sources and the receivers for the deep focus travel time data are distributed at two different radii. Provided that the sources and the receivers are uniformly distributed at their respective radii, (J.4) and (J.5) will be valid also for the deep focus travel times.

APPENDIX K

The Baseline Correction in the P Wave Travel Times of the Jeffreys-Bullen Tables (1940)

We have used throughout this study the baseline correction to the J-B times (1940) of P wave as previously determined by Sengupta (1972). The P wave arrival times reported in the seismological bulletins (1964-1971) were used in that study. To avoid the systematic bias due to near-source heterogeneity in the upper mantle, only the deepest earthquakes were selected from those Benioff zones around the world which extended beyond 450 km depth. The selected earthquakes are listed in Table K-1. In general two or more events were selected from the same source region. Gross errors in the times reported in the bulletins were removed through a check that each station had a similar residual (within ± 1 second of the median residual) for the events in the same source zone. Before this check was performed, all hypocenters were relocated through the master event method (Evernden, 1969) to assure a similar bias, if any, in the hypocenters from the same source region. When the bad data were eliminated this way (about 8% of the original collection), a process of iteration, similar to that of Tucker *et al.* (1968) was adopted. In this process (a) each earthquake was relocated with the help of the J-B travel time tables (1940), (b) corrections to these standard

travel times were estimated, and (c) the station anomalies were determined. During the relocation, each sector of the earth's surface of size 10° in distance and 10° in azimuth were given equal weights irrespective of the number of observations. Following a process similar to Flinn's (1965), the standard errors for determination of the focal parameters and the joint confidence regions for the epicentral coordinates were estimated. The data from 12 events (marked in Table K-1) for which the area of the 95% confidence ellipse was greater than 500 km^2 were omitted from the analysis, since it was likely that those data were contaminated by some type of large errors. Final analysis of the travel times was carried out by about 3,300 arrival times from 47 deep earthquakes. Corrections to J-B times, for the focal depth of 550 km, were estimated by averaging the travel time residuals in 2° cells of distance. Station anomalies were estimated by the average of travel time anomalies at each station. Selection of sinusoidal azimuthal variation in station anomaly used by Herrin and Taggart (1968) or the spherical harmonics expansion in distance and azimuth carried out by Shimshoni and Pekeris (1966) did not show (see Table K-2) any appreciable reduction in the standard error of the travel time residuals at a station as compared to that given for the representation of station anomalies by the average of

travel time residuals at a station. The station anomalies determined according to this definition are listed separately in Appendix L. Corrections to the J-B times estimated from those 3300 travel time data are shown in Fig. K-1 (left). To the right of this figure we show the corrections to the same J-B times determined similarly from about 1200 P wave travel time data of this study. Note that the data of this study came from twelve deep earthquakes (see Table 2-1 in Chap. 2) and two intermediate earthquakes (one at Hindukush and the other at Greece) whose depths were constrained by the depth phases (see Appendix A). The differences in the shapes of the two travel time curves shown in Fig. K-1 are apparently insignificant.

The correct baseline value of the systematic errors in J-B times was difficult to determine because such error was absorbed in the determination of the origin times of the earthquakes which were not known. So, in the second part of the study, Sengupta (1972) used the P wave travel time data from the explosions whose locations and origin times were known precisely. Five explosions (Table K-1) were chosen at the Nevada Test Site (NTS), where the structure of the crust and the upper mantle are known (Green and Hales, 1968; Archambeau et al., 1969). The observed P wave J-B residuals from those explosions were corrected for the effect of the

downgoing path near the source from 0 to 550 km depth. In particular, the WNA model (Julian, personal communication) and the NTS1 model (Green and Hales, 1968) were chosen for representing the upper mantle structure beneath the NTS. Fig. K-2 shows the computed corrections to the observed J-B residuals for P times when the J-B model for the upper mantle (0-550 km depth) was replaced by the WNA model.

The P wave arrival time data of the five NTS explosions as taken from the bulletins, were also screened by the same check of consistency as mentioned earlier regarding the earthquake travel time data. After this process, the average standard deviation of P wave travel time residuals at a station for those five explosions was found to be 0.3 seconds. With a background of this standard deviation for the reading error, Table K-3 shows the mean and the standard deviation of the 487 observed P wave J-B residuals of the five explosions at different stages of correcting these residuals. The raw J-B residuals (without any correction) as well as the final residuals are shown in Fig. K-3. Note that the final residuals in this figure were corrected (i) for the upper mantle structure beneath the NTS by the use of the WNA model instead of the J-B model; (ii) for the error in the shape of the J-B times shown in Fig. K-2 (left) and (iii) for the station travel time anomalies as listed in Appendix L. In spite of these corrections, scatter in the explosion

residuals was not reduced and remained very large compared to the reading error (Table K-3). The use of the NTS1 model instead of the WNA model also produced the similar scatter. The most plausible cause for this scatter is then the absence of spherical symmetry in the upper mantle structure beneath the NTS. Therefore, at this stage without correcting for the lateral variation beneath the NTS, an error of $\pm$ 1 second is very likely to be present in the estimated baseline error of the P wave J-B times given by the average of the final residuals.

The value we have adopted throughout this study for the baseline error in the P wave J-B times for the focal depth of 550 km is -1.3 ± 1.0 seconds. This figure is based on (i) the use of the WNA model as a first approximation to the upper mantle structure beneath the Nevada test site, (ii) the use of correction to J-B times found from the depth constrained events (Fig. K-1, right), (iii) the use of correction for the station anomalies as given in Appendix L and, (iv) the formal specification of uncertainty of one second as noted earlier.

Table K-1

List of Earthquakes and Explosions

(a) Earthquakes

Source Region	Event No.	Date	Origin Time	Lat	Lon	Depth	Mag	Ref. of data	Reported maximum depth
West Tonga	1	12/09/65	13h 12m 55. s	18.12S	178.12W	649	5.4	ISC	680 km (Gutenberg, 1954)
	2	12/25/65	02h 57m 5 . s	18.14S	179.13W	624	5.5	ISC	
	x† 3	7/21/66	18h 30m 15.0s	18.85S	178.56W	589	5.6	ISC	650 (Sykes,1966; Sykes,Isacks & Oliver, 1969)
	4	12/25/65	19h 20m 45.6s	18.21S	179.13W	631	5.2	ISC	
	5	12/30/66	01h 00m 24.4s	18.06S	179.16E	650	5.1	ISC	
South Fiji	6	12/28/64	16h 16m 08.7s	22.13S	179.62W	577	5.7	ISC	680 km (Gutenberg, 1954)
	x 7	3/17/66	15h 50m 32.3s	21.08S	179.15W	627	5.9	ISC	
	*	3/14/64	04h 45m 51.9s	21.96S	179.62E	627	5.0	ISC	650 km (Sykes, 1966; Sykes, Isacks & Oliver 1969)
	8	10/17/66	18h 20m 07.0s	22.32S	179.21E	620	5.2	ISC	
	9	09/21/64	04h 23m 18.9s	21.96S	179.46W	603	5.2	ISC	
Colombia	10	7/31/70	17h 08m 05.4s	1.5S	72.6W	651	7.1	USCGS	650 km (Gutenberg,1954;Santo 1969)
	x 11	11/03/65	01h 39m 03.2s	9.04S	71.32W	587	5.9	ISC	
Peru-Brazil Border	12	12/22/64	00h 24m 48.8s	9.48s	71.21W	6615	5.2	ISC	650 km (Gutenberg,1954;Santo 1969)
	*	11/28/64	16h 41m 34.3s	7.90s	71.32W	651	5.3	ISC	
	*	11/28/64	16h 49m 30.5s	7.87S	71.32W	651	5.3	ISC	
	*	02/18/65	22h 32m 19.1s	9.99S	71.06W	593	5.2	ISC	
South Bolivia	13	5/13/65	02h 23m 24.2s	19.24S	63.84W	602	5.0	ISC	660 km(Gutenberg, 1954)
Argentina	14	12/09/64	13h 35m 41.9s	27.46S	63.23W	578	5.8	ISC	660 km (Gutenberg, 1959)
	*	09/19/67	10h 06m 44.1s	27.7S	63.1W	578	5.8	ISC	
	15	03/05/65	14h 32m 17.9s	26.89S	63.25W	555	5.6	ISC	
	x 16	12/20/66	12h 26m 53.6s	26.06S	63.10W	571	5.8	ISC	
	17	07/25/69	06h 06h 42.4s	25.6S	63.3W	579	5.5	USCGS	
Java Sea	x 18	04/29/65	15h 48m 58.9s	5.65S	110.24E	524	5.7	ISC	660 km (Gutenberg 1954)
	*	03/24/67	09h 00m 19.5s	6.0S.	112.3E	600	6.0	UUSCGS	
	19	01/30/68	03h 44m 24.4s	6.1S	113.3E	594	6.2	USCGS	650 km (Santo, 1969; Fitch & Molner, 1970)
	20	02/13/70	15h 43m 28.7s	5.9S	113.0E	636	5.8	USCGS	
Bali Sea	21	03/26/68	00h 41m 56.9s	6.6S	116.1E	520	5.9	USCGS	600 km (Gutenberg, 1954)
Philippines	*	01/23/65	23h 24m 30.1s	7.43N	123.86E	628	5.2	ISC	610 km (Gutenberg, 1954)
	x 22	12/22/65	00h 52m 56.8s	6.67N	124.11E	552	5.2	ISC	
	23	12/18/70	23h 50m 12.2s	5.1 N	123.5E	511	5.5	USCGS	
Celebes Sea Flores Sea	24	11/25/64	09h 24m 08.9s	4.34S	122.14E	607	5.8	ISC	670 km (Gutenberg, 1954)
	*	01/06/65	00h 55m 27.7s	7.13S	122.84E	554	5.3	ISC	
	x *	05/13/69	14h 30m 19.6s	7.2S	120.9 E	616	5.6	USCGS	
Banda Sea	25	08/17/66	19h 54m 11.1s	5.01S	125.15E	555	5.5	ISC	720 km (Gutenberg, 1954)
	26	06/14/66	16h 39m 47.9s	5.39S	124.41E	616	5.4	ISC	
	*	10/18/64	12h 32m 24.9s	7.17S	123.86E	585	5.8	ISC	

Table K-1 (continued)

Source Region	Event No.	Date	Origin Time	Lat	Lon	Depth	Mag	Ref. of data	Reported maximum depth
Okhotsk Sea (north)	27	08/22/66	14h 21m 13.6s	50.28 N	147.71E	626	5.0	ISC	
	×28	08/30/70	17h 46m 09.0s	52.4 N	151.6 E	645	6.6	USCGS	650 km (Gutenberg, 1954)
	29	01/29/71	21h 58m 05.4s	51.7 N	150.9 E	544	6.1	USCGS	
	30	09/05/70	07h 52m 27.9s	52.2 N	151.4E	580	5.7	USCGS	
USSR	×31	06/30/66	08h 59m 49.5s	43.40 N	132.41E	476	5.0	ISC	
	32	04/10/69	14h 54m 03.9s	42.0 N	130.9 E	555	5.6	USCGS	590 km (Gutenberg, 1954)
	33	10/12/70	09h 33m 36.6s	42.8 N	131.0 E	555	5.2	USCGS	
Japan Sea	34	12/11/64	16h 04m 58.4s	38.9 N	130.22E	551	5.1	ISC	580 km (Gutenberg 1954)
	×†35	01/24/64	17h 17m 46.7s	38.75 N	129.54E	557	5.3	ISC	
	36	08/06/65	18h 15m 11.1s	41.39 N	131.34E	554	5.0	ISC	590 km (Santo 1969)
Bonnin Island	×37	05/23/64	11h 23m 34.6s	25.58 N	139.56E	423	5.2	ISC	540 km (Gutenberg, 1954)
	38	03/02/65	21h 36m 39.6s	28.12 N	139.51E	507	5.1	ISC	
	*	10/07/68	19h 20m 20.3s	26.3 N	140.6 E	516	6.1	USCGS	500-600 km (Katsumata & Sykes, 1969; Miyamura 1969; Santo, 1969)
Marianas (south)	39	05/10/70	20h 05m 15.9s	18.6 N	145.2 E	602	5.6	USCGS	570 km (Gutenberg, 1954) 685 km (Santo, 1969)
Solomon Islands	×40	07/06/65	18h 36m 47.3s	4.48 S	155.07 E	509	5.6	ISC	560 km (Gutenberg, 1954)
	41	06/13/64	14h 01m 40.5s	3.93SS	154.36 E	476	5.2	ISC	=500 km (Denham, 1969)
	42	08/28/66	10h 03m 03.3s	4.59 S	155.21 E	511	5.4	ISC	
	43	11/25/65	22h 35m 37.9s	4.00 S	150.54 E	460	5.2	ISC	516 km (Santo, 1970)
New Hebrides	44	03/14/64	15h 05m 54.4s	13.82 S	172.38 E	613	5.0	ISC	370 km (Gutenberg, 1954)
	×45	04/10/65	22h 53m 04.55	13.45 S	170.30 E	641	5.3	ISC	
	46	11/04/68	09h 07m 38.5s	14.2 S	172.0 E	585	5.8	USCGS	655 km (Sykes 1964)
	47	01/08/68	03h 17m 12.6s	13.7 S	171.5 E	630	5.2	USCGS	649 km (Santo, 1970)
	*	01/30/65	18h 06m 20.8s	12.93 S	169.63 E	641	5.1	ISC	

* Events deleted for confidence ellipse area greater than 500 sq. km.
† Test events
× Master event for the source region

(b) Explosions

Explosion Site	Explosion Name	Date	Origin Time	Lat.	Lon.	Elev.	Mag.	Ref. of data
Nevada Test Site	Greely	12/20/66	15h 30m 00.1s	37°18'07"N	116°24'30"W	740.7m	6.3	ISC
	Half Beak	06/30/66	22h 15m 00.7s	37°18'57"N	116°17'56"W	1190.9m	6.1	ISC
	Boxcar	04/26/68	15h 00m 00.1s	37°17'44.0"N	116°27'21"W	6370ft.	6.3	USCGS
	Jorum	09/16/69	14h 30m 00.0s	37°18'51"N	116°27'38"W		6.1-6.3	USCGS
	Handley	03/26/70	19h 00m 00.2s	37°18'01.7"N	116°32'02.8"W		6.2-6.3	USCGS

Table K-2

Comparison of the methods to compute station anomalies

Station	No. of data	Standard error of estimate for station-anomaly (sec.)		
		*1	*2	*3
BKS	20	0.55	0.52	0.40
EUR	31	0.43	0.46	0.46
PAS	27	0.68	0.67	0.69

*1 station anomaly is found from the average of all residuals at the station

*2 station anomaly is given in the form of A + B sin Az + C cos Az where Az is the back azimuth from the station to the epicenter. Values of A, B, and C are found by linear regression.

*3 station anomaly is given in the form of $a_0 + a_1 \cos\Delta + a_2 \sin\Delta \cos Az + a_3 \sin\Delta \sin Az$ where 'Δ' is the epicentral distance between source to station, 'Az' is the back azimuth from station to hypocenter. a_0, a_1, a_2 and a_3 were found by linear regression.

Table K-3

The baseline error in the Jeffreys-Bullen (J-B) times from travel time data of five Nevada Test Site (NTS) explosions

Correction to the observed J-B residual	1* No. of data	1* Average (sec.)	1* Standard deviation (sec.)	2+ No. of data	2+ Average (sec.)	2+ Standard deviation (sec)
A. None (raw J-B residuals)	487	-1.71	1.19	487	-1.71	1.19
B. Correction for the upper mantle model beneath the source between 0 to 550 km depth.	487	-1.59	1.06	487	-2.45	0.99
C. Correction to the shape of J-B travel time curves (focal depth 550 km)	487	-1.63	1.03	487	-2.52	0.92
D. Correction for station anomalies	487	-1.49	0.92	487	-2.35	0.86

1* WNA model (Julian, personal communication) instead of J-B model is chosen for the upper mantle structure beneath NTS

2+ NTS1 model (Green and Hales, 1968) instead of J-B model is chosen for the upper mantle structure beneath NTS.

Figure K-1. Error in the 'shape' of the Jeffreys-Bullen times (1940) of P wave for the focal depth of 550 km.

(left) As determined by Sengupta (1972) from 3300 bulletin data from 47 deep earthquakes without constaining the depths from the depth phases.

(right) As determined in this study from 1200 bulletin data from 14 deep earthquakes (two being of intermediate depth - one at Hindukush and the other at Greece) whose depths were constrained from the depth phases.

Figure K-2. Correction to the travel time residuals calculated from the Jeffreys-Bullen (J-B) times [or, 1968-P (Herrin) times] when the upper mantle (0-550 km) velocity structure beneath the source region is replaced by the WNA model (Julian, personal communication) or the NTS1 model (Green and Hales, 1968). These velocity models are shown in the upper inset. Note that the WNA model or the NTS1 model has been proposed for the upper mantle structure beneath the Nevada Test Site (NTS). Roughness in the correction curves is due to numerical interpolation.

Figure K-3. J-B travel time residuals of P wave for five explosions at the Nevada Test Site (NTS). The locations and origin times of these explosions are given in Table K-1 (b). The dashed line is the average of all residuals giving equal weight to each 2° distance cell.

(top) the J-B residuals without any correction.

(bottom) the J-B residuals corrected for (i) the upper mantle (0-550 km) structure beneath the Nevada Test Site by use of the WNA model (Fig. K-2) instead of the J-B model; (ii) the error in the shape of J-B times (Fig. K-1, right); (iii) the station anomalies, as listed in Appendix L.

Note that scatter in observed residuals remained almost the same in spite of these corrections, which strongly suggested the spherical asymmetry in the upper mantle structure beneath the NTS. The dashed line in the figure below represents the adopted baseline error in the wave J-B times for the focal depth of 550 km.

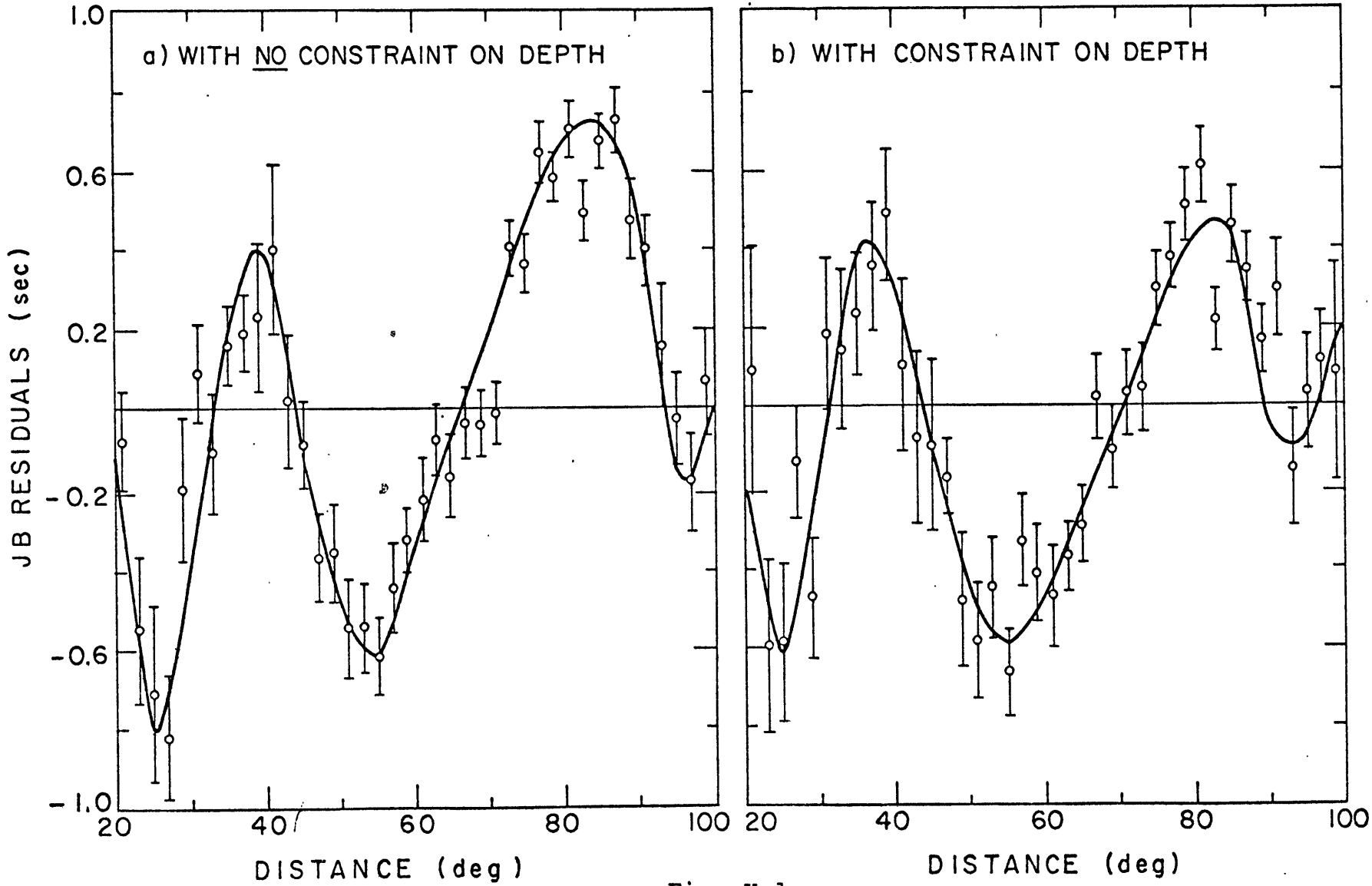

a) WITH NO CONSTRAINT ON DEPTH
b) WITH CONSTRAINT ON DEPTH
JB RESIDUALS (sec)
1.0
0.6
0.2
-0.2
-0.6
-1.0
20
40
60
80
100
DISTANCE (deg)
DISTANCE (deg)

Fig. K-1

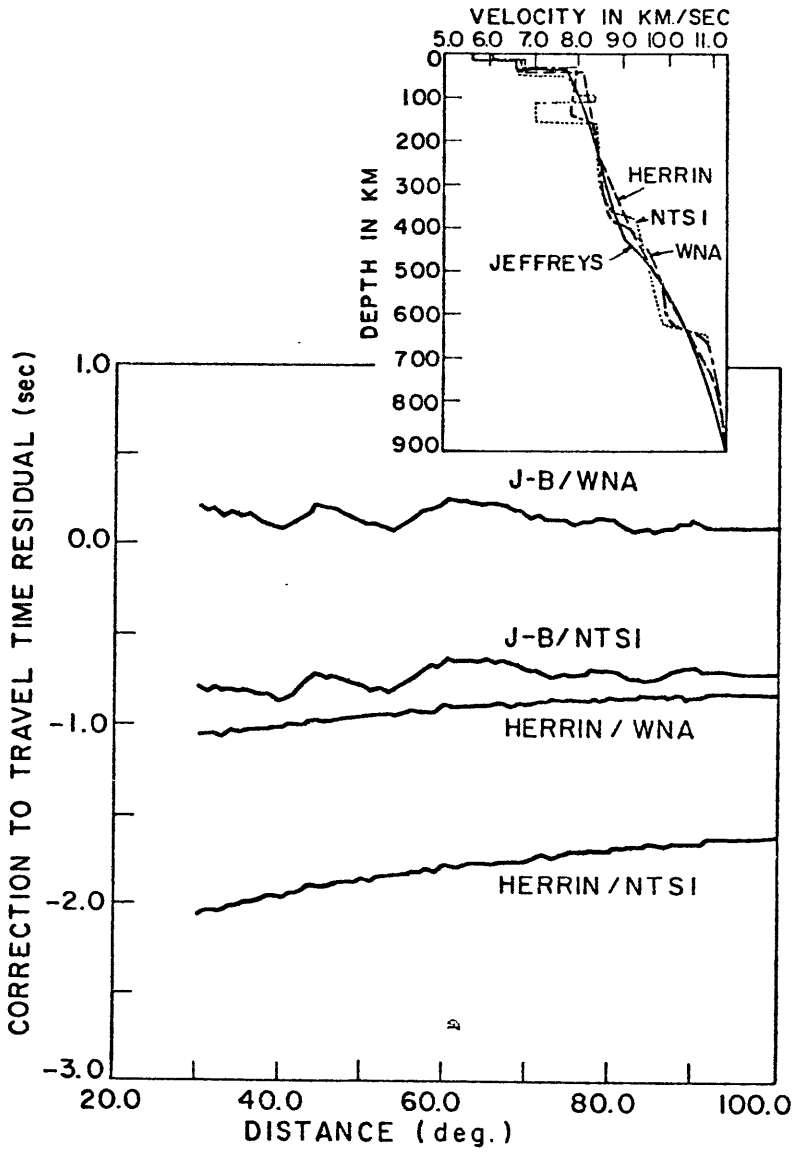

VELOCITY IN KM./SEC
5.0 6.0 7.0 8.0 9.0 10.0 11.0
0
100
200
300
400
500
600
700
800
900
DEPTH IN KM
HERRIN
NTS I
WNA
JEFFREYS
1.0
0.0
-1.0
-2.0
-3.0
CORRECTION TO TRAVEL TIME RESIDUAL (sec)
J-B/WNA
J-B/NTSI
HERRIN / WNA
HERRIN / NTSI
20.0
40.0
60.0
80.0
100.0
DISTANCE (deg.)

Fig. K-2

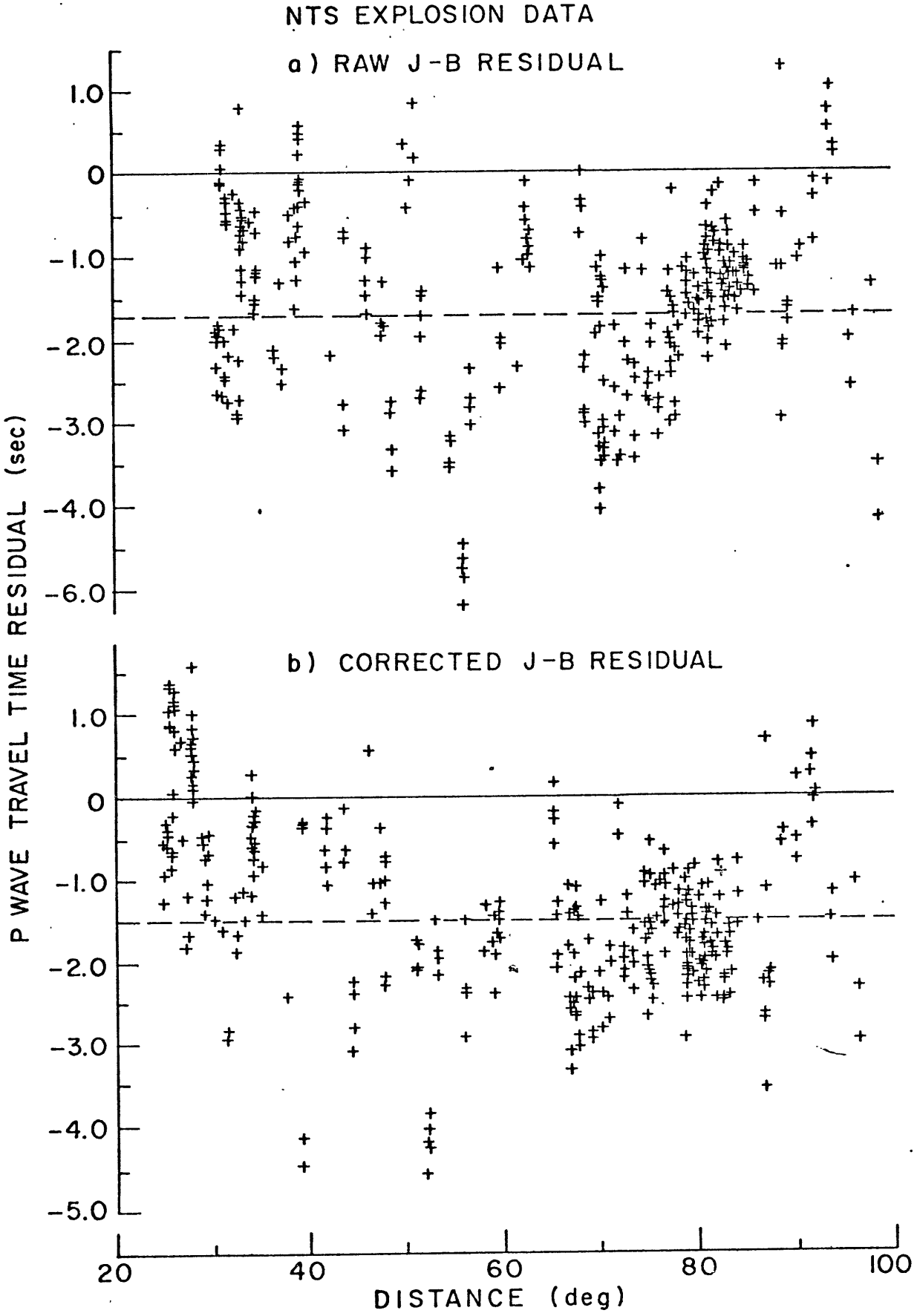

NTS EXPLOSION DATA
a) RAW J-B RESIDUAL
b) CORRECTED J-B RESIDUAL
P WAVE TRAVEL TIME RESIDUAL (sec)
1.0
0
-1.0
-2.0
-3.0
-4.0
-6.0
-5.0
20
40
60
80
100
DISTANCE (deg)

Fig. K-3

APPENDIX L

Station Anomalies for P and S Wave Travel Times

This appendix presents two tables. Table I shows our S wave station anomalies as determined from the deep focus travel times, in comparison with those of Doyle and Hales (1967) and Hales and Roberts (1970a). Table II shows our deep focus P wave travel time station anomalies in comparison with those of Cleary and Hales (1966), Herrin and Taggart (1968) and Lilwall and Douglas (1970). We have listed in these tables only the average station anomalies of Herrin and Taggart (1968) and Lilwall and Douglas (1970) who introduced also two other parameters related to a sinusoidal variation of the station anomaly with azimuth. We have also converted the confidence limits given by Lilwall and Douglas (1970) to standard deviations for convenience in comparison. N in these tables refers to the number of data used in computing the station anomalies and 'S.D.' is the abbreviation of 'standard deviation' as opposed to 'standard error'! Note that the positive values of these station anomalies (or, 'VALUE' as listed in these tables) mean later arrivals and the negative values imply the earlier arrivals as compared to those on the average earth. The units of these station anomalies are seconds.

TABLE I

S WAVE STATION ANOMALIES

	THIS STUDY			HALES + ROBERTS (1970)			DOYLE + HALES (1967)			P STN. ANOMALY (THIS STUDY)		
STA	VALUE	S.D.	N	VALUE	S.D.	N	VALUE	S.D.	N	VALUE	S.D.	N
AAE	+5.88	2.82	4							+1.13	0.28	4
AAM	-2.27	3.39	9	-3.21		6	-2.93	3.53	6	-0.95	0.26	4
ADE	-2.19	0.82	13							-0.19	0.58	8
AFI	-0.88	0.32	4							+0.03	0.43	11
ALQ	+1.25	2.87	21	+1.11		20	-0.28	5.54	14	+0.52	0.49	24
ANP	-0.66	4.09	12							+0.69	0.78	9
ANT	-0.46	1.68	3							-0.89	1.19	5
ARE	+4.15	6.22	2							+0.10	1.35	9
ATL	-2.49	0.49	14							-0.43	0.27	5
ATU	-5.26	1.72	6									
BAG	+0.37	2.47	13							-0.99	0.59	18
BEC	-1.32	0.00	1									
BHP	+0.33	0.14	2							+1.16	1.24	4
BKS	+1.78	2.86	12	+2.26		18	+0.19	5.07	11	+0.49	0.54	20
BLA	-0.52	2.65	9	-0.84		12	-4.29	4.74	9	-0.19	0.38	3
BUL	-0.98	2.27	7							+0.16	0.63	10
CAR	-4.33	0.76	2							-0.27	0.98	6
CHG	-1.07	2.07	13							+0.39	0.69	9
CMC	-2.07	1.50	20	-2.51		2	-4.05	3.30	2	-0.40	0.88	4
COL	-0.57	4.08	17							-0.64	0.86	33
COP	-3.06	3.11	8							+0.20	0.82	10
COR	+2.40	2.57	15	+2.37		11	+1.51	4.36	8	+0.87	0.54	10
CTA	-1.68	1.02	10							-0.43	0.46	33
DAL	-2.19	0.58	2	-1.42		11	-2.95	3.70	4	-0.35	0.17	2
DAV	+2.15	3.28	6							+0.36	0.70	11
DUG	+2.01	3.24	17	+0.65		6	-4.40	2.97	1	+0.50	0.37	28
EIL	-4.44	0.00	1									
ESK	-1.71	2.06	13							-0.79	0.30	11
FLO	-2.30	1.02	3	-2.35		11	-4.72	4.42	7	-1.68	0.01	2
GDH	-2.37	0.53	9				-3.29	3.98	5	-0.70	0.56	6

TABLE I (CONTINUED)

	THIS STUDY			HALES + ROBERTS (1970)			DOYLE + HALES (1967)			P STN. ANOMALY (THIS STUDY)		
STA	VALUE	S. D.	N	VALUE	S. D.	N	VALUE	S. D.	N	VALUE	S. D.	N
GEO	-0. 95	1. 83	6	-1. 38		12	-3. 93	4. 64	8	-0. 42	0. 59	6
GIE	+3. 68	1. 64	2									
GOL	+0. 07	3. 77	14	+1. 60		19	-1. 47	5. 09	12	+0. 65	0. 40	16
GSC	+4. 08	2. 50	7	-2. 80		3	-3. 42	3. 24	3	+0. 51	0. 71	6
GUA	-1. 55	4. 41	7							-0. 30	0. 48	16
HKC	+3. 42	1. 48	9							+1. 70	0. 39	6
HLW	-3. 16	0. 00	2							-0. 37	0. 83	5
HNR	-1. 63	0. 97	3							-1. 01	0. 47	3
HOW	+1. 63	0. 93	2									
IST	-4. 04	3. 99	3							-0. 45	0. 52	4
JCT	+0. 98	2. 74	11							+0. 13	0. 60	5
JER	-2. 63	4. 00	7							-0. 30	0. 54	10
KBL	-4. 72	0. 42	2							-0. 24	0. 48	4
KBS	-4. 39	4. 14	2									
KEV	-3. 90	1. 65	7							-0. 61	0. 54	15
KIP	+2. 33	3. 50	6							+0. 47	0. 45	17
KOD	+0. 00	2. 75	14							+0. 22	0. 42	8
KON	-2. 29	1. 12	8							-0. 58	0. 50	11
KTG	-0. 63	1. 86	4							-0. 09	0. 40	7
LAH	-2. 43	0. 28	2							-0. 47	0. 27	5
LEM	-2. 38	2. 03	10							-0. 20	0. 56	14
LON	-0. 86	2. 63	12	-0. 61		6	-2. 58	3. 46	4	+0. 03	0. 54	17
LPS	+0. 74	3. 30	10							-0. 21	0. 95	7
LUB	+0. 26	2. 73	7	-0. 10		11	-2. 35	4. 80	9	-0. 32	0. 88	3
MAL	-0. 93	1. 93	5									
MAN	+1. 58	1. 82	5							+0. 86	1. 11	12
MNN	-1. 18	0. 00	1	-2. 51		14	-5. 53	4. 53	9			
MSH	+0. 03	1. 54	5							+0. 64	0. 47	6
MUN	-2. 31	1. 70	8							-0. 70	0. 42	27
NAI	+5. 67	3. 21	7							+1. 04	0. 44	6

TABLE I (CONTINUED)

	THIS STUDY			HALES + ROBERTS (1970)			DOYLE + HALES (1967)			P STN. ANOMALY (THIS STUDY)		
STA	VALUE	S. D.	N	VALUE	S. D.	N	VALUE	S. D.	N	VALUE	S. D.	N
NDI	-3. 47	1. 99	15							-0. 99	0. 52	16
NHA	+3. 19	0. 66	5							+0. 88	1. 24	8
NIL	-1. 80	0. 42	2									
NNA	+3. 20	4. 33	4							+0. 24	0. 76	4
NOR	-1. 71	1. 73	17							-0. 78	0. 55	12
NUR	-4. 36	1. 26	8							-0. 65	0. 67	20
OGD	-2. 94	3. 98	3	-5. 78		3	-4. 06	3. 14	1			
OXF	-3. 08	0. 98	11	+1. 38		1				-1. 15	1. 22	7
PEL	-2. 58	0. 42	2							-0. 47	0. 29	7
PMG	-0. 30	2. 45	10							-0. 28	0. 45	32
POO	-2. 59	1. 32	12							-0. 39	0. 32	13
PRE	-0. 06	3. 73	6							-0. 39	0. 36	4
PTO	+0. 17	2. 84	10							-0. 81	0. 53	7
QUE	-1. 30	2. 37	10							-0. 10	0. 52	22
QUI	+1. 00	0. 00	1							+1. 60	1. 10	2
RAB	-0. 36	2. 90	4							-0. 49	0. 93	8
RAR	-0. 03	2. 23	9							+0. 92	0. 51	8
RCD	+2. 58	2. 30	11	-4. 57		6				+0. 58	0. 91	6
RIV	+1. 94	1. 76	12							+0. 86	0. 67	23
SBA	+3. 01	1. 23	15							+1. 20	0. 62	15
SCP	-2. 20	2. 28	12	-1. 47		10	-1. 61	4. 44	7	-0. 68	0. 27	2
SDB	-2. 21	3. 13	5							-0. 51	0. 99	8
SEO	+2. 08	4. 78	3							+0. 68	0. 37	6
SHA	-3. 12	0. 34	3	+0. 53		8	-1. 98	3. 98	5			
SHI	-3. 24	0. 92	9							-0. 81	0. 41	17
SHK	+0. 34	2. 57	4							+0. 31	0. 79	7
SHL	-2. 26	0. 67	18							-0. 02	0. 52	22
SJG	-3. 16	1. 48	4							-1. 04	0. 92	5
SPA	-1. 74	1. 39	12							-0. 05	0. 63	20
TAB	-0. 79	2. 36	6							+0. 36	0. 42	8

TABLE I (CONTINUED)

	THIS STUDY			HALES + ROBERTS (1970)			DOYLE + HALES (1967)			P STN. ANOMALY (THIS STUDY)		
STA	VALUE	S.D.	N	VALUE	S.D.	N	VALUE	S.D.	N	VALUE	S.D.	N
TAU	-0.80	2.50	7							+0.23	0.46	29
TOL	+4.43	0.81	5							-0.12	0.49	5
TRI	-3.21	2.53	7							-0.55	0.98	2
TRN	+0.66	0.59	4							+0.09	0.40	5
TUC	+1.68	2.27	23	+1.67		5	+1.50	3.45	3	+0.64	0.60	10
UME	-2.38	2.15	7							-0.85	0.87	9
VAL	-1.37	1.12	7							-0.57	0.56	6
WEL	-2.93	1.40	7							-1.75	0.37	8
WES	-1.48	2.98	3	-0.97		10	-2.46	4.44	7	+0.14	0.28	10
WIN	-0.05	1.37	10							-0.20	1.21	5

TABLE II

P WAVE STATION ANOMALIES

	THIS STUDY			HERRIN ET. AL. (1968)			LILWALL + DOUGLAS (1970)			CLEARY + HALES (1966)		
STA	VALUE	S. D.	N	VALUE	S. D.	N	VALUE	S. D.	N	VALUE	S. D.	N
AAB	1.49	0.37	8	0.06	0.99	110				0.30	0.73	6
AAE	1.13	0.28	4	1.12	1.12	16	2.16	0.88	30	1.50	0.17	3
AAM	-0.95	0.26	4	-0.01	0.87	18	0.19	0.98	24	-0.30	0.54	6
ABU	0.33	0.47	10				0.29	0.57	9			
ADE	-0.19	0.58	23	0.03	1.04	118	-0.29	0.96	30	-1.20	0.73	6
ADK	-0.61	0.54	8				-0.37	0.87	17			
AFI	0.03	0.43	11	0.60	1.37	60	0.90	0.94	27	0.10	2.40	4
AKU	1.15	0.30	2				1.42	0.80	21			
ALE	-0.30	0.42	6	-0.06	0.84	120	-0.94	0.87	48	-0.68	0.64	14
ALQ	0.52	0.49	24	0.23	0.86	72	0.47	0.83	38	0.26	0.69	21
ANP	0.69	0.78	9				0.86	0.94	21			
ANT	-0.89	1.19	5	-0.52	1.47	17	-1.08	0.98	10	-0.90	0.57	2
APA	-0.91	0.39	9	-0.28	0.92	129	-0.83	1.15	18	-0.90	0.73	6
ARE	0.10	1.35	9	0.54	1.30	39	-0.04	1.72	11			
ATL	-0.43	0.27	5	0.04	0.62	16	-0.05	1.00	25			
AVE	-0.19	0.65	5									
BAG	-0.99	0.59	18	-0.03	1.20	63	-0.38	0.98	33	-2.00	0.60	9
BCN	0.85	0.61	22	0.91	0.88	83	0.85	0.88	37	1.10	0.60	4
BHP	1.16	1.24	4	-0.09	1.21	24	-0.20	0.78	13	-0.10	1.34	5
BKR	0.93	0.42	7	0.57	0.92	51	0.87	1.20	15			
BKS	0.49	0.54	20	0.84	0.68	81	0.78	0.85	25	0.26	0.66	17
BLA	-0.19	0.38	3	-0.03	0.73	64	0.18	0.78	24	-0.48	0.61	13
BLC	-0.96	0.48	8									
BMO	0.18	0.37	23	-0.41	0.81	145	-0.57	0.90	61	-0.22	0.61	13
BNG	-0.68	0.60	5				-0.88	0.90	12	-0.80	0.69	3
BNH	0.33	0.73	10				0.03	1.33	21			
BNS	-0.21	0.53	11	0.14	0.66	45	-0.37	0.90	41	0.20	0.40	4
BOD	0.15	0.71	14	-0.22	0.87	137	-1.05	1.20	22	-1.10	0.60	4
BOG	1.30	0.61	6	0.96	1.03	34	1.10	0.97	15	1.10	1.12	5
BOZ	0.46	0.58	20	-0.25	0.66	22	-0.06	0.87	42	-0.20	0.67	5

TABLE II

P WAVE STATION ANOMALIES

	THIS STUDY			HERRIN ET. AL. (1968)			LILWALL + DOUGLAS (1970)			CLEARY + HALES (1966)		
STA	VALUE	S.D.	N	VALUE	S.D.	N	VALUE	S.D.	N	VALUE	S.D.	N
AAB	1.49	0.37	8	0.06	0.99	110				0.30	0.73	6
AAE	1.13	0.28	4	1.12	1.12	16	2.16	0.88	30	1.50	0.17	3
AAM	-0.95	0.26	4	-0.01	0.87	18	0.19	0.98	24	-0.30	0.54	6
ABU	0.33	0.47	10				0.29	0.57	9			
ADE	-0.19	0.58	23	0.03	1.04	118	-0.29	0.96	30	-1.20	0.73	6
ADK	-0.61	0.54	8				-0.37	0.87	17			
AFI	0.03	0.43	11	0.60	1.37	60	0.90	0.94	27	0.10	2.40	4
AKU	1.15	0.30	2				1.42	0.80	21			
ALE	-0.30	0.42	6	-0.06	0.84	120	-0.94	0.87	48	-0.68	0.64	14
ALQ	0.52	0.49	24	0.23	0.86	72	0.47	0.83	38	0.26	0.69	21
ANP	0.69	0.78	9				0.86	0.94	21			
ANT	-0.89	1.19	5	-0.52	1.47	17	-1.08	0.98	10	-0.90	0.57	2
APA	-0.91	0.39	9	-0.28	0.92	129	-0.83	1.15	18	-0.90	0.73	6
ARE	0.10	1.35	9	0.54	1.30	39	-0.04	1.72	11			
ATL	-0.43	0.27	5	0.04	0.62	16	-0.05	1.00	25			
AVE	-0.19	0.65	5									
BAG	-0.99	0.59	18	-0.03	1.20	63	-0.38	0.98	33	-2.00	0.60	9
BCN	0.85	0.61	22	0.91	0.88	83	0.85	0.88	37	1.10	0.60	4
BHP	1.16	1.24	4	-0.09	1.21	24	-0.20	0.78	13	-0.10	1.34	5
BKR	0.93	0.42	7	0.57	0.92	51	0.87	1.20	15			
BKS	0.49	0.54	20	0.84	0.68	81	0.78	0.85	25	0.26	0.66	17
BLA	-0.19	0.38	3	-0.03	0.73	64	0.18	0.78	24	-0.48	0.61	13
BLC	-0.96	0.48	8									
BMO	0.18	0.37	28	-0.41	0.81	145	-0.57	0.90	61	-0.22	0.61	13
BNG	-0.68	0.60	5				-0.88	0.90	12	-0.80	0.69	3
BNH	0.33	0.73	10				0.03	1.33	21			
BNS	-0.21	0.53	11	0.14	0.66	45	-0.37	0.90	41	0.20	0.40	4
BOD	0.15	0.71	14	-0.22	0.87	137	-1.05	1.20	22	-1.10	0.60	4
BOG	1.30	0.61	6	0.96	1.03	34	1.10	0.97	15	1.10	1.12	5
BOZ	0.46	0.58	20	-0.25	0.66	22	-0.06	0.87	42	-0.20	0.67	5

TABLE II (CONTINUED)

	THIS STUDY			HERRIN ET. AL. (1968)			LILWALL + DOUGLAS (1970)			CLEARY + HALES (1966)		
STA	VALUE	S. D.	N	VALUE	S. D.	N	VALUE	S. D.	N	VALUE	S. D.	N
ISK	-0. 62	0. 42	5									
ISO	-0. 42	1. 11	10	0. 04	1. 00	74	-0. 24	0. 85	32	0. 30	0. 69	3
IST	-0. 45	0. 52	4	0. 39	0. 98	74	-0. 31	0. 77	41	0. 00	0. 63	10
JAS	0. 36	0. 44	24				0. 23	0. 55	37			
JCT	0. 13	0. 60	5									
JER	-0. 30	0. 54	10	0. 83	0. 91	68	0. 62	0. 89	38	0. 70	0. 57	8
KAT	0. 86	1. 03	7	0. 94	0. 97	58	0. 75	1. 41	23			
KBL	-0. 24	0. 48	4									
KEV	-0. 61	0. 54	15	0. 15	0. 91	56	-0. 25	0. 89	47	-0. 80	0. 63	10
KEW	-0. 86	0. 37	7	0. 14	0. 98	55	-0. 63	0. 78	19	0. 10	0. 72	13
KHC	-0. 46	0. 38	12	-0. 60	0. 89	62	-0. 98	0. 90	48	-0. 60	0. 80	4
KHO	0. 99	0. 42	7	0. 86	0. 95	97	0. 30	1. 20	19	1. 30	0. 40	4
KIP	0. 47	0. 45	17	1. 06	1. 13	113	1. 30	0. 87	28	-0. 10	0. 85	8
KIR	-0. 71	0. 55	18	-0. 20	0. 83	161	-0. 85	0. 89	51	-0. 70	0. 72	13
KJN	-0. 77	0. 54	15	0. 09	0. 95	66	-1. 02	0. 52	37	-0. 50	0. 85	8
KLG	-1. 07	0. 69	24				-1. 23	0. 62	17			
KOD	0. 22	0. 42	8				0. 43	0. 81	13			
KON	-0. 58	0. 50	11	0. 17	0. 69	27	-0. 39	0. 96	44	0. 50	0. 60	9
KOU	0. 11	0. 94	14	0. 86	0. 96	41	0. 26	0. 99	14	0. 20	0. 49	6
KRK	-0. 29	0. 48	7				-0. 25	0. 96	34			
KRP	0. 58	0. 49	17				0. 07	0. 88	16			
KRV	-0. 54	0. 40	5				-1. 18	0. 80	21	-0. 10	0. 00	3
KSA	0. 43	0. 34	6	1. 15	1. 19	48	-0. 21	1. 65	20	-0. 10	0. 90	9
KTG	-0. 09	0. 40	7	0. 97	0. 75	19	0. 42	0. 87	26			
KUR	-0. 38	1. 15	6	0. 40	1. 30	33	0. 80	1. 01	5			
LAH	-0. 47	0. 27	5	-0. 42	0. 96	69				-0. 50	1. 34	5
LAN	1. 07	0. 86	6	0. 63	0. 81	149				0. 00	0. 49	6
LAO	0. 44	1. 07	8				-0. 07	0. 45	17			
LAW	-1. 04	0. 22	6	-0. 73	0. 91	76	-0. 75	0. 86	33	-1. 00	0. 66	11
LEM	-0. 20	0. 56	14	-0. 98	1. 22	58	0. 00	1. 35	12	-0. 80	1. 73	3

TABLE II (CONTINUED)

	THIS STUDY			HERRIN ET. AL. (1968)			LILWALL + DOUGLAS (1970)			CLEARY + HALES (1966)		
STA	VALUE	S. D.	N	VALUE	S. D.	N	VALUE	S. D.	N	VALUE	S. D.	N
FCC	-0. 90	0. 34	4									
FFC	-0. 67	0. 28	3									
FGU	0. 57	0. 42	12	-0. 09	0. 98	58	-0. 25	0. 57	12	-0. 60	0. 35	3
FHC	1. 43	0. 55	3									
FLN	-0. 73	0. 56	11	-0. 18	1. 05	63	-0. 54	0. 94	26			
FLO	-1. 68	0. 01	2	-0. 53	0. 85	39	-0. 92	0. 61	4	-0. 95	0. 64	14
FRU	0. 77	0. 27	9	0. 74	0. 90	115	1. 57	2. 77	3	0. 40	0. 79	7
FSJ	0. 41	0. 45	9				-0. 03	0. 33	3			
FUR	-0. 15	1. 10	8				-0. 52	0. 99	21			
GAR	0. 16	0. 23	8	-0. 35	0. 88	40	-0. 77	0. 94	19			
GCA	0. 91	0. 54	17	0. 62	0. 79	38	0. 40	0. 81	19	0. 60	0. 40	4
GDH	-0. 70	0. 56	6	-0. 05	1. 04	23	-0. 26	0. 86	27	-0. 40	0. 57	8
GEO	-0. 42	0. 59	6	0. 12	0. 35	43	-0. 55	0. 86	16	-0. 48	0. 62	12
GNZ	-0. 64	0. 71	6				0. 80	1. 35	13			
GOL	0. 65	0. 40	16	0. 25	0. 73	109	0. 46	0. 86	38	0. 24	0. 68	18
GOT	-1. 38	0. 87	5	-0. 05	0. 97	60	-1. 13	0. 84	10	-0. 30	0. 90	9
GRC	-0. 81	0. 81	9	-0. 27	0. 88	30	-0. 68	0. 61	19	-0. 50	0. 45	5
GRR	-0. 60	0. 51	10				-0. 37	0. 83	27			
GRS	0. 12	0. 76	6	0. 47	1. 03	107	0. 42	1. 18	16	1. 50	1. 27	2
GUA	-0. 30	0. 48	16	-0. 03	1. 51	52	-0. 66	0. 94	20			
GWC	-1. 83	1. 00	3									
HHM	0. 36	0. 45	20	0. 13	1. 01	107	-0. 32	0. 89	43	-0. 50	0. 79	7
HKC	1. 70	0. 39	6	0. 83	1. 19	78	0. 69	0. 96	30	0. 60	0. 57	2
HLW	-0. 37	0. 83	5	0. 42	1. 26	20	-0. 71	0. 97	15			
HNR	-1. 01	0. 47	13	-0. 69	1. 20	53	-1. 38	0. 93	25	-0. 20	1. 00	4
HON	0. 71	0. 59	8	1. 32	1. 28	96	0. 97	0. 83	24	0. 60	0. 45	5
HUA	1. 93	0. 72	5	1. 58	1. 26	37	1. 38	0. 92	14			
HVO	0. 74	0. 45	12	0. 48	1. 03	89	0. 93	0. 89	31	0. 10	0. 79	7
IFR	0. 35	1. 11	9				-0. 05	0. 88	37			
INK	-0. 48	0. 40	4									

TABLE II (CONTINUED)

	THIS STUDY			HERRIN ET. AL. (1968)			LILWALL + DOUGLAS (1970)			CLEARY + HALES (1966)		
STA	VALUE	S. D.	N	VALUE	S. D.	N	VALUE	S. D.	N	VALUE	S. D.	N
NHA	0. 88	1. 24	8	0. 55	1. 31	31	-0. 23	1. 57	6	-0. 30	0. 66	11
NNA	0. 24	0. 76	4	-0. 09	1. 04	14	-0. 40	0. 92	6	-1. 00	1. 21	3
NOR	-0. 78	0. 55	12	-0. 55	1. 12	86	-0. 84	0. 88	49	-0. 20	0. 40	4
NOU	0. 02	0. 47	22	0. 23	1. 26	50	0. 42	1. 20	15	0. 90	0. 60	4
NUR	-0. 65	0. 67	20	-0. 33	0. 78	166	-0. 87	0. 91	62	-0. 60	0. 32	10
NVL	-0. 39	0. 45	9	0. 66	0. 93	56						
ORV	-0. 03	0. 71	26	-0. 11	0. 66	67	-0. 20	0. 89	47			
OTT	-0. 81	0. 54	3	-0. 62	0. 95	78	-0. 96	0. 86	38	-1. 24	0. 57	9
PAL	-0. 63	0. 72	5	-0. 06	1. 10	87	-0. 07	0. 87	26	0. 30	0. 85	8
PAS	0. 18	0. 68	27	0. 36	0. 88	185	0. 32	0. 64	50	-0. 04	0. 67	20
PEL	-0. 47	0. 29	7									
PET	-0. 25	0. 76	8	0. 06	1. 19	114	0. 50	1. 89	14			
PHC	0. 51	0. 51	2				0. 36	1. 39	8			
PLV	1. 67	1. 03	5				1. 75	1. 17	10			
PNG	-0. 28	0. 45	32	-0. 38	1. 00	122	-0. 62	0. 91	32	-0. 90	0. 60	9
PNT	0. 27	0. 37	14	-0. 21	0. 89	81	-0. 48	0. 50	15	0. 06	0. 68	16
POO	-0. 39	0. 32	13	0. 66	1. 03	31	-0. 56	0. 82	30	-0. 50	0. 52	3
PPT	1. 15	0. 65	13				1. 97	0. 90	12			
PRE	-0. 39	0. 36	4				-0. 39	1. 00	44	-0. 20	0. 17	3
PRI	0. 83	0. 44	24	0. 83	0. 80	136	0. 71	0. 70	44	0. 80	0. 92	21
PRS	0. 39	0. 48	9	0. 69	0. 81	107				0. 50	0. 73	6
PRU	0. 08	0. 89	10	0. 02	0. 84	146	-0. 56	0. 94	61	0. 50	0. 69	12
PTO	-0. 81	0. 53	7	-0. 11	1. 80	16	-0. 45	1. 11	38	-1. 20	0. 57	2
PVC	-0. 04	0. 64	14	0. 94	1. 13	17	0. 65	1. 28	12			
QUE	-0. 10	0. 52	22	0. 09	1. 00	125	0. 08	0. 66	24	0. 30	0. 90	9
QUI	1. 60	1. 10	2				1. 11	0. 87	5			
RAB	-0. 49	0. 93	8	-0. 71	1. 07	73	-0. 11	0. 78	21	-2. 10	1. 20	4
RAR	0. 92	0. 51	8				0. 74	1. 31	7			
RBA	-0. 27	0. 76	5				-0. 42	1. 14	15			
RCD	0. 58	0. 91	6	0. 30	1. 05	30	-0. 03	1. 51	43	-0. 12	0. 50	4

TABLE II (CONTINUED)

	THIS STUDY			HERRIN ET. AL. (1968)			LILWALL + DOUGLAS (1970)			CLEARY + HALES (1966)		
STA	VALUE	S. D.	N	VALUE	S. D.	N	VALUE	S. D.	N	VALUE	S. D.	N
LHA	1 50	0. 40	5	1. 23	0. 89	131				1. 70	0. 87	3
LHN	0. 05	0. 85	5				-0. 01	0. 96	24			
LJU	-0. 61	0. 49	5	0. 12	0. 93	54	-0. 41	0. 82	16	0. 10	0. 53	7
LNS	-0. 30	0. 58	5									
LON	0. 03	0. 54	17	0. 02	0. 78	31	-0. 11	0. 86	23	-0. 02	0. 57	10
LOR	-0. 75	0. 66	12				-0. 80	0. 88	30			
LPB	0. 15	0. 64	6	0. 38	1. 44	19	0. 47	0. 98	20	1. 00	0. 42	2
LPS	-0. 21	0. 95	7							0. 10	0. 73	6
LUB	-0. 32	0. 88	3	-0. 06	0. 71	71	0. 08	0. 87	28	-0. 20	0. 60	4
LUG	0. 02	1. 09	14				-0. 04	0. 70	5			
MAG	-0. 10	1. 03	6	0. 33	1. 09	109	-0. 28	1. 28	13			
MAN	0. 86	1. 11	12	0. 83	1. 77	61	-0. 11	0. 90	14	-0. 10	0. 79	7
MAT	-0. 93	0. 52	22	-0. 67	0. 89	156	-1. 24	0. 96	41	-1. 20	1. 13	8
MAW	-0. 22	0. 41	17	0. 08	0. 80	67	0. 43	0. 85	18	-1. 70	0. 69	3
MBC	-0. 12	0. 32	10	-0. 05	1. 01	157	-0. 58	0. 89	60	-0. 41	0. 60	10
MEK	-1. 06	0. 36	5									
MHC	0. 74	0. 50	21				0. 72	0. 87	48	0. 70	0. 42	18
MIN	-0. 07	0. 70	19				-0. 46	0. 80	16			
MIR	-0. 55	0. 72	18	-0. 37	0. 94	88	-0. 06	0. 92	14	-1. 90	0. 57	2
MMA	0. 67	0. 47	6									
MNG	-1. 63	1. 41	3									
MNT	-0. 24	0. 38	10	0. 00	0. 88	76	-0. 36	0. 87	34	-0. 10	0. 60	9
MNW	-0. 01	0. 42	6				-0. 39	0. 68	4			
MOO	0. 56	0. 66	15	0. 91	1. 10	65	0. 97	0. 90	14	1. 10	0. 69	3
MOX	0. 14	0. 58	7				-0. 70	0. 91	53			
MSH	0. 64	0. 47	6				1. 30	0. 53	11			
MUN	-0. 70	0. 42	27	-0. 42	0. 97	117	-0. 74	0. 83	29	-1. 20	0. 80	4
NAI	1. 04	0. 44	6				1. 99	0. 91	27			
NDI	-0. 99	0. 52	16	0. 33	1. 10	24	-0. 46	0. 97	45	-0. 80	0. 53	7
NEW	-0. 03	0. 36	16				-0. 83	0. 76	32			

TABLE II (CONTINUED)

	THIS STUDY			HERRIN ET. AL. (1968)			LILWALL + DOUGLAS (1970)			CLEARY + HALES (1966)		
STA	VALUE	S. D.	N	VALUE	S. D.	N	VALUE	S. D.	N	VALUE	S. D.	N
STU	-0. 44	0. 41	14	-0. 30	0. 87	143	-0. 41	0. 91	45	0. 00	0. 80	16
SVE	0. 19	0. 49	5	-0. 23	0. 99	160	-0. 63	0. 94	21	-0. 30	0. 57	8
TAB	0. 36	0. 42	8				0. 48	0. 87	19			
TAC	1. 77	1. 28	4	2. 33	1. 54	27	1. 13	0. 87	12	1. 60	0. 71	2
TAS	0. 32	0. 36	9	0. 72	1. 03	151	0. 40	0. 98	25	0. 20	0. 90	9
TAU	0. 23	0. 46	29	0. 61	1. 16	65	0. 26	1. 24	21	0. 40	1. 20	4
TFO	1. 12	0. 31	19	0. 64	1. 30	109	0. 66	0. 90	56	0. 69	0. 49	5
TIK	-1. 04	0. 40	16	-0. 70	1. 14	132	-1. 87	1. 17	22	-0. 60	1. 21	3
TNG	-2. 13	0. 47	5				-1. 53	1. 23	3	-1. 50	0. 80	4
TNP	0. 46	0. 47	10				0. 70	1. 70	18			
TOL	-0. 12	0. 49	5	0. 24	1. 00	101	-0. 06	0. 73	24	-0. 30	0. 77	15
TOO	0. 20	0. 33	31	0. 17	0. 87	107	-0. 51	0. 98	33	0. 30	0. 73	6
TRI	-0. 55	0. 98	2	0. 45	0. 98	66	-0. 97	0. 94	27	-0. 50	0. 79	7
TRN	0. 09	0. 40	5	0. 42	1. 10	45	-0. 08	0. 89	20	-0. 20	0. 67	5
TRO	-0. 71	0. 60	16	-0. 01	0. 94	130	-0. 68	0. 81	39	-0. 60	0. 75	14
TRR	0. 81	0. 42	22	0. 53	1. 03	63	0. 72	0. 94	21	0. 80	0. 35	3
TSK	-1. 14	0. 83	5				-0. 95	1. 07	12			
TUC	0. 64	0. 60	25	0. 33	0. 76	94	0. 14	0. 87	48	0. 19	0. 54	6
TUL	-0. 46	0. 32	10	-0. 60	0. 86	69	-0. 52	0. 87	36	-0. 40	0. 69	12
TUM	0. 68	0. 60	10	0. 55	1. 03	13	0. 60	0. 85	15			
UBO	0. 60	0. 31	26	0. 10	0. 75	125	0. 03	0. 88	58	0. 02	0. 54	9
UME	-0. 85	0. 87	9	-0. 34	0. 97	56	-1. 49	0. 67	23	-0. 60	0. 28	8
UNM	0. 03	0. 96	2									
UPP	-1. 07	0. 94	22	-0. 58	0. 80	167	-1. 24	0. 91	57	-0. 80	0. 72	13
UZH	-1. 02	0. 64	6	0. 51	0. 80	94	-0. 10	1. 03	17	0. 40	0. 20	4
VAL	-0. 57	0. 56	6	0. 63	0. 89	26	-0. 04	0. 89	35			
VIC	0. 42	0. 76	4	0. 18	0. 87	112	-0. 06	0. 77	14	-0. 18	0. 66	15
VLA	1. 21	0. 31	8	-0. 19	1. 20	70				-1. 00	0. 14	2
VUN	0. 46	0. 67	5				0. 53	0. 51	4			
WEL	-1. 75	0. 37	8	-0. 09	1. 15	56	-0. 11	0. 94	22	0. 20	1. 57	5

TABLE II (CONTINUED)

	THIS STUDY			HERRIN ET. AL. (1968)			LILWALL + DOUGLAS (1970)			CLEARY + HALES (1966)		
STA	VALUE	S. D.	N	VALUE	S. D.	N	VALUE	S. D.	N	VALUE	S. D.	N
RIV	0.86	0.67	23	0.45	1.16	85	1.03	0.94	23	0.50	0.60	4
ROX	-0.28	0.69	5				0.52	1.76	11			
RSL	-1.38	1.67	7				-0.22	1.06	11	-0.20	0.90	9
SAP	-1.16	0.69	5	-0.48	1.40	16	-1.01	0.87	5			
SAV	1.01	0.60	21				1.19	0.90	16			
SBA	1.20	0.62	15	0.97	0.99	73	1.57	0.95	17	0.00	0.14	2
SCH	-0.51	0.60	9	-0.43	0.70	33	-0.71	0.91	15	-0.80	0.68	18
SCP	-0.68	0.27	2	-0.12	0.85	75	-0.36	1.48	20	-0.20	0.64	16
SDB	-0.51	0.99	8	0.29	1.04	15	0.10	0.91	22	-0.20	0.49	6
SEM	-0.90	0.32	6	-0.27	1.02	118	-1.06	0.99	21	-0.70	0.85	8
SEO	0.68	0.37	6				-0.64	0.90	12			
SES	-0.28	0.43	13									
SFA	-0.41	0.54	4				-0.34	1.02	5			
SHF	-0.32	0.45	5	-0.11	0.87	51				-0.37	0.60	11
SHI	-0.81	0.41	17	-0.59	0.88	102	-0.71	0.92	43	-0.50	0.28	8
SHK	0.31	0.79	7				-0.51	0.88	12			
SHL	-0.02	0.52	22	-0.48	1.20	138	-0.53	0.97	37	-1.50	0.53	7
SIC	-0.46	0.39	6				-0.41	1.42	7	-0.22	0.48	2
SIT	0.92	0.63	9	1.00	1.07	49	1.25	0.77	15	0.90	1.04	3
SJG	-1.04	0.92	5				-0.21	1.32	15			
SKA	-0.66	0.80	5	0.25	0.85	66	-0.87	0.99	21	-0.60	0.79	7
SLC	0.28	0.23	15	0.30	0.83	74	0.26	0.86	38	0.40	0.24	6
SLD	0.93	0.39	15				0.75	0.86	27			
SNA	0.04	0.54	4									
SOD	-0.55	0.54	15	-0.23	0.90	172	-0.81	0.54	45	-0.60	0.69	12
SPA	-0.05	0.63	20	0.19	1.08	74	0.43	0.94	21	-1.10	1.12	5
SPO	0.59	0.43	11	0.42	0.79	33	0.31	1.17	22	-0.20	0.49	6
SSC	-0.90	0.63	11				-0.50	0.82	30			
SSF	-0.59	0.59	12				-0.82	0.90	28			
STR	-0.12	0.62	8	0.13	0.87	96	-0.16	0.90	41	0.20	0.77	15

TABLE II (CONTINUED)

	THIS STUDY			HERRIN ET. AL. (1968)			LILWALL + DOUGLAS (1970)			CLEARY + HALES (1966)		
STA	VALUE	S. D.	N	VALUE	S. D.	N	VALUE	S. D.	N	VALUE	S. D.	N
WES	0.14	0.28	10	0.91	1.07	35	-0.11	0.87	17	-0.05	0.57	8
WIL	-0.18	0.42	12	0.48	1.10	64	0.18	1.37	12	-0.40	0.89	5
WIN	-0.20	1.21	5	-0.99	1.07	11	0.90	0.92	16	0.30	0.49	6
WMO	0.01	0.63	9	-0.70	0.85	162	-0.91	0.89	47	-0.87	0.70	22
WRA	-0.99	0.47	10				-1.24	0.74	12			
WRS	-0.48	0.78	9	-0.83	1.26	85	-0.35	1.27	23	-0.20	0.85	8
YKC	-0.51	0.50	11	-0.76	1.01	13	-0.52	0.48	23			
YSS	0.29	0.52	16	0.26	0.88	117	0.25	1.34	17			

APPENDIX M

Station Anomalies for P and S Wave Amplitudes

In this Appendix the station amplitude anomalies are presented in two tables. Table I shows the short period (period <3 seconds) station anomalies for $\log_{10}$-amplitude (microns) data of the deep focus P, SV and SH waves. Table II shows the similar station anomalies for long period (period >5 seconds) data. N in these tables refers to the number of data used in computing the station anomalies and 'S.D.' stands for the abbreviation of 'standard deviation' as opposed to 'standard error'. Note that the positive values of these station anomalies (or 'VALUE' as shown in these tables) mean higher amplitudes and the negative values imply smaller amplitudes than those on the average earth.

TABLE I

STATION ANOMALIES FOR LOGARITHMIC(COMMON) AMPLITUDE (PERIOD $\leq$ 3 SECONDS)

	P WAVE			SV WAVE			SH WAVE		
STA	VALUE	S. D.	N	VALUE	S. D.	N	VALUE	S. D.	N
AAE	0.58	0.00	1	0.97	0.00	1			
AAM	0.25	0.00	1						
ADE	-0.26	0.23	4						
AFI	-0.25	0.37	2						
AKU	0.25	0.00	1						
ALQ	0.10	0.74	3	-0.34	0.33	2	0.21	0.09	2
ANP	-0.20	0.59	3	-0.33	0.00	1			
AQU	0.16	0.00	1						
ARE									
ATL	0.44	0.17	2				0.78	0.00	1
ATU	0.38	0.30	3	0.11	0.00	1			
BAG	-0.05	0.23	3	0.33	0.00	1	0.17	0.00	1
BEC									
BKS	0.22	0.45	6	1.02	0.73	2	0.14	0.09	2
BLA				0.89	0.00	1	0.88	0.00	1
BUL	0.21	0.00	1						
CHG				0.04	0.00	1	-0.55	0.00	1
CMC				0.76	1.35	2	0.43	0.43	2
COL	0.21	0.43	5						
COP	0.38	0.00	1	0.40	0.00	1			
COR	0.19	0.13	4						
CTA	-0.26	0.30	2	0.71	0.81	2			
DAL									
DAV	0.51	0.48	4						
DUG	0.31	0.27	5	0.45	0.00	1	-0.05	0.00	1
EIL									
ESK	-0.29	0.14	2	-0.08	0.67	3	-0.54	0.00	1
FLO									
GDH	-0.09	0.23	2						
GEO	0.20	0.09	3	-0.14	0.00	1			

TABLE I (CONTINUED)

	P WAVE			SV WAVE			SH WAVE		
STA	VALUE	S.D.	N	VALUE	S.D.	N	VALUE	S.D.	N
GIE									
GOL	0.13	0.41	4	0.26	0.16	2	-0.04	0.03	2
GRM	0.63	0.00	1						
GSC				0.20	0.00	1	0.10	0.00	1
GUA	0.84	0.00	1	-0.40	1.55	2	0.40	0.00	1
HKC	-0.16	0.49	3						
HLW	-0.60	0.00	1						
HNR				0.86	0.00	1			
IST	-0.26	0.15	3	-0.24	0.00	1			
JCT	-0.77	0.00	1	0.41	0.08	2	-0.06	0.12	2
JER	-0.34	0.13	2						
KBL									
KBS									
KEV	0.07	0.85	2						
KIP	0.37	0.59	3	0.66	0.00	1	0.36	0.00	1
KOD	-0.23	0.33	2						
KON	-0.13	0.00	1						
KTG	0.39	0.34	4	0.16	0.00	1			
LAH									
LEM	0.02	0.09	2						
LON	-0.11	0.47	5	-0.08	0.53	3	-0.28	0.16	3
LPS				0.05	0.00	1	-0.49	0.00	1
LUB	0.09	0.66	2						
MAL	-0.08	0.45	3						
MAN							-0.30	0.00	1
MAT	-0.21	0.00	1						
MNN									
MSH	-0.17	0.06	2						
MUN	0.24	0.21	3						
NAI	-0.08	0.20	2	0.80	0.00	1	0.33	0.00	1

TABLE I (CONTINUED)

	P WAVE			SV WAVE			SH WAVE		
STA	VALUE	S. D.	N	VALUE	S. D.	N	VALUE	S. D.	N
NDI	0.66	0.00	1	0.18	0.56	3	0.10	0.68	2
NHA	-0.42	0.38	2	-0.03	0.00	1			
NIL	0.35	0.00	1						
NNA									
NOR	-0.03	0.44	3						
NUR	0.62	0.41	3	0.00	0.00	1	-0.10	0.00	1
OGD	-0.43	0.30	2						
OXF	0.79	0.19	2	0.09	0.35	2	0.69	0.71	2
PMG	0.84	0.00	1	0.18	0.43	2			
POO	0.06	0.00	1						
PRE	-0.08	0.33	3	0.11	0.00	1	0.55	0.00	1
PTO	0.61	0.00	1	0.70	0.00	1			
QUE	-0.36	0.29	3	-0.30	0.11	2	-0.04	0.33	2
RAB	-0.26	0.00	1						
RAR	0.15	0.21	3						
RCD	0.34	0.35	2	0.54	0.31	2	1.12	0.19	2
RIV	-0.06	0.00	1	-0.02	0.06	2	0.93	0.00	1
SBA	-0.01	0.96	5						
SCP	-0.10	0.12	2	0.97	0.00	1			
SDB	-0.32	0.55	3	-0.50	0.00	1			
SEO	0.10	0.00	1						
SHA									
SHI	-0.49	0.66	2	0.32	0.00	1	-0.12	0.00	1
SHK				-0.73	0.00	1			
SHL	-0.72	0.42	2	0.09	0.00	1	-0.74	0.00	1
SJG				0.27	0.00	1	-0.81	0.00	1
SPA									
STU									
TAB	0.09	0.43	2	0.38	0.00	1			
TAU	0.68	0.00	1	0.50	0.00	1	1.46	0.00	1

TABLE I (CONTINUED)

	P WAVE			SV WAVE			SH WAVE		
STA	VALUE	S.D.	N	VALUE	S.D.	N	VALUE	S.D.	N
TOL	0.20	0.09	3						
TRI	-0.30	0.30	2						
TRN				0.07	0.00	1	-0.23	0.00	1
TUC	0.15	0.49	3	-0.67	0.00	1			
UME	-0.38	0.00	1						
UNM	0.00	0.00	1						
VAL	0.16	0.17	4	0.07	0.23	2			
WEL	-0.46	0.00	1	-0.92	0.00	1			
WES	0.78	0.00	1						
WIN	-0.28	0.48	4	-0.30	0.46	2			

TABLE II

STATION ANOMALIES FOR LOGARITHMIC(COMMON) AMPLITUDE (PERIOD > 5 SECONDS)

	P WAVE			SV WAVE			SH WAVE		
STA	VALUE	S. D.	N	VALUE	S. D.	N	VALUE	S. D.	N
AAE	-0.04	0.25	2	0.17	0.00				
AAM	0.12	0.04	2	0.25	0.12		0.11	0.00	1
ADE	0.02	0.18	3	-0.07	0.14	3	0.07	0.10	2
AFI	-0.13	0.00	1	-0.14	0.00	1			
AKU	0.19	0.00	1						
ALQ	0.02	0.13	4	0.16	0.12		-0.01	0.42	2
ANP	0.16	0.11	3	0.10	0.35		-0.23	0.09	3
AQU									
ARE				0.02	0.00	1			
ATL	0.18	0.00	1	0.34	0.00		0.49	0.00	1
ATU	0.22	0.16	3	-0.21	0.00	1	0.16	0.00	1
BAG	0.06	0.03	3	0.36	0.24		0.31	0.19	3
BEC	-0.27	0.00	1				0.25	0.00	1
BKS	0.17	0.08	3	-0.08	0.33	2	0.24	0.40	2
BLA	0.14	0.00	1	0.27	0.13		0.27	0.15	2
BUL	0.16	0.08	2	0.45	0.00	1			
CHG	-0.11	0.21	3	0.05	0.09	3	-0.02	0.23	3
CMC	0.22	0.00	1	0.17	0.12	4	0.17	0.23	2
COL	0.12	0.03	2	-0.04	0.50	2	0.19	0.08	2
COP	0.23	0.10	4	0.57	0.10	2			
COR	0.41	0.10	2						
CTA	-0.01	0.00	1	0.09	0.31	2			
DAL				0.88	0.00	1	-0.09	0.00	1
DAV	0.16	0.12	3	0.38	0.00	1	0.16	0.34	2
DUG	0.23	0.01	2	-0.11	0.03	2	0.14	0.00	1
EIL	0.24	0.00	1						
ESK	0.24	0.12	3	-0.18	0.00	1			
FLO	-0.00	0.25	2						
GDH	0.09	0.08	2	0.18	0.21	2			
GEO	0.26	0.12	3						

TABLE II (CONTINUED)

	P WAVE			SV WAVE			SH WAVE		
STA	VALUE	S. D.	N	VALUE	S. D.	N	VALUE	S. D.	N
GIE							0.19	0.00	1
GOL	0.07	0.14	3	-1.53	0.00	1	-0.05	0.00	1
GRM	0.53	0.00	1						
GSC									
GUA	0.37	0.06	2	0.38	0.00	1			
HKC	0.19	0.13	2	0.12	0.08	3	-0.19	0.00	1
HLW	-0.33	0.00	1	0.43	0.00	1	0.56	0.00	1
HNR				0.15	0.00	1			
IST	0.09	0.08	2	0.33	0.00	1			
JCT	-0.25	0.00	1	0.35	0.00	1	0.08	0.00	1
JER	0.31	0.00	1	-0.12	0.00	1	0.46	0.00	1
KBL				0.34	0.00	1	0.04	0.00	1
KBS	0.12	0.00	1	0.34	0.00	1			
KEV	0.21	0.00	1	-0.79	0.00	1	0.04	0.00	1
KIP				0.14	0.36	3	0.01	0.61	2
KOD	0.16	0.00	1	0.19	0.13	2	-0.02	0.00	1
KON	0.01	0.11	2						
KTG	0.18	0.05	2	-0.83	0.29	2			
LAH	-0.05	0.00	1						
LEM	0.01	0.35	2	-0.36	0.00	1	-0.42	0.00	1
LON	0.08	0.24	3	0.01	0.00	1	0.34	0.00	1
LPS				0.22	0.13	2	0.32	0.63	2
LUB	0.05	0.00	1						
MAL	0.16	0.27	3	0.03	0.04	2			
MAN				-0.02	0.18	2	0.25	0.00	1
MAT	-0.05	0.00	1						
MNN				0.21	0.00	1			
MSH									
MUN	0.04	0.04	2	-0.07	0.36	4	-0.08	0.07	3
NAI	-0.07	0.03	2	-0.30	0.55	2	0.32	0.14	2

TABLE II (CONTINUED)

	P WAVE			SV WAVE			SH WAVE		
STA	VALUE	S. D.	N	VALUE	S. D.	N	VALUE	S. D.	N
NDI	0 13	0. 00	1	-0. 16	0. 67	2	0. 11	0. 21	2
NHA	0. 10	0. 13	2	-0. 53	0. 00	1	0. 05	0. 25	2
NIL				0. 60	0. 00	1	0. 44	0. 00	1
NNA				-0. 08	0. 00	1	0. 78	0. 00	1
NOR	0. 18	0. 16	2	0. 14	0. 23	2			
NUR	0. 25	0. 10	2	-0. 11	0. 00	1	0. 04	0. 00	1
OGD									
OXF	0. 01	0. 09	2	0. 16	0. 00	1	-0. 37	0. 00	1
PMG	0. 04	0. 06	2	0. 15	0. 00	1			
POO	0. 23	0. 00	1	0. 04	0. 47	2	-0. 01	0. 09	2
PRE	0. 01	0. 24	4	0. 04	0. 19	2	0. 07	0. 00	1
PTO	0. 26	0. 07	2	0. 38	0. 00	1			
QUE	0. 07	0. 10	3	0. 14	0. 08	2	-0. 04	0. 05	2
RAB	0. 05	0. 00	1	0. 00	0. 00	1			
RAR	0. 21	0. 00	1						
RCD	0. 32	0. 06	2	0. 08	0. 05	2	0. 50	0. 55	2
RIV	0. 31	0. 00	1	-0. 03	0. 40	2	0. 78	0. 00	1
SBA	0. 59	0. 28	2	0. 21	0. 37	5	-0. 23	0. 69	5
SCP	0. 21	0. 08	2	0. 48	0. 00	1			
SDB	-0. 05	0. 25	3	0. 26	0. 00	1			
SEO				-0. 16	0. 29	2	0. 11	0. 00	1
SHA	0. 35	0. 00	1						
SHI				0. 50	0. 33	2	0. 19	0. 23	2
SHK									
SHL	-0. 06	0. 00	1	-0. 03	0. 31	2	0. 12	0. 07	3
SJG									
SPA	0. 51	0. 00	1	0. 53	0. 00	1	0. 47	0. 00	1
STU	0. 09	0. 38	3						
TAB	0. 05	0. 00	1	0. 33	0. 00	1	0. 37	0. 00	1
TAU	0. 04	0. 28	2	-0. 13	0. 42	3	0. 40	1. 01	2

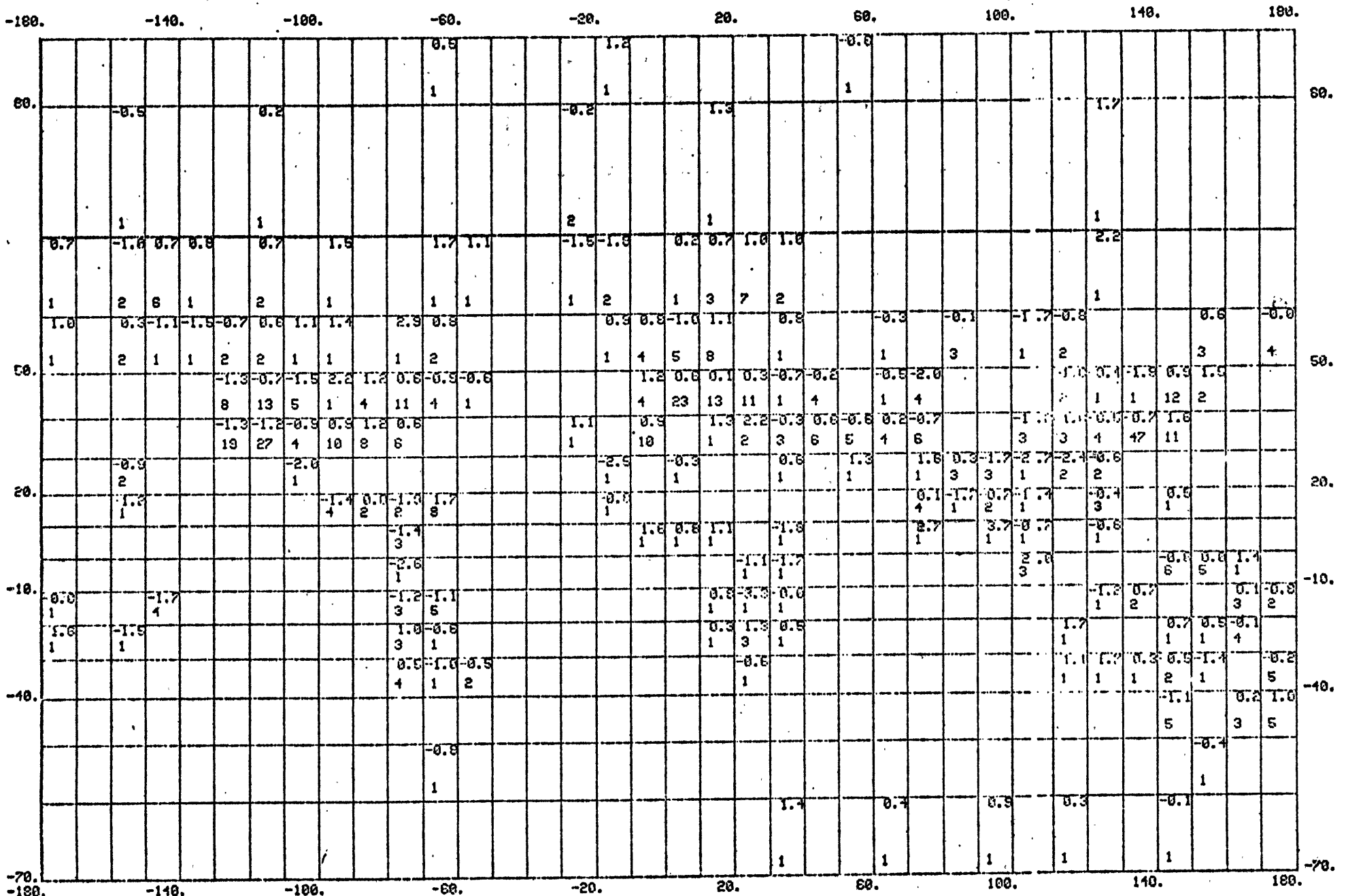
TABLE II (CONTINUED)

	P WAVE			SV WAVE			SH WAVE		
STA	VALUE	S.D.	N	VALUE	S.D.	N	VALUE	S.D.	N
TOL	0.30	0.00	1	0.54	0.00	1			
TRI	0.12	0.00	1						
TRN				0.32	0.00	1	0.50	0.00	1
TUC	0.10	0.10	3	-0.14	0.44	4	-0.14	0.83	3
UME	-0.32	0.00	1				-0.32	0.00	1
UNM									
VAL	0.29	0.04	2	0.10	0.19	2			
WEL	-0.12	0.00	1	-1.04	0.00	1			
WES	0.12	0.06	2						
WIN	-0.14	0.18	3						

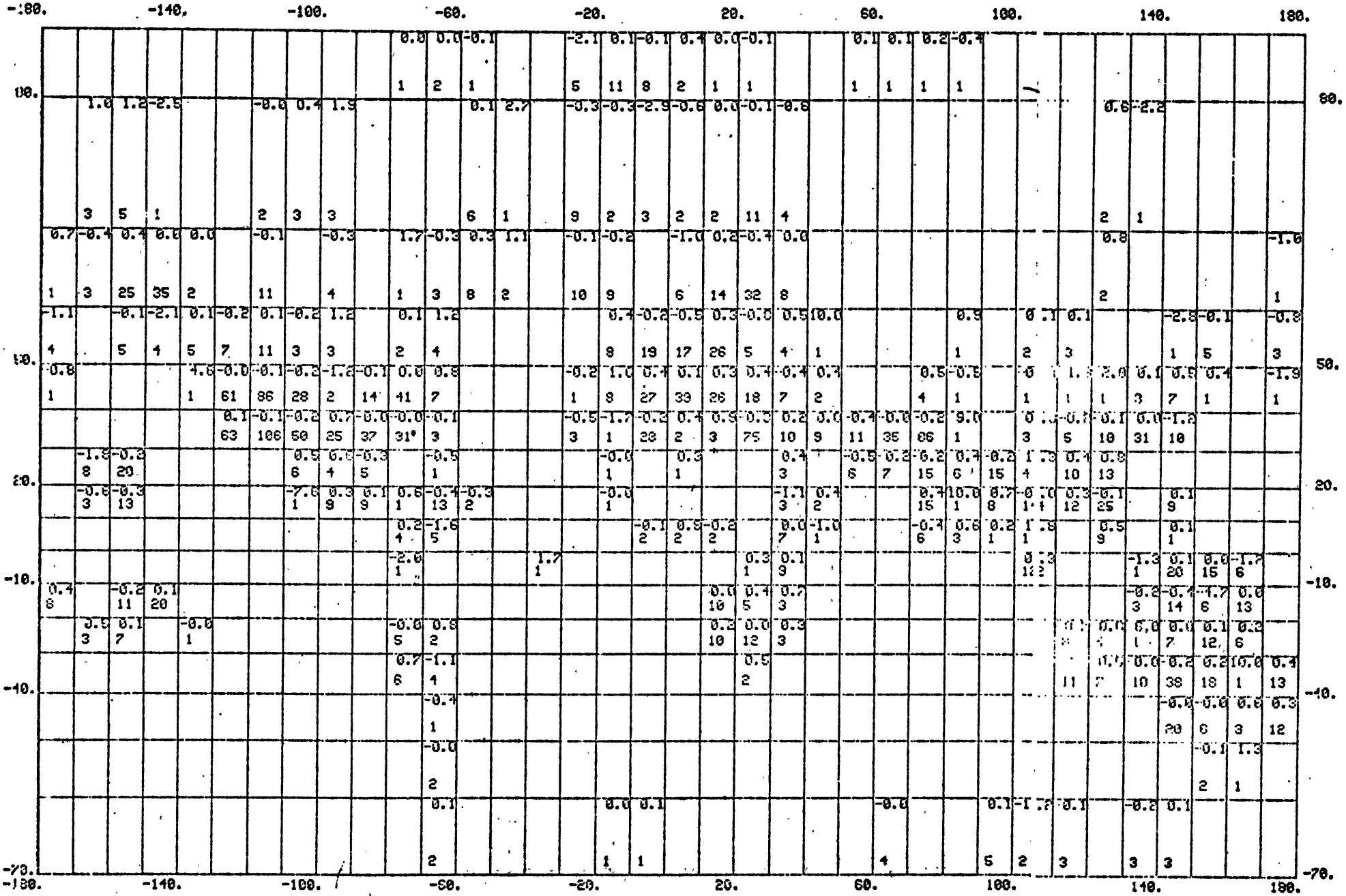
APPENDIX N

Three-dimensional Models for P and S Wave Velocities

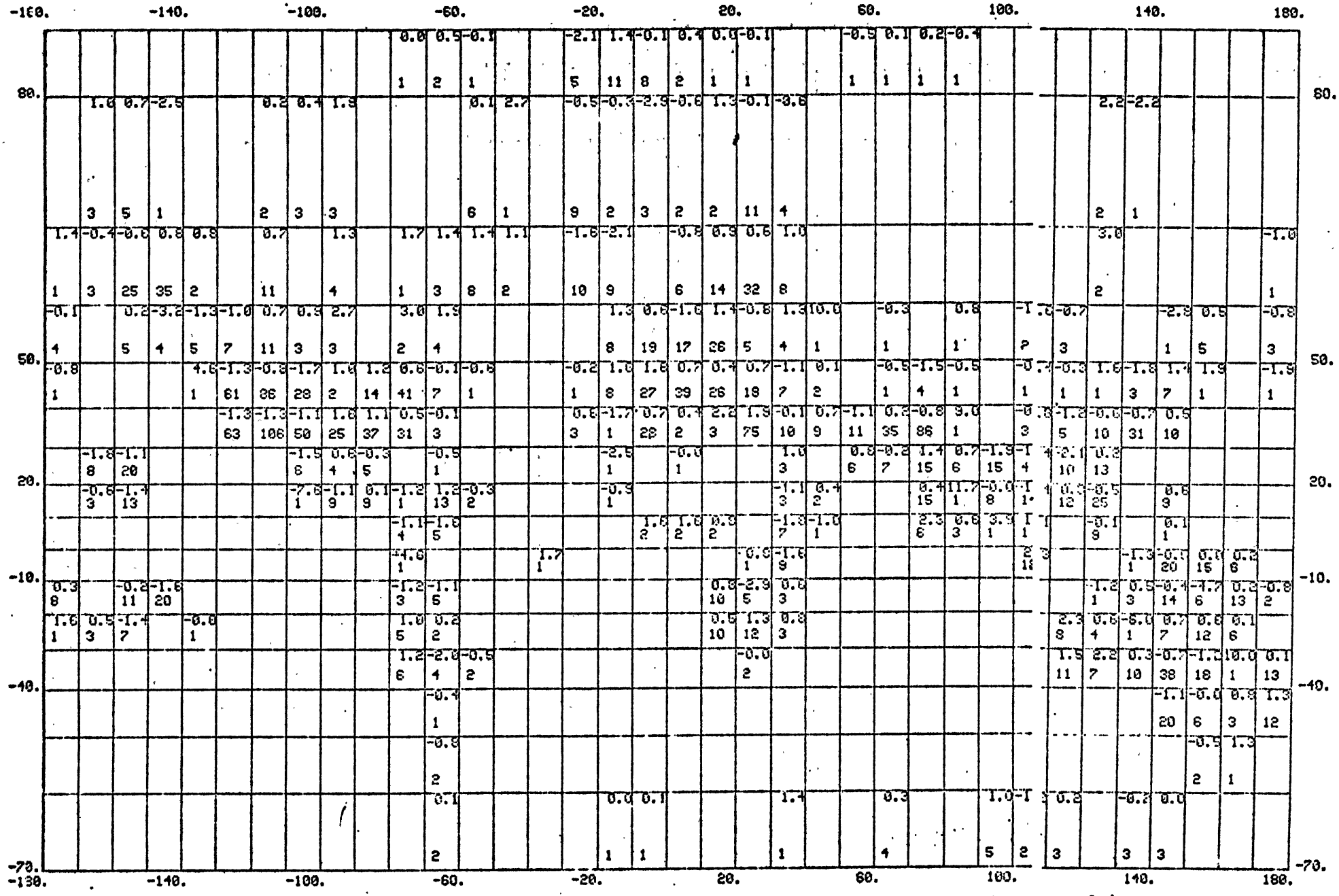
In this appendix, we present the lateral velocity variations for MODEL 3, obtained by the random sequencing of three-dimensional blocks during inversion (Chap. 5). Lateral velocity perturbations corresponding to the station anomalies are also presented. For each block sampled, we show, at the top, the relative velocity perturbation in percent, and at the bottom, the number of rays that passed through that block. Note that the positive values of velocity perturbation mean higher velocities and the negative perturbations imply lower velocities than the spherically symmetric model (Chap. 3).



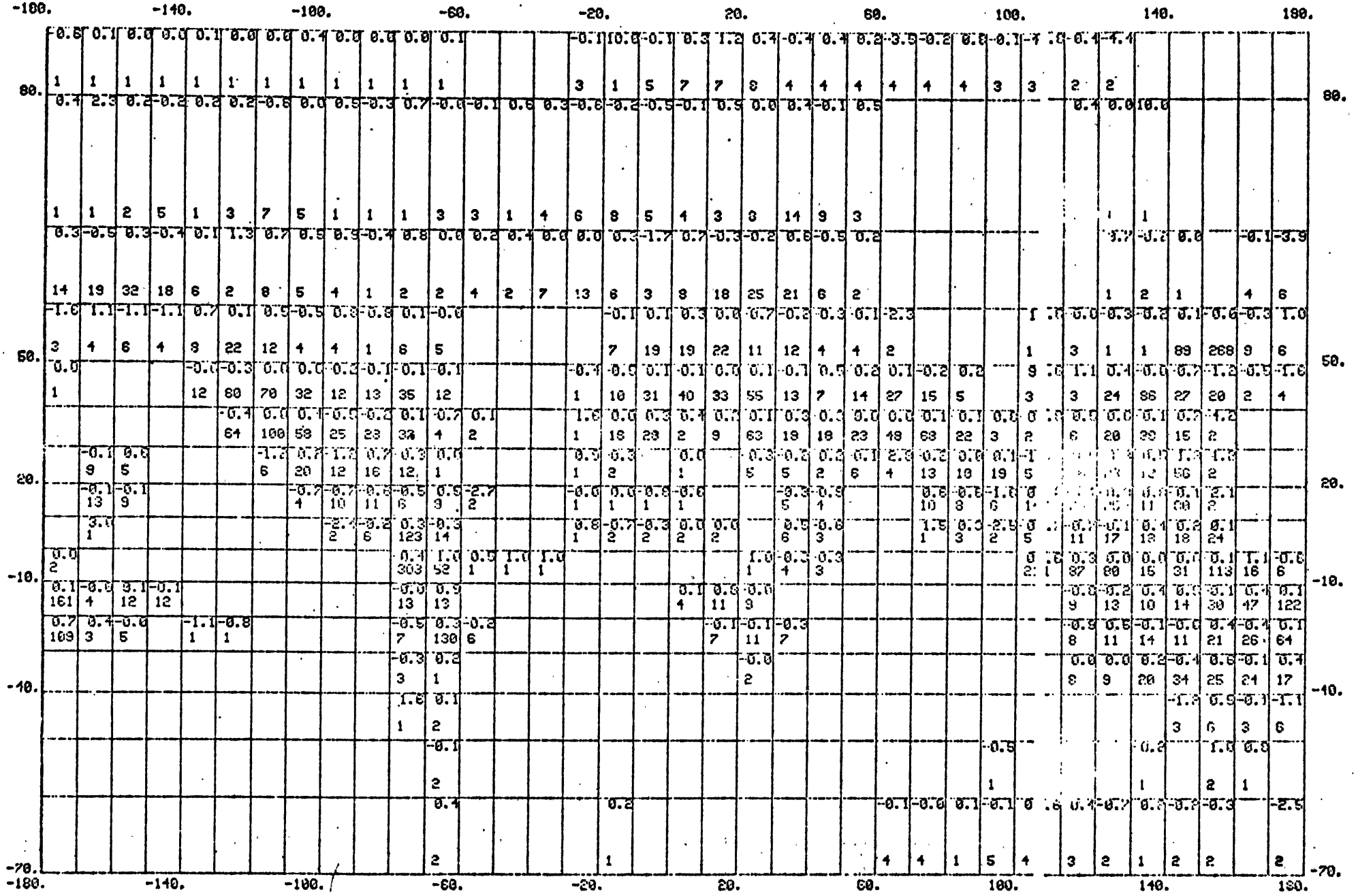
P wave velocity: 0-500 km depth (station anomaly)



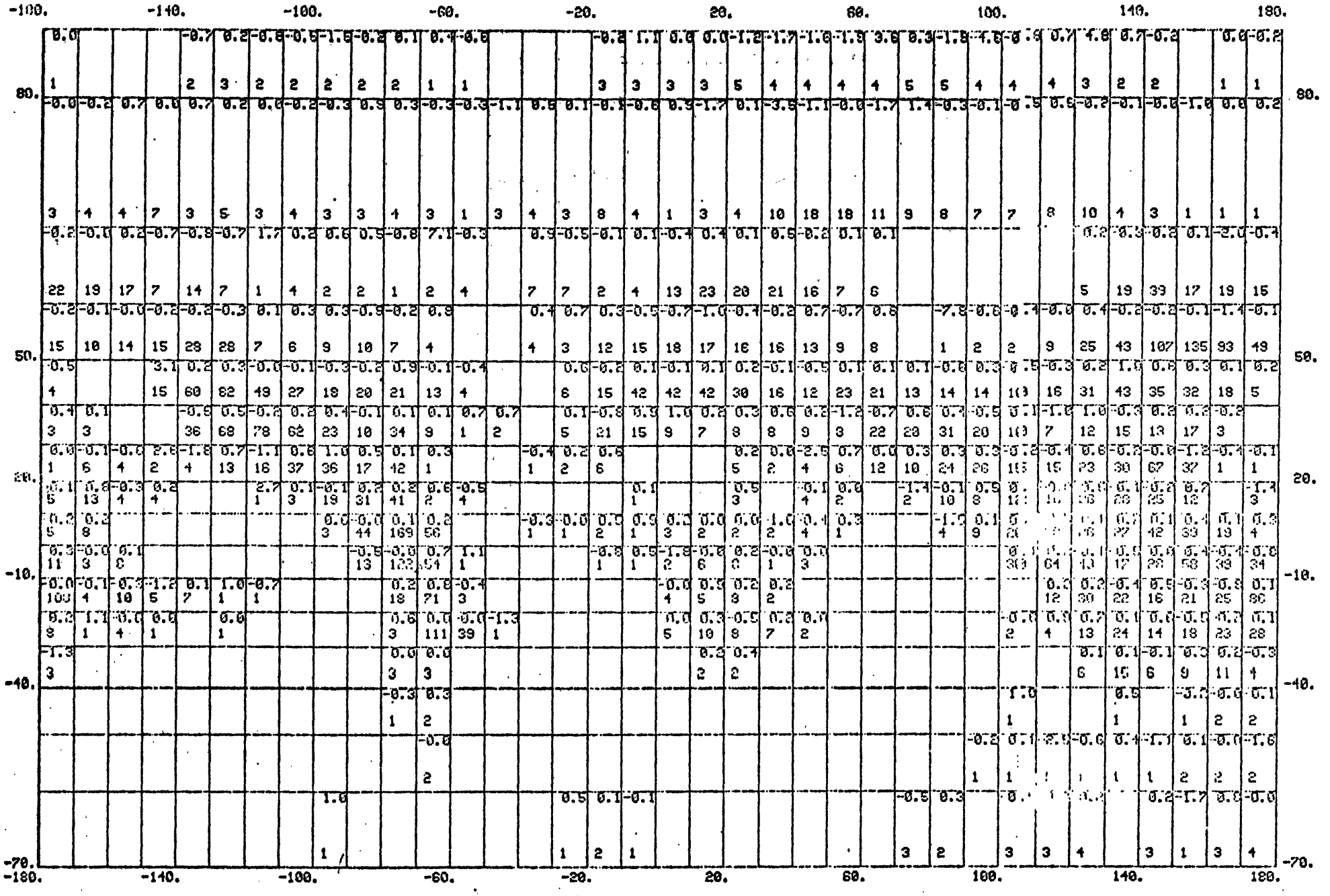
MODEL 3: P wave velocity: 0-500 km depth



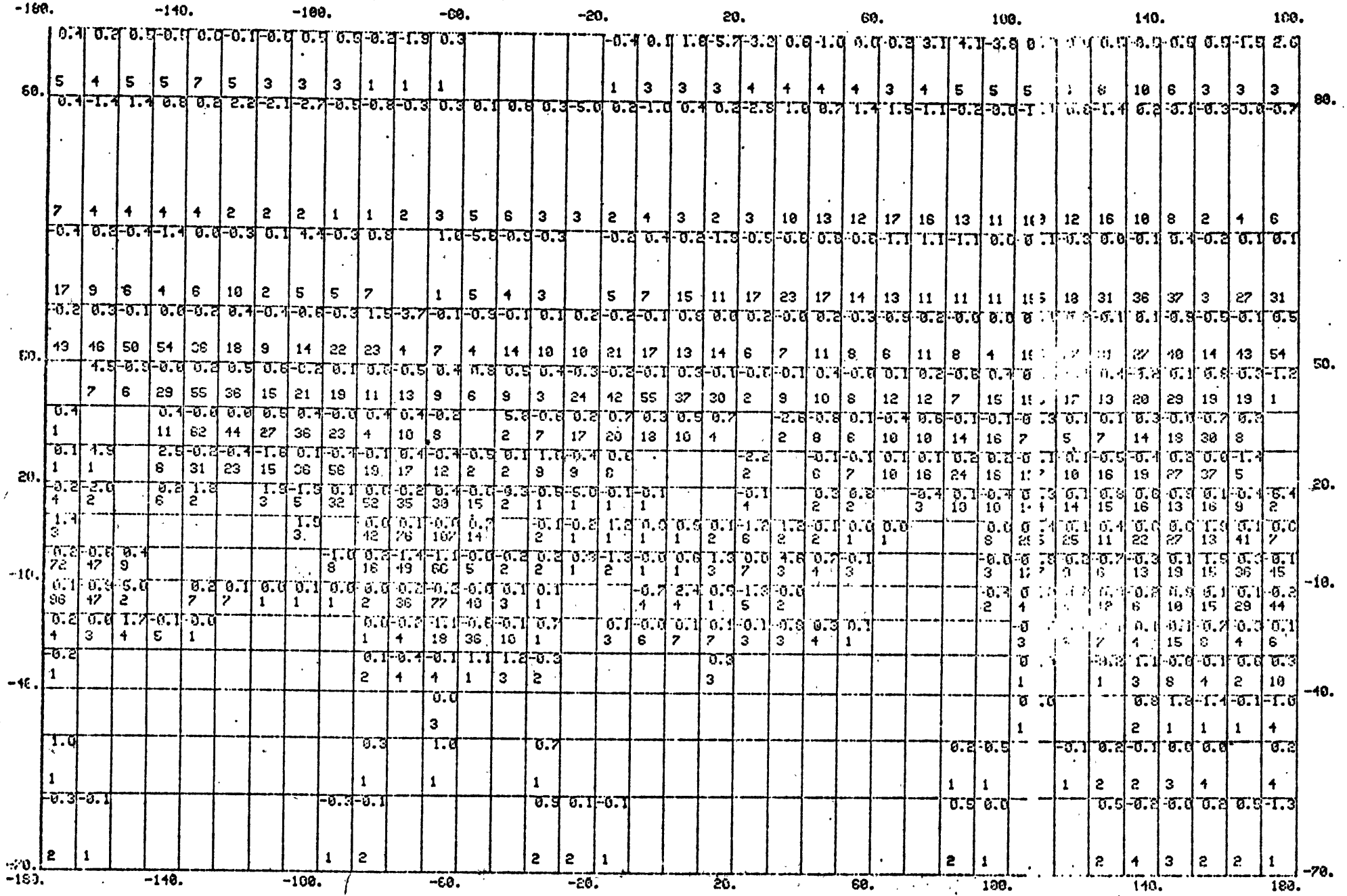
MODEL 3: P wave velocity: total perturbation in 0 to 500 km (including station anomaly)



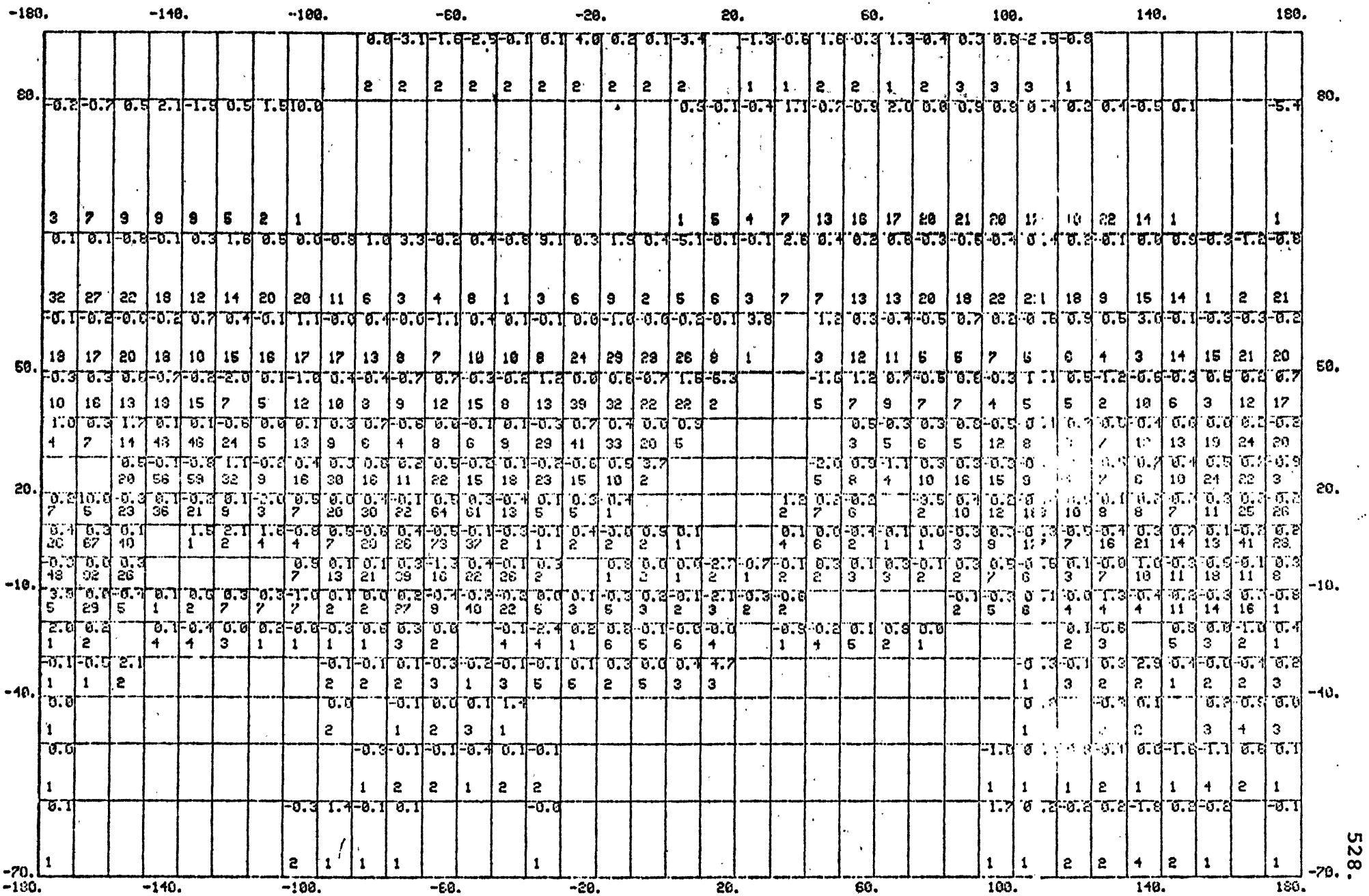
MODEL 3: P wave velocity: 500-1000 km



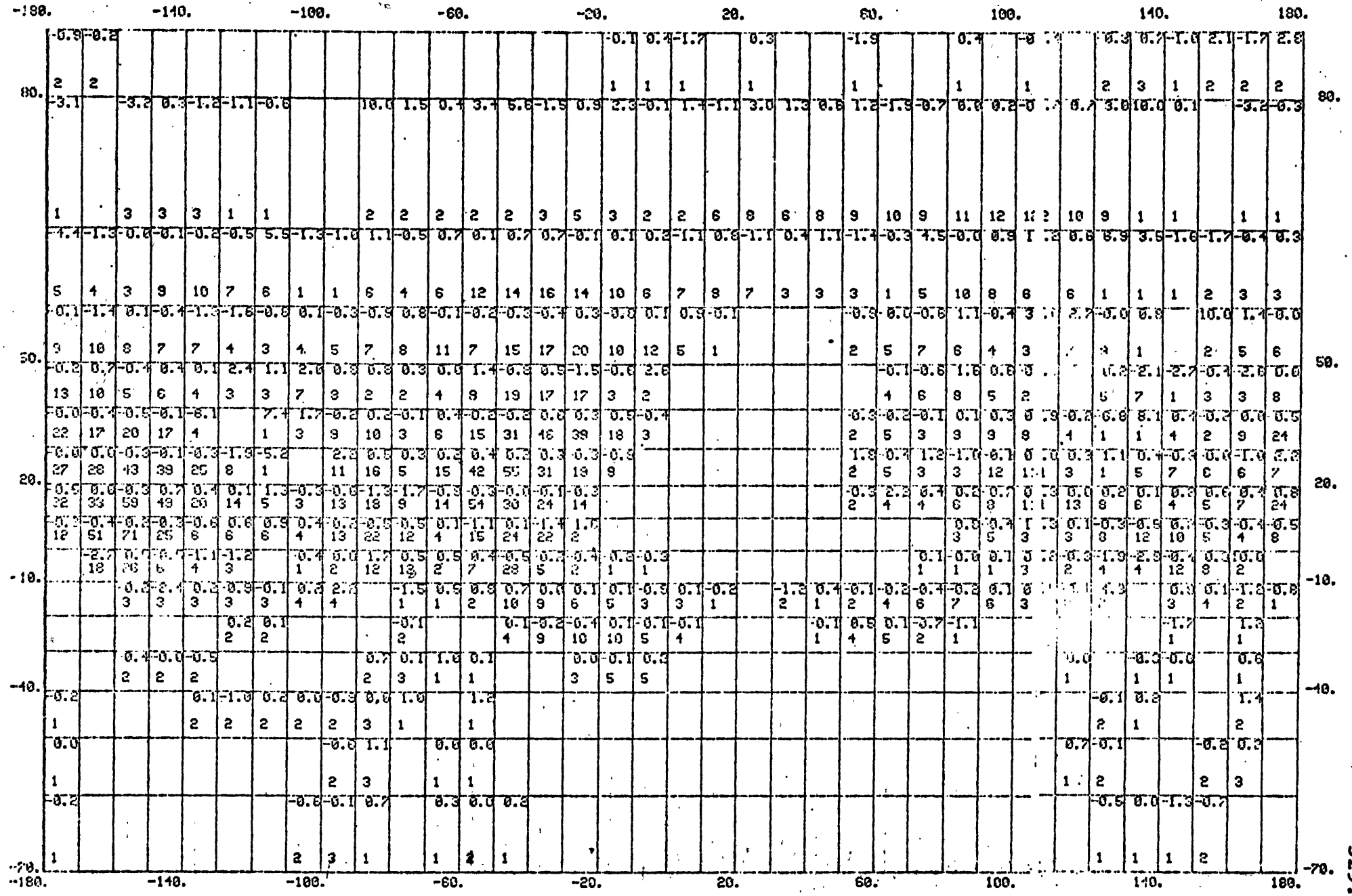
MODEL 3: P wave velocity: 1000-1500 km depth



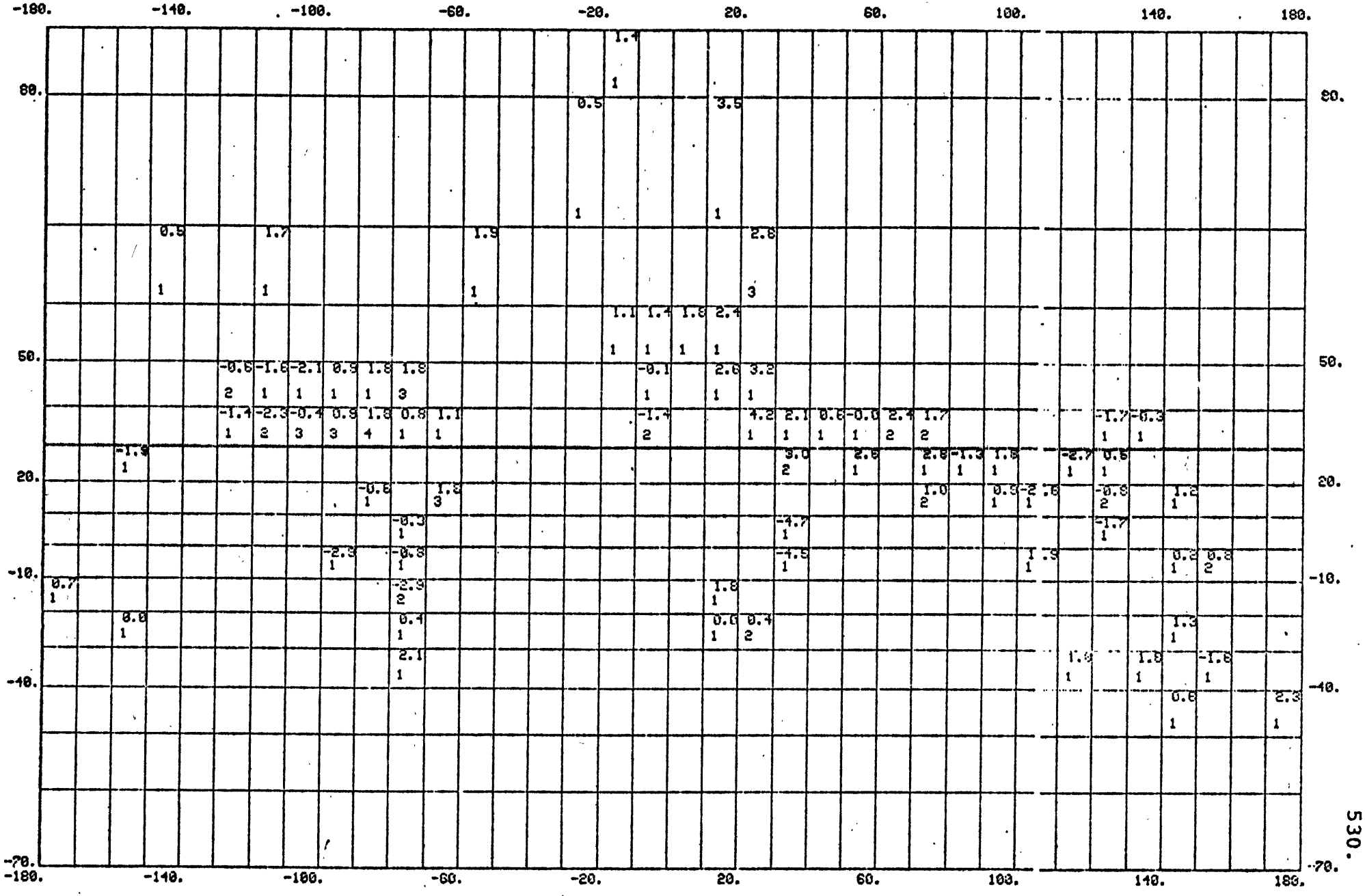
MODEL 3: P wave velocity: 1500-2000 km depth



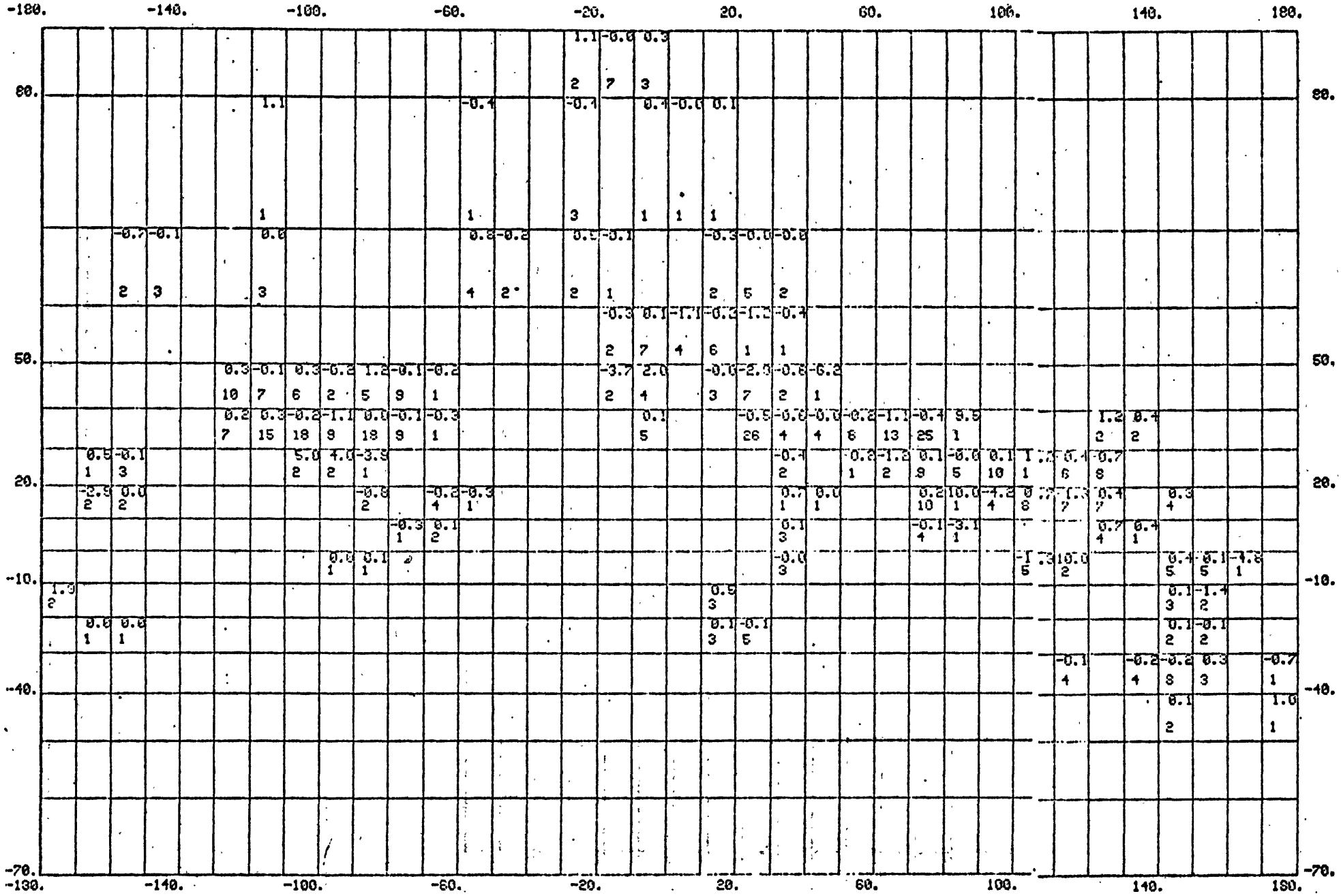
MODEL 3: P wave velocity: 2000-2500 km depth



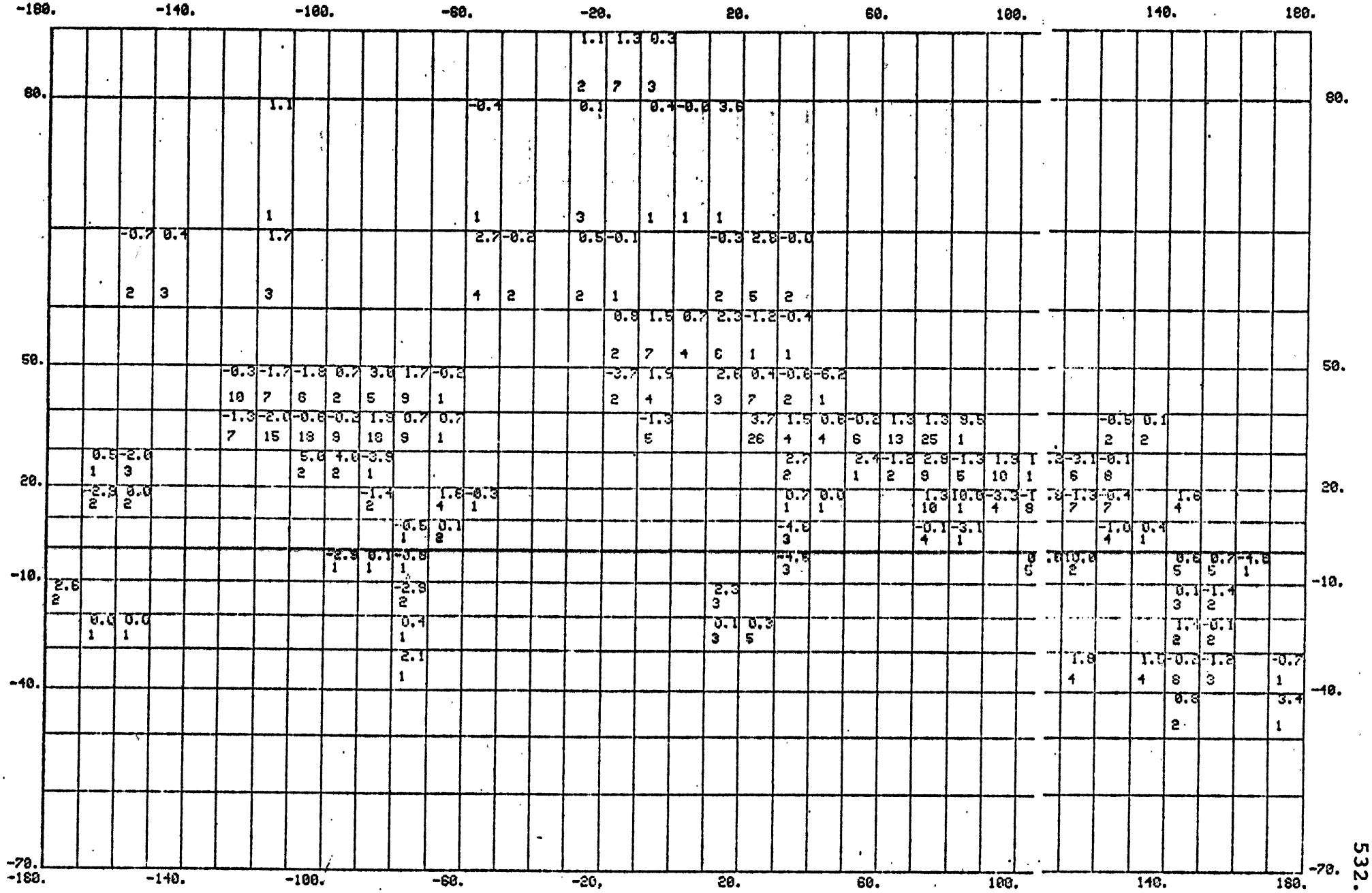
MODEL 3: P wave velocity: 2500 km to core-mantle boundary



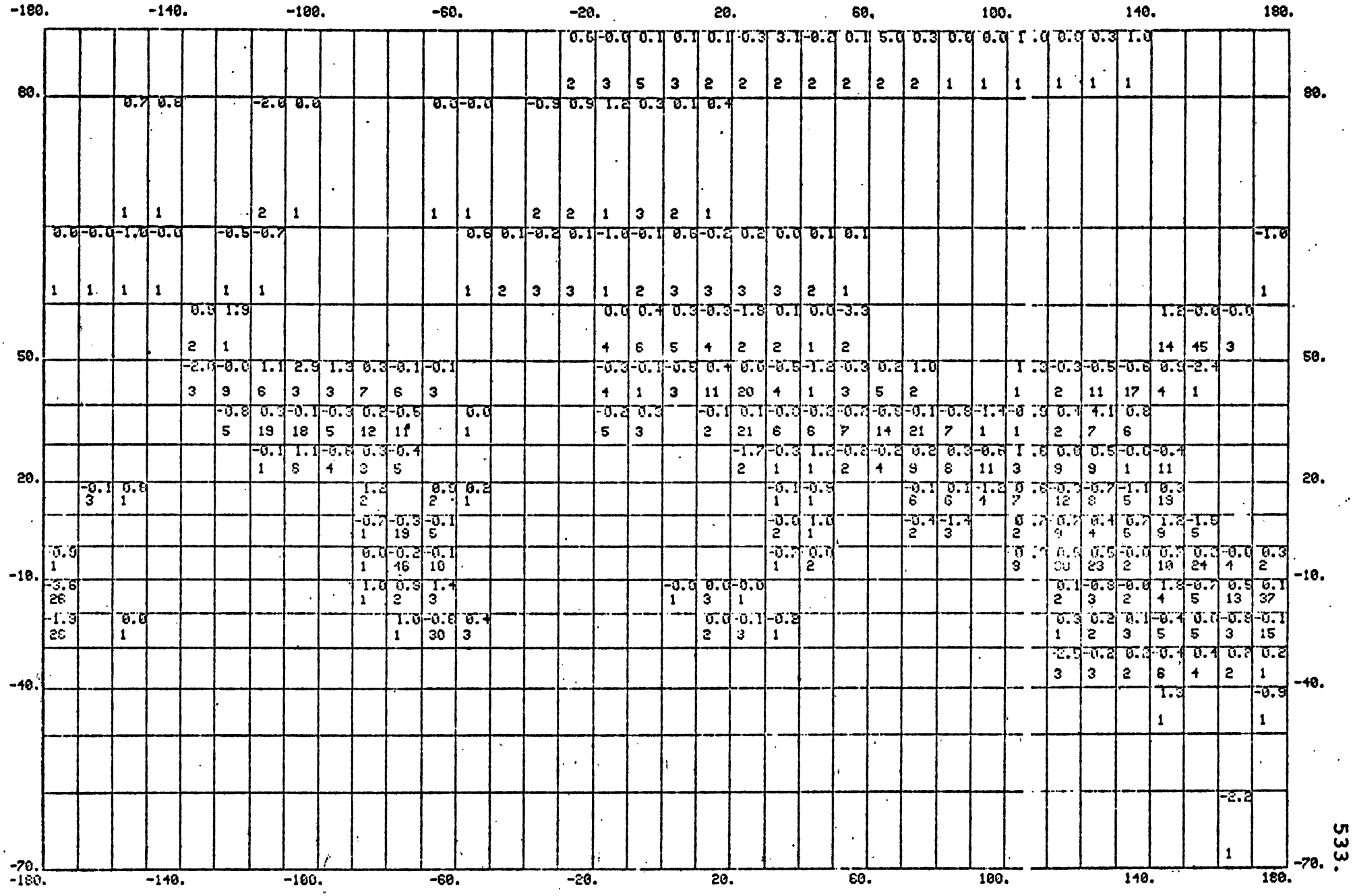
S wave velocity: 0-500 km depth (station anomaly)



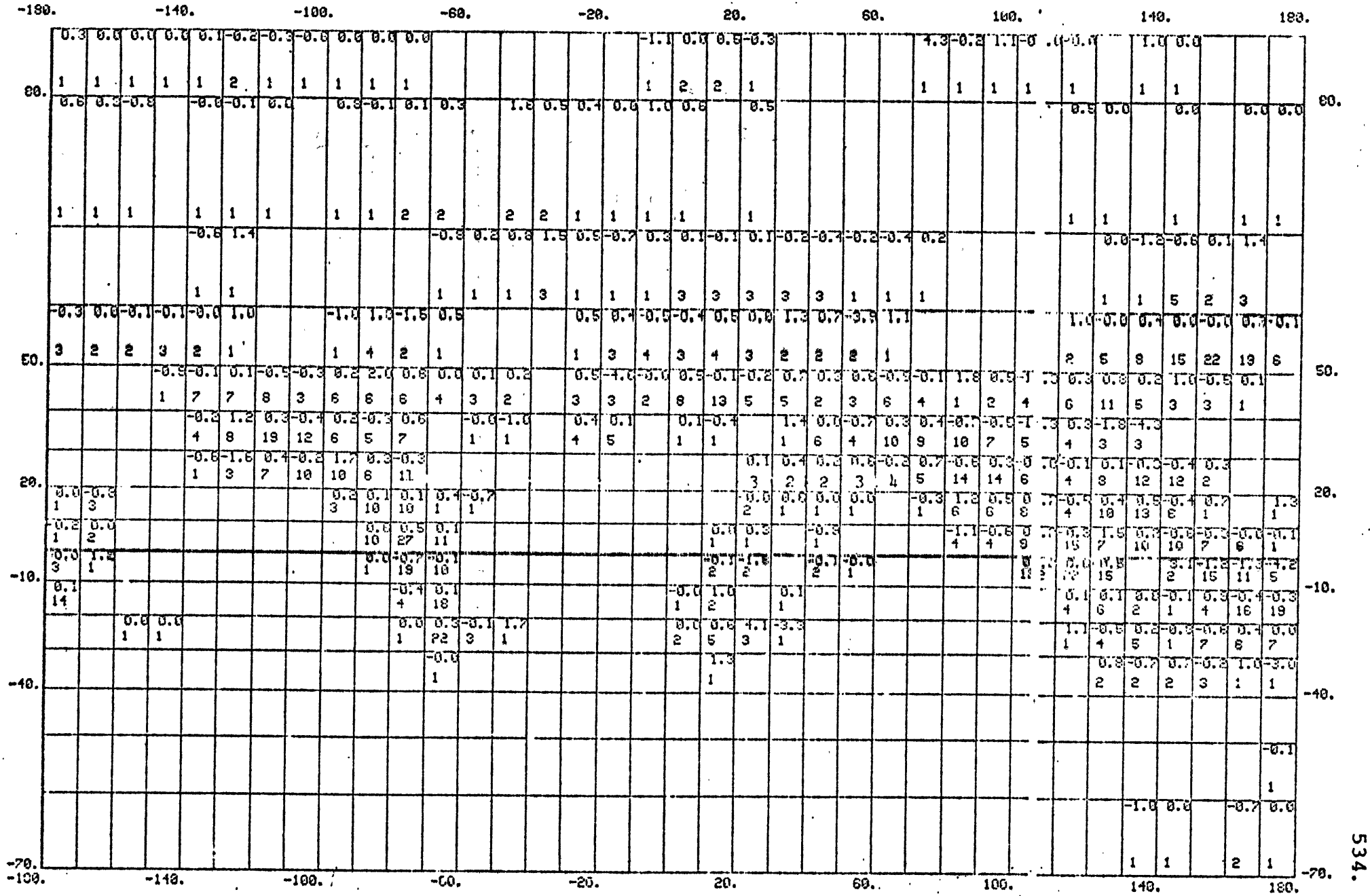
MODEL 3: S wave velocity: 0-500 km depth



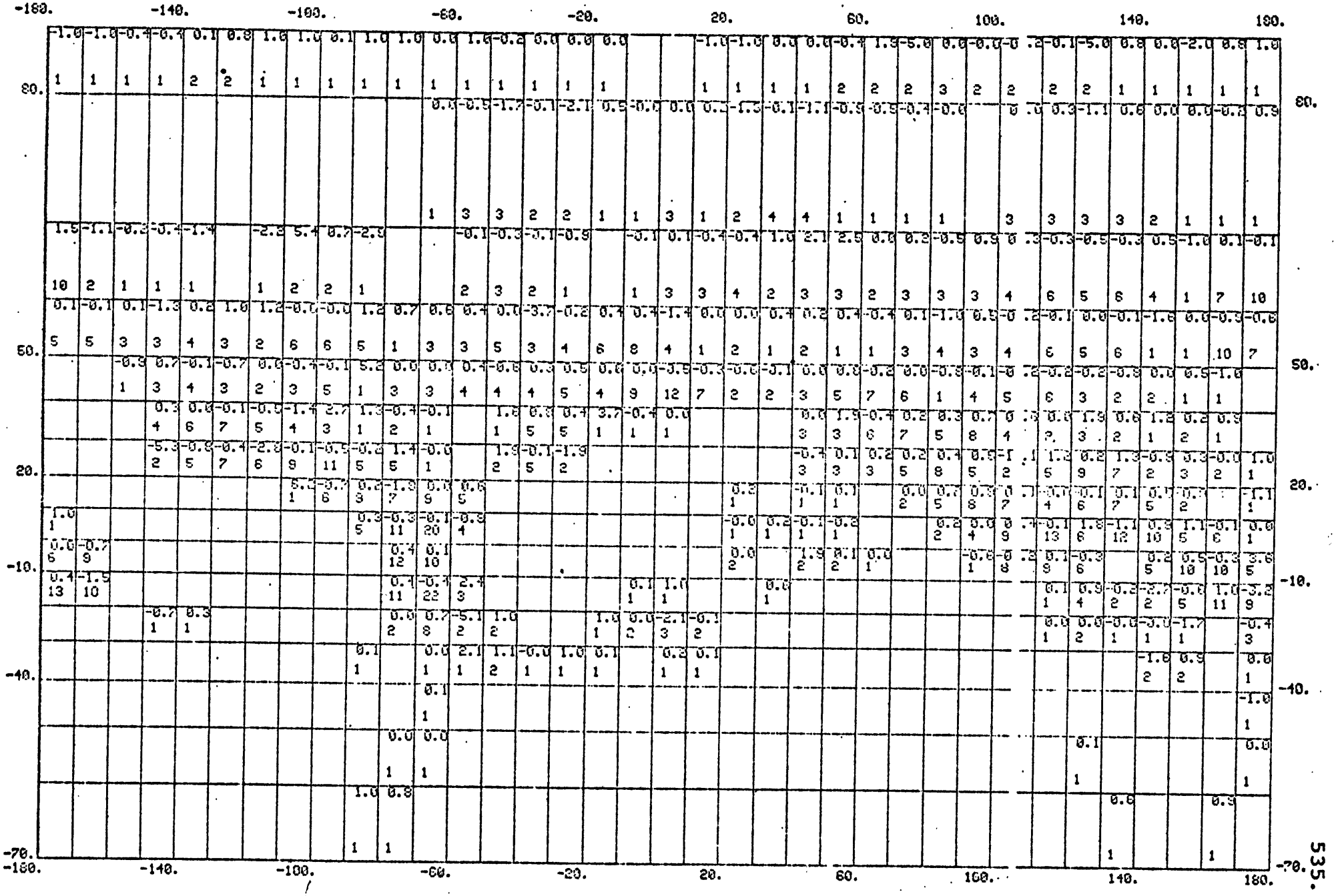
MODEL 3: S wave velocity: 0-500 km depth (total perturbation, including station anomaly)



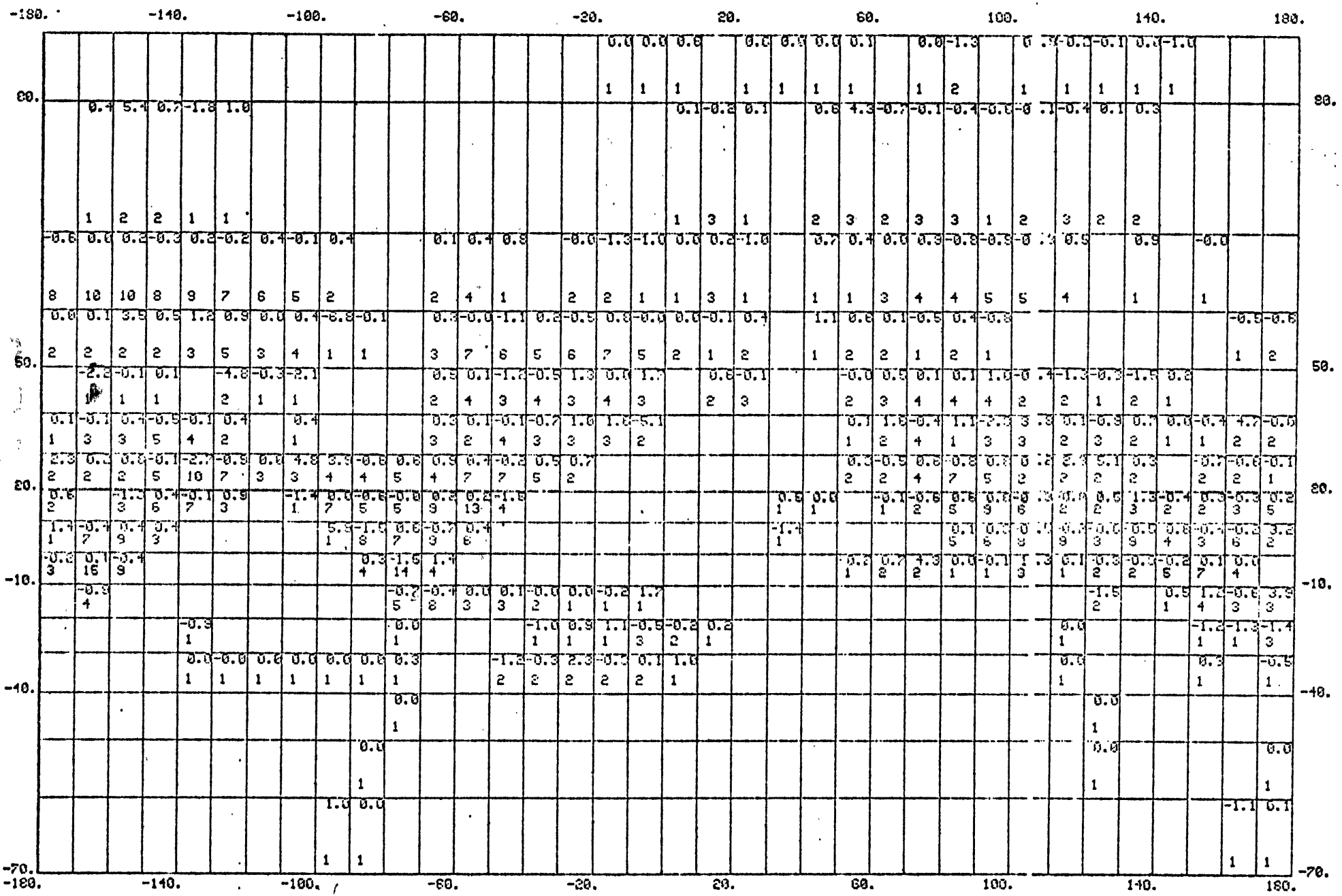
MODEL 3: S wave velocity: 500-1000 km depth



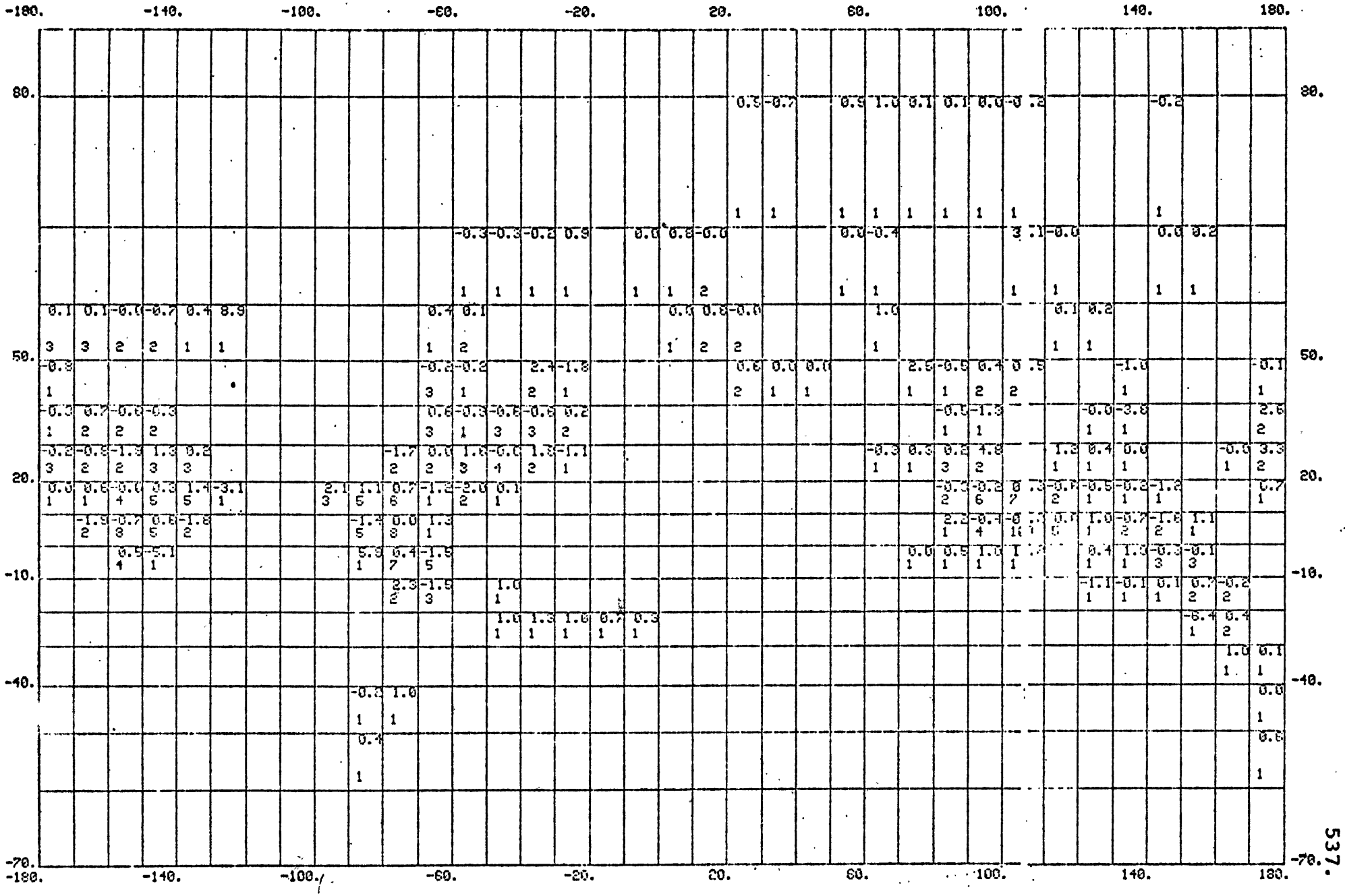
MODEL 3: S wave velocity: 1000-1500 km depth



MODEL 3: S wave velocity: 1500-2000 km depth



MODEL 3: S wave velocity: 2000-2500 km depth



MODEL 3: S wave velocity: 2500 km to core-mantle boundary

APPENDIX O

List of Deep Focus Travel Time and Amplitude Data

In this Appendix we present the travel time and amplitude data from 14 deep events (Table 2-1 in Chap. 2) for which we read the data personally from WWSSN seismograms. In this listing EVENT is serial number of data, IVENT is the event number corresponding to Table 2-4, in Chap. 2, STN is three-letter code of WWSSN stations; NCMP is seismograph component (1-3: short period vertical, N-S, E-W; and 4-6: long period vertical, N-S, E-W). INDX is code for seismic phases (1: P; 2: PcP; 3: pP; 4: sP; 5: ScP; 6: S; 7: ScS; 8: PcS; 9: SKS). TH, TM, TS is arrival time in hours, minutes and seconds, AMP is amplitude of the phase (in millimeters) as measured on ITEK projection screen from 70 mm film chips. To obtain the amplitude on original seismograms, one must multiply these amplitudes by a factor of 0.53. 'PRD' is the period (in seconds) of dominant signal.

See at the back
NKS.

This Appendix titled "List of Deep Focus Travel Time and Amplitude Data" (pp. 538-577) is available in the form of microfiches from the National Archives, Washington, D.C.

Biographical Notes

De jure, the author's life began on the 16th of December, 1947; de facto, he saw the light on this earth on July the 30th, 1946. Being born and brought up amidst din and bustle of a city like Calcutta (India), he developed automatically a sense of appreciation for nature over society. It is no wonder then that eventually his career also will be in Earth Sciences rather than in Medical Sciences.

After graduation from high school with honors in Physics, he was advised to go in for Geophysics by his beloved Physics-major private tutor Mr. Samaresh Bhattacharya - an unforgettable name in his life's history who shaped up much of the author's philosophy in his tender ages. So, he got admission into the Indian Institute of Technology at Kharagpur - an epitome of western style education and culture in India. Five short years of enjoyable stay there also were marked with several achievements. He earned his Bachelor's Degree in Geological Sciences in 1967 and Master's Degree in Exploration Geophysics in 1969, graduating both times first in the class. He was also given a book award for his Master's Thesis which was considered to be the best for the year 1969. During these college years, he became also the founder-secretary (1964-1966) of the alumni association of his high school and then the general

secretary (1967-1968) of the student's union of his department in I.I.T. For his achievements in the latter capacity, he was honored also by an award for the best outgoing student of the department for the year 1969.

After his college education in I.I.T. was over, he was more keen to prepare his final career in management and administration rather than higher education. During that time fortunately or unfortunately, his application for admission into graduate school at M.I.T., Cambridge, Massachusetts, U.S.A. was approved and he was given also a research assistantship. The offer was too glorious for him (including his guardians and professors) to turn down. So, in the fall of 1969 he launched into an adventurous journey of Higher Education Abroad. Surviving the storms at sea, his career-boat has ultimately entered into the Port of Eden where live Drs. Adam and Eve. During this voyage, he recorded some of his experience in literature or scientific gatherings. They include:

Julian, B.R. and M.K. Sengupta (1973):
Seismic travel time evidence for lateral heterogeneity in the deep mantle, Nature, 242, 443-447.

Sengupta, M.K. and B.R. Julian (1975): P wave travel times from deep earthquakes, to be submitted to Bull. Seismo. Soc. Am.

Sengupta, M.K. and B.R. Julian: A travel time study using deep earthquakes; Spring AGU Meeting, 1972.

Sengupta, M.K. and B.R. Julian: Travel times and lateral heterogeneity in the deep mantle; Spring Meeting, AGU, 1973.

Sengupta, M.K. and B.R. Julian: Mantle velocity and its regional variation, Spring Meeting, AGU, 1974.

THE END!